Precise measurements of charmed baryon properties with the LHCb detector at the LHC

Elisabeth Maria Niel

université
PARIS-SACLAY

Precise measurements of charmed baryon properties with the LHCb detector at the LHC

Mesures précises des propriétés des baryons charmés avec le détecteur LHCb au LHC

Thèse de doctorat de l'université Paris-Saclay

École doctorale n°576 Particules, Hadrons, Énergie, Noyau, Instrumentation, Imagerie, Cosmos et Simulation (PHENIICS)
Spécialité de doctorat: physique des particules
Unité de recherche: Université Paris-Saclay, CNRS, IJCLab, 91405, Orsay, France
Référent: Faculté des sciences d'Orsay

Thèse présentée et soutenue à Paris-Saclay, le 16 Septembre 2021, par

Elisabeth Maria Niel

Composition du jury

Marie-Hélène Schune Directrice de recherche, Université Paris-Saclay	Présidente
Bostjan Golob Professeur des Universités, University of Ljubljana	Rapporteur & Examinateur
Antonin Maire Chargé de recherche, Institut Pluridisciplinaire Hubert Curien, Strasbourg	Rapporteur & Examinateur
Marianna Fontana Docteure, Sorbonne Université	Examinatrice
Lesya Shchutska Professeure assistante, École polytechnique fédérale de Lausanne	Examinatrice

Direction de la thèse

Patrick Robbe Directeur de recherche, Université Paris-Saclay	Directeur
Achille Stocchi Professeur, Université Paris-Saclay	Co-Directeur

Thèse de doctorat

NNT: 2021UPASP075

A mia madre, per il tuo amore senza limiti.
A Arianna, Vincent e Michela, per il vostro sorriso senza tempo.

Acknowledgements

This thesis has been for me a long and rich journey shared with many people that I wish to thank here.

I would like to start by thanking Bostjan Golob and Antonin Maire who kindly accepted to be rapporteurs of my thesis; thank you for the careful reading of my manuscript and for helping me improving the quality of my work. I also want to thank Marianna Fontana and Lesya Shchustska for accepting to be in my jury and for being present today despite the complicated sanitary situation. Je remercie Marie-Hélène Schune non seulement pour avoir accepté de faire partie de mon jury, mais surtout pour m'avoir accueilli en stage il y a désormais 5 ans, quand la physique des particules n'était pour moi qu'un univers fascinant et mystérieux.

Je te remercie Patrick pour m'avoir guidé tout le long de ce chemin, j'ai énormément appris au près de toi, du point de vue scientifique et humain. Tu as été un guide et un modèle pour moi; grâce à toi je sais quel type de chercheuse j'ai envie d'être. Ta compréhension profonde de la physique, ta gentillesse et ton calme ne sont que quelques-unes des qualités qui ont rendu ton encadrement formidable. Je te remercie aussi pour les moments de convivialité et les conversations toujours intéressantes au tour de la musique, la culture, les voyages, la bouffe et bien plus encore! (Merci aussi de m'avoir appris à préparer des présentations en toutes conditions, notamment en ayant passé la nuit dans un train entre Pekin et Shanghai...).

Je remercie aussi Achille pour avoir ouvert la voie à la mesure des moments magnétiques des baryons charmés. Parler de physique avec toi c'est un peu comme revivre les émotions des premières découvertes en physique des hautes énergies. Avec toi j'ai aussi appris ce que veut dire faire partie d'un grand laboratoire et créer une vie scientifique et sociale au sein d'un groupe.

I want to especially thanks Sergey Barsuk for having me in the PLUME team. It was a great pleasure to work with you and learn from someone with such a knowledge of the past, present and future of particle physics. The coffees discussion were always rich and fun, especially when discussing about Ukrainian chocolate an Italian coffee. I will never forget the late evening fighting against the minidaq and the feeling of joy when it was finally working! À cette occasion, je souhaite aussi remercier Monique, Christophe et Frédéric pour m'avoir appris à utiliser la minidaq et les cartes d'acquisition. Merci Christophe pour les discussions d'escalade toujours intéressantes !

Merci Louis Henry pour avoir travaillé avec moi sur cette analyse extrêmement compliquée. I also thanks all the people of the LHCb Milan and IFIC groups with whom I shared this path towards the baryons polarization measurement. I would like to warmly thank Emi Kou for the careful reading of the helicity amplitudes chapter of my thesis and for the path we shared together on the charmed baryons polarization and MDM understanding. I would like to thank Mikhail Mikhasenko for sharing his knowledge about amplitudes for three body decays with me; your sharp and clear vision has been extremely useful to me.

Je te remercie Yasmine du fond du cœur. Ma co-bureau et guide spirituel, ma copine de destruction du patriarcat (nous allons y arriver en douceur). Tu es une force de la nature, tu m'as appris tout ce qu'on ne lit pas dans les livres. Mais aussi, merci pour les tablettes de chocolat de fin de chapitre!

I want to warmly thank the LHCb group of IJCLab (previously LAL). I have a lot of good memories with all of you. I will start with Carla, the queen of macarena; you are my model of calm in the middle of the storm. It looks like we are getting closer to the understanding the pK-razy spectrum! I would also like to thank Anja for the fruitful and fun discussions about helicity amplitudes. Thank you Vitalii, the explorer, for teaching me many things about LHCb, from the software and physics part to the collaboration dynamics. I hope you will be able to travel a lot again! Thanks to Andrii and Victor for sharing the first part of this journey together. I say goodbye and thanks all the phD students of the LHCb-IJCLab group, I'm sure that you are going to have a lot of fun now that things are going back to normal. Thanks to Felicia, Gaelle, Yuya, Valeriia, Vsdevolod and Chiara (che continua la tradizione delle dottorande italiane nel gruppo!). You have the chance to be with very kind and competent people so enjoy it! Je vais remercier la « Yellow Pecora team » composée par les presque meilleurs blaguers d'LHCb: Fabrice Desse, Guillaume Pietr{ykz} (je vais laisser le lecteur reconstruire ton nom de famille en essayant toutes les permutations circulaires possibles des 3 dernières lettres) et Martino Borsato. Merci aussi à Adam pour les journées passés ensemble atour du CERN et les soirées au R1.

Merci aux cousins du LLR, Frédéric, Vlad et Emilie; l'aventure avec SMOG ne s'arrête pas ici. Merci pour les beaux moments partagés lors des repas à Gif et les pizzas aux semaines LHCb, et surtout merci Emilie pour m'avoir appris à montrer que la physique des particules est aussi aguichante que la recherche sur les petits pandas! Grazie a Felipe (ormai parli italiano meglio di me), il viaggio in California resterà per sempre nei miei ricordi: i parchi nazionali Yosemite e Sequoia Park, Los angeles, il surf sull'oceano, le serate con gli altri studenti. C'est bon j'oublie personne du LLR...ah oui le bon vieux Ben! On s'est rencontré au R1 pendant mon stage, quand tu étais un jeune postdoc plein d'espoir, on a de suite bien accroché ! Puis on était MC liaisons ensemble, je pense que je n'aurais jamais survécu au looong meeting simulation sans toi! J'ai beaucoup appris sur le monde de la physique des ions lourds dont tu es désormais Grand Maitre ! J'espère qu'on pourra encore partager plein de beaux moments ensemble autour de l'escalade, la bouffe, la bière mais aussi la musique, les voyages, les échecs, les blagues et l'Italie évidemment. La recherche a besoin de personnes comme toi ! Merci à Michael Winn, lors de mon premier stage tu étais là en train de me parler de mesurer obscure en

physique des ions lourd alors que moi je sortais à peine d'un cours de mécanique quantique de base ! Ils ont de la chance de t'avoir au CEA, même si tu es recherché pour conduite illégale de bateau sur lac privé! Merci aussi à Francesco Bossu pour m'avoir appris à bien structurer mes classes en C++.

Je remercie tous les professeurs et professeures qui m'ont formée et accompagnée le long de ce chemin: Tripiciano (du college), Labella e Cardone (du lycée), Marianne Dufour et Daniel Husson (MPA), Patrick Puzo, Xavier Garrido et Claire Marrache (du Magistère d'Orsay), que je remercie aussi pour avoir été une super marraine de thèse. Merci d'avoir été à l'écoute et de m'avoir transmis votre passion.

I would like to thanks all the IJCLab students for the nice movie nights, barbecues, galette, breakfasts, concerts and other activities that we had the chance to share. I only realize now that we are deprived of these activities, how important they were. Thanks to Shaymaa, Manar, JG, Noé, Loic, Angelique, Antoine, Henri and everyone I may have forgotten.

Thanks to the student's seminars team!! Mais bon, est-ce que je vais vraiment remercier Clo et Rems pour avoir organisé les séminaires étudiants hein? Je remercie toute la team Deblé: Clo, Rems, Toto, GuiGui, Smeg, Sly, Tguy (oui Louis aussi), pour les innombrables journées d'escalade, les soirées de vrille et de camping à Fontainebleau, les bonnes chutes au Viaduc! Vous êtes tous des personnes incroyables que je souhaite garder à mes coter pour toute la vie, nous allons nous retrouver au quatre coins du monde avec nos petits vans et notre soif d'aventure! Que la vrille soit avec nous mes amis! Grazie a Giorgia per le bellissime cene, pranzi e barbecues sempre incredibili e accompagnati da dolci a 16 strati, spero che la Francia possa darti una nuova casa, anche se non hanno il bidet...

Merci Mister Baptiste, ca fait 8 ans qu'on se connait et notre amitié a tellement évolué, je sais déjà que ça sera pour toujours! Nous avons été collègues, colocs, erasmus, runners, randonneurs, road-trippeurs ensemble et ce n'est pas près de s'arrêter là! Mister Donald, nous avons aussi partager beaucoup d'aventures ensemble de Londres à Paris (en passant par l'Espagne, la Norvege, La Suède...). Les longues discussions sur comment changer le système vont me manquer, je sais que tu auras un rôle très important dans ce changement ; mais n'oublies pas, la solution c'est l'éducation ! My Chiquita, you will always have a special place in my heart. Thanks for sharing this amazing year in London and later in any country, you're such a mature and spontaneous person, I will always want to roll down a hill with you or dance Mentirosa! Je te remercie mon cher Valentin, nous avons partagé plus que quelques soirées, nous sommes compagnons de vie, dans les bonnes et les mauvaises situations. J'ai hâte d'écouter tes histoire californiennes ! Merci à la team Erasmus: Guilhain et Charlies (Royal Albert Hall in the heart), Thomas et Thibault.

Je remercie Léo Pe, Zoé et Robin : nos chemins se sont croisés l'été 2017 en tant que Summer Students. Merci Léo pour avoir été un super coloc' avec pleins d'initiative et envie de vivre. Je suis obligée d'avouer que tes blagues et celles de Baptise étaient parfois aussi marrantes que les miennes ! Merci aussi à Zoé pour toutes les activités que tu as organisé et ton envie de découvrir toujours quelque

chose de nouveau. Merci Robin, l'homme qui repoussait ces limites sans cesse. Merci à Christelle pour m'avoir fait découvrir plein de resto coréen et japonais. Merci à Thomas pour avoir mangé de l'avocat avec du hummus pendant cette fameuse semaine LHCb. Merci à Tomachin et Dounia pour les soirée spartagées autour de repas exquis, quand j'y pense je peux pas m'empêcher de sourire. Merci à Joff et Olivia tout d'abord pour avoir laissé Louis gagner au Catane, mais aussi pour avoir partagé autant de belles soirées ensemble. Je remercie aussi tous mes potes du Magistère pour les innombrables soirées partagées au rythme de Sean Paul et Britney Spears: Leo, Victor, Flo, Mic, Julien, Clemence, Djémé mais aussi Lena et Vincent. Merci à la meilleure prof du monde, Mado Martin, ton énergie et ton honnêteté font le bonheur des personnes autour de toi!

Ringrazio profondamente mia madre, la migliore madre che potessi desiderare. La tua profonda gentilezza, la tua intelligenza, la tua immensa cultura, la tua finezza di spirito e il tuo riguardo verso le persone illuminano il cammino di tutti coloro che ti incontrano. Senza di te, non sarei neanche metà di quello che sono ad oggi. Grazie per avermi supportato (e sopportato) in tutto: la musica, la fisica et la mia partenza in Francia. Sarai sempre un modello per me. Grazie al mio Papà che ha cultura e battute da vendere, la tua storia fa parte del mio percorso e la porterò sempre con me. Ringrazio anche te per avermi supportato e sopportato, anche se effettivamente sono una figlia quasi perfetta. On ira à Paris en vélo, pour dépasser les autos.. Saluto e ringrazio i miei fratelli e nipoti: Henry, Simone, Irene e i piccoli avventurosi Leo, Thiago e Margherita.

Ringrazio le mie migliori amiche, Lyuba e Elsa, la vostra amicizia è un dono prezioso. Ricordo i tempi del liceo, quando studiavamo insieme sul trenino per preparare le interrogazioni; ne abbiamo fatta di strada! Ringrazio le mie amiche di una vita, Lavinia, Giorgia e soprattutto Michela, il cui sorriso illumina ancora i miei pensieri. Abbiamo attraversato insieme la prova più difficile che la vita potesse metterci davanti, ma in un certo senso saremo sempre tutte e quattro insieme.

Mon dernier remerciement s'adresse à toi, Louis. Tu ne fais que remplir ma vie et la rendre plus incroyable chaque jour. Tu es la seule personne avec qui je pourrais vivre confinée dans 15 m^2 sans jamais en avoir marre. Mais je ne peux pas te remercier ici pour tout ce que tu m'as donnés et que tu me donnes chaque jour car quelques lignes ne suffiraient pas... Je te remercie ici pour avoir partagé ces années de thèse avec moi, pour m'avoir épaulé dans les moments de difficulté (surtout avec latex, ou quand je cherchais une these en neurosciences lorsque mes codes ne marchaient pas...), pour avoir attendu jusqu'à tard avant d'aller à l'escalade et surtout merci de m'avoir appris à avoir confiance en moi et à être (presque) satisfaite de mon travail. Tout simplement, merci d'avoir été présent et toujours encourageant et compréhensif. J'ai hâte de découvrir le monde avec toi dans notre petit Mushu. Il y a en a pas deux comme toi...

Che il viaggio continui!

Contents

1 Introduction

The Standard Model of particle physics (SM) is an elegant theory describing the fundamental structure of the matter surrounding us. It focuses on the description of the elementary particles, for instance quarks q, and the way they combine into more complex elements, for instance baryons (qqq) or mesons ($\bar{q}q$). Among baryons, protons and neutrons form the ordinary matter as we know it. The interactions between those particles are also described within the SM. Although the large amount of successful predictions has made of the SM a well established theory, there are few experimental observations which are not accounted for. Among those, the significant asymmetry between matter and antimatter that we observe in our Universe, is not explained within the SM. The violation of the charge and parity symmetries, called CP violation, could help understanding why matter and antimatter are not present in same quantities, however it is still not enough to explain such a large difference.

The need of physics models going beyond the Standard Model theory pushes the experimental searches to test the limits of the SM predictions and look for New Physics (NP) beyond it. Within those searches, the measurement of the magnetic dipole moment (MDM) of charmed baryons and ultimately of the charm quark, allows to test the validity of the SM predictions and especially of the Quantum Chromo Dynamics (QCD) theory. The magnetic moments of leptons have been measured for electrons and muons and the latter has been found to be in tension with the SM prediction. The tau's MDM is technically harder to measure due to the very short lifetime of tau leptons; as of today the tau leptons anomlaous MDM is known with a precision of only 10^{-2}, which is not competitive with the 10^{-8} precision of the SM prediction. Similarly, for the MDM of charm baryons and charm quark, few predictions exist however there is no experimental measurement available to confirm or reject them, hence a measurement is needed. In Chapter 2, the Standard Model is described in details with a particular focus on charmed baryons and the status of the magnetic dipole moment and polarization measurement for baryons.

An experiment for measuring the charmed baryons magnetic moment is proposed in Refs. [1, 2, 3, 4, 5]; all proposals are based on a well known physics principle, which is the precession of charged particles in a magnetic field. The idea of these experiments is to measure the precession angle of the baryons spin vector, which gives access to the MDM of the baryon. However, since the lifetime of charmed baryons is very short (around few hundreds fm), the precession must happen before the baryon decays to other particles and this requires a very strong magnetic field which is not achievable

with conventional magnets. A possible solution is to channel the baryons in a crystal, where the magnetic field between the planes is high enough to make the precession happen before the baryon decay; this method was successfully used in the past for the measurement of the Σ^+ baryon MDM [6]. The way charmed baryons could be produced at the Large Hadron Collider (LHC) and then redirected to the precession crystal is the subject of extensive R&D which go behind the scope of this thesis. One of the proposed setups includes a sequence of two crystals where a deflecting crystal is used to extract protons from the halo of the LHC beam to direct them on a second one, a target-crystal, which is used to produce the charmed baryons. The crystal dedicated to the precession of the polarization vector is placed right after these two other crystals.

In order to measure the magnetic moment, the initial polarization of the baryon (before it enters the crystal) is needed. In principle, the initial polarization could be obtained from other experiments which runs in similar conditions as in the double crystal setup, *i.e.* an experiment producing baryons from the interaction of a proton beam with a target. The LHCb experiment [7] is suited for this measurement since it can run in fixed-target mode thanks to the SMOG system, which allows to inject tiny quantities of gas close to the interaction point. The pNe fixed-target sample collected with the LHCb detector at a center of mass energy of $\sqrt{s} = 68$ GeV in 2017 reproduces similar condition as the one needed for the input polarization measurement discussed above. However, due to the lack of statistics in the fixed-target sample (around 250 Λ_c^+ are seen in the data) and to the complexity of the amplitude analysis which is necessary to measure the polarization, a preliminary measurement of the polarization is performed using the high statistic pp samples collected by LHCb. This allows to fix some of the parameters of the model which do not depend on the production mechanism involved in the baryon production and which are thus independent on the experiment. This is the subject of this work. The model built on the pp data can be then used to measure the polarization in the fixed-target sample.

In this thesis, the amplitude analysis of the three-body decay $\Lambda_c^+ \to pK^-\pi^+$ is presented. The goal of this analysis is to establish a model describing this three-body decay and extract the Λ_c^+ polarization vector. The choice of this channel is guided by the need of a weak decay to be sensitive to the polarization, since the amplitude is proportional to the asymmetry parameter α which is non zero only in case of parity violating interactions; and the fact that this channel has a large branching ratio. Furthermore, this decay allows for intermediate states which can interfere with each other, enhancing the sensibility to the polarization. The measurement is performed on the data containing pp collisions collected with the LHCb detector in 2016, at a center of mass energy of 13 TeV. The analysis is performed for Λ_c^+ baryons produced right after the collisions, called "prompt", and not for baryons coming from the decay of heavier particles, called "secondaries". Around 800 000 $\Lambda_c^+ \to pK^-\pi^+$ prompt decays have been selected with negligible background contributions and negligeable residual contamination from secondary decays. The large amount of statistics allows to describe this decay and its numerous intermediate resonant states. First, in Chapter 5, the equations describing the amplitude of the $\Lambda_c^+ \to pK^-\pi^+$ decays are derived within the helicity formalism, based on Ref. [8], making sure that no unphysical dependence or bias are introduced in this complex amplitude. Then the obtained formalism is used to describe the data. For the analysis of the data, first an amplitude model is built using an iterative procedure where the intermediate resonances are added one by one until the model is not

sensitive to them anymore. Then, the nominal model obtained is used to measure the polarization vector and the helicity couplings, along with the asymmetry parameters and the fit fractions. The measurement is performed separately for Λ_c^+ and $\overline{\Lambda}_c^-$ decays, since different production mechanisms are involved for baryons and anti-baryons and their polarization may differ. In Chapter 3, the LHCb detector is described, highlighting the excellent capabilities which allowed to study charm baryons and, finally, in Chapter 6 the amplitude analysis is presented.

Shifting toward the future, LHCb has been upgraded to take data during the next 3 years at the conditions foreseen for Run 3 (2022-2025). The upgraded detector will operate at a five times higher luminosity level than the previous runs, Run 1 and Run 2. However the performances of the LHCb detector, even for the upgraded version, degrades at high occupancy since it was designed to work at a lower luminosity level than the other general purpose experiments installed at the LHC. For this reason, the luminosity is voluntarily reduced at the LHCb interaction point and this procedure requires the measurement of the luminosity in real time. Furthermore, during Run 3 the LHCb detector will switch to an entire software trigger scheme, which requires very precise knowledge of the running conditions of the experiment. Those are only few of the reasons that motivated the construction of a new luminosity detector, the PLUME detector, which will be installed near the LHCb interaction point for Run 3. The PLUME detector is designed to determine if there was an interaction or not in a bunch crossing and it is based on the measurement of the Cherenkov light produced by charged particles crossing the detector. In the Chapter 4 of this thesis, the work on the front-end electronics (FEE) of the PLUME detector is presented. The FEE of PLUME has been defined; it will be based on the front-end electronics of the LHCb electromagnetic calorimeter which have been proven to be adapted for the expected signal shape obtained during tests beam. Finally, the possibility to use the PLUME detector to measure the shift of the LHCb clock with respect to the main LHC clock is also explored. This measurement will be beneficial for the performances of the LHCb detector during Run 3.

2 Theoretical and experimental overview

2.1 The Standard Model of particle physics

The Standard Model (SM) of particle physics is a quantum field theory (QFT) describing precisely fundamental particles and their interactions. Its construction has been guided by principles of symmetry expressed using the mathematics of group theory. It accounts for many phenomenological predictions which have been extensively tested and which are found to agree well with experimental measurements. The SM has become the main theory used to describe and predict particle physics phenomena, the recent discovery of the Higgs boson in 2012 by ATLAS [9] and CMS [10] represents one of its greatest achievements and corroborates fifty years of successful discoveries. Although the SM is an elegant and precise theory, it cannot be the ultimate theory describing nature; there exist few experimental observations, discussed in Sec. 2.2.2, which are not accounted for in the SM. Furthermore, the SM describes very well three out of four fundamental interactions (electromagnetic, weak and strong interactions) however it does not include gravity, which is currently understood within classical physics by the theory of General Relativity (GR). Even though the effects of gravity are not seen at small distance scales, a theory unifying the four forces is needed to provide a complete description of nature. On top of that, a growing number of cosmological and astrophysical evidences point towards the need of an extension of the SM theory. Consequently, the SM of particle physics is the subject of an extensive research program across the world, grouping together the efforts of theorists and experimentalists, whose goal is to discover and understand the missing blocks of this beautiful theory. All the particles discovered up to now, have a place in the SM description. The classification of particle is an outstanding result of symmetry considerations within group theory, rather than a simple listing or labelling process. The way particles arise within the SM as well as the interactions between them are discussed in the next sections.

2.1.1 Particle content in the Standard Model

In QFT, particles appear as quantized excitations of a field and they are fundamental entities without any substructure. Depending on the nature of the underlying field, they can have different properties. To begin with, particles are classified in two major categories: bosons, with integer spin, and fermions,

	Quarks			Leptons		
Gen.	Flavour	Mass	Charge	Flavour	Mass	Charge
1st	u	$2.2^{+0.5}_{-0.4}\,\mathrm{MeV}/c^2$	$+2/3$	ν_e	$< 2\,\mathrm{eV}/c^2$	0
	d	$4.7^{+0.5}_{-0.3}\,\mathrm{MeV}/c^2$	$-1/3$	e^-	$0.511\,\mathrm{MeV}/c^2$	-1
2nd	c	$1.275^{+0.025}_{-0.035}\,\mathrm{GeV}/c^2$	$+2/3$	ν_μ	$< 190\,\mathrm{keV}/c^2$	0
	s	$95^{+9}_{-3}\,\mathrm{MeV}/c^2$	$-1/3$	μ^-	$105.66\,\mathrm{MeV}/c^2$	-1
3rd	t	$173.0 \pm 0.4\,\mathrm{GeV}/c^2$	$+2/3$	ν_τ	$< 18.2\,\mathrm{MeV}/c^2$	0
	b	$4.18^{+0.04}_{-0.03}\,\mathrm{GeV}/c^2$	$-1/3$	τ^-	$1776.9 \pm 0.1\,\mathrm{MeV}/c^2$	-1

Table 2.1: Summary of leptons and quarks properties, from [11].

with half-integer spin. Together with the spin, particles have other quantum numbers such as the electric, colour and hyper charges, the lepton and baryon numbers and other properties such as their flavours and masses. For each particle, there exists an antiparticle which shares the same mass and spin but opposite electrical charge, as well as lepton and baryon number. The antiparticles form the so-called antimatter which is present in tiny quantities in the Universe; the predominance of particle over antiparticles is not understood up to now. A difference in the behaviour of matter with respect to antimatter seems to be a necessary condition to justify this imbalance and would directly imply the violation of charge and parity symmetries; this is discussed in Sec. 2.2.

Fermions are considered as the "building blocks" of matter, since they are the main constituents of nuclei and consequently of atoms[1]. They are divided in two categories: leptons, which do not interact strongly and have a zero colour charge, and quarks, which are sensitive to any type of interaction. The masses anc charges of fermions are summarized in Tab. 2.1. There are 6 types (or "flavours") of leptons and 6 of quarks, for a total of 12 fundamental fermions. They are organized in three generations with increasing mass and in pairs of two, called "doublets" (this is related to the SU(2) nature of the weak interaction). The reason why matter is organized in three generations with similar properties but different masses is not explained within the SM. For quarks, the first and lighter generation, are the up (u) and down (d) quarks, forming the ordinary matter. The second generation, is made of a charm (c) and a strange (s) quark and the third one by the top (t) and bottom (b), also called beauty, quarks. The *up-type* quarks have the same electric charge, $\frac{2}{3}$, and the *down-type* quarks have charge $-\frac{1}{3}$. Since quarks interact strongly, they carry a colour charge which can take 6 discrete values: red, green, blue and anti-red, anti-green, anti-blue. In nature, only colourless objects are observed, thus the elementary quarks cannot be observed alone. When quarks are produced, they "combine" (hadronise) very quickly (in less than 10^{-23} s) with other quarks to form colourless and bound combinations, called *hadrons*. This is however not the case for the heaviest quark t which is so heavy that it decays before having the time to form a hadron. Typical colourless combinations are a pair of quark and antiquark ($q\overline{q}$) called *mesons*, or a group of three quarks (qqq) called *baryons*. There exist other "exotic" combinations, such as tetraquarks ($qq\overline{q}\overline{q}$) and pentaquarks ($qqqq\overline{q}$), which have been observed first by Belle [12] and BaBar [13] and recently by LHCb [14] [15]. Baryons composed by the heavier quarks b or c, allow for

[1]Nuclei are composed of u and d quarks, forming protons (uud) and neutrons (udd), and electrons.

Gauge bosons			
Name	Mass	Charge	Spin
Gluon	0	0	1
Photon	0	0	1
Z boson	$91.1876 \pm 0.0021\,\mathrm{GeV}/c^2$	0	1
W boson	$80.379 \pm 0.012\,\mathrm{GeV}/c^2$	± 1	1
Higgs	$125.10 \pm 0.14\,\mathrm{GeV}/c^2$	0	0

Table 2.2: Gauge bosons properties, from [11].

a large amount of decay modes and they are widely studied within LHCb and Belle II; in this thesis, the Λ_c^+ (udc) baryon properties are studied. Depending on the quark content, baryons have different quantum numbers, this is understood within the so-called *quark model*, described in Sec. 2.3.

For leptons, the same classification in three generations holds. Each leptonic doublet is formed by an electrically (-1) charged lepton the electron (e), muon (μ) or tau (τ), and an associated neutral neutrino ν_e, ν_μ or ν_τ. Since neutrinos are electrically neutral, they interact only via the weak force. Up to now, it has been observed that the difference between the number of leptons and the number of antileptons, called lepton number $L = n_l - n_{\bar{l}}$, is a conserved quantity. Thus, the concept of family lepton numbers was introduced: L_e, L_μ and L_τ, where the lepton number L_i of a family i is 1 for the particle and -1 for the antiparticle. For instance the electron has $L_e = +1$ and the antimuon $L_\mu = -1$. For other particles which are not leptons, the lepton number is zero. Family lepton numbers are conserved quantities so that the sum of lepton numbers (for each family) before and after any interaction must be the same. This is called "lepton flavour number conservation" and it is believed to be respected for the charged leptons (up to now, no lepton-flavour violating decays have been observed), however it is violated in the case of neutrino oscillations. These oscillations have been measured by different experiments [16] [17] [18] and imply that neutrinos have a non-zero mass. The origin of the neutrino masses is not completely understood within the SM yet.

The second type of particles are bosons, with integer spin. In the SM, spin-1 bosons, or gauge bosons, are the "carriers" of the interactions. Thus, there are 3 force carriers: photons (γ) for electromagnetic interactions, Z and W bosons for neutral and charged weak interactions and finally gluons (g) for strong interactions. One extra spin-0 boson, the Higgs boson, exists in the SM and it is not precisely a force carrier. It is the boson responsible for the Brout-Englert-Higgs (BEH) mechanism, causing the electroweak symmetry breaking discussed in Sec. 2.1.2. It is the way masses were introduced and justified in the SM, before which only massless fermions and bosons were considered. The masses, charges and spins of the SM bosons are summarized in Tab. 2.2.

2.1.2 The Standard Model interactions

There are four fundamental forces in nature: gravitational, electromagnetic, strong and weak forces. Mathematically, the last three forces arise as quantum fields in the SM and their dynamics and kinematics are determined by the Lagrangian density and local symmetries. The latter are transformations determined by a specific group and if the system is unchanged by those transformations, then the transformation is a symmetry. The SM Lagrangian is invariant under local transformation of the

Force	Relative strength	Mediator	Type of charge	Coupling constant	Time scale decay
Strong	1	8 Gluons	colour	α_s	$\sim 10^{-24}$ s
Electromagnetic	10^{-2}	Photon	Electric	α_{em}	$\sim 10^{-16}$ s
Weak	10^{-5}	W and Z bosons	Hypercharge Y	α_W	$\sim 10^{-6} - 10^{-8}$ s
Gravity	10^{-42}	Graviton(?)	Mass	✗	✗

Table 2.3: The 4 fundamental forces seen in nature. The graviton has not been observed up to now.

composite group

$$\mathrm{SU}(3)_C \times \mathrm{SU}(2)_I \times \mathrm{U}(1)_Y \tag{2.1}$$

where the colour charge C, the weak isospin I and hypercharge Y are conserved quantities. The three interactions arise as gauge fields when requiring the Lagrangian to be invariant under transformations belonging to those 3 groups. The $\mathrm{SU}(3)_C$ symmetry is associated with QCD and strong interactions and $\mathrm{SU}(2)_I \times \mathrm{U}(1)_Y$ with electroweak interactions (EW), describing the electromagnetic and weak forces. The bosons carrying the forces, listed in Table. 2.2, correspond to the generators of these groups[1]. The strength of those interactions is characterized by a coupling constant, which is, despite the name, a non-constant adimensional parameter which depends on the energy scale. The characteristics of the four forces are summarized in Table. 2.3 where the last column shows the typical time scale of decays where the interaction is involved, and the other quantities have been defined in the text. In the following, the Lagrangian formulation of the electroweak and strong interactions as well as the Higgs mechanism are presented in a concise way, a more detailed description can be found in the classical textbooks [19][20][21].

Electroweak theory The Lagrangian ($\mathcal{L}_0$) describing a freely propagating fermion ψ of mass M, is

$$\mathcal{L}_0 = \bar{\psi}(i\gamma^\mu \partial_\mu - M)\psi. \tag{2.2}$$

where γ^μ are the Dirac matrices which satisfy the anticommutation relation: $\{\gamma^\mu, \gamma^\nu\} = \gamma^\mu\gamma^\nu + \gamma^\nu\gamma^\mu = 2\eta^{\mu\nu} I_4$, where $\eta^{\mu\nu}$ is the Minkowski metric, and I_4 is the 4×4 identity Matrix. $\mathcal{L}_0$ is invariant under global U(1) transformation which transforms the ψ field as $\psi(x) \xrightarrow{U(1)} \psi'(x) \equiv e^{iq\theta}\psi(x)$, corresponding to a rotation of the field phase by an arbitrary real constant θ. The gauge principle however, requires the U(1) phase invariance to hold locally. This means that the phase transformation becomes space-time coordinates dependent ($\theta(x)$) and that the partial derivative term in $\mathcal{L}_0$ transforms as:

$$\partial_\mu \psi(x) \xrightarrow{U(1)} e^{iq\theta(x)} \left(\partial_\mu + iq\partial_\mu \theta(x)\right) \psi(x) \tag{2.3}$$

where an extra term that breaks the invariance appears. The "free" Lagrangian transforms now as

$$\mathcal{L}_0 \overset{U(1)}{=} \bar{\Psi} \left(i\gamma^\mu \partial_\mu - M\right) \Psi - \bar{\Psi}\gamma^\mu \partial_\mu q\theta(x) \Psi \tag{2.4}$$

[1]The group generators are elements of the group which form a subset such that every element of the group can be expressed as a combination (under the group operation) of it and their inverses.

Field	Generations			T	T_3	$SU(3)_C$	$SU(2)_L$	$U(1)_Y$	$Q = T_3 + Y$
Q_L	$\begin{pmatrix} u_L \\ d_L \end{pmatrix}$	$\begin{pmatrix} c_L \\ s_L \end{pmatrix}$	$\begin{pmatrix} t_L \\ b_L \end{pmatrix}$	1/2	$\begin{pmatrix} +1/2 \\ -1/2 \end{pmatrix}$	3	2	+1/6	$\begin{pmatrix} +2/3 \\ -1/3 \end{pmatrix}$
U_R	u_R	c_R	t_R	0	0	3	1	+2/3	+2/3
D_R	d_R	s_R	b_R	0	0	3	1	−1/3	−1/3
L_L	$\begin{pmatrix} \nu_{eL} \\ e_L \end{pmatrix}$	$\begin{pmatrix} \nu_{\mu L} \\ \mu_L \end{pmatrix}$	$\begin{pmatrix} \nu_{\tau L} \\ \tau_L \end{pmatrix}$	1/2	$\begin{pmatrix} +1/2 \\ -1/2 \end{pmatrix}$	1	2	−1/2	$\begin{pmatrix} 0 \\ -1 \end{pmatrix}$
E_R	e_R	μ_R	τ_R	0	0	1	1	−1	−1

Table 2.4: Representations of the fermion sector with relative charges.

where the second term breaks the invariance under the U(1) local phase transformation. This indicates that local phase invariance is not possible for a free theory, which does not include any interaction term by definition. To compensate for this extra term, a new degree of freedom A_μ is introduced, which transforms under local U(1) as:

$$A_\mu \xrightarrow{U(1)} A'_\mu = A_\mu + \partial_\mu \theta(x). \tag{2.5}$$

It can be seen that $\mathcal{L}_0$ becomes invariant under the local U(1) transformation if the derivative is replaced by the covariant derivative D_μ:

$$D_\mu = \partial_\mu - iqA_\mu. \tag{2.6}$$

Finally, the "free" Lagrangian $\mathcal{L}_0$ becomes

$$\mathcal{L}_A \equiv \bar{\psi}(x)(i\gamma^\mu D_\mu - M)\psi(x) = \mathcal{L}_0 + \underbrace{qA_\mu(x)\bar{\psi}(x)\gamma^\mu\psi(x)}_{\text{interaction term}} \tag{2.7}$$

where $\mathcal{L}_A$ fulfils the local U(1) invariance requirements and a new term appears, corresponding to the interaction of the fermion with a gauge field A_μ. The new field corresponds to the photon, interacting with other fermions with a strength $q = e$. This is a typical example of how a gauge boson, force carrier of an interaction, arises in the SM as a consequence of local symmetries.

In a similar way, the unification of electromagnetic and weak forces results by requiring local gauge invariance under the group $\mathrm{SU(2)}_L \times \mathrm{U(1)}_Y$. In this case, the gauge bosons appear as combinations of four fields $W_\mu^{1,2,3}$ and B_μ and the covariant derivative is

$$D_\mu = \partial_\mu - ig\frac{\tau_a}{2}W_\mu^a - ig'\frac{Y}{2}B_\mu, \quad a = 1,2,3 \tag{2.8}$$

where τ_a are the group generators of $\mathrm{SU(2)}_L$ and Y of $\mathrm{U(1)}_Y$; g and g' are the coupling constants of $\mathrm{SU(2)}_L$ and $\mathrm{U(1)}_Y$ respectively. The W and B bosons are massless, so they do not correspond to the W and Z bosons of the weak interactions yet. The origin of gauge bosons masses requires a specific mechanism which is explained in the following.

The EW theory is a chiral theory, meaning that the right-handed and left-handed particles are not interacting in the same way. The W_μ^a fields couple only to left-handed particles (or right-handed

antiparticles), while the B_μ field couples to particles carrying the weak hypercharge. The left-handed fermions are organized in doublets whereas right-handed fermions are organized in singlets, the particle representations under the EW group are shown in the sixth column of Table 2.4. The EW chirality results in the violation of parity, a phenomenon observed experimentally for the first time in 1956 [22]; a complete discussion about parity violation is given in Sec. 2.2.

It appears clearly here that the way particles are organized in the SM is a direct consequence of the underlying groups chosen to describe them and their interactions. Hence one can refer to a particle either by its name, or by the way it behaves with respect to the standard model group(s), thus a bottom quark can be referred to as $(3, 2, +1/6)$, meaning that it is a triplet under $\mathrm{SU}(3)_C$, a doublet under $\mathrm{SU}(2)_L$ and a singlet with hypercharge $+1/6$ for $\mathrm{U}(1)_Y$.

Strong force The strong interactions are described by a theory called Quantum Chromodynamics (QCD). The force carriers are the gluons G_μ which have a colour charge and can couple to quarks or other gluons. They lie in the adjoint representation of SU(3). As for the electroweak theory, there exists a covariant derivative allowing for gauge invariance under SU(3):

$$D_\mu = \partial_\mu - i g_s \frac{\lambda_a}{2} G^a_\mu, \quad a = 1 \dots 8 \tag{2.9}$$

where λ_a are the 8 generator Gell-Mann matrices and g_s is the strong coupling constant.

Then, the QCD Lagrangian can be written as:

$$\mathcal{L}_{QCD} = \bar{\Psi} \left(i \gamma^\mu D_\mu - m \delta_{ij} \right) \Psi - \frac{1}{4} G^a_{\mu\nu} G^{\mu\nu}_a \tag{2.10}$$

where m is the mass of the quark corresponding to the field Ψ. Quarks and gluons carry a colour charge however it has been observed up to now that only colourless combinations of particles can exist in nature. This means that a colour charged particle alone cannot exist in nature, it needs to combine with other particles to form colourless combinations (the hadrons). This feature can be understood when looking at the behaviour of the strong coupling constant ($\alpha_s \propto g_s^2$) as a function of the energy scale Q, shown in Fig. 2.1. At small Q values, corresponding to large distances[1], α_s takes large values whereas for large Q, corresponding to short distances, it decreases. This means that at large energy (short distances), quarks and gluons interact less intensively and can be treated as free particles, this is called asymptotic freedom and it is specific to QCD. On the other hand, at low energy (large distances), quarks and gluons must form bound states (hadrons) and cannot be isolated, this phenomenon is known as colour confinement. When α_s is small (*i.e.* in the energy $100\,\mathrm{GeV} - 1\,\mathrm{TeV}$ range, where the coupling is around 0.1), QCD calculations can be simplified and developed in a perturbative way (pQCD), while for large α_s (below 1 GeV) more sophisticated methods are needed, as for instance lattice QCD.

Higgs mechanism The theory as presented up to now do not account for fermion and boson masses. Indeed, if a simple mass term $m\bar{\psi}\psi$ is added for fermions, then mixed terms such as $m\bar{\psi}_R\psi_L$ would

[1] Momentum and position are conjugate variables, related by a Fourier transform (FT). The properties of FT lead to the famous Heisenberg relation: $\Delta x \Delta p \geqslant \hbar/2$, thus for large distance x the momentum p has to be small and vice versa.

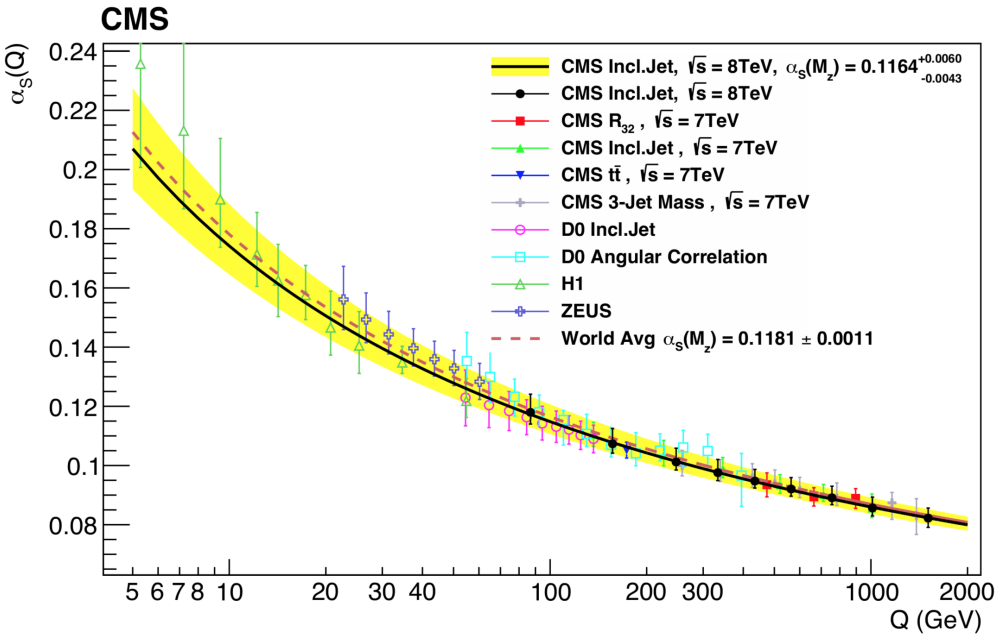

Figure 2.1: Strong coupling constant α_s as a function of the energy scale of the interaction Q. Several measurements are superimposed, the brown dashed line represents the world average, from [23].

appear and the gauge invariance would be broken, due to the fact that the EW theory treats right and left handed particles in a different way. Nevertheless, the masses of the W and Z bosons have been measured experimentally and found to be different from zero, 80.4 and 91.2 GeV [24][25] respectively. This was a sign that the SM theory was not complete yet. A way out, allowing to generate the gauge bosons masses within the SM, is the now famous Brout-Englert-Higgs mechanism [26][27]. It consists in adding a scalar field Φ, hereon called Higgs, resulting in a Lagrangian of the form:

$$\mathcal{L}_{\text{Higgs}} = \underbrace{(D^\mu\phi)^\dagger (D_\mu\phi)}_{\text{Kinetic term}} - \underbrace{V(\phi)}_{\text{Potential}} \tag{2.11}$$

where the scalar potential $V(\phi)$ is defined as:

$$V(\phi) = \mu^2\phi^\dagger\phi + \lambda\left(\phi^\dagger\phi\right)^2 \quad \text{with} \quad \phi = \begin{pmatrix} \phi^+ \\ \phi^0 \end{pmatrix} \tag{2.12}$$

with $\lambda > 0$ and $\mu^2 < 0$ and ϕ, the Higgs field, is an SU(2) doublet composed of two complex scalar fields ϕ^+ and ϕ^0. The vacuum expectation value of the Higgs potential is at $v = \sqrt{-\mu^2/\lambda}$ and there are infinite degenerate states that have the minimum energy, choosing one state would break the EW symmetry "spontaneously". For the arbitrary choice

$$\phi_0 = \frac{1}{\sqrt{2}} \begin{pmatrix} 0 \\ v \end{pmatrix} \tag{2.13}$$

there is still a subgroup which stays unbroken and which is associated to QED hence $\mathrm{SU}(2)_L \times \mathrm{U}(1)_Y \rightarrow \mathrm{U}(1)_Q$. The potential can be expanded around the ground state to obtain the Higgs doublet:

$$\phi(x) = \frac{1}{\sqrt{2}} \begin{pmatrix} 0 \\ v + h(x) \end{pmatrix} \tag{2.14}$$

From there, the gauge boson masses are obtained expanding the kinetic term of Eq. 2.11 while the potential term of the same equation describes the Higgs self-interactions; thus inserting the definition of D_μ given in Eq. 2.8 and after few simplifications one obtains

$$(D_\mu \phi)^\dagger (D_\mu \phi) = \frac{1}{2} (\partial_\mu h)(\partial^\mu h) + \frac{g^2}{4}(v+h)^2 W_\mu^+ W^{\mu -} + \frac{1}{8}\left(g^2 + g'^2\right)(v+h)^2 Z_\mu Z^\mu \tag{2.15}$$

$$V(\phi) = \frac{\mu^2}{2}(v+h)^2 + \frac{\lambda}{4}(v+h)^4 \tag{2.16}$$

The physical gauge fields are then two charged fields, $W^\pm$, and two neutral gauge bosons, Z and γ. For this reason, weak interactions are classified as "neutral currents" mediated by the Z boson, and "charged currents", mediated by the charged bosons $W^\pm$. The EW gauge bosons appear in Eq. 2.15 as combinations of W_μ^a and B_μ fields:

$$\begin{aligned} W_\mu^\pm &= \frac{1}{\sqrt{2}}\left(W_\mu^1 \mp i W_\mu^2\right) \\ Z^\mu &= \frac{-g' B_\mu + g W_\mu^3}{\sqrt{g^2 + g'^2}} \\ A^\mu &= \frac{g B_\mu + g' W_\mu^3}{\sqrt{g^2 + g'^2}} \end{aligned}$$

For the neutral bosons, this relation is also expressed as a rotation of the mass basis by the weak mixing angle θ_w,

$$\begin{pmatrix} Z_\mu \\ A_\mu \end{pmatrix} = \begin{pmatrix} \cos\theta_w & -\sin\theta_w \\ \sin\theta_w & \cos\theta_w \end{pmatrix} \begin{pmatrix} W_\mu^3 \\ B_\mu \end{pmatrix} \text{ where } \cos\theta_w = \frac{g}{\sqrt{g^2 + g'^2}} \tag{2.17}$$

The gauge bosons masses arise naturally from the covariant derivative expansion, Eq. 2.15, and the Higgs boson mass (along with the self-interaction couplings) from the potential term one, Eq. 2.16. They read:

$$\begin{aligned} M_W^2 &= \frac{1}{4} g^2 v^2 \\ M_Z^2 &= \frac{1}{4}\left(g^2 + g'^2\right) v^2 \\ M_A &= 0 \\ M_{Higgs} &= \sqrt{2\lambda v^2} \end{aligned}$$

The spontaneous symmetry breaking (SSB) allowed to generate boson masses, starting with a complex scalar doublet Φ with 4 degree of freedoms (dofs), one massless B with 2 dofs and three massless W^a gauge fields with 6 dofs, for a total number of 12 dofs. After SSB, the dofs repartition is changed: one

real scalar Higgs field (1 dof), 3 massive weak bosons (9 dofs) and 1 massless photon with 2 dofs, for a total of 12 again. The scalar dofs have been absorbed by the massive gauge field to describe their longitudinal polarization. Finally, fermion masses are also obtained thanks to the Higgs field by mean of the Yukawa Lagrangian:

$$\mathcal{L}_Y = -Y^D_{ij}\bar{Q}_{Li}\phi D_{Rj} - Y^U_{ij}\bar{Q}_{Li}\phi^* U_{Rj} - Y^L_{ij}\bar{L}_{Li}\phi E_{Rj} + \text{h.c.}^1 \tag{2.18}$$

where the quark and lepton left- and right-handed fields are the one shown in Table 2.4 and appear multiplied by the Yukawa couplings Y_{ij}, where the indices i, j run over the three fermion generations. The fermion masses can be expressed as $m_i = y_i \frac{v}{\sqrt{2}}$. It should be noted that the Yukawa couplings and in turn the fermion masses are free parameters in the SM and they cannot be predicted theoretically. Therefore, they have been measured experimentally and the origin of the large mass difference between the three generations is not predicted within the SM.

2.2 Symmetries and CP violation

Symmetries and conservation laws are at the core of physics and especially particle physics. As derived in the previous sections, particle fields arise in the SM by applying symmetry transformations to the Lagrangian. The symmetries discussed above are continuous symmetries, parametrized by a set of continuous parameters. More generally, the invariance of a system under a continuous symmetry leads to the conservation law for a physics quantity, this is stated in the notorious Noether's theorem. For instance, the invariance under rotation leads to the angular momentum conservation, similarly the space and time translations to the momentum and energy conservation. A list of particle quantum numbers and their conservation laws for different interactions is given in Table 2.5. Beside continuous symmetries, discrete symmetries, which are instead parametrized by discrete values, play also an important role especially in modern particle physics. In particular, there are three important discrete symmetries widely exploited in particle physics: parity (P), charge conjugation (C) and time reversal (T). Parity operation inverts spatial coordinates, which is equivalent to applying a mirror transformation followed by a rotation of π. The effect of parity transformation (along with charge and time reversal) on physical quantities is summarized in Tab. 2.6. For instance, position and momentum change sign under parity, while spin is unaffected. The action of parity on a quantum state is simply $P\psi(\vec{r}) = \psi(-\vec{r})$ and the eigenvalues of P satisfy,

$$P|\psi(\vec{r},t)\rangle = \eta_P|\psi(-\vec{r},t)\rangle \tag{2.19}$$

where $\eta_P = e^{i\xi_P}$ is a phase factor: $|\eta_P|^2 = 1$, with ξ_P real. This is required since the normalisation of the physical state $|\psi\rangle$ must stay unchanged:

$$1 = \langle\psi|\psi\rangle = \langle\psi|P^\dagger P|\psi\rangle = |\eta_P|^2\langle\psi|\psi\rangle \tag{2.20}$$

[1] h.c. = hermitian conjugate.

Quantum number	Strong	EM	Weak
Electric charge (Q)	✓	✓	✓
Energy (E)	✓	✓	✓
Momentum ($\vec{p}$)	✓	✓	✓
Spin ($\vec{J}$)	✓	✓	✓
Baryon number (B)	✓	✓	✓
Lepton numbers (L_e, L_μ, L_τ)	✓	✓	✓
Strange (s)	✓	✓	✗
Charm (c)	✓	✓	✗
Beauty (b)	✓	✓	✗
Top (t)	✓	✓	✗
Strong isospin (I)	✓	✗	✗
Isospin projection (I_3)	✓	✓	✗

Table 2.5: Conservation laws for the three fundamental forces and SM quantum numbers, ✓ means that the quantum number is conserved, ✗ that is not.

Obs.	P	C	T
Time (t)	t	t	$-t$
Position ($\vec{r}$)	$-\vec{r}$	$\vec{r}$	$\vec{r}$
Energy (E)	E	E	E
Momentum ($\vec{p}$)	$-\vec{p}$	$\vec{p}$	$-\vec{p}$
Angular momentum ($\vec{J}$)	$\vec{J}$	$\vec{J}$	$-\vec{J}$
Helicity (λ)	$-\lambda$	λ	λ
Electric charge (e)	e	$-e$	e

Table 2.6: Transformation of physical observables under parity (P), charge conjugation (C) and time reversal (T) operations.

Furthermore, the parity operator applied a second time restores the original state, implying that $P^2 = 1$, which, along with the condition $P^\dagger P = 1$ imposed by the normalisation, means that P is an hermitian operator. A physical state can either have a defined parity, meaning that it is an eigenstate of P with either even, $\eta_P = 1$, or odd parity, $\eta_P = -1$, or it can have no defined parity, in which case it is not an eigenstate of P. In the contest of quantum field theory, every particle is described as a state in the Hilbert space with a parity eigenvalue, called *intrinsic parity*. For instance, fermions have even intrinsic parity, while anti-fermions odd. According to their parity, spin-0 particles can be scalars (even) or pseudo-scalars (odd), while spin-1 can be vectors (odd) or axial vectors (even). For hadrons, the intrinsic parity is often determined experimentally by observing a decay process and using conservation laws.

The charge conjugation operation reverses the sign of all charges associated to the quantum state (electric, colour and weak hyper-charges), transforming a particle in its antiparticle. Similarly to the P case, a C-parity quantum number can be defined for the charge eigenstates. Its effect on a state with definite momentum $\vec{p}$, spin projection s and charge q is

$$C|\vec{p}, s, q\rangle = \eta_C|\vec{p}, s, -q\rangle \tag{2.21}$$

Discrete symmetry	Strong	EM	Weak
Parity, P	✓	✓	✗
Charge parity, C	✓	✓	✗
Time reversal invariance, T	✓	✓	✗
Combined parity, CP	✓	✓	✗
CPT invariance	✓	✓	✓

Table 2.7: Conservation laws for the three fundamental forces, ✓ means that the symmetry is conserved, ✗ that it is not.

where $\eta_C = e^{i\xi_C}$ is a phase factor, $|\eta_C|^2 = 1$, with ξ_C real.

The last operation, time reversal, inverses the time direction; the spatial coordinates are unchanged but the direction of momenta are reversed, as a consequence the initial and final states are exchanged, $T(a \to b) = (b \to a)$. Time inversion operator is unitary as P and C, however it is antilinear [1], for this reason, it cannot be an observable in the same way as P and C. Requiring the conservation of one of these three symmetries, or the combination of two of them, for a physics process results in the prohibition of certain transitions in nature. For instance, if P is a symmetry of the system, the transition to states with different parities is forbidden and any observable which is odd under parity must have a zero expectation value. This gives rise to a set of selection rules for the observables describing the transition amplitude, which are usually derived starting from the Lagrangian terms. Not all the three fundamental interactions (weak, strong and EM) conserve the P, C and T symmetries. Parity violation was first theorized in 1956 by Lee and Yang [28] as a solution to the famous "$\tau - \theta$" puzzle; two particles, with same lifetime and mass, were found to decay to two different final states with different parities: $\theta^+ \to \pi^+\pi^0$ and $\tau^+ \to \pi^+\pi^-\pi^+$. At the time, parity was believed to be conserved implying that the two particles could not be the same one as the measurement suggested. Lee and Yang proposed an easier solution, θ and τ were actually the same particle, a K meson, which decays violating parity. Then, in 1957, parity violation in weak interactions was observed for the first time in the β decay of cobalt-60 by C.S.Wu et al. [29]. Thereafter, it was clear that the weak interaction was violating parity, and the C violation was also shown right after, whereas there were still no evidence for CP violation. This is strictly linked to the chiral structure of the weak interactions, allowing for the existence of a left-handed neutrino but not of a right-handed neutrino or a left-handed antineutrino. Since the right-handed antineutrino, the CP conjugate of the left-handed neutrino, exists in the SM, one would expect the CP symmetry to be conserved. However, in 1964, CP violation was observed in kaon decays [30] and although unexpectedly small, it was a breakthrough. The Fermi theory which was successfully describing the weak interaction as a point-like interaction, needed to be extended, it was for this reason that the V-A structure was introduced in the weak interaction.

Up to now, only the combination of the three symmetries, CPT, is considered an exact symmetry of nature and no violation of it has been observed. The CPT symmetry follows from the most fundamental assumption of the current quantum field theory, local Lorentz invariance, and the breaking of the CPT symmetry would imply the breaking of the entire SM theory. It is worth to notice that if

[1] This appears when imposing the conservation of the commutation relation between momentum and position $[x, p] = i\hbar$. The time reversal of this relation implies that T maps i to $-i$.

CP is violated then, as a consequence of the *CPT* theorem, T must also be violated. As a conclusion, a summary of the symmetries laws for the three fundamental interactions is given in Table 2.7.

2.2.1 Quark mixing and the CKM matrix

At the time the SM was built, only 3 quarks were known: u, d and s. They were classified as representations of $\mathrm{SU}(2)_L$ as a doublet $\begin{pmatrix} u \\ d \end{pmatrix}$ and a singlet $\{s\}$. Nevertheless, this organization would not allow the interaction of u and d with a s, contradicting the observation of the strangeness violation in the $K^+ \to \mu^+\nu_\mu$ decay. A solution to this problem was proposed by N. Cabibbo in 1963 [31], who proposed the idea that the observed isospin eigenstates (the primed states here) are actually an admixture of the mass eigenstates. Thus when they interact, the u and d are a u quark, d' doublet and a s' singlet. The mixing is represented as a rotation matrix of angle $\theta_C \sim 13°$, the so-called Cabibbo angle,

$$\begin{pmatrix} d' \\ s' \end{pmatrix}_{\mathrm{F}} = \begin{pmatrix} \cos\theta_C & \sin\theta_C \\ -\sin\theta_C & \cos\theta_C \end{pmatrix} \begin{pmatrix} d \\ s \end{pmatrix}_{\mathrm{M}} = \begin{pmatrix} d\cos\theta_C + s\sin\theta_C \\ -d\sin\theta_C + s\cos\theta_C \end{pmatrix} \tag{2.22}$$

In this way, the interaction of u and s quarks is allowed. Since $\cos\theta_C > \sin\theta_C$, the u-d transition is classified as *Cabibbo favoured*, while the u-s is *Cabibbo suppressed*. However this rotation implies the existence of transitions $d \to s$, known as flavour changing neutral current (FCNC), which were not observed experimentally. In 1970, the Glashow-Iliopoulos-Maiani (GIM) mechanism [32] proposing the existence of a fourth quark c forming a doublet with the s, was proposed. Now two quark doublets exist (u,d) and (c,s), with interaction eigenstates

$$\begin{pmatrix} u \\ d\cos\theta_C + s\sin\theta_C \end{pmatrix} \quad \text{and} \quad \begin{pmatrix} c \\ s\cos\theta_C - d\sin\theta_C \end{pmatrix} \tag{2.23}$$

and the FCNC are forbidden. The c quark was discovered in 1974 by the Brookhaven National Laboratory and SLAC [33][34]. They both observed it as the J/ψ [1] resonance decaying into an electron-positron pair. As for the third family of quarks, t and b, it was predicted in 1973, by M. Kobayashi and T. Maskawa [35] to explain the observed *CP* violation in kaon decays. The observation came in 1977, with the b discovery at Fermilab as the Y resonance [36]. The t quark was harder to discover because, due to its high mass, it decays before hadronising; it was first seen in 1994 by the CDF and D0 collaborations [37].

In order to include the third family, the Cabibbo rotation matrix is to be replaced by the Cabibbo-Kobayashi-Maskawa (CKM) matrix, which fully describes the quark mixing between the three SM families. It is usually written as

$$\begin{pmatrix} d' \\ s' \\ b' \end{pmatrix}_{F} = \begin{pmatrix} V_{ud} & V_{us} & V_{ub} \\ V_{cd} & V_{cs} & V_{cb} \\ V_{td} & V_{ts} & V_{tb} \end{pmatrix} \begin{pmatrix} d \\ s \\ b \end{pmatrix}_{M} \tag{2.24}$$

[1] The resonance was called J at Brookhaven and ψ at SLAC, thus finally it was named J/ψ.

and as for the Cabibbo case, it represents the change of basis between the quark interaction eigenstates, or flavour eigenstates (F), and the quark mass eigenstates (M). The V_{ij} matrix elements determine the strength of the quark couplings between different families. Once the arbitrary phases of the quark fields are fixed, the CKM matrix can be parametrized by three real mixing angles and one complex phase, corresponding to 3 real numbers (λ, A and ρ) and one phase (η), as proposed by L. Wolfenstein [38]:

$$V_{CKM} = \begin{pmatrix} 1-\lambda^2/2 & \lambda & A\lambda^3(\rho - i\eta) \\ -\lambda & 1-\lambda^2/2 & A\lambda^2 \\ A\lambda^3(1-\rho-i\eta) & -A\lambda^2 & 1 \end{pmatrix}. \tag{2.25}$$

This form was obtained by expanding each element as a power series in $\lambda \equiv |V_{us}| \sim \sin\theta_C$. With this parametrization, the hierarchy of transition strength becomes clear: the diagonal elements are of the order of 1 corresponding to transitions inside the same family; transitions between the first and second families are of order λ, between second and third λ^2 and between the second and the third families λ^3. The only matrix elements allowing for CP violation are V_{ub} and V_{td}, since they contain a complex phase[1], however they are suppressed by a factor $\lambda^3 \sim 0.01$ which means that they provide a very small amount of CP violation and they are hard to measure.

From the unitarity of the CKM matrix $V_{\mathrm{CKM}} V_{\mathrm{CKM}}^{\dagger} = \mathbb{1}$, two relations are obtained:

$$\sum_{j=1}^{3} V_{ij} V_{kj}^{*} = \delta_{ik} \quad \text{and} \quad \sum_{j=1}^{3} V_{ji} V_{jk}^{*} = \delta_{ik}. \tag{2.26}$$

For the case $i \neq j$, these six relations can be represented in the (ρ, η) complex plane as triangles and their areas quantify the amount of CP violation. These 6 triangles have all the same surface, which is not zero if CP is not conserved. Nevertheless, the triangles have very different shapes due to the different orders of magnitude of the V_{ij} coefficients, the only not-flat triangles are those including $\mathcal{O}(\lambda^3)$ elements:

$$\begin{aligned} V_{ud}V_{td}^{*} + V_{us}V_{ts}^{*} + V_{ub}V_{tb}^{*} = 0 \\ V_{ud}V_{ub}^{*} + V_{cd}V_{cb}^{*} + V_{td}V_{tb}^{*} = 0 \end{aligned} \tag{2.27}$$

The triangles are usually represented as a function of the transformed coordinates $\bar{\rho} = (1-\lambda^2/2)\rho$ and $\bar{\eta} = (1-\lambda^2/2)\eta$, one of them is shown in Fig. 2.2, where the angles shown are defined as:

$$\alpha = \mathrm{Arg}\left(-\frac{V_{td}V_{tb}^{*}}{V_{ud}V_{ub}^{*}}\right) \tag{2.28}$$

$$\beta = \mathrm{Arg}\left(-\frac{V_{cd}V_{cb}^{*}}{V_{td}V_{tb}^{*}}\right) \tag{2.29}$$

$$\gamma = \mathrm{Arg}\left(-\frac{V_{ud}V_{ub}^{*}}{V_{cd}V_{cb}^{*}}\right) \tag{2.30}$$

At present, the CKM matrix elements account for the CP violation observed experimentally. The status of the CKM measurements as for 2019 is shown in Fig. 2.2 (right). However, the amount

[1] CP violation implies that a complex phase is present in the decay amplitudes, as a consequence a particle and its antiparticle decay differently. For a $N \times N$ matrix there are $(N-1)(N-2)/2$ complex phases, hence if only 2 generations existed ($N = 2$), there would be no room for CP violation.

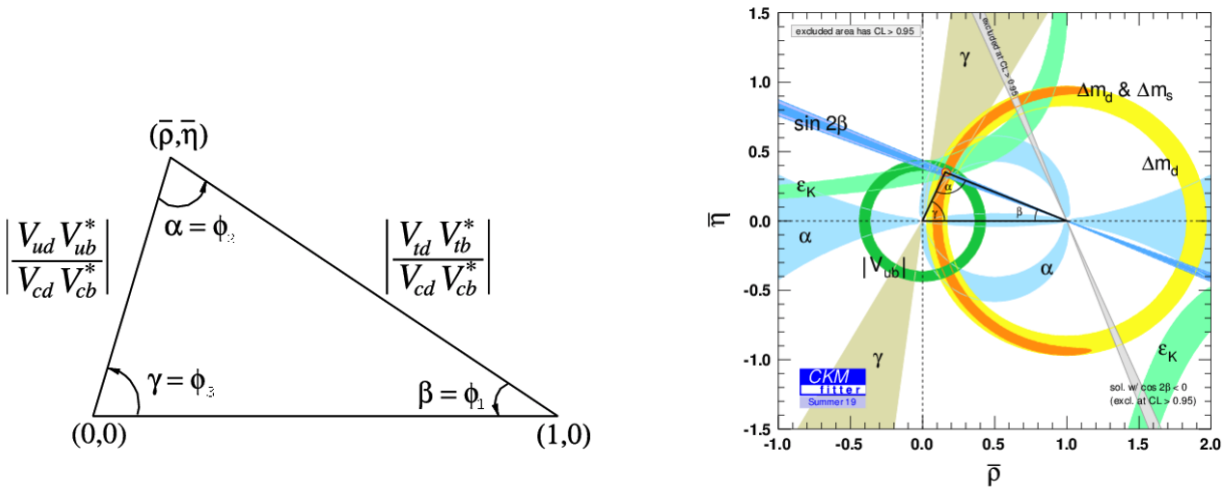

Figure 2.2: Left: illustration of the unitarity triangle. Right: global fit of the CKM triangle in black, based on the experimental constraints in colours, from the CKMfitter collaboration [39, 40].

of *CP* violation observed is really small and it cannot explain the large predominance of matter on anti-matter in the Universe as it was hoped for. Indeed, *CP* violation is one necessary condition needed to explain the observation of such an asymmetry between matter and anti-matter. The origin of this asymmetry stays unrevealed and it is one of the open questions of the SM (Sec. 2.2.2). For the neutrino sector, there exists an equivalent matrix called the Pontecorvo-Maki-Nakagawa-Sakata (PMNS) matrix explaining the neutrino oscillations, observed experimentally by Super-Kamiokande and SNO [41][42]. Up to now, no *CP* violation has been observed in the neutrino sector.

Beside the electroweak forces, the SM Lagrangian actually allows for CP violation in strong interactions, however it has never been measured experimentally. The terms breaking CP symmetry in the Lagrangian are proportional to the QCD angle θ, which has been tightly constrained to be smaller than 10^{-10}, by the measurement of the electric dipole moment of the neutron [1][43]. The reason why this angle is so small it is not understood and it is known as the "strong CP problem".

2.2.2 Open questions of the Standard Model

Although the SM is a very corroborated and successful theory, there are few questions which remain unanswered. Some of them have been mentioned in the previous sections: the strong *CP* problem, which requires an unjustified fine tuning of the strong angle θ; the incompatibility with the general relativity theory describing the gravitational force; the origin of the differences between fermion masses; the origin of neutrino masses; the very small amount of *CP* violation. Indeed, the universe is mainly composed of matter, however within the SM, matter and antimatter should be present in a similar amount and this prediction contradicts the experimental observations. The *CP* violation could account for this, however the observed violation until now within the SM is too small to justify such a difference. Along with those problem there are few other open questions: the SM account for only 4.5 % of the

[1]The presence of a *CP* violation term for the strong interactions in the Lagrangian would produce a non zero neutron electric dipole moment.

visible world, the rest seems to interact weakly or not interact at all with the SM fields and it is called dark matter, representing 26 % of the visible world. The remaining 69%, goes in the so-called dark energy, responsible for the accelerating expansion of the universe. Furthermore, the SM has a large number of free parameters, 19 in total, which can only be measured experimentally, for instance the quark and lepton masses. The Higgs mass as well is an open problem, since it gets very large corrections which must be compensated with a fine tuning of the bare mass. This is known as the hierarchy problem. These open questions are at the center of the current research program in particle physics and they motivate the search for physics beyond the SM, also called New Physics (NP). There are two ways to address them, either performing "direct searches", going to the highest possible energy to find new particles; or "indirect searches", performing precision measurements at low-energy by looking at virtual processes where new particles could contribute and shift the results from the SM prediction. These second methods are widely used in flavour physics and at LHCb, where the most powerful searches involve very suppressed, even forbidden, processes so that even a tiny deviation could reveal the presence of NP effects. Recently, two major results have been produced by LHCb using these techniques. The first one is the measurement of the rare decay $B_s^0 \to \mu^+\mu^-$, which is predicted to be very small in the SM and which has been measured to be $(3.09^{+0.46+0.15}_{-0.43-0.11}) \times 10^{-9}$ [44]. There is a set of theories predicting a significant modification of this branching ratio making it a smoking gun for NP searches; from now on, any new theory will have to account for this new measurement which is compatible with the SM. The second NP measurement consists in probing the lepton-flavour-universality (LFU) predicted by the SM, i.e. the interaction couplings are independent of the flavour of the lepton involved. In order to do so, LHCb studied the decay of B^+ mesons to muons and to electrons, namely $B^+ \to K^+e^+e^-$ and $B^+ \to K^+\mu^+\mu^-$. If their couplings are different, then the ratio of the two decays should be different from 1, meaning that new particles contribute to the virtual loop describing the transition $b \to s\ell^+\ell^-$. The ratio is measured to be $R_K = 0.846^{+0.044}_{-0.041}$ [45], being the most precise measurement to date and is 3.1σ away from the SM prediction, thus this is a new evidence for the violation of lepton flavour universality, which need to be confirmed by further measurements. Another interesting sign for new physics came from the measurement of the anomalous magnetic dipole moment of muons performed by the Fermilab experiment $g-2$. For charged leptons, the magnetic moment g should be close to 2, and the deviation from 2 is due to higher order QED corrections which are very precisely predicted by the SM, see Sec. 2.4. This recent measurement [46] resulted in a tension between experiment and theory at 4.2 standard deviation. These recent results, along with the still unanswered questions listed here, point to the fact that the SM theory is not complete and flavor physics is a very powerful tool to search for new physics.

2.3 Charmed baryons and their polarization

The quark model classifies hadrons in terms of their valence quarks properties, for instance their quantum numbers, flavour or colour. It successfully describes a large number of light hadrons, containing the u and d quarks. It was proposed, independently, by two physicists: M. Gell-Mann [47] and G. Zweig [48]. The model is constructed starting from the representations of flavour SU(3) and the Pauli exclusion principle, which states that two identical fermions cannot occupy the same quantum state

with the same quantum numbers. The quark model is also known as the "Eightfolds Way", after the group representations of the mesons in an octet plus one singlet. The 3 quark flavours lie in the fundamental representation[1] (**3**) of SU(3), and the antiquark in the complex conjugate representation ($\overline{\mathbf{3}}$); the nine states of a pair of quark and anti-quark can be decomposed in one trivial representation, the singlet (**1**) and the adjoint representation, the octet (**8**). The decomposition can be written in group theory as: $\mathbf{3}\otimes\overline{\mathbf{3}}=\mathbf{8}\oplus\mathbf{1}$. This work aims at measuring the Λ_c^+ baryon properties, for this reason only the quark model for baryon will be described in detail and the meson case will not be treated here, although it relies on very similar considerations.

Baryons are made of three quarks and as a three-body system it can have two angular momenta (l and l') between the 2 pairs of particles. Let's start with the easier case where $l=l'=0$, the ground state of a baryon for which the angular momentum of the baryon depends entirely on the spin of the three constituent quarks. Quarks have spin 1/2 thus they can occupy two states, spin up $\uparrow$, with spin projection $+1/2$ or spin down $\downarrow$, with spin projection $-1/2$, giving 8 possible combinations: 4 *symmetric* combinations, for which the interchange of two particles leaves the state unchanged, and 4 partially *antisymmetric*, where the interchange of two particles flip the sign of the state.

$$\left.\begin{aligned}\left|\tfrac{3}{2}\tfrac{3}{2}\right\rangle &= (\uparrow\uparrow\uparrow)\\ \left|\tfrac{3}{2}\tfrac{1}{2}\right\rangle &= (\uparrow\uparrow\downarrow+\uparrow\downarrow\uparrow+\downarrow\uparrow\uparrow)/\sqrt{3}\\ \left|\tfrac{3}{2}-\tfrac{1}{2}\right\rangle &= (\downarrow\downarrow\uparrow+\downarrow\uparrow\downarrow+\uparrow\downarrow\downarrow)/\sqrt{3}\\ \left|\tfrac{3}{2}-\tfrac{3}{2}\right\rangle &= (\downarrow\downarrow\downarrow)\end{aligned}\right\}\quad \text{Fully symmetric, spin } \frac{3}{2},\ \psi_s \tag{2.31}$$

$$\left.\begin{aligned}\left|\tfrac{1}{2}\tfrac{1}{2}\right\rangle_{12} &= (\uparrow\downarrow-\downarrow\uparrow)\uparrow/\sqrt{2}\\ \left|\tfrac{1}{2}-\tfrac{1}{2}\right\rangle_{12} &= (\uparrow\downarrow-\downarrow\uparrow)\downarrow/\sqrt{2}\end{aligned}\right\}\quad \text{Antisymmetric in particle 1 and 2 , spin } \frac{1}{2},\ \psi_{1\leftrightarrow 2} \tag{2.32}$$

$$\left.\begin{aligned}\left|\tfrac{1}{2}\tfrac{1}{2}\right\rangle_{23} &= \uparrow(\uparrow\downarrow-\downarrow\uparrow)/\sqrt{2}\\ \left|\tfrac{1}{2}-\tfrac{1}{2}\right\rangle_{23} &= \downarrow(\uparrow\downarrow-\downarrow\uparrow)/\sqrt{2}\end{aligned}\right\}\quad \text{Antisymmetric in particle 2 and 3 , spin } \frac{1}{2},\ \psi_{2\leftrightarrow 3} \tag{2.33}$$

The two-dimensional representation of SU(2) is thus decomposed into the direct sum of 1 four-dimensional representation and 2 two-dimensional representations as: $\mathbf{2}\otimes\mathbf{2}\otimes\mathbf{2}=\mathbf{4}\oplus\mathbf{2}\oplus\mathbf{2}$, or using spin labels $\frac{1}{2}\otimes\frac{1}{2}\otimes\frac{1}{2}=\frac{3}{2}\oplus\frac{1}{2}\oplus\frac{1}{2}$. Beside spin, a baryon is described by other quantum numbers, colour and flavour, and the total wave function is a product of 4 sub-wave functions:

$$\psi_{\text{baryon}}=\psi_{\text{spin}}\,\psi_{\text{flavour}}\,\psi_{\text{colour}}\,\psi_{\text{space}} \tag{2.34}$$

where ψ_{space} describes the spatial part, ψ_{colour} and ψ_{flavour} the colour and flavour parts and ψ_{spin} the spin part. The possible combinations of each component of the wave function are strongly reduced by the conditions imposed by the spin statistic theorem, which states that half-integer-spin particles (fermions) have an antisymmetric wave function and integer spin particles (bosons) a symmetric one.

[1] More details on group theory and its applications to particle physics can be found in Ref. [49] [50].

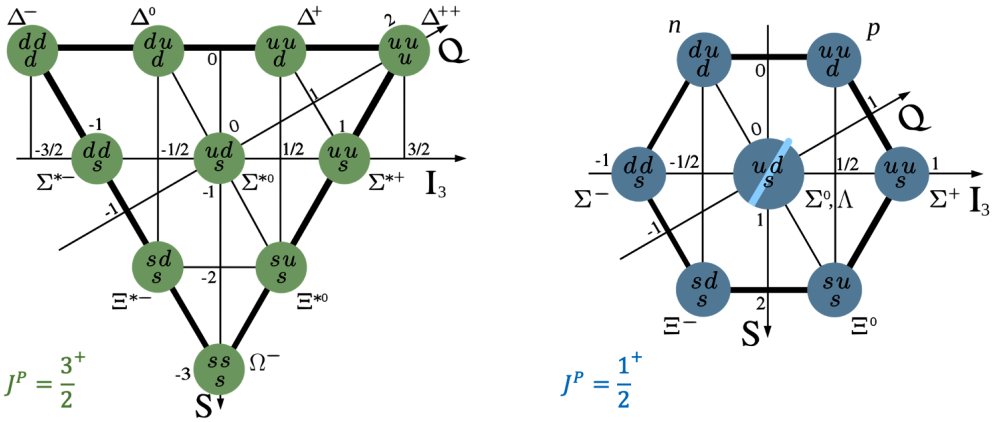

Figure 2.3: The SU(3) multiplet formed by the three quarks u, d and s. Left: the decuplet. Right: the octet. Adapted from Refs. [51] [52].

It follows that the total wave function of Eq. 2.34 must be antisymmetric under the exchange of any pair of quarks. For the ground states, with zero angular momentum, the spatial wave function is symmetric. The colour wave function is the same for all baryons, this is a consequence of the fact that only colourless combinations of quarks exist and thus the combination of the three colours can only exist as a colour singlet state[1],

$$\psi_{\text{colour}} = \frac{1}{\sqrt{6}}(RGB - RBG + BRG - BGR + GBR - GRB) \tag{2.35}$$

which is antisymmetric. Thus the product of the spatial and space parts is always antisymmetric for the ground state baryons. This implies that the remaining product of ψ_{spin} and ψ_{flavour} has to be symmetric, in order to obtain an antisymmetric total wave function. The explicit form for the possible spin states ψ_s, $\psi_{2\leftrightarrow3}$ and $\psi_{1\leftrightarrow2}$ is given in Eq. 2.31. Regarding the flavour states, the 3 lightest quarks u, d and s form an approximate SU(3) symmetry. They lie in the 3 dimensional representation which can be reshuffled, as in the spin case, into a set of symmetric, antisymmetric and mixed symmetry states. In terms of group theory, the direct product of three SU(3) representations is decomposed in $\mathbf{3}\otimes\mathbf{3}\otimes\mathbf{3} = \mathbf{10}\oplus\mathbf{8}\oplus\mathbf{8}\oplus\mathbf{1}$, corresponding to one decuplet of ψ_s^f symmetric states, two octuplets with $\psi_{1\leftrightarrow2}^f$ and $\psi_{2\leftrightarrow3}^f$ states of mixed symmetry, and one singlet, with a completely antisymmetric state ψ_A^f. Combining all together, there are two possibilities to create a symmetric combination of the flavour and the spin parts. The easiest way is to combine the fully symmetric parts: $\psi_{\text{decuplet}} = \psi_s \times \psi_s^f$. This form the spin-$\frac{3}{2}$ baryon decuplet. For the mixed symmetry states, the combination of one state alone can be symmetric under the exchange of 2 particles, for instance $\psi_{2\leftrightarrow3} \times \psi_{2\leftrightarrow3}^f$ for the 2 to 3 exchange. By adding the three possibilities, $\psi_{\text{octet}} = \psi_{2\leftrightarrow3}\psi_{2\leftrightarrow3}^f + \psi_{1\leftrightarrow2}\psi_{1\leftrightarrow2}^f + \psi_{1\leftrightarrow3}\psi_{1\leftrightarrow3}^f$, the state is symmetric under the exchange of any pair of quarks, giving rise to the baryon octet. The baryon decuplet and octet obtained are shown in Fig. 2.3. Few considerations can be derived from this, for instance the corners of the decuplet contain states with identical quarks in a symmetric flavour state, hence they can only exist in the symmetric spin state $j = 3/2$. Furthermore, this classification naturally implies

[1] colours generate a SU(3) symmetry, as for flavours, but in this case it is an exact symmetry, whereas for the flavour case the symmetry is only approximate due to the differences in quark masses.

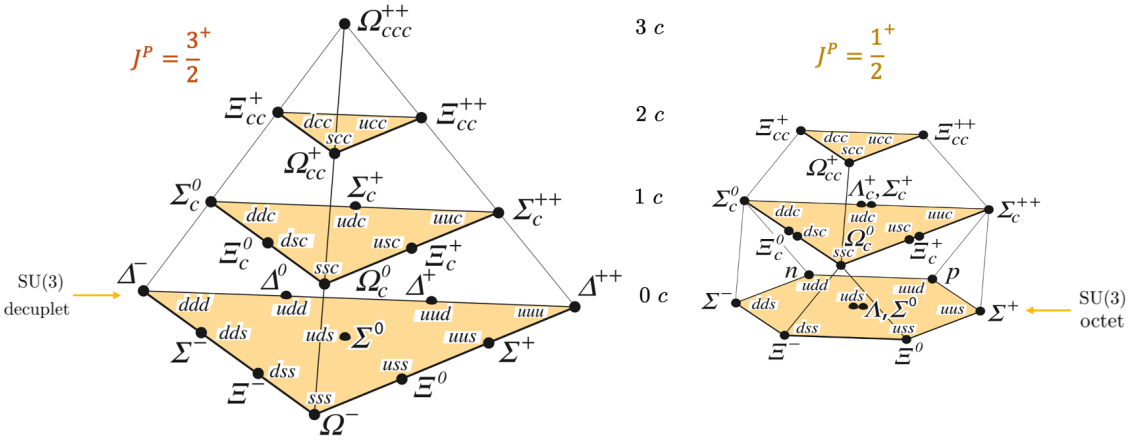

Figure 2.4: The SU(3) multiplet formed by the four quarks u, d, s and c. Left: the 20-plet $\mathbf{20}_M$. Right: the 20-plet $\mathbf{20}_S$. Adapted from Ref. [11].

an ordering based on the charge Q, strangeness S and isospin projection I_3, also shown in Fig. 2.3.

The multiplets classification considered only the three lightest quarks, which form an approximate SU(3) symmetry. The addition of the c quark would require the extension of the flavour symmetry to SU(4) and since the c mass is large, this would break the symmetry even more. However the approximate SU(4) symmetry can give predictions for charmed baryon spectrum up to corrections of the order of 20 % [11].

Let's describe first charmed baryons with only one charm quark. Single-charmed baryons $q_1 q_2 c$ can be decomposed as a di-quark pair plus a charm quark. The two light quarks are SU(3) representations decomposed as $\mathbf{3} \otimes \mathbf{3} = \mathbf{6} \oplus \overline{\mathbf{3}}$, hence they can either form a spin-0 colour antitriplet antisymmetric which can combine with the c to form $1/2^+$ states, or a spin-1 colour antitriplet that is symmetric, combined with the c into $1/2^+$ or $3/2^+$ states. The wave function for the $\overline{\mathbf{3}}$ charmed baryons with $J^P = 1/2^+$ is composed of a flavour part and a spin part which are both antisymmetric under the exchange of light quark flavours (see Eq. 2.32 for the spin part):

$$\left|\Lambda_c^+; \frac{1}{2}, +\frac{1}{2}\right\rangle = \frac{1}{2}\left(u_\uparrow d_\downarrow c_\uparrow - u_\downarrow d_\uparrow c_\uparrow - d_\uparrow u_\downarrow c_\uparrow + d_\downarrow u_\uparrow c_\uparrow\right) \tag{2.36}$$

$$\left|\Xi_c^+; \frac{1}{2}, +\frac{1}{2}\right\rangle = \frac{1}{2}\left(u_\uparrow s_\downarrow c_\uparrow - u_\downarrow s_\uparrow c_\uparrow - s_\uparrow u_\downarrow c_\uparrow + s_\downarrow u_\uparrow c_\uparrow\right) \tag{2.37}$$

$$\left|\Xi_c^0; \frac{1}{2}, +\frac{1}{2}\right\rangle = \frac{1}{2}\left(d_\uparrow s_\downarrow c_\uparrow - d_\downarrow s_\uparrow c_\uparrow - s_\uparrow d_\downarrow c_\uparrow + s_\downarrow d_\uparrow c_\uparrow\right) \tag{2.38}$$

where $q_\uparrow (q_\downarrow)$ indicates a quark in spin up (down) state. In order to extend the quark model representation to baryons with 2 or 3 charm quarks, quarks are rather embedded in the approximate SU(4) symmetry broken as $\mathrm{SU(4)} \to \mathrm{SU(3)} \times \mathrm{U(1)}_{\mathrm{charm}}$ and the tensor product becomes: $\mathbf{4} \otimes \mathbf{4} \otimes \mathbf{4} = \mathbf{20}_S \oplus \mathbf{20}_M \oplus \mathbf{20}_M \oplus \overline{\mathbf{4}}$, where the subscript M stand for mixed symmetry states and S symmetric states. The $\mathbf{20}_S$ representation obtained is shown in Fig. 2.4 (left); on the bottom layer there is the baryon decuplet of Fig. 2.3 and in the next one lies the single charmed baryon $\mathbf{6}$ representation, the last two layers are for the doubly and triply-charmed baryons. On the right of Fig. 2.4, the $\mathbf{20}_M$

Baryon	flavour	$SU(3)_f$ rep.	I	I_3	Mass [MeV]	Cross section [μb] Fixed target	Collider	Life-length or decay width
Λ_c^+	$[ud]c$	$\overline{3}$	0	0	2286.5 ± 0.1	10.13	758.1	$60.0 \pm 1.2\mu$m
Ξ_c^+	$[us]c$	$\overline{3}$	$\frac{1}{2}$	$+\frac{1}{2}$	2467.9 ± 0.2	0.588	65.5	$132.5 \pm 7.8\mu$m
Ξ_c^0	$[ds]c$	$\overline{3}$	$\frac{1}{2}$	$-\frac{1}{2}$	2470.9 ± 0.3	0.510	65.6	$33.6 \pm 3.6\mu$m
Σ_c^{++}	uuc	6	1	+1	2454.0 ± 0.1	0.863	42.0	1.9 ± 0.1MeV
Σ_c^+	$\{ud\}c$	6	1	0	2452.9 ± 0.4	0.697	42.2	< 4.6MeV
Σ_c^0	ddc	6	1	−1	2453.8 ± 0.1	0.461	41.6	1.8 ± 0.1MeV
$\Xi_c'^+$	$\{us\}c$	6	$\frac{1}{2}$	$+\frac{1}{2}$	2578.4 ± 0.5	0.083	6.3	–
$\Xi_c'^0$	$\{ds\}c$	6	$\frac{1}{2}$	$-\frac{1}{2}$	2579.2 ± 0.5	0.072	6.6	–
Ω_c^0	ssc	6	0	0	2695.2 ± 1.7	0.028	3.0	$80.3 \pm 10\mu$m
Ξ_{cc}^{++}	ccu	3	$\frac{1}{2}$	$+\frac{1}{2}$	3621.4 ± 0.8	$< 10^{-4}$	$\sim 10^{-3}$	$76.7 \pm 10\mu$m
Ξ_{cc}^+	ccd	3	$\frac{1}{2}$	$-\frac{1}{2}$	3518.9 ± 0.9	$< 10^{-4}$	$< 10^{-3}$	–
Ω_{cc}^+	ccs	3	0	0	–	$< 10^{-4}$	$\sim 10^{-3}$	–

Table 2.8: Properties of singly and doubly charmed baryons. The flavour functions are defined by the two lightest quarks as $[q_1q_2] \equiv \frac{1}{\sqrt{2}}(q_1q_2 - q_2q_1)$ (antisymmetric) and $\{q_1q_2\} \equiv \frac{1}{\sqrt{2}}(q_1q_2 + q_2q_1)$ (symmetric). The explicit wave function for the first three charmed baryons is given in Eq. 2.36. The production cross sections are obtained with a Pythia simulation for the LHC fixed-target mode at $\sqrt{s} = 110\,\text{GeV}$ and in collider mode at $\sqrt{s} = 13\,\text{TeV}$, from [3].

representation is shown, the bottom is the SU(3) light baryon octet and the subsequent layer the $\overline{\mathbf{3}}$ and **6** representations derived above, where the Λ_c^+ baryon lies. Properties of single and double charmed baryons are summarized in Tab. 2.8. The multiplet classification shown above holds only for the ground states. For the excited states, *i.e.* baryons with angular momentum different from zero, it is more tricky. Baryons can get radial or orbital excitations, on top of that there can be a further splitting due to spin-spin or spin-orbit couplings, giving rise to a spectrum of possible excited baryons which are studied experimentally. For a complete review of charmed baryons physics, see [53].

2.3.1 Baryon polarization

The rich structure of baryons, composed of three fermions, allows for different configurations for the spin of the constituents and their orbital angular momentum. The mechanism responsible for the alignment of the spin, and the consequent emergence of a polarization, is the subject of extensive research programs. Experimentally, more and more polarization measurements for baryons appeared to give intriguing results, not explained by the theory. In general, the information on the polarization is extracted by looking at the angular distribution of weak decay products, which depends on both the original baryon polarization and the parity violating decay asymmetry. For instance for the Λ_c^+ baryon, the angular distribution for the two body decay $\Lambda_c^+ \to BP$ (with B a baryon and P a pseudoscalar meson) in the Λ_c^+ rest frame is

$$\frac{1}{N}\frac{dN}{d\cos\theta} = \frac{1}{2}(1 + \alpha P \cos\theta) \tag{2.39}$$

where P is the Λ_c^+ polarization projection, θ is the angle between the polarization axis and the final baryon B direction, and α is the decay-asymmetry parameter. This equation holds for a longitudinally (along the direction of motion) polarized Λ_c^+. On the one hand, the asymmetry parameter α is

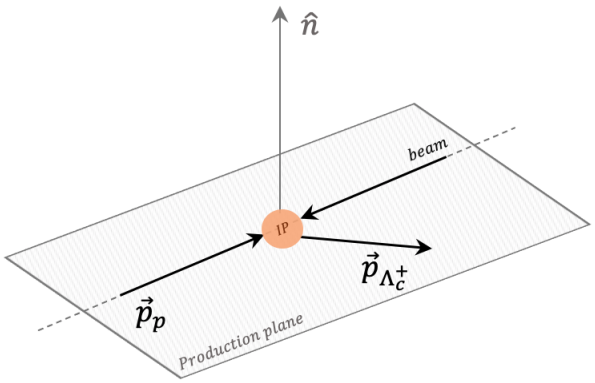

Figure 2.5: Direction of the production polarization for a Λ_c^+ produced via strong interaction at the LHC, where $\vec{p}_p$ and $\vec{p}_{\Lambda_c^+}$ are the proton (belonging to the beam) and Λ_c^+ momenta in the laboratory frame.

independent of the production conditions and it represents the asymmetry between the parity violating and the parity conserving amplitudes of the decay. This means that if the decay conserves parity, α will be null and the angular distribution would be flat, preventing the polarization measurement. The asymmetry is non zero for decays induced by parity violating interactions and the sensitivity to the polarization depends on the value of α, the bigger is α the higher is the sensitivity. On the other hand, the polarization depends strictly on the production mechanism and consequently on the experiment, that is to say it depends on the beam type, the collision mode (fixed-target or not), the parent decay chain, the center-of-mass energy of the system. For baryons produced via parity conserving interactions, strong or electromagnetic, the polarization vector $\vec{P}$ must be perpendicular to the production plane, see Fig. 2.5. This constraint is a consequence of symmetry considerations as explained in the following.

For parity symmetric interactions, the Lagrangian is invariant under the action of the parity operator P, consequently the transition matrix $\mathcal{T}$ describing the process should be invariant too. The matrix $\mathcal{T}$ can be always decomposed in a parity-even and a parity-odd part, $\mathcal{T} = \mathcal{T}^{P_+} + \mathcal{T}^{P_-}$, and since parity reverses momenta, the momentum dependence of the transition amplitudes will guide the behaviour of the matrix element under the action of parity. Given a generic transformation described in term of momenta $\vec{p}$ and spin $\vec{S}$ by a matrix $\mathcal{A}(\vec{p}_i, \vec{S}_i)$, in order to conserve parity, $\mathcal{A}$ must satisfy:

$$\mathcal{A}(\vec{p}_i, \vec{S}_i) = \mathcal{A}(-\vec{p}_i, \vec{S}_i). \tag{2.40}$$

This implies that odd terms combining $\vec{p}$ or $\vec{S}$ are not allowed and must have zero expectation value, for instance $\vec{S} \cdot \vec{p}$ or $\vec{p}_1 \cdot (\vec{p}_2 \times \vec{p}_3)$ [54]. For the Λ_c^+ production, there are few vectors available: the (beam) proton momentum $\vec{p}_p$, the baryon direction $\vec{p}_{\Lambda_c^+}$ and the polarization vector $\vec{\mathcal{P}}$, giving the spin direction. The only scalar term allowed in parity conserving decays would be $\vec{\mathcal{P}} \cdot (\vec{p}_p \times \vec{p}_{\Lambda_c^+})$, which requires the polarization to be perpendicular to the production plane defined by $\vec{p}_p$ and $\vec{p}_{\Lambda_c^+}$. Thus the polarization vector has no component in the production plane and its projection is maximized along

the direction $\hat{n} = \hat{p}_p \times \hat{p}_{\Lambda_c^+}$ [1]. Equation 2.39 gets more complicated when considering several two-body decays happening in sequence. This is the case for the three-body decay $\Lambda_c^+ \to pK^-\pi^+$, which can be decomposed in subsequent decays passing through an intermediate resonant state, for each pair of final state particles. In this case, there are multiple asymmetry parameters and the different chains interfere between each other, hence the angular distribution is not trivial anymore. The development of the equations for the $\Lambda_c^+ \to pK^-\pi^+$ case is the subject of Chapter 5. It is important to notice that in order to observe a parity violating transition producing an asymmetry $\vec{p} \to -\vec{p}$, the parity-odd part $\mathcal{T}^{P-}$ alone is not sufficient since the amplitude of the process will be the squared modulus of it. Hence the presence of both the parity conserving and the parity violating terms are necessary and the asymmetry is generated by the interferences between them; this is strictly linked to the meaning of the α asymmetry parameter of Eq. 2.39 and it will be further discussed for the specific case of the $\Lambda_c^+ \to pK^-\pi^+$ decay.

Experimental status

The polarization of different kinds of baryons has been measured in a variety of experiments. The measurements are usually shown as a function of the center of mass energy E^*, the fraction of incident proton momentum carried by the baryon in the center of mass system x_F or the transverse momentum p_T. The first measurements were performed in fixed-target experiments focusing on hyperons[2] Λ^0. In 1976, the Λ^0 baryon polarization has been measured in a Fermilab experiment [55] sending 300 GeV protons on a Beryllium target, the result showed an increasing polarization with p_T, up to 28%: this was the first unexpected result. Two years later, the same experiment with 400 GeV protons [56] has confirmed the previous result, measuring a polarization of 24% at $p_T = 2.1\,\text{GeV}/c$ and more intriguing, the anti-hyperon $\bar{\Lambda}^0$ polarization was found to be zero. These results triggered the interest on baryon polarization and other hyperons and anti-hyperons have been studied in fixed-target experiments with different targets (Cu, Be) with proton beams up to 940 GeV, and polarization ranging from 0 to 28% [57, 58, 59, 60, 61, 62, 63, 64, 65, 66, 67, 68]. The experimental results are summarized in Table 2.9 to give an idea of the trend depending of the type of baryon and the energy of the proton beam used.

The characteristics that seem to emerge from those measurements are: an increasing polarization with increasing transverse momentum, a (not well-defined) dependence on the target type and a different polarization between hyperon and anti-hyperon. The latter was explained at the time, see for instance [70], by arguing that baryons are more easily produced from the valence quarks of the proton than anti-baryons, which need antiquarks from the sea, and for this reason antibaryons are expected to be produced unpolarized. However, at a later stage, a similar polarization was measured for Ξ^+ and Ξ^- [71][72], contradicting this naive explanation which predicts zero polarization for all anti-baryons. When looking at heavier baryons, less measurements have been performed since, due to their higher mass, they are harder to produce. For the Λ_c^+ baryon, the first measurement was performed in 1992 at CERN-SPS, in the NA32 experiment colliding 230 GeV/c π^- on a Cu target, they collected 121 $\Lambda_c^+ \to pK^-\pi^+$ decays and found the product αP to be $-0.65^{+0.22}_{-0.18}$ for a $p_T > 1.1\,\text{GeV}/c$

[1] The "hat" notation indicate a unit vector, thus $\hat{p} = \vec{p}/|\vec{p}|$.

[2] Hyperons are baryons with at least one strange quark and no charm, bottom nor top quark, belonging to the baryon octect and decuplet shown in Fig. 2.3.

Baryon	System	Beam energy [GeV]	Result	p_T range [GeV/c]	Ref.
Λ^0	pBe	300	18%	1.5	[55]
	pBe	400	24%	2.1	[56]
	pC and pW	920	~ 0	~ 0.8	[63]
	pN	450	up to 0.29%	0.86	[64]
$\bar{\Lambda}^0$	pBe	400	0	up to 1.2	[56]
	p-X	400	0	up to 2.4	[60]
Ω^-	pBe	800	~ 0	[0.5, 1.3]	[61]
Σ^+	pCu	800	16%	1.0	[62]
Ξ^0	pCu and pBe	400	$\sim 20\%$	1.6	[69]
Ξ^+	pBe	800	up to 0.09%	0.76	[67]
Ξ^-	pBe	400	up to 10%	1.21	[65]
	pCu	400	up to 0.07%	0.63	[66]
	pBe	800	up to 0.1%	>0.8	[68]

Table 2.9: Summary of hyperon polarization measurements at different energies and targets. The polarization results cited are approximate and without the uncertainties, more details about the measurements can be found in the references given in the last column. This list is non exhaustive.

[73]. Then in 1999, the E791 experiment studied the same decay for 500 GeV/c pion-nucleus collisions, with as target five thin target foils (one platinum, four diamond), with 946 ± 38 reconstructed decays. The results showed an increasingly negative polarization as a function of p_T^2, the highest polarization being -0.67 ± 0.15 in the bin $1.24 < p_T^2 < 5.20$ GeV$^2/c^2$, the results are shown in Fig. 2.6 (right). The polarization dependence as a function of p_T is well described by the model proposed in [74], where the spin dependent fragmentation functions are calculated in a quark-diquark model. However the formalism used in the E791 experiment was incomplete, as explained in Chapter 5, furthermore they mixed baryons and anti-baryons which are expected to have different polarizations, as in the Λ^0 case, since the production mechanisms involved are different. Recently, in 2008, data from the E831 experiment with photons beam, have been re-analyzed to measure Λ_c^+ polarization from the two body decays: $\Lambda_c^+ \to \Lambda^0 \pi$ and $\Lambda_c^+ \to K_s p$. A small polarization, consistent with zero, was found for the photoproduced baryons and antibaryons in the range $p_T < 4$ GeV/c [75].

The hyperon polarization has been measured in e^+e^- colliders at the Belle and BESIII experiments. In the first, a non zero Λ and $\bar{\Lambda}$ polarization was measured for the first time in a collider experiment, at a center of mass energy of 10.58 GeV [76]. In the second experiment, the $\Lambda\bar{\Lambda}$ baryons are produced in an entangled state from $e^+e^- \to J/\psi \, \Lambda\bar{\Lambda}$; a polarization up to 25% was measured [77].

Regarding pp colliders, there are few measurements, however in the absence of any polarization mechanism at high center-of-mass energy collisions, polarization is expected to be zero since it is diluted in the decay and in the hadronization processes. At $\sqrt{s} = 53$ and 62 GeV, a mean Λ polarization of $-(0.357 \pm 0.055)$ was measured at the CERN intersecting storage ring [78]. However, the ATLAS experiment measured Λ and $\bar{\Lambda}$ polarizations, at $\sqrt{s} = 7$ TeV, to be compatible with zero for $0.8 < p_T < 15$ GeV/c [79]. This result nicely compare with other measurements, see Fig. 2.6, giving an idea of the dependence of the hyperon polarization as a function of the variable Feynman $x_F = p_z/p_{beam}$.

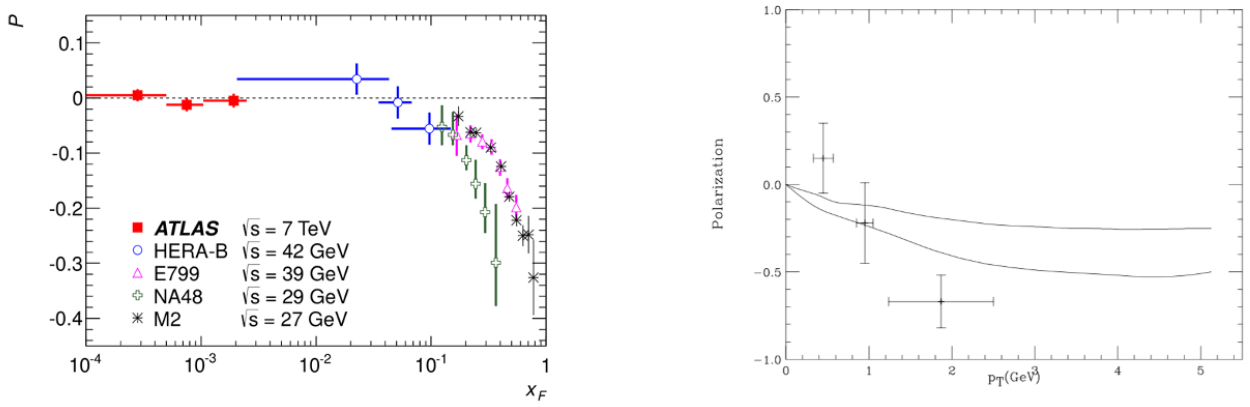

Figure 2.6: Left: comparison of different experimental results for the Λ transverse polarization as a function of x_F, from [79]. Right: Λ_c^+ polarization as a function of the p_T obtained by the E791 experiment, the two full lines are the theory prediction from [74].

The Λ_b^0 polarization was also measured at 7, 8 and 13 TeV by LHCb [80, 81], ATLAS [82] and CMS [83], all measurements are compatible with zero.

Baryon polarization has been also measured in ion-ion collisions at the STAR experiment, they measured a Λ polarization component in the beam direction in Au-Au collisions at $\sqrt{s_{\rm NN}} = 200$ GeV [84]. The polarization was found to increase in more peripheral collisions, and shows no strong transverse momentum dependence at $p_T > 1$ GeV/c. The ALICE collaboration measured a Λ and $\bar{\Lambda}$ polarization compatible with zero in Pb-Pb collisions at $\sqrt{s_{\rm NN}} = 2.76$ and 5.02 TeV [85]. These result are interpreted theoretically in [86][87], however the heavy ions case is very different from the pp or fixed-target one, since the production process is influenced by the dynamics of Quark Gluon Plasma that forms in heavy-ion collisions.

There are no straightforward conclusions to draw from these experimental results and the only theory prediction available for heavy baryons is [74], published in 2000. For the hyperon case, a first prediction aiming at describing the hyperon polarization measured in fixed-target data using spin fragmentation function is given in [88], published in 2001. Although fixed-target results did not show an energy dependence, the ATLAS result, shown in Fig. 2.6, indicates a dependence on the energy for the Λ polarization. In general, the polarization, when present, seems to increase with the $|p_T|$ and it is expected to be small at LHC energies. What is clear is that more measurements are needed to better constrain and understand the polarization behaviour. In this work, the polarization of the Λ_c^+ baryon will be measured in pp collissions at a center-of-mass energy of $\sqrt{s} = 13\,\text{TeV}$, adding one measurement to help understanding the origin of baryon polarization.

2.4 Magnetic and electric dipole moments to probe new physics

The magnetic dipole moment (MDM) μ of a particle is a property induced by the spin. For spin $S = 1/2$ particles the magnetic moment μ is, in natural units $\hbar = c = 1$,

$$\vec{\mu} = \frac{g}{2}\frac{q}{2m}\vec{S} \quad \text{and} \quad \mu = \frac{g}{2}\frac{q}{2m} \tag{2.41}$$

where q is the electric charge of the fermion, m is its mass and g is the gyromagnetic factor, also known as g-factor. At the classical level, $g = 2$, however quantum corrections from loop effects can modify this value. The anomalous magnetic moment is defined as $a_p \equiv \frac{g-2}{2}$, where the subscript p indicates the particle, and is commonly used to quantify the higher order contributions, which are very precisely calculated by QED. Any deviation of a_p from the SM prediction would indicate the presence of NP effects. The magnetic moments of the electron and the muon have been measured very precisely: $g_e/2 = 1.00115965218073(28)$ [89] and $a_\mu = 116592061(41) \times 10^{-11}$ [90]. The theoretical predictions are also computed with a very good accuracy, resulting in a 4.2σ tension between theory and experiment for the muon magnetic moment. This is one of the most significant evidence for new physics as of today.

Moving to composite particles, such as baryons, their magnetic moment can be predicted, within the quark model, starting from the magnetic moment of the constituents. The magnetic moment of a baryon $|B\rangle$ is thus:

$$\mu_B = \langle B|(\vec{\mu}_1 + \vec{\mu}_2 + \vec{\mu}_3) \cdot \vec{S}|B\rangle = \sum_i \langle B| \frac{g_i}{2} \frac{q_i}{2m_i} |B\rangle \tag{2.42}$$

where the sum runs over the flavour of the quarks composing the baryon. For instance, the proton magnetic moment is :

$$\mu_p = \frac{1}{3}(4\mu_u - \mu_d) \quad \text{where} \quad \mu_q = \frac{g_q}{2} \frac{Q_q}{2m_q} \tag{2.43}$$

In the isospin symmetry limit $m_u = m_d = M$ and $g_u = g_d = g$, thus $\mu_p = \frac{g}{2} \frac{e}{2m_q}$, where the main uncertainty is coming from the quark mass. The proton MDM has been measured very precisely $g_p = 5.585694702(17)$ and it is different from 2 due to the substructure of the proton. Within the quark model $M = m_p/3$, thus the quark gyromagnetic factor is: $g_q = g_p/3 \simeq 1.862$, which is close to 2, indicating that the light quark (u,d) have little substructure. However it is difficult to conclude whether or not the quark g-factor is SM-like for three main reasons: one can only measure the ratio g_q/mq thus the result depends on the quark mass (reversely, assuming the classical limit $g_p = 2$ one obtains $m_q = 0.336\,\text{GeV}$ for the u or d quarks mass); differently from the lepton case, the anomalous MDM is introduced by strong interactions and it may be very large; it has been claimed that the spin of the proton is not carried by quarks but mainly by gluons. The neutron magnetic moment relates to the proton's one as:

$$\mu_n = \frac{1}{3}(4\mu_d - \mu_u) = -\frac{g_p}{2} \frac{1}{3m_q} = -\frac{2}{3}\mu_p \tag{2.44}$$

This relation between μ_n and μ_p is quark mass and g-factor independent and it is very well satisfied by the experimental measurements: $\mu_p = (2.79284734462 \pm 0.00000000082)\mu_N$ and $\mu_n = () - 1.91304273 \pm 0.00000045)\mu_N$, where μ_N is the nuclear magneton, a physical constant defined as $\mu_N = e\hbar/2m_p$. For the Λ_c^+ baryon, Eq. 2.42 translates to:

$$\mu_{\Lambda_c^+} = \langle \Lambda_c^+; \frac{1}{2}, +\frac{1}{2}|(\vec{\mu}_1 + \vec{\mu}_2 + \vec{\mu}_3) \cdot \vec{S}_z|\Lambda_c^+; \frac{1}{2}, +\frac{1}{2}\rangle \tag{2.45}$$

where $|\Lambda_c^+; \frac{1}{2}, +\frac{1}{2}\rangle$ is the Λ_c^+ wave function, explicitly given in Eq. 2.36. Let's compute each term

separately:

$$(\mu_1 S_{1z} + \mu_2 S_{1z} + \mu_3 S_{1z})|u_\uparrow d_\downarrow c_\uparrow\rangle = (\mu_u - \mu_d + \mu_c)|u_\uparrow d_\downarrow c_\uparrow\rangle \tag{2.46}$$

$$-(\mu_1 S_{1z} + \mu_2 S_{1z} + \mu_3 S_{1z})|u_\downarrow d_\uparrow c_\uparrow\rangle = -(-\mu_u + \mu_d + \mu_c)|u_\downarrow d_\uparrow c_\uparrow\rangle \tag{2.47}$$

$$-(\mu_1 S_{1z} + \mu_2 S_{1z} + \mu_3 S_{1z})|d_\uparrow u_\downarrow c_\uparrow\rangle = -(\mu_d - \mu_u + \mu_c)|d_\uparrow u_\downarrow c_\uparrow\rangle \tag{2.48}$$

$$(\mu_1 S_{1z} + \mu_2 S_{1z} + \mu_3 S_{1z})|d_\downarrow u_\uparrow c_\uparrow\rangle = (-\mu_d + \mu_u + \mu_c)|d_\downarrow u_\uparrow c_\uparrow\rangle \tag{2.49}$$

$$\tag{2.50}$$

Putting this back in Eq. 2.45 leads to

$$\mu_{\Lambda_c^+} = \frac{1}{4}\left[(\mu_u - \mu_d + \mu_c) + (-\mu_u + \mu_d + \mu_c) + (\mu_d - \mu_u + \mu_c) + (-\mu_d + \mu_u + \mu_c)\right] = \mu_c \tag{2.51}$$

meaning that the Λ_c^+ MDM is equal to the charm quark one. This results in an interesting relation between the g factor of the Λ_c^+ and of the charm quark: $g_{\Lambda_c} = \frac{q_c m_{\Lambda_c}}{m_c} g_c \simeq 0.9\, g_c$, meaning that although the Λ_c^+ has a substructure, its g-factor is very close to the c quark one. Finally, by inserting the constituent mass $m_c = m_{\Lambda_c^+} - m_u - m_d = 1.66\,\text{GeV}$, one obtains:

$$\mu_{\Lambda_c^+} = 0.37\,\frac{g_c}{2}\,\mu_N. \tag{2.52}$$

Beyond the quark model, there are few models giving a prediction for the Λ_c^+ MDM. The contribution of the light quarks (u,d) is considered to be small with respect to the charm quark one, as predicted by the heavy quark effective theory (HQET) [91][92][93]. This is because in heavy baryons with light quarks, there are two distinct scales, and the heavy quark mass ($m_c \approx 1.27\,\text{GeV}$) is much larger than the mass scale $\Lambda_{\text{QCD}} \approx 200\,\text{MeV}$ associated with the light quarks. Thus the MDM of the charmed baryon is expected to be close to the charm quark one, in agreement with the quark model prediction. The various model predictions are summarized in Tab. 2.10, no attempt to explain those models in details is done here. The latest prediction is obtained in Ref.[3], $\mu_{\Lambda_c^+} = 0.48 \pm 0.03$, where radiative charmonium decays results from BES III are used. This result is remarkable since it doesn't suffer from the charm quark uncertainty and it offers an alternative method based on experimental results. Furthermore, the result is slightly different from the majority of other theoretical predictions (especially when comparing to rows 1 to 8 in Tab. 2.10). If the precision on the radiative charmonium decays measurement is further improved, for instance at BES III or at future charm factories, this discrepancy could eventually transform in a sizeable tension. A direct measurement of the Λ_c^+ MDM would certainly help to probe these predictions and discriminate between the different models available. However this measurement is really challenging due to the very short lifetime of charmed-baryon, a proposal to perform such a measurement using bending crystals is discussed in the next section.

2.5 Measuring charmed-baryons magnetic moment

The magnetic dipole moment of a particle can be seen classically as a small magnet which will precess in the presence of an external magnetic field. The precession phenomenon is well known in quantum

nb.	$\mu_{\Lambda_c^+}[\mu_N]$	Approach	Ref.
1	0.15 ± 0.05	QCD spectral sum rule	[94]
2	0.24 ± 0.02	NNLO in the HHCPT	[95]
5	$0.33 - 0.34$	Interquark potential and Fadeev formalism	[96]
3	0.34	Independent quark model, power-law potential	[97]
4	$0.369 - 0.385$	Hyper central Coulomb plus power potential	[98]
5	$0.36 - 0.41$	5q components contributions	[99]
6	0.37	Chiral perturbation theory	[100]
7	0.38	Soliton model and chiral perturbation theory	[101]
8	0.392	SU(4) chiral constituent quark model	[102]
9	0.40 ± 0.05	Light cone QCD sum rules	[103]
10	0.411	Bag model reexamined	[104]
11	0.42 ± 0.01	Relativistic three-quark model	[105]
12	0.48 ± 0.03	Radiative charmonium decays	[3]
13	0.52	Dirac point-form dynamics	[106]

Table 2.10: Summary of existing theoretical predictions for the Λ_c^+ magnetic moment.

electrodynamics and in the non-relativistic case it is described by:

$$\frac{d\vec{S}}{dt} = \vec{\mu} \times \vec{B}^* + \vec{\delta} \times \vec{E}^* \tag{2.53}$$

where the electromagnetic fields $\vec{B}^*$ and $\vec{E}^*$ are expressed in the particle rest frame. The first term accounts for the MDM precession and second term for the electric dipole moment (EDM) δ precession. The precession frequency, or Larmor frequency, for the MDM is :

$$\omega_s = \frac{geB}{2mc} + (1-\gamma)\frac{eB}{mc\gamma} \tag{2.54}$$

where the second term is due to a relativistic correction called "Thomas precession", and all the other quantities have been previously defined. This basic physics phenomenon is exploited to measure the MDM of particles. For instance, the muon magnetic moment has been measured using this physics principle, by the (g-2) experiment at Fermilab [90]. The polarized muons are produced from the pion decay $\pi^+ \to \mu^+\nu_\mu$ and analyzed through the weak decay $\mu^+ \to e^+\nu_e\bar{\nu_\mu}$, where the positron direction follows the muon spin. The precession has to happen before the muon decay (the lifetime of a muon is 2.19×10^{-6} s), this can be achieved via a strong magnetic field of 1.45 T. The extension of this technique to charmed baryons is not trivial. Charmed baryons have a very short lifetime of order 10^{-13} s, thus, in order to make the precession happen before the decay, a much stronger magnetic field would be required. For instance, for the Λ_c^+ baryon, with a lifetime of 200 fs, the precession frequency should satisfy: $\omega_s > 5 \times 10^{12}\,\mathrm{s}^{-1}$. At the LHC center of mass energy of 13 TeV, $\gamma_{\Lambda_c^+} \approx 40$ (looking at the average Λ_c^+energy), thus using Eq. 2.54, a magnetic field $B > 5 \times 10^9$ T would be necessary to observe a sizeable precession. Knowing that the strongest magnetic field achieved in a laboratory up to now is around 45 T, it would be impossible to use a conventional magnetic field to make the Λ_c^+ precession happen before it decays. A new technique was proposed to overcome this problem, consisting in using the effective magnetic field produced inside a crystal to induce the precession of

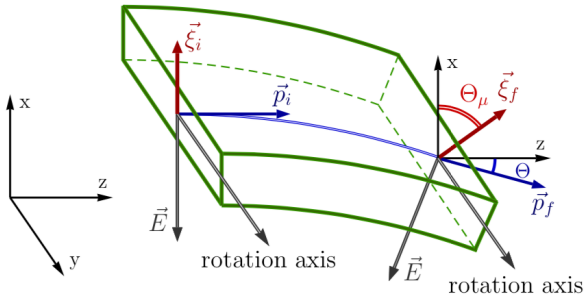

Figure 2.7: Sketch of the precession of the polarization vector (in red) in the bending crystal, the precession angle Θ_μ is also shown. From Ref.[2].

the polarization vector and measure the magnetic moment [107] [108][109].

This technique has already been used to measure the MDM of Σ^+ (uus) baryons at Fermilab [6]. The strange baryons were produced on a Cu target and have an average polarization of $12 \pm 1\%$. The precession was performed in a bent silicon single crystal providing an effective magnetic field of 45 T resulting in a precession of the polarization vector by $\approx 60°$. The Σ^+ MDM was measured to be: $(2.40 \pm 0.46_{\text{stat}} \pm 0.40_{\text{syst}})\mu_N$, which was consistent with the world average. Let's discuss the extension of this technique to the charmed baryons case.

The principle of the charmed-baryons MDM measurement is the following. First polarized baryons are produced in fixed target collision with a polarization $\vec{\xi}_i$. Then they are captured in the bent crystal where they precess under the effect of an effective magnetic field. This step is sketched in Fig. 2.7. After the crystal, the polarization has changed $\vec{\xi}_f$, the precession angle Θ_μ gives direct access to the g factor of the baryon as [110],

$$\Theta_\mu = \gamma \left(\frac{g}{2} - 1 - \frac{g}{2\gamma^2} + \frac{1}{\gamma} \right) \Theta \approx \gamma \left(\frac{g}{2} - 1 \right) \Theta \tag{2.55}$$

where $\Theta = L/R$ is the deflection angle of the baryon momentum after the channelling, L is the length and R the bending radius of the crystal. The precession angle Θ_μ can be obtained by measuring the initial and final polarization of the baryon. Hence a complete experiment for measuring the MDM of short-live baryon would require: a proton beam on a target to produce polarized baryons, a bending crystal to make the precession and an apparatus to measure the polarization of the outgoing baryons after the channelling. The initial polarization can be measured in a system which has similar conditions as the fixed-target production, in both polarization measurements the polarization is extracted using the angular distribution of Eq. 2.39.

This measurement presents many challenges and new developments are necessary. For instance, the crystal bending radius and orientation must be optimized to maximize the precession efficiency, which includes the deflection efficiency of the crystal. Then the polarization of the final and initial state baryons (along with the α parameter) should be measured with high accuracy. There are several studies ongoing on the crystal optimization and on the feasibility of such an experiment [1, 2, 3, 4, 5].

Two options are considered to perform the experiment at CERN [111]: one at IR3, which is the

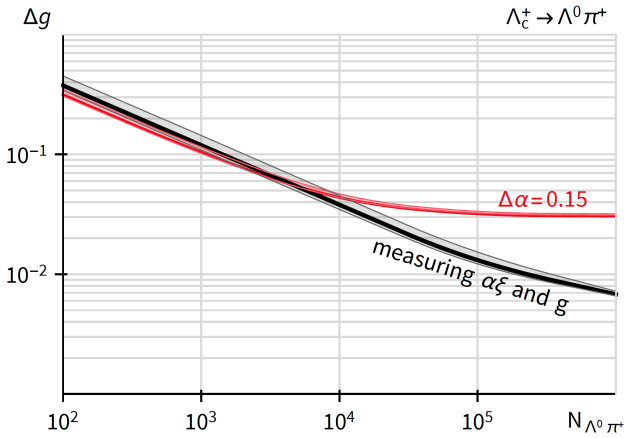

Figure 2.8: Absolute statistical error on the g-factor as a function of the number of reconstructed events N, for $\Lambda_c^+ \to \Lambda^0\pi^+$ decays and for IR3 configuration. The red line corresponds to the case where pre-measured values of the product $\alpha\xi$ are used. The black line instead, corresponds to a simultaneous measurement of $\alpha\xi$ and the g-factor. From Ref. [3].

insertion region 3 where a collimation system for momentum cleaning[1] is located, and one at IP8, which is the interaction point of the LHCb experiment. In the first case, a dedicated detector would need to be built, whereas in the second case the LHCb detector could be used to analyze the channeled Λ_c^+. In both cases the sensitivity on the baryon g factor depends on (from Ref. [3])

$$\Delta g = \sqrt{\frac{12}{\alpha_j^2 Br_j \eta_j^{\text{det}} N_{\text{def}}\, \eta_{\text{MDM}}}}, \quad \eta_{\text{MDM}} = \left\langle \xi_x^2 \gamma^2 \right\rangle \omega^2 \tag{2.56}$$

where $\alpha_j = \alpha \|\xi\|$, Br_j is the branching ratio and η_j the detector efficiency for the j decay channel; η_{MDM} is the efficiency of the target plus crystal setup. The first 3 terms in the denominator only depend on the Λ_c^+ decay channel and on the detector efficiency. The last two terms, $N_{\text{def}}\, \eta_{\text{MDM}}$, depend on the channelling efficiency of the crystal and on the properties of the accelerator used (e.g. the energy of the protons), the product of the two is the precession efficiency. The knowledge of the weak decay parameter α is crucial to achieve the desired accuracy, which is $\Delta g = 0.1$. In [3], it is shown that this same result can be more efficiently achieved by measuring the product $\alpha\xi$ simultaneously[2], if reconstructing at least 10^4 Λ_c^+ decays (after channelling), because at higher statistics the systematic error on $\Delta\alpha$ becomes dominant. This can be seen in Fig. 2.8 where the absolute statistical error on the g factor (Δg) is computed as a function of the number of reconstructed $\Lambda_c^+ \to \Lambda^0\pi^+$ decays for the two cases where the product $\alpha\xi$ is measured simultaneously with the g factor (in black) or it is taken from another experiment (red curve). For $N > 10^4$, the simultaneous measurement (black curve) leads to a smaller error on g. The measurement of the weak decay parameter and the polarization of the Λ_c^+ baryon can be performed in combination exploiting LHCb data in pp and fixed-target collisions. In this work, a model to measure Λ_c^+ polarization is built using the high statistics sample of pp collisions at $\sqrt{s} = 13$ TeV of Run 2. Then, the model built will be used in the future to extract the polarization

[1] The "momentum cleaning" consists in intercepting off-momentum particles close to the top or bottom of the RF buckets.

[2] When measuring the product $\alpha\xi$, Eq. 2.56 is slightly modified and the error on g increases.

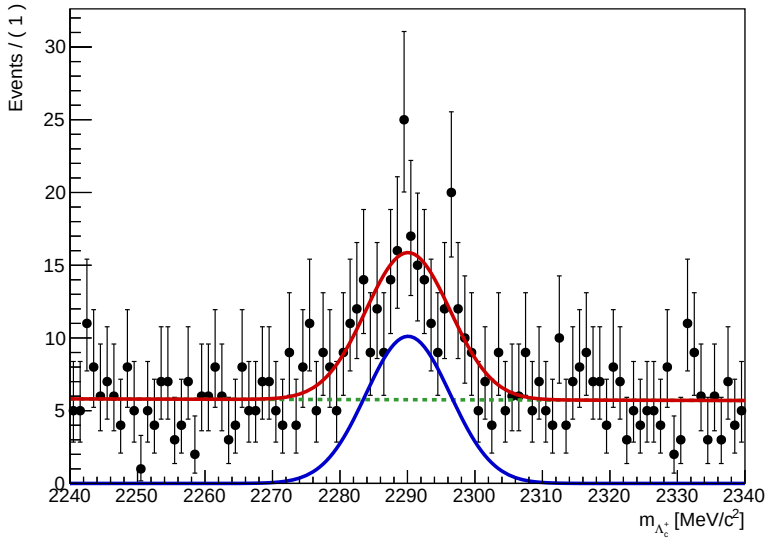

Figure 2.9: Invariant mass distribution from the reconstructed $\Lambda_c^+ \to pK^-\pi^+$ decays in the pNe sample at $\sqrt{s} = 68\,\text{GeV}$. The red line represents the total fit, the dashed-green line is the polynomial background contribution and the full blue line the Gaussian signal (from this thesis).

from the pNe fixed-target sample collected with the SMOG system at $\sqrt{s} = 68\,\text{GeV}$. The fixed-target collisions are obtained with one filled bunch in one beam and one empty bunch on the other beam; the empty bunches are alternated with full ones so the fixed-target collisions are run at the same time as proton proton collisions. This ended up to be a problem, because the bunches which were supposed to be empty for the fixed-target collisions are sometime filled with some debunched protons from the previous full bunch. These parasitic proton-proton collisions have been studied in detail here [112] where the fraction of Ghost-Charge (GC) residual contamination is given as a function of the collision zone studied, *i.e.* the z position of the primary vertex. The invariant mass plot obtained from the $\Lambda_c^+ \to pK^-\pi^+$ reconstructed decays before cleaning the GC is shown in Fig. 2.9, the number of signal events (in a 3 standard deviations window around the mean value obtained from the fit to the data) is 169 ± 23 and the number of background event 586 ± 31. This plot is obtained with a non refined selections based on the daughters PID and on the DIRA variable (defined in Sec. 6.2.1.). After applying the selections to remove GC, the number of reconstructed Λ_c^+ is significantly reduced. An optimization of the signal extraction using neural network needs to be performed to maximize the signal over noise ratio. Furthermore, the number of signal events will be increased during Run 3 thanks to the SMOG2 system (see Sec. 3.3); for instance for pAr collisions at $\sqrt{s}$ =115 GeV, 300 000 Λ_c^+ are expected. The measurement of the asymmetry parameter $\alpha_{\Lambda_c^+} = 0.715 \pm 0.005$, performed in this thesis using the pp sample at $\sqrt{s} = 13$ TeV, proves that the three-body decay $\Lambda_c^+ \to pK^-\pi^+$ is sensitive to the polarization (since the asymmetry is not zero) and that the strategy for the Λ_c^+ MDM measurement described above is valid. The model obtained in the pp analysis is currently being used to measure the polarization in the pNe sample collected by the LHCb experiment and the results will be an important input for the MDM experiments using bent crystals discussed above.

3 The LHCb experiment at the LHC

3.1 The Large Hadron Collider

The Large Hadron Collider (LHC)[113] is a circular accelerator designed to collide proton (and ion) beams. It is, to this day, the most powerful hadron accelerator for research in particle physics. It is located 100 m underground in the 26.7 km tunnel originally designed for the Large Electron-Positron collider (LEP) and built in 1984-1985. The LHC is the last step of an accelerator complex shown in Figure 3.1. The protons are first extracted from a bottle of hydrogen gas using an electric field to remove the valence electron from each hydrogen atom [1]. They are then sent to LINAC2 and accelerated up to 50 MeV using radiofrequency cavities made of an alternation of conductors charged positively and negatively, which are respectively pushing and pulling the protons to accelerate them. To keep the protons focused in a beam, small quadrupole magnets are used at this stage. From there, protons are injected in the Proton Synchroton Booster (PSB), this is a set of 4 superimposed synchrotron rings accelerating the protons to 1.4 GeV. Then they enter two successive circular accelerators: the Proton Synchrotron (PS) and the Super Proton Synchrotron (SPS), with a circumference of 628 m and 7 km, accelerating protons to 25 GeV and 450 GeV respectively. Finally the proton beams are injected in two different beam pipes circulating in opposite directions. On the other hand, the ion accelerator chain is slightly different. Ions are produced via electron cyclotron resonance (ECR) and then sent to another adapted linear accelerator, the LINAC3. From there, they are sent into the Low Energy Ion Ring (LEIR) which makes the bunches shorter and denser and accelerates them from 4.2 MeV to 72 MeV. From here on, the ions follow the proton chain going to the PS, with a lower number of bunches with respect to the protons case. The final energy is reached in the LHC. The beam pipes in which protons circulate, operate in ultra high vacuum with a pressure of the order of 10^{-10} to 10^{-11} mbar, a vacuum almost as rarefied as on the Moon's surface. This is to avoid unwanted collisions. The protons are accelerated up to 6.5 TeV using radiofrequency cavities and they are guided using a strong magnetic field (up to 8.3 T) provided by 1232 superconducting dipole magnets which operate

[1] As a curiosity, at the LHC there are $\sim 3 \times 10^{14}$ protons per beam and one cubic centimeter of gas contains 5×10^{19} hydrogen atoms, which means that one hydrogen bottle could refill the LHC for ∼200 000 years. In 2016, 1.34×10^{20} protons were accelerated, this is equivalent to the number of protons in a grain of sand and only 0.1% of these protons are actually used by the LHC, the rest goes to other smaller experiments shown in Fig. 3.1.

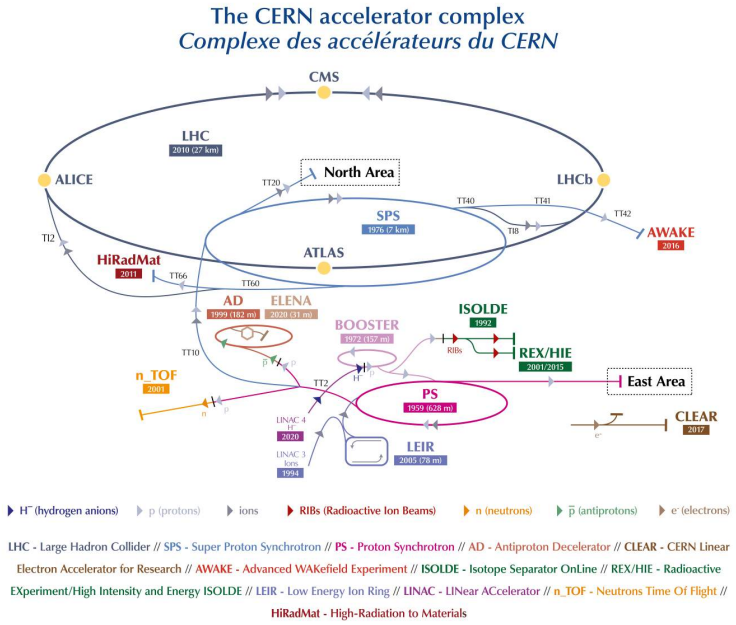

Figure 3.1: The CERN accelerator complex as in 2019, from [114]. Other accelerators not mentioned in the text are also presents, they provides beams for other experiments mentioned at the bottom.

at -271.3 °C. This temperature is achieved using superfluid helium all along the LHC. In addition, 392 quadrupole magnets are used to focus the beam. Once the desired energy is reached, the two beams are travelling nearly at the speed of light and they are ready to cross at the four collision points where the biggest experiments are located, namely ATLAS [115], CMS [116], ALICE [117] and LHCb [7]. The final beam energy increased over time: 3.5 TeV in 2010 and 2011, 4 TeV in 2012 (Run 1) and 6.5 TeV in 2015, 2016 and 2017, 2018 (Run 2), corresponding to a center-of-mass collision energy of 7 TeV, 8 TeV and 13 TeV. At the end of the chain, the proton bunches were spaced 50 ns apart for Run I and 25 ns for Run 2. The maximum number of bunches was 2556 for Run 2 and 1300 for Run 1. At this point, when the two beams cross, a fraction of the 1.15×10^{11} protons in the bunches collides and produces new particles, transforming their kinetic energy into mass. The result of the collisions are studied by the four large detectors with a different focus. ATLAS and CMS are general purpose detectors covering the 4π solid angle around the beam pipe, designed to measure high-transverse-momentum particles. They discovered the Higgs boson [10][9] in 2012 and they still study its properties. Their physics programs also include searches for New Physics (e.g. SUSY particles [118], dark photons [119]) and study of top quark physics. The ALICE experiment instead has been designed to study heavy-ion collisions where matter reaches extreme densities and a new phase called Quark Gluon Plasma (QGP) forms. The 4^{th} experiment, LHCb, is designed to study flavour physics phenomena and it operates at lower luminosity with respect to ATLAS and CMS. It is better suited for the study of B physics thanks to its good performance in vertex reconstruction and particle identification. The ATLAS and CMS experiments have very tight thresholds in their trigger selections (to cope with the busy environment), at LHCb instead the lower pile-up [1] and the

[1] The pile-up is the superposition of several collisions in the detector during the same bunch crossing.

consequently lower track multiplicity allows to have looser trigger selections and study a wider range of flavour physics processes. The LHCb detector will be described in details in the following sections.

3.2 The LHCb detector

At B factories, at the $\Upsilon(4S)$ energy, B mesons are produced in pairs. This characteristic is used to flag one of the B mesons as a "flavor-tag" and use it to identify the other B flavour, since they are coherently produced. To do so, a crucial need is to be able to distinguish one meson from its companion. This is only possible if the detector is able to separate the origin of the two decays (in space and hence in time) and this requires a sufficiently long decay length. At e^+e^- colliders, again at the $\Upsilon(4S)$ energy, mesons are produced almost at rest in the laboratory frame thus, to distinguish the $B\bar{B}$ pair, an unachievable resolution would be necessary. A workaround was proposed for the first time in 1992 by P. J. Oddone [120]. He suggested to use asymmetric beam energies to boost the particles in a specific direction and make the decay length sizeable, in this way the separation of the B and $\bar{B}$ mesons would become possible. This was a breakthrough for the design of future flavour physics experiments. At the LHC, the beam have the same energies, however the dominant process for pp collisions at the TeV scale is gluon fusion. Gluons can have very asymmetric momenta, hence the $b\bar{b}$ pairs are still produced with a boost along the direction of the higher momentum gluon, which can be forward or backward with respect to the beam axis. It is for this reason that LHCb has been design as a forward spectrometer. Despite is narrow coverage, from 10 mrad to 300 mrad, corresponding to 4% of the 4π solid angle, it covers 24 % of the $b\bar{b}$ production cross section at $\sqrt{s} = 14$ TeV. As a comparison, ATLAS and CMS cover 95 % of the solid angle and 41% of the $b\bar{b}$ production cross section. The $b\bar{b}$ cross section as a function of the polar angles and pseudorapidities[1] is shown in Fig. 3.2. However, the average detection efficiency for B hadrons is lower for ATLAS and CMS with respect to LHCb, this is due to the hard selections applied on the p_T and η of particles which reduce considerably the number of visible B hadrons. Even if LHCb has been originally designed for observing beauty hadrons, it is also suited for studying charm physics. The $c\bar{c}$ cross section has been measured to be $\sigma(pp \to c\bar{c}X) \approx 1.4\,\text{mb}$ at 7 TeV [122] and $\sigma(pp \to c\bar{c}X) \approx 2.4\,\text{mb}$ at 13 TeV [123], both in the kinematic range $p_T < 8\,\text{GeV}/c$ and $2.0 < y < 4.5$. These measurements are performed using the fragmentation functions (f_i) obtained from e^+e^- data [11]. The f_i have not been proved to be independent of the production system and hence they could differ in the hadron colliders case. For instance, the $f(b \to \Lambda_b)$ has been measured and proven to be different between the pp and e^+e^- case [124]. Even though the f_i are not necessary adapted to the pp case, we use those numbers here to estimate the amount of charm hadrons produced at the LHC. The number of expected $\Lambda_c^+ \to pK^-\pi^+$ events can be computed using:

$$N = \sigma_{\Lambda_c^+\overline{\Lambda}_c^-} \times \mathcal{L} \times \mathcal{B}(\Lambda_c^+ \to pK^-\pi^+)\epsilon \tag{3.1}$$

[1] The pseudorapidty is a quantity used in high energy physics to describe the angle (θ) of a particle with respect to the beam axis. It is defined as: $\eta = -\ln\left(\tan\left(\frac{\theta}{2}\right)\right)$. For $\eta \to \infty$, the particles are close to the beam axis and $\theta \to 0$, whereas for $\eta \to 0$, particles are produced at a 90° angle. It is also convenient to express η as a function of the longitudinal momentum p_L as: $\eta = \ln\left(\frac{|p|+p_L}{|p|-p_L}\right)$.

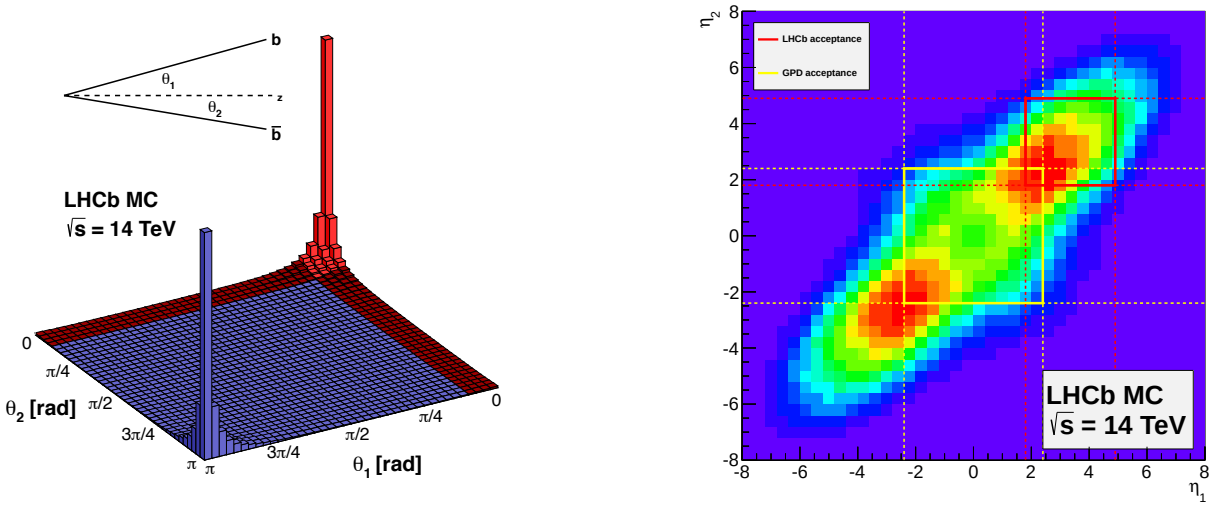

Figure 3.2: Left: production cross section as a function of the polar angles of b and $\bar{b}$ with respect to the beam direction. Right: same cross section as a function of the pseudorapidity. The yellow square indicates the ATLAS and CMS acceptance, the red one the LHCb acceptance. The simulation is done using PYTHIA8 and CTEQ6 NLO parton density function, including the following processes weighted according to their cross sections: $\bar{q}q \to b\bar{b}$, $gg \to b\bar{b}$, $\bar{q}q \to b\bar{b}g$(where $q \neq b$), $b\bar{b} \to b\bar{b}g$ and $gg \to b\bar{b}g$, from [121].

where $\sigma_{\Lambda_c^+\overline{\Lambda}_c^-}$ is the $\Lambda_c^+\overline{\Lambda}_c^-$ production cross section, also expressed as $\sigma_{\Lambda_c^+\overline{\Lambda}_c^-} = 2 \times \sigma_{c\bar{c}} \times f(c \to \Lambda_c^+)$, where $f(c \to \Lambda_c^+)$ is the fragmentation function describing the probability for a c quark to hadronize in a Λ_c^+ baryon and the factor 2 accounts for the charge-conjugate decay. $\mathcal{L}$ is the integrated luminosity and ϵ the total detection efficiency. It is shown in [125] that at 7 TeV $f_{\Lambda_c^+} = 0.10$ describes better LHCb data, instead of the $f_{\Lambda_c^+} = 0.05$ pre-LHC result, hence this value is chosen here. The branching ratio of $\Lambda_c^+ \to pK^-\pi^+$ has been measured to be $\mathcal{B}(\Lambda_c^+ \to pK^-\pi^+) = 6.84 \pm 0.24 \pm 0.23\%$ in 2014 by Belle [126] with ≈ 1359 decays reconstructed, and $\mathcal{B}(\Lambda_c^+ \to pK^-\pi^+) = 5.84 \pm 0.24^{+0.21}_{-0.27}\%$ in 2016 by BESIII [127] with ≈ 6300 decays reconstructed. The PDG fit, combining the two measurements and scaling the error by a factor 1.4, gives as final average: $\mathcal{B}(\Lambda_c^+ \to pK^-\pi^+) = 6.28 \pm 0.32\%$, which is closer to the Belle result. For instance, the total efficiency for the reconstruction (and selection) of the $\Lambda_c^+ \to pK^-\pi^+$ decays in this analysis is estimated to be 0.03. Thus, from Eq. 3.1, one would expect $\mathcal{O}(10^6)$ $\Lambda_c^+ \to pK^-\pi^+$ decays to be seen with LHCb Run 2 (2016 only, corresponding to an integrated luminosity of 3 fb^{-1}) data. The final number of reconstructed decays will be discussed in Chapter 6, yet this estimation already proves that LHCb (and the LHC) is after all a charm factory.

3.2.1 General layout

As aforementioned, the LHCb detector as been designed for the study of beauty (and charm) hadrons. It is a spectrometer covering the forward direction corresponding to a pseudorapidity range $2 < \eta < 5$. It separates particle by their mass, momentum or energy. To do so, it is equipped with several subdetectors, each of which is used to measure (or help measuring) one of these properties. The general layout is shown in Fig. 3.3. The coordinate system of LHCb is defined with origin at the

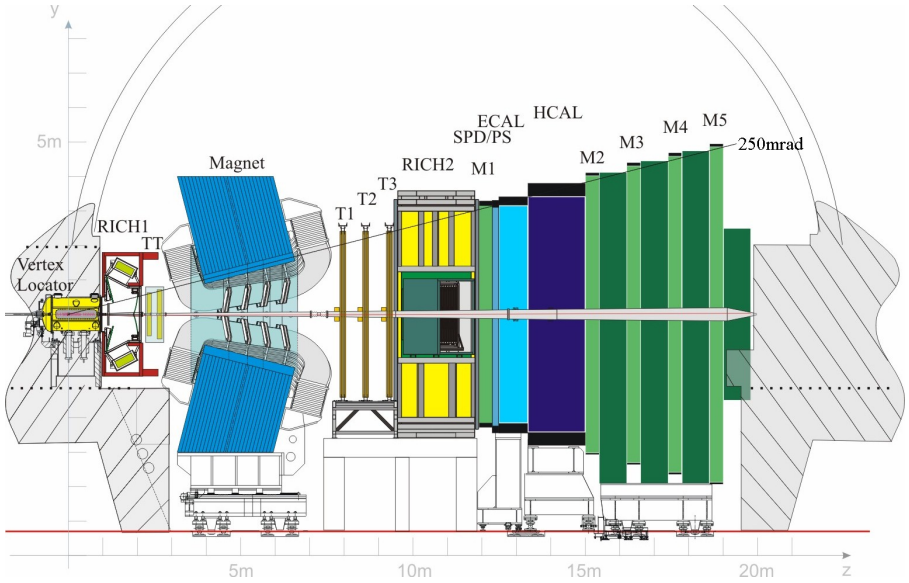

Figure 3.3: Layout of the LHCb detector. The coordinate system is also shown. From [7].

interaction point. The z axis is oriented along the beam direction pointing from the interaction point towards the LHCb muon stations. The y axis is vertical, perpendicular to the LHC and pointing towards the surface. The x axis is defined using the two others to form a right-handed coordinate system. The B (and other) hadrons are reconstructed using their decay products, mainly charged leptons, charged and neutral hadrons and photons. Some particles traverse all the detector and pass through almost each subdetectors (typically the muons). Others, are stopped before the end of the detector but they still cross the majority of it, they are called "stable" particles (in LHCb jargon) as opposed to "unstable" particles, which have a short lifetime and decay before crossing the detector. The latter are detected only via their decay products. Within the stable and directly detectable particles, there are: charged pions ($\pi^{\pm}$), charged kaons ($K^{\pm}$), protons ($p,\bar{p}$), electrons ($e^{\pm}$), muons ($\mu^{\pm}$) and photons (γ). Within the unstable particles, some hadrons such as K^0_S, Λ or Ξ^-, have a longer lifetime and cross some detectors before decaying, they are classified as "*long-lived*". The neutrinos are not reconstructed directly in LHCb. To give a global idea of the detector design, the sequence of sub-detectors is introduced here, however the detailed description of each subdetector is given in the next sections. The collisions happen in the VErtex LOcator (VELO), a precise tracking detector capable of measuring the coordinates of vertices near the interaction point. It is used to distinguish between prompt and secondary particles, i.e. particles produced directly after the collision (at the primary vertex) or produced from the (displaced) decay of other particles. The discrimination is performed using the impact parameter (IP), which is the transverse distance of closest approach between the particle trajectory and a vertex (in this case the interaction vertex). The tracking system is completed by two other tracking detectors: the Tracker Turicensis (TT) upstream of the dipole magnet and the three tracking stations upstream the magnet (T1-T3). The magnet is used to bend the charged particles, determine their charge sign and estimate their momentum using the induced track curvature. The charged particle identification is performed by two RIng Cherenkov Detectors (RICH1 and RICH2), placed upstream and downstream the magnet. Two calorimeters provide the

information on the energy of the particles and participate to the Level 0 hardware trigger: those are the Electromagnetic CALorimeter (ECAL) and the Hadronic CALorimeter (HCAL). At the end of the detector, the muon chambers (M2-M5) are used to detect muons with one additional station M1 placed before ECAL. Each sub-detector is described in details in the following.

3.2.2 Tracking and vertex reconstruction

The tracking system goal is to reconstruct the trajectories of charged particles from their hits left in the tracking detectors. It is composed by the VELO and the tracking stations. Depending on their length, tracks are classified in three categories shown in Fig. 3.4 (right). Long tracks which have hits in the VELO and in the tracking stations T1-T3. Downstream tracks, without hits in the VELO but with hits in the rest of the tracking system. Upstream tracks, which have hits in the VELO and TT stations without any hits in the tracking stations T1-T3. VELO tracks, which only have hits in the VELO. The last type, the T tracks are only measured in the T stations and they are typically produced in secondary interactions. Usually in physics analysis (and in this analysis) long tracks are used due to their better momentum resolution. The downstream tracks are typically used for the analysis of *long-lived* particles. The VELO tracks instead, are used to reconstruct the primary vertex (PV). If a particle is reconstructed more than once with different track types, the track crossing the larger number of subdetectors is chosen. The number of unique (long) tracks in an event, nTracks, is used as a measure for the event multiplicity.

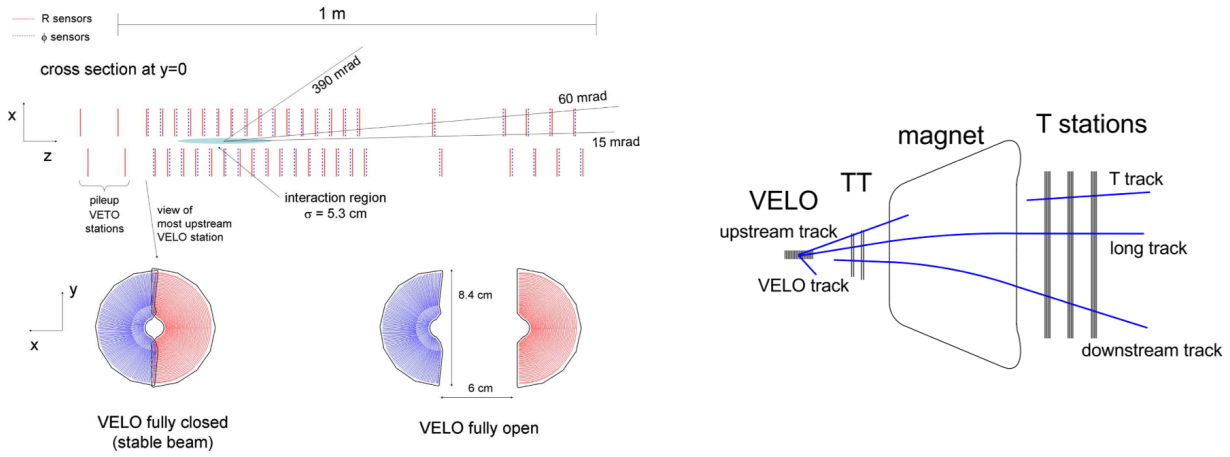

Figure 3.4: Left: a schematic view of the VELO half modules on the bottom and of the position of the VELO stations along the z axis on the top. Right: a sketch of the track types of LHCb. From [7].

Vertex locator

The VELO [128] is placed close to the interaction region and it measures track coordinates. It is probably one of the most peculiar detector of LHCb, it allows to distinguish secondary displaced vertices from prompt ones with an outstanding precision. This characteristic is an essential feature in flavour physics and it is widely used in this analysis. VELO is made of a series of silicon modules

Baryon	τ	$c\tau$	γ	Flight distance
Λ_c^+	200 fs	59.9 µm	≈ 20	≈ 0.2 mm
Λ_b^0	1.47 ps	441.0 µm	≈ 40	≈ 8.82 mm

Table 3.1: Comparison between the flight distances of Λ_c^+ and Λ_b^0 baryons produced at the LHC, at a center of mass energy of 13 TeV, where γ is obtained using the average particle energy.

along the beam direction. Upstream of the main VELO sensors there are two planes perpendicular to the beam as shown in Fig. 3.4 (left). These are the *pile-up veto stations* and they were built for the L0 trigger and for measuring the centrality of heavy-ion collisions, even though they have not been used for this purpose in the end due to the poor performances, and in the fixed target mode they are used to reduced the background induced by *pp* collisions by vetoing on only forward tracks, (*i.e.* tracks without hits in these stations). The modules are movable and specialized in measuring either the r or ϕ coordinates, using respectively the R-sensors or the ϕ-sensors. The third coordinate is deduced knowing the position of each sensor plane within the experiment. These modules operate under vacuum and they are separated from the beam by a thin aluminium sheet called RF-foil (used to protect the electronics from radio frequency interferences). The foil must be as thin as possible to reduce to the minimum the interactions length of particles going into the sensors, which is in average $0.0175\ X_0$. When the modules are aligned, *i.e.* VELO is "closed", the space left for the beam is smaller than the size of the beam during the injection phase. This implies that the detector would be damaged if closed during the injection phase and the beam would be destabilized. For this reason the VELO modules are movable and the detector is only closed when the beam has reached the desirable size. When closed, the modules overlap as shown in Fig. 3.4. The position of the modules is constrained by the angular acceptance and by the requirement that a track in the LHCb acceptance crosses at least three stations. This is sketched in the upper part of Fig. 3.4 (left), the interaction region is also shown in blue. Due to its vicinity to the beam, the radiation environment is extremely hard (an accumulated luminosity of 2 fb^{-1} is equivalent to a $1.3 \times 10^{14}\,\text{n}_{\text{eq}}/\text{cm}^2$ flux of 1-MeV neutrons). For this reason, the detector is cooled down between -10 and 0 °C. In this work, the VELO detector is used to measure the impact parameter (IP) of the daughter particles. The IP is used to separate prompt Λ_c^+, which are originating from the primary interaction, from secondaries Λ_c^+, produced by the decay of long-lived hadron, e.g. $\Lambda_b^0 \to \Lambda_c^+ l \nu_l$. In Fig. 3.5, a sketch of the decay topology is shown, with the prompt decay depicted in red and the secondary decays in green, the IP of the pion is also shown. The performances of the VELO detector for Run 1 are discussed in [129] and the resolution on the impact parameter (IP) (per track) was around $\sim 30\,\mu$m for Run 2, as shown in Fig. 3.6 (right). The intrinsic resolution of the detector on the decay time is of the order of ~ 40 fs, see Fig. 3.6 (left) for the D^0 meson case. This is enough to distinguish not only prompt from secondaries decays, but also to reconstruct the prompt Λ_c^+ vertex which is displaced from the primary vertex (PV) of less than a mm at the LHC energies, see Table 3.1.

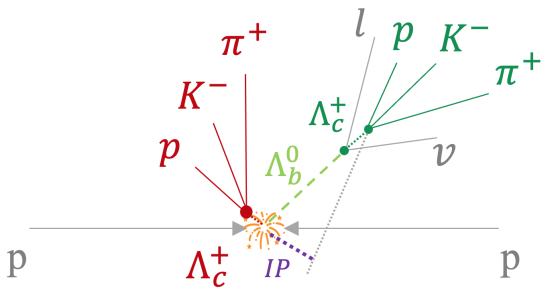

Figure 3.5: Sketch of the Λ_c^+ decay for prompt (red) and secondary production (green). The impact parameter (IP) of the pion is also shown (purple) as an example.

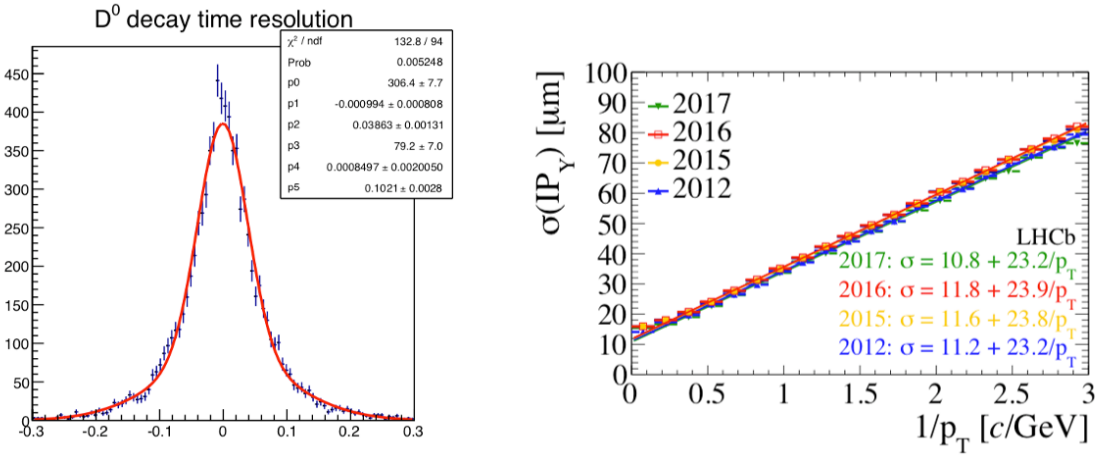

Figure 3.6: Example of decay time resolution obtained from simulation, for D^0 mesons, from [130]. Resolution on the impact parameter along the y direction as a function of $1/p_T$, from [129].

Silicon Tracker

The Silicon Tracker (ST) is formed by two detectors: the Tracker Turicensis (TT) [131], placed upstream the magnet, and the Inner Tracker (IT)[132], close to the beam axis at the level of the tracking stations (see Fig. 3.3 and the purple part of Fig. 3.7). Both use silicon microstrip sensors with a strip pitch of about 200 µm. The charged particles crossing the silicon p-n junction create electron-holes pairs in the depletion zone, those pairs can move freely and they are directed by an electric field to the microstrip to be collected and to finally generate an electric signal that can be read out. The TT has an active area of 8.4 m^2 and the IT of 4.0 m^2. Each station has four detection layers with vertical strips in the first and last layers and tilted strips in the second and third layer (+5° and -5°) to obtain optimal spatial resolution, the layout is shown in Fig. 3.7 (right). Both detectors have a spatial resolution of about 50 µm.

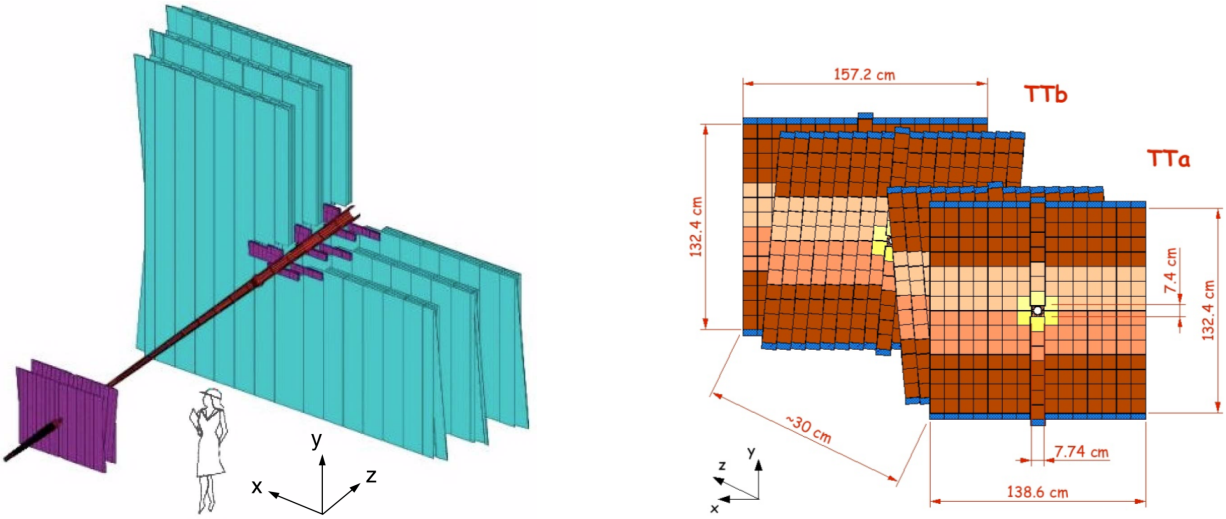

Figure 3.7: Left: the TT detector with the first three stations (T1-T3) followed by the Outer Tracker (OT) and Inner Tracker (IT) forming the downstream tracking stations T1-T3. Right: a schematic view of the TT stations. From [7].

Outer Tracker

The Outer Tracker (OT) [133] covers the region further away from the beam axis, shown in blue in Fig. 3.7 (left). It is an array of gas straw-tube modules containing a gas mixture of Argon (70%) and CO_2 (30%) which has been chosen in order to have a drift time below 50 ns and a 200 µm resolution. The straw tubes are arranged in two layers and the modules are tilted in the same way as in the IT. The charged particles ionizing the gas produce charges which are collected by anode wires. This technology is much cheaper than the silicon sensors, but it has a worse resolution and it is less radiation hard.

Tracking strategy and performance

The track reconstruction begins with the search of track seeds in the VELO and in the T stations, building the first track candidates. When the tracks are found, the trajectories are fitted using tracking algorithms based on the Kalman filter [134], which takes into account multiple scattering and energy loss effects and can reject fake tracks, called "ghost tracks". The quality of the fit is monitored by a χ^2 test, and the normalized χ^2/ndf is used in the physics analysis to apply requirements on the track quality. The trajectories of particles are bent in the horizontal x-z plane by the dipole magnet providing a magnetic field of 4 Tm which is known at a very high precision, $\delta B/B \sim 4 \times 10^{-4}$. It is used to measure the momentum of the particles using the relation: $p = \frac{qB}{\rho}$ where B is the magnetic field, ρ the bending radius, q the electric charge and p the particle momentum. Combining the magnet and the tracking system, the final relative momentum resolution $\delta p/p$ ranges from 0.4% to 1%, as shown in Fig. 3.8 (left). Track reconstruction efficiencies at LHCb have been measured using a tag-and-probe method with $J/\psi \to \mu^+\mu^-$ or $D^0 \to K^-\pi^+$ decays [135]. The average efficiency is better than 95 % in the momentum region $5\,\text{GeV}/c < p < 200\,\text{GeV}/c$, as shown in Fig. 3.8 for 2012 and 2015 data. The final uncertainty per track is below 0.5% for muons and below 1.5% for pions and kaons [135].

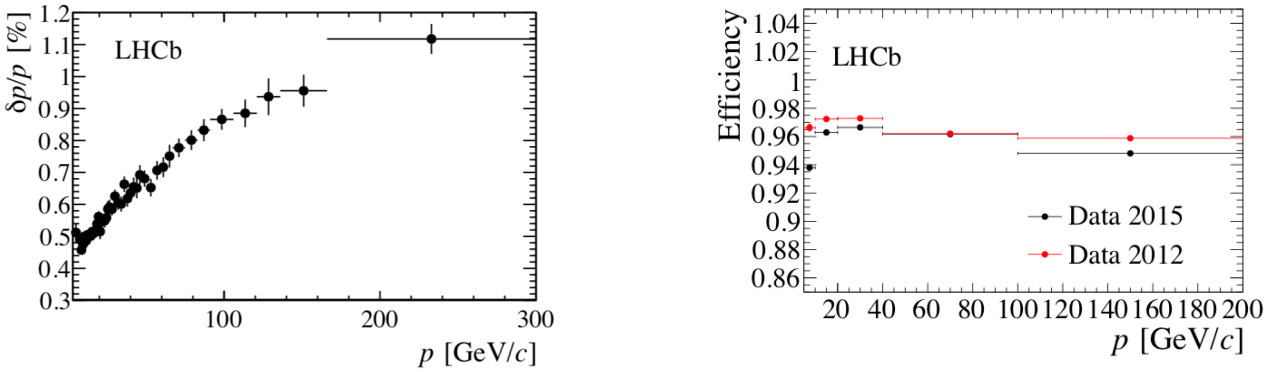

Figure 3.8: Left: Relative momentum resolution versus momentum for long tracks in data, from [129]. Right: tracking efficiency versus momentum, from [136].

3.2.3 Particle identification and energy measurement

A particle is "identified" when its mass (m) is known, then once the particle's momentum (p) is measured (by the tracking system previously described), the energy (E) can be deduced using the relativistic relation:

$$E = \sqrt{p^2c^2 + m^2c^4} \tag{3.2}$$

Thus the identification of particles is performed combining the information from several subdetectors. A system of calorimeters allows to distinguish between photons and electrons (interacting only electromagnetically) and hadrons. On top of that the RICH detectors perform the separation between pions, kaons and protons. Photons belong to a special category, since they are massless and not charged, they do not leave hits in the tracking stations. Only their energy is measured, using the electromagnetic calorimeter, and their momentum is deduced from Eq. 3.2 for the massless case: $E = pc$. Electrons

are special too, since they suffer from Bremsstrahlung [1] they need a dedicated reconstruction algorithm based on the information in the ECAL and trackers. Finally, muons are measured by the muon chambers.

Calorimeters

There are two calorimeters, the electromagnetic calorimeter (ECAL) and the hadronic calorimeter (HCAL)[137]. As the names suggest, the ECAL is dedicated to the detection of particles interacting electromagnetically whereas HCAL to the ones interacting hadronically (via strong and weak interactions). They identify hadrons against electrons or photons and measure their energy. The measurement of the transverse energy[2] is used by the first level trigger (L0) to decide, within 4 µs, if the event is kept or rejected, hence the calorimeters play a crucial role in the trigger system. The calorimeters are preceded by the PreShower (PS) and the Scintillator Pad Detector (SPD). These are planes of scintillator pads with wavelength shifting fibers (WLS) to transmit the scintillation light to the photomultiplier tubes (PMTs). They are separated by a layer of lead used as converter, corresponding to 2.5 radiation lengths X_0 and 0.06 of the hadronic interaction length[3]. Thus, electrons and photons start the electromagnetic shower in the lead plate, whereas hadrons do not. This is used to distinguish between them. Furthermore, any charged track will leave hits in the SPD, allowing the separation of electrons from photons and the rejection of the high background of charged pions. However, several processes can lead to an energy deposit in the SPD and result in the misidentification of photons, these effect are studied using simulations. The energy deposit of particles in the calorimeters is sketched in Fig. 3.9 (left) and it schematically summarizes how to identify electrons, photons and hadrons depending on which part of the calorimeter system has detected something.

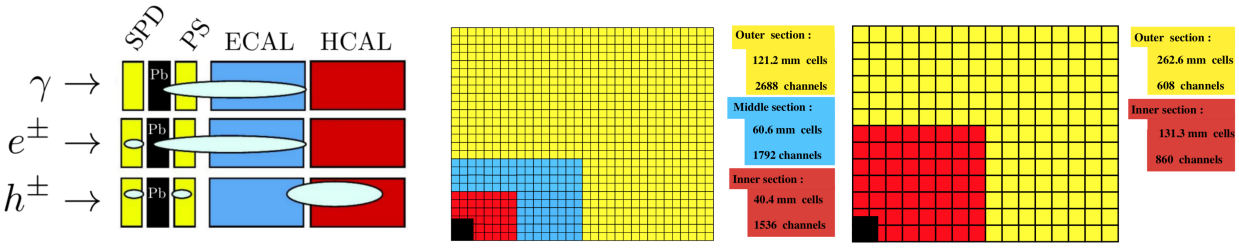

Figure 3.9: Left: a schematic view of the calorimeters system and the particle identification method, from [138]. Center and right: lateral segmentation of the SPD/PS/ECAL and of HCAL respectively. One quarter of the detector front face is shown, from [7].

The ECAL is made of an alternation of lead plates and scintillating tiles (the so-called shashlik technology) along a 42 cm stack corresponding to 25 radiation lengths and a Moliere radius of 3.5 cm.

[1] Bremsstrahlung is the phenomenon of photon emission by a charged particle interacting with nuclei, with consequent loss of kinetic energy. The probability of this process is $\propto 1/M^2$, hence it is more pronounced for electrons than muons. Above a few tens of MeV, it is the dominant process for electrons. It becomes important for muons (and pions) at few hundred GeV.

[2] The transverse energy is is defined as $E_T = \sum E_i \sin\theta_i$, where E_i is the energy deposited in the cell i and θ_i is the angle between the z axis and a line joining the center of the calorimeter cell to the interaction point.

[3] The radiation length X_0 represents the average distance x that an electron needs to travel in a material to reduce its energy to $1/e$ of its original energy E.

This is enough to contain all the electromagnetic shower and measure the full energy deposit. The light from the scintillator tiles is collected by WLS fibers (as for the SPD and PS) and readout with Hamamatsu R7899-20 phototubes. The granularity of the detector (*i.e.* the size of the cells) is adapted depending on the distance to the beam pipe. The PS and SPD have the same segmentation, shown in Fig. 3.9 (center), to achieve a one-to-one projective correspondence with the ECAL segmentation. The designed energy resolution is $\sigma_E/E = 10\%/\sqrt{E} \oplus 1\%$ (E is expressed in GeV). This results in an expected B mass resolution of 65 MeV/c^2 for the $B^0 \to K^*\gamma$ decay and 75 MeV/c^2 for $B^0 \to \pi^+\pi^-\pi^0$ decay. The final invariant mass resolution for $B^0 \to K^*\gamma$ decays is shown Fig. 3.10, it has improved from about 91 MeV/c^2 for Run 1 to 87 MeV/c^2 for Run 2.

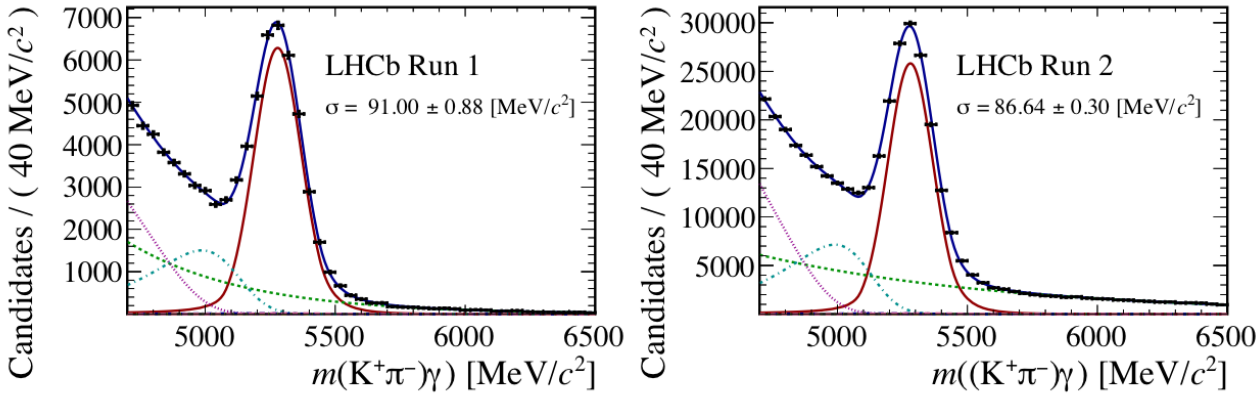

Figure 3.10: Invariant mass of $B^0 \to K^*\gamma$ candidates in Run 1 (left) and Run 2 (right). The fit model includes the (red) signal component, (dashed green) combinatorial background, (dot-dashed turquoise and purple) misidentified physics backgrounds, from [136].

On the other hand, the HCAL is made from iron (absorber) and scintillating tiles (active material). It has a thickness of 5.6 hadronic interaction lengths (plus 1.2 interactions lengths coming from the ECAL upstream). The segmentation is different from the ECAL one and it is shown in Fig. 3.9 (right). The designed resolution is $\sigma_E/E = 65\%/\sqrt{E} \oplus 9\%$ (E is expressed in GeV). The HCAL is used in combination with ECAL to identify hadrons, which start the shower in the lead layer and ends it in the HCAL. It is mainly used for the hardware trigger stage since its energy resolution is too modest to use it for other purposes.

RICH detectors

The RICH detectors [139], RICH1 and RICH2, are used to separate protons, kaons and pions and to help identifying muons and electrons. When charged particles travel in a medium faster than the phase velocity of light (in this medium), they produce light by Cherenkov effect. The RICH detectors measure this light. If the refraction index of the medium is n and the particle travels at a speed v_p, then the threshold for the emission of photons is $v_p > c/n$. The Cherenkov photons are emitted in the direction defined by a cone with opening angle θ:

$$\cos\theta = \frac{1}{n\beta} \tag{3.3}$$

where $\beta = v_p/c$. Hence by measuring the opening angle of the cone one can deduce the velocity of the particle. From the velocity and the momentum (measured by the tracking system), the mass of the particle can be inferred using:

$$m = \frac{p}{\beta\gamma c} = \frac{pn\cos\theta}{c\gamma} \tag{3.4}$$

RICH 1 is placed upstream right after VELO, the medium (called absorber) is an aerogel and fluorobutane C_4F_{10} gas with refractive index $n = 1.0014$ and it covers low momentum charged particles around $\sim 1-60$ GeV. For Run 2, the aerogel part was removed since it did not have any significant impact. The RICH 2 radiator instead is made of CF_4 gas with a smaller refraction index $n = 1.0005$, this implies that particles must have a higher momentum to pass the emission threshold $v_p > c/n$ and RICH 2 covers a higher momentum range $\sim 15-100\,\text{GeV}/c$. RICH 2 is placed after the TT stations, covering the higher pseudo-rapidity range which correspond to an area where the more energetic particles are expected. A schematic view of the RICH detectors is presented in Fig. 3.11. In both detectors the Cherenkov light is focused by a system of spherical and flat mirrors to be redirected to Hybrid Photon Detectors (HPDs). In Fig. 3.11 (bottom right) the reconstructed Cherenkov angle as a function of the particle momentum is shown, it can be seen by eye that there are kinematic regions where a reliable separation of different hadrons is not possible. At low momentum, kaons and protons do not have a sufficient velocity to create a Cherenkov ring, hence their identification is challenging. On the other hand, at high momentum the Cherenkov angles look very similar for all particles types. In Fig. 3.11 (up right) a simulated event display of RICH 1 is shown. A dedicated algorithm is used to reconstruct the rings and compute the Cherenkov angle. A track is then assigned to the reconstructed rings and a likelihood (of being a certain particle type), called DLLX, is computed for each track. Differences of likelihoods are used as discriminating variables in the offline selection, typically the likelihood of the kaon (proton) compared to the pion one, called PIDK (PIDp). From these, a neural network is trained to combine the information of several subdetectors and return a probability for each charged particle candidate (pion, kaon, proton, muon, electron or deuteron), called ProbNNX, which will have a higher discrimination power than the DLLX [140]. The ProbNNX are used in the $\Lambda_c^+ \to pK^-\pi^+$ analysis to eliminate backgrounds coming from other decays where one particle, either proton, kaon or pion, has been mis-identified.

The performance of the RICH detectors is studied using a high-statistic sample of decays selected without PID requirements, namely $K^0_S \to \pi^+\pi^-$, $\Lambda \to p\pi^-$ and $D^{*+} \to D^0(K^-\pi^+)\pi^+$ where the signal is extracted using the *sPlot* technique (see Sec. 6.2.2). As an example, the kaon identification efficiency (kaons identified as kaons) and the pion misidentification rate (pions misidentified as kaons) are shown as a function of particle momentum in Fig. 3.12 (left) for pp collisions at 7 TeV in 2011. These are shown with two different requirements: $(\text{DLL}K - \text{DLL}\pi) > 0$ or 5, which corresponds to requiring the likelihood of each track with the kaon mass hypothesis to be larger than the one with the pion hypothesis. In this case, the average kaon efficiency is 95% and the pion misidentification fraction 10%. The tighter requirement (DLLK-DLLπ) > 5 reduces the pion misidentification fraction to 3% and the kaon efficiency goes to 85%. Similar performances are obtained for the following data taking periods, see [142]. For comparison, the same plot for proton identification efficiency and kaon misidentification rate is shown in Fig. 3.12 (center). From this, one can notice that separating protons

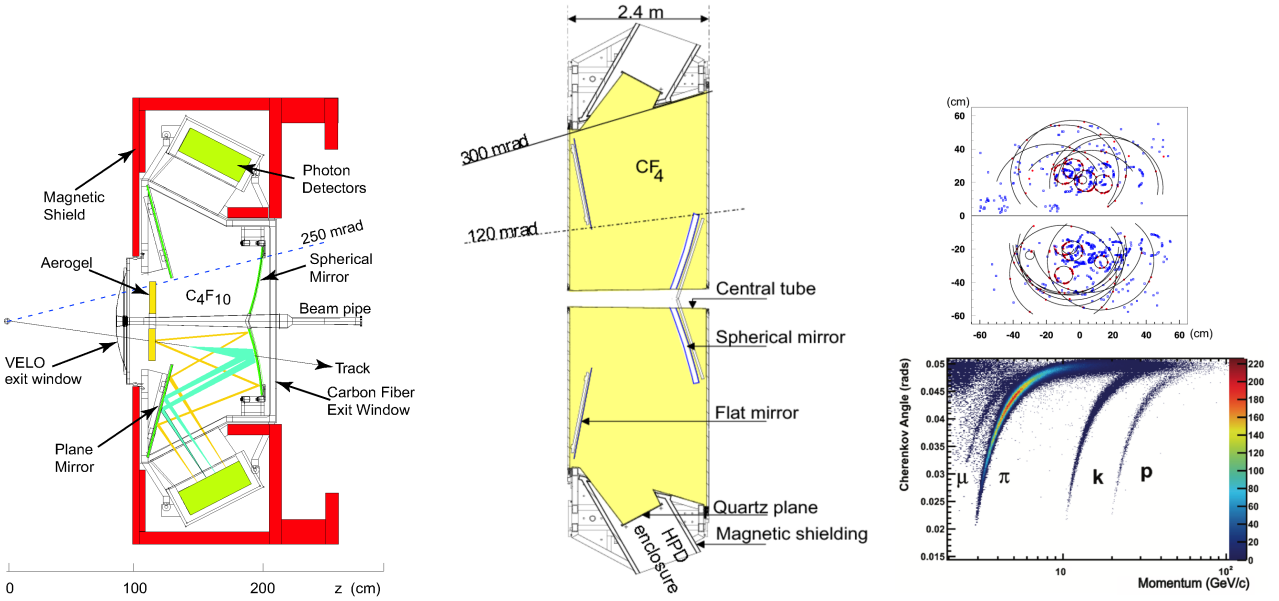

Figure 3.11: Left: schematic view of the RICH detectors [7]. Right top: Cherenkov rings from simulation [139]. Right bottom: measured Cherenkov angles as a function of the track momentum for RICH1, using 2011 LHCb data [141].

from kaons is harder than separating kaons from pions. This behaviour can be guessed intuitively looking at the separation of the scattered lines in Fig. 3.11 (bottom right). Fig. 3.12 (right) shows the pion misidentification fraction versus the kaon identification efficiency as a function of the track multiplicity, indicating that the PID efficiency degrades at higher multiplicity.

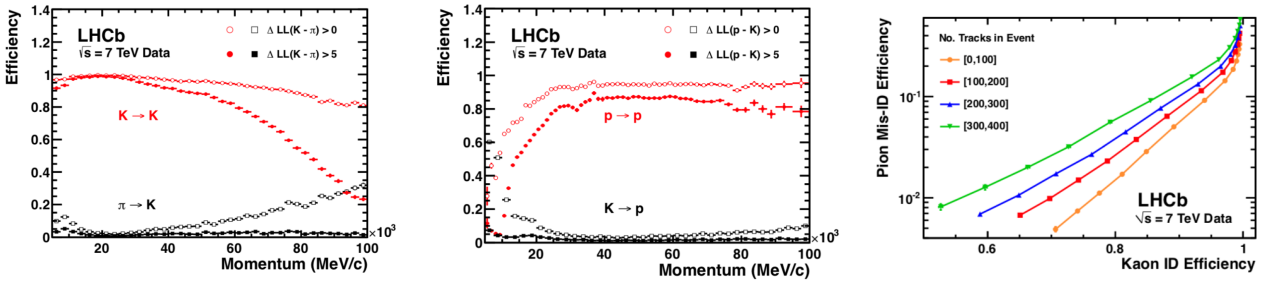

Figure 3.12: Left: Kaon identification efficiency and pion misidentification rate measured on data as a function of track momentum, with two different requirements, DLLK − DLL$\pi > 0$ (open marker) and DLLK − DLL$\pi > 5$ (filled marker), as measured in 7 TeV LHCb collisions. Center: same plot for proton identification efficiency and kaon misidentification fraction. Right: pion misidentification fraction versus kaon identification efficiency as a function of the track multiplicity. From [141].

Muon system

The muon system [143] is shown in Fig. 3.13. It is composed of five stations M1-M5, located along the beam axis. The first station M1 is placed before the calorimeter, to provide a better transverse momentum measurement, which is used by the hardware trigger to select high-p_T particles. The other stations M2-M5 are placed after the calorimeters and they are interleaved with layers of 80 mm

thick iron absorbers. The total absorber thickness of the muon system (including the calorimeters) is equivalent to 20 interaction lengths, this means that only muons with a momentum higher than 6 GeV can cross all the stations. This is also the reason why all the muons stations are not placed upstream other detectors, otherwise they would stop any particle. To cover the LHCb angular acceptance set by the previous subdetectors, they cover a large area of in total 435 m^2. The inner and outer angular acceptances area of 20 (16) mrad and 306 (258) mrad in the bending (non-bending) plane respectively. This allows to detect 20 % of the muons from inclusive b semileptonic decays. Each station is divided in 4 regions R1-R4, each of which is segmented in a different way to have a uniform overall occupancy. To achieve that, the size of the segmentation cells decreases from the external regions towards the beam pipe, where the occupancy is much higher, see right side of Fig. 3.13. The stations are multi-wire proportional chambers (MWPC) except for the inner region (R1) of M1 equipped with triple-GEM detectors, which can stand higher particle rates (for radiation protection issues). The trigger algorithm requires that the efficiency of each station is high enough to give a total efficiency of at least 95% within the 25 ns window. This is achieved using a fast gas mixture (Ar/CO2/CF4 with 40% Ar and variable concentrations of CO2/CF4) and an optimized charge-collection geometry. The efficiency of

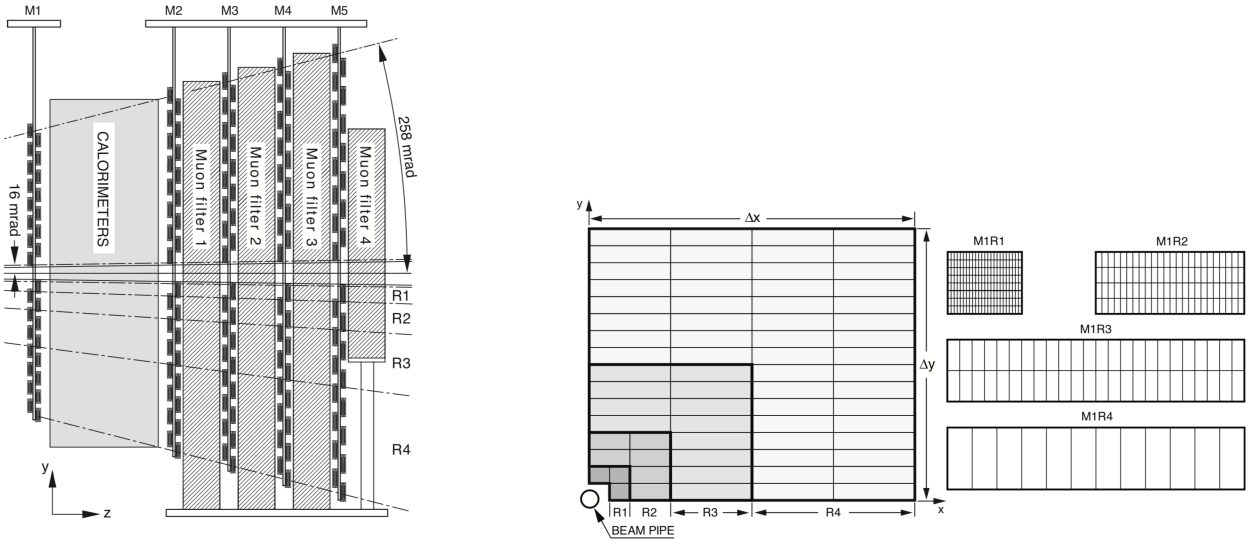

Figure 3.13: Left: Schematic side view of the muon system. Right: A quadrant of one of the muon stations, where each square represents one muon chamber. The segmentation of the chambers for each different R region is shown on the right-hand side of the picture, for M1 from[7].

the muon system for the full 2010 sample was between 98.66 to 100% depending on the station and the region [144], and it is similar for the other data taking periods. The muon identification algorithm [145] exploits tracks with $p > 3\,\mathrm{GeV}/c$ in the muon stations. The identification strategy works as follows. First the muon candidates are selected based on the penetration in the calorimeter and iron filters, a variable called isMuon is created. Similarly, two other boolean variables are constructed: IsMuonLoose and IsMuonTight, whose requirements are respectively looser and tighter with respect to IsMuon. Then the tracking information is used to extrapolate the particle trajectories to the muons station and study their hits pattern. A variable called muDLL is used as discriminating variable, it is defined as the logarithm of the ratio of likelihoods for the muon to the non-muon hypotheses. At

the end, a combined likelihood is built using the information from calorimeters and RICH systems. Then, the logarithm of the ratio between the likelihood for the muon and pion hypotheses forms a discriminating variable called PIDmu. This information is used by the software trigger HLT. The average muon identification efficiencies are around 98% level for pion and kaon misidentification below 1%. The high-level trigger algorithm, based on the variables described above, has been improved for Run 2 [146] since larger computing power has been made available, an increase in efficiency around 15% has been obtained with respect to Run 1.

3.2.4 The SMOG system

The SMOG system (System for Measuring Overlap with Gas), shown in Fig. 3.14 (right), is a system allowing to inject gas inside the VELO vessel. It was originally designed for precise luminosity measurements [147]. Since 2015, LHCb has started exploiting SMOG to study fixed-target collisions using special fills not devoted to *pp* physics. When injecting the gas the LHC vacuum pressure rises by two orders of magnitude, from about 10^{-9} mbar to slightly above 10^{-7} mbar. The injected gas pressure can be monitored by four cold-cathode gauges (Penning type) and one hot-filament ionization (Bayard-Alpert type) gauge around VELO. The first system calibration is not precise enough to perform a density measurement, the second one instead allows to have a measurement of the gas density at 10% precision level [148].

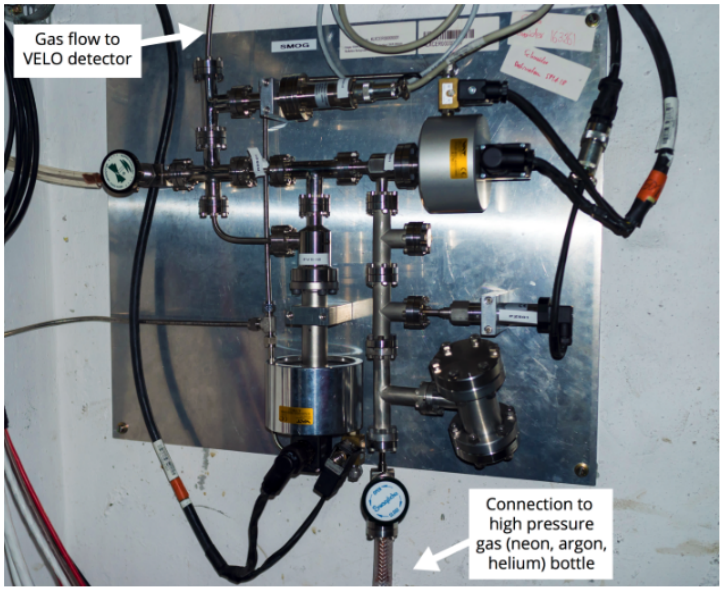

Figure 3.14: Left: simulation. Right: the SMOG gas feed system.

The SMOG system opened a new set of possible measurements for LHCb, making LHCb the only LHC detector capable of doing fixed-target physics. The first physics measurement using SMOG was the antiproton cross-section in collisions of 6.5 TeV proton beam on helium corresponding to a dataset of 0.4 nb^{-1} [149] published in 2018. This was the first measurement of antimatter production in pHe and it has strong implications for the astrophysics experiments PAMELA and AMS-02. The second

measurement is the J/ψ and D^0 production in collisions of 6.5 TeV proton beam on Argon [150], published in 2019.

3.2.5 Trigger system

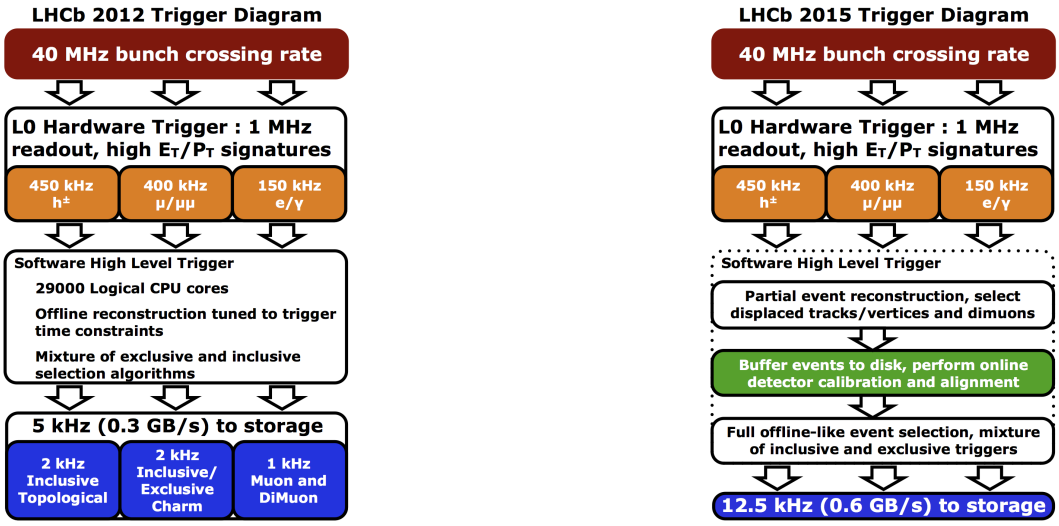

Figure 3.15: Sketch of the trigger sequence starting from the collision to the final event reconstruction for Run 1 (left) and Run 2 (right) from [151].

At the LHC, the bunches cross every 25 ns corresponding to a frequency of 40 MHz. However at the LHCb interaction point, not all the bunches are filled. This is due to the forward geometry of the LHCb detector which imposes a shift of the interaction point away from the center of the cavern (on the z direction). Hence the LHCb bunch crossing frequency is lower, $\sim 30\,\text{MHz}$ and the maximum number of colliding bunches is 2036, whereas for ATLAS and CMS it is 2208. In each collision, the majority of the events are not interesting for physics and saving them all would require an enormous amount of disk space (the 40 MHz rate corresponds to ~ 1.92 Tbytes/s) resulting in a considerable waste of resources. Each single bunch collides at a frequency of ~ 11 kHz, however in each collision not all the protons interact. The average number of visible interactions per bunch crossing (called μ) allows to estimate the fraction of visible interaction per bunch crossing, $1-\exp(-\mu) \sim 0.7$ (for Run 1, $\mu \sim 1-2$), meaning that the frequency of visible interactions per bunch crossing is eventually reduced to 7.26 kHz (a more complete discussion about luminosity can be found in Chapter 4). Looking at the Λ_c^+ case, for a luminosity of $4\times10^{32}\,\text{cm}^{-2}\,\text{s}^{-1}$ for Run 2, the rate of $c\bar{c}$ pairs is 0.96 MHz *i.e.* almost 1 millions of pairs produced per second. Out of this, the production rate of Λ_c^+ decaying into $pK^-\pi^+$, reduces to $N_{\Lambda_c^+}(\text{Hz}) = BR(\Lambda_c^+ \to pK^-\pi^+) \times f_{\Lambda_c^+} \times 0.96\,\text{MHz} = 0.0628 \times 0.10 \times 0.96\,\text{MHz} = 602$ Hz in total. Thus the rate of interesting events is significantly lower than the official LHCb bunch crossing rate. The role of the trigger is to find and keep the events that may contain interesting physics and save it to disk while discarding the rest. The LHCb trigger is implemented in two levels: the Level 0 trigger (L0), which is an hardware trigger, and the High Level Trigger HLT, which is software and divided in two steps HLT 1 and HLT 2. The first level brings the rate down to 1 MHz, the second level to few kHz. The rate reduction after the trigger sequence is schematically shown in Fig. 3.15

TCK	L0hadron E_T[MeV]	L0muon p_T[MeV/c]	L0Electron E_T[MeV]	L0photon E_T[MeV]	nSPD Hits (upper limit)	yearly luminosity fraction [%]
0x1603	3216	1320	2112	2304	450	2.1
0x1604	3552	1560	2256	2784	450	1.5
0x1605	3696	1800	2592	2976	450	4.7
0x1609	3696	1560	2352	2832	450	44.7
0x160E	3696	1800	2592	2976	450	3.3
0x160F	3744	2160	2400	2784	450	34.8
0x1611	3888	1800	2616	2976	450	2.7
0x1612	3888	1920	2616	2976	450	5.4

Table 3.2: Most relevant 2016 TCKs with associated energy and transverse momentum thresholds (minimum value) for L0hadron, L0muon, L0electron, L0photon.

for 2012 and 2015 settings, the final output rate of the LHCb trigger was of 5 kHz for 2012 and 12.5 kHz for 2015 scheme. These 3 stages (L0, HLT 1 and HLT 2) run several parallel lines and each of them run only if the previous trigger step gave a positive decision (except for L0). The combination of the trigger selections (also called trigger lines) are configured at the start of each fill using a unique sequence called Trigger Configuration Key (TCK), this information is then used offline to know exactly the trigger configuration used during the data taking. The TCKs are used to reproduce the trigger response in the simulation. The two trigger steps are detailed in the following.

Level 0 trigger

The first level of trigger in LHCb, the Level 0 (L0), is an hardware trigger. It uses information from the VELO pile-up system, the calorimeters and the muon stations to make decisions and reduce the rates from 40 MHz to 1 MHz. The L0 requirements are based on physics considerations: since the B hadrons have large masses, their decay products will have large transverse momentum (p_T) and transverse energy (E_T) thus the calorimeter and muon triggers reconstruct and select high E_T electrons, hadrons and photons and high p_T muons or di-muons respectively. Two other quantities are extracted at this stage: the number of hits in the SPD (nSPD), which is an estimation of the number of charged particles produced (nTracks), and the total measured energy using the calorimeters. The maximum number of SPD hits is limited (by the L0 trigger) to reject events with a too large multiplicity which would require a long computing time for HLT1. The total energy (the sum of E_T) is used to identify empty bunch crossing to determine the luminosity. The L0 Decision Unit (DU) evaluates the final trigger decision for each bunch crossing within 2 µs (the total latency including cables is 4 µs). If the event passes the L0 decision (*i.e.* more than one trigger line is fired) then the entire detector is read out and the data are sent to the HLT computing farm. The requirement of the most relevant TCK for 2016 used in this analysis are summarized in table 3.2. The calorimeter builds clusters of 2×2 cells and selects the highest E_T candidate, the identification (electron, photon, pion or hadron) is determined combining the information from the SPS, PS, ECAL and HCAL as explained in Sec. 3.2.3. The muon trigger performs a standalone decision, it looks for high p_T tracks which have hits in the 5 muon stations and which point towards the interaction point.

High Level Trigger

The second stage of the trigger is implemented as software applications written in C++ code. It runs on the Event Filter Farm (EFF) and reduces the 1 MHz rate of L0 to 5 (12.5) kHz for Run 1 (Run 2). The HLT1 performs a simplified track reconstruction looking for VELO segments and forming pp vertices (starting from at least 5 VELO tracks). Segments not associated to a PV or not matched to any track in the muons stations are discarded. The remaining ones are matched to hits in the T-stations to form long tracks. To save computing time, arising due to combinatorics, the search window is reduced to $3 < p < 6\,\text{GeV}/c$ and $0.5 < p_T < 1.25\,\text{GeV}/c$. Events passing HLT1 are sent to the HLT2, at a rate of 80 kHz. Since more time is available, the full reconstruction using all the information available in the sub-detectors is performed. This step changed between Run 1 and Run 2. In Run 1 a simplified reconstruction was performed "online" and the calibration and alignment of the detector was not taken into account at this stage. This required yet another reconstruction step and reprocessing of the full dataset "offline". At this point, the entire raw event is saved to be able to reprocess the data later on to improve the reconstruction (full stream). To reduce the dataset size an extra step is needed. Based on the HLT2 lines, a central selection, called *stripping*, is run to reconstruct the decays. The output lines are grouped into *streams* having similar selections. The HLT2 lines are classified as either *inclusive*, where generic signatures are searched and *exclusive*, where decays are fully reconstructed. This processing chain is complicated since the set of selection offline and online is not matching. In Run 2 an automatic real-time procedure for calibration and alignment was developed. The calibration, ran while data are kept in the HLT1 buffer, can now be applied during the reconstruction step performed by HLT2. Thus the online reconstruction was significantly improved and it ended up performing at the same level as the offline one. Furthermore, since the additional offline processing is not necessary anymore, the raw detector information is not saved, this stream is called "Turbo stream" (since it is "faster"). The information saved to disk depends on the configuration, one can save the entire event, only signal candidates, or only signal candidates together with pre-defined tracks of interest. In this analysis, the data are selected from the Turbo stream called "Hlt2CharmHadLcpToPpKmPipTurbo" with exclusive selections optimized to select the $\Lambda_c^+ \to pK^-\pi^+$ candidates.

3.2.6 Data processing and simulation

The software framework used to run all LHCb applications is called Gaudi [152]. The various steps of data processing within Gaudi are shown in Fig. 3.16. The trigger is run by the Moore application [154] and its output is reconstructed by the Brunel application to be stored in "data summary type" files (dst). It is at this point that the new Turbo stream has been added in Run 2. For the full stream, the Stripping is run using the DaVinci application. For the Turbo stream instead, data are directly ready for analysts to make ntuples[1] out of it (using DaVinci). Since the stripping is performed offline, it can be run again if new lines or a change in the selections of existing lines are required. The re-stripping usually happens around 4 times per year. After the ntuples are created from the stripping or from the

[1]ntuples are used in high energy physics for data organisation, they are files written by python scripts using LHCb classes and stored in ROOT files. They contain the properties of the particles *e.g.* energy, mass, momentum etc...

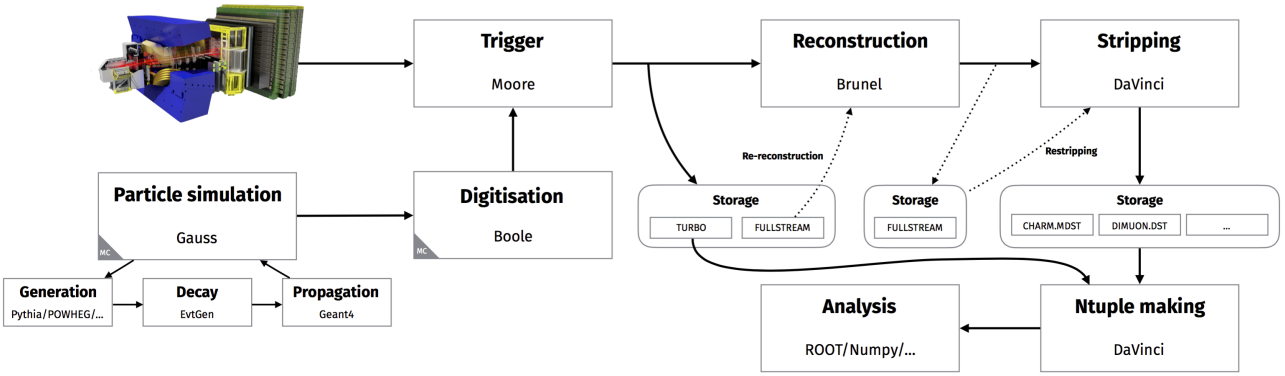

Figure 3.16: Data flow and processing in LHCb [153]

Turbo stream, data are ready to be analysed, usually using ROOT or python code. The above tasks require a large computing power which is obtained by combining computers from all over the world. LHCb is part of the Worldwide LHC Computing Grid (WLCG) project [155], a global computing infrastructure counting 47 countries, 170 computing centers and 1 million computer cores with over 2 million jobs running every day. The simulation, reconstruction and the physics analysis are done on this "grid" of computers. The (large) output of these processes is also stored on the grid, making the data available for all the collaboration. This synergy of resources has made possible to perform computations that no single local cluster could perform alone.

Simulation In order to study the detector response and to include it in the physics analysis, Monte Carlo simulations modelling real data are used. The generic pp collisions and the signal events are generated within the Gauss application [156] using the PYTHIA package [157] with a specific LHCb configuration [158]. Other generators are also available, for instance EPOS [159] to generate heavy-ion collision, HIJING [160] for beam gas events or STARLIGHT [161] for $\gamma\gamma$ and γP initial states. The decay of signal particle is handled by EvtGen [162], along with Photos [163], used to generate final state radiations. The full LHCb detector response is simulated with the Geant4 software [164] [165]. The digitization of the simulated data is done by the Boole application to obtain raw data similar to that produced by the detector. Then the same reconstruction as in data is ran in order to have a description as close as possible to the real data. In LHCb jargon TRUE variables are the generator level variables corresponding to the output of Pythia. On the other hand, the reconstructed variables are the output of the full simulation chain. In this thesis some work has been done to allow the production of polarized spin one half baryons in the Gauss framework and a new EvtGen decay model has been developed (called LAMBDAC_PHH) to simulate $\Lambda_c^+ \to pK^-\pi^+$ decays with three intermediate resonances.

3.3 LHCb upgrade I

Particle physics and especially flavour physics has advanced enormously thanks to the LHCb collaboration. Although a large amount of precise measurements has been performed, LHCb is limited since it is running at a lower luminosity level than ATLAS and CMS. This limitation is due to the detector

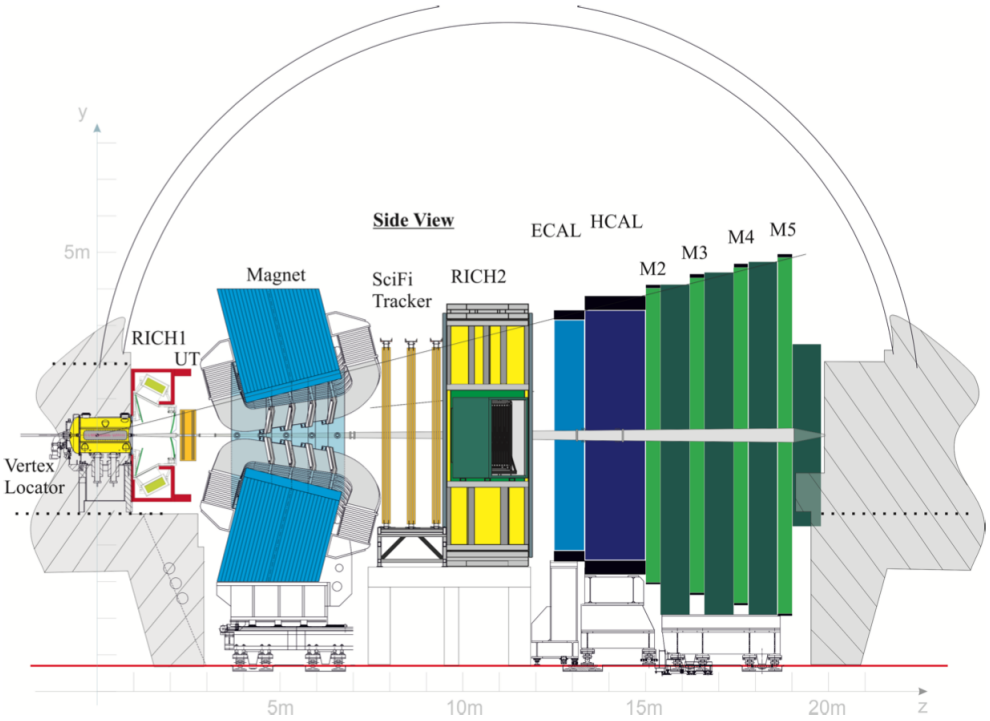

Figure 3.17: Schematic view of the LHCb upgrade detector from [166].

capabilities rather than the LHC performances. Furthermore, few years ago, it has been decided to run the LHC at a higher luminosity level to perform more precise measurements. Hence the LHCb detector needs to be upgraded to profit from this increase in luminosity and perform studies beyond the reach of the current detector. After the long shutdown 2 (LS2) 2018-2021 the instantaneous luminosity will be increased by a factor 5, from $4 \times 10^{32}\,\mathrm{cm}^{-2}\mathrm{s}^{-1}$ to $2 \times 10^{33}\,\mathrm{cm}^{-2}\mathrm{s}^{-1}$, achieved with a 25 ns spacing with an average number of interactions per bunch crossing $\mu = 3.8 - 7.6$. To cope with this luminosity, most of the subdetectors have to be upgraded to increase the radiation hardness, the readout speed, the granularity and the trigger configuration. During Run 1 and Run 2 the luminosity was intentionally reduced by two orders of magnitude at the LHCb interaction point with a procedure called luminosity levelling (see Sec. 4.1). On top of that, the hardware trigger was reducing the readout rate from the 40 MHz collision rate to 1 MHz. To fully exploit the higher luminosity delivered by the LHC, the hardware trigger will be replaced by a software trigger operating online (called RTA, Real Time Trigger) and allowing for more flexible and complete trigger decisions. Along with the new trigger paradigm, almost all the subdetectors will be upgraded, the layout of the upgraded detector is shown in Fig. 3.17. The new layout is very close to the original one, the main changes are: the trajectories and momenta of particles will be measured by a new tracking system composed of VELO, the new planar tracking stations (UT) upstream the magnet and three new stations downstream (SciFi). The L0 hardware trigger will be removed along with the PS and SPD. Finally the injection gas system, SMOG, will be also upgraded to improve the target gas density and allow for a wider choice of gas species. A summary of the upgraded sub-detectors is given below.

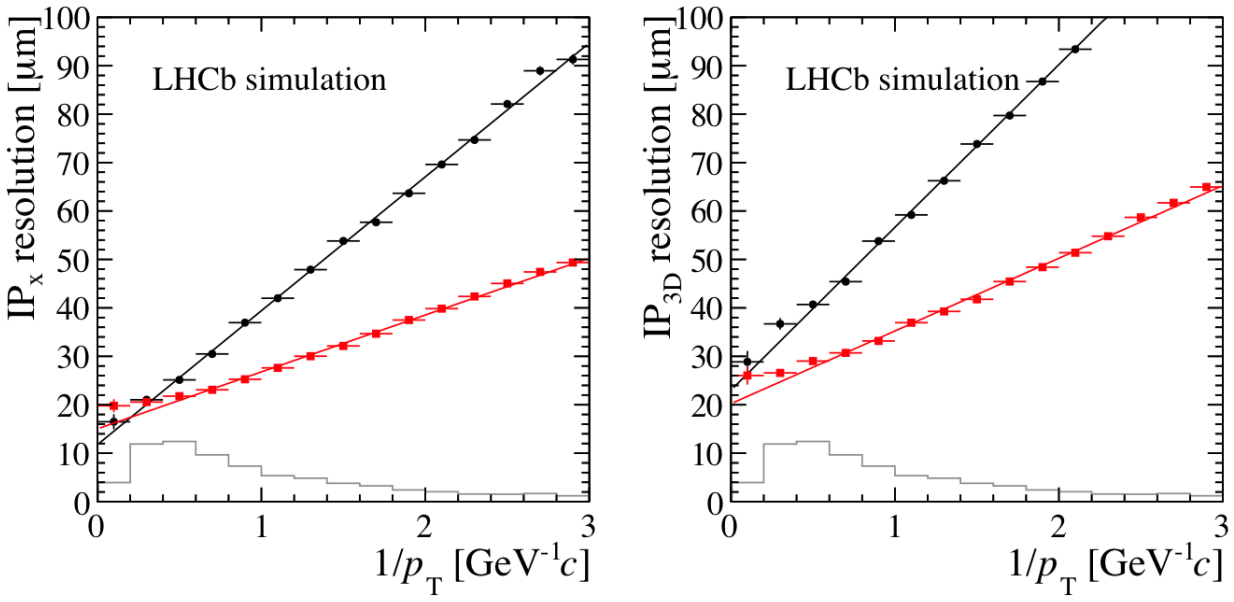

Figure 3.18: Left: IP$_x$ resolution. Right: 3D IP resolution as a function of the inverse transverse momentum. In black with round markers, the resolution of the original VELO is shown. In ref with round squared the resolution of the upgraded VELO is shown. In light grey, the population of b-hadron daughter tracks is shown. Taken from [167].

The upgraded vertex locator The upgraded VELO [167] will be made of 26 planar stations (5 more than before) of hybrid silicon pixel detectors. In total there are 41 million pixels with a size of $55 \times 55\,\mu$m, read out by the new custom VeloPix ASIC [168]. The detector will be placed closer to the beam (5.1 mm distance) and the thickness of the aluminium foil will be reduced from 300 μm to 200-250 μm. The lowered material budget and shorter distance from the beam will result in an improvement of the impact parameter resolution, shown in Fig. 3.18, to be compared with Fig. 3.6.

The upstream tracker The Upstream Tracker (UT) [166] will replace the TT. It will be made of four detection layers of silicon strip detectors. In the outer region, silicon strips of 10 cm with a 190 μm pitch are used. In the intermediate region the pitch is reduced to 95 μm. In the inner region the length is reduced to 5 cm with 95 μm pitch. Close to the beam pipe, the sensors are cut in the form of a quarter circle to improve the acceptance at small polar angles. The readout is made by a new front-end ASIC, the SALT [169] compatible with the 40 MHz rate. Simulations show that the UT can help reducing the number of ghost tracks and improve the resolution on the transverse momentum, see Fig. 3.19.

The downstream tracker The downstream tracker (SciFi) is going to replace the IT and OT. It is a scintillating fiber tracker made of three stations of four planar detection layers each. The detector modules will have 2.5 m long scintillating fibers with a diameter of 250 μm. The fibers are readout by Silicon Photomultipliers (SiPMs) at the top and bottom of the detector, operating at -40 °C to avoid radiation damage. The goal is to have a resolution smaller than 100 μm over a surface of 340

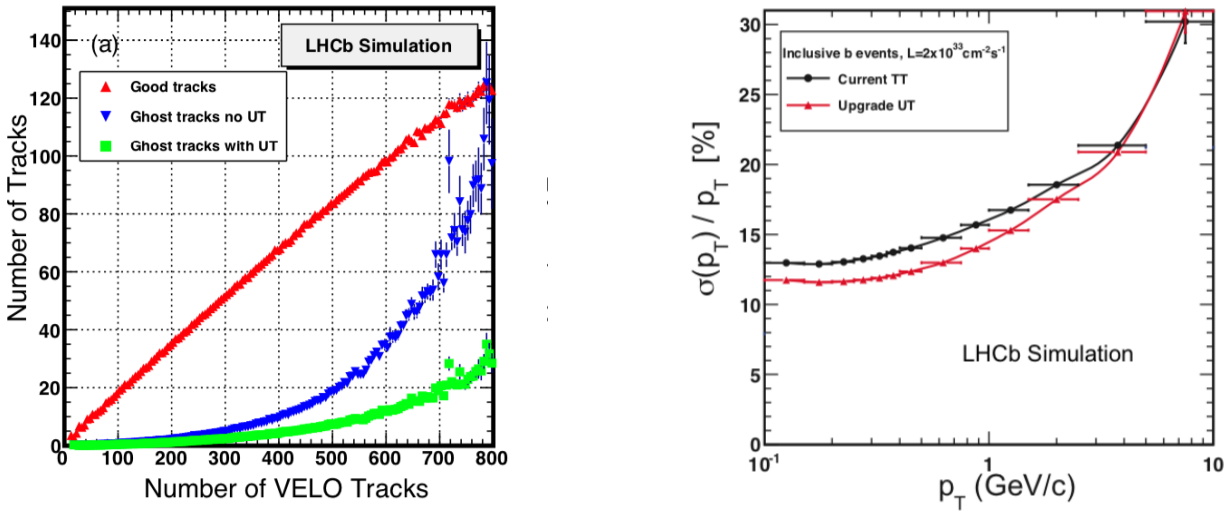

Figure 3.19: Left: simulation of the number of real reconstructed downstream tracks and ghost tracks as a function of the number of VELO tracks for a luminosity of $2 \times 10^{33}\,\mathrm{cm}^{-2}\,\mathrm{s}^{-1}$, for inclusive b-hadron decays in pp collisions at 14 TeV center-of-mass energy. Two categories of tracks are shown, with UT or without UT match. Right: resolution on the p_T as a function of p_T, for the current TT (closed circles) and the upgraded UT (red triangles). From [166].

m^2. Simulations show, Fig. 3.20, that the tracking efficiency will be lower for events with a small number of PV due to the less fine granularity. Nevertheless the detector is more performing for a higher number of PVs hence the global efficiency as a function of the pseudorapidity is higher.

Calorimeters The PS and SPD detectors, which were used by the L0 trigger, are removed. The present calorimeters will be kept as they are. The PMT gain will be reduced by a factor five to limit the PMT degradation and the Front-End electronics will be upgraded to compensate the gain for the readout at 40 MHz. The upgraded Front-End boards will be described in detail in the next Chapter.

RICH detectors and muon system The upgraded RICH detectors [170] will be similar to their predecessors, at the same position and with the same gas radiators. The system of mirrors used by RICH1 will be replaced by a new optical design to deal with the higher particle density. The light detection will be ensured by Multi-anode Photo Multiplier Tubes (MaPMT), replacing the HPDs, with a granularity of $2.9 \times 2.9\mathrm{mm}^2$ [171]. The front-end electronics will be updated to readout at 40 MHz using a new front end chip: CLARO [172]. Regarding the muon system, the first of the five muons station, M1, will be removed. Indeed it was essentially used for the L0 trigger which will not exist anymore. The M2 inner region will be equipped with Triple-GEM detectors to cope with the increased particle flux. The electronics will be also updated to readout at 40 MHz.

SMOG2 The SMOG2 system constitutes an upgrade of its predecessor SMOG. It is made of a storage cell installed upstream of the VELO which is designed to reach a much higher gas density than SMOG, by a factor of about 8 (with H_2) to 35 (with Ar). Other novelties with respect to SMOG are: a more advanced gas feed system allowing for a precise determination of the target density, the

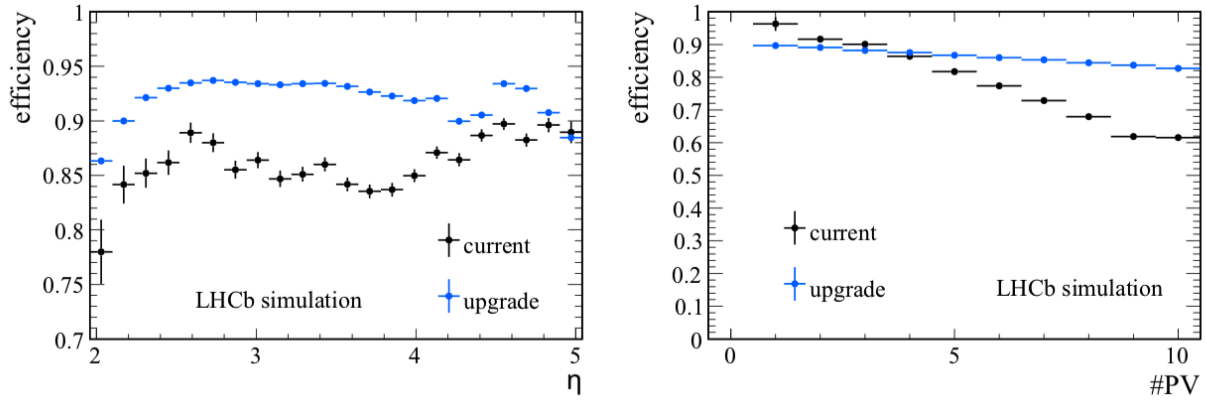

Figure 3.20: Expected track reconstruction efficiency as a function of the pseudorapidity (η) of the track (left) and of the number of reconstructed pp interaction vertices (right). From [166].

possibility to inject H_2 and D_2 in addition to the noble gases, a better defined interaction region, the possibility to run in parallel during *pp* collisions. More details on the complex design of the storage cell can be found in Ref. [148], whereas the new physics opportunities achievable with SMOG2 are discussed in Ref. [173].

Trigger The hardware trigger L0 will be removed and replaced by a full software trigger [174], which will reduce the rate to 30 MHz instead of 1 MHz. The main goal is to select beauty and charm hadron decays with the highest efficiency and purity possible. The conditions that the new software trigger has to fulfil are summarized in Tab. 3.3.

Instantaneous luminosity	$2 \times 10^{33}\,\mathrm{cm}^{-2}\mathrm{s}^{-1}$
Pile-up	7.6
Input rate	30 MHz
Maximum processing time per event	13 ms
Output bandwidth	$20\,\mathrm{kHz} \times 100\,\mathrm{kbytes} = 2\mathrm{GByte/s}$

Table 3.3: Conditions to be fulfilled by the software trigger for the upgraded LHCb detector. From [175].

In the new software trigger, the High Level Trigger (HLT), the event selection is ran on two software stages. The first one, HLT1, selects event based on the one or two-track algorithms. Here, only the calibration and alignment constants obtained from the previous run are used. The event rate is reduced by a factor 30 to 60. In the second stage, the detector is calibrated and aligned almost online and HLT2 will identify decays without keeping the raw data (following the example of the Turbo stream of Run 2). The total output volume is 80 Gbit/s. In the baseline proposal, the data from subdetectors are treated by 250 event building x86 servers to reconstruct the full event. Complete events are sent to a separate "event filter farm" (EFF) where both HLT1 and HLT2 stages are run. Recently a new project called Allen [176] proposed to run the reconstruction and selections using Graphics Processing Units (GPUs). LHCb embraced this project and decided to run the track reconstruction of HLT1 on 500 GPUs. This will reduce the global data volume of a factor 30-60, reducing considerably the cost

associated to the sending of the data to the EFF. The reconstruction and the physics selections are run at a rate of 40 Gbit/s. The limits of the rate is mainly due to the rate at which the CPU hosting server can communicate with GPU, rather than the GPUs themselves. A comparison of the data acquisition system between the baseline proposal and the new GPU proposal is shown in Fig. 3.21, where the event building step is shown in the second light blue box. The physics performances of the

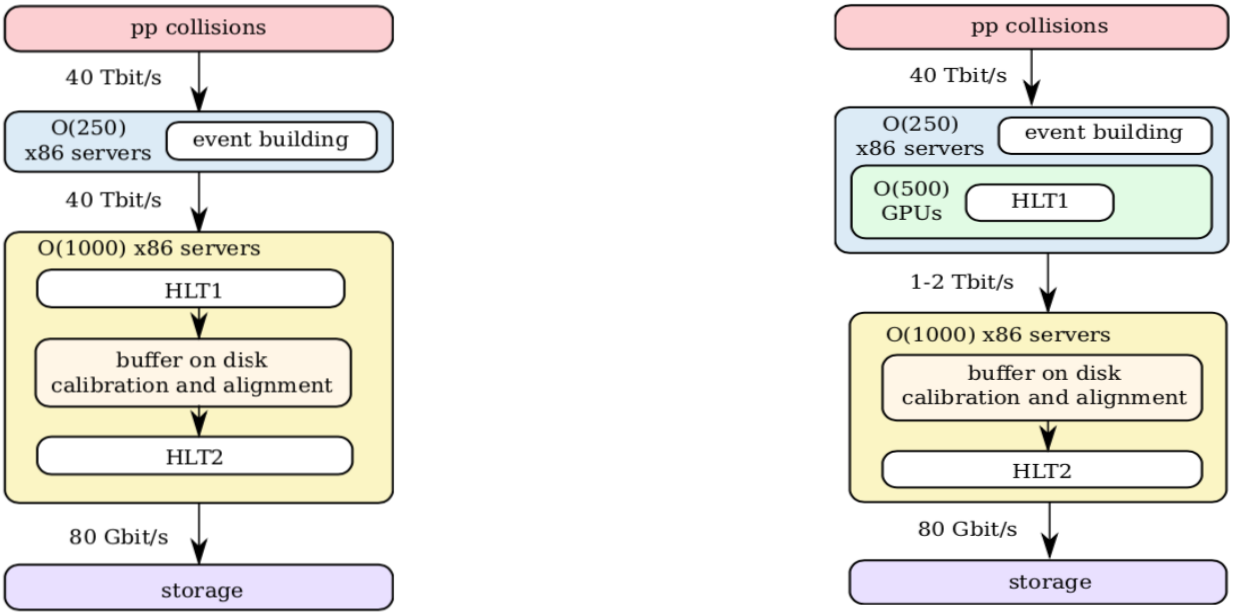

Figure 3.21: Baseline proposal (left) and GPU based proposal (right) for the upgraded LHCb data acquisition system [176].

Allen reconstruction are shown in Fig. 3.22 (left). The momentum resolution is better than 1% and it can be compared to the 0.5-1% resolution obtained from offline track reconstruction in Run 2. The PV reconstruction efficiency versus track multiplicity is also shown Fig. 3.22 (right). The performances for track and vertex reconstruction efficiencies, muon identification and momentum resolution are sufficient for efficient trigger selections for LHCb physics analyses.

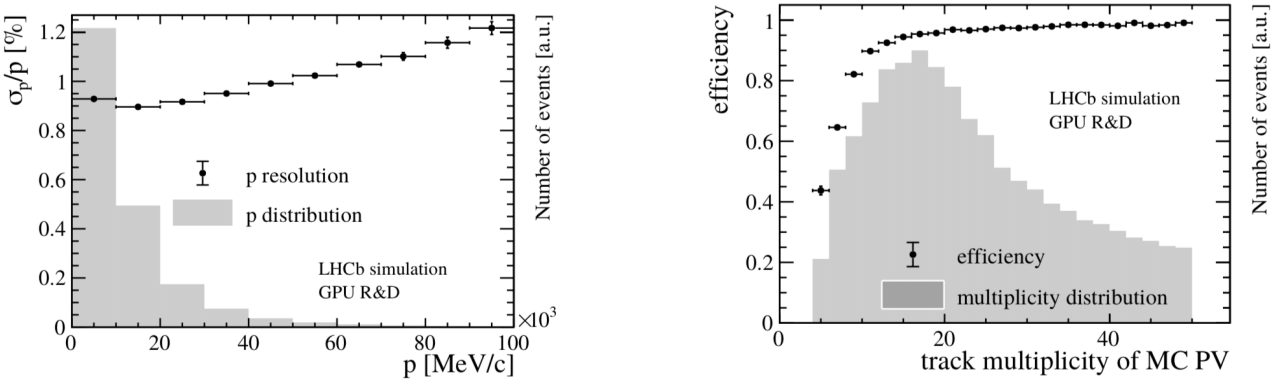

Figure 3.22: Left: relative momentum resolution of tracks passing through the VELO, UT and SciFi detectors versus momentum. Right: PV reconstruction efficiency versus track multiplicity of the Monte Carlo (MC) PV for minimum bias events, from [176].

4 Front-End electronics for the PLUME detector

In this chapter, my work on the choice of the front-end electronics for the PLUME detector will be presented. In Sec. 4.1 an introduction on the luminosity as measured in LHCb is given. Then in Sec. 4.2 the PLUME detector is described, including an overview of the intermediate steps that preceded the final detector design. In Sec. 4.3 the front-end electronics is described in details and in the following section, my work on the adaptability of the ECAL electronics for PLUME is presented. Finally, in Sec. 4.5, a promising timing measurement that could be performed thanks to the ECAL electronics is discussed.

4.1 Luminosity at LHCb

When proton bunches collide at the LHC, three processes can happen: protons can either pass close to each other without interacting, they can interact elastically without changing their structure, or finally they can collide and interact inelastically. Each of these processes is quantified by its cross section, which is representative of the probability for a process to occur. By multiplying the cross section of a process by the number of collisions taking place within a bunch crossing, one obtains the rate at which this same process occurs. Hence, the differential rate of LHC pp collisions, dR/dt, is proportional to the cross section of proton collisions $\sigma_{vis}(pp \to X)$, the subscript vis indicates a collision which is visible by the LHCb detector,

$$\frac{dR}{dt} = \mathcal{L} \times \sigma_{vis}(pp \to X) \tag{4.1}$$

where $\mathcal{L}$ is called *instantaneous luminosity*, expressed in units of $\mathrm{cm}^{-2}\mathrm{s}^{-1}$. From this, the total number of collisions R is obtained integrating the differential rate as $R = \sigma \times \int \mathcal{L}dt$, where L is the integrated luminosity, $L = \int \mathcal{L}dt$. In other words, luminosity is a quantity giving a measure of the number of collisions happening during a period of time; it is proportional to the average number of visible proton-proton interactions per beam-beam crossing, called μ_{vis}. It is measured in units of cm^{-2} because the number of collisions strictly depends on the probability for a proton proton interaction to happen, which in turn is quantified as a function of the size of the crossing area. The instantaneous

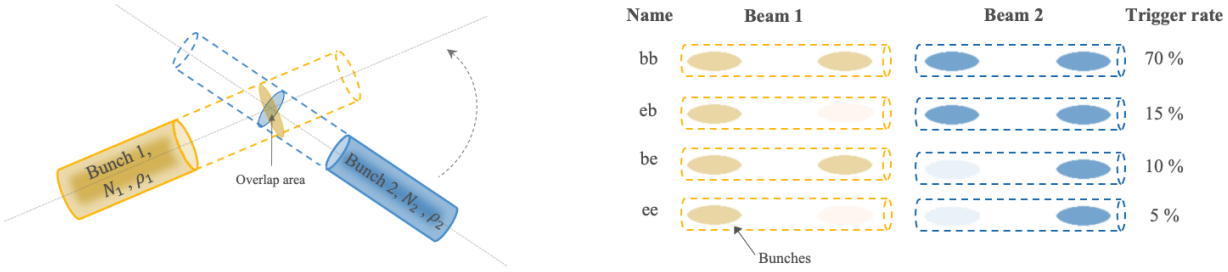

Figure 4.1: Left: sketch of two bunches crossing, N_1 and N_2 are the number of protons in the colliding bunches, the overlap area is also shown. Right: naming convention for the four possible bunches configurations described in the text (bb, eb, be, ee) with relative trigger rates.

luminosity for a pair colliding bunches can be generally written as:

$$\mathcal{L} = \frac{N_1 N_2 v_{coll}}{I_{overlap}} \tag{4.2}$$

where v_{coll} is the frequency of collisions, which is equal to the revolution frequency; N_1 and N_2 are the number of protons in the colliding bunches of beam 1 and 2 respectively; $I_{overlap}$ is the overlap integral, embodying the area of the two bunches which actually overlaps when the crossing happens. On one hand, v_{coll}, N_1 and N_2 are measured by the LHC, with an uncertainty smaller than 0.5%. On the other hand, the overlap integral (at IP8) is unknown, but it can be measured within LHCb. A drawing showing these quantities is shown in Fig. 4.1 (left). The luminosity measurement is crucial for the physics analysis, especially for cross section measurements which are directly derived from Eq. 4.1, and need to be performed with the best possible accuracy. In general, there exist two methods to measure luminosity classified as indirect or direct. The first, is based on external quantities *e.g.* the measurement of the elastic and total cross sections [177] or the comparison with a process for which the absolute cross-section is known precisely from another measurement, or, when possible, from theory. The direct methods instead consist in measuring some of the beam parameters to determine the luminosity, these are the "van der Meer scan method" (VDM) [178] and the beam-gas imaging method (BGI) [179]. The VDM method consists in making a scan of the beam by moving them across the transverse plane (*i.e.* along x and y) and record the rates of collisions as a function of the transverse beam separation to infer the cross section. This method was first used at CERN ISR [178] and it is now widely used at the LHC. The BGI method instead consists in reconstructing interaction vertices between beam particles and the gas in the beam vacuum, in order to measure the shapes, angles and positions of the beams without having to move them. From this, the overlap integral of Eq. 4.2 can be inferred. This method makes use of the unique capability of the LHCb experiment of injecting gas in the VELO using the SMOG system, described in Sec. 3.2.4. An illustration of the BGI method is shown in Fig. 4.2, where the shape of the beam emerges from the distribution of reconstructed vertices. These two methods combined, VDM and BGI, allowed to determined the luminosity with a precision of 1.16% for pp collisions at $\sqrt{s} = 8\,\text{TeV}$ [147], more details are given in the following section.

At the LHCb interaction point (IP8) the luminosity is voluntarily reduced in order to optimize the physics reach. This is done via a procedure called luminosity levelling, which consists in increasing

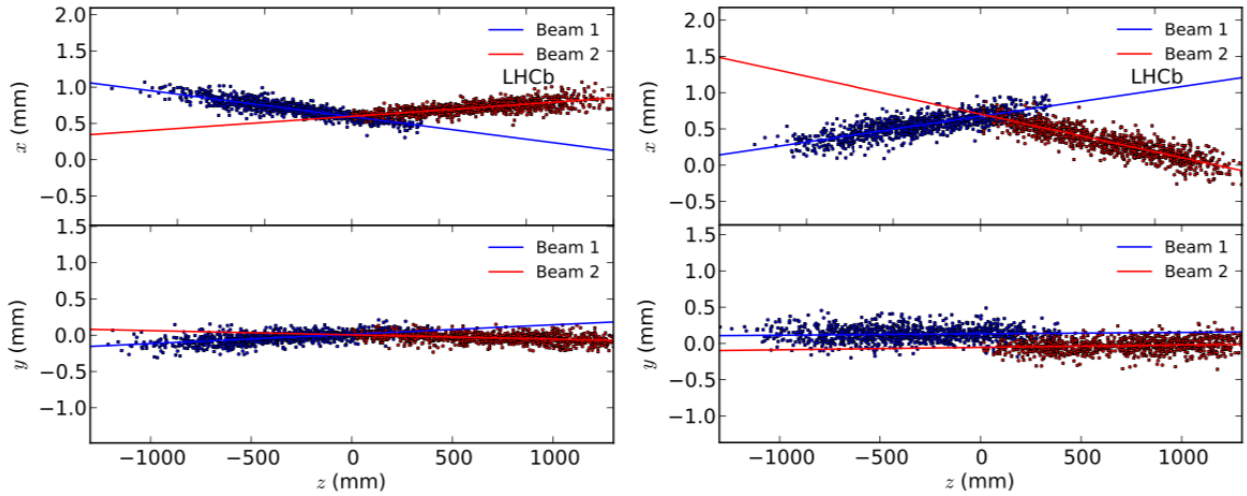

Figure 4.2: Positions of the reconstructed vertices in the $x-z$ (top) and $y-z$ (bottom) planes for two different fills of 2012 (left-right) at $\sqrt{s} = 8\,\text{TeV}$. From [147].

the distance between the two colliding beams in the plane perpendicular to the beam direction, at the beginning of a fill, and then progressively reduce it in order to maintain the luminosity level constant. This procedure results in a reduction of the luminosity from the $10^{34}\,\text{cm}^{-2}\text{s}^{-1}$ delivered by the LHC for ATLAS and CMS to $4\times10^{32}\,\text{cm}^{-2}\text{s}^{-1}$ at IP8 (for Run 2). This procedure is necessary in order to reduce and maintain constant the pile up in the LHCb detector[1]. The LHCb trigger efficiencies decrease quickly when the pile-up increases since a higher occupancy requires a larger bandwidth and the total bandwidth is limited. Thus, the low pile-up condition is essential for LHCb to be able to associate primary vertices of the proton-proton collisions to the corresponding displaced b or c hadron vertices, without mixing primary vertices and decay products coming from different collisions[2]. The full luminosity recorded by LHCb during Run 1 and Run 2 is shown in Fig. 4.3 (left), a total of respectively 3.2 fb^{-1} and 5.9 fb^{-1} has been collected. In Fig. 4.3 (right), the instantaneous luminosity for one fill (fill 2006) is shown as a function of time for ATLAS, CMS and LHCb. One can see that while the instantaneous luminosity in ATLAS and CMS decreases exponentially, at LHCb it has an approximately constant value thanks to the luminosity levelling technique.

4.1.1 From calibration runs to a luminosity measurement for physics analysis

The VDM scans and BGI methods are used during dedicated short runs to perform calibration measurements, then the results obtained need to be translated to the complete data-taking period. The translation is performed using some standard processes for which the interaction rate is measured continuously during physics runs. As mentioned above, luminosity is proportional to the average number of visible pp interactions per beam crossing μ_{vis}. Any interaction rate measurable at LHCb (and any "counting" detector) can in principle be used as a luminosity monitor for the luminosity measurement,

[1]The pile up is the superposition of several collisions in the detector during the same bunch crossing.

[2]For each bunch crossingx there can be more than one interaction between protons, also called "collision". An event is the ensemble of interactions for a given bunch crossing. In LHCb jargon, an "empty event" indicates a bunch crossing where no interaction happened.

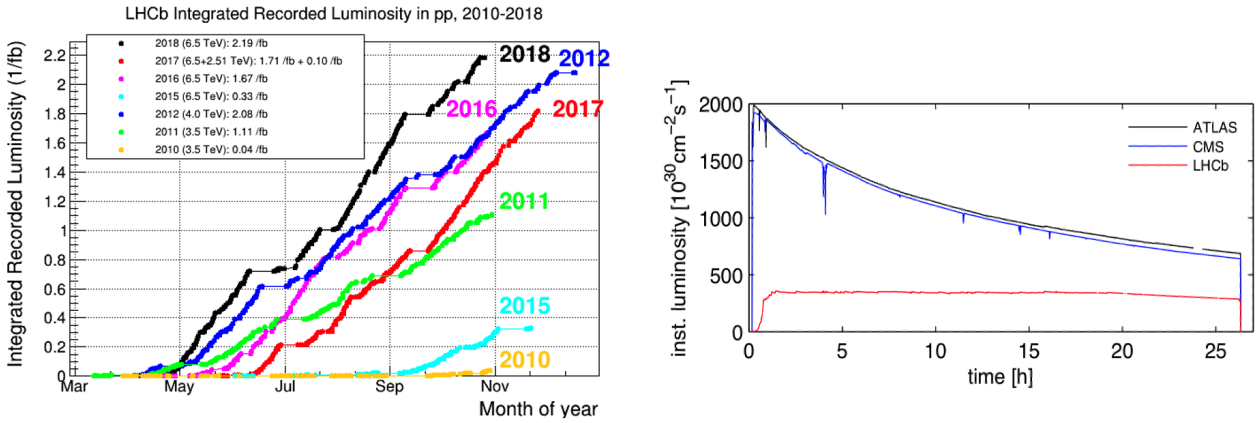

Figure 4.3: Left: recorded integrated luminosity for *pp* collisions between 2010 and 2018, from the LHCb public website http://lhcb-public.web.cern.ch/lhcb-public/. Right: Instantaneous luminosity of fill 2006 (in 2011) as a function of time, for three different LHC experiments, from [180]. The instantaneous luminosity in ATLAS and CMS decreases exponentially, whereas at LHCb the luminosity levelling technique allows to have an approximately constant value.

thus the subscript *vis* doesn't point to a specific physics process here. In LHCb, there are specific trigger lines dedicated to measure quantities used for luminosity purposes. These lines, called "luminosity triggers", are run on random beam crossings with an overall frequency of 1 kHz. Of this rate, 70% is assigned to slots where two bunches cross (bb), 15% to slots with only a beam-1 bunch (be), 10% to those with only a beam-2 bunch (eb) and the remaining 5% to empty slots (ee). A sketch of these 4 possible configurations is shown in Fig. 4.1 along with the respective trigger rates. The be, eb and ee types are used for background subtraction and beam monitoring. Those luminosity triggers store a small number of observables comprising: the number of vertices and tracks reconstructed in the VELO, the number of muons reconstructed in the muon stations, the number of hits in the PS and in the SPD (in front of the ECAL) and finally the total transverse energy deposit in the calorimeters. All of these observables are obtained directly in the hardware trigger unit L0, except for the VELO related ones which require a software reconstruction; all these observables are proportional to the luminosity. In principle, luminosity can be obtained by integrating one of the observables above, however this method heavily relies on the stability of the observable itself and on its linearity in the presence of multiple interactions. What is used instead, is the fraction of empty (or invisible) events during beam-beam crossings (bb), denoted here as P_0. The empty events are measured by setting a threshold below which it is considered that no *pp* interaction occurs in the bunch crossing. The way luminosity is measured from those events is explained in the following. The number of interactions in one bunch crossing follows the Poisson probability distribution:

$$P(n,\mu) = \frac{\mu^n}{n!} e^{-\mu} \tag{4.3}$$

where n is the number of pile-up interactions occurring in one bunch crossing and μ is the average number of interactions (proportional to the luminosity, $\mathcal{L}$, and the inelastic cross section, σ_{inel}: $\mu \propto$

$\mathcal{L}\sigma_{inel}$). Thus μ is given by:

$$\mu = -\log(P_0) = -\log\left(\frac{N_0}{N}\right) - \frac{1}{2}\left(\frac{1}{N_0} - \frac{1}{N}\right) \tag{4.4}$$

where N_0 and N are the numbers of empty and all events and the second term are second order corrections [181]. This is called the "logZero method" [182] and it is more robust than the proportionality method described above, since it is not sensitive to any non-linearity due to multiple events or any gain and efficiency variations of the observables. The possible backgrounds coming from beam parasitic interactions are subtracted using the information from the other bunch types:

$$\mu_{\text{vis}} = -\left(\log P_0^{\text{bb}} - \log P_0^{\text{be}} - \log P_0^{\text{eb}} + \log P_0^{\text{ee}}\right) \tag{4.5}$$

where P_0^i with $(i = bb, ee, be, eb)$ are the probabilities to find an empty event in a bunch-crossing slot for the four different bunch crossing types. The contribution from P_0^{ee} is negligible. Note that this formula is only valid if the bunch crossing of the same type have similar properties, otherwise the thresholds set to determine if an event is empty or not could vary between different bunches of the same type.

The most stable results for this method are obtained using as observable the number of tracks and vertices reconstructed in VELO, where an empty event is defined to have less than 2 tracks in the VELO. After processing, the luminosity information from the best luminometer is added to the end of every LHCb file, the File Summary Record (FSR), and it is used offline.

4.1.2 Beam monitoring systems during Run 1 and Run 2

During Run 1 and Run 2, the monitoring of the beam-induced background and radiation at IP8 was ensured by three systems: the Radiation Monitoring System (RMS) [183], a set of Beam Loss Scintillators (BLS) [184] and a Beam Condition Monitoring System (BCM) [185]. The RMS is based on Metal Foil Detector (MDF) technology, which consists in a 5-layer structure of 50 μm thick aluminum foils. When particles impinge in the metal foil surface, electrons are emitted causing the presence of positive charge in an isolated metal. Those charges are then collected and readout by Charge Integrators (ChI). It is placed at the second Inner Tracker (IT) station close to the beam, in order to monitor the dose of radiation absorbed by the IT and the related increase of leakage current. This detector will be upgraded for Run 3. The BLS is dedicated to the study of beam losses at a rate of 40 MHz and it was the only real time system providing feedback bunch by bunch. It is placed close to VELO and it is made of two quartz radiators and four plastic scintillators, readout by photomultipliers tubes (PMTs). It is an inexpensive detector which runs continuously to give feedback to the LHC operators about fast and small beam losses, along with the BCM which covers large and accumulated losses instead. The BLS is also used as online luminometer during collisions. However, the BLS presents strong non linearity and important detector effects, thus it cannot be used as a reliable luminometer by itself. Finally, the BCM is a safety system monitoring continuously the radiation conditions for LHCb. It is composed of diamond sensors symmetrically distributed around the beam pipe, placed 2131 mm upstream (BCM-U) and 2765 mm downstream (BCM-D) from the interaction

point. They are positioned close to the beam at respectively 50.5 mm and 37.0 mm of radial distance. The readout operates at 25 kHz. If the three adjacent sensors detect an activity above threshold, the BCM triggers a beam dump. This system will be upgraded for Run 3.

The online luminosity was monitored using minimum bias transverse energy thresholds (L0CALO trigger) requiring at least one hit in the SPD and one energy cluster in the HCAL. From those events, μ is measured using the "logZero method" explained above, then the cross section for this selection σ_{sel} is simulated using PYTHIA [157] and the luminosity is inferred using $\mu \propto \mathcal{L}\sigma_{sel}$.

In conclusion, during Run 1 and Run 2, these three beam monitoring systems operated successfully. The RMS was the only fully electrical device and the main purpose of it was the measurement of the radiation load for the inner tracker sensors. The BLS was the only live system doing bunch-by-bunch measurements of beam induced background with a readout system independent of LHCb and thus running 24/7. However in 2018, the BLS plastic scintillators were not usable anymore due to aging. Finally, the BCM system was the LHCb lifeguard, triggering a beam dump if dangerous radiation levels were reached. In 2018, two of the upstream BCM sensors were unusable due to the radiation damage.

4.1.3 Luminosity measurement and monitoring system for Run 3

During Run 3 and Run 4, LHCb will see a five-fold increase of the luminosity up to $\mathcal{L} = 2 \times 10^{33}\,\mathrm{cm}^{-2}\,\mathrm{s}^{-1}$. The same luminosity levelling as in Run 1 and Run 2 will be perform to lower the luminosity delivered by the LHC, which will be of $2 \times 10^{34}\,\mathrm{cm}^{-2}\,\mathrm{s}^{-1}$. This procedure allows to maintain a constant μ during the operations within a $\pm 5\%$ range and it relies on the possibility to measure some necessary quantities in real time. These quantities are expected to vary from fill to fill, and more importantly from one bunch crossing to another, even more than during Run 1 and Run 2; hence they need to be monitored to give a real time feedback to the LHC operators. It has been estimated that a precision of 5% on the particle multiplicity is needed for the online operation. Moreover, for the upgrade of the LHCb fixed-target program the multiplicity determination will be also crucial to separate the signal (*i.e.* beam-gas collisions) from parasitic proton or ion beam collisions. Furthermore, the upgraded LHCb detector will be running with a fully software trigger, as explained in Sec. 3.3; this also requires that the running conditions are precisely known and maintained stable in "real time". On top of that, the increase of luminosity makes the monitoring of the radiation level and beam-induced background even more crucial to keep the LHCb detector running safely and prevent fast aging of the fragile detector components. As a consequence of the new requirements listed above, the necessity of a new detector dedicated to the online luminosity measurement and monitoring of the beam conditions has become evident. This new system should be able to fulfil the following requirements:

1. Provide a measurement of the luminosity (and μ) online for the luminosity levelling procedure.
2. Measure the luminosity per bunch.
3. Measure the radiation background and ghost charges level[1] and produce alarms.

[1]The base RF of the LHC is 400 MHz. This gives 35640 buckets, spaced of 2.5 ns, which can be empty or filled with bunches. Only one bucket out of ten is filled with a bunch, for a total of 3564 bunches. All particles should be contained within the filled bunches. However, the nominally empty buckets may contain some protons, these are called "satellite

4. Monitor the LHC filling scheme in real time.
5. Help determining the centrality of heavy-ion collisions.
6. Provide accurate offline luminosity.
7. Run independently of the LHCb DAQ system to provide continuous monitoring.
8. If possible, provide a timing measurement to monitor the LHCb clock shift.

The PLUME project started working in 2019 on a possible system to cover the above requirements and provide a luminosity measurement during Run 3. The path leading to the final detector design as well as the final detector choice are presented in the following sections.

4.2 The PLUME detector

The luminosity measurement is performed using the "logZero method" which is based on the quantification of number of empty events, as discussed in the previous section. In order to determine if a bunch crossing is empty or not (*i.e.* if the protons within the bunches interacted or not), PLUME will measure the number of charged particles produced (within the PLUME acceptance) in a bunch crossing and if this number is below a certain threshold then the collision is considered as "empty". On top of that, it also has to monitor the activity of the beam by measuring if there are particles produced outside the nominal filled bunches defined by the LHC. The physics principle used to detect charged particles is the Cherenkov effect, *i.e.* the emission of light by charged particles passing through a medium at a phase velocity bigger then the velocity of light in this same medium. The PLUME detector aims at collecting the Cherenkov light produced by the charged particles, which has a wavelength lying between 300 - 650 nm. Several solutions have been studied both for the choice of the medium (radiator) and of the photodetector; they are briefly discussed in Sec. 4.2.1. The final choice is to use photomultiplier tubes (PMTs) to detect the light and fused silica (quartz) as radiator. The detector design has been mainly guided by the constraints on the radiation resistance, available space and time (it has to be ready before the start of Run 3 beginning of 2022). The final design is described in Sec. 4.2.2. The main contributions of this work to the PLUME detector concern the choice and testing of the readout electronics and the timing measurement described in Sec. 4.3 and Sec. 4.5 respectively.

4.2.1 First prototypes

At the time the project started, few options for the radiator and photodetector have been considered. Several setups have been tested at DESY facilities, in December 2019, with a beam of electrons bunches of 6.5 GeV at 2 kHz and using an Hamamatsu R7378 PMT. The following setups have been tested and more details can be found in Ref. [186]. The first option implies a quartz fiber bundle as radiator positioned at 45° with respect to the incoming particles (corresponding to the opening angle of the Cherenkov cone) to maximize the light yield. The bundles allow to transport the light outside the high

bunches" if they are within one of the other 9 buckets (hence within 25 ns), or "ghost charges", if they are in an empty slot within two groups of 10 buckets.

radiation zone. A yield of about 7 photoelectrons[1] (p.e.) per incoming electron has been measured. The second configuration consists in adding a garnet scintillator as radiator and use the bundles to transport the light to the PMT. The measured light yield was lower, 4 p.e. per incoming electron, due to the small size of the tested crystal. Moreover, the signal was too long in time. The third tested configuration consisted in placing the garnet directly on the PMT. This gave a much higher yield, 400 p.e. per incoming electron, with a decay time of 14 ns for the output signal pulse. As fourth option, the PMT alone with its quartz window has been tested. The latter option has been inspired by the design of the LUCID detector [187][188], a luminosity detector placed in the ATLAS experiment. This gave a short signal pulse (3 ns) and a reasonable yield of 24 p.e. per incoming electron; the signal obtained is shown in Fig. 4.4. The fifth and last option tested consisted in a system of parabolic

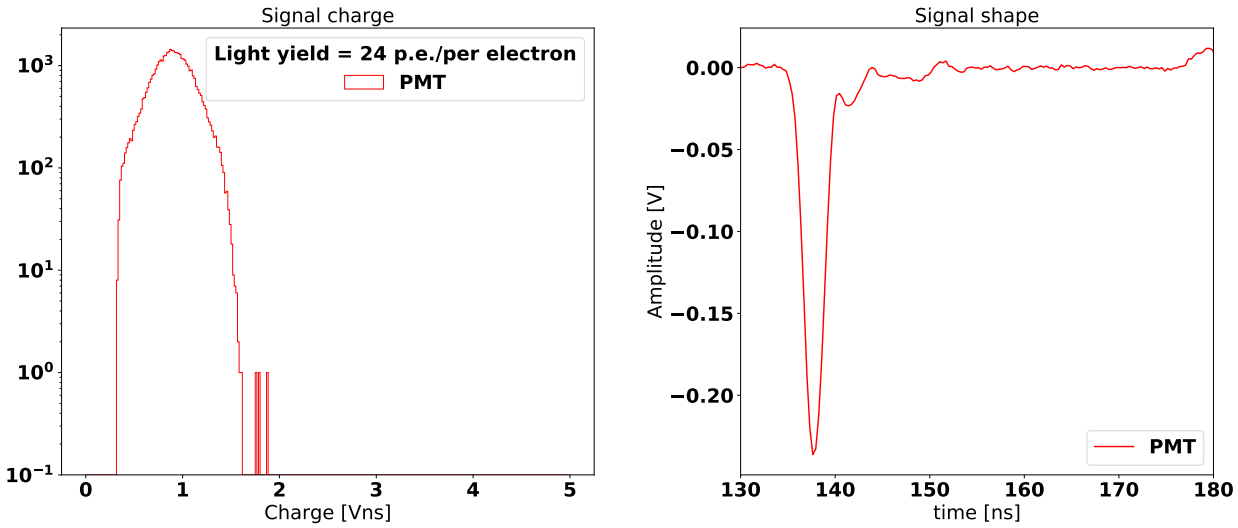

Figure 4.4: Signal from the DESY test beam for the PMT coupled to a quartz tablet. Left: response of the PMT, the charge was measured in $V \cdot ns$ over 50 Ohm, hence one unit corresponds to 20 pC. Right: signal shape out from the PMT. From Ref. [186].

mirrors to transport the light, produced in a radiator or in a scintillating crystal, to the PMT thus avoiding again the high radiation zone. The light yield was found to be lower due to the poor optical tuning of the system. Furthermore, this option would require more space and a complex mechanical configuration. Out of this test beam, the PMT with a quartz tablet on top appeared to be the most suitable option in terms of signal speed, radiation resistance, light yield and mechanical complexity. In this system, the native PMT quartz window serves as radiator and the additional quartz tablet is used to increase the signal yield. This increase is however moderated by the quality of the contact between the tablet and the PMT window.

[1]Photoelectrons are the electrons created in the PMT photocathode by the incoming photon (via photoelectric effect), see Sec. 4.2.2 for a detailed description of the working principle of a PMT.

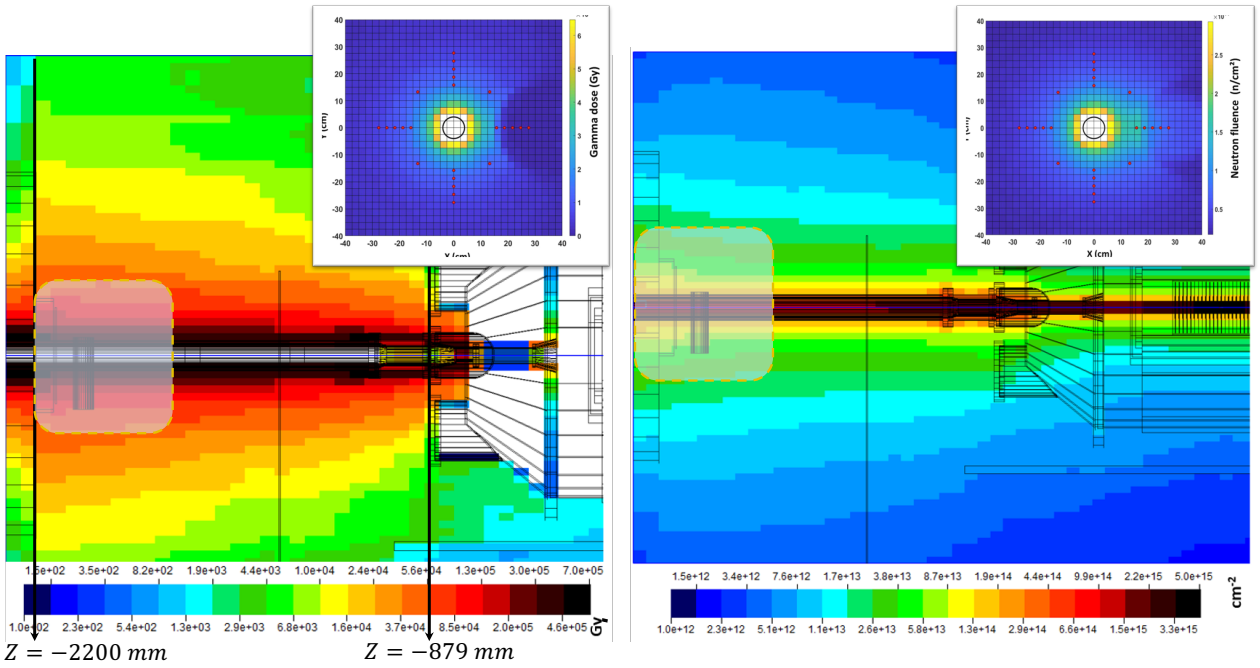

Figure 4.5: Total simulated dose in the region upstream the LHCb VELO detector that will be accumulated during the LHC Run 3 corresponding to an integrated luminosity of 50 fb^{-1} [189]. Left: ionizing dose in Gy. Right: radiation dose expressed in 1 MeV neutron equivalents per cm^{-2}. The yellow dashed transparent boxes show the approximate position of the PLUME detector. Overlaid on the top right of each figure, a slice of the xy plane at $z = -1570\,\text{cm}$ is shown. The red dots indicate the approximate PMTs positions. Adapted from Ref. [190].

4.2.2 Final design of the detector

The PLUME detector will be composed of 48 PMTs placed around the beam pipe in a double cross structure formed by a two-layers hodoscope as shown in Fig. 4.10. It will be placed upstream the collision region and it will be used in a counting mode (yes or no response with a changeable threshold). This is possible thanks to the small detector size, so that the probability to have two particles crossing one detector cell is small. The main constraints for the detector design were the available space, the radiation hardness and the need of a fast signal lying within 25 ns to avoid spillover [1] and ensure an efficient readout. The expected radiation dose around the VELO detector for 50 fb^{-1} of data collected during Run 3 is shown in Fig. 4.5. The technology based on the measurement of the Cherenkov light allows to produce and collect a signal within a short time ($\sim 10\,\text{ps}$). The choice of the PMT (instead of MaPMT for instance) has been guided by the DESY test beam described in the previous section and by the precious experience inherited from the LUCID detector [188], a luminometer placed at the ATLAS experiment that ran successfully during Run 1 and Run 2. Another constraint was set by the positioning of the detector with respect to the VELO detector. In order to use VELO tracks for calibration, the two layers of the PLUME hodoscope should be placed between 5 ° and 10 ° with respect to the beam axis. This means that the PMTs will be placed at a distance between 7 cm and

[1] The spillover are collisions from an adjacent bunch crossing leaking and producing signal in the next or previous bunch crossing.

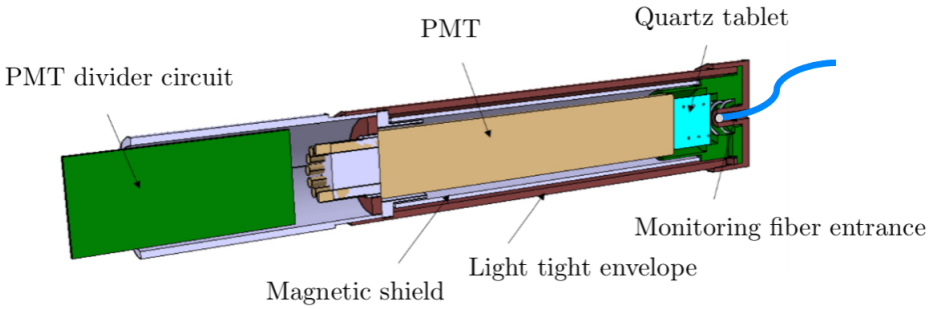

Figure 4.6: Schematic view of the PLUME elementary detection module.

15 cm from the beam pipe, where the radiation dose ranges from 80 and 200 kGy and the neutron fluence is around 1×10^{14} neutrons/cm^2, see the radiation map in Fig. 4.5. An additional not negligible constraint was the short time available to produce and test the detector. From these requirements the design of the PLUME detector has been defined. Ultimately, PLUME will be a relatively simple detector based on the collection of Cherenkov light using the same PMTs as in LUCID and positioned in a double ring shape for calibration with the VELO tracks. The single detector modules along with the characteristics of the PMTs, the final layout of the detector, the choice of the readout electronics and the calibration system are discussed in the following sections.

Single detection module

A single detection module is shown in Fig. 4.6. The PMT is connected to its socket (named PMT divider circuit in the picture) and placed along with the quartz tablet in an Aluminum light tight tube. At the end of it, there is a hole to inject light with fibers for monitoring purposes (see the paragraph on calibration and monitoring below). The PMT is surrounded by a permalloy screen to provide a shielding against the residual magnetic field at the PLUME position. The total length of the detection module is 153 mm with a diameter of 24 mm. Then the module will be encapsulated in a polyetheretherketone (light) material comprising the PMT, its socket and the quartz tablet.

The photomultipliers tubes The photomultipliers chosen for PLUME are the R760 PMT produced by HAMAMATSU and successfully used in the LUCID detector [187][188]. A picture of a R760 PMT and a schematic view of its working principle are shown in Fig. 4.7. The charged particles striking the PMT window, produce Cherenkov light (either in the window itself or in the PLUME case after crossing the additional quartz tablet placed in front of the PMT). These Cherenkov photons are converted to electrons (called photoelectrons) in the photocathode, as a consequence of the photoelectric effect. Then they are accelerated by an electric field and directed to a chain of dynodes. After striking the first dynode, more low energy electrons are emitted, and these electrons are in turn accelerated toward the second dynode and so on until the last dynode. An exponentially increasing number of electrons is produced at each dynodes and at the end all the electrons (around 10^6 electrons depending on the gain) are collected and form a sharp current pulse which can be detected. The R760 PMT has a 1.2 mm thick silica glass (*i.e.* quartz) window and a photocathode of 10 mm of diameter.

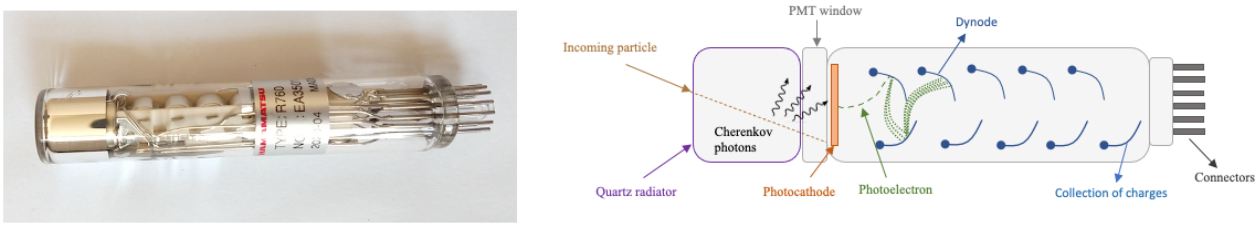

Figure 4.7: Left: a picture of the R760 HAMAMATSU PMT. Right: a schematic view of the PMT amplification chain.

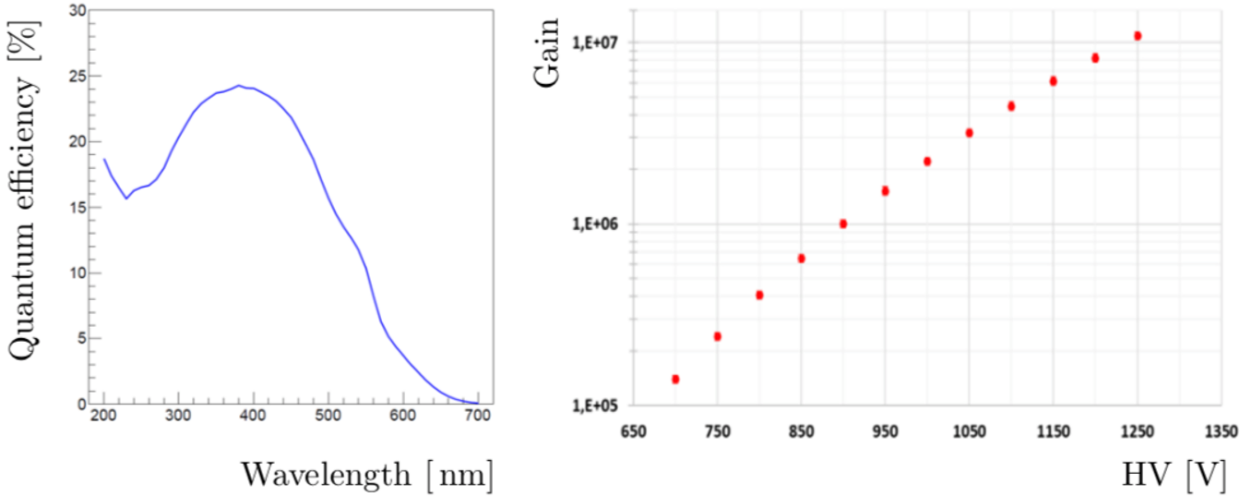

Figure 4.8: On the left the quantum efficiency of the R760 HAMAMATSU PMT is shown as a function of the wavelength. On the right, the gain curve as a function of the biasing voltage.

It has 10 dynode stages and the gain for an average voltage of 900 V is around 1×10^6. The variation of the gain as a function of the applied voltage is shown in Fig. 4.8 (right). The PMT is sensible to wavelengths within 160 to 650 nm. Its quantum efficiency (Q.E.)[1] as a function of the wavelength is shown in Fig. 4.8 (left). The higher is the Q.E. the higher will be the current at the output of the PMT and hence the easier it will be to read a signal above the pedestal of the electronics. For this PMTs, the Q.E. reaches its maximum ($\sim 23\%$) around 420 nm. These PMTs have been tested under irradiation with gamma rays up to 2×10^5 Gy dose and up to 2.7×10^{14} neutrons/cm^2 fluence [191]. The only sizeable effect observed after radiation is the increase of the dark current[2] of about one order of magnitude.

Quartz tablet The addition of a quartz tablet glued on top of the PMT window is expected to increase the light yield, this has been confirmed by a complete GEANT4 simulation. The simulation showed that assuming an ideal optical coupling between a 5 mm quartz and the PMT, the light yield should be increased by a factor 5 [186]. The gluing procedure is complex, several radiation resistant materials are under study for achieving the best optical contact possible minimizing the loss photons or inducing reflections. The choice of the quartz tablet on the other hand, has been guided by a second test beam performed at DESY, in September 2020, with 5.4 GeV electrons. A PMT coupled to a polished quartz tablet (Corning HPFS 7980) of 10×10 mm^2 and 5 mm thickness with a TSF451-50M grease is the option retained from the tests. The radiation resistance of the quartz and of several optical contact materials has been studied with neutrons at the Kharkov Institute of Physics and Technology, with a 1 MeV equivalent neutron fluence of 10^{14} neutrons/cm^2. A degradation between 4% and 18% has been observed for the transmittance measured at 200 and 250 nm. The final choice for the quartz material is the Corning HPFS 7980. For the grease the Seiko-Silicone grease (TSF451-50M) is chosen as baseline candidate based on the irradiation test results.

Final layout

The final detector layout is shown in Fig. 4.9 and Fig. 4.10. The two PMT layers are placed at $z = 1680$ mm and $z = 1900$ mm from the nominal interaction point. Each layer forms a double cross shape in the $x - y$ plane, as shown in the left picture of Fig. 4.10. The double cross should allow to detect asymmetries in the beam positions and may provide information on the beam crossing angle, this is yet to be proven. In total there are 48 PMTs positioned at angles between 10° and 5°, covering a pseudorapidity (η) range between 2.4 and 3.1. The two layers allow to use the detector as an hodoscope[3], the coincidence of the two layers allows to perform a standalone calibration. The addition of the VELO track segments reconstructed upstream and entering in the PLUME acceptance, allows to get a further clean sample for calibration purposes; more details on that are given in the next section. The final box containing the detector is shown on the right side of Fig. 4.10. The entire

[1] The PMT quantum efficiency is the ratio of the number of photoelectrons emitted from the photocathode (primary electron) to the number of incident photons, where the number of emitted electrons per incident photon is either one or zero.

[2] The dark current is the current present in the PMT even if no light falls on the photomultiplier tube.

[3] A hodoscope (from the Greek "hodos" for way or path, and "skopos" for observer) is an instrument used to detect passing charged particles and determine their trajectories.

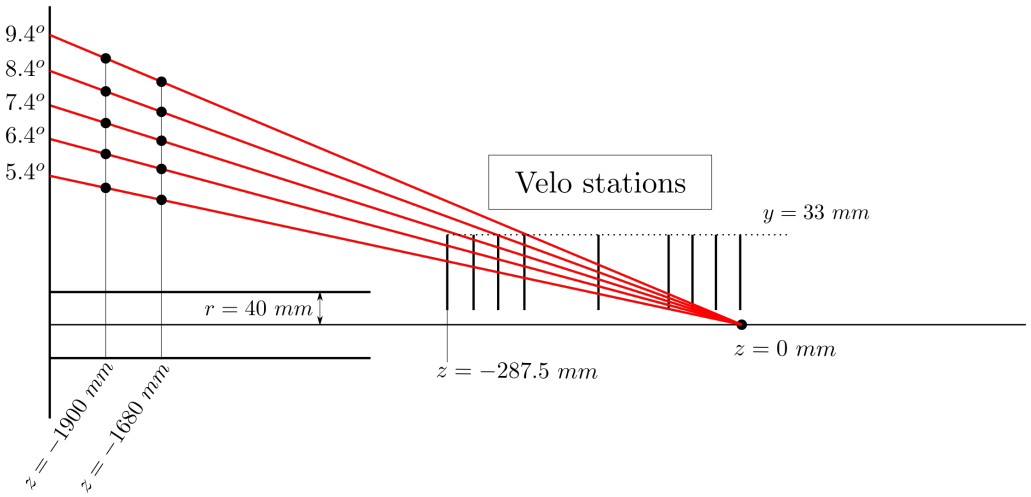

Figure 4.9: Position of the two projective layers of PMTs forming the PLUME detector. Side view showing the position along the LHCb beam direction at $z = -1680$ and $z = -1900$ mm. The VELO stations are shown as black vertical lines and the red lines illustrate which VELO stations are expected to reconstruct a track entering in the acceptance of the two projective layers of PLUME. From Ref. [190].

detector can be dismounted in less than one day if an urgent intervention on VELO is necessary.

Calibration and monitoring

The stability of the detector changes with time, thus a monitoring system is needed to monitor the variations and perform regular calibrations during the entire data taking period. The gain and efficiency of the PMT are the two quantities that can undergo large variation depending on the detector occupancy, current, temperature or radiation dose. The monitoring system designed for PLUME follows the solutions implemented for the LHCb ECAL [192], based on LEDs light injection, and complements it with an additional calibration method using upstream VELO tracks. The LED light is injected into the elementary PLUME modules using fibers (shown in blue in Fig. 4.6). The response of the PMTs to the injected light is monitored at regular time intervals and since the LED signal can last more than 25 ns (FWHM of the pulses is ~ 15 ns), the monitoring is performed during the abort gaps[1] of the LHC filling scheme. The stability of the LED pulses is in turn monitored by PIN photodiodes (Hamamatsu S1223-01) placed on the balcony next to the LEDs. Based on the monitoring response, the gain can be corrected by adjusting the high voltage with steps of 0.5 V, corresponding to a 2 % gain variation. The calibration using the upstream VELO tracks imposes a strong constraint on the detector geometry. The calibration sample will require 4-5 reconstructed upstream VELO tracks pointing towards PLUME and a coincidence signal matching the PMT of the second hodoscope layer. The coincidence allows to suppress secondaries (*i.e.* tracks which are not coming from the primary *pp* interaction vertex). This requirement strongly influenced the positioning

[1]The abort gap is a sequence of buckets in a row which are supposed to be unfilled for the beam dump procedure. When a beam dump is triggered, it takes a certain amount of time to switch on the deviating magnets used to deflect the beam into the dump. During this time the superconducting magnets should not receive any particle, that is why the abort gap exists. During Run 2 it was 3.05 µs long (121 slots).

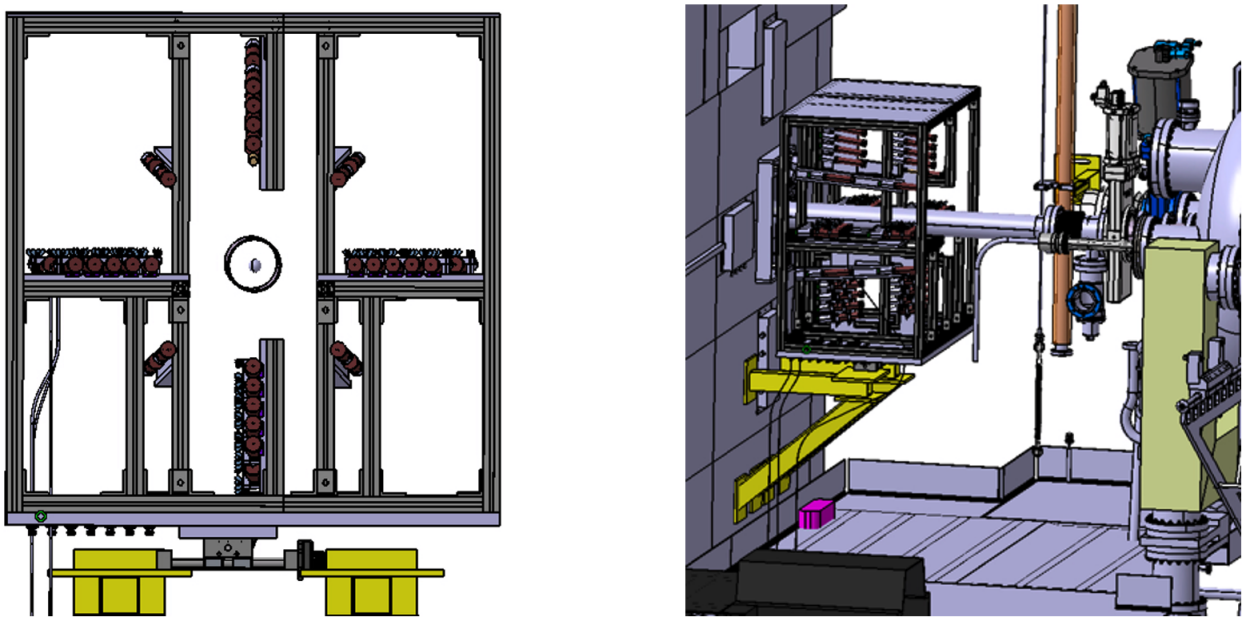

Figure 4.10: Left: PLUME (crossed shape) detector view on the $x-y$ plane. Right: view of the entire detector box upstream VELO. From [190].

of the PMTs with respect to the VELO detector, in order to have 4 or 5 upstream VELO tracks in the PLUME acceptance the PMTs layers must be placed as shown in Fig. 4.9. A simulation (based on PYTHIA8 and GEANT4) has been performed and according to it the coincidence between the two layers is detected in 1.5 % of the cases leading to a ratio of primaries to secondaries of 1:2. This proves that the coincidence is needed to deliver a clean signal of particles coming from the interaction point. In addition to the quartz fibers transmitting the LEDs light, one plastic fiber (Eska CK-40) per LED sends light to the PIN diode to monitor the LED itself and four short fibers (passing in the PLUME box) are used to loop the light back into the bundle. This light is measured by four R760 PMTs to monitor the quartz fiber transparency variation due to radiation. The entire monitoring system will be readout by an extra ECAL front-end board and will be configured by a LED timing unit (LEDTSB).

4.3 Front-end electronics for PLUME

Three options have been considered for the PLUME front-end electronics (FEE), all based on existing boards to be adapted to the PLUME case. Indeed, due to the short time available, the production of a new customized board was not possible. The first option considered was to use the updated Front End electronics of the LHCb electromagnetic calorimeter (ECAL). The second option considered, was to use a RICH-like electronics, based on the CLARO chip [172]. Both options allow for a fast integration in the data acquisition system (DAQ) and the Experiment Control (ECS) of LHCb. The third option was based on the LUCID detector readout experience. The PLUME readout should be able to run online, offline and as well independently of the other detectors, especially for the luminosity levelling procedure and the beam monitoring tasks. The advantage of using existing LHCb boards is that they

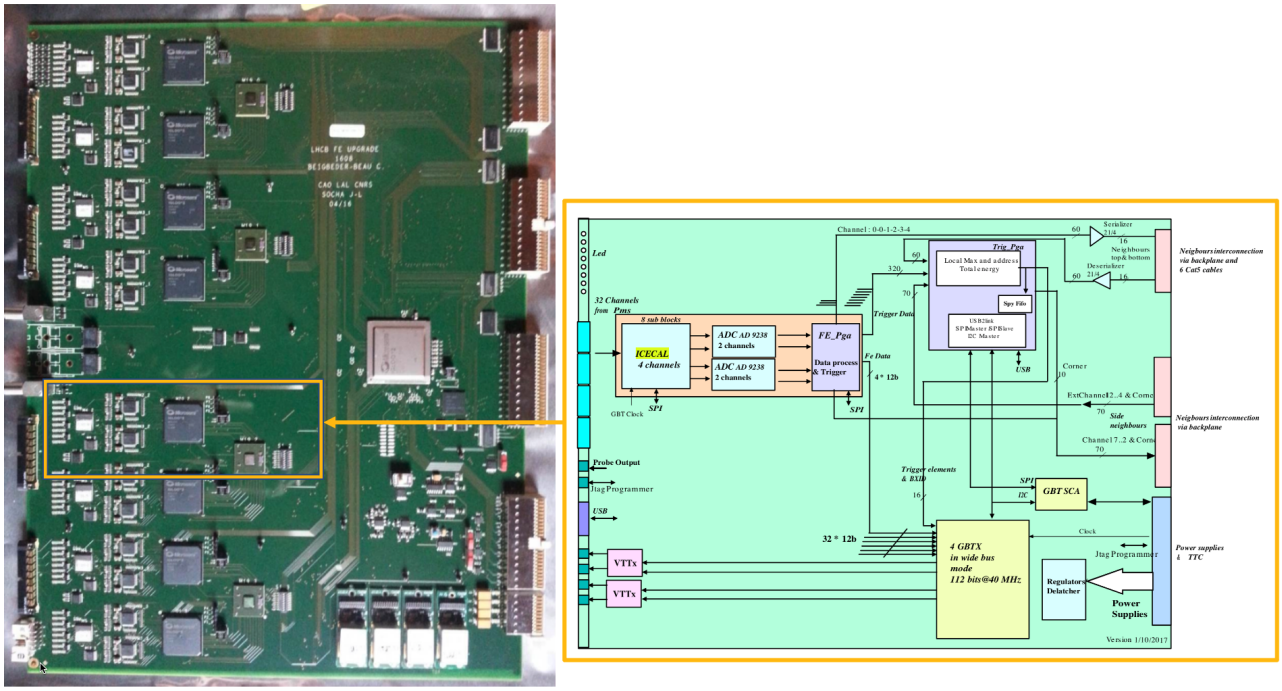

Figure 4.11: Picture of one ECAL FEB with a zoom on the front end block, showing a functional schematics of the front-end block, the power circuitry, the slow control (GBT-SCA) and trigger module, adapted from[193].

are already adapted to readout a signal at the LHC rate within the LHCb data acquisition system. However the expected signal shape from the PLUME's PMT is different from the usual ECAL PMT one. A much shorter pulse is expected, see Fig. 4.4 (right), with a pulse width[1] varying between 3 and 5 ns. In this work, the ECAL electronics has been tested to prove that it can be used to read-out the PLUME-like signal. Ultimately, the RICH and LUCID electronics have not been directly tested since the first option was already working and it was more easily accessible since the boards are tested at IJCLab.

4.3.1 ECAL-like read-out chain

The electronics chain consists of a front-end part (FE) located close to the detector, and a back-end part (BE). The FE part is composed by the front-end boards (FEB) and the control unit board (3CU). The BE is ensured by a TELL40 (PCIe40) board.

Front-end boards The ECAL Front-End Boards (FEB) have been re-designed for the readout of the upgraded calorimeter [193]. Their role is to amplify, shape, integrate and digitize the signal coming from the detector's PMTs. A picture of a FEB is shown in Fig. 4.11. A functional schematic of one front end block is also shown to help following the description. Each board is composed of 4 FE blocks treating 8 channels each, thus one board can handle 32 channels. One front-end block has 2 ICECAL analog chips, for a total of 8 chips treating 4 channels each. Then two 12 bits Analog to

[1]Here width is the Gaussian Full Width at Half Maximum (FWHM)

Bits	ECAL	PLUME
0 .. 95	ADCs: 12 bits per channel	ADCs: 12 bits per channel
96 .. 103	LLT information	Over threshold: 1 bit per channel, 8 channels
104 .. 111	BCIds, only 8 bits out of the 12 bits are transferred	BCIds, same as ECAL

Table 4.1: Data format, comparison between ECAL and PLUME organisation.

Digital Converter (ADCs) AD9238, convert the analog output into a digital one. The digital output of the 2 ADCs is processed by one FPGA (4 in total). As each FEB treats 32 channels, the ADC data requested bandwidth is $12 \times 32 = 384$ bits, 12 bits per channel and 32 channels, at 40 MHz. The FPGA re-synchronises the signal of each ADC channel to the LHC clock and performs a subtraction of the pedestal (when required) based on the previous samples reducing the low-frequency noise. The data are then sent via GBT-X chips and optical fibers to the DAQ back-end boards (PCIe40) for processing by the software trigger. There are 4 GBT-X chips, one per optical fiber. To summarize, one front-end block reads 8 channels and it is composed of 2 ICECAL, 2 dual-channel ADC chips, 2 FPGA, one GBT-X. A FEB contains 4 of these front-end blocks.

Back-end electronics and data format The back-end electronics (BE) is ensured by PCIe boards [194], widely used for the LHCb upgrade. It receives data from the FEE in a 12-bit ADC word per channel. The data processing is done in a TELL 40 board with a firmware specifically designed for PLUME. This board has three main tasks: compute the instantaneous luminosity, format the data to be sent to the high level trigger for offline storage and send an alarm in case of too high occupancy. The first task consists in filling histograms with the number of hits in coincidence (between the two hodoscope layers) measured by PLUME. The luminosity is inferred from the number of events without any hits over the total number of events, as explained in Sec. 4.1.1. The luminosity histograms can be also produced per bunch since the FEB RAW data contains the Bunch Crossing Id (BCId) information. The content of the histogram is read and updated at a rate of 1 Hz, then the content is sent to the LHC control system and stored in the central ECS database. Histograms are also sent to the online monitoring system to check that the calculations are done correctly by comparing with other quantities measured by PLUME. The second task performed by the TELL40 is to format the data. The firmware for the data formatting is similar to the one used by the calorimeter, the only difference being that the calorimeter LLT (Low Level Trigger) information is not needed. The bits used to transfer the LLT information for the calorimeter are used to store the threshold information instead. Each FEB has 4 optical fibers with 112 bits organized as shown in Table 4.1. Along with the TELL40, one other board, the SOL40, is needed for handling the configuration, timing and control commands. This board does not need to be modified for PLUME. The BE must provide measurements even when the LHCb DAQ is not running, hence the system will be running independently and constantly.

Calorimeter Control Card Unit The Calorimeter Control Card Unit (3CU) is in charge of sending the commands received from the main LHCb control system to the front-end boards via the backplane.

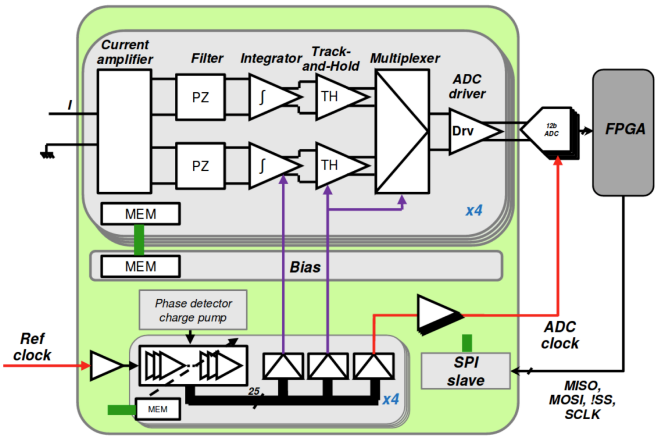

Figure 4.12: Schematic view of the analog electronics. From Ref. [193].

Each calorimeter crate needs to have at least one 3CU board plugged in, positioned in the central slot. The information sent to the FEBs are the 40 MHz clock, the Time Fast Control (TFC) and the Experiment Control System (ECS) commands. First the 3CU receives the clock and the TFC commands through optical transmitter (VTRx) decoded inside the GBTX. Then the data are processed by a FPGA (IGLOO2 family) and finally the board communicates with the FEBs via the 3U backplane. A more detailed description of the board components can be found in Ref. [195]. The 3CU do not need to be additionally tested for the PLUME detector since it only treats commands which are not related to the signal shape itself or the detector choice. However, one 3CU board is needed for PLUME to communicate with the FEBs.

ICECAL chip The ICECAL chip [196] is schematically shown in Fig. 4.12. The signal coming from PLUME is transported by a ~ 25 m CK50 cable to be injected in the ICECAL chip, which is positioned at the very beginning of the front-end block, shown in Fig. 4.11 (right). Inside the ICECAL chip, the signal is first amplified with a current amplifier. Then, the ICECAL contains two processing lines running at 20 MHz each, synchronized with the 40 MHz global LHC clock (called "Ref clock" in the figure) which arrives from the GBT-X of the front-end module. Each processing line shapes the signal with a pole zero compensation, then it either integrates the signal or is reset. The signal is then sent in a "track-and-hold module", which stores the signal and does the sampling. The two lines are followed by a multiplexer which selects the correct sub channel and presents the integrated signal at the output. An ADC driver matches the input impedance to the ADC one and sends the input charges to it. The ADC needs a clock to properly sample the ICECAL output. The phase of this clock can be tuned (ClockADC); it is synchronized with the phase of the track and hold clock (ClockTH) to perform the sampling correctly. The polarity of the FPGA clock (positive or negative depending on the phase shift between the two clocks), can also be set. The entire chip is configured through the TrigSeq FPGA with the SPI protocol (Serial Peripheral Interface). This allows to set the pole zero compensation parameters, the gain of the integration processing and the clock phase to synchronise the signal integration within 25 ns. This chip plays a crucial role in the timing measurement discussed in Sec. 4.5.4.

4.4 Test of the adaptability of ECAL FEBs for PLUME

In order to assess if the ECAL FEBs can be used for PLUME, a first test has been performed using the signal shape observed in the data collected during the DESY test beam, for the configuration with a PMT with a quartz window, see Sec. 4.2.1. The signal shape, shown in Fig. 4.4, has been emulated with a Tektronik (DP0 4104) generator. The shape obtained with the generator is a Gaussian pulse of width 3.34 ns and an amplitude of 210 mV, which corresponds to a total charge of roughly 6.68×10^{-12} C. The data acquisition is performed using the miniDAQ system available for the ECAL FEB test bench

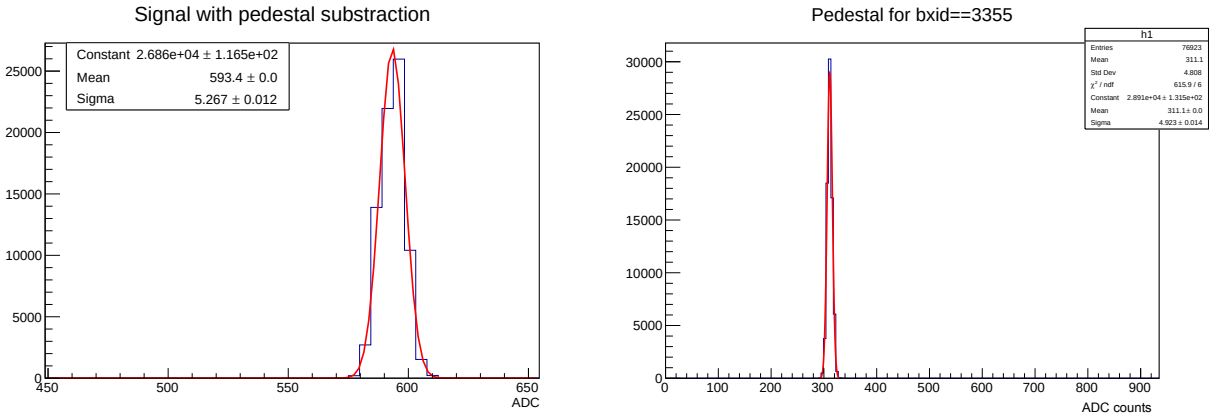

Figure 4.13: Example of reading out the expected signal shape with the ECAL FEE. Left: signal after pedestal subtraction. Right: pedestal from following bunch crossing.

which is equivalent to the LHCb DAQ system that will be used in Run 3 (the firmware version used was updated in February 2020). At first the acquisition of 100 000 events was performed running with random bunch crossing identification value (called, BCIDs or bxid) from 0 to 3563[1]. The bxid are synchronized with the LHC clock and sent to the FEBs by the miniDAQ. This has to be done since there is an unknown delay between the moment the input signal is collected and the moment it arrives in the FEBs, hence the corresponding bxid of the input signal has to be determined. The delay is mainly due to the length of the cables sending the signal from the generator to the board. Each ICECAL has 2 time integrators working in parallel, each at 20 MHz: one for odd and one for even bunch crossings. The input signal width is short with respect to the time window of the ADC integrators (25 ns). However, one needs to check that the signal is well comprised in a single BX sampling (i.e. one single integrator), otherwise a part of the signal could be lost. The signal was found to be at bxid 3353, hence the second data acquisition was performed in a window of 3350 ± 6 bxids in order to acquire the entire signal data. In this acquisition, the clock's phase was set to 12 ns for the odd integrator and 0 ns for the even one, in order to collect all the signal with the odd integrator. The pedestal was subtracted using the next odd bx-id (see Fig. 4.13, right) and it was found to be around 311.1 ADC counts. The signal after pedestal subtraction is also shown in Fig. 4.13 (left) and found to be at 593.4 ADC counts. More details on the pedestal subtraction are given in Sec. 4.5.3. The gain is thus estimated to be $\frac{6.68 \times 10^{-12} \text{C}}{593.4 \text{ ADC}} = 11.26$ fC/ADC. This test has been repeated with a more complete setup including a LED or a laser, one Hamamatsu PMT and the low attenuation CK50 cable that

[1] 3564 is the total number of bunches at the LHC

will be used to send the signal from PLUME to the FEE. This second test was also successful. The details are not given here since the setup is further discussed in Sec. 4.5.4, and some examples of signals are also shown there. These tests proved that the LHCb calorimeter FEBs can be used for the PLUME readout without additional hardware modifications, making this option the most convenient and easily adaptable one for the PLUME readout. This studies have thus defined the final choice for the PLUME front-end electronics.

4.5 Timing measurement

In order to readout synchronously the entire LHCb detector when a collision happens, a global clock set by the LHC is used to track the crossing bunches. Each of the subdetectors electronics is synchronized relative to the LHC clock to sample correctly the signal within 25 ns. The LHC clock arrives to the LHCb experiment via optical fibers travelling underground. Due to variations of temperature, the clock can undergo a shift up to few ns before arriving to LHCb inducing a desynchronization of the detector readout with respect to the LHC collisions. This shift has to be monitored in order to achieve optimal performances during Run 3, especially with respect to the calibration and alignment of the detector. For this reason, a measurement of the clock delay using the PLUME detector is proposed here.

4.5.1 Run 1 and Run 2 case

During Run 1 and Run 2, a clock shift has been observed and it has been corrected using the Outer Tracker timing measurement. The OT is a gaseous straw tube detector composed of drift tubes, see Sec. 3.2.2 for more details. The OT electronics measures the drift-times of the ionization clusters produced by the charged particles hitting the straw tubes with respect to the beam crossing signal. This time is converted into position information to reconstruct particle's trajectories. The shift of the global LHCb clock contributes to the total drift time and it can be extracted from the average of the drift-time residual distribution over the whole OT calculated for every run. During Run 1 and Run 2, this drift was automatically corrected if it changes by more than 0.5 ns. An example of average drift time residuals as measured for Run 1 is shown in Fig. 4.14. It has been shown that, if kept under 0.5 ns, the overall shift of the LHCb clock is well below the time resolution of 3 ns and therefore it does not contribute significantly to the detector resolution [197].

4.5.2 PLUME timing strategy

The OT detector will be removed during Run 3. The new tracking detector, the SciFi, does not use the straw tubes technology but rather scintillating fibers, hence the timing measurement cannot be performed anymore by means of the tracking system. A new way of monitoring the time drift of the LHCb clock using the PLUME detector is proposed here. The PLUME detector is based on the Cherenkov technology, this means that the production of light, by charged particle hitting the quartz tablet, and the transmission to the PMT happens within 7-10 ps (depending on the detector geometry). The PMT itself takes around 22 ns to produce a signal, with a raising time of 2.1 ns.

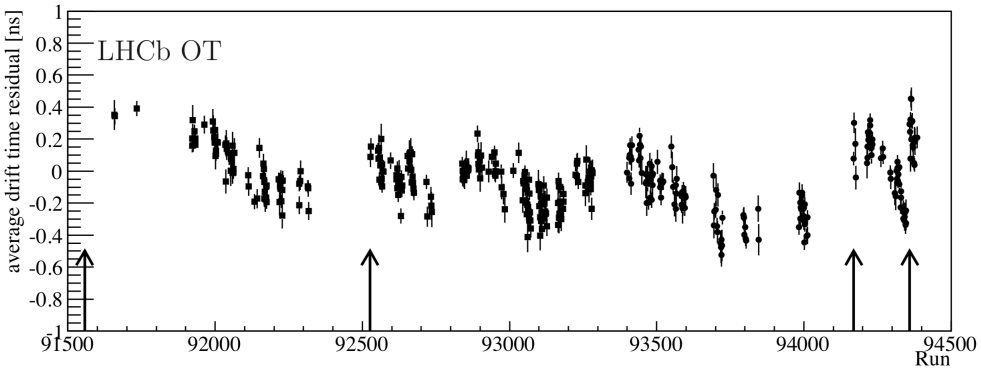

Figure 4.14: Average drift time residuals measured by the LHCb OT. Every point is a one hour run. The arrows show the adjustment of the LHCb clock, from [197].

Hence, the production and collection of the signal within PLUME is very fast. Furthermore, in the front-end electronics, a delay of the sampling time with respect to the central LHCb clock can be easily adjusted for each of the 32 channels independently with a step size of 1 ns. These two features, the fast signal and the tunable delays, can be exploited to perform a timing measurement as explained in the following. The integration of the signal is performed in the ICECAL chip. As explained in Sec. 4.3.1, there are two integration lines running in parallel at 20 MHz each, alternating 25 ns of integration and 25 ns of rest mode. The alternation of these two integrators has been designed to minimize the losses due to dead-time within two consecutive integrations. A schematic view of the integration process happening in the ICECAL is shown in Fig. 4.15. From top to bottom, the LHC clock, the PMT pulse, the integration and the track-and-hold systems (T/H) are shown as a function of time, with the 2 integrating lines drawn in green and red. This drawing is not to scale, it is aimed at guiding the reader through the explanation. The input pulse (from PMTs) is integrated by the first integrator during 25 ns. At the same time, the output charge is transferred to the hold capacitors of the T/H system. Meanwhile the other integrator stays in reset state. During the following 25 ns, the first integrator switches to reset mode and the second one performs the integration of the tail of the signal which did not fit in the first integration window. Here again, the signal is transferred to the (second) T/H system. Then the multiplexer combines the two signals to send them to the ADC drivers after selecting the correct integration channel. Each integrator is tagged using the bunch crossing ID. Since the BCID changes every 25 ns and the two integration lines operation last 50 ns with 25 ns per line [1], it is possible to associate a BCID to the first integrator and the subsequent BCID to the second integrator. In this way, once the initial assignment is done, one integrator will always have odd BCIDs and the other even ones. The phase of the T/H clock can be adjusted, which implies that the output charge of the integrator is moved to the track and hold phase earlier (or later depending on the delay). This is equivalent to changing the starting time (t_0^{int}) of the signal integration process and thus applying a delay with respect to the LHC clock. By moving t_0^{int}, the first integrator is not integrating the whole signal anymore and the second integrator integrates a bigger part of the signal

[1]The first BCID is assigned randomly to one of the two integrators at the beginning of a run, hence the odd/even association with the first/second integrator can be inverted depending on the run. However it is also possible to require having always the same odd/even association by changing the settings of the FEBs at the beginning of each run.

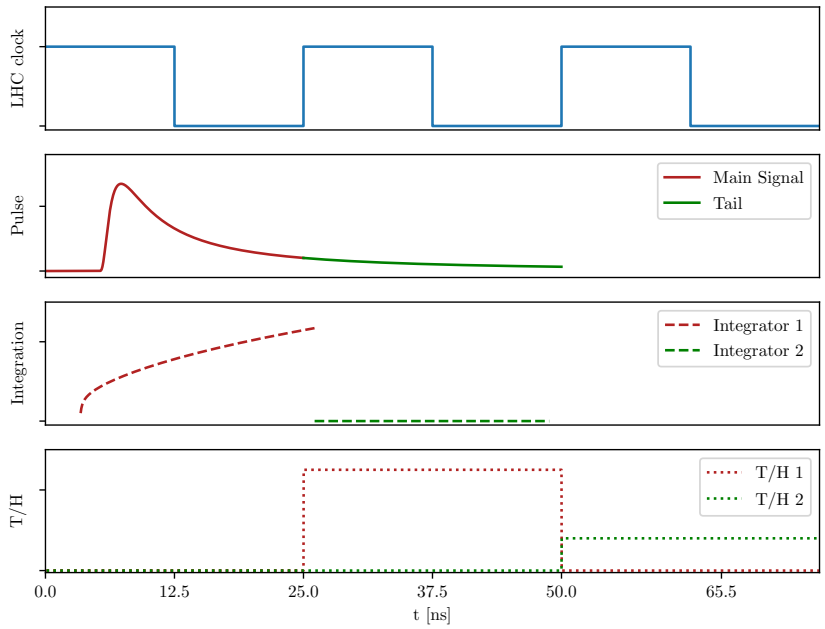

Figure 4.15: Sketch of the integration process within the ICECAL chip (arbitrary units on y axis) for an ECAL-like signal.

rather than only the tail. Thus by gradually increasing the delays from 0 to 25 ns, it is possible to perform a scan, monitoring the gradual shift of the signal (previously fully contained in the first integrator) from one integrator to the other. This shift is shown schematically in Fig. 4.16 where the area of the Gaussian signal[1] integrated by the integrator tagged as BCID 39 is shown in magenta and for the BCID 40 in cyan, three different delays are shown (10.5, 12.5 and 14.5 ns), to help visualizing the shift of the signal integration window. If the LHCb clock is perfectly synchronized with the LHC clock, for a delay of $d_{split} = 12.5$ ns the signal should be half-half split between the two integrators. By drawing the difference of signals between the two integrators (*i.e.* between two consecutive BCIDs) as a function of the delay applied, it is possible to measure where is the half-half splitting point situated. This should give a curve, with a typical S-shape, where the inflection point correspond to d_{split}. The ideal S-shape curve that one should obtain is shown in Fig. 4.17. The tails correspond to a signal fully integrated by only one integrator. A shift from the expected $d_{split} = 12.5$ ns value would indicate a desynchronization of the LHCb clock with respect to the LHC one. The resolution required for this measurement should be at least as good as the 0.5 ns obtained with the OT for Run 1 and Run 2.

[1]Note that the signal shape is only approximately Gaussian.

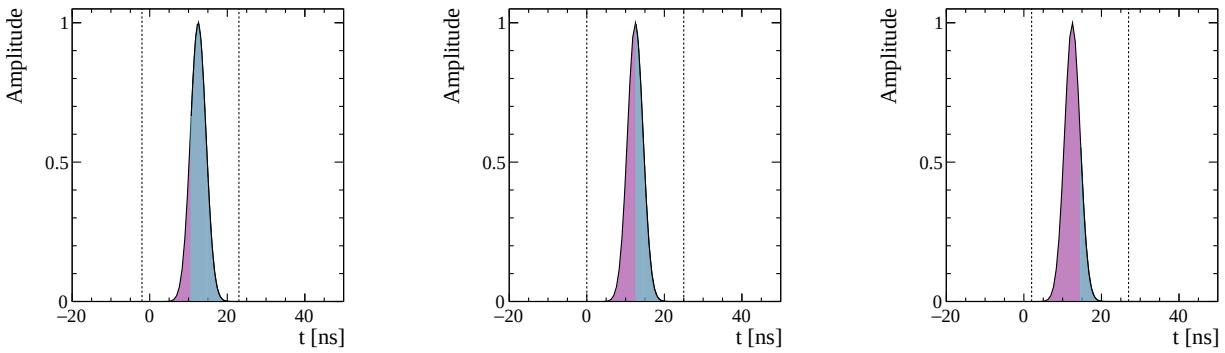

Figure 4.16: Gaussian signal shape for different delays (10.5, 12.5 and 14.5 ns). The magenta region represent the signal integrated by the integrator tagged as BCID 39 and the cyan as the BCID 40. The dashed vertical lines represent the 25 ns window.

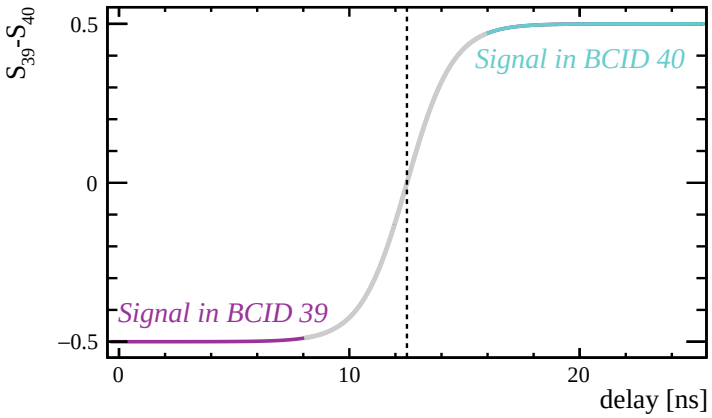

Figure 4.17: Ideal S-shape for delays from 0 to 25 ns. The dashed vertical line indicates the point $d_{split} = 12.5$ ns. The magenta region correspond to a signal integrated by the integrators tagged as BCID 39 and the cyan one to the integrator BCID 40. The grey part of the curve represents the region where the signal integration is gradually shifting from one integrator to the other.

4.5.3 First timing measurement

General setup

The setup used to perform the time measurement is sketched in Fig. 4.18 and described in the following. A laser with a wavelength of 405 nm and an output power of 700 mW is used as light source. It is brought inside a light tight box via an optical fiber. The laser is controlled via a EIG 1000D controller (Advanced Laser Diode Systems A.L.S. GmbH). The trigger is given to the laser controller by the 3CU control board at a 11.25 kHz rate synchronized with the BCIDs. The laser's controller input for trigger can only read signals in a range of ±5 V and the output signal provided by the 3CU is much smaller (~ 800 mV) hence an intermediate step is needed. The 3CU trigger is used to trigger a generator which will in turn produce a pulse with an amplitude up to 4 V synchronized with the BCID, that can be used to trigger the laser. In the light tight box, in front of the laser,

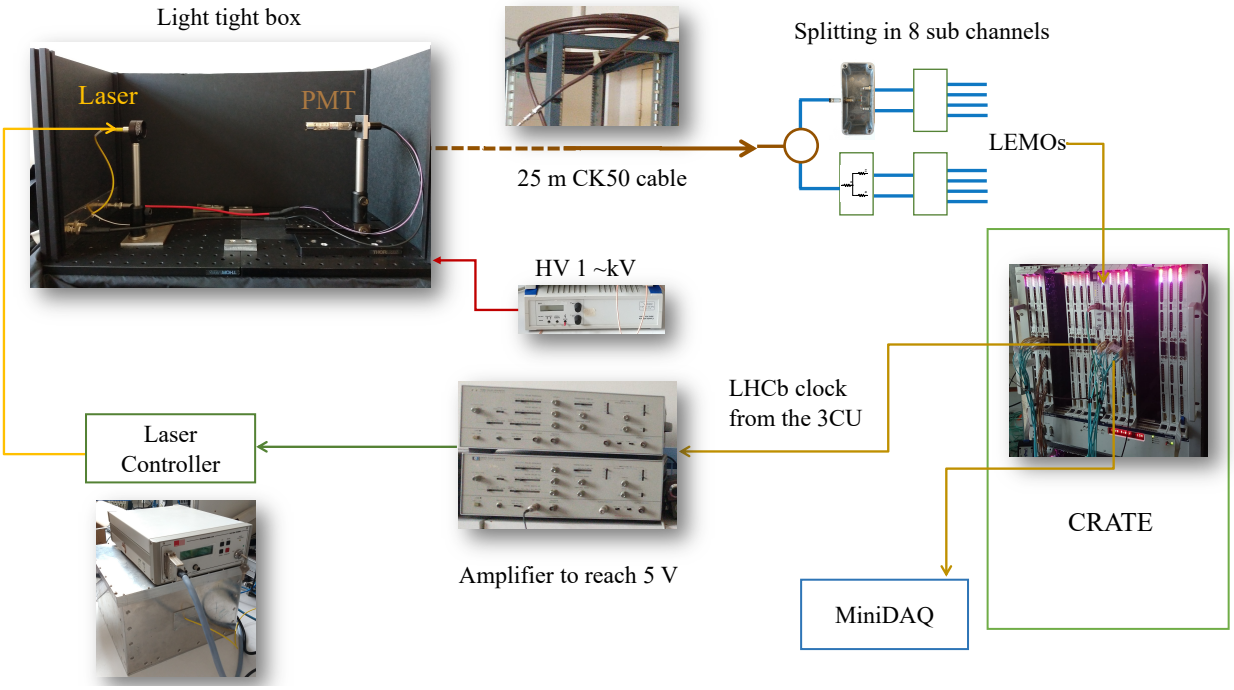

Figure 4.18: Schematic view of the setup. A picture of the inside of the box showing the laser (in yellow) and the PMT on the right is shown. The CK 50 cable (in brown), the PMT high voltage supply, the amplifier, the laser controller box and the FEBs (on the right) are also shown.

one Hamamatsu R760 (shown in Fig. 4.7) is placed in a socket with customized divider circuit. The inside of the box is shown in Fig. 4.18, top left corner. The PMT high voltage is provided by a high voltage power supply module (T1DP 050 205 EPU) set to negative polarity. The PMT signal is sent to the FEBs via a 25 m long CK50 cable (the length expected for the final PLUME detector); these cables are chosen because they have very low attenuation effects. The cable is then connected to the FEB channels using mini-LEMO connectors. The data acquisition is performed using the same miniDAQ system as the previous test, with the firmware version of November 2020. This setup is used to perform two measurements. For the first one, the signal is directly injected to one of the FEBs channels (this option will be called *internal delay mode*), in the second one the signal is split in 8 sub-channels via 4 subsequent one-to-two splitters (this options will be called *split mode*), each sent to one of the 8 input channels of one front-end block. In the first case, the delays are applied changing the FEBs settings for one channel via the miniDAQ, and taking data for each new delay configuration. In the second case, different delays are applied to each of the 8 channels simultaneously and data are taken only once. The disadvantage of the second configuration is that the input signal amplitude is decreased at each splitting step, hence the PMT signal amplitude should be at least 8 times bigger than the electronics pedestal to be readable after splitting. This problem could be partially solved by increasing the high voltage of the PMT up to 1.2 kV to have a larger signal amplitude, however this would cause a fast aging of the PMT. On the other hand, even if the first configuration has larger amplitude it would require further developments of the firmware to perform an automated scan for different delays starting from the single signal acquired and it would probably lead to a worse precision

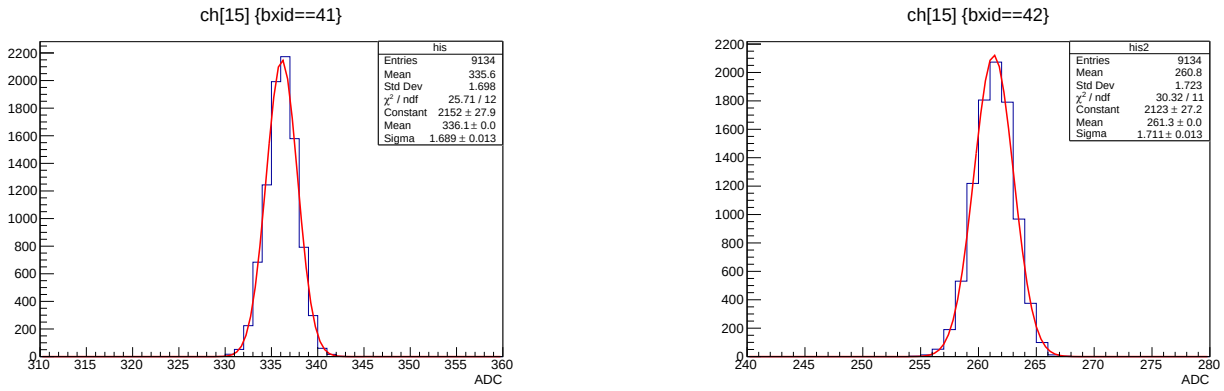

Figure 4.19: Example of the pedestal shapes for the two integrators: (left) odd and (right) even, from run 1049.

since it is impossible to have identical signals at the input. Data are taken with the calorimeter FEBs (at IJCLab) in March 2021. The FEBs are used without the internal pedestal subtraction. The pedestals are carefully removed offline using the previous odd or even BCID corresponding to the odd or even "tagged" integrator. It is not possible to simply use the pedestal of the previous (or next) BCID, mixing odd and even BCIDs, because the two integrators have different pedestals. An example of pedestals are shown in Fig. 4.19; the even pedestal mean varies around 260 ADC counts with a standard deviation of 1.7 ADC counts, the odd one varies around 336 ADC with a similar standard deviation. The two setups, *internal delay mode* and *split mode*, are discussed below, where the first one can be seen as a test to see if the general approach works.

Internal delay mode

The PMT are powered with a high voltage of $HV = 1.0011\,\text{kV}$ resulting in an output signal amplitude of ~ 100 mV and a width of 6 ns (for a 50 Ohm impedance), corresponding to roughly ~ 6 pC. The entire signal is sent to one of the 32 channels of one FEB and several runs are taken with different delay settings. The purpose of this preliminary test is to prove that when the signal is split within the two integrators, it is still measurable. This proof is necessary since the FEBs were not designed for this end, on the contrary in the ECAL case, the delay settings are used to make the PMT signal (except the tails) fit in one integrator. When the signal is integrated by two different integrators, the dead time around 1 ns to switch from one to the other could cause a loss of part of the signal, however this can be partially recovered after calibration. In total, 19 runs are taken with delays from 5 to 30 ns. For each run, 4 BCIDs are taken, and an example of signal without pedestal subtraction is shown in Fig. 4.20 for runs 2486 and 2469, corresponding to a delay of 5 and 26 ns. The results are summarized in Table 4.2, from the left to the right the mean in ADC counts measured for the two integrators (*i.e.* for two subsequent BCIDs), the delay and run number are shown. This test shows that the signal can be split between the two integrators and still readout by the electronics. The under-pulse, which is a signal below the pedestal, seen when shifting the signal is due to the pole-zero (PZ) compensation circuit in the ICECAL, the parameters of which can be changed easily. These parameters were optimized for the ECAL PMT signal which is larger than the expected PLUME one,

Mean BCId 31 [ADCs]	Mean BCId 32 [ADCs]	Delay [ns]	Run number
464.73	562.29	5	2469
592.01	441.00	6	2470
707.42	342.21	7	2471
773.40	280.29	8	2472
881.00	206.95	9	2473
911.78	179.04	10	2474
955.79	155.94	11	2475
999.61	145.26	12	2476
1000.74	152.30	13	2477
994.13	166.37	14	2478
966.41	188.84	15	2479
963.56	201.39	16	2480
944.86	219.10	17	2481
910.17	241.67	18	2482
889.51	256.20	19	2483
878.95	266.66	20	2484
883.53	265.44	21	2485
842.07	296.10	26	2486
388.95	651.88	30	2487

Table 4.2: Mean value of the signal without pedestal subtraction for two integrators (BCIDS 31 and 32) with different delays.

hence it will be necessary to tune again those parameters to remove the effect of the PZ filter which is not necessary for PLUME.

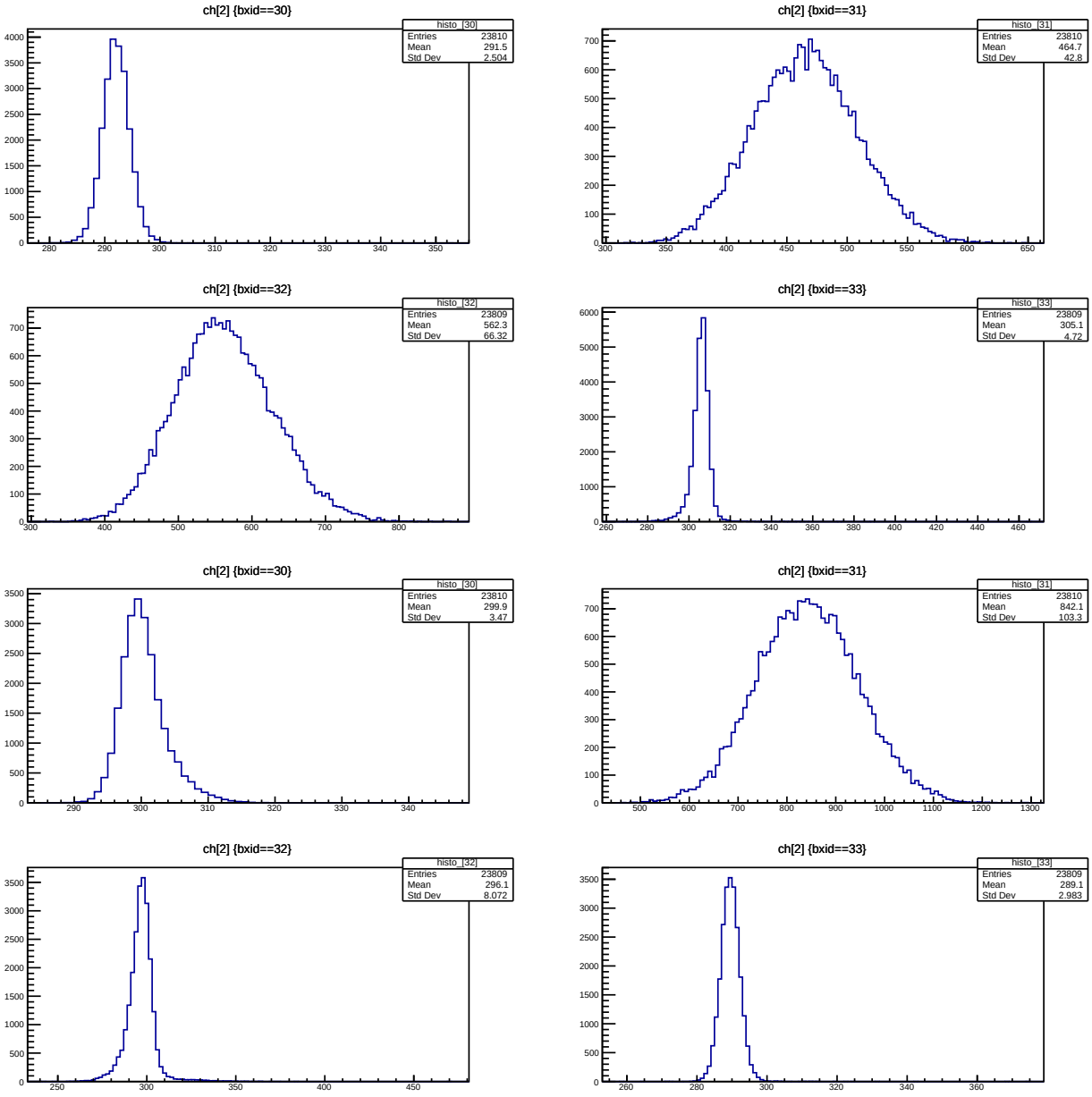

Figure 4.20: Example of signal shift without pedestal subtraction, for 4 different BCIDs. The x axis shows the number of ADC counts. Top run 2469, bottom run 2486. For both the top and bottom plots, starting from the top left corner, the BCIDs are 30, 31, 32 and 33.

Split mode

In this configuration, the signal is first split into two sub-channels using a Suhner power divider with a 6 dB attenuation (corresponding to an attenuation factor of 3.98) and 50 Ohm impedance for each branch. From these two branches the signal is further split into a total of 8 copies using Wye splitters. A picture of the splitters, with a sketch of the circuit and a schematic view of the complete splitting chain are shown in Fig. 4.21. Then the signal is connected to 8 channels of one FEB and the delays

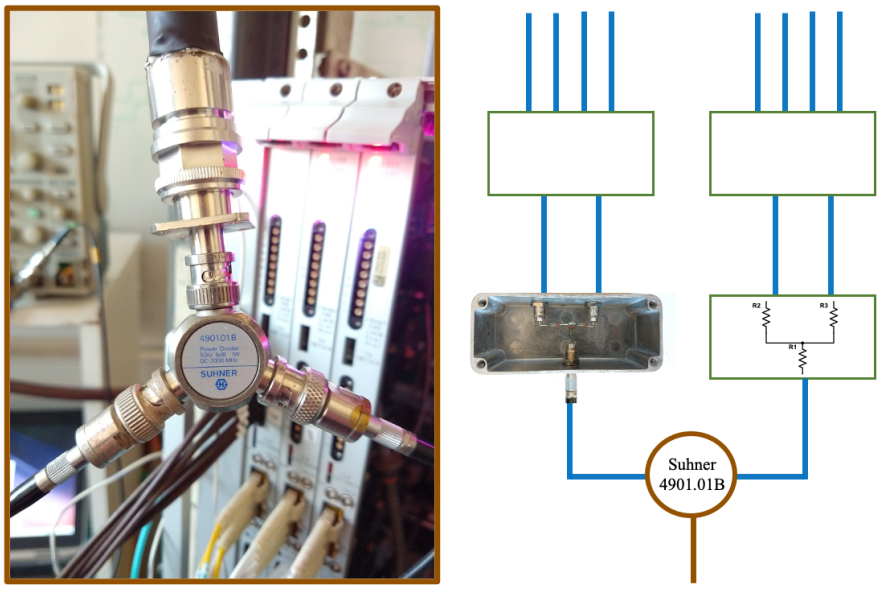

Figure 4.21: Picture of the splitters used to separate the signal in 8 signal copies.

are applied to each channel (using WinCC[1] panels). The PMTs are supplied with 989 V. Four runs are taken, with different delay ranges and steps, the running conditions are summarized in Table 4.3. Then, event by event, an histogram is filled with the difference of ADC counts between two

Run	Step [ns]	First [ns]	Last [ns]
1008	3	0	21
1049	3	0	21
1051	2	10	24
1053	2	6	20

Table 4.3: Run conditions.

subsequent integrators, $\Delta S = S_N - S_{N+1}$. Only 8 channels are used, hence the other channels will have a distribution around 0 ADC count after pedestal subtraction, showing the mean noise. The result for Run 1008 is shown in Fig. 4.22, where the signal was connected to the channels 8 to 15, corresponding to the red shaded sub-plots. The histograms are fitted with a double Gaussian function, and the result (mean and width) are overlaid on the plots[2] Similar plots for runs 1049, 1051 and 1053 are shown in appendix A The mean values obtained for the signal channels from the fit are summarized in Tab. 4.4. From these measurements ΔS can be plotted as a function of the delay. The S-shape obtained is shown in Fig. 4.23.

[1]WinCC is a system, created by Siemens, which provides a human-machine interface (HMI) to control processes and perform data acquisition of several machines (in this case several FEBS) at a time and on a large scale.

[2]The width is computed using quantiles since the distributions are not always Gaussian, it is obtained by removing the 100 worst outliers with extreme ADC values, then the width is defined as the region containing all the data but 100 events (i.e. $X\%$ of the data where $X = 1 - 110/n_{events}$). This width is then scaled to the number of corresponding sigma for $X\%$, in other words it is scaled back to contain 68% of the data which would correspond to the 1 sigma region for a Gaussian distribution.

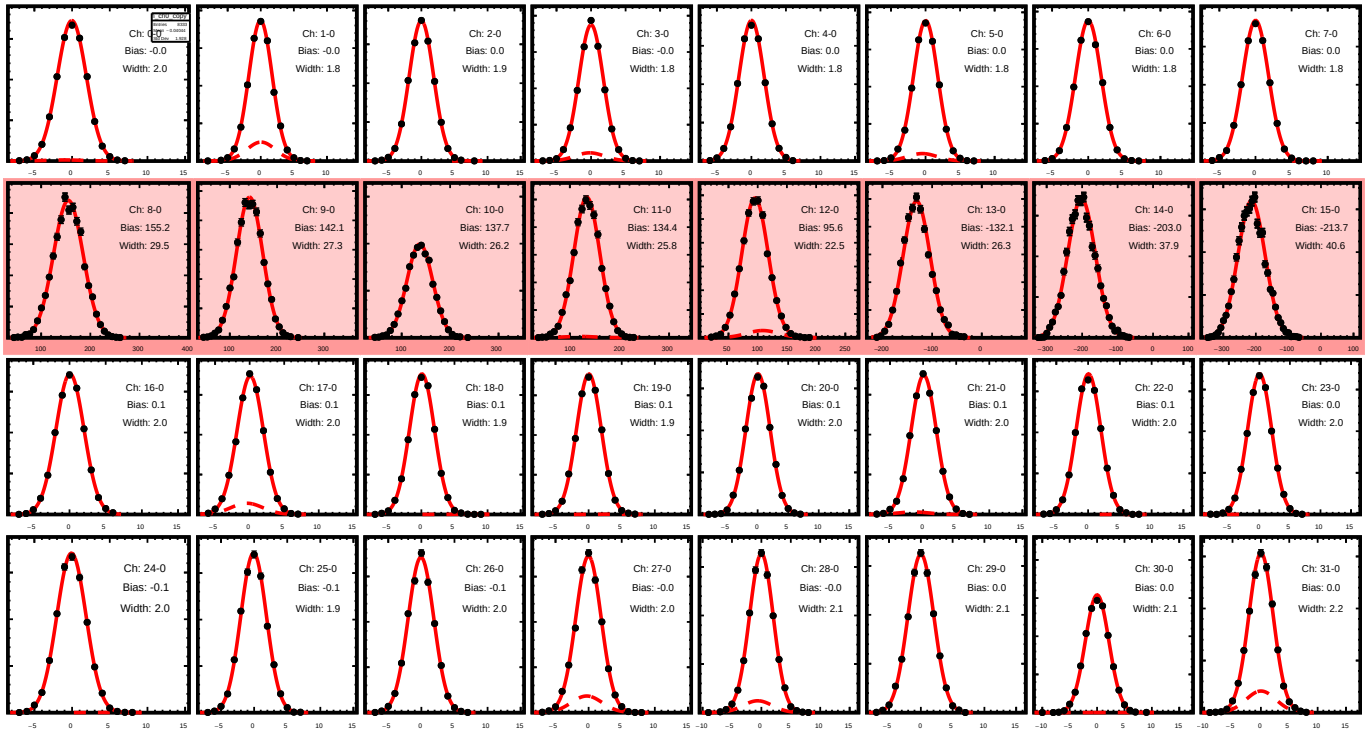

Figure 4.22: ΔS distributions for Feb 4, 32 channels (Run 1008) as a function of the ADC counts after pedestal subtraction. The red bold lines are double Gaussian fit to the distributions and the bias and the width results are shown on the sub-plots. The red shaded channels have a non zero mean and correspond to the channels where a signal is seen.

Channel	ΔS[ADCs]	Error [ADCs]	Delay [ns]
8	-155.15	0.09	0
9	-141.85	0.29	3
10	-137.42	0.29	6
11	-134.27	0.52	9
12	-94.92	0.52	12
13	131.26	0.29	15
14	201.83	0.15	18
15	213.25	0.41	21

Table 4.4: Result of the fit to the signal after pedestal subtraction for Run 1008.

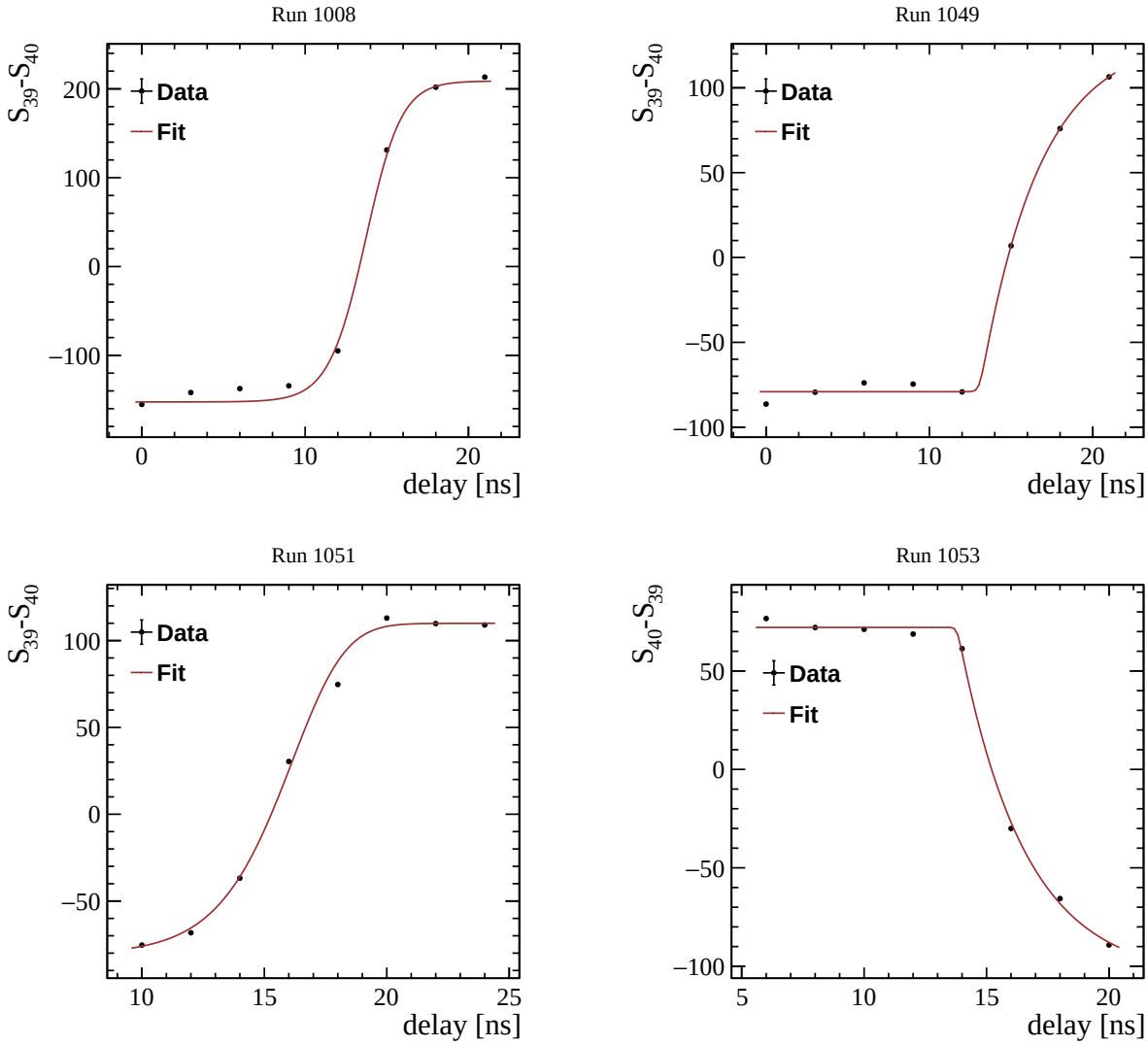

Figure 4.23: S-shape distributions for runs 1008, 1049, 1051 and 1053. The bottom right plot shows $-\Delta S = S_{40} - S_{39}$ as a function of the delay.

Parameter	Fit results			
	Run 1008	Run 1049	Run 1051	Run 1053
a	-361.24 ± 0.55	-209.548 ± 1.17	-190.82 ± 0.33	178.04 ± 0.66
b	0.87 ± 0.02	7.69 ± 0.75	0.59 ± 0.01	16.32 ± 0.62
c	1.14 ± 0.08	0.04 ± 0.01	3.47 ± 0.35	0.0223 ± 0.00
d	-208.82 ± 0.55	-130.43 ± 1.17	-109.98 ± 0.04	105.92 ± 0.62
f	13.89 ± 0.11	13.07 ± 0.03	18.24 ± 0.23	13.80 ± 0.02
χ^2/ndf	1877.82	722.76	477.95	146.84

Table 4.5: Result of the fit to the S shape for runs 1008, 1049, 1051 and 1053.

The S shape is fitted with a composite function:

$$f(x) = \frac{a}{(1 + \exp(b(x-f))^c) - d} \tag{4.6}$$

where the parameters b, d, a and f corresponds to the slope, a constant, the maximum asymptote and the inflection point. The results of the fit are shown in Table 4.5.3. Note that for run 1053 the shape is inverted since it is $-\Delta S = S_{40} - S_{39}$ that is shown. Even though the fit is not describing the data perfectly (one can see that looking at the large values of χ^2/ndf), this shape is found to give an approximation of the inflection point, corresponding to the fitted parameter f to be compared with the expected value of 12.5 ns. The resolution on the inflection point needs to be measured with more runs in the same conditions in order to monitor how is the inflection point varying for each measurement. The spread around the inflection points will give an idea of the resolution that could be achieved with this measurement. Here as a preliminary measurement only two runs have been taken with the same conditions, run 1008 and run 1049, and the results are shifted of 1.39 ns and 0.57 ns from the expected value, meaning that the resolution of the measurements could be eventually larger than 0.5 ns, which is the resolution achieved by the OT in Run 1, but no conclusions on the expected resolution can be given here. The other two runs, 1051 and 1053, show an even larger variation around the expected value of 12.5, meaning that noise effects are dominant and need to be further investigated. A possible improvement could be obtained by selecting only runs where the input signal is stable within a few percent level for instance. Furthermore, the noise could be better controlled by using an improved splitter system which would allow to have less variations of the input signal shape after the splitting. A more detailed study measuring the expected resolution with an improved splitter is on-going at IJCLab, few measurements with a resolution below 80 ps have been obtained and all the measurements show a resolution at least smaller than 250 ps. This work will be continued by other PhD. students in the near future.

4.5.4 Conclusions on the timing measurement

The results obtained for the S-shapes are promising, however there is still room for improvement. The *split mode* option will be chosen as baseline for this measurement with two dedicated PMTs, within the ones positioned in the smaller tilted cross (see Fig. 4.10), and 8 channels of the front-end boards will be (permanently) dedicated to this measurement. The *internal delay mode* relies on the

reproducibility of the input signal which cannot be ensured whereas for the *split mode* the signal copies after the splitting are all approximately the same making the measurement more stable, this is way the latter is chosen as baseline solution. The choice of the delay steps size can be further optimized. In total there are 8 channels available and the delay steps is chosen depending on which region is scanned within the 25 ns. For instance, with a step of 3 ns, one can scan a window from 0 to 24 ns or for a delay step of 2 ns, from 0 to 16 ns. To optimize the S-shape measurement one needs an high number of points (and hence a smaller delay step) around the inflection region to better constrain the fit in this region. Choosing 1 ns steps would allow to perform the scan only on a small time window (maximum 1×8 ns), the inflection point region would be better constrained however in order to fit the S-shape few points outside the inflection region are needed, thus this would probably not be the optimal step size. A possible way to determine the optimal step size would be to perform first a scan with a large step size, for instance 3 ns, to find the inflection point region and few other extreme points at the beginning of one of the first runs of PLUME. Then, perform the successive scans with smaller steps around the inflection region, including some points outside it obtained from the previous measurement to constrain the S-shape fit. Another possibility would be to take the first two points with a 6 ns step covering from 0 to 12 ns, then 4 points with 1 ns steps from 9 to 13, and finally two other points with a 6 ns step; this options would allow to cover the full 0 to 25 ns window with an higher precision around the inflection region. The splitting of the signal could be also optimized using a printed circuit instead of the "homemade" splitter used for the tests discussed above, to be placed inside the FEBs. Finally, one could eventually verify if better connectors and cables (mini-LEMO) would reduce the noise and improve the precision of the timing measurement.

4.6 Conclusions

The PLUME detector, which will be installed for Run 3 in 2021, is an inexpensive detector which will provide a fundamental measurement for physics analysis, the luminosity, and which in addition allows to monitor the beam conditions and the time shift of the LHCb clock with respect to the LHC clock. In this work the FEBs of the LHCb ECAL have been shown to be suitable for the readout of the PLUME detector. The FEBs have been first tested with a simple generator emulating the signal obtained in the test beams and then with a more realistic setup where the signal is obtained with a laser pointing to one of the PLUME PMTs. A preliminary timing measurement has been performed and the setup will be used for further measurements which will allow to determine the expected resolution achievable with the PLUME electronics and which are already on going. The aimed resolution is at least below 250 ps and can be improved up to 70 ps (following the results obtained while writing this manuscript). Even if very preliminary and incomplete (due to the lack of time partially linked to the COVID-19 pandemic), these results open the way to a promising and unexpected additional timing measurement that the PLUME detector could perform. As an outcome of this work, the ECAL FEBs have been chosen for the front-end electronics of the future PLUME detector and a preliminary timing measurement has been performed giving promising results.

5 Helicity formalism for baryonic three body subsequent decays

5.1 Introduction

The conventional way to describe a decay to multi-body final states relies on the isobar model which is describing the process as a succession of two-particles decays. The intermediate resonance states are called "isobars" and they are described by dynamic functions, usually called “lineshapes". For a three-body decay $A \to a+b+c$ there are three possible combinations giving three different isobars: $A \to (R_1 \to a+b)+c$, $A \to a+(R_2 \to b+c)$ and $A \to (R_3 \to c+a)+b$. The decay amplitude is factorized in a dynamic part $\Delta_{r_i}(m_{r_i})$ and an angular part $\psi_{r_i}(\vec{\Omega})$:

$$\mathscr{A}(\vec{\Omega}) = \sum_i \psi_{r_i}(\vec{\Omega})\Delta_{r_i}(m_{r_i}) \tag{5.1}$$

where $\vec{\Omega}$ are the phase space variables, r_i is the i^{th} resonance and m_{r_i} its mass. The choice of the lineshape $\Delta_{r_i}(m_{r_i})$ parametrization is guided by experimental data or existing models and it introduces a bias in the amplitudes since it requires a specific modeling. The angular amplitudes ψ_{r_i} instead are derived from first principles of quantum mechanics without any a priori assumption on the physical process studied. They can be described using different approaches (helicity amplitudes, covariant formalism, Zemach tensor formalism, ...) and they only depend on the spin and angular momentum of the particles. In this work the helicity formalism is chosen. Starting from the decomposition in Eq. 5.1, the final amplitude for the three body decay is obtained by summing coherently over the different isobars, which can have different spin, and incoherently over the final and initial state helicities. Another usual choice for the description of the spin amplitudes is the partial-wave basis, the main difference with the helicity basis is that the spin of the daughters particles are defined in their own rest-frame and not in the rest frame of the mother particle. It is possible to write a decomposition of one basis as a function of the other and since the final state spins are summed over, the two descriptions must give the same angular distribution. In this chapter, after a brief introduction on the arise of the concept of spin in quantum mechanics and in group theory, the helicity formalism is explained and the polarized helicity amplitudes for the $\Lambda_c^+ \to pK^-\pi^+$ decay are derived in details. As a conclusion, a set of benchmark tests, which should be verified by any model, are shown for the $\Lambda_c^+ \to pK^-\pi^+$ helicity amplitudes.

5.2 Spin in relativistic processes

In quantum mechanics, spin is an intrinsic property of a particle and it has been introduced in the early $20'$s to explain the results of the Stern-Gerlach experiment [198]. In this experiment, a non-relativistic beam of silver atoms (treated as a single valence electron of charge $-e$ in the s orbital) is sent through a magnet producing an inhomogeneous magnetic field. The deflection of the beam was found to have a peculiar shape. If the particles were classical magnetic dipoles, their distribution after deflection would have been expected to be continuous, instead the particles were deflected either up or down by a certain amount without any intermediate possibility. This was one of the first proof of the effect of spin, albeit it seems that the early Stern-Gerlach experiments did not have a great influence on the discovery of the spin due to its poor precision. The concept of spin formally appeared instead when studying the separations in line spectra to explain an effect known today as **LS** splitting. In 1924, Kronig first proposed the spin to explain the observed spectra but he did not dare publishing his results, the reason for that seems to be that Pauli did not appreciate his work. One year later, Uhlenbeck and Goudsmit confirmed that the spin was responsible for the splitting seen in the spectra. Some months later Thomas [199] understood the last missing piece to match the theory to the experiment which was the mysterious factor $\frac{1}{2}$ missing in the measured magnetic moment w.r.t. the theory prediction. Nowadays spin is a well established quantum number describing the intrinsic angular momentum rotational degree of freedom of particles.

5.2.1 State vector and representations of the Poincaré group

To describe particles with spin, a set of mathematical tools has been developed in the framework of group theory. In quantum mechanics, a particle is described by a *state* vector, which is a vector in an Hilbert space [1] associated with a physical system. The nature of the Hilbert space to which this vector belongs will give more information on the possible physical states that one can associate to it. The Hilbert space can be decomposed in a direct sum of two sub-spaces one labelled by the momentum and mass $\mathscr{H}_p$ and the other one by the spin $\mathscr{H}_s$, then the Hilbert space $\mathscr{H}$ can be defined as the direct sum $\mathscr{H} = \mathscr{H}_p \otimes \mathscr{H}_s$. If $\mathscr{H}_p$ (often called h, little Hilbert space) is spanned by vectors $|p_\mu\rangle$ and $\mathscr{H}_s$ by $|\alpha\rangle$, then the total Hilbert space $\mathscr{H}$ is spanned by the direct product of these two vectors: $|p_\mu\rangle \otimes |\alpha\rangle$. A general vector of $\mathscr{H}$ transforms under a unitary representation of the Poincaré group $U(\Lambda, a)$ as follows:

$$\begin{aligned} U(\Lambda,a)(|p_\mu\rangle \otimes |\alpha\rangle) &= \exp(-iP_\mu a^\mu)(|p_\mu\rangle \otimes |\alpha\rangle) \\ &= \exp(-ip_\mu{}' a^\mu)(|p_\mu{}'\rangle \otimes |\alpha'\rangle) \end{aligned}$$

where $p' = \Lambda p$ and $|\alpha'\rangle = \mathscr{D}(R)|\alpha\rangle$ where $\mathscr{D}(R)$ is a representation of the rotation group on $\mathscr{H}_s$ and Λ is a Lorentz transformation. Starting with an irreducible representation of the rotation group one can construct an irreducible representation of the Restricted Poincaré Group (RPG), labelled by the

[1] A Hilbert space is a generalized notion of Euclidean space with any infinite or finite number of dimension. The algebra of observables in quantum mechanics is described on Hilbert spaces, more details can be found in [200][201].

eigenvalues of the M^2 and J^2 operators which are m and j. Any representation of the RPG can be expressed as a direct sum over these irreducible representations. The vector corresponding to an irreducible representation can be written as:

$$|\vec{p}, m\rangle \otimes |j, \mu\rangle \equiv |m, j; \vec{p}, \mu\rangle \tag{5.2}$$

and the transformation law under an element of the RPG reads:

$$U(\Lambda, a)|m, j; \vec{p}, \mu\rangle = \exp\Big(-ip'_\mu a^\mu\Big) \sum_{\mu'} D^j_{\mu',\mu}(R)|m, j; \vec{p}', \mu'\rangle \tag{5.3}$$

where $R \equiv R(\Lambda, p) = \Lambda^{-1}_{p'} \Lambda \Lambda_p$ and $\mathscr{D}^j(R)$ is a matrix of the irreducible representation of the rotation group labelled by j. More details and a precise derivation of this can be found in [21]. What is interesting here, is that the physical system described by these vectors is labelled by two quantities: m, corresponding to the mass of the particle, a well known property, and a new number j. This parameters is labeling the rotations and it introduces a $(2j+1)$ degeneracy in the momentum eigenstates, thus it would be compatible with the spin of a particle. To confirm this hypothesis we should look at how the state vector transforms in the rest frame under a rotation R using Eq. 5.3:

$$U(R)|m, j; 0, \mu\rangle = \sum_{\mu'} D^j_{\mu',\mu}(R)|m, j; 0, \mu'\rangle \tag{5.4}$$

This means that they transform under an irreducible representation j of the rotation group, exactly as a particle with spin j would do. What is important to retain from this discussion is that starting from the most general Hilbert space and building the irreducible representation acting on the corresponding vector, the description of a particle with mass m and spin j is naturally obtained. In other words, the concept of particle with spin arises from basic principles of invariance and group theory considerations when looking for an irreducible representation of the (restricted) Poincaré group on the Hilbert space. Here on the label m, indicating the mass of the particle, will be dropped since it leads to confusion with the projection of the spin, usually denoted as m too. Hence from now, a particle with momentum $\vec{p}$ and spin j is represented by the state vector $|j; \vec{p}, m\rangle$, with m the eigenvalue of the spin operator $\vec{J}_3$ previously denoted as μ.

5.2.2 Rotation operator

A n dimensional rotation group is a group composed by all the rotations around a fixed point in a space of dimension n which can be complex or real. An example of a rotation group is $SO(3)$, which is the group of all rotations about the origin of three-dimensional Euclidean space and it is represented by 3×3 orthogonal rotation matrices ($R^T R = I$) of determinant 1. Hence each rotation is represented by an operator R and it can be described univocally by three Euler angles α, β, γ. In this work, the active rotations convention is used where the Cartesian coordinate axes are fixed and the state is rotated, i.e. the rotation acts on the system itself and not on the coordinate axes. The angles of the rotation are specified by attaching new axes $\{x'', y'', z''\}$ to the physical system. The Euler angles of

the rotated system with respect to the original one will be the angles of the rotated $\{x'', y'', z''\}$ with respect to $\{x, y, z\}$. In the z-y-z convention, an arbitrary rotation can be written as:

$$R(\alpha, \beta, \gamma) = R''_z(\alpha) R'_y(\beta) R_z(\gamma) \tag{5.5}$$

where $R_n(\theta)$ means a rotation of an angle θ around the n-axis. Hence the rotation $R(\alpha, \beta, \gamma)$ means a rotation of γ around the z-axis, then a rotation of β around the rotated y'-axis followed by a rotation of α around the z''-axis which has been rotated twice. It is shown in [8] that by exploiting the unitarity of the rotation operators, $R(\alpha, \beta, \gamma)$ can be expressed as a rotation with respect to the original coordinate axis x, y, z which are fixed, without passing through the intermediate system x', y', z' and the final one x'', y'', z''. Then R can be written as

$$R(\alpha, \beta, \gamma) = R_z(\alpha) R_y(\beta) R_z(\gamma) \tag{5.6}$$

The 3 Euler angles are defined in the ranges: $\alpha \in [-\pi, \pi]$, $\beta \in [0, \pi]$ and $\gamma \in [-\pi, \pi]$. It can be shown that the inverse rotation is simply

$$R^{-1}(\alpha, \beta, \gamma) = R(-\gamma, -\beta, -\alpha) \tag{5.7}$$

The generators of infinitesimal rotations of angle ϵ are the components of the angular momentum operator $\hat{J}$ such that $R_{\hat{n}}(\epsilon) = I - i\epsilon \vec{J} n$. From this, the operator corresponding to a finite rotation can be written as $R_n(\theta) = \exp\left(-i\theta \hat{J} \cdot \hat{n}\right)$ and the complete rotation in Eq. 5.6 becomes:

$$R(\alpha, \beta, \gamma) = e^{-i\alpha J_z} e^{-i\beta J_y} e^{-i\gamma J_z} \tag{5.8}$$

The $\hat{J}_i$ are hermitian operators satisfying the commutation relations:

$$\left[\hat{J}_i, \hat{J}_j\right] = i\hbar \epsilon_{ijk} \tag{5.9}$$

From these three operators $\hat{J}_i$, an invariant operator (also called "Casimir" operator) $J^2 = J_x^2 + J_y^2 + J_z^2$ commuting with each $\hat{J}_i$ can be defined. Then $\hat{J}^2$ and one of the $\hat{J}_i$, for instance $\hat{J}_z$, can be used to define a complete commuting set of these operators. Using the commutation relations and the *ladders* operators $\hat{J}_\pm \equiv \hat{J}_x \pm \hat{J}_y$ the eigenvalues of these operators can be derived [201]:

$$\begin{aligned} \hat{J}^2 |jm\rangle &= j(j+1)|jm\rangle \\ \hat{J}_z |jm\rangle &= m|jm\rangle \end{aligned}$$

where $|jm\rangle$ are eigenstates of spin $j = \{0, 1/2, 1, 3/2, ...\}$ and m is the spin projection along a chosen axis (conventionally called z axis) and it takes values $m = \{-j, -j+1, ..., j-1, j\}$. For a given j, there are $(2j+1)$ vectors spanning a subspace $\mathscr{H}^{(j)}$ which is invariant under rotations. The group of operators R acting in $\mathscr{H}^{(j)}$ forms an irreducible representation of the rotation group labelled by the angular momentum j. The kets $|jm\rangle$ form an orthonormal set of eigenvectors of the group and they

transform as, following Eq. 5.4,

$$R(\alpha,\beta,\gamma)|jm\rangle = \sum_{m'=-j}^{j} D^{j}_{m',m}(\alpha,\beta,\gamma)|jm'\rangle \tag{5.10}$$

$$\langle jm''|R(\alpha,\beta,\gamma)|jm\rangle = D^{j}_{m',m}(\alpha,\beta,\gamma) \tag{5.11}$$

where $D^j(\alpha,\beta,\gamma) = D^j(R)$ are the rotation matrices and they are representations of the SU(2) group, which is the set of all 2×2 complex matrices of determinant 1 that satisfies $A^\dagger A = I$. A useful way of writing the SU(2) rotation matrices is, using Eq. 5.8,

$$D^{j}_{m',m}(\alpha,\beta,\gamma) = \langle jm'|e^{-i\alpha J_z}e^{-i\beta J_y}e^{-i\gamma J_z}|jm\rangle \tag{5.12}$$

$$= e^{-i\alpha m'}d^{j}_{m'm}(\beta) - e^{im\gamma} \tag{5.13}$$

where $d^j(\beta)_{m'm}$ are the Wigner d-matrix elements, defined as:

$$d^{j}_{m'm}(\beta) = \langle jm'|e^{-i\beta J_y}|jm\rangle = \left[(j+m')!\,(j-m')!(j+m)!(j-m)!\right]^{\frac{1}{2}} \sum_s \left[\frac{(-1)^{m'-m+s}\left(\cos\frac{\beta}{2}\right)^{2j+m-m'-2s}\left(\sin\frac{\beta}{2}\right)^{m'-m+2s}}{(j+m-s)!s!\,(m'-m+s)!\,(j-m'-s)!}\right] \tag{5.14}$$

Although the definition seems complicated, they take very simple trigonometric forms and they inherit some useful symmetries properties from the rotation group. Starting from Eq. 5.14, some useful relations can be obtained, for instance:

$$d^{j}_{m',m}(-\beta) = (-1)^{m'-m}d^{j}_{m',m}(\beta)\,, \tag{5.15}$$

$$d^{j}_{m',m}(\pi) = (-1)^{j-m}\delta_{m',-m}\,, \tag{5.16}$$

$$d^{j}_{m',m}(\pi\pm\beta) = (-1)^{j\mp m'}d^{j}_{m',-m}(\beta)\,, \tag{5.17}$$

$$d^{j}_{m',m}(2\pi+\beta) = (-1)^{2j}d^{j}_{m',m}(\beta)\,. \tag{5.18}$$

From the unitarity of SU(2) instead, the following relation is obtained:

$$d^{j}_{m',m}(\beta) = (-1)^{m'-m}d_{m,m'}(\beta) = d_{-m,-m'}(\beta)\,. \tag{5.19}$$

The last property in Eq. 5.18 is particularly relevant since it shows that a 2π rotation is not always leaving the system invariant. For integer value of j, the equation gives the identity but for half-integer values a minus sign arises. This means that for half integer spins, a rotation of 2π, written as $D^j(0,0,2\pi) = (-1)^{2j}$, is not returning the system to its original state. From a group theory point of view, this is because the rotation operators over half-integer spin states belong to $SU(2)$, which is the covering group of $SO(3)$. Between these two groups it exists a two-to-one homomorphism $SU(2)\to SO(3)$, implying that representations of $SO(3)$ are also representations of $SU(2)$, but there are (spinor) representations of $SU(2)$ that have no analog in $SO(3)$. In other words, for half-integer

values of j the representation is double-valued hence for any rotation there are two possible matrices differing by a sign. This will impact the definition of the helicity amplitudes later on since if the 2π invariance is broken, one needs to be careful when defining the angles.

Finally it is important to mention that the D-Wigner functions are orthogonal, the orthogonality relation is (from Ref. [8]):

$$\int_0^{2\pi} d\alpha \int_0^{2\pi} d\gamma \int_0^{\pi} \sin\beta d\beta \left[D^{j*}_{mn}(\alpha\beta\gamma) D^{j'}_{m'n'}(\alpha\beta\gamma) \right] = \frac{8\pi^2}{2j+1} \delta_{mm'}\, \delta_{nn'}\, \delta_{jj'}. \tag{5.20}$$

5.2.3 Spin in relativistic quantum mechanics

Summarizing the results discussed above, the state vector $|j;\vec{p},m\rangle$ of a particle is labelled by the total angular momentum j. The total angular momentum operator $\vec{J}$ is defined to be the sum of the orbital angular momentum $\vec{L}$ and the spin $\vec{S}$. The spin is usually seen as an intrinsic degree of freedom of the particle whereas $\vec{L}$ is an external degree of freedom. The two angular momenta act on different spaces hence they commute:

$$\vec{J} = \vec{L} + \vec{S} \quad \text{and} \quad \left[\vec{L}, \vec{S}\right] = 0 \tag{5.21}$$

These three angular momenta obey the same kind of algebra:

$$\left[\hat{J}_i, \hat{J}_j\right] = i\hbar\epsilon_{ijk}\hat{J}_k \quad \text{and} \quad \left[\hat{L}_i, \hat{L}_j\right] = i\hbar\epsilon_{ijk}\hat{L}_k \quad \text{and} \quad \left[\hat{S}_i, \hat{S}_j\right] = i\hbar\epsilon_{ijk}\hat{S}_k\,. \tag{5.22}$$

The spin state $|sm\rangle$ is a simultaneous eigenstate of the commuting operators S^2 and S_z with eigenvalues $\hbar s(s+1)$ and m, where s can be zero, integer or half integer and m can take values $-s < m < s$ in steps of 1. The second quantum number, $m = \hat{s_z}$ describes the projection of the spin on a given axis z, this implies working with a well-defined coordinate reference system with a fixed origin O. However, this description of the spin only holds for the non-relativistic case. The transition to a relativistic description of spin is not trivial, this is because for relativistic particles the spin is only defined if the particle is at rest. The heart of the problem is then the generalization from the rest state case to any state. The general approach to solve this is to generate states with any momentum, starting from the spin states at rest, by applying Lorentz transformations to it. Consider a particle A at rest in a state $|s, s_z\rangle$ and an observer B moving with velocity $-\vec{v}$ with respect to A. It is clear that from the point of view of B, A is moving with velocity $\vec{v}$. The choice of B is not unique, a rotation of this frame could give another equivalent frame where the particle A is seen moving with the same velocity but with a different spin configuration. To fix this choice, there are two usual conventions:

- *the canonical choice*, where the B reference frame is obtained from the reference frame of A via a boost $l(-\vec{v})$. In this case, the state seen by B would be $|\vec{p}, s_z\rangle$.

- *the helicity choice* where B first transforms via a boost to a frame S' in the direction of the negative z axis of A, and then S' is rotated by $R(\alpha = \phi, \beta = \theta, \gamma)$ to have the momentum $\vec{p} = (\theta, \phi, p)$ aligned to the z_A-axis of A. In other words, the particle spin quantization axis z_A is aligned to be along the particle direction in the observer frame B. This means that if the observer B sees the particle A in a state $|\vec{p}, \lambda\rangle$, then A is found to be at rest with $s_z = \lambda$ and

$|\vec{p},\lambda\rangle \equiv |p=0,s,s_z=\lambda\rangle$.

In this work the helicity convention is chosen to describe a relativistic particle with spin. It is important to notice that the γ angle in the rotation $R(\alpha,\beta,\gamma)$ is not fixed by the helicity choice, any rotation around the momentum of A would lead to the same spin state. Here again, it is a choice and there are two conventions used in the literature $\gamma=0$ and $\gamma=-\phi$, where the first one lead to easier equations. For completeness, the helicity amplitudes will be written using first the $\gamma=-\phi$ convention, then the simplified case $\gamma=0$ will be deduced.

5.3 The helicity formalism

In this section the helicity formalism will be introduced in details and then used to derive the amplitude of the three-body baryonic decay $\Lambda_c^+ \to pK^-\pi^+$. Consider a particle of total angular momentum $\vec{J}=\vec{L}+\vec{S}$ where $\vec{S}$ is the spin vector and $\vec{L}$ the orbital angular momentum. The usual way of describing a particle in quantum mechanics is to use a basis formed by the simultaneous eigenstates of $\vec{J}^2$, J_z, $\vec{L}^2$ and $\vec{S}^2$ or $\vec{L}^2$, L_z, $\vec{S}^2$ and S_z where we can switch from one basis to another using the Clebsch-Gordon coefficients. There is a third basis which is convenient to describe relativistic processes involving particles with spin, the so called helicity basis. The helicity operator Λ is defined as the projection of the total angular momentum along the particle momentum:

$$\hat{\Lambda} = \frac{\vec{J}\cdot\vec{p}}{\|\vec{p}\|} = (\hat{L}+\hat{S})\cdot\hat{\mathbf{p}} = \hat{S}\cdot\hat{\mathbf{p}}. \tag{5.23}$$

Λ commutes with $\vec{J}$ and $\vec{S}^2$ hence we can build a basis of simultaneous eigenstates of $\vec{J}^2$,J_z,$\vec{S}^2$ and Λ. A very useful property of the helicity operator is the invariance under rotations, since $\hat{\mathbf{p}}$ and $\vec{S}$ are rotated at the same time, the product of the two is invariant. As discussed in the previous section, the spin state $|\vec{p},\lambda\rangle$ describes the particle in its helicity frame, i.e. the frame where the particle momentum is aligned to the z-axis and the particle is at rest. The state $|\vec{p},\lambda\rangle$ is an eigenstate of the helicity operator Λ with eigenvalue λ and it is called helicity state. Thus the projection of the total angular momentum of the particle along the z axis coincides by construction with the helicity.

5.3.1 Helicity frame

The helicity frame of a particle can be reached by mean of boosts and rotations, the reasons are explained in Sec. 5.2.3. These transformations can be applied either to the particle four-momenta itself or to the reference frames leading to *active* transformations, *i.e.* the coordinates of the reference frames are fixed and the particle momenta change under boosts and rotations, or *passive* transformations, *i.e.* the particle four-momenta are fixed and the coordinates of the reference frame change. Consider a particle A and a frame S_L (where the label L stands for laboratory), in this frame the particle is described by the state vector $|\vec{p},\lambda\rangle$, where $\vec{p}$ is the momentum and λ helicity. The helicity frame of A, S_A, is defined as the frame where $\vec{p}$ is aligned with the z-axis and A is at rest. The transformation to go to the helicity frame is

$$h(\vec{p}) = R(\phi,\theta,0)L_z(v) \tag{5.24}$$

where $R(\phi,\theta,0)$ is a rotation , see 5.2.2, and $L_z(v)$ is a boost of speed v along the z direction. Hence the relation between the two frames, A and S_L, can be written as :

$$S_L = h^{-1}(\vec{p})S_A = R^{-1}(\phi,\theta,0)L_z(v)S_A = R^{-1}(0,\theta,-\phi)L_z(v)S_A \tag{5.25}$$

For the *active* convention instead, the transformation is applied to the states as follows, using Eq. 5.7:

$$|\vec{p},\lambda\rangle = L(\vec{p})R(\phi,\theta,0)|\vec{p}=0,\lambda\rangle\,, \tag{5.26}$$

where $L(\vec{p})$ is a boost along $\vec{p}$ with velocity $\vec{v}=\vec{p}/m$. The particle in its helicity frame will acquire a momentum $\vec{p}$ after the boost. The above comparison between the two conventions, active and passive, can be summarized as follows: if the helicity state for particle A is defined in another frame (here S_L) via the transformation in Eq. 5.26, then λ is the z-component of the spin of particle A measured in the rest frame S_A which is obtained using Eq. 5.25. In the following the *active* convention is chosen. The interchange of Lorentz boost and the rotation has no impact on the definition of the helicity states, mathematically this is because:

$$\begin{aligned}|\vec{p},s,\lambda\rangle &= L(\vec{p})R(\phi,\theta,-\phi)|\vec{p}=0,s,\lambda\rangle \\ &= R(\phi,\theta,-\phi)R^{-1}(\phi,\theta,-\phi)L(\vec{p})R(\phi,\theta,-\phi)|\vec{p}=0,s,\lambda\rangle \\ &= R(\phi,\theta,-\phi)L(\vec{p_z})|\vec{p}=0,s,\lambda\rangle\end{aligned} \tag{5.27}$$

using the fact that $L(\vec{p}) = R^{-1}(\phi,\theta,-\phi)L(\vec{p}_z)R(\phi,\theta,-\phi)$. This can be also understood intuitively: in the first case the boost is applied along $\vec{p}=p\hat{z}$ which has been previously rotated, in the second case the boost will be along $\hat{p}(\theta,\phi)$ and the alignment is done afterwards by applying the same rotation of (θ,ϕ) but using the angle computed in the S_L frame, giving an equivalent result.

5.3.2 Helicity states

The definition of helicity states can be now described in details. Starting from the rest state $|\vec{p}=0,\lambda\rangle$ with spin s and spin projection $s_z=\lambda$ and exploiting the rotational invariance of the helicity operator, one can define a state with any momentum $\vec{p}$ as in Eq. 5.26. This invariance is due to the fact that the quantization axis $\hat{p}(\theta,\phi)$ rotates along with the spin $\vec{s}$ of the system, hence the product is invariant under rotation. Those states are normalized using the Lorentz invariant normalization:

$$\langle\vec{p}',s',\lambda'|\vec{p},s,\lambda\rangle = (2\pi)^3 2E\delta^3(\vec{p}'-\vec{p})\delta_{ss'}\delta_{\lambda\lambda'}\,. \tag{5.28}$$

Following the definition of the one-particle helicity state, the two-particle plane-wave helicity states are the direct products of the one-particle states

$$|\vec{p}_1,\lambda_1;\vec{p}_2,\lambda_2\rangle = |\vec{p}_1,s_1,\lambda_1\rangle\otimes|\vec{p}_2,s_2,\lambda_2\rangle \tag{5.29}$$

where s_1 and s_2 are the spins of the two particles. They are fixed and the label can be dropped. When defining two particles states care must be taken. Particles one and two will be back-to-back in the

two-particle center-of-mass frame, hence if $\vec{p_1} = (p, \theta, \phi)$ then $\vec{p_2} = -\vec{p_1} = (p, \pi - \theta, \phi \pm \pi)$, this relation can be easily verified for the particular case $\theta = 0$ and $\phi = 0$, where we define $p = |\vec{p_1}| = |\vec{p_2}|$. There is an ambiguity on the choice of ϕ_2 which can be removed imposing the condition:

$$\lim_{-\vec{p_z} \to 0} |-\vec{p_z}, \lambda\rangle = \lim_{\vec{p_z} \to 0} |\vec{p_z}, -\lambda\rangle \tag{5.30}$$

requiring that for a particle at rest, if the spin projection along p_z is λ then the projection along $-p_z$ is $-\lambda$. This condition gives rise to a phase, $(-1)^{s-\lambda}$,between particle 1 and particle 2, see [8] for detailed calculations :

$$|-\vec{p_z}, s, \lambda\rangle = (-1)^{s-\lambda} \exp\{-i\pi J_y\} |\vec{p_z}, s, \lambda\rangle \,. \tag{5.31}$$

This phase is optional and it can be either dropped (*no-phase convention*) or kept (*particle-2-phase-convention*). It is important to be consistent with this choice, especially when looking at the action of the parity operator on the two particles state. Now, because the particles are back-to-back the two-particle state can be specified using only the coordinates p, θ and ϕ, thus the state is written as $|p, \theta, \phi; \lambda_1, \lambda_2\rangle$. These states are called plane-wave helicity states and they are not eigenstates of total angular momentum, meaning that they do not have definite angular momentum. It is possible to define a new basis, the spherical-wave helicity basis, formed by vectors which instead are eigenstates of the total angular momentum. The states of this basis are $|p, J, M, \lambda_1, \lambda_2\rangle$, where p is the magnitude of the momentum of one of the two particles, J the total angular momentum of the two-particle system, M is the projection of the total angular momentum along z and λ_1, λ_2 are the helicities of the particles. These states transform irreducibly under rotations according to Eq. 5.10. The plane-wave states can be written in terms of the spherical-waves states [8]:

$$|p, \theta, \phi, \lambda_1, \lambda_2\rangle = \sum_{J,M} c_{JM}(p, \theta, \phi, \lambda_1, \lambda_2) |p, J, M, \lambda_1, \lambda_2\rangle. \tag{5.32}$$

The coefficients c_{JM} are determined starting from the easier case $\theta = \phi = 0$. In this case, the two particles are moving in opposite directions (in plane-wave states) along the z-axis. The orbital angular momentum $\vec{L} = \vec{r} \times \vec{p}$ is zero by definition. Hence $|p, \theta, \phi, \lambda_1, \lambda_2\rangle$ is an eigenstate of J_z with eigenvalue $\lambda = \lambda_1 - \lambda_2$. On the right-hand side $M = \lambda$ and

$$|p, \theta = 0, \phi = 0, \lambda_1, \lambda_2\rangle = \sum_{J} c_{J\lambda}(p, \theta = 0, \phi = 0, \lambda_1, \lambda_2) |p, J, \lambda, \lambda_1, \lambda_2\rangle. \tag{5.33}$$

Thanks to the invariance of the helicity under rotation discussed in Sec. 5.3.1 one can rotate back to the original state leaving the helicities unchanged using the D-Wigner matrices:

$$|p, \theta = 0, \phi = 0, \lambda_1, \lambda_2\rangle = \sum_{JM'} \sqrt{\frac{2J+1}{4\pi}} D^J_{M'\lambda}(\phi, \theta, -\phi) |p, J, M', \lambda_1, \lambda_2\rangle \tag{5.34}$$

where the coefficients $c_{J\lambda}(p, \theta = 0, \phi = 0, \lambda_1, \lambda_2)$ are determined up to a phase and found to be [8] $c_{J\lambda}(p, \theta = 0, \phi = 0, \lambda_1, \lambda_2) = c_J = \sqrt{\frac{2J+1}{4\pi}}$. To invert Eq. 5.34 the orthogonality relations of the D

functions in Eq. 5.20 can be used, giving:

$$|J, M', \lambda_1, \lambda_2\rangle = \sqrt{\frac{2J+1}{4\pi}} \int_0^{2\pi} d\phi \int_{-1}^{1} d\cos\theta \, D^J_{M'\lambda^*}(\phi, \theta, -\phi)|\theta, \phi, \lambda_1, \lambda_2\rangle. \tag{5.35}$$

.

5.3.3 Helicity amplitudes

The amplitude for a two-body decay $a \to 1\ 2$ can be obtained working in the rest frame of a and using Eq. 5.34. The decaying particle a has a spin J and spin projection M along an arbitrary chosen z-axis. The final and initial two-particle plane-wave helicity states are:

$$|i\rangle = |J, M\rangle \text{ and } |f\rangle = |p_f \theta_f \phi_f \lambda_1 \lambda_2\rangle \tag{5.36}$$

where λ_1, λ_2 are the helicities of the final state particles, $\vec{p}_1 = \vec{p}_f$ and $\vec{p}_2 = -\vec{p}_f$, θ_f and ϕ_f are the polar and azimuthal angles of $\vec{p}_f$. The amplitude for $a \to 1\ 2$ is, neglecting the overall constants which are not affecting the angular distribution,

$$\mathscr{A}_{M,\lambda_1,\lambda_2} = \langle f|\mathscr{O}|i\rangle = \langle p_f \theta_f \phi_f \lambda_1 \lambda_2|\mathscr{O}|J, M\rangle \tag{5.37}$$

where $\mathscr{O}$ is the operator describing the transition $a \to 1\ 2$. As explained in Sec. 5.3.2, the conservation of angular momentum is applicable only to spherical-wave states, hence it is useful to insert a complete set of spherical-wave states $|J_f M_f \lambda_1 \lambda_2\rangle$, such that

$$\begin{aligned}\mathscr{A}_{M,\lambda_1,\lambda_2}(a \to 12) &= \sum_{J_f M_f} \langle p_f \theta_f \phi_f \lambda_1 \lambda_2|J_f M_f \lambda_1 \lambda_2\rangle \langle J_f M_f \lambda_1 \lambda_2|\mathscr{O}|J, M\rangle \\ &= \sum_{J_f M_f} \sqrt{\frac{2J+1}{4\pi}} D^{*J}_{M_f \lambda}(\phi_f, \theta_f, -\phi_f) \delta_{J_f, J} \delta_{M_f, M} \langle \lambda_1 \lambda_2|\mathscr{O}|M\rangle\end{aligned}$$

$$\mathscr{A}_{M,\lambda_1,\lambda_2}(a \to 1\ 2) = \sqrt{\frac{2J+1}{4\pi}} D^{*J}_{M\lambda}(\phi_f, \theta_f, -\phi_f) H_{\lambda_1,\lambda_2} \tag{5.38}$$

where $\lambda = \lambda_1 - \lambda_2$. $H_{\lambda_1,\lambda_2} = \langle \lambda_1 \lambda_2|\mathscr{O}|M\rangle$ is rotational invariant, this means that it cannot depend on the projection on a given axis and the M index can be dropped. The complex parameters H_{λ_1,λ_2} encode the dynamics of the transition and they are usually called "helicity couplings". If the final state helicities of the particles cannot be measured, one needs to sum over the final state helicities λ_1, λ_2.

As explained in the introduction, a three-body decay $a \to 1+2+3$ can proceed via intermediate states. In this case, the decay can be decomposed in two sequential two body decays, for instance $a \to (R \to 1+2)+3$, where the final state and intermediate particles have helicities $\lambda_1, \lambda_2, \lambda_3, \lambda_R$ and spins s_1, s_2, s_3, s_R. The amplitude of this process can be written using the two-body decay amplitude

in Eq. 5.38 as

$$\mathscr{A}_{M,\lambda_1,\lambda_2,\lambda_3}(a \to 1+2+3) = \sum_{\lambda_1} \langle \theta_3\phi_3\lambda_3\lambda_4|\mathscr{O}(R)|s_1, M_1 = \lambda_1\rangle\langle\theta_1\phi_1\lambda_1\lambda_2|\mathscr{O}(a)|J, M\rangle \tag{5.39}$$

$$\mathscr{A}_{M,\lambda_1,\lambda_2,\lambda_3}(a \to 1+2+3) = \sum_{\lambda_1} D^{*J}_{M,\lambda_R-\lambda_3}(\phi_1,\theta_1,-\phi_1) D^{*s_R}_{\lambda_R,\lambda_1-\lambda_2}(\phi_3,\theta_3,-\phi_3) H^{a\to R3}_{\lambda_R,\lambda_3} H^{R\to 12}_{\lambda_1,\lambda_2} \tag{5.40}$$

where $H^{a\to R3}_{\lambda_1,\lambda_2}$ are the helicity couplings for the decay of the mother particle to the resonance R and $H^{R\to 12}_{\lambda_3,\lambda_4}$ the one for the decay of the resonance R to its decay products. The angles are computed each time in the rest frame of the decaying particle, thus θ_1 and ϕ_1 are computed in the a reference frame reached from the laboratory frame and θ_3 and ϕ_3 are computed in the R reference frame reached from the a reference frame. This is a crucial point; the spin states of the a and R decay products are defined in helicity frames reached from different starting points, therefore the helicity are projected on different axes, the consequences of this are discussed in Sec. 5.4.2. Finally, the total angular momentum is conserved by construction thus the allowed helicities are constrained by

$$|\lambda_R| \leq s_R \qquad |\lambda_3| \leq s_3 \qquad |\lambda_R - \lambda_3| \leq s_a \tag{5.41}$$

Helicity couplings The definition of the helicity couplings depends on the convention chosen for the particle 2 phase. Labelling the helicity couplings for the *no-phase convention* by capital H and the *particle-2-phase-convention* ones by small h, the relation between the two is given in [202]

$$h^{R\to i,j}_{\lambda_i,\lambda_j} = H^{(ij)\to i,j}_{\lambda_i,\lambda_j}(-1)^{j_j-\lambda_j} \quad h^{a\to R,k}_{\lambda_R,\lambda_k} = H^{a\to(ij),k}_{\lambda_R,\lambda_k}(-1)^{j_k-\lambda_k} \tag{5.42}$$

Furthermore, the number of allowed helicity couplings can be reduced if parity is conserved in the decay. The action of the parity operator on spherical-wave helicity states is not trivial since they are not eigenstates of parity. It is worked-out in Ref [8]; starting from the plane-wave states at rest and exploiting the properties of the d functions, the action of the parity operator Π on the two-particle spherical helicities state is

$$\Pi\,|p, J, M, \lambda_1, \lambda_2\rangle = \eta_1\eta_2(-1)^{J-s_1-s_2}\,|p, J, M, -\lambda_1, -\lambda_2\rangle\,. \tag{5.43}$$

where η_i are the eigenvalues of the parity operator. This means that the parity changes the sign of the daughter's helicity but not the sign of the spin projection of the mother M. By applying this relation to the helicity couplings (for a strong decay), the following constraints are obtained:

$$\begin{aligned} h_{\lambda_1,\lambda_2} &\equiv \langle\lambda_1\lambda_2|\mathscr{O}|JM\rangle = \langle\lambda_1\lambda_2|\Pi(\Pi^\dagger\mathscr{O}\Pi)\Pi^\dagger|JM\rangle = \langle\lambda_1\lambda_2|\Pi\mathscr{O}\Pi^\dagger|JM\rangle \\ h_{\lambda_1,\lambda_2} &= \eta_a\eta_1\eta_2(-1)^{s_1+s_2-s_a}h_{-\lambda_1,-\lambda_2} \end{aligned} \tag{5.44}$$

For the *no-phase convention* case the constraints are slightly modified and they can be derived from Eq. 5.42 and Eq. 5.44,

$$H_{\lambda_1,\lambda_2} = \eta_a\eta_1\eta_2(-1)^{s_1+s_2-s_a}H_{-\lambda_1,-\lambda_2}(-1)^{2\lambda_2}. \tag{5.45}$$

In the introduction, the Partial Wave (PW) basis was discussed as another possible option to derive the amplitudes. The advantage of this basis is that the parity conservation is automatically included and there is no need to enforce it using the relations in Eq. 5.42. The relation between the helicity basis and the PW basis (also called LS-basis) is [203]

$$h^{a\to R,3}_{\lambda_R,\lambda_3} = \sum_{S=|J_R-J_3|}^{|J_R+J_3|} \sum_{J=|L-S|}^{|L+S|} h^{a\to R,3}_{LS} \sqrt{\frac{2L+1}{2J+1}} \langle j_R, \lambda_R; j_3, -\lambda_3 \mid S, \lambda_R - \lambda_3\rangle \langle L, 0; S, \lambda_R - \lambda_3 \mid J, \lambda_R - \lambda_3\rangle \tag{5.46}$$

where the first Clebsch-Gordan coefficient is for the coupling of j_R and j_3 to a spin S which is the total spin of the system $(J_R J_3)$ and the second one for the coupling of L and S to the total angular momentum $J = J_R + J_3$. Note that here the projection L_z of the orbital angular momentum is always zero since z is perpendicular to p. Similarly, the LS decomposition for the isobar helicity couplings is

$$h^{R\to 1,2}_{\lambda_1,\lambda_2} = \sum_{S'=|J_1-J_2|}^{|J_1+J_2|} \sum_{J=|L'-S'|}^{|L'+S'|} h^{R\to 1,2}_{L'S'} \sqrt{\frac{2L'+1}{2J'+1}} \langle j_1, \lambda_1; j_2, -\lambda_2 \mid S', \lambda_1 - \lambda_2\rangle \langle L', 0; S', \lambda_1 - \lambda_2 \mid J', \lambda_1 - \lambda_2\rangle \tag{5.47}$$

where the first Clebsch-Gordan coefficient is for the coupling of j_1 and j_2 to a spin S' which is the total spin of the system $(J_1 J_2)$ and the second one for the coupling of L' and S' to the total angular momentum $J' = J_1 + J_2$. The decomposition of the helicity couplings in the LS basis, allows to separate the different waves i.e. different L of the decay (partial wave decomposition). This further allows to identify a parity violating and a parity conserving part in the decay. This differentiation is particularly relevant for the Λ_c^+ weak decay to the isobars, where parity is not conserved and both contributions are there. For the strong decay of the isobars itself, there is only one possible wave and the decomposition is equivalent to the parity conservation relations in Eq. 5.44.

5.3.4 Polarized decay rate

In this work, the main goal is to measure the polarisation of the charmed baryon Λ_c^+. In scattering experiments usually an un-polarized or spin averaged cross section is measured. Up to now, it is not possible to create an experiment where all the particles are produced (on purpose) in a well defined spin state, hence polarized. Instead, it is possible to polarize the target particles or the beam itself, for instance using a strong magnetic field. At the LHC, the proton beams are produced in a mixture of spin states without a well-defined polarization. The particles created in a collision form a statistical ensemble where each of them can be produced in a different spin state, on an event-by-event basis. In this case particles are produced in a *mixture* of spin states, as opposed to a *pure* state system where the particles are all in the same spin state. The unpolarized partial decay rate of a particle of mass M in an initial state $|i\rangle$ decaying in some n-body final state $|f\rangle$ is given in its rest frame by [11]:

$$d\Gamma \sim \frac{(2\pi)^4}{2M} |\mathscr{M}|^2 d\Phi_n\left(P; p_1, \ldots, p_n\right) \tag{5.48}$$

where $d\Phi_n$ is an element of the n-body phase space and the matrix element $\mathscr{M}$ describes the amplitude of the process, where the squared of the amplitude gives the decay probability. For a three-body decay,

this is the helicity amplitude $\mathscr{A}_{M,\lambda_1,\lambda_2,\lambda_3}(a \to 1+2+3)$ described above and it is written using defined spin states $|i\rangle = |J,M\rangle$ and $|f\rangle = |\vec{p_1}\vec{p_2}\vec{p_3};\lambda_1,\lambda_2,\lambda_3\rangle$. To take into account the fact that Λ_c^+'s are produced in a mixture of states, the probability in Eq. 5.48 has to be modified.
When a particle is produced in a mixed state $|\chi\rangle$, it can be written as a coherent sum of pure states $|e_i\rangle$ occurring with a statistical weights p_i (where $\sum_i p_i = 1$). The expectation value of an observable A can then be written as [21]:

$$\langle A\rangle = \sum_i p_i \langle\chi_i|A|\chi_i\rangle = \sum_{j,k}\langle e_j|A|e_k\rangle \sum_i \langle e_k|\chi_i\rangle p_i \langle\chi_i|e_j\rangle = \sum_{j,k} a_{jk}\rho_{kj} \tag{5.49}$$

where $a_{jk} = \sum_{j,k}\langle e_j|A|e_k\rangle$ and $\rho_{kj} = \sum_i \langle e_k|\chi_i\rangle p_i \langle\chi_i|e_j\rangle$ is the density matrix, which is hermitian $\rho = \rho^\dagger$, it has trace $\mathrm{tr}(\rho) = 1$ and $\mathrm{tr}(\rho^2 \leq 1)$ (leaving only N^2-1 independent parameters, with N the dimension of ρ). The diagonal elements ρ_{kk} represent the probability to find the system in a pure state $|e_k\rangle$ and the expectation value of A can be written as:

$$\langle A\rangle = \sum_{j,k} a_{jk}\rho_{kj} = \mathrm{tr}(A\rho) \tag{5.50}$$

Therefore, the spin orientation of an ensemble of spin j particles is described by a $(2j+1)(2j+1)$ density matrix containing $(2j+1)^2-1$ independent real parameters, with $|e_i\rangle = |s,m\rangle$.

In the $\Lambda_c^+ \to pK^-\pi^+$ case, $j = \frac{1}{2}$ hence ρ is a 2×2 matrix parametrized by 3 real numbers. The most general way to write ρ is using the Pauli matrices σ_i and the identity matrix $\mathcal{I}$

$$\rho = \frac{1}{2}\left(\mathcal{I} + \vec{P}\cdot\vec{\sigma}\right) = \begin{pmatrix} \rho_{\frac{1}{2},\frac{1}{2}} & \rho_{\frac{1}{2},-\frac{1}{2}} \\ \rho_{-\frac{1}{2},\frac{1}{2}} & \rho_{-\frac{1}{2},-\frac{1}{2}} \end{pmatrix} = \frac{1}{2}\begin{pmatrix} 1+P_z & P_x - iP_y \\ P_x + iP_y & 1-P_z \end{pmatrix} \tag{5.51}$$

Inverting the equation and using the properties of Pauli matrices, $\vec{P}$ is obtained:

$$\vec{P} = \mathrm{tr}(\dot{\rho}\vec{\sigma}) \tag{5.52}$$

$\vec{P} = \{P_x, P_y, P_z\}$ is the polarization vector representing the degree and direction of the state's spin orientation. The condition $\mathrm{tr}(\rho^2) \leq 1$ ensures that $\vec{P} \leq 1$. A pure state corresponds to a state fully polarized with $P = \pm 1$. Introducing the spin density matrix using Eq. 5.50, the decay rate becomes:

$$d\Gamma(\Omega) \propto \sum_{\{\lambda_i\}}\sum_{m,m'} \rho_{m,m'}\mathscr{A}_{m,\lambda_1,\lambda_2,\lambda_3}\mathscr{A}^*_{m',\lambda_1,\lambda_2,\lambda_3} \tag{5.53}$$

where Ω describes the phase space.

5.3.5 Isobars dynamics

In the previous section, the amplitude for the three body resonant decay of a particle a with mass m_a has been derived. As explained in the introduction, in the isobar model the amplitude is factorized into an angular part, which is spin dependent and derived from first principles, and a dynamical part describing the intermediate states, the so-called isobars. The isobars are not stable particles with

defined mass, but rather resonant states with complex mass distributions. In most of the cases, the mass distribution can be described by a relativistic Breit-Wigner function (RBW). This parametrization is valid for narrow resonances far from all relevant thresholds or other resonances. If this is not the case and if there are overlapping resonances with the same quantum numbers, a more complex parametrization has to be used. In general, a resonance is parametrized by its pole position s_R which is independent of the reaction studied and its residues, which quantify the couplings to various channels and can be used to calculate branching ratios. The relation with the usual mass m_0 and width Γ_0 of the resonance is $\sqrt{s_R} = m_R - \mathrm{i}\frac{\Gamma_R}{2}$. It is important to note that the BW poles (m_0, Γ_0) agrees with its pole position (m_R, Γ_R) only for narrow and well separated resonances, far away from the opening of decay channels. The RBW lineshape is

$$\mathrm{BW}(m) = \frac{1}{m_0^2 - m^2 - i m_0 \Gamma(m)}, \quad \Gamma(m) = \Gamma_0 \left(\frac{p}{p_0}\right)^{2L_R+1} \frac{m_0}{m} F_{L_R}^2(p, p_0) \tag{5.54}$$

where all the quantities are defined in the following. The RBW is multiplied by the barrier factors, also called "angular momentum barrier", which suppress the amplitude at low values of break-up momenta (p and q). However, the barrier factors grow rapidly with increasing break-up momenta for positive values of L. The Blatt-Weisskopf form factors, F_L, are introduced to compensate for this behavior. The final lineshape after multiplication is

$$\mathcal{X}_{\mathrm{BW}}(m) = \underbrace{\left(\frac{q(m)}{q_0}\right)^{L_{\Lambda_c^+}} \left(\frac{p(m)}{p_0}\right)^{L_R}}_{\text{barrier factors}} \underbrace{F_{L_{\Lambda_c^+}}(q, q_0)\, F_{L_R}(p, p_0)}_{\text{form factors}} \mathrm{BW}(m) \tag{5.55}$$

where $L_{\Lambda_c^+}$ is the orbital angular momentum between the resonance and the spectator particle, while L_R is the orbital angular momentum between the resonances decay products. Then $q(m)$ is the momentum of one of the products of the $\Lambda_c^+ \to Rh$ decay in the (Rh) system. Similarly $p(m)$ is the momentum of one of the products of the R decay in the R's rest frame. The explicit expression of p is simply [11]

$$|p| = \frac{\left[\left(M^2 - (m_1+m_2)^2\right)\left(M^2 - (m_1-m_2)^2\right)\right]^{1/2}}{2M} \tag{5.56}$$

where M is the mass of the decaying particle, m_1 and m_2 the masses of the decay products. Next, $q_0 = q(m_0)$ and $p_0 = p(m_0)$ are the momenta calculated at the resonance BW mass, finally m_0 and the width Γ_0 are the BW mass and width. The Blatt-Weisskopf form factors $F_L(z, z_0)$ are parametrized as:

$$\begin{cases} F_0(z, z_0) & = 1 \\ F_1(z, z_0) & = \sqrt{\frac{1+z_0}{1+z}} \\ F_2(z, z_0) & = \sqrt{\frac{(z_0-3)+9z_0}{(z-3)^2+z}} \\ F_3(z, z_0) & = \sqrt{\frac{z_0(z_0-15)^2+9(2z_0-5)}{z(z-15)^2+9(2z-5)}} \end{cases} \tag{5.57}$$

where for the Λ_c^+ decay, $z = (q(m)d)^2$ and $z_0 = (q_0 d)^2$ and d is the radius of interaction and is taken to be $d = 5.0\ \hbar\mathrm{c}/\mathrm{GeV}$. For the resonance decay $z = (p(m)d)^2$ and $z_0 = (p_0 d)^2$ with d the "radius of the

resonance" are taken to be: $d'_{\overline{\mathrm{K}}^{*0}} = 3.4\ \hbar\mathrm{c}/\mathrm{GeV}$, $d'_{\Delta^{++}} = 5.22\ \hbar\mathrm{c}/\mathrm{GeV}$ and $d'_{\Lambda^*} = 6.29\ \hbar\mathrm{c}/\mathrm{GeV}$, as in Ref. [204]. These values are chosen as reference values for the main model. The choice of the radius values has a minor influence on the final amplitude, this is shown in Fig. 5.1, where the BW function in Eq. 5.55 with $L_{\Lambda_c^+} = 0$ is plotted for one resonance per channel and for three different values of d. The grey curves are for $d' = 1$, it can be seen that changing d' has a small effect on the BW shape, affecting mostly the tail of the distribution. The same value of d' for each channel will be set in the fit so that the effect is the same for every resonance in the same channel. The influence of the barrier factor's radii on the final amplitude will be studied as a systematic effect.

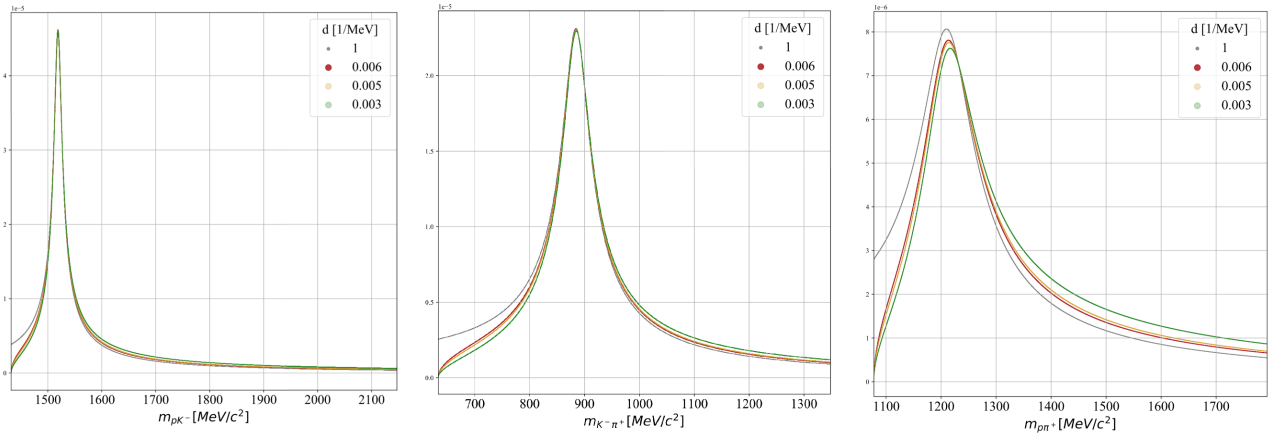

Figure 5.1: Breit Wigner functions for $\Lambda^*(1520)$, $K^*(892)$ and $\Delta^{++}(1232)$ with three different values of d are shown: $d = [0.006, 0.005, 0.003]$ MeV^{-1}, as a comparison the case $d = 1$ MeV^{-1} is shown in grey. The masses and width are from [11].

The same comparison is done for the Λ_c^+ radial parameter in Fig. 5.2, this time Eq. 5.55 is shown for $L_R = 0$. The effect of d is even smaller and it is expected to have a small influence in the fit result.

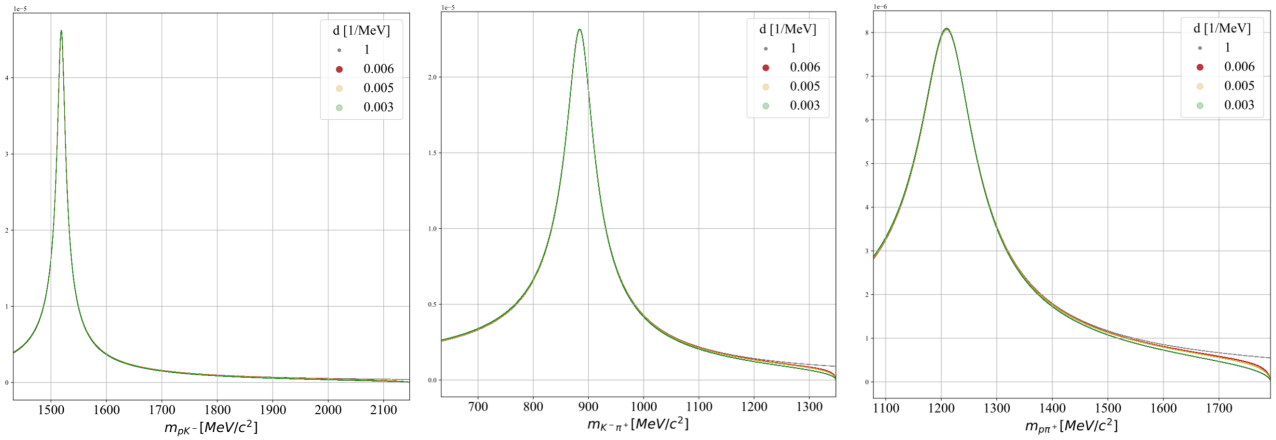

Figure 5.2: Breit Wigner functions for $\Lambda^*(1520)$, $K^*(892)$ and $\Delta^{++}(1232)$ for three different values of d $0.006, 0.005, 0.003$ MeV^{-1}, as a comparison the case $d = 1$ MeV^{-1} is shown in grey. The masses and width are fixed to the values in Ref. [11].

For some of the resonances present in the $\Lambda_c^+ \to pK^-\pi^+$ decay, the RBW is not a suitable parametrization. For instance, the scalar mesons of the $K\pi$ channel are difficult to describe since

they can have large widths and thus interfere with the non-resonant component or other resonances. The S-wave scattering has two possible isospins, $I = \frac{1}{2}$ containing $K_0^*(1430)$ and $K_0^*(700)$ and $I = \frac{3}{2}$, which contains no known resonances. They are commonly parametrized by the LASS lineshape [205].

$$\mathcal{X}_{\text{LASS}}\left(m^2\right) = \frac{m}{q\cot\delta_B - iq} + e^{2i\delta_B}\frac{m_0\Gamma_0\frac{m_0}{q_0}}{m_0^2 - m^2 - im_0\Gamma_0\frac{q}{m}\frac{m_0}{q_0}} \tag{5.58}$$

$$\tag{5.59}$$

where $\cot\delta_B = \frac{1}{aq} + \frac{1}{2}rq$, a is the scattering length and r the effective range and the other quantities are defined as in Eq. 5.55.

Another special case is the $\Lambda^*(1405)$ resonance which has its pole mass about 30 MeV below the threshold of the pK^- mass ($\sim 1432\,\text{MeV}/c^2$). Even if the mass peak is below the threshold, its high mass tail can contribute to the spectrum. To parametrize this effect, the pole mass m_0 in the RBW is replaced by an effective mass m_0^{eff}, given by:

$$m_0^{\text{eff}} = m^{\min} + \frac{1}{2}\left(m^{\max} - m^{\min}\right)\left[1 + \tanh\left(\frac{m_0 - \frac{m^{\min}+m^{\max}}{2}}{m^{\max} - m^{\min}}\right)\right] \tag{5.60}$$

where $m^{\min} = m_{K^-} + m_p$ and $m^{\max} = m_{\Lambda_c^+} - m_{\pi^+}$ are the minimum and maximum allowed masses. Another parametrization exists for the $\Lambda(1405)$ which accounts for the opening of another decay channel above $1328\,\text{MeV}/c^2$ with final state $\Sigma^+\pi^-$. This increases the width above the threshold and thus modifies the shape of the RBW. This effect is taken into account by adding a lineshape for the other possible opening channels, $\text{BW}_{\Lambda(1520)}(m) = \text{BW}_{pK^-}(m) + \text{BW}_{\Sigma^+\pi^-}(m)$, where q and q_0 in the second term are calculated assuming the decay to $\Sigma\pi$ and the resonance width Γ_0 is set to the $\Lambda(1405)$ width for both cases. This is called Flatté lineshape [206].

5.4 The $\Lambda_c^+ \to pK^-\pi^+$ case

The decay studied in this analysis is the Cabibbo favored decay $\Lambda_c^+ \to pK^-\pi^+$. As discussed when deriving the helicity amplitudes in Sec. 5.3.3, this three-body decay can be decomposed in subsequent two-body decays passing through intermediate resonances. The possible intermediate chains are (pK^-), $(K^-\pi^+)$ and (π^+p) and each resonance is labeled either by the two decay products or by the name of the resonant particle: Λ^* chain, K^* chain and Δ chain. Note that the ordering of the decay products is important, if the cyclic order is broken, the final result may change, especially when defining the angles and the helicity coupling relations. This can be understood looking for instance at Eq. 5.42, where the choice of the particle ordering changes the relations between the couplings. Regarding the angles, those of one decay product differ from the ones of the other decay product by a factor of π; thus for $a \to 1+2$, in the rest frame of a, particle 1 is traveling in the (θ_1, ϕ_1) direction and particle 2 must be traveling in the $(\theta_2, \phi_2) = (\pi - \theta_1, \phi_1 + \pi)$ direction. This is further discussed in Sec. 5.5. The total amplitude is the sum of the amplitudes of each resonance, where the single resonance angular distributions are multiplied by the corresponding lineshape. To describe the total

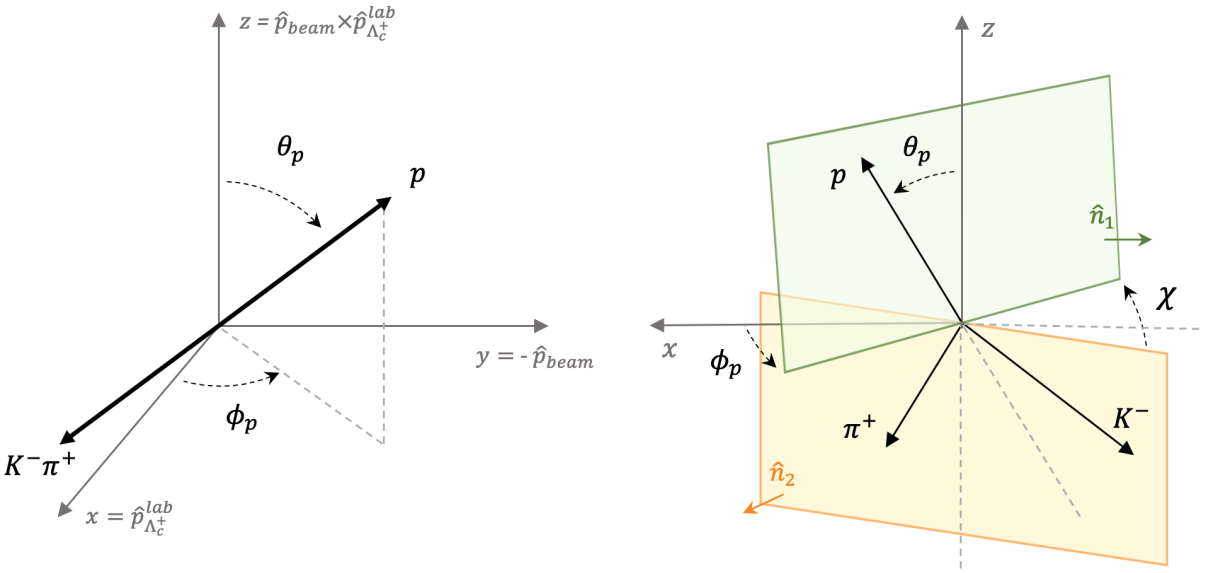

Figure 5.3: Definitions of the Euler angles in the polarization frame. Left: θ_p and ϕ_p angles. Right: χ angle. The ($\vec{p}$,z) plane is shown in green and the (K^-,π^+) plane in orange. The unitary vectors, $\hat{n}_1$ and $\hat{n}_2$, perpendicular to those planes are also shown.

amplitude for the $\Lambda_c^+ \to pK^-\pi^+$ decay, first the necessary frame and the angles are defined, then the individual amplitudes of each chain are derived following Eq. 5.40 and finally the polarized decay rate can be obtained.

5.4.1 Three-body phase space description

The kinematics of the Λ_c^+ three-body decay is described by the four-momenta of the 3 daughter particles, leading to $3 \times 4 = 12$ degrees of freedom (dofs). Fixing the 3 masses and using the energy-momentum conservation, there are only 5 dofs left. In the Λ_c rest frame, the decay products are in the same plane and the angles between them are determined by two pairs of invariant masses. The orientation of the plane is given by 3 Euler angles, the polar and azimuthal angle of the proton (θ_p, ϕ_p), and the angle χ, which is the angle between the planes formed by the z axis and the proton direction and the plane formed by the resonance decay product, as shown in Fig. 5.3. The angles are defined in the polarization frame $\{\hat{x}, \hat{y}, \hat{z}\}$, described in the next section, as:

$$\begin{cases} \theta_p & = \arccos(\hat{p_p} \cdot \hat{z}) \\ \phi_p & = \operatorname{atan2}(\hat{p_p} \cdot \hat{y}, \hat{p_p} \cdot \hat{x}) \\ \chi & = \arccos(\hat{n}_1 \cdot \hat{n}_2) \end{cases} \tag{5.61}$$

where $\hat{p}_p$ is the unit vector along the proton direction, $\hat{n}_1 = \hat{p}_p \times \hat{z}$ and $\hat{n}_2 = \hat{p}_{\pi^+} \times \hat{p}_{K^-}$. The five phase space variables are thus

$$\Omega = \left(m^2_{pK^-}, m^2_{p\pi^+}, \cos\theta_p, \phi_p, \chi\right) \tag{5.62}$$

These three angles describe a rotation which brings the initial frame (x, y, z) into the frame (x'', y'', z'') where the z'' axis direction is the proton direction, and p, K and π lie in the (x'', z'') plane. The rotation is the rotation of angle ϕ_p around the z axis, followed by the rotation of angle θ_p around the y' axis, and followed by the rotation of angle χ around the $z' = z''$ axis. For zero polarization the dependence on the three Euler angles is dropped (see Sec. 5.5) and the decay is fully determined by two variables, usually the two invariant masses. For non-zero polarisation, the decay will have a non trivial dependence on the angles. This means that the effects of the polarization can be seen in the angular distribution of the decay and not on the invariant masses distributions. The choice of the axis is arbitrary but it can be guided by physics considerations, it is detailed in Sec. 5.4.2.

The magnitudes of the p, K and π momenta in the Λ_c^+ polarization frame are given by:

$$|\vec{p}_p| = \frac{\sqrt{m_K^4 - 4M_{\Lambda_c}^2 m_p^2 + 2m_K^2(m_\pi^2 - m_{pK}^2 - m_{p\pi}^2) + (m_{p\pi}^2 + m_{pK}^2 - m_\pi^2)^2}}{2M_{\Lambda_c}}, \tag{5.63}$$

$$|\vec{p}_K| = \frac{\sqrt{\left(M_{\Lambda_c}^2 - (m_{p\pi} + m_K)^2\right)\left(M_{\Lambda_c}^2 - (m_{p\pi} - m_K)^2\right)}}{2M_{\Lambda_c}}, \tag{5.64}$$

$$|\vec{p}_\pi| = \frac{\sqrt{\left(M_{\Lambda_c}^2 - (m_{pK} + m_\pi)^2\right)\left(M_{\Lambda_c}^2 - (m_{pK} - m_\pi)^2\right)}}{2M_{\Lambda_c}}. \tag{5.65}$$

In the (x'', y'', z'') frame instead,

$$\vec{p}_p'' = \begin{pmatrix} 0 \\ 0 \\ |\vec{p}_p| \end{pmatrix}. \tag{5.66}$$

The angle between the proton and pion directions is equal to $\theta_{p\pi}$ and

$$\cos\theta_{p\pi} = \frac{-m_{p\pi}^2 + m_p^2 + m_\pi^2 + 2E_pE_\pi}{2|\vec{p}_p||\vec{p}_\pi|}, \tag{5.67}$$

with

$$E_p = \sqrt{|\vec{p}_p|^2 + m_p^2} \tag{5.68}$$

and

$$E_\pi = \sqrt{|\vec{p}_\pi|^2 + m_\pi^2}. \tag{5.69}$$

Thus

$$\vec{p}_\pi'' = \begin{pmatrix} -|\vec{p}_\pi|\sqrt{1 - \cos^2\theta_{p\pi}} \\ 0 \\ |\vec{p}_\pi|\cos\theta_{p\pi} \end{pmatrix}. \tag{5.70}$$

Similarly,

$$\cos\theta_{pK} = \frac{-m_{pK}^2 + m_p^2 + m_K^2 + 2E_pE_K}{2|\vec{p}_p||\vec{p}_K|}, \tag{5.71}$$

with

$$E_K = \sqrt{|\vec{p}_K|^2 + m_K^2} \tag{5.72}$$

and

$$\vec{p}''_K = \begin{pmatrix} |\vec{p}_K|\sqrt{1-\cos^2\theta_{pK}} \\ 0 \\ |\vec{p}_K|\cos\theta_{pK} \end{pmatrix}. \tag{5.73}$$

The vectors in the original frame are then obtained with the rotations given above and using the rotation matrix

$$R = \begin{pmatrix} \cos\phi_p\cos\chi\cos\theta_p - \sin\phi_p\sin\chi & -\sin\phi_p\cos\chi - \cos\phi_p\cos\theta_p\sin\chi & \cos\phi_p\sin\theta_p \\ \sin\phi_p\cos\chi\cos\theta_p + \cos\phi_p\sin\chi & \cos\phi_p\cos\chi - \sin\phi_p\cos\theta_p\sin\chi & \sin\phi_p\sin\theta_p \\ -\sin\theta_p\cos\chi & \sin\chi\sin\theta_p & \cos\theta_p \end{pmatrix}: \tag{5.74}$$

$$\vec{p}_p = R\begin{pmatrix} 0 \\ 0 \\ |\vec{p}_p| \end{pmatrix} = \begin{pmatrix} |\vec{p}_p|\cos\phi_p\sin\theta_p \\ |\vec{p}_p|\sin\phi_p\sin\theta_p \\ |\vec{p}_p|\cos\theta_p \end{pmatrix}, \tag{5.75}$$

$$\vec{p}_\pi = R\begin{pmatrix} -|\vec{p}_\pi|\sqrt{1-\cos^2\theta_{p\pi}} \\ 0 \\ |\vec{p}_\pi|\cos\theta_{p\pi} \end{pmatrix}, \tag{5.76}$$

$$\vec{p}_K = R\begin{pmatrix} |\vec{p}_K|\sqrt{1-\cos^2\theta_{pK}} \\ 0 \\ |\vec{p}_K|\cos\theta_{pK} \end{pmatrix}. \tag{5.77}$$

The minus sign in Eq. 5.76 depends on the configuration of the resonance decay products. Looking at Fig. 5.4, the direction of the unit vector $\hat{n}_2$ depends on the position of the π and K^- vectors. There are two possible configuration for the K-π ordering corresponding the blue and orange case in the figure, giving a minus sign in a different position when projecting the momentum on the x axis for the π^+ or for the K^- respectively. Eq. 5.76 and 5.77 are written in the "blue" configuration.

5.4.2 Frames definition

To describe the $\Lambda_c^+ \to pK^-\pi^+$ decay two frames are needed: the polarization frame, for the Λ_c^+ decay to the isobars, and the resonance frame, for the decay of the isobar itself. As explained in the introduction (Sec. 5.1), for promptly produced Λ_c in a pp collider, the polarization vector is expected to be perpendicular to the production plane due to parity conservation in strong interactions. Hence it is convenient to define a z axis along the normal to the production plane using the beam direction and the Λ_c direction in the lab frame

$$\hat{z} = \hat{p}_{\text{beam}} \wedge \hat{p}^{\text{lab}}_{\Lambda_c} \tag{5.78}$$

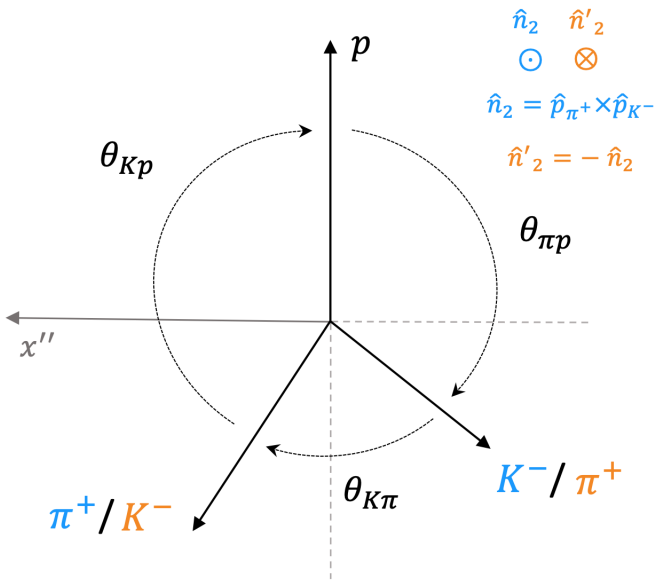

Figure 5.4: Sketch of the $pK\pi$ momenta in the $x'' - z''$ plane. The two possible configurations are shown in blue and orange, the n_2 vector, perpendicular to the (K^-,π^+) plane, is shown for the two configurations.

where $\vec{p}_{\text{beam}}$ is the beam direction in the laboratory frame (z axis for the LHCb reference frame) and $\vec{p}^{\,\text{lab}}_{\Lambda_c}$ is the Λ_c direction in the laboratory frame. The choice of the x and y axes is not important since parity conservation ensures the independence on the azimuthal angle. A possible choice is taking as $\hat{x}$ axis the direction of the Λ_c in the lab frame, the $\hat{y}$ axis is then automatically defined

$$\hat{x} = \hat{p}^{\text{lab}}_{\Lambda_c} \text{ and } \hat{y} = \hat{z} \wedge \hat{x}. \tag{5.79}$$

Then the polarization frame, shown in Fig. 5.3, is the frame where the Λ_c^+ is at rest and the axes $\{\hat{x},\hat{y},\hat{z}\}$ have been defined above. The helicity frame of the isobars is defined starting from the polarization frame, using a sequence of boosts and rotations, where the z axis is the direction of the resonance in the laboratory frame. This new coordinate system (x',y',z') is thus obtained by rotating the axis by the Euler rotation $R(\phi_R,\theta_R,-\phi_R)$ i.e. a rotation of angle ϕ_R around the z axis, followed by a rotation of angle θ_R around the rotated y axis and followed by a rotation of angle $-\phi_R$ around the rotated z axis. The angles θ_R,ϕ_R are the polar angles of the resonance in the polarization frame,

$$\theta_R = \arccos(\hat{p}_R \cdot \hat{z}) \tag{5.80}$$

$$\phi_R = \text{atan2}(\vec{p}_R \cdot \hat{y}, \vec{p}_R \cdot \hat{x}) \tag{5.81}$$

This defines six angles: $\theta_R = \{\theta_{K*},\theta_\Lambda,\theta_{\Delta^{++}}\}$ and $\phi_R = \{\phi_{K*},\phi_\Lambda,\phi_{\Delta^{++}}\}$. These rotations are followed by a boost along the new z axis, i.e. z' is the direction of $\vec{p}_R$ in the Λ_c rest frame. The momentum $\vec{p}'$ of one of the R decay product in this frame is described by the angles (θ',ϕ'). Note that ϕ' is the same in the Λ_c rest frame and in the R rest frame since the boost is perpendicular to

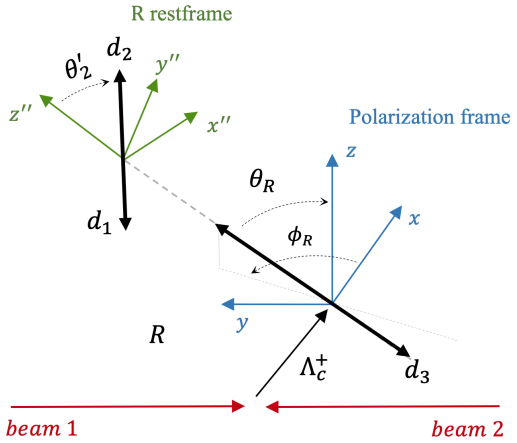

Figure 5.5: Definitions of the reference frames and angles for $\Lambda_c^+ \to pK^-\pi^+$

the plane defining ϕ'. The angles in the resonance frame are defined as:

$$\theta'_i = \arccos\left(\vec{p}'_i \cdot \vec{p}_R^{\,\text{lab}}\right) = \arccos\left(\vec{p}'_i \cdot \hat{z}'\right) \tag{5.82}$$

$$\phi'_i = \text{atan2}\left(\vec{p}'_i \cdot \hat{y}', \vec{p}'_i \cdot \hat{x}'\right) \tag{5.83}$$

In total 6 angles are needed to describe the one resonance per decay channel: θ'_{K^-},ϕ'_{K^-} for the K^* decay, θ'_{π^+} ,ϕ'_{π^+} for the Δ decay and θ'_p,ϕ'_p for the Λ decay. The resonance and polarization frames are shown in Fig. 5.5. The resonance frame of the three chains is equally shown in Fig. 5.8.

5.4.3 Quantization axis and proton's helicity frame

The proton helicity frame is then reached from the resonance helicity frame via a rotation $R(\phi', \theta', -\phi')$ and boost along the proton momentum. For each chain the proton helicity frame is reached passing through a different sequence of boosts and rotations leading to a different definition of the proton helicity state. In the end, the decay amplitudes are obtained summing coherently the amplitudes of the different resonances, hence the proton helicity state must be defined using the same quantization axis (which is defined w.r.t the Λ_c^+) for the three chains.

- For the $\Lambda_c^+ \to p\bar{K}^{*0}(\to K^-\pi^+)$ decay, the proton quantization axis is the direction of the proton in the Λ_c rest frame,
- for the $\Lambda_c^+ \to K^-\Delta^{++}(\to p\pi^+)$ decay, the proton quantization axis is the direction of the proton in the Δ (or $p\pi$) rest frame,
- for the $\Lambda_c^+ \to \pi^+\Lambda^*(\to pK^-)$ decay, the proton quantization axis is the direction of the proton in the Λ^* (or pK) rest frame.

If we measure the proton spin projection using as quantization axis for all decays in the proton rest frame, the direction of the proton in the Λ_c frame, one needs to rotate the projection axis (or equivalently the proton helicity state) of the chain which is not aligned with this quantization axis.

These are called Wigner rotations and they are due to the fact the boosts used to reach the proton rest frame within one chain are not collinear.

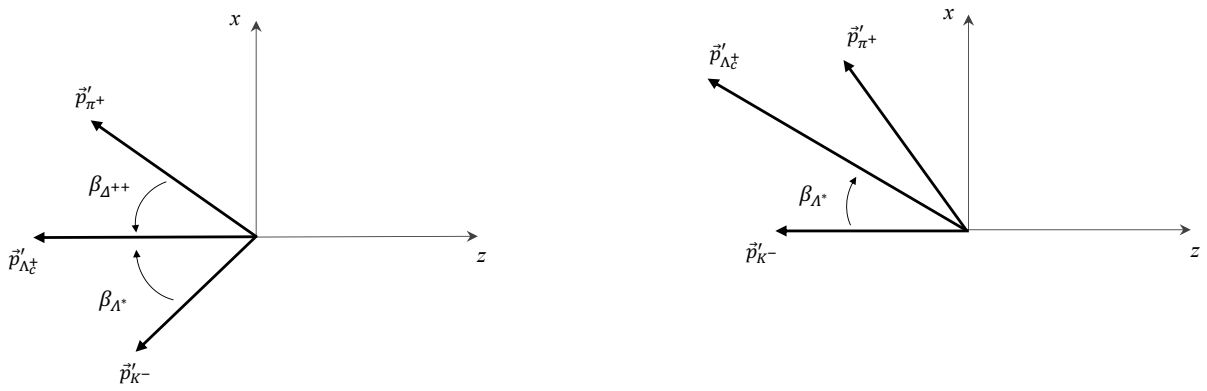

Figure 5.6: View of the $(x-z)$ plane of the proton rest frame reached from the K^* resonant decay on the left and from the Λ^* resonant decay on the right. The Wigner angles $\beta_{\Delta^{++}}$ and β_{Λ^*} are shown.

For the K^* chain the sequence of boosts is shown in Fig. 5.8. The proton quantization axis in the p rest frame reached from the K^* rest frame is aligned with the one reached from the Λ_c^+ rest frame. For the other two chains this is not the case and an additional rotation is needed to align the proton quantization axis as in the K^* chain, see right side of in Fig. 5.8. The polar Wigner angles, named β_R here, are shown in Fig. 5.6. On the left, the proton helicity frame is reached from the K^* chain, the momentum of Λ_c^+ is parallel to $-\hat{z}$ and there is no need of a rotation, hence $\beta_{K^*} = 0$. On the right of the figure, the Λ chain is shown, where the resonance daughter momentum $\vec{p}_{K^-}$ is aligned to $-\hat{z}$ in the proton rest frame. Here β_{Λ^*} is the angle in the p rest frame between the direction of the Λ_c and that of the K. In the right figure, the Δ chain is shown, where the $\vec{p}_{\pi^+}$ is aligned to $-\hat{z}$ and $\beta_{\Delta^{++}}$ is the angle in the p rest frame between the direction of the Λ_c and that of the π.

The azimuthal part of these rotations is less obvious. One could think that since p, K^- and π^+ are in the same plane, there is no need of an azimuthal rotation. However, looking at the $x-y$ plane it is clear that the K^* chain is in a different configuration, since the azimuthal part of the daughter is not zero after boosting to the p rest frame. This is shown in Fig. 5.7. The Δ and Λ chains need to be rotated by ϕ'_K around the z-axis. Hence the final Wigner rotation is:

$$R(0, \beta_{\text{res}}, \phi'_K) \tag{5.84}$$

and it appears when combining the amplitudes of the three chains in Eq. 5.103.

5.4.4 The $\Lambda_c^+ \to pK^-\pi^+$ amplitudes

Now that all the necessary elements have been introduced, the helicity amplitudes for the $\Lambda_c^+ \to pK^-\pi^+$ decays are derived first for each chain separately and finally for the total amplitude, including the spin-density matrix. Compared to the equations given in Ref.[204], these amplitudes include the Wigner rotations and the additional α factors, defined in Eq. 5.4.4, which compensate for the two-to-one

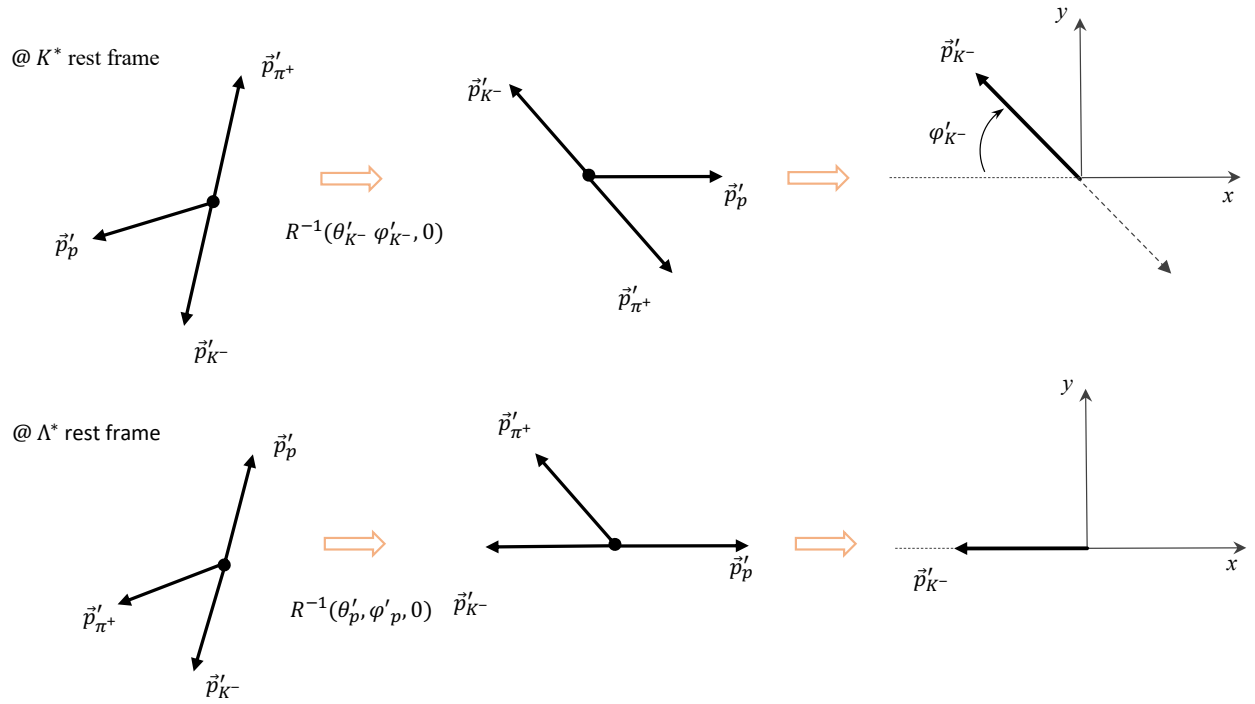

Figure 5.7: Sketch of the rotation and boost sequence for the K^* and Λ^* chains, the azimuthal angle of the Wigner rotation ϕ'_K is shown on the last drawing, showing the final particles configuration in the $x-y$ plane plane.

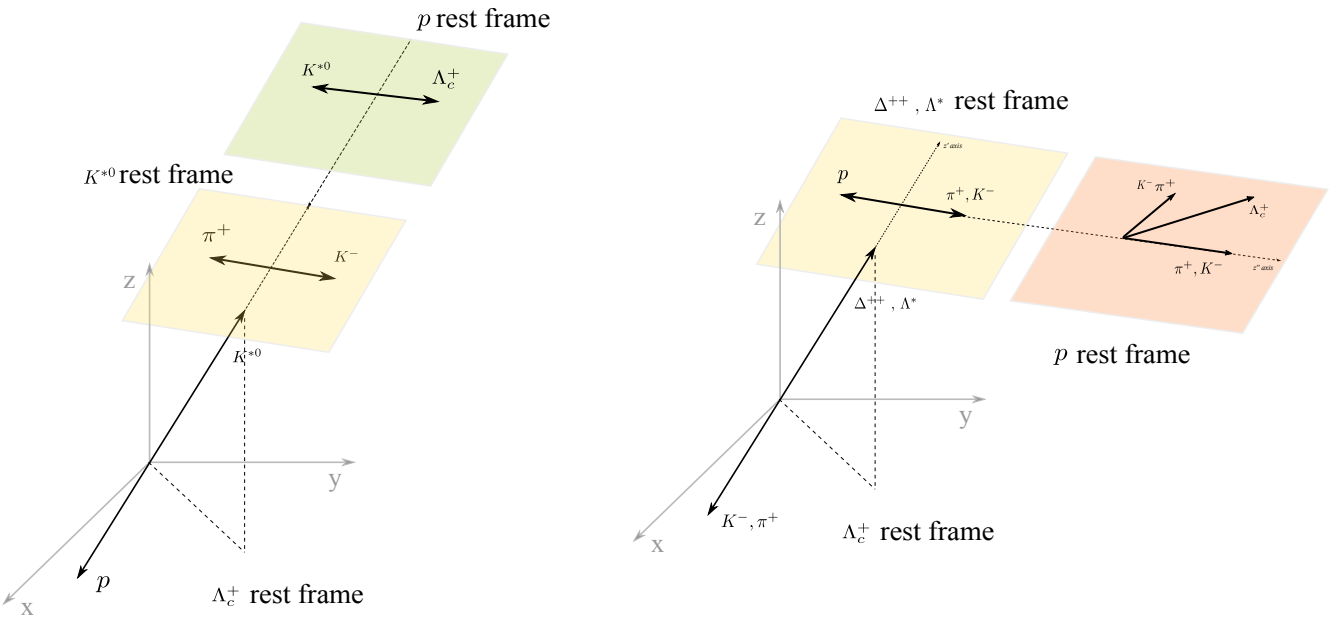

Figure 5.8: Definition of the frames and angles for the three decay chains, K^* on the left, Δ^{++} and Λ^* on the right.

homomorphism $SU(2) \to SO(3)$.

Partial amplitude for $\Lambda_c^+ \to \bar{K}^{*0}(\to K^-\pi^+)p$

Consider the chain $\Lambda_c^+ \to \bar{K}^{*0}p(\to K^-\pi^+)$. The spin projection of Λ_c on the z axis (polarization axis) is labeled by $m_{\Lambda_c^+}$. In this case, Eq. 5.40 gives with $s_R = s_K^*$, $\lambda_R = \lambda_{K^*}$, $\lambda_1 = \lambda_{K^-} = 0$, $\lambda_2 = \lambda_{\pi^+} = 0$, $\lambda_3 = \lambda_p = \pm\frac{1}{2}$ and $J = J_{\Lambda_c^+} = \frac{1}{2}$,

$$\mathcal{A}^{K^*}_{m,\lambda_p} = B_{K^*}(M_{K\pi}) \times \sum_{s_{K^*}} \sum_{\lambda_{K^*}} D^{s_{K^*}}_{\lambda_{K^*},0}(\phi'_K, \theta'_K, -\phi'_K) \\ D^{\frac{1}{2}*}_{m,\lambda_{K^*}-\lambda_p}(\phi_{K^*}, \theta_{K^*}, -\phi_{K^*})\, H^{\bar{K}^{*0}\to K^-\pi^+}_{\lambda_{K^-},\lambda_{\pi^+}} H^{\Lambda_c^+\to\bar{K}^{*0}p}_{\lambda_{K^*},\lambda_p} \quad (5.85)$$

where $B_{K^*}(M_{K\pi})$ is the K^* RBW, $H^{\Lambda_c^+\to\bar{K}^{*0}p}_{\lambda_{K^*},\lambda_p}$ is the helicity coupling for the decay $\Lambda_c^+ \to \bar{K}^{*0}p$, and $H^{\bar{K}^{*0}\to K^-\pi^+}_{\lambda_{K^-},\lambda_{\pi^+}}$ the one for the $\bar{K}^{*0} \to K^-\pi^+$ decay, where the *no-phase convention* is used. Note that the sum over s_{K^*} takes in consideration the fact that within a chain, different resonances with different spins can contribute.

The projection of the total angular momentum of the $p\bar{K}^{*0}$ system on the axis defined by the momentum of p is given by $\lambda_{K^*} - \lambda_p$ (the projection of the orbital angular momentum is 0). Since the total angular momentum of the Λ_c^+ is conserved, the projection $|\lambda_{K^*} - \lambda_p| \leq J_{\Lambda_c^+}$ can only take certain values (see Eq. (5.41)). This reduces the number of allowed terms in Eq. (5.85). For spin one K^* resonances, there are 4 allowed values, for spin zero only 2, this is shown in Table. 5.1: Hence the only allowed helicity couplings are: $H^{\Lambda_c^+\to\bar{K}^{*0}p}_{0,\frac{1}{2}}$, $H^{\Lambda_c^+\to\bar{K}^{*0}p}_{0,-\frac{1}{2}}$, $H^{\Lambda_c^+\to\bar{K}^{*0}p}_{1,\frac{1}{2}}$ and $H^{\Lambda_c^+\to\bar{K}^{*0}p}_{-1,-\frac{1}{2}}$.

λ_{K^*} \ λ_p	$\frac{1}{2}$	$-\frac{1}{2}$
1	✓(E_1^{res})	✗
0	✓(E_2^{res})	✓(E_3^{res})
-1	✗	✓(E_4^{res})

Table 5.1: Allowed helicity values for K^* decay. The notation E_i^{res} is defined in the text below.

For the strong decay $\bar{K}^{*0} \to K^-\pi^+$ there is only one contribution $H^{\bar{K}^{*0}\to K^-\pi^+}_{0,0}$ and it is absorbed in $H^{\Lambda_c^+\to\bar{K}^{*0}p}_{\lambda_{K^-},\lambda_{\pi^+}}$. For convenience, the couplings are renamed as E_i^{res}, as $H^{\Lambda_c^+\to\bar{K}^{*0}p}_{0,\frac{1}{2}} * H^{\bar{K}^{*0}\to K^-\pi^+}_{0,0} = E_2^{res}$, $H^{\Lambda_c^+\to\bar{K}^{*0}p}_{0,-\frac{1}{2}} * H^{\bar{K}^{*0}\to K^-\pi^+}_{0,0} \equiv E_3^{res}$, $H^{\Lambda_c^+\to\bar{K}^{*0}p}_{1,\frac{1}{2}} * H^{\bar{K}^{*0}\to K^-\pi^+}_{0,0} \equiv E_1^{res}$ and $H^{\Lambda_c^+\to\bar{K}^{*0}p}_{-1,-\frac{1}{2}} * H^{\bar{K}^{*0}\to K^-\pi^+}_{0,0} \equiv E_4^{res}$, where the superscript res is used distinguish between different K^* resonances, for example $res = K^*(892), K^*(1410)$.

Partial amplitude for $\Lambda_c^+ \to \Delta^{++}(\to p\pi^+)K^-$

For the Δ chain, Eq. 5.40 gives with $s_R = s_\Delta^{++}$, $\lambda_R = \lambda_{\Delta^{++}}$, $\lambda_1 = \lambda_{\pi^+} = 0$, $\lambda_2 = \lambda_p = \pm\frac{1}{2}$, $\lambda_3 = \lambda_{K^-} = 0$ and $J = J_{\Lambda_c^+} = \frac{1}{2}$,

$$\mathcal{A}^{\Delta^{++}}_{m,\lambda_p} = B_{\Delta^{++}}(M_{p\pi}) \times \sum_{s_{\Delta^{++}}} \sum_{\lambda_{\Delta^{++}}} D^{s_{\Delta^{++}}*}_{\lambda_{\Delta^{++}},-\lambda_p}(\phi'_\pi, \theta'_\pi, -\phi'_\pi) \\ D^{\frac{1}{2}*}_{m,\lambda_{\Delta^{++}}}(\phi_{\Delta^{++}}, \theta_{\Delta^{++}}, -\phi_{\Delta^{++}})\, H^{\Delta^{++}\to p\pi^+}_{\lambda_{\pi^+},\lambda_p} H^{\Lambda_c^+\to\Delta^{++}K^-}_{\lambda_{\Delta^{++}},\lambda_{K^-}} \quad (5.86)$$

where $H^{\Lambda_c^+\to\Delta^{++}K^-}_{\lambda_{\Delta^{++}},\lambda_{K^-}}$ is the helicity coupling for the decay $\Lambda_c^+ \to \Delta^{++}K^-$, and $H^{\Delta^{++}\to p\pi^+}_{\lambda_{\pi^+},\lambda_p}$ the one for the $\Delta^{++} \to p\pi^+$ decay. The sum over $s_{\Delta^{++}}$ runs over the possible resonances in the Δ^{++} chain. The projection of the total angular momentum of the $K^-\Delta^{++}$ system on the axis defined by the momentum of K^- is $|\lambda_{\Delta^{++}} - \lambda_K| = \lambda_{\Delta^{++}}$ (the projection of the orbital angular momentum is 0). Here again, since the total angular momentum $J_{\Lambda_c} = \frac{1}{2}$ is is conserved, the projection $\lambda_{\Delta^{++}}$ can only take the values $+\frac{1}{2}$ or $-\frac{1}{2}$, whatever the value of $J_{\Delta^{++}}$ is. This reduces the number of allowed terms Eq. (5.86). In addition, because of parity conservation in the strong decay $\Delta^{++} \to p\pi^+$ see Eq. 5.45, the number of possible couplings can be further reduced using Eq. 5.45,

$$H^{\Delta^{++}\to p\pi^+}_{\lambda_{\pi^+},\lambda_p} = \eta_{\Delta^{++}}\eta_{\lambda_{\pi^+}}\eta_{\lambda_p}(-1)^{s_{\lambda_{\pi^+}}+s_{\lambda_p}-s_{\Delta^{++}}}H_{-\lambda_{\pi^+},-\lambda_p}(-1)^{2\lambda_p} \tag{5.87}$$

$$= \eta_{\Delta^{++}}(-1)^{\frac{3}{2}-s_{\Delta^{++}}+2\lambda_p}H_{-\lambda_{\pi^+},-\lambda_p} \tag{5.88}$$

where $\eta_\pi = -1$ and $\eta_p = 1$. Hence $H^{\Delta^{++}\to p\pi^+}_{0,\lambda_p} = \eta_{\Delta^{++}}(-1)^{\frac{3}{2}-s_{\Delta^{++}}+2\lambda_p}H^{\Delta^{++}\to p\pi^+}_{0,-\lambda_p} = \pm H^{\Delta^{++}\to p\pi^+}_{0,-\lambda_p}$ where the sign is determined by the spin of the resonance. This reduces the number of possible helicity couplings to 2, F_1^{res} and F_2^{res}, here again the superscript res is used to distinguish between the possible Δ^{++} resonances.

λ_p \ $\lambda_{\Delta^{++}}$	$\frac{1}{2}$		$-\frac{1}{2}$	
$\frac{1}{2}$	$H^{\Delta^{++}\to p\pi^+}_{0,\frac{1}{2}}$	$H^{\Lambda_c^+\to\Delta^{++}K^-}_{\frac{1}{2},0} \equiv F_1^{res}$	$H^{\Delta^{++}\to p\pi^+}_{0,\frac{1}{2}}$	$H^{\Lambda_c^+\to\Delta^{++}K^-}_{-\frac{1}{2},0} \equiv F_2^{res}$
$-\frac{1}{2}$	$\pm H^{\Delta^{++}\to p\pi^+}_{0,\frac{1}{2}}$	$H^{\Lambda_c^+\to\Delta^{++}K^-}_{\frac{1}{2},0} \equiv \pm F_1^{res}$	$\pm H^{\Delta^{++}\to p\pi^+}_{0,\frac{1}{2}}$	$H^{\Lambda_c^+\to\Delta^{++}K^-}_{-\frac{1}{2},0} \equiv \pm F_2^{res}$

Regarding the couplings of Λ_c^+ decay to the Δ^{++} resonances, they can be rewritten in the LS basis separating the parity conserving and the parity violating part using Eq. 5.46. In this chain, $J_3 = J_{K^-} = 0$, the spin of the $(R3) = (\Delta^{++}K^-)$ system can only be $S = S_\Delta^{++}$ and since $J = \frac{1}{2}$ by conservation of the total angular momentum, L is constrained by $|\frac{1}{2} - S_\Delta^{++}| < L < |\frac{1}{2} + S_\Delta^{++}|$, thus

$$h^{\Lambda_c^+\to\Delta^{++}K^-}_{\lambda_{\Delta^{++}},0} = \sum_{L=|\frac{1}{2}-S_{\Delta^{++}}|}^{|\frac{1}{2}+S_{\Delta^{++}}|} h^{\Lambda_c^+\to\Delta^{++}K^-}_{LS}\sqrt{\frac{2L+1}{2}}\,\langle j_R,\lambda_R;0,0 \mid S_{\Delta^{++}},\lambda_{\Delta^{++}}\rangle\,\langle L,0;S_{\Delta^{++}},\lambda_{\Delta^{++}} \mid J=1/2,\lambda_{\Delta^{++}}\rangle \tag{5.89}$$

where $\sqrt{\frac{2L+1}{2}}\,\langle j_R,\lambda_R;0,0 \mid S_{\Delta^{++}},\lambda_{\Delta^{++}}\rangle$ is a constant term and $\lambda_{\Delta^{++}}$ can only take the values $+\frac{1}{2}$ or $-\frac{1}{2}$. Writing

$$\langle L,0;S_{\Delta^{++}},\lambda_{\Delta^{++}} \mid J=1/2,\lambda_{\Delta^{++}}\rangle = C_{L,S_{\Delta^{++}},\lambda_{\Delta^{++}}}, \tag{5.90}$$

$$\sqrt{\frac{2L+1}{2}}\,\langle j_R,\lambda_R;0,0 \mid S_{\Delta^{++}},\lambda_{\Delta^{++}}\rangle = d_L, \tag{5.91}$$

then the decomposition would look like:

$$h^{\Lambda_c^+\to\Delta^{++}K^-}_{\lambda_\Delta^{++},0} = \sum_L h^{\Lambda_c^+\to\Delta^{++}K^-}_{LS} \times C_{L,S_{\Delta^{++}},\lambda_{\Delta^{++}}}\,d_L. \tag{5.92}$$

This is a sum over all possible waves, $\{S(L=0),\ P(L=1),\ D(L=2),\ F(L=3)...\}$ weighted by the Clebsh-Gordon coefficients $C_{L,S_{\Delta^{++}},\lambda_{\Delta^{++}}}$. The parity conservation relation

$$\eta_{\Lambda_c^+} = \eta_{\Delta^{++}}\eta_{K^-}(-1)^L = \eta_{\Delta^{++}}(-1)^{L+1} \tag{5.93}$$

can be used to identify the L values corresponding to the parity violating and the parity conserving couplings.

As an example, let's look at the $\Delta^{++}(1232)$ case, with $J^P = \frac{3}{2}^+$. The possible values for the orbital angular momentum are $L = 1, 2$, which implies as possible Clebsh-Gordon coefficients: $C_{1,3/2,\pm 1/2} = -\sqrt{1/3}$ and $C_{2,3/2,\pm 1/2} = \pm\sqrt{1/5}$. Then Eq. 5.92 gives

$$h^{\Lambda_c^+\to\Delta^{++}K^-}_{\lambda_\Delta^{++},0}\sqrt{2}(h^{\Lambda_c^+\to\Delta^{++}K^-}_{1,3/2}\times C_{1,3/2,\lambda_{\Delta^{++}}} + h^{\Lambda_c^+\to\Delta^{++}K^-}_{2,3/2}\times C_{2,3/2,\lambda_{\Delta^{++}}}) = \\ \sqrt{\frac{3}{2}}(h^{\Lambda_c^+\to\Delta^{++}K^-}_{1,3/2}\left(-\sqrt{\frac{1}{3}}\right) + \sqrt{\frac{5}{2}}h^{\Lambda_c^+\to\Delta^{++}K^-}_{2,3/2}\left(\pm\sqrt{\frac{1}{5}}\right). \tag{5.94}$$

The parity relation is $+1 = (-1)^{L+1}$, hence L odd corresponds to the parity conserving part (PC) and L even to the parity violating one (PV), thus by defining $h^{\Delta^{++}}_{\rm PC} \equiv h^{\Lambda_c^+\to\Delta^{++}K^-}_{1,3/2}$ and $h^{\Delta^{++}}_{\rm PV} \equiv h^{\Lambda_c^+\to\Delta^{++}K^-}_{2,3/2}$, the LS decomposition gives:

$$\begin{cases} h^{\Lambda_c^+\to\Delta^{++}K^-}_{\frac{1}{2},0} &= -\sqrt{\frac{1}{2}}\left(h^{\Delta^{++}}_{\rm PC} - h^{\Delta^{++}}_{\rm PV}\right) \\ h^{\Lambda_c^+\to\Delta^{++}K^-}_{-\frac{1}{2},0} &= -\sqrt{\frac{1}{2}}\left(h^{\Delta^{++}}_{\rm PC} + h^{\Delta^{++}}_{\rm PV}\right) \end{cases} \tag{5.95}$$

Partial amplitude for $\Lambda_c^+ \to \pi^+\Lambda^*(\to pK^-)$

For the Λ chain, Eq. 5.40 gives with $s_R = s_\Lambda^{++}$, $\lambda_R = \lambda_{\Lambda^{++}}$, $\lambda_1 = \lambda_p = \pm\frac{1}{2}$, $\lambda_2 = \lambda_{K^-} = 0$, $\lambda_3 = \lambda_{\pi^+} = 0$ and $J = J_{\Lambda_c^+} = \frac{1}{2}$.

$$\mathcal{A}^{\Lambda^*}_{m,\lambda_p} = B_{\Lambda^*}(M_{pK}) \times \sum_{\Lambda^*}\sum_{\lambda_{\Lambda^*}} D^{s_{\Lambda^**}}_{\lambda_{\Lambda^*},\lambda_p}(\phi'_p,\theta'_p,-\phi'_p) \\ D^{\frac{1}{2}*}_{m,\lambda_{\Lambda^*}}(\phi_{\Lambda^*},\theta_{\Lambda^*},-\phi_{\Lambda^*})\, H^{\Lambda^*\to pK^-}_{\lambda_p,\lambda_{K^-}}\, H^{\Lambda_c^+\to\pi^-\Lambda^*}_{\lambda_{\Lambda^*},\lambda_{\pi^+}} \tag{5.96}$$

where $H^{\Lambda_c^+\to\pi^-\Lambda^*}_{\lambda_{\Lambda^*},\lambda_{\pi^+}}$ is the helicity coupling for the decay $\Lambda_c^+ \to \pi^-\Lambda^*$, and $H^{\Lambda^*\to pK^-}_{\lambda_p,\lambda_{K^-}}$ the one for the $\Lambda^* \to pK^-$ decay. The sum over s_{Λ^*} run over the possible resonances in the Λ^* chain. The projection of the total angular momentum of the $\pi^-\Lambda^*$ system on the axis defined by the momentum of K^- is $\lambda_{\Lambda^*} - \lambda_\pi = \lambda_{\Lambda^*}$ (the projection of the orbital angular momentum is 0). Here again, since the total angular momentum $J_{\Lambda_c} = \frac{1}{2}$ is is conserved, the projection λ_{Λ^*} can only take the values $+\frac{1}{2}$ or $-\frac{1}{2}$, whatever the value of J_{Λ^*} is. This reduces the number of allowed terms in Eq. (5.96). In addition, in this case as well parity conservation in the strong decay $\Lambda^* \to pK^-$ helps to further reduce the number

of allowed couplings.

$$H^{\Lambda^*\to pK^-}_{\lambda_p,\lambda_{K^-}} = \eta_{\Lambda^*}\eta_{\lambda_p}\eta_{\lambda_{K^-}}(-1)^{s_{\lambda_p}+s_{\lambda_{K^-}}-s_{\Delta^{++}}} H^{\Lambda^*\to pK^-}_{-\lambda_p,-\lambda_{K^-}}(-1)^{2\lambda_{K^-}} \tag{5.97}$$

$$= \eta_{\Lambda^*}(-1)^{\frac{3}{2}-s_{\Lambda^*}} H^{\Lambda^*\to pK^-}_{-\lambda_p,-\lambda_{K^-}} \tag{5.98}$$

where $\eta_{K^-} = -1$ and $\eta_p = 1$. Hence $H^{\Lambda^*\to p\pi^+}_{\lambda_p,0} = \pm H^{\Lambda^*\to p\pi^+}_{\lambda_p,0}$, where the sign is determined by the spin of the resonance. This reduces the number of possible couplings to 2: G_1^{res} and G_2^{res}, where again the superscript res is used to distinguish between the possible Λ^* resonances.

λ_p \ λ_{Λ^*}	$\frac{1}{2}$	$-\frac{1}{2}$
$\frac{1}{2}$	$H^{\Lambda^*\to pK^-}_{\frac{1}{2},0}\ H^{\Lambda_c^+\to\Lambda^*\pi^+}_{\frac{1}{2},0} \equiv G_1^{res}$	$H^{\Lambda^*\to pK^-}_{\frac{1}{2},0}\ H^{\Lambda_c^+\to\Lambda^*\pi^+}_{-\frac{1}{2},0} \equiv G_2^{res}$
$-\frac{1}{2}$	$\pm H^{\Lambda^*\to pK^-}_{\frac{1}{2},0}\ H^{\Lambda_c^+\to\Lambda^*\pi^+}_{\frac{1}{2},0} \equiv \pm G_1^{res}$	$\pm H^{\Lambda^*\to pK^-}_{\frac{1}{2},0}\ H^{\Lambda_c^+\to\Lambda^*\pi^+}_{-\frac{1}{2},0} \equiv \pm G_2^{res}$

Similarly to the Δ^{++} case, the Λ^* couplings can be rewritten in the LS basis using Eq. 5.46. Since the π^+ and K^- have the same spin parity $J^P = 0^-$, Eq. 5.92 holds for the Λ^* and by changing the labels, the LS decomposition reads:

$$h^{\Lambda_c^+\to\Lambda^*\pi^+}_{\lambda^*_\Lambda,0} = \sum_L h^{\Lambda_c^+\to\Lambda^*\pi^+}_{LS} \times F_{L,S_{\Lambda^*},\lambda_{\Lambda^*}} e_L. \tag{5.99}$$

with

$$\langle L,0;S_{\Lambda^*},\lambda_{\Lambda^*} \mid J=1/2,\lambda_{\Lambda^*}\rangle = F_{L,S_{\Lambda^*},\lambda_{\Lambda^*}}, \tag{5.100}$$

$$\sqrt{\frac{2L+1}{2}}\,\langle j_R,\lambda_R;0,0 \mid S_{\Lambda^*},\lambda_{\Lambda^*}\rangle = e_L, \tag{5.101}$$

As an example, lets' look at the LS coupling decomposition for $\Lambda^*(1520)(\frac{3}{2}^-)$. The parity conservation relation gives: $\eta_{\Lambda_c^+} = \eta_{\Lambda^*}\eta_{\pi^+}(-1)^L = (-1)^L$, meaning that even L corresponds to the parity conserving couplings and odd L to the parity violating ones. After the same steps as for the Δ^{++} case, one obtains:

$$\begin{cases} h^{\Lambda_c^+\to\Lambda^*\pi^+}_{\frac{1}{2},0} = -\sqrt{\frac{1}{2}}\left(h^{\Lambda^*}_{\rm PC} + h^{\Lambda^*}_{\rm PV}\right) \\ h^{\Lambda_c^+\to\Lambda^*\pi^+}_{-\frac{1}{2},0} = -\sqrt{\frac{1}{2}}\left(h^{\Lambda^*}_{\rm PC} - h^{\Lambda^*}_{\rm PV}\right) \end{cases} \tag{5.102}$$

where $h^{\Lambda^*}_{\rm PC} \equiv h^{\Lambda_c^+\to\Lambda^*\pi^+}_{2,3/2}$ and $h^{\Lambda^*}_{\rm PV} \equiv h^{\Lambda_c^+\to\Lambda^*\pi^+}_{1,3/2}$.

Total amplitude

The final amplitude is obtained summing over the final helicities (since they cannot be measured) and including the polarization. In this case, the only final non null helicity is the one of the proton. To be able to do this sum, the Wigner rotation must be included to have a coherent definition of

the quantization axis, hence using the usual D functions to represents rotations, the amplitude for each helicity configurations $\mathcal{A}^{\Lambda_c^+\to pK^-\pi^+}_{m,\lambda_p,\lambda_{K^-},\lambda_{\pi^+}} = \mathcal{A}_{m,\lambda_p}$, where to improve readability the $\Lambda_c^+ \to pK^-\pi^+$ superscript is dropped:

$$\mathcal{A}_{m,\lambda_p}(\Omega) = \mathcal{A}^{K^*}_{m,\lambda_p}(\Omega_{K^*}) + \sum_{\lambda'_p} \mathcal{A}^{\Lambda^*}_{m,\lambda'_p}(\Omega_{\Lambda^*})\, D(\alpha_1, \beta_{\Lambda^*}, \phi'_{K^-}) + \sum_{\lambda'_p} \mathcal{A}^{\Delta^{++}}_{m,\lambda'_p}(\Omega_{\Delta^{++}})\, D(\alpha_2, \beta_{\Delta^*}, \phi'_{K^-}) \tag{5.103}$$

where

$$\alpha_1 = \begin{cases} 2\pi & \text{if } |\phi_p - \phi_\pi| > \pi \\ 0 & \text{else} \end{cases} \qquad \alpha_2 = \begin{cases} 2\pi & \text{if } |\phi_p - \phi_K| > \pi \\ 0 & \text{else} \end{cases} \tag{5.104}$$

The alpha conditions are coming from the fact that spin $\frac{1}{2}$ particles are not invariant under a 2π rotation but under a 4π one. This is explained in Sec. 5.2.2 and further investigated in Sec. 5.5. The total decay rate including the spin density matrix described in Sec. 5.3.4 is given by

$$\begin{aligned} \Gamma =& \rho_{\frac{1}{2},\frac{1}{2}} \left(|\mathcal{A}_{\frac{1}{2},\frac{1}{2}}|^2 + |\mathcal{A}_{\frac{1}{2},-\frac{1}{2}}|^2 \right) \\ &+ \rho_{\frac{1}{2},-\frac{1}{2}} \left(\mathcal{A}_{\frac{1}{2},\frac{1}{2}} \mathcal{A}^*_{-\frac{1}{2},\frac{1}{2}} + \mathcal{A}_{\frac{1}{2},-\frac{1}{2}} \mathcal{A}^*_{-\frac{1}{2},-\frac{1}{2}} \right) \\ &+ \rho_{-\frac{1}{2},\frac{1}{2}} \left(\mathcal{A}_{-\frac{1}{2},\frac{1}{2}} \mathcal{A}^*_{\frac{1}{2},\frac{1}{2}} + \mathcal{A}_{-\frac{1}{2},-\frac{1}{2}} \mathcal{A}^*_{\frac{1}{2},-\frac{1}{2}} \right) \\ &+ \rho_{-\frac{1}{2},-\frac{1}{2}} \left(|\mathcal{A}_{-\frac{1}{2},\frac{1}{2}}|^2 + |\mathcal{A}_{-\frac{1}{2},-\frac{1}{2}}|^2 \right) \end{aligned} \tag{5.105}$$

and by applying parity conservation for the production of Λ_c which is done via strong interactions, the cross terms $\rho_{\frac{1}{2},-\frac{1}{2}}(..)$ and $\rho_{-\frac{1}{2},\frac{1}{2}}(..) = 0$ are zero. The final differential rate for the $\Lambda_c^+ \to pK^-\pi^+$decay is:

$$d\Gamma \propto (1+P_z) \left(|\mathcal{A}_{\frac{1}{2},\frac{1}{2}}|^2 + |\mathcal{A}_{\frac{1}{2},-\frac{1}{2}}|^2 \right) + (1-P_z) \left(|\mathcal{A}_{-\frac{1}{2},\frac{1}{2}}|^2 + |\mathcal{A}_{-\frac{1}{2},-\frac{1}{2}}|^2 \right) \tag{5.106}$$

5.4.5 $D(\phi,\theta,0)$ convention

As mentioned in Sec. 5.2.3, there exists two equivalent conventions to describe the rotations: $D(\phi,\theta,-\phi)$ and $D(\phi,\theta,0.)$. The second convention leads to easier equations, Eq. 5.85, 5.86, 5.96 become:

$$\mathcal{A}^{K^*}_{m,\lambda_p} = B_{K^*}(M_{K\pi}) \times \sum_{s_{K^*}} \sum_{\lambda_{K^*}} D^{s_{K^*}}_{\lambda_{K^*},0}(\phi'_K, \theta'_K, 0) \times D^{\frac{1}{2}*}_{m,\lambda_{K^*}-\lambda_p}(\phi_{K^*}, \theta_{K^*}, 0)\, H^{\bar{K}^{*0}\to K^-\pi^+}_{\lambda_{K^-},\lambda_{\pi^+}} H^{\Lambda_c^+\to \bar{K}^{*0}p}_{\lambda_{K^*},\lambda_p} \tag{5.107}$$

$$\mathcal{A}^{\Lambda^*}_{m,\lambda_p} = B_{\Lambda^*}(M_{pK}) \times \sum_{\Lambda^*} \sum_{\lambda_{\Lambda^*}} D^{s_{\Lambda^**}}_{\lambda_{\Lambda^*},\lambda_p}(\phi'_p, \theta'_p, 0) \times D^{\frac{1}{2}*}_{m,\lambda_{\Lambda^*}}(\phi_{\Lambda^*}, \theta_{\Lambda^*}, 0)\, H^{\Lambda^*\to pK^-}_{\lambda_p,\lambda_{K^-}} H^{\Lambda_c^+\to \pi^-\Lambda^*}_{\lambda_{\Lambda^*},\lambda_{\pi^+}} \tag{5.108}$$

$$\mathcal{A}^{\Delta^{++}}_{m,\lambda_p} = B_{\Delta^{++}}(M_{p\pi}) \times \sum_{s_{\Delta^{++}}} \sum_{\lambda_{\Delta^{++}}} D^{s_{\Delta^{++}}*}_{\lambda_{\Delta^{++}},-\lambda_p}(\phi'_\pi, \theta'_\pi, 0) \times D^{\frac{1}{2}*}_{m,\lambda_{\Delta^{++}}}(\phi_{\Delta^{++}}, \theta_{\Delta^{++}}, 0)\, H^{\Delta^{++}\to p\pi^+}_{\lambda_{\pi^+},\lambda_p} H^{\Lambda_c^+\to\Delta^{++}K^-}_{\lambda_{\Delta^{++}},\lambda_{K^-}} \quad (5.109)$$

The definition of the primed angles Eq. 5.82 also changes since the helicity frame is reached via a different rotation and as a consequence the $\{x', y', z'\}$ axis are changed. The definition of the resonance angles is unchanged.

5.4.6 Isobars

When building the amplitude for the single chains, one needs to sum over different possible resonances. This is due to the fact that hadrons can have different mass states, depending on their quantum mechanical properties, engendering a spectrum of possible resonances with different masses and spins. The already observed resonances of each chain are listed in Table 5.2, where the mass and width values are from Ref. [11]. Only the resonances which are classified as "Likely (***)" or "Certain (****)" are shown, plus the $\Lambda^*(2000)$ which will be used in the fit later on. Any state with a different mass (and spin) from the ground state is called excited state or resonance. For the Λ baryons the ground state is the $\Lambda^0(\frac{1}{2}^+)$ particle and it has a mass of $1116\,\mathrm{MeV}/c^2$. It is below the pK^- threshold, hence the decay will proceed only via Λ^* resonances, the PDG lists 13 of them in the range $m_{pK^-} \in [1432, 2147]\,\mathrm{MeV}/c^2$. For Δ baryons, the ground state is $\Delta^{++}(\frac{3}{2}^+)$ with mass $1232\,\mathrm{MeV}/c^2$, it is included in the $p\pi^+$ spectrum $m_{p\pi^+} \in [1078, 1792]\,\mathrm{MeV}/c^2$, with 3 other resonances (4 in total). For the K^* mesons, the ground state is $K^*(0^+)$ with mass $824\,\mathrm{MeV}/c^2$ which is inside the $K^-\pi^+$ mass window which is $m_{K^-\pi^+} \in [634, 1348]\,\mathrm{MeV}/c^2$. For the K^* there are 4 resonances in total which may contribute to the amplitude.

All the resonances can possibly be there in the data, but some of them have a smaller influence on the final fit. During the analysis, a procedure is established to select only the resonances that give major contributions to the likelihood and to build the final model (i.e. a list of resonances) which will be used to fit the polarization. For the pK channel, there exists two possible baryons with the same quark content (uds), depending on the (strong) isospin configuration. Those are the Σ baryons with isospin ($I = 1, I_3 = 0$) and the Λ baryons with isospin ($I = 0, I_3 = 0$). Since they are produced via weak decays, the (strong) isospin is not conserved. In the literature [207] some considerations on the isospin suppressions are done in similar decays. These are based on the fact that the isospin is carried by the u ($I = \frac{1}{2}, I_3 = \frac{1}{2}$) and d ($I = \frac{1}{2}, I_3 = -\frac{1}{2}$) quarks. The π^+ has isospin ($I = 1, I_3 = 1$). In the transition $\Lambda^* \to pK^-$, the quark content of the Λ_c^+ baryon *(ucd)* is transformed to *(uds)*. The isospin of the Λ_c^+ is zero hence the (ud) pair should be zero too. In the quark spectator limit, the spin of the pair of quarks (ud) is expected to be unchanged by the weak transition, therefore the final isospin of the (uds) baryons is likely to be zero. Thus the isospin transition giving Σ resonances are expected to be suppressed. Nevertheless, the decay $\Lambda_c^+ \to \Sigma^0\pi^+$ has been measured experimentally, with a branching fraction of $1.29 \pm 0.07\%$ [11] very close to the $\Lambda_c^+ \to \Lambda\pi^+$ branching fraction which is $1.30 \pm 0.07\%$ [11]. Thus the Σ baryons contributions should be studied in details to be able to assert that their influence on the final amplitude is minor; this will be considered as a systematic effect.

Resonance	Mass (approx)[MeV]	Width (approx)[MeV]	J^P	$L_{\Lambda_c^+}$	L_R	PDG status
pK channel						
$\Lambda^*(1405)$	$1405.1^{+1.3}_{-1.0}$	50.5 ± 2.0	$1/2^-$	0,1	0	****
$\Lambda^*(1520)$	1517 ± 4	15^{+10}_{-8}	$3/2^-$	1,2	2	****
$\Lambda^*(1600)$	1544 ± 3	112^{+12}_{-2}	$1/2^+$	0,1	1	***
$\Lambda^*(1670)$	1669^{+3}_{-8}	19^{+18}_{-2}	$1/2^-$	0,1	0	****
$\Lambda^*(1690)$	1697 ± 6	65 ± 14	$3/2^-$	1,2	2	****
$\Lambda^*(1800)$	1720-1850	200-400	$1/2^-$	0,1	0	***
$\Lambda^*(1810)$	1750-1850	50-250	$1/2^+$	0,1	1	***
$\Lambda^*(1820)$	1824^{+2}_{-1}	77 ± 2	$5/2^+$	2,3	3	****
$\Lambda^*(1830)$	1899 ± 40	80^{+100}_{-34}	$5/2^-$	2,3	2	****
$\Lambda^*(1890)$	1850-1910	60-200	$3/2^+$	1,2	1	****
$\Lambda^*(2000)$	2000	0.150	-	-	-	*
$\Lambda^*(2100)$	2090-2110	100-250	$7/2^-$	3,4	4	****
$\Lambda^*(2110)$	2090-2140	150-250	$5/2^+$	2,3	3	***
$\Sigma^*(1660)$	$1660 \in [1640-1680]$	$220 \in [100-300]$	$1/2^+$	0,1	1	***
$\Sigma^*(1670)$	$1675 \in [1665-1685]$	$70 \in [40-100]$	$3/2^-$	1,2	2	****
$\Sigma^*(1750)$	$1750 \in [1700-1800]$	$150 \in [100-200]$	$1/2^-$	0,1	0	***
$\Sigma^*(1775)$	$1775 \in [1770-1780]$	$120 \in [105-135]$	$5/2^-$	2,3	2	****
$\Sigma^*(1910)$	$1910 \in [1870-1950]$	$220 \in [150-300]$	$3/2^-$	1,2	2	****
$\Sigma^*(1915)$	$1915 \in [1900-1935]$	$120 \in [80-160]$	$5/2^+$	2,3	3	****
$\Sigma^*(2030)$	$2030 \in [2015-2040]$	$180 \in [150-200]$	$7/2^+$	3,4	3	****
$p\pi$ channel						
$\Delta^{++}(1232)$	1209-1211	98-102	$3/2^+$	1,2	1	****
$\Delta^{++}(1600)$	1460-1560	200-340	$3/2^+$	1,2	1	****
$\Delta^{++}(1620)$	1590-1610	100-140	$1/2^-$	0,1	0	****
$\Delta^{++}(1700)$	1640-1690	200-300	$3/2^-$	1,2	2	****
$K\pi$ channel						
$K^*(700)$	824 ± 30	478 ± 50	0^+	0	0	****
$K^*(892)$	891.66 ± 0.26	50.8 ± 0.9	1^-	0,1,2	1	****
$K^*(1410)$	1414 ± 15	232 ± 21	1^-	0,1,2	1	****
$K_0^*(1430)$	1425 ± 50	270 ± 80	0^+	0	0	****

Table 5.2: Summary of the known resonances that may contribute to the $\Lambda_c^+ \to pK^-\pi^+$ decay amplitude. The mass, widths and spins are from Ref. [11], the values of $L_{\Lambda_c^+}$ and L_R are obtained from angular momentum conservation rules, as explained in the text. The last column shows the status of the knowledge on the resonances where (*) and (**) mean that evidence of existence is poor and fair, (***) means "likely" and (****) "Certain".

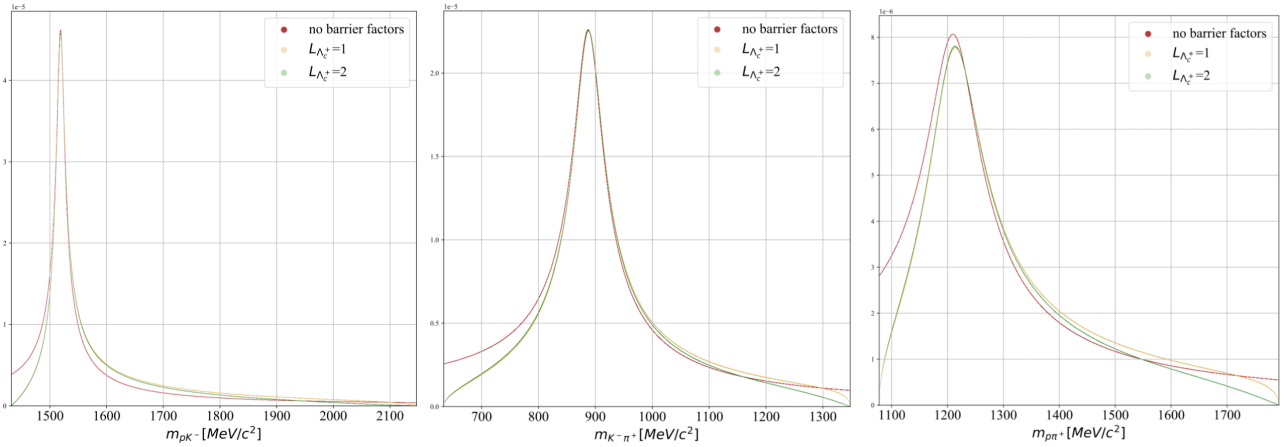

Figure 5.9: Comparison of the relativistic RBW lineshape for different values of $L_{\Lambda_c^+}$. One resonance per channel is shown: $\Lambda^*(1520)$, $K^*(892)$ and $\Delta^{++}(1232)$ with masses and width from Ref. [11]. The value of the barrier factors radii are the one used for the main model, mentioned in Sec. 5.3.5. The red line is the RBW without barrier factors. The yellow curve represent the case $L_{\Lambda_c^+} = 1$ and the green one $L_{\Lambda_c^+} = 2$.

The mass-dependent width and the form factors entering in the lineshape functions in Eq. 5.55 depend on the orbital angular momentum of the 2 two-body decays. For the Λ_c^+ decay to the resonances, since the decay is weak, the orbital angular momentum $L_{\Lambda_c^+}$ is only constrained by the conservation of angular momentum in the decay $\Lambda_c^+ \to Rh$. For Δ^* and Λ^* resonances the possible values are $|J_R - \frac{1}{2}| < L_{\Lambda_c^+} < |J_R + \frac{1}{2}|$, where J_R is the spin of the resonance. For K^* resonances the possible values reduce to $L_{\Lambda_c^+} = 0$ for spin zero resonances and $|J_R - 1| < L_{\Lambda_c^+} < |J_R + 1|$ for higher spins. For the isobar decays, in the Δ^* and Λ^* cases, the decay is strong hence the orbital angular momentum L_R is further constrained by parity conservation. Thus, $|J_R - \frac{1}{2}| < L_R < |J_R + \frac{1}{2}|$ and $\eta_R = \eta_p \eta_{K,\pi} = (-1)^{L_R+1}$, where η_i is the parity of particle i, and $\eta_\pi = \eta_K = -1$ and $\eta_p = +1$. For K^* resonances, $J_R = L_R$ since $J_{\pi^+} = J_{K^-} = 0$, parity conservation holds, giving the relation: $\eta_R = (-1)^{L_R}$, which forbids some decays. The higher $L_{\Lambda_c^+}$ contributions have a minor influence on the amplitude, the effect on the lineshapes for three resonances, one per channel, are shown in Fig. 5.9. The higher L have a slightly different tail of the distribution for the 3 channels, however one needs to add the two possible values of L weighted by the C-G coefficients following the LS coupling decomposition in Eq. 5.46, after adding them the effect will be mitigated. The influence on the complete amplitude is expected to be small thus only the lowest $L_{\Lambda_c^+}$ are kept, however this effect will be included in the systematic uncertainties studies. The values of $L_{\Lambda_c^+}$ and L_R for each resonance are shown in the 5$^{\text{th}}$ and 6$^{\text{th}}$ column of Table 5.2.

5.4.7 Dalitz plot decomposition

In Ref. [202] a decomposition of the amplitude separating the invariant mass and the orientation angles dependence is proposed, called "Dalitz plot decomposition" (DPD). The main idea behind this approach is to disentangle the effect due to the production polarization from phase space effects. The factorization consists in using the same rotation $D(\alpha^1, \beta^1, \gamma^1) = D(\phi_1, \theta_1, \phi_{23})$ for the 3 chains to go

from the polarization frame to the frame where the decay products are in the $(x-z)$ plane and the proton momentum points to $-\hat{z}$, called "*aligned center-of-mass frame*". For the $\Lambda_c^+ \to pK^-\pi^+$ decay, the DPD amplitude is written as:

$$M_\lambda^\Lambda = \sum_\nu D^{1/2*}_{\Lambda,\nu}(\phi_1,\theta_1,\phi_{23})\, O_\lambda^\nu(\{\sigma\}) \tag{5.110}$$

where (ϕ_1,θ_1) are the proton angles in the polarization frame, $\phi_{23}=\chi$ and

$$\begin{aligned} O_\lambda^\nu(\{\sigma\}) = & \sum_s^{K^*\to K\pi} \sum_\tau \sqrt{2} n_s \delta_{\nu,\tau-\lambda} H^{0\to(23),1}_{\tau,\lambda} X_s(\sigma_1) d^s_{\tau,0}(\theta_{23}) H^{(23)\to 2,3}_{0,0} \\ & + \sum_s^{\Delta\to\pi p} \sum_{\tau,\lambda'} \sqrt{2} n_s d^{1/2}_{\nu,\tau}(\hat{\theta}_{2(1)}) H^{0\to(31),2}_{\tau,0} X_s(\sigma_2) d^s_{\tau,-\lambda'}(\theta_{31}) H^{(31)\to 3,1}_{0,\lambda'} d^{1/2}_{\lambda',\lambda}(\zeta^1_{2(1)}) \\ & + \sum_s^{\Lambda\to pK} \sum_{\tau,\lambda'} \sqrt{2} n_s d^{1/2}_{\nu,\tau}(\hat{\theta}_{3(1)}) H^{0\to(12),3}_{\tau,0} X_s(\sigma_3) d^s_{\tau,\lambda'}(\theta_{12}) H^{(12)\to 1,2}_{\lambda'} d^{1/2}_{\lambda',\lambda}(\zeta^1_{3(1)}) \end{aligned} \tag{5.111}$$

$O_\lambda^\nu(\{\sigma\})$ is called the "Dalitz plot function". The H are the usual helicity couplings, X_s is the lineshape. Regarding the angles, $\zeta^1_{2(1)} = \beta_{\Delta^{++}}$ and $\zeta^1_{3(1)} = -\beta_{\Lambda^*}$ are the angles for the Wigner rotation, and $\theta_{23} = \theta'_K$, $\theta_{31} = \theta'_\pi$ and $\theta_{12} = \theta'_p$. The correspondence between the DPD and the amplitude in Sec. 5.4.4 is given by the following equivalences:

$$\begin{aligned} & D\left(\alpha^1,\beta^1,\gamma^1\right) \longleftrightarrow D^{s_{K^*}}_{\lambda_{K^*},0}(\phi'_K,\theta'_K,0)\, D^{\frac{1}{2}*}_{m,\lambda_{K^*}-\lambda_p}(\phi_{K^*},\theta_{K^*},0) \\ & D\left(\alpha^1,\beta^1,\gamma^1\right) d(\hat{\theta}_{2(1)}) \longleftrightarrow D^{s_\Delta}_{\lambda_\Delta,\lambda_p}(\phi'_\pi,\theta'_\pi,0)\, D^{\frac{1}{2}*}_{m,\lambda_\Delta}(\phi_\Delta,\theta_\Delta,0) \\ & D\left(\alpha^1,\beta^1,\gamma^1\right) * d(\hat{\theta}_{3(1)}) \longleftrightarrow D^{s_{\Lambda^*}}_{\lambda_{\Lambda^*},\lambda_p}\left(\phi'_p,\theta'_p,0\right) D^{\frac{1}{2}*}_{m,\lambda^*_\Lambda}(\phi_{\Lambda^*},\theta_{\Lambda^*},0) \end{aligned} \tag{5.112}$$

The amplitudes have been compared numerically, the result is shown in Fig. 5.10, where 1M phase space events have been simulated with $\vec{P}=\{0,0,1\}$ and BW=1, three resonances are included $K^*(892)$, $\Lambda^*(1520)$ and $\Delta^{++}(1232)$, with random helicity couplings: $E_4^{res}=0.9$, $E_3^{res}=0.7$, $E_2^{res}=0.8$, $E_1^{res}=0.5$, $H_2^{res}=1.$, $H_1^{res}=0.6$, $F_2^{res}=0.8$ and $F_1^{res}=0.6$.

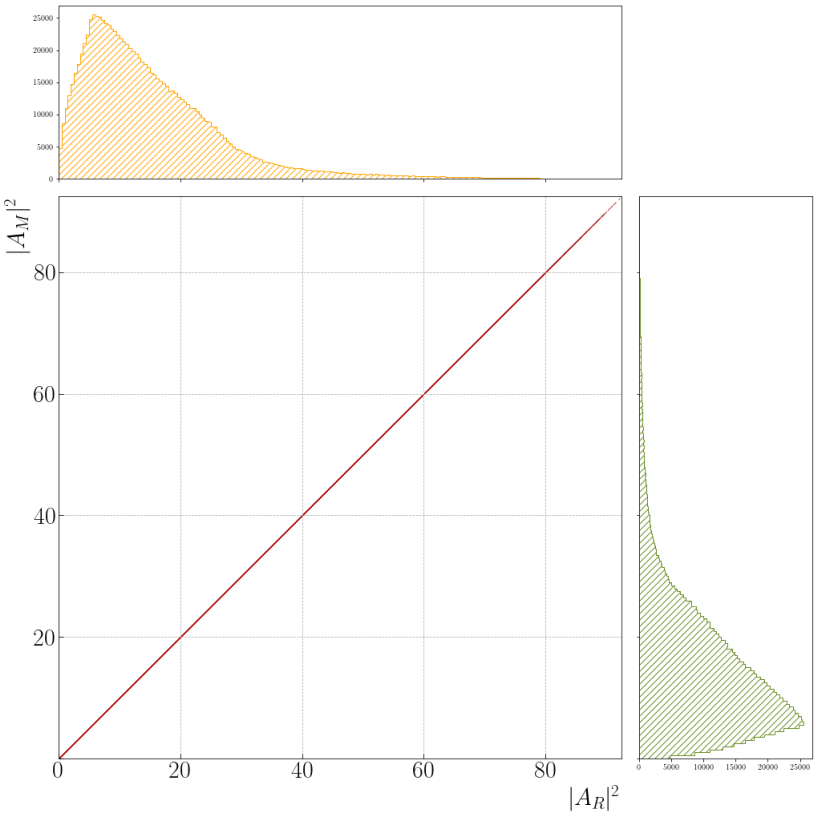

Figure 5.10: Comparison between the DPD amplitude $|A_M|^2$ (y axis) and the one obtained with this formalism $|A_R|^2$ (x axis), using 1M simulated phase space events with $\vec{P} = \{0,0,1\}$ and BW=1. In the total amplitude, named A here, three resonances are included: $K^*(892)$, $\Lambda^*(1520)$ and $\Delta^{++}(1232)$. The helicity couplings values are given in the text.

5.5 Properties of the helicity amplitudes and benchmark tests

In this section the properties of the helicity amplitude for the $\Lambda_c^+ \to pK^-\pi^+$ decay are discussed, with a particular focus on the polarization. The polarization of the Λ_c^+ depends on the production mechanism. The angular distribution takes the general form:

$$d\Gamma \propto N(1 + \alpha P_z \cos\theta_p + ...) \tag{5.113}$$

where α is the asymmetry parameter. It is clear that to be able to measure the polarization, one needs to know α ahead and if $\alpha = 0$ the information on the polarization is lost. If the polarization depends on the specific conditions of the experiment where the particle is produced, the asymmetry parameter on the contrary is universal and independent of the production mode. At the LHC, Λ_c^+ can be produced via strong interactions right after the collision or via weak interactions in a secondary decay (for instance $\Lambda_b \to \Lambda_c^+ l\nu_l$). To acquire a polarization, the Λ_c^+ must be produced from a particle with spin and polarized. For the weak interaction, this particle is the weak boson $W^\pm$. For the strong interaction, the Λ_c^+ can be produced through different mechanisms (e.g. gluon fusion,qg interaction etc..) however by the time the quark c is created and hadronized to a Λ_c^+ many intermediate interactions happen and the polarization is diluted. Since the number of particle produced and interactions increases with the energies, the loss of polarization increases likewise. After production, the Λ_c^+ itself decays via strong or weak interaction. In the first case, as the parity is conserved, the decay amplitude must be symmetric under space inversion and the polarization cannot be measured since there is no asymmetry in the decay i.e. $\alpha = 0$. For weakly produced Λ_c^+ instead, parity violation can occur and $\alpha \neq 0$, hence the polarization is measurable. The $\Lambda_c^+ \to pK^-\pi^+$ decay is a weak decay, this means that the polarization is accessible.

Linearity The angular distributions take a simple form if derived for each single chain separately with one resonance per chain. As an example, the $K^*(892)(1^-)$ angular distribution is computed here [208], with the lineshape set to 1. Starting from the polarized decay rate of Eq. 5.106, let's compute the first term of the equation:

$$|\mathcal{A}_{\frac{1}{2},\frac{1}{2}}|^2 = |D^{1*}_{00}(\phi'_K,\theta'_K,-\phi'_K) D^{\frac{1}{2}*}_{\frac{1}{2},-\frac{1}{2}}(\phi_{K^{*0}},\theta_{K^{*0}},-\phi_{K^{*0}})\, H^{\Lambda_c^+\to pK^*}_{0,\frac{1}{2}} + D^{1*}_{10}(\phi'_K,\theta'_K,-\phi'_K) D^{\frac{1}{2}*}_{\frac{1}{2},\frac{1}{2}}(\phi_{K^{*0}},\theta_{K^{*0}},-\phi_{K^{*0}})\, H^{\Lambda_c^+\to pK^*}_{1,\frac{1}{2}}|^2 \tag{5.114}$$

then using the relation between D and d-Wigner matrices in Eq. 5.12, one finds:

$$D^{1*}_{00}(\phi'_K,\theta'_K,-\phi'_K) = d^1_{00}(\theta'_K) = \cos\theta'_K \tag{5.115}$$

$$D^{\frac{1}{2}*}_{\frac{1}{2},-\frac{1}{2}}(\phi_{K^{*0}},\theta_{K^{*0}},-\phi_{K^{*0}}) = d^{\frac{1}{2}}_{\frac{1}{2},-\frac{1}{2}}(\theta_{K^{*0}}) e^{i\phi^{*0}_K} = -\sin\left(\frac{\theta_{K^{*0}}}{2}\right) e^{i\phi^{*0}_K} \tag{5.116}$$

$$D^{1*}_{10}(\phi'_K,\theta'_K,-\phi'_K) = d^{1*}_{10} e^{i\phi'_K}(\theta'_K) = -\frac{1}{\sqrt{2}} \sin\theta'_K e^{i\phi'_K} \tag{5.117}$$

$$D^{\frac{1}{2}*}_{\frac{1}{2},\frac{1}{2}}(\phi_{K^{*0}},\theta_{K^{*0}},-\phi_{K^{*0}}) = d^{\frac{1}{2}}_{\frac{1}{2},\frac{1}{2}}(\theta_{K^{*0}}) = \cos\frac{\theta_{K^{*0}}}{2}. \tag{5.118}$$

The other three terms of Eq. 5.106,$\mathcal{A}_{-\frac{1}{2},\pm\frac{1}{2}}$ and $\mathcal{A}_{\frac{1}{2},-\frac{1}{2}}$, can be obtained using the d-Wigner functions properties: $d^1_{1,0} = -d^1_{-1,0}$, $d^{\frac{1}{2}}_{\frac{1}{2},\frac{1}{2}} = d^{\frac{1}{2}}_{-\frac{1}{2},-\frac{1}{2}}$ and $d^{\frac{1}{2}}_{\frac{1}{2},-\frac{1}{2}} = -d^{\frac{1}{2}}_{-\frac{1}{2},\frac{1}{2}}$, the results are shown in Table 5.3.

m	λ_p	A_{m,λ_p}
$\frac{1}{2}$	$\frac{1}{2}$	$\cos\theta'_K \sin\left(\frac{\theta_{K^{*0}}}{2}\right) e^{i\phi^{*0}_K} + \frac{1}{\sqrt{2}} \sin\theta'_K \cos\frac{\theta_{K^{*0}}}{2} e^{i\phi'_K}$
$\frac{1}{2}$	$-\frac{1}{2}$	$\cos\theta'_K \cos\frac{\theta_{K^{*0}}}{2} + \frac{1}{\sqrt{2}} \sin\theta'_K \sin\left(\frac{\theta_{K^{*0}}}{2}\right) e^{-i(\phi'_K - \phi^{*0}_K)}$
$-\frac{1}{2}$	$\frac{1}{2}$	$\cos\theta'_K \cos\frac{\theta_{K^{*0}}}{2} - \frac{1}{\sqrt{2}} \sin\theta'_K \sin\left(\frac{\theta_{K^{*0}}}{2}\right) e^{i(\phi'_K - \phi^{*0}_K)}$
$-\frac{1}{2}$	$-\frac{1}{2}$	$\cos\theta'_K \sin\left(\frac{\theta_{K^{*0}}}{2}\right) e^{-i\phi^{*0}_K} - \frac{1}{\sqrt{2}} \sin\theta'_K \cos\frac{\theta_{K^{*0}}}{2} e^{-i\phi'_K}$

Table 5.3: Summary of the A_{m,λ_p} terms obtained.

Integrating over $d\Omega = \sin\theta'_K d\theta_K d\phi'_K d\phi_{K^*}$ in Eq. 5.106, many of the terms of Table 5.3 integrate to zero and the angular distribution takes the simple form:

$$\frac{d\Gamma}{d\cos\theta} \sim \frac{4}{3}\left(1 + P_{\Lambda_c} \alpha^{K^*}_{\Lambda_c} \cos\theta_{K^*}\right) \tag{5.119}$$

where

$$\alpha^{K^*}_{\Lambda_c} = \frac{|H^{\Lambda_c^+ \to \bar{K}^{*0} p}_{1,1/2}|^2 - |H^{\Lambda_c^+ \to \bar{K}^{*0} p}_{0,1/2}|^2 + |H^{\Lambda_c^+ \to \bar{K}^{*0} p}_{0,-1/2}|^2 - |H^{\Lambda_c^+ \to \bar{K}^{*0} p}_{-1,-1/2}|^2}{|H^{\Lambda_c^+ \to \bar{K}^{*0} p}_{1,1/2}|^2 + |H^{\Lambda_c^+ \to \bar{K}^{*0} p}_{0,1/2}|^2 + |H^{\Lambda_c^+ \to \bar{K}^{*0} p}_{0,-1/2}|^2 + |H^{\Lambda_c^+ \to \bar{K}^{*0} p}_{-1,-1/2}|^2} = \frac{|E_1|^2 - |E_2|^2 + |E_3|^2 - |E_4|^2}{|E_1|^2 + |E_2|^2 + |E_3|^2 + |E_4|^2} \tag{5.120}$$

where the res superscript (here $res = K^*(892)(1^-)$) has been dropped for sake of readability and the $H^{\bar{K}^{*0} \to K^- \pi^+}_{0,0}$ coupling has been dropped too since it is absorbed in $H^{\Lambda_c^+ \to \bar{K}^{*0} p}_{i,j}$. The same can be done for the two other chains, with always one resonance per chain. For the Δ chain, let's take the case of $\Delta^{++}(1232)(\frac{3}{2}^+)$, the angular distribution is,

$$\frac{d\Gamma}{d\cos\theta} \sim \frac{4}{3}\left(1 + P_{\Lambda_c} \alpha^{\Delta^{++}}_{\Lambda_c} \cos\theta_{\Delta^{++}}\right) \tag{5.121}$$

where

$$\alpha^{\Delta^{++}}_{\Lambda_c} = \frac{|H^{\Lambda_c^+ \to \Delta^{++} K^-}_{1/2,0}|^2 - |H^{\Lambda_c^+ \to \Delta^{++} K^-}_{-1/2,0}|^2}{|H^{\Lambda_c^+ \to \Delta^{++} K^-}_{1/2,0}|^2 + |H^{\Lambda_c^+ \to \Delta^{++} K^-}_{-1/2,0}|^2} = \frac{|F_1|^2 - |F_2|^2}{|F_1|^2 + |F_2|^2} \tag{5.122}$$

where the res superscript (here $res = \Delta^{++}(1232)(\frac{3}{2}^+)$) has been dropped for sake of readability and the coupling $H^{\Delta^{++} \to p\pi^+}_{1/2,0}$ has been absorbed in the $H^{\Lambda_c^+ \to \Delta^{++} K^-}_{i,j}$ since it is the same for all the configurations. Following the decomposition in the LS basis in Eq. 5.95, $\alpha^{\Delta^{++}}_{\Lambda_c}$ can be rewritten as:

$$\alpha^{\Delta^{++}}_{\Lambda_c} = -2\frac{\mathrm{Re}\left\{h^{\Delta^{++}}_{PC} h^{\Delta^{++}*}_{PV}\right\}}{|h^{\Delta^{++}}_{PC}|^2 + |h^{\Delta^{++}}_{PV}|^2} \tag{5.123}$$

this shows that both the parity violating and the parity conserving parts of the decay are needed. This supports the previous argument, for a parity conserving decay the polarization cannot be measured since h_{PV} would be zero and so would α. This argument has also been discussed in the introduction, Sec. 2.3.1.

Similarly for the Λ^* chain, let's look at $\Lambda^*(1520)(\frac{3}{2}^-)$:

$$\frac{d\Gamma}{d\cos\theta} \sim \frac{4}{3}\left(1 + P_{\Lambda_c}\alpha_{\Lambda_c}^{\Lambda^*}\cos\theta_{\Lambda^*}\right) \tag{5.124}$$

where

$$\alpha_{\Lambda_c}^{\Lambda^*} = \frac{|H_{1/2,0}^{\Lambda_c^+\to\Lambda^*\pi^+}|^2 - |H_{-1/2,0}^{\Lambda_c^+\to\Lambda^*\pi^+}|^2}{|H_{1/2,0}^{\Lambda_c^+\to\Lambda^*\pi^+}|^2 + |H_{-1/2,0}^{\Lambda_c^+\to\Lambda^*\pi^+}|^2} = \frac{|G_1|^2 - |G_2|^2}{|G_1|^2 + |G_2|^2} \tag{5.125}$$

where the res superscript (here $res = \Lambda^*(1520)(\frac{3}{2}^-)$) has been dropped for sake of readability and the coupling $H_{1/2,0}^{\Lambda^*\to pK^-}$ has been absorbed in the $H_{i,j}^{\Lambda_c^+\to\Lambda^*\pi^+}$ since it is the same for all the configurations. Following the decomposition in the LS basis in Eq. 5.102 $\alpha_{\Lambda_c}^{\Delta^{++}}$ can be rewritten as:

$$\alpha_{\Lambda_c}^{\Lambda^*} = -2\frac{\mathrm{Re}\left\{h_{PC}^{\Lambda^*}h_{PV}^{\Lambda^**}\right\}}{|h_{PC}^{\Lambda^*}|^2 + |h_{PV}^{\Lambda^*}|^2} \tag{5.126}$$

The linearity of a single chain can be used as a test to check if the implementation of the amplitude is correct. This was useful to assert the necessity of the polar and azimuthal Wigner rotations as well as the 2π factors coming from the representation of spin $\frac{1}{2}$ particles.

Setting the polarization to be $\vec{P} = \{0,0,1\}$ the $\cos\theta$ distributions in Eq. 5.120, Eq. 5.125 and Eq. 5.122 should be straight lines with positive slope, if only one chain is included in the amplitude. The distribution for 10 000 simulated phase space $\Lambda_c^+ \to pK^-\pi^+$ decays with $P_z = 1$ are shown in Fig. 5.11. The dynamic part is not included, meaning that all the Breit-Wigners are set to 1. The helicity couplings have been chosen in order to obtain $\alpha_{K^*} = \alpha_{\Lambda^*} = \alpha_{\Delta^{++}} = 1$, namely:$E_1^{K^*(892)} = E_3^{K^*(892)} = 1$ and $E_2^{K^*(892)} = E_4^{K^*(892)} = 0$, $F_1^{\Delta^{++}(1232)} = G_1^{\Lambda^*(1520)} = 1$ and $F_2^{\Delta^{++}(1232)} = G_2^{\Lambda^*(1520)} = 0$. From the right to the left the K^*, Λ^* and the Δ^{++} polar angles are shown, the amplitude has been computed including only one chain at the time, for instance $\cos\theta_{\Delta^{++}}$ only contains the Δ^{++} contribution in the amplitude. The linearity is kept when adding the three chains together but the computations are more complex and they are not shown here.

The zero polarization case When the polarization is zero, the dependence on the Euler angles θ_p, ϕ_p, χ is dropped and the angular distributions are uniform. This is because the polarization axis becomes a random axis and there is no reference direction to define for instance the θ_p angle. This means that for each event the angles are equally probable and in the end the angular distribution will be uniform. This can be easily seen for the case with only one chain and one resonance, if $P = 0$ in Eq. 5.119, 5.124, 5.121, the angular distribution is indeed flat. This is a benchmark test that any amplitude formalism should pass, it can be used to spot problems in the amplitude model and in the implementation of the code itself. A test with 1 000 000 (1M simulated phase space events with zero polarization has been performed including only three resonances: $K^*(892)$, $\Lambda^*(1520)$ and $\Delta^{++}(1232)$ with random helicity couplings and BW lineshapes set to 1. The helicity couplings random values are: $E_4^{K^*(892)} = 0.9$, $E_3^{K^*(892)} = 0.7$, $E_2^{K^*(892)} = 0.8$, $E_1^{K^*(892)} = 0.5$, $G_2^{\Lambda^*(1520)} = 1$, $G_1^{\Lambda^*(1520)} = 0.6$, $F_2^{\Delta^{++}(1232)} = 0.8$ and $F_1^{\Delta^{++}(1232)} = 0.6$. The results are shown in Fig. 5.12. This test has been used to assess the necessity of the azimuthal part of the Wigner rotation and of the "2π" condition, discussed

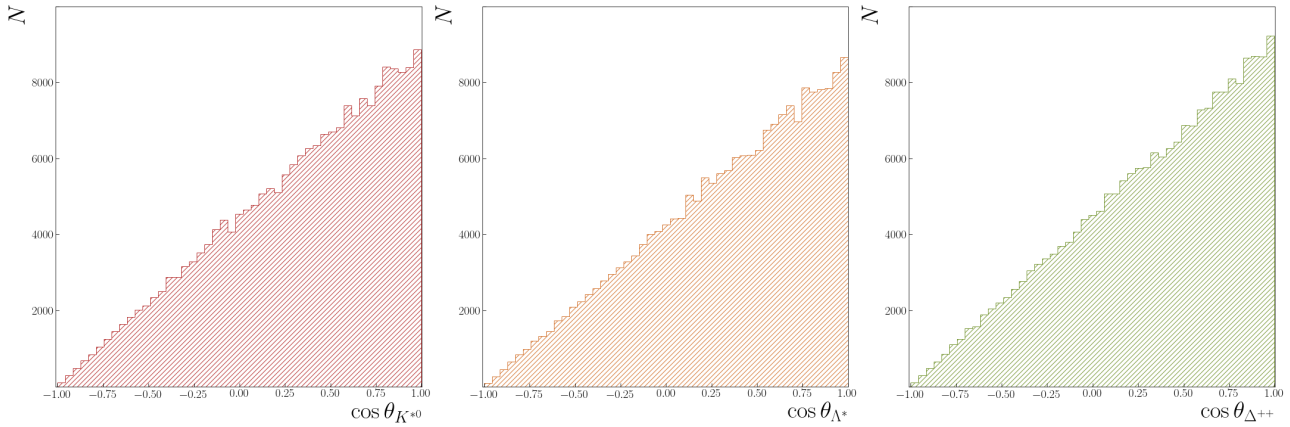

Figure 5.11: Angular distribution $\cos\theta_p$, $\cos\theta_\pi$ and $\cos\theta_K$ simulated for 10 000 phase space events with polarization $\vec{P} = \{0,0,1\}$, the amplitude contains only the resonance studied, *i.e.* the decays $\Lambda_c^+ \to p\bar{K}^{*0}(892)(\to K^-\pi^+)$, $\Lambda_c^+ \to \pi^+\Lambda^*(1520)(\to pK^-)$ and $\Lambda_c^+ \to K^-\Delta^{++}(1232)(\to p\pi^+)$ respectively.

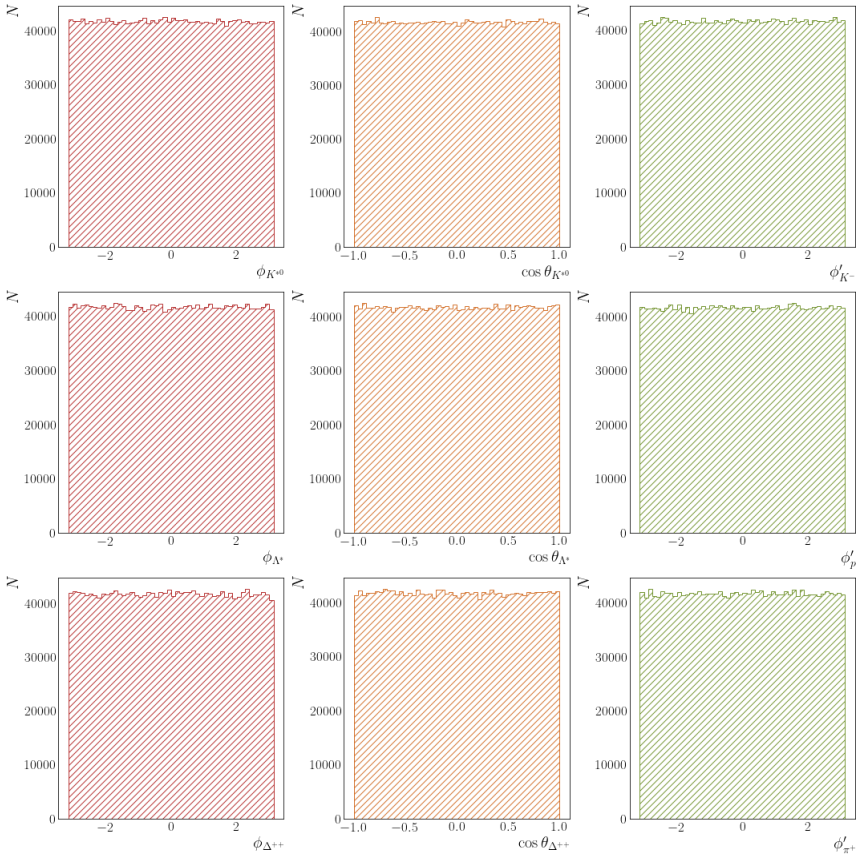

Figure 5.12: Phase space simulation of 1M events with $\vec{P} = \{0,0,0\}$ and BW=1,including only three resonances: $K^*(892)$, $\Lambda^*(1520)$ and $\Delta^{++}(1232)$ with random helicity couplings. From the left to the right column the angular distributions for the three Euler angles are shown. From the top to the bottom line the K^*, Λ^* and Δ^{++} chains are shown.

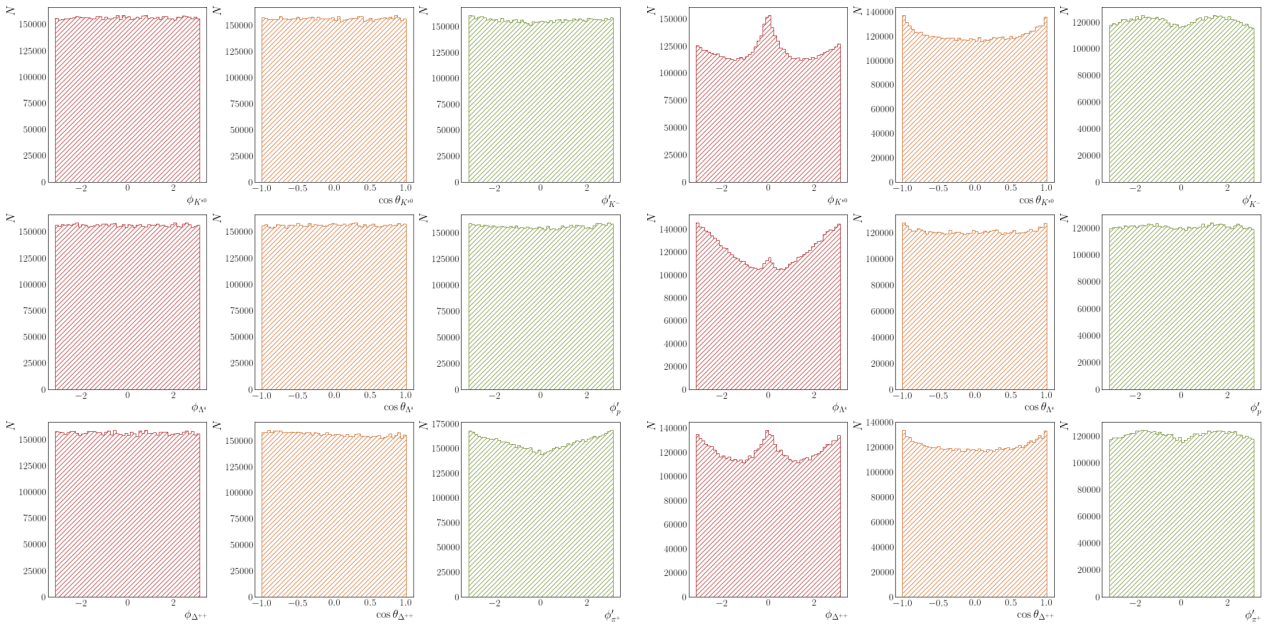

Figure 5.13: Phase space simulation of 1M events with $\vec{P} = \{0,0,0\}$ and BW=1,including only three resonances: $K^*(892)$, $\Lambda^*(1520)$ and $\Delta^{++}(1232)$ with random helicity couplings given in the text. From the left to the right column the angular distributions for the three Euler angles are shown. From the top to the bottom line the K^*, Λ^* and Δ^{++} chains are shown. Left: the azimuthal part of the Wigner rotation has been removed. Right: the "2π" condition has been removed.

in Sec. 5.4.2 and Sec. 5.4.4. If one of the two condition is removed, then the angular distributions have some unphysical dependence for the zero polarization case and they are not flat as expected. This is shown in Fig. 5.13, where on the left the azimuthal Wigner rotation has been removed and on the right the "2π" condition, parametrized by the α factors of Eq. 5.103, has been removed. This has to be compared to the expected flat distributions shown in Fig. 5.12.

Parity conservation of the Λ_c^+ decay If parity is conserved in the $\Lambda_c^+ \to Rh$ decays then the angular distribution is flat and it is not possible to measure the Λ_c^+ polarization. This can be seen easily in the case of single resonance asymmetry parameters, looking at Eq. 5.122 and 5.125, for a parity conserving decay $h^R_{PV} = 0$, implying that the asymmetry parameters α_R would be zero and the angular distribution would be flat. Hence if the conservation of parity for the Λ_c^+ decay is enforced, the angular distribution should be flat for the single resonance amplitudes. The same holds when adding three resonances from different chains. This physics condition allows to perform another useful test of the amplitude formalism, that is for a non-zero polarization if the conservation of parity for the Λ_c^+ decay to the resonances is required, then the angular distributions must be flat as for the zero polarization case in Fig. 5.12. This test has been useful to prove that the 2π condition is needed. Parity conservation implies additional relations for the helicity couplings, using Eq. 5.45 for the decay $\Lambda_c^+ \to Rh$

$$H_{\lambda_R,\lambda_h} = \eta_{\Lambda_c^+}\eta_R\eta_h(-1)^{s_R+s_h-s_{\Lambda_c^+}} H_{-\lambda_R,-\lambda_h}(-1)^{2\lambda_h}, \tag{5.127}$$

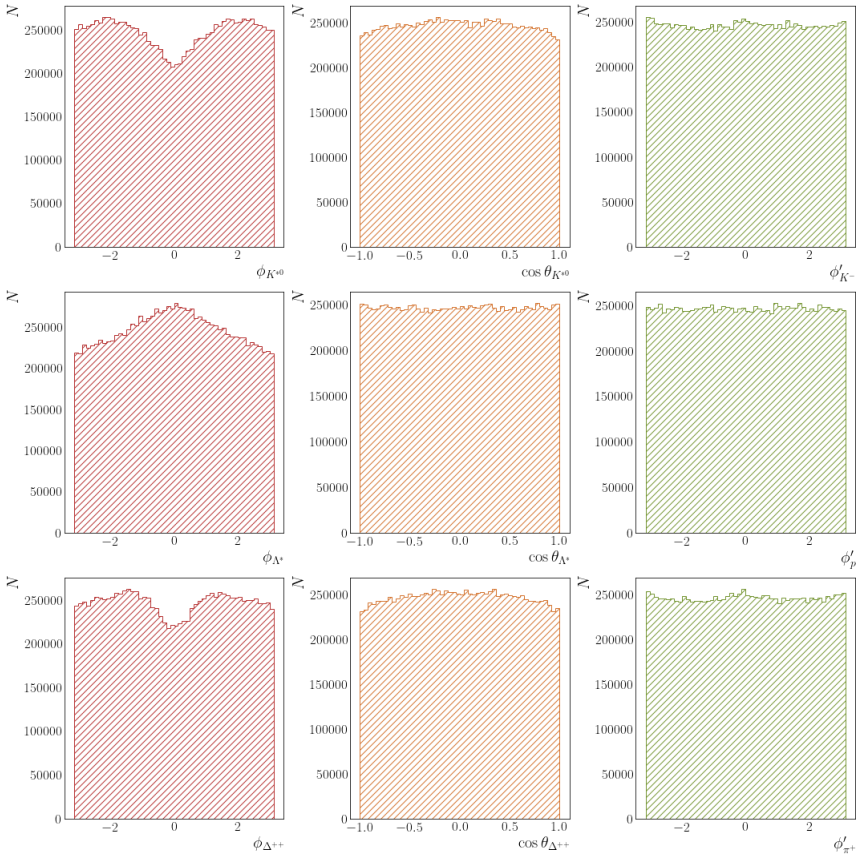

Figure 5.14: Phase space simulation of 1M events with $\vec{P} = \{0, 0, 1\}$ and BW=1,including only three resonances: $K^*(892)$, $\Lambda^*(1520)$ and $\Delta^{++}(1232)$ with helicity couplings relations of Eq. 5.14. From the left to the right column the angular distributions for the three Euler angles are shown. From the top to the bottom line the K^*, Λ^* and Δ^{++} chains are shown. The "2π" condition has been removed, resulting in a not flat distribution.

one can deduce the relations for $K^*(892)$, $\Lambda^*(1520)$ and $\Delta^{++}(1232)$ helicity couplings:

$$\begin{cases} H^{\Lambda_c^+ \to \bar{K}^{*0} p}_{0,1/2} & = -H^{\Lambda_c^+ \to \bar{K}^{*0} p}_{0,-1/2} \\ H^{\Lambda_c^+ \to \bar{K}^{*0} p}_{1,1/2} & = -H^{\Lambda_c^+ \to \bar{K}^{*0} p}_{-1,-1/2} \\ H^{\Lambda_c^+ \to \Delta^{++} K^-}_{1/2,0} & = H^{\Lambda_c^+ \to \Delta^{++} K^-}_{-1/2,0} \\ H^{\Lambda_c^+ \to \Lambda^* \pi^+}_{1/2,0} & = -H^{\Lambda_c^+ \to \Lambda^* \pi^+}_{-1/2,0} \end{cases} \iff \begin{cases} E_1^{K^*(892)} & = -E_4^{K^*(892)} \\ E_2^{K^*(892)} & = -E_3^{K^*(892)} \\ F_1^{\Delta^{++}(1232)} & = F_2^{\Delta^{++}(1232)} \\ G_1^{\Lambda^*(1520)} & = -G_2^{\Lambda^*(1520)} \end{cases} \tag{5.128}$$

Similarly to the zero polarization case, a phase space simulation has been performed with 1M events, $\vec{P} = \{0, 0, 1\}$, requiring parity conservation using the relations in Eq. 5.128 and removing the "2π" condition. The results are shown in Fig. 5.14, the angular distribution are not flat as expected, whereas they are flat when the "2π" condition is included. This means that this condition is necessary otherwise the amplitude would present unphysical dependences in the angular distributions.

Origin of the "2π condition" The origin of this condition is linked to the half-integer nature of fermions spin, which breaks the 2π invariance. This is explained in Sec. 5.2.2. An extra minus sign

can arise depending on the configuration of the angles and this has to be compensated somehow in the amplitude. In this formalism, the "2π condition" by introducing an extra term in the Wigner rotation, corresponding to the α angles in Eq. 5.103. In practice this condition imposes that for the Λ^* and Δ^{++} chains, an extra rotation of 2π is applied if $\phi_p - \phi_K > \pi$ or $\phi_p - \phi_\pi > \pi$. The domain where the condition applies is shown in Fig. 5.15.

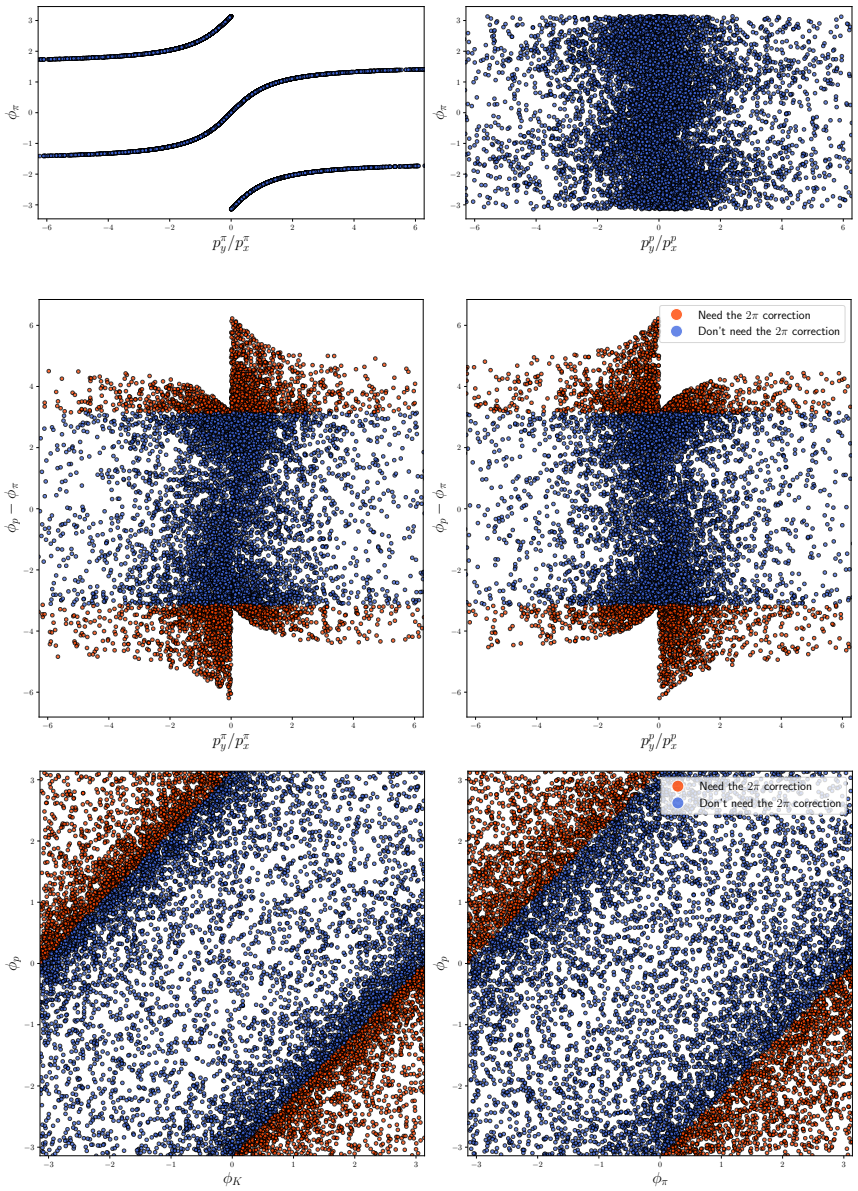

Figure 5.15: Simulation of 1M phase space events. The middle plot shows $\phi_p - \phi_\pi$ as a function of on the left p_y^π/p_x^π and on the right p_y^p/p_x^p. The top plot shows the dependence of ϕ_π as a function of on the left p_y^π/p_x^π and on the right p_y^p/p_x^p. Bottom: ϕ_p as function of ϕ_K and ϕ_π is shown. In both plots, the points in orange corresponds to the points requiring the "2π condition".

Note on particle ordering The ordering of the daughter particles matters when writing the amplitude of Eq. 5.40, a phase difference (minus sign) between amplitudes could be introduced if a pair of particles is swapped. For a decay $M \to 123$ the cyclic ordering should be respected, meaning that the resonances daughters pairs are: (12)3, 1(23) and (31)2. For the $\Lambda_c^+ \to pK^-\pi^+$ case this implies the ordering: $(pK^-)\pi^+$, $p(K^-\pi^+)$ and $(\pi^+p)K^-$. For instance in the Δ^{++} channel, (π^+p), daughter one (d_1) is the pion and two (d_2) the proton. By exchanging the ordering, $d_1 = p$ and $d_2 = \pi^+$, Eq. 5.40 get modified as:

$$D^{s_{\Delta^{++}}*}_{\lambda_{\Delta^{++}},\lambda_\pi-\lambda_p}(\phi'_\pi,\theta'_\pi,-\phi'_\pi) \to D^{s_{\Delta^{++}}*}_{\lambda_{\Delta^{++}},\lambda_p-\lambda_\pi}(\phi'_p,\theta'_p,-\phi'_p) \tag{5.129}$$

The indices change and the angles of the proton and the pion are not the same: $(\theta'_p,\phi'_p) = (\pi-\theta'_\pi,\phi'_\pi+\pi)$. Using the properties of the d-Wigner matrices, Eq. 5.15 and Eq. 5.12, and the relations between the proton and pion angles, it can be shown that the two rotations are not equivalent, mathematically there is a sign difference between the two D-functions which depends on λ_p and $s_{\Delta^{++}}$,

$$D^{s_{\Delta^{++}}*}_{\lambda_{\Delta^{++}},\lambda_p-\lambda_\pi}(\phi'_p,\theta'_p,-\phi'_p) = (-1)^{s_{\Delta^{++}}+\lambda_p+1}e^{-2i\lambda_p\phi'_\pi}D^{s_{\Delta^{++}}*}_{\lambda_{\Delta^{++}},\lambda_\pi-\lambda_p}(\phi'_\pi,\theta'_\pi,-\phi'_\pi) \tag{5.130}$$

Furthermore, the relations between the helicity couplings are also modified, see Eq. 5.87. This short example shows that breaking the cyclic ordering of the resonance daughters introduces an unphysical phase difference between the amplitudes.

5.6 Conclusions

In this chapter the helicity formalism for two subsequent two-body decays has been introduced. The helicity amplitude for the $\Lambda_c^+ \to pK^-\pi^+$ decays including the initial state polarization have been derived and studied in detail. A set of test has been performed to prove that this formalism is correct: the linearity of the single resonance amplitude, the zero polarization test and the parity conserving Λ_c^+ decay test. The relations between the helicity couplings have been derived explicitly for the *no-phase convention* and the *particle-2-phase-convention*. These two conventions can lead to confusions, in [8] the relations for parity conservation is given for the *particle-2-phase-convention* whereas in the amplitude the *no-phase convention* is used. The relations between the couplings in the two conventions are given in Eq. 5.42. The necessity of the azimuthal part of the Wigner rotation has been assessed thanks to the zero polarization test. An extra factor of 2π has been found to be necessary to describe the amplitude correctly. This factor is due to the spin 1/2 nature of fermions and needs to be included to pass the third test which enforce parity conservation for the Λ_c^+ decay to the isobars, and the zero polarization test. This formalism has been proven to be exactly equivalent to the DPD formalism proposed in [202], if the 2π condition is included.

6 Amplitude analysis for $\Lambda_c^+ \to pK^-\pi^+$ decay

6.1 Introduction to the measurement

In this chapter the Λ_c^+ polarization measurement, via the amplitude analysis of the Cabibbo favored $\Lambda_c^+ \to pK^-\pi^+$, is presented. The dataset used contains pp collisions collected by the LHCb detector in 2016 (Run 2) at a center of mass energy of 13 TeV, for an integrated luminosity of 1.7 fb^{-1}. The LHCb detector collected millions of $\Lambda_c^+ \to pK^-\pi^+$ events and among it, only the Λ_c^+ produced directly after a pp collisions (called prompt), and not from the decay of B particles (secondaries), are selected. A tight selection is applied in order to have an almost pure prompt signal with a contamination from secondaries under 2%. This requirement eliminates a major part of the dataset, nevertheless the final sample contains more than 600 000 events, allowing to perform a full 5 dimensional amplitude analysis where the helicity couplings and the polarization vector are measured simultaneously on the Dalitz plane. A first amplitude analysis of the $\Lambda_c^+ \to pK^-\pi^+$ decays has been performed by the E791 experiment at Fermilab [204], on a data sample containing ~ 1000 events for Λ_c^+ produced in π-N collisions. An evidence of non-zero polarization was found and three main resonances were identified: $K^*(892)$, $\Lambda^*(1520)$, $\Delta(1232)$ and a non-resonant component. However, the model used in this analysis has been proven to be incomplete, since the Wigner rotations discussed in Sec. 5.4.3 were not included, and the low statistics sample did not allow to see other resonant contributions, which are instead visible in the LHCb data. The helicity amplitudes derived in Chapter 5 are used to describe the amplitude of the decay and measure the Λ_c^+ polarization vector. As discussed in the same chapter, the $\Lambda_c^+ \to pK^-\pi^+$ decay presents a very rich structure; each of the three possible channels (pK, $K\pi$ and πp) can involve several intermediate states. Even though all the well-established resonances listed in Ref.[11] could contribute to the amplitude, some of them give a negligible contribution or cannot even be distinguished from other resonances. For this reason, the resonance content of the amplitude needs to be assessed in a recursive way; ultimately three models, all giving similar results, are retained. The choice of the model gives the larger systematic uncertainties on the polarization measurement. In order to avoid introducing any bias in the analysis, the value of the polarization is blinded. The unblinding will be performed once the model and the details of the analysis will be definitively fixed. Such a high-statistics sample require large computational resources and an unavoidable optimization of the amplitude fit procedure, the code has been developed in C++ within the RooFit framework,

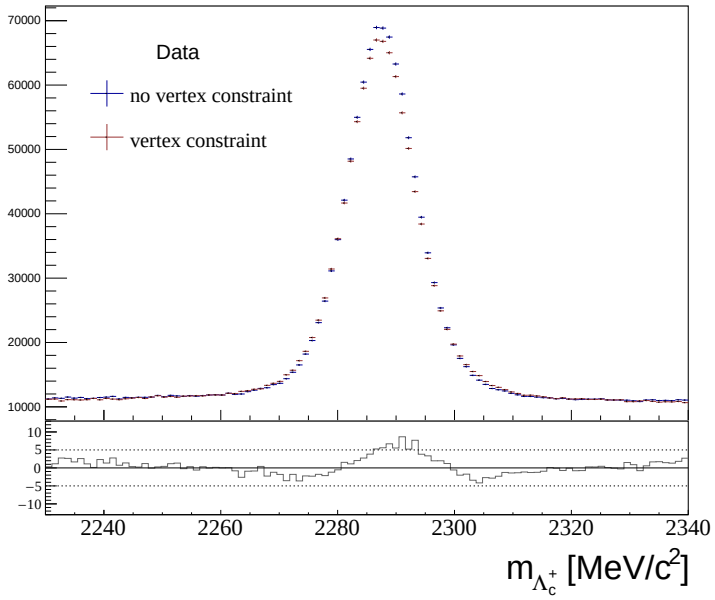

Figure 6.1: The $m_{pK^-\pi^+}$ invariant mass distribution with (red) and without (blue) the DTF vertex constraint. The bottom pad shows the difference between the two distributions divided by the error.

using OpenMP libraries for multi-threading[1].

6.2 Selection of $\Lambda_c^+ \to pK^-\pi^+$ events in pp

The data sample used for this analysis contains pp collisions collected with the LHCb experiment in 2016, for a luminosity of $1.7\,\text{fb}^{-1}$ at a center of mass energy $\sqrt{s} = 13\,\text{TeV}$ [2]. Data are selected from the Turbo stream, this means that there is no offline stripping and the reconstruction is performed online by the HLT steps. The ntuples are build using the DaVinci software. An additional step is applied to the whole dataset (and to the simulated samples) which adds two constraints: the vertex constraint, which imposes that the daughters' reconstructed momenta point to the Λ_c^+ decay vertex (DV), and the mass constraint, which requires that the Λ_c^+ reconstructed invariant mass coincides with the "known" value from Ref. [11]. This is done within the LHCb software using the "Decay Tree Fitter" (DTF) algorithm [209], which re-fits the entire decay chains including the mass and vertex constraints, resulting in a better estimate of the track momenta. This procedure can induce some biases which should be carefully studied, an example of the effect of the vertex constraint on the $m_{pK^-\pi^+}$ invariant mass distribution is given in Fig. 6.1. The mass resolution changes from 5.59 MeV (without DTF) to 5.51 MeV (with DTF).

[1] Multi-threading is a feature that allows to run several tasks at a time, it allows to compute the amplitude concurrently on several batches of data.

[2] The detector conditions during the data taking are summarized in the tag: "dddb-20200424-3" with conditions "cond-20191004-1". The bookepping path where the data are stored is : $/LHCb/Collision16/Beam6500GeV-VeloClosed-Mag(Up/Down)/RealData/Turbo03a/94000000/CHARMSPECPARKED.MDST$.

6.2.1 Trigger

Due to the very high rate of collisions at the LHC, 40 MHz, the LHCb detector cannot register all the events hence some criteria are set to decide whether an event is kept (because it contains "interesting" physics) or not: this is done by the trigger system of LHCb. The first step for the trigger, is the level 0 hardware trigger L0. Since it is an hardware trigger, only the events passing its requirements are saved and go to the next processing stage. In general, the trigger can be fired either using the signal candidates, called Triggered On Signal (TOS) events, or without using the signal candidates, called Triggered Independent of Signal (TIS) events. In the first case the signal candidate alone (via its decay products) is sufficient to fire the trigger line. In the second case, the signal candidate is not used (and actually removed) and the trigger is fired by the rest of the event. These "non signal" events can still contain signal candidates because at LHCb, b hadrons are produced in pairs, one hadron of the pair can produce the signal candidate and the other can produce other decay products that fire the trigger by itself (if the signal is not enough to fire the trigger). Note that an event can be TIS and TOS at the same time (Triggered On Both TOB). In this analysis, the Λ_c^+ candidates are selected using the following L0 requirements:

- *L0 Hadron TOS*: requiring that at least one of the charged tracks of the signal decay creates a cluster in the HCAL with a transverse energy higher than the *L*0 Hadron threshold, which is ranging from 3216 MeV to 3888 MeV depending on the TCK used during the data taking period. For any TCK it is also required to have less then 450 SPD hits to exclude busy events.

- L0 TIS: requiring energetic muons or electrons, which are not from the signal decay, but which indicates that something that may be signal has been produced in the event. More precisely the lines used in the analysis are: *L0MuonTIS, L0DiMuonTIS, L0ElectronTIS, L0PhotonTIS*.

The specific requirements of these lines are summarized in Sec. 3.2.5, Table 3.2. It is of major importance to understand how these requirements influence the shape of the phase space distribution of the Λ_c^+ candidates (and the backgrounds) since they could introduce a bias in the amplitude fit and consequently in the polarization measurement. The MC simulation is used to study these effects and the results are shown and discussed in Sec. 6.2.7. In order to master these efficiency effects, which depend on the type of trigger required, the two trigger categories, TIS and TOS[1], are studied separately. The samples are also separated according to their polarities, positive (MagUp) or negative (MagDown). In total four separated samples are studied: MagUp TIS, MagUp TOS, MagDown TIS and MagDown TOS. If not stated otherwise, all along this chapter the figures shown are for the MagDown TOS category, the other three categories give similar results and the relative plots are shown in the Appendices when needed.

On top of the L0 trigger requirement, the events are required to fire some HLT lines, see Sec. 3.2.5 for a detailed explanation of the HLT. A summary of the L0 and HLT trigger lines used in the analysis is given in Tab. 6.2. The HLT1 lines are based on generic track information, the transverse momentum p_T, the track quality χ^2_{track}, the ghost probability, the $\chi^2_{\rm IP}$ of the track, the $\chi^2_{\rm vtx}$ and the DIRA angle.

[1]Where TIS and TOS hereon refers to the specific TIS and TOS requirements applied in this analysis and listed in the text.

Name	Symbol	Definition
Vertex quality	χ^2_{vtx} or χ^2_{vtx}/ndf	χ^2 or χ^2/ndf of the fit of the decay vertex.
Track quality	χ^2_{track}	Quality of the track reconstruction
Ghost probability	$p_{ghost}(a)$	Probability to be a fake track, coming from a random combination of hits.
Impact Parameter	IP	The transverse distance of closest approach between a particle trajectory and the Primary Vertex (PV), sketched in Fig. 6.2 (right).
	χ^2_{IP}	The change in vertex χ^2 when adding or not a track in the vertex fit.
Direction angle	DIRA	The angle between a line drawn from the PV to the DV of the particle and the sum of the 4-momentum of its decay products, sketched in Fig. 6.2 (left). One typically uses the cosine of the direction angle in selections.
Flight Distance (FD)	χ^2_{FD}	Flight distance of a particle divided by its uncertainty.
PID	$ProbNN_b(a)$	Probability of the track a of being a particle of type b, where a can be p, K, π, μ, e, d, obtained using a neural network combining the information from sub-detectors.
	$PID_b(a)$	Same as the $probNN$ variables, without the neural network training.

Table 6.1: Definition of the variables used in the trigger and offline selections.

Trigger level	Lines
L0 TOS	L0Hadron (TOS)
L0 TIS	(L0Muon OR L0DiMuon OR L0Electron OR L0Photon)(TIS)
HLT1	Hlt1TrackMVA (TOS) OR Hlt1TwoTrackMVA (TOS)
HLT2	Hlt2CharmHadLcpToPpKmPipTurbo (TOS)

Table 6.2: Trigger requirements applied on all samples. Details about the selection contained in the HLT 1 and HLT 2 lines are given in Table 6.3 (right).

Some of these variables have been already defined in Chap. 3, however to facilitate the reading a short definition of each of them is given in Tab. 6.1. The complete list of selections contained in the HLT lines, with the numerical values, is given Tab. 6.3 (right).

The HLT2 requirements instead are designed to select the three-body decay $\Lambda_c^+ \to pK^-\pi^+$ specifically, the selections are listed in Tab. 6.3 (left). The decay products have requirements on the same variables as for the HLT 1 with on top some loose PID selections to remove particles which have been very luckily misidentified. All tracks are required to point away from the PV. Additional selections applied to the combination of the three decay products are applied on the flight distance (FD), the Λ_c^+ lifetime (τ), the DIRA angle and finally a mass window around the Λ_c^+ mass $m_{\Lambda_c^+} = 2286.46 \pm 0.14\,\text{MeV}/c$ [11] is set. Since the majority of these variables will be also used in the offline selection, the detailed explanation and justification of it is given in Sec. 6.2.2.

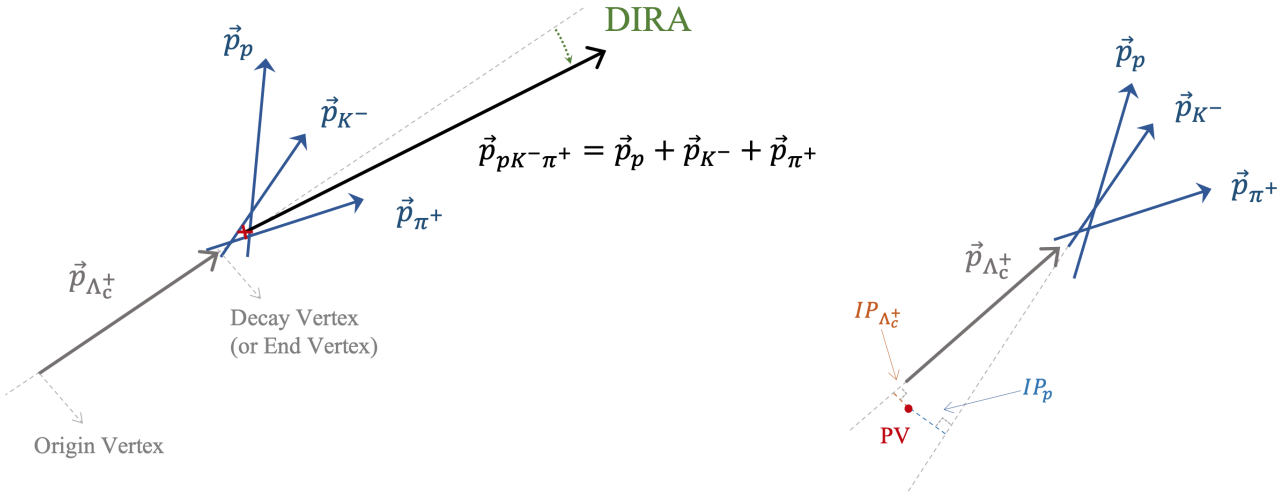

Figure 6.2: Sketch of the DIRA angle (left) and the impact parameter (right), as defined within LHCb.

Particle	Selection
Proton	$p > 10\,\text{GeV}/c$ $\text{PID}_p > 5$ $\text{PID}_p - \text{PID}_K > 5$
Kaon	$\text{PID}_K > 5$
Pion	$\text{PID}_K < 5$
All tracks	$p_T > 200$ MeV/c $p > 1\,\text{GeV}$ $\chi^2_{\text{IP}} > 6$ $\chi^2_{\text{track}}/\text{ndf} < 3$
At least two tracks	$p_T > 400$ MeV/c $\chi^2_{\text{IP}} > 9$
At least one track	$p_T > 1000$ MeV/c $\chi^2_{\text{IP}} > 16$
Combination	2211 MeV/$c^2 < m < 2543$ MeV/c^2 $\sum_{\text{daughters}} p_T > 3000$ MeV/c $\text{acos(DIRA)} < 0.01\,\text{mrad}$ $\tau > 0.15\,\text{ps}$ $\chi^2_{\text{FD}} > 25$

TrackMVA
$p_T > 1000$ MeV/c
$p_T < 25000$ MeV/c
$\chi^2_{\text{IP}} > 7.4$
$\chi^2_{\text{track}} > 2.5$
Ghost probability < 0.2

TwoTrackMVA
$p > 5000$ MeV/c
$p_T > 500$ MeV/c
$\chi^2_{\text{track}} > 2.5$
$\chi^2_{\text{IP}} > 4$
$2 < \eta < 5$
$\chi^2_{\text{vtx}} < 10$
DIRA > 0
$m_{\text{corr}} > 1000$ MeV/c

Table 6.3: Left: selections in the HLT 2 trigger lines. Right: selections in the HLT 1 trigger lines.

6.2.2 Offline selection

On top of the trigger requirements described above, additional selections are applied offline to achieve an optimal signal purity. The selections are first designed by tightening the HLT ones on the transverse momenta of the decay products and they are listed in Tab. 6.4. Then, additional requirements on the daughter's momenta are applied to select the range where the particle identification performs better,

see Fig. 3.2.3 to have an idea of the PID efficiency as a function of the particle momentum. The quality of the particle identification (PID) is enforced by mean of the $ProbNN_a(b)$ variables, the value chosen for these selections is the result of an optimization procedure discussed in Sec. 6.2.4. Finally the $\chi^2_{\rm IP}$ of the decay products is required to be between 9 and 200, where the lower limit allows to select candidates with tracks pointing to the Λ_c^+ decay vertex and not to the PV, and the upper limit allows to remove tracks far from the PV arising from the creation of particles due to the interaction with the detector. The proton candidates are also required to have a small probability to be fake tracks, $p_{ghost}(p)$. Regarding the mother particle Λ_c^+, it is required to have a significant flight distance in order to remove the combinatorics arising from the large amount of particles produced at the PV during collisions, this is quantified by the $\chi^2_{\rm FD}$. The Λ_c^+ decay vertex (DV) is required to have a good χ^2, meaning that the fit performed to the reconstructed DV is good. The Λ_c^+ momentum is required to be aligned with the momentum obtained when joining the PV and the Λ_c^+ DV, by mean of the $DIRA$ variable, which is sketched in Fig. 6.2. The measured Λ_c^+ lifetime is 0.20 ± 0.03 ps [11], based on that a requirement for τ to be smaller than 1.5 ps is added. Finally, a selection on the $\log(\chi^2_{\rm IP})$ of the Λ_c^+ candidates is applied to remove secondary decays. This is probably the most important selection for this analysis since the polarization depends on the production mechanism and the secondary and prompt Λ_c^+ are produced via different interactions (weak and strong respectively). The optimization of the $\log(\chi^2_{\rm IP})$ selection is discussed in detail in the next section.

The *sPlot* technique

The *sPlot* technique [210] is a method (used in this analysis) which allows to unfold the contributions from different sources in a given data samples. A "discriminating" variable is used to separate the events into different categories of choice. A typical example is the use of the invariant mass as discriminating variable to separate the signal candidates from the background. The mass is described by a model which includes the two components, signal and background, and which is used to classify the events. An event-by-event weight (usually called "sWeights") is extracted from this model and it can be used on other variables (called "control" variables) to separate the contribution of each category. An essential assumption for this technique to work is that the control variable is uncorrelated with the discriminating variables. In this analysis, the *sPlot* technique is used to separate signal from background events using the $m_{pK^-\pi^+}$invariant mass as discriminating variable, see Sec. 6.2.6, and to separate prompt from secondary Λ_c^+ decays using the $\log(\chi^2_{\rm IP})$as discriminating variable, see Sec. 6.2.3.

6.2.3 Separation of prompt and secondary Λ_c^+

In this analysis, only the Λ_c^+ produced directly in the pp interaction (called prompt) are studied, hence the Λ_c^+ produced from the decay of other baryons (secondaries) are considered as background. The separation between prompt and secondaries is performed using the Λ_c^+ impact parameter: if the IP is large then the Λ_c^+ have been produced from a secondary decay, for instance the decay $\Lambda_b^0 \to \Lambda_c^+ l^- \bar{\nu}_l$, however if the IP is small, then the Λ_c^+ momentum is pointing to the primary vertex, meaning that it has been produced promptly. In practice, the variable used is the $\chi^2_{\rm IP}$, defined in Tab. 6.1, which takes

Particle	Selections
Λ_c^+	$\log(\chi^2_{\rm IP}) < -2.$
	$\tau < 0.0015\,$ns
	$\chi^2_{FD} > 40$
	$\chi^2_{\rm vtx}/{\rm ndf} < 5$
	$acos(DIRA) > 10\,$mrad
Proton	$\chi^2_{\rm IP} > 9$
	$\chi^2_{\rm IP} < 200$
	$p_{ghost}(p) < 0.4$
	$10000 < p < 100000$ MeV/c
	$p_T > 1000$ MeV/c
Kaon	$\chi^2_{\rm IP} > 9$
	$\chi^2_{\rm IP} < 200$
	$3000 < p < 150000$ MeV/c
	$p_T > 500$ MeV/c
Pion	$\chi^2_{\rm IP} > 9$
	$\chi^2_{\rm IP} < 200$
	$3000 < p < 150000$ MeV/c
	$p_T > 500$ MeV/c
PID	$(ProbNN_p(p) - ProbNN_K(p)) > 0.1$
(MC15TuneV1)	$(ProbNN_p(p) - pProbNN_\pi(p)) > 0.4$
	$ProbNN_K(K) > 0.1$

Table 6.4: Offline selections. The variables used are described in the text.

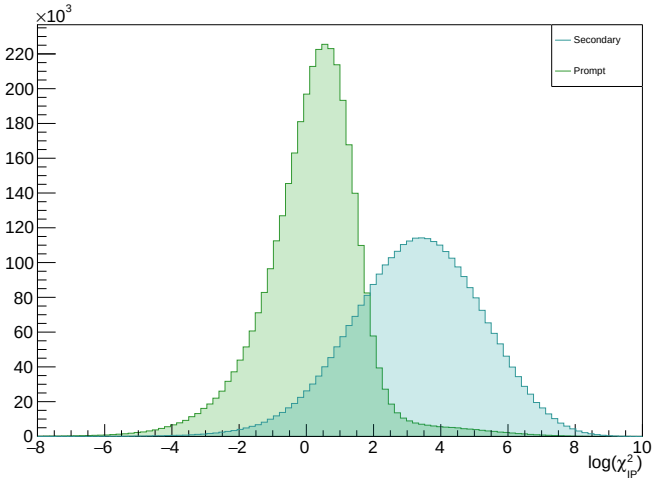

Figure 6.3: Comparison of the $\log(\chi^2_{\rm IP})$ distributions in 2016 Monte-Carlo simulations for prompt produced (green) and weakly produced (cyan) Λ_c^+ baryons.

into account the associated error coming from the track fit procedure, where the simple IP variable instead does not. An even better discrimination between prompt and secondaries Λ_c^+ is obtained using the logarithm of the $\chi^2_{\rm IP}$, which allows to distinguish these two categories clearly even by eye. Indeed, in Fig. 6.3 the comparison of the $\log(\chi^2_{\rm IP})$ for prompt and secondary Λ_c^+ simulated decay shows two well separated peaks and one can already see that promptly produced Λ_c^+ starts to be dominant at $\log(\chi^2_{\rm IP}) < 0$. The selection is optimized in order to have a prompt signal as pure as possible and the optimization is performed in 3 steps. First the MC distributions for prompt and secondaries are fitted using a Bukin function in order to extract the shape parameters. Then a fit of the $\log(\chi^2_{\rm IP})$ distribution of the signal data, selected using the sWeights obtained from the invariant mass fit, is performed. Finally, the contamination of the prompt sample is estimated by computing the number of prompt (N_p) over the number of secondary decays (N_S), $N_P/(N_S+N_P)$, as a function of the $\log(\chi^2_{\rm IP})$ selection. The Bukin function is a modified Novosibirsk distribution defined as

$$f_{\rm Bukin}(x;\mu,\sigma,\xi,\rho_{\rm L},\rho_{\rm R}) = \begin{cases} e^{-\ln 2\left[\frac{\ln\left(1+2\xi\sqrt{\xi^2+1}\frac{x-\mu}{\sigma\sqrt{2\ln 2}}\right)}{\ln\left(1+2\xi^2-2\xi\sqrt{\xi^2+1}\right)}\right]^2} & x_{\rm L} < x < x_{\rm R} \\ e^{\frac{\xi\sqrt{\xi^2+1}(x-x_{\rm L})\sqrt{2\ln 2}}{\sigma(\sqrt{\xi^2+1}-\xi)^2\ln\left(\sqrt{\xi^2+1}+\xi\right)}+\rho_{\rm L}\left(\frac{x-x_{\rm L}}{\mu-x_{\rm L}}\right)-\ln 2} & x \le x_{\rm L}, \\ e^{\frac{\xi\sqrt{\xi^2+1}(x-x_{\rm R})\sqrt{2\ln 2}}{\sigma(\sqrt{\xi^2+1}-\xi)^2\ln\left(\sqrt{\xi^2+1}+\xi\right)}+\rho_{\rm R}\left(\frac{x-x_{\rm R}}{\mu-x_{\rm R}}\right)-\ln 2} & x \ge x_{\rm R}, \end{cases} \tag{6.1}$$

where

$$x_{\rm L,R} = \mu + \sigma\sqrt{2\ln 2}\left(\frac{\xi}{\sqrt{\xi^2+1}} \mp 1\right). \tag{6.2}$$

where μ and σ are the mean and the width of the central peak, ξ is the asymmetry parameter, $\rho_{\rm L}$ and $\rho_{\rm R}$ are the left and right tail exponential coefficients. The results of the MC fits are shown in Fig. 6.4 and Table 6.5. The fit on data is done fixing ρ_1 for the prompt and secondary component and

Parameter	Value	
	Prompt	Secondary
ξ	$-0.17 \pm 3.74 \times 10^{-5}$	$0.03 \pm 2.37 \times 10^{-3}$
μ	$0.05 \pm 2.24 \times 10^{-3}$	$3.35 \pm 6.06 \times 10^{-3}$
ρ_1	$-0.10 \pm 1.04 \times 10^{-4}$	$-0.30 \pm 6.79 \times 10^{-3}$
ρ_2	$0.12 \pm 3.29 \times 10^{-5}$	$-1.70 \pm 2.76 \times 10^{-2}$
σ	$0.10 \pm 1.71 \times 10^{-3}$	$1.94 \pm 2.96 \times 10^{-3}$

Table 6.5: Results of the fit to the simulation using a Bukin function for prompt and secondary Λ_c^+.

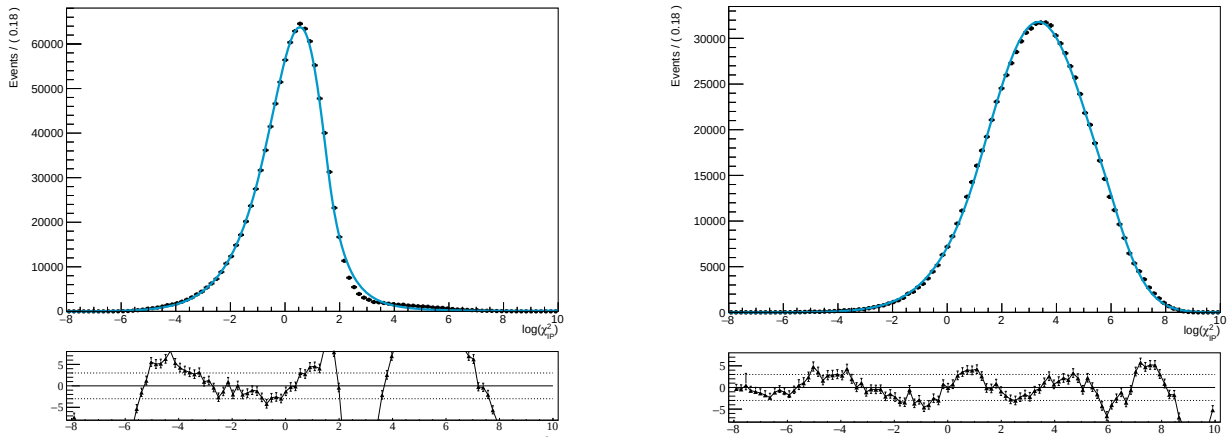

Figure 6.4: Fit of the $\log(\chi^2_{\rm IP})$ simulated MC distributions for prompt (left) and secondary (right) produced Λ_c^+.

letting the other parameters free with as a starting value the results of the MC fit. An example of fit to the $\log(\chi^2_{\rm IP})$ distribution in data (without any selection) is shown in Fig. 6.5. Then the number of secondary and prompt decays is extracted from this fit for different $\log(\chi^2_{\rm IP})$ selections to compute the ratio $N_P/(N_S+N_P)$. The results are shown in Fig. 6.6, the selection chosen for the analysis is $\log(\chi^2_{\rm IP}) < -2.0$, resulting in a residual contamination from secondary of 1.05% and a signal purity of 98.9%.

To ensure that the $\log(\chi^2_{\rm IP})$ selection does not introduce any dependence on the phase space variables, the efficiency of the $\log(\chi^2_{\rm IP})$ selection has been studied as a function of the 5 phase-space variables in MC and data. For the MC simulation, the efficiency of the selection $-7 < \log(\chi^2_{\rm IP}) < -2$ for prompt signal particles is shown in Fig. 6.7. The efficiency distributions obtained are not flat over the phase space as expected. The efficiency over ϕ_p drops in the middle, similarly it drops on the extreme right for the invariant masses case. For the other variables, χ and $\cos(\theta_p)$ the efficiency looks flat as expected. This efficiency variation could be introduced by the refitting procedure that is performed on the tuples, the "Decay Tree Fitter" (DTF) [209]. The quality of the (re)fit of the tracks, especially after the vertex constraint, is strongly correlated with the $\chi^2_{\rm IP}$ variable. This could introduce a bias in the phase space distributions depending on the $\log(\chi^2_{\rm IP})$ selections chosen, the larger is the selection on the *logIpChiSq* variable the larger is the correlation between the two variables. This effect has been studied by plotting the $\chi^2/{\rm ndf}_{\rm DTF}$ against the five phase space variables in four bins of

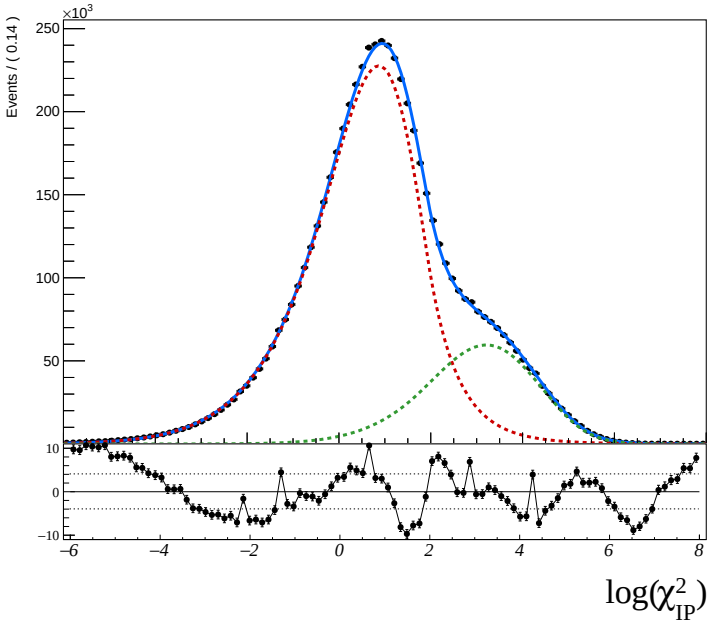

Figure 6.5: Fit to the $\log(\chi^2_{\text{IP}})$ distribution on the data, two Bukin functions are used. The red dashed line represent the prompt contribution and the green one the secondary one.

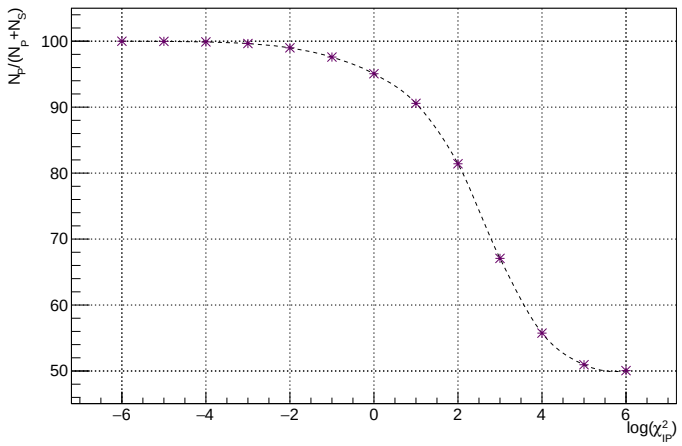

Figure 6.6: Purity of the signal computed as $N_P/(N_S + N_P)$ as a function of the $\log(\chi^2_{\text{IP}})$ selection.

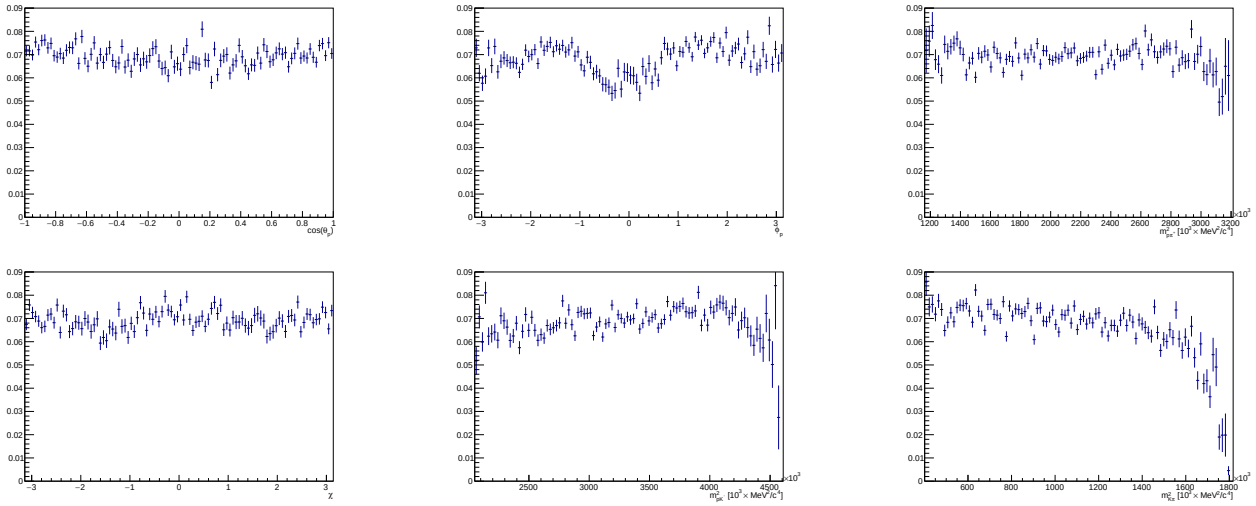

Figure 6.7: Efficiencies for $-7. < \log(\chi^2_{\rm IP}) < -2.$.

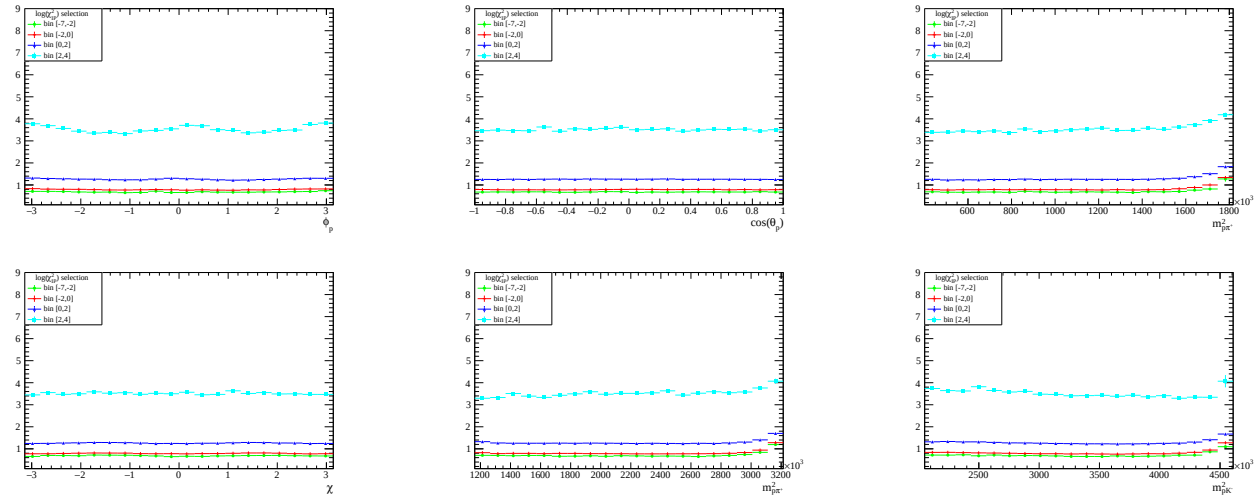

Figure 6.8: Profile histograms featuring the $\chi^2/\mathrm{ndf}_{\rm DTF}$ versus the phase space variables $\left(m^2_{pK^-}, m^2_{p\pi^+}, \cos\theta_p, \phi_p, \chi\right)$, the mass $m^2_{K^-\pi^+}$ is also shown. The colors represent the $\log(\chi^2_{\rm IP})$ bins: [-7,-2] (in green), [-2,0] (in red), [0,2] (in blue), [2,4] (in cyan). The results shown are for the TOS category and positive polarity.

$\log(\chi^2_{\rm IP})$: [-7,-2], [-2,0], [0,2] and [2,4]. The result are shown in Fig. 6.8. An effect on the border of the mass distribution and a non flat dependence on the angular variable ϕ_p is seen, the effect is larger for the [2,4] $\log(\chi^2_{\rm IP})$ bin. For the bin used in the analysis [-7,-2], no effect is seen on the angular variables, however a variation at the border of the mass distributions is seen. What is important to verify is whether this effect is also present in data. In order to do so, the prompt and secondary decays are selected in the data using sweights obtained form the fit to the $\log(\chi^2_{\rm IP})$ in data. Then the $\log(\chi^2_{\rm IP})$ selection efficiency for the prompt decays is obtained on a sample with loose preselections by dividing the number of events in the $\log(\chi^2_{\rm IP})$ bin over the total number of events. The comparison is shown in Fig. 6.9 where the green histograms are the efficiencies from simulated events, the blue histograms from data and the red histograms are the ratio of the two previous histograms where the corresponding y-axis is displayed in red on the right side of the plot. Both samples, MC and data, have passed the same DTF procedure and it appears that the effect is well reproduced in the simulation. In conclusion, the $\log(\chi^2_{\rm IP})$ selection is introducing an effect over the phase space which is well reproduced in the simulation, this means that it will be taken into account when correcting for the efficiencies and no unphysical behavior will be introduced over the phase space variables.

6.2.4 Optimization of the PID selections

The selections on the particle identification variables, $ProbNN$, aims at increasing the probability to have tracks which are correctly identified as proton, kaon or pion. This allows to reduce the background considerably, however since the $\log(\chi^2_{\rm IP})$ selections already remove a major part of the dataset, an optimization of this selection is performed to avoid any unnecessary further reduction of it. The PID requirements have been optimized using a recursive method. Starting with the proton variables, $probNN_p(p)$, $probNN_K(p)$ and $probNN_\pi(p)$ two variables are constructed: $\Delta_{pK} = probNN_p(p) - probNN_K(p)$ and $\Delta_{p\pi} = probNN_p(p) - probNN_\pi(p)$. These variables are chosen to better contrast the hypothesis that the proton has been well identified against the hypothesis where the proton has been misidentified as a kaon or a pion, this allows to better remove the background from misidentification of a proton as a pion or a kaon described in Sec. 6.2.5. First the Δ_{pK} is optimized against $\Delta_{p\pi}$ by looking at how the purity of the signal and the significance varies in the mass region $[2281.47, 2293.33]$ MeV/c for each combination of selections. A fit to the $m_{pK^-\pi^+}$ invariant mass is performed to extract the number of signal (N_S) and background (N_B) events, from which the purity is estimated as the ratio N_S/N_B and the significance as $N_S/\sqrt{N_B + N_S}$. The optimization is performed only on a reduced sample for the TIS category MagUp, since it is not expected to vary among trigger categories or magnet polarities. The model used to fit the invariant mass includes two Crystal Ball functions sharing the mean and standard deviation and one Gaussian, sharing the mean but not the standard deviation. The invariant mass fit is not shown since a detailed description of it is given in Sec. 6.2.6. Several values have been studied, the optimal point is found around $\Delta_{pK} > 0.1$ hence a zoom on this region has been performed. The results are shown in Fig. 6.10 (left), the optimal selection for Δ_{pK} and $\Delta_{p\pi}$ is found around the region $\Delta_{pK} > 0.1$ and $\Delta_{p\pi} > 0.4$, which has been chosen based on the significance ratio plot (upper, left). The purity increases monotonically so it cannot be used to make a decision alone. Note that the selection $\Delta_{pK} > 0.08$ could also work, however the purity plot indicates

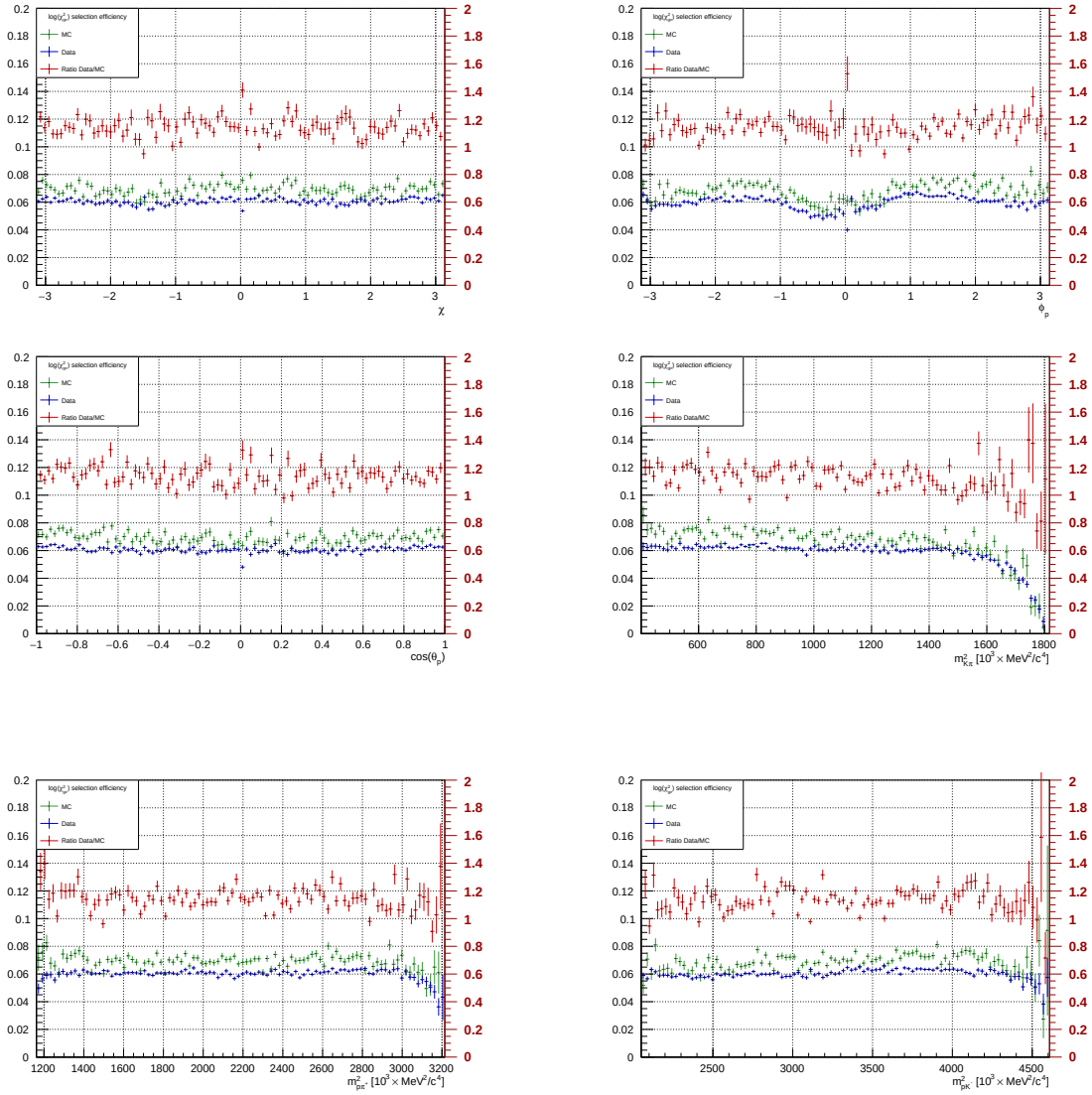

Figure 6.9: Comparison between the $\log(\chi^2_{\rm IP})$ selection efficiency obtained in the simulation (green) and in data (blue). The red histograms are the ratio of the green and blue ones, with the corresponding y axis displayed in red on the right side of the plot.

a higher purity for higher values of Δ_{pK}, hence the selection $\Delta_{pK} > 0.1$ has been chosen. Once the selection on the proton variables has been fixed, the pion and kaon variables are also studied using the same technique. Based on the significance ratio shown in the upper right plot of Fig. 6.10, the values $probNN_K(K) > 0.1$ and $probNN_\pi(\pi) > 0.0$ have been chosen, which select 98% of signal events and leave 2.2% of background events. A similar optimization has been performed using another set of PID

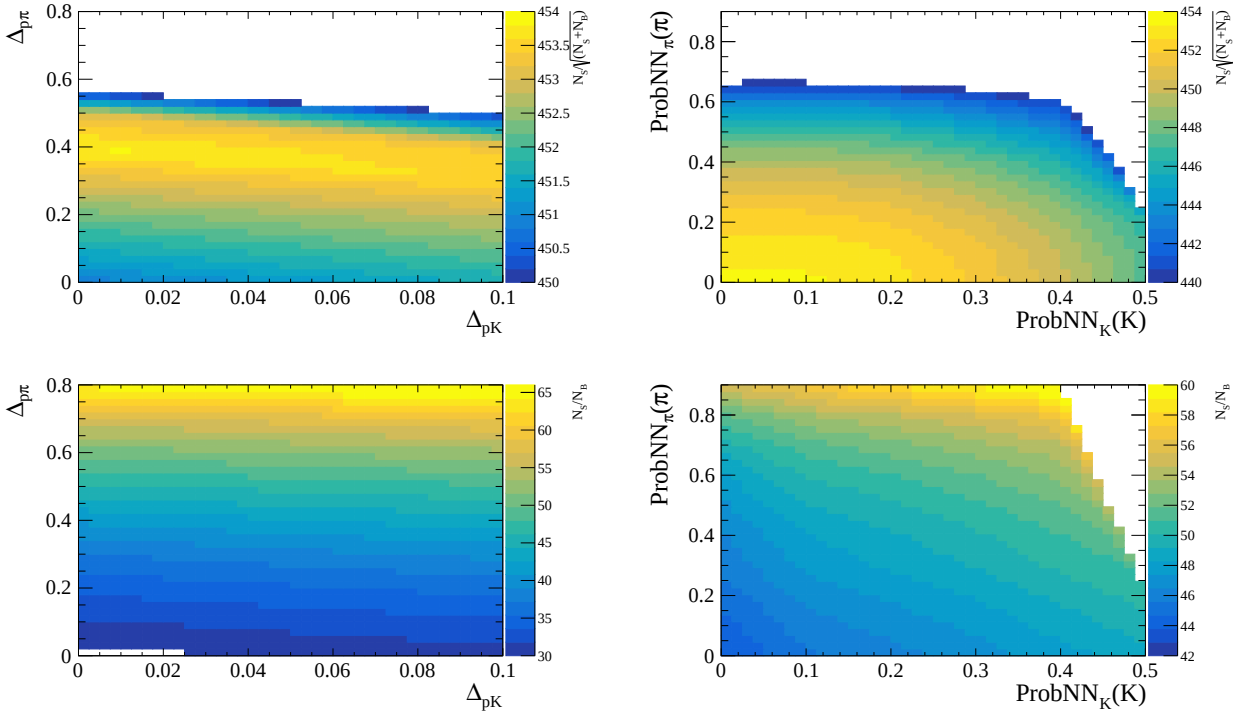

Figure 6.10: Left: the combination of ProbNN variables $\Delta_{p\pi}$ vs Δ_{pK} are shown as a function of (top) $N_S/\sqrt{N_B+N_S}$ and (bottom) N_S/N_B. Right: the $probNN_\pi(\pi)$ selections are shown as a function of (top) $N_S/\sqrt{N_B+N_S}$ and (bottom) N_S/N_B, with the additional selection $\Delta_{pK} > 0.1$ and $\Delta_{p\pi} > 0.4$ fixed.

variables, the $PIDx$ variables. They are obtained in a different way than the ProbNN variables, as explained in Sec. 3.2.3, and they are used in the HLT lines already. The equivalent optimized selection is obtained for $PID_p(p) > 13.5$ and $(PID_p(p) - PID_p(K)) > 6$, corresponding also to 98% of signal events and 2.2% of background events. The two set of variables are thus equivalent with respect to this optimization procedure. Finally, the probNN variables have been chosen since they show a better agreement between data and simulation.

6.2.5 Backgrounds

There exists three types of possible backgrounds:

1. *Mis-ID background*: three-body decays where one of the final-state particles is wrongly identified.

Mis-ID	Final state	Possible decays	BR	Comments
$\pi^+ \to K^+$	pK^-K^+	$\Lambda_c^+ \to pK^-K^+$	$(1.06 \pm 0.06) \times 10^{-3}$	
$K^- \to \pi^-$	$p\pi^-\pi^+$	$\Lambda_c^+ \to p\pi^+\pi^+$	$(4.61 \pm 0.28) \times 10^{-3}$	
$p \to \pi^+$	$\pi^+K^-\pi^+$	$D^+ \to K^-\pi^+\pi^+(\pi^0)$	9.13 ± 0.19 (5.99 ± 0.18)	SEEN, additional π^0 not reconstructed
$p \to K^+$	$K^+K^-\pi^+$	$D_s^+ \to K^+K^-\pi^+(\pi^0)$, $D^+ \to K^+K^-\pi^+$	5.39 ± 0.15 (6.2 ± 0.6), $(9.54 \pm 0.26) \times 10^{-3}$	SEEN, additional π^0 not reconstructed
$p \to K^+$ & $K^- \to \pi^-$	$K^+\pi^-\pi^+$	$D^+ \to K^+\pi^-\pi^+$, $D_s^+ \to K^+\pi^-\pi^+$	$(5.28 \pm 0.23) \times 10^{-4}$, $(6.5 \pm 0.4) \times 10^{-3}$	$D+$ mode is DCS[1]
$p \to \pi^+$ & $K^- \to \pi^-$	$\pi^-\pi^+\pi^+$	$D^+ \to \pi^-\pi^+\pi^+$, $D_s^+ \to \pi^+\pi^-\pi^+$	$(3.18 \pm 0.18) \times 10^{-3}$, 1.08 ± 0.04	
$\pi^+ \to K^+$ & $K^- \to \pi^-$	$pK^+\pi^-$	$\Lambda_c^+ \to pK^+\pi^-$	$(1.11 \pm 0.18) \times 10^{-4}$	DCS[1]
$p \to \pi^+$ & $\pi^+ \to p$	π^+pK^-	$\Lambda_c^+ \to \pi^+pK^-$	6.28 ± 0.32	SEEN, signal final state
$p \to K^+$ & $K^- \to \pi^-$& $\pi^+ \to K^+$	$K^+K^+\pi^-$	$D_s^+ \to K^+K^+\pi^-$	$(1.28 \pm 0.04) \times 10^{-4}$	DCS

Table 6.6: Mis-ID backgrounds, BR are from Ref. [11]. DCS stands for "Doubly Cabibbo Suppressed" decays.

2. Partially reconstructed backgrounds: those are four-body decays where one of the final particles (Y) has not been reconstructed, $X \to pK^-\pi^+Y$.

3. Combinatorial background: random combinations of p, K and π particles which are not originating from a Λ_c^+ decay.

For the first type of background, there are few decays that may mimic the signal or peak in the signal region. The mis-identification can happen for one particle (6 possibilities), two particles (12 possibilities) or even three particles at the time (24), for a total of 42 possibilities. However not all the misidentification have the same probability to occur; for instance the double misidentification is less likely than the single one and the probability to misidentify three particles at a time is very small. Furthermore, each particle has a different mis-id probability itself, see Sec. 3.2.3, Fig. 3.12, for instance the proton is more likely misidentified than the kaon. Not all the combinations correspond to a specific decay mode, the list of physically possible decay mode is given in Tab. 6.6, along with the associated branching ratios. For the partially reconstructed backgrounds, the mass of the non reconstructed particle has to be small or the reconstructed mass $m_{pK^-\pi^+}$ would be outside the region of interest. There are three-body decays to hadronic final states with an additional non reconstructed photons, for instance $D^+ \to K\pi^+\pi^+\pi^0$ and $D_s^+ \to K^+K^-\pi^+\pi^0$, where, in addition to the non reconstructed photon, a proton has been misidentified either as a pion or as a kaon ($p \to \pi^+$ and $p \to K^+$); however those decay would peak outside the mass window since the D^+ mass is $m_{D^+} = 1869.65 \pm 0.05\,\mathrm{MeV}/c^2$[11], and the D_s^+ mass, $m_{D_s^+} = 1968.34 \pm 0.07\,\mathrm{MeV}/c^2$ [11]. In addition those decays are suppressed with

respect to the signal, since they are Doubly Cabibbo Suppressed (DCS[1]). The presence of these physical backgrounds is studied by reconstructing the invariant mass of the three daughter particles with different mass hypotheses, where the particle's four-vector is computed again changing the value of the mass to a new mass hypothesis. Then, two-dimensional plots featuring the three-body invariant mass $m_{pK^-\pi^+}$ against the same invariant mass with the new mass hypothesis are drawn, the mis-ID contributions appear as lines on these two-dimensional plots. The three mis-ID combinations giving a sizable background contributions to the $\Lambda_c^+ \to pK^-\pi^+$ decays are shown in Fig. 6.11 for the TOS category (magnet up): $(p \to \pi^+)$ (bottom-left),$(p \to K^+)$ (bottom-right) and the double mis-ID $(p \to \pi^+)$ and $(\pi^+ \to p)$ (top-right), along with one combination which has no significant contribution $(p \to \pi^+)$ and $(K^- \to \pi^-)$ (top-left). In Fig. 6.12 the one-dimensional projections, with the new modified hypothesis (same as the x axis on the left plots), are shown. The same figures for the TIS category, along with other misidentification combinations of Table 6.6 that may contribute, are shown in Appendix B. Two lines appear clearly in Fig. 6.12, one around the D^+ mass, $m_{D^+} = 1869.65 \pm 0.05\,\text{MeV}/c^2$[11], for the $(p \to \pi^+)$ misidentification, the second one around the D_s^+ mass, $m_{D_s^+} = 1968.34 \pm 0.07\,\text{MeV}/c^2$[11], for the $(p \to K^+)$ misidentification. For the third line appearing in the double misidentification case $(p \to \pi^+)$ and $(\pi^+ \to p)$, this exchange results in the same final state as the signal, however this is still a background, especially when taking a pair of particles to compute the invariant masses: $m^2_{pK^-}$, $m^2_{\pi^+p}$ or $m^2_{K^-\pi^+}$. The same misidentification plots after applying the final offline selections, listed in Tab. 6.4, are shown in Fig. 6.13 and Fig. 6.14. The mis-id contributions are considerably reduced but still present. The residual contribution has been estimated using the following method.

1. Using the data after the final selections, a fit of the invariant mass is performed to obtain the mean value ($\mu_{\Lambda_c^+}$), the standard deviation ($\sigma_{\Lambda_c^+}$) and the number of signal events in the window $\Delta m_{3\sigma} = \mu \pm 3\sigma$, the fit results are shown in Fig. 6.15 (left).

2. In order to fit the misidentification peaks appearing in the one dimensional distribution of $m_{(p\to\pi^+)K^-\pi^+}$ and $m_{(p\to K^+)K^-\pi^+}$, a pre-fit of the data without selections and outside the signal window $\Delta m_{3\sigma}$ is performed to find the mean value and the standard deviation of those peaks.

3. A second fit of the misidentification peaks is then performed to the data after offline selections, always outside the signal window $\Delta m_{3\sigma}$, fixing the mean and sigma values to the results found in the previous step. The results are shown in Fig. 6.15 (right), the number of D^+ ($N^{!3\sigma}_{D^+}$) and D_s^+ ($N^{!3\sigma}_{D_s^+}$) is extracted from the corresponding fit.

4. Finally, the number of residual background is extrapolated to the $\Delta m_{3\sigma}$ signal region as

$$N^{3\sigma}_{D^+/D_s^+} = N^{!3\sigma}_{D^+/D_s^+} \times \frac{\Delta m_{3\sigma}}{\Delta m_{down} + \Delta m_{up}} \tag{6.3}$$

   where Δm_{down} and Δm_{up} are the sideband regions outside $\Delta m_{3\sigma}$, shown in Fig. 6.15 (left).

[1]The singly *Cabibbo suppressed* (SCS or CS) decays have been discussed in Sec. 2.2.1. I The DCS decays are more suppressed than the singly CS decays (which are $\mathcal{O}(\lambda)$) since they involve two suppressed quark transitions implying a CKM factor $\mathcal{O}(\lambda^2)$.

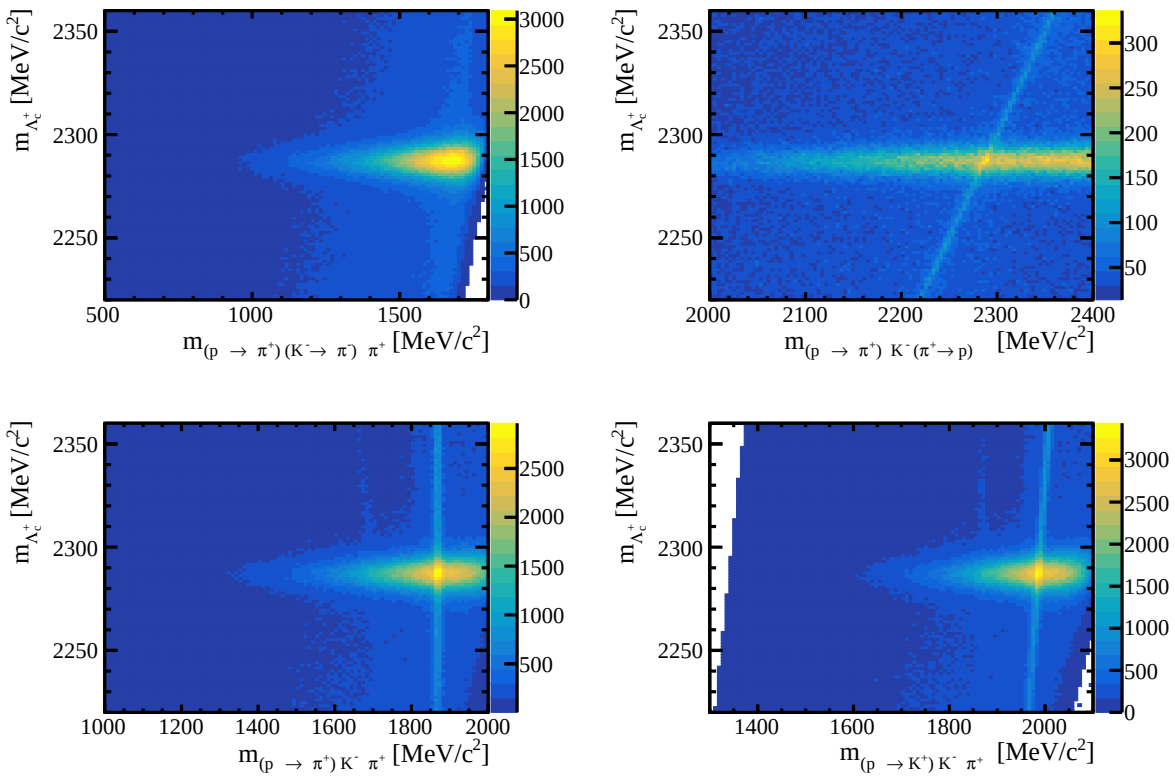

Figure 6.11: Left: reconstructed $m_{pK^-\pi^+}$ invariant mass vs different mass substitutions for reconstructed $\Lambda_c^+ \to pK^-\pi^+$ decays without offline selections. Top: double misidentification $p \to \pi^+$ and $K^- \to \pi^-$, double misidentification $p \to \pi^+$ and $\pi^+ \to p$. Bottom: simple misidentification $p \to \pi^+$ and $p \to K^-$. The horizontal band is the signal, vertical and diagonal bands are the misidentification backgrounds described in the text.

The percentage of remaining mis-ID background from D^+ and D_s^+ in the $\Delta m_{3\sigma}$ window is shown in Tab. 6.7. The number of signal Λ_c^+ and residual background obtained from the invariant mass fit are also shown. The residual contamination from D^+ and D_s^+ decays is less than 1% and 2% respectively.

Trigger	TIS [%]		TOS[%]	
Polarity	Mag Up	Mag Down	Mag Up	Mag Down
D^+	0.85	0.90	0.69	0.80
D_s^+	1.37	1.37	1.25	1.35
Λ_c^+	97.23	97.08	97.27	97.11
Background	2.78	2.92	2.73	2.89

Table 6.7: Fraction of events in the $\Delta m_{3\sigma}$ window for the D^+, D_s^+, Λ_c^+ and residual background. The percentages have been computed on the data after applying the offline selections. The two polarities and two trigger categories are shown.

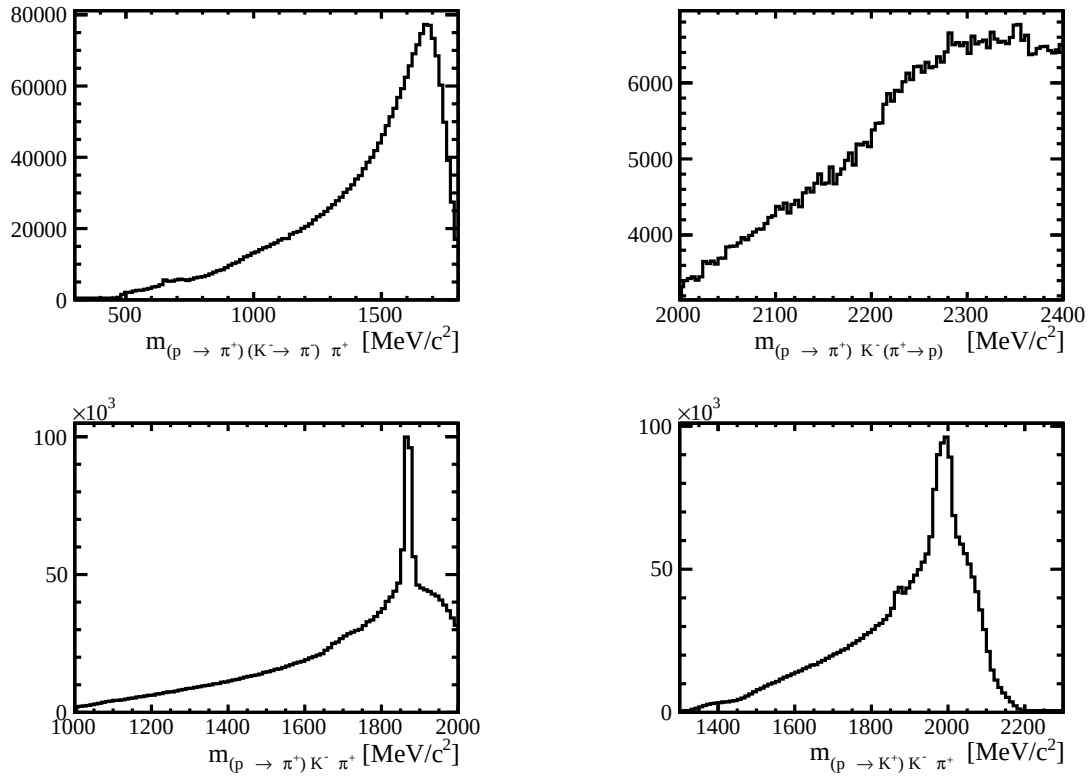

Figure 6.12: One dimensional projection of the $m_{pK^-\pi^+}$ invariant mass with different mass substitutions for reconstructed $\Lambda_c^+ \to pK^-\pi^+$ decays without offline selections. Top: double misidentification $p \to \pi^+$ and $K^- \to \pi^-$, double misidentification $p \to \pi^+$ and $\pi^+ \to p$. Bottom: simple misidentification $p \to \pi^+$ and $p \to K^-$. Two peaks appear around the mass of the D^+ (bottom left) and D_s^+ (bottom right), which correspond to the mother particles of the misidentified decays listed in Tab. 6.6.

6.2.6 Purity of the signal

After the offline selections, the residual background is evaluated by mean of fit to the $pK^-\pi^+$ invariant mass, which is also used to separate the signal candidates from the background. The signal shape is modeled by two Crystal-Ball (CB) functions and a Gaussian function, the background is modeled by an exponential function. The CB is a probability density function (PDF) which has a Gaussian core and power-low tails allowing for asymmetric tails, both the function itself and the first derivative are continuous,

$$CB(x;\bar{x},\sigma,\alpha,n) = N \begin{cases} \exp\left(-\frac{(x-\bar{x})^2}{2\sigma^2}\right) & \text{for } \alpha > 0, \frac{(x-\bar{x})}{\sigma} > -\alpha \\ A\left(B - \frac{(x-\bar{x})}{\sigma}\right)^{-n} & \text{for } \alpha > 0, \frac{(x-\bar{x})}{\sigma} \leq -\alpha \end{cases}, \tag{6.4}$$

in which $A = \left(\frac{n}{|\alpha|}\right)^n \exp\left(-\frac{|\alpha^2|}{2}\right)$, $B = \frac{n}{|\alpha|} - |\alpha|$ and N is a normalisation factor. Then $\bar{x}$ can be seen as the mean value of the Gaussian part of the CB distribution, and it is common to the 2 CBs and to the Gaussian. Finally, the n is the exponent of the power law tail and α sets the limits between the Gaussian and the power law shapes. There is one set of parameter per CB: $(n_1, \alpha_1, \sigma_1)$ for CB1 and $(n_1, \alpha_1, \sigma_2)$ for CB2. The fit to the $pK^-\pi^+$ invariant mass for the candidates passing the selections

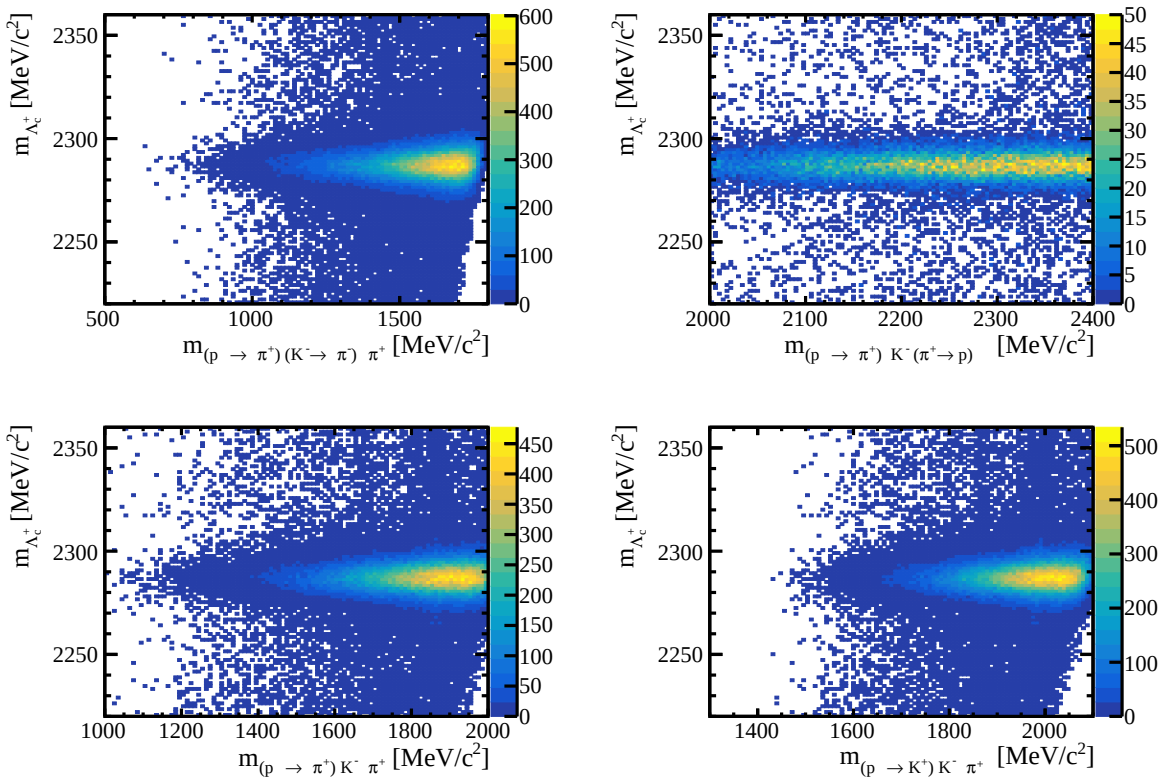

Figure 6.13: Left: reconstructed $m_{pK^-\pi^+}$ invariant mass vs different mass substitutions for reconstructed $\Lambda_c^+ \to pK^-\pi^+$ decays after offline selections. Top: double misidentification $p \to \pi^+$ and $K^- \to \pi^-$, double misidentification $p \to \pi^+$ and $\pi^+ \to p$. Bottom: simple misidentification $p \to \pi^+$ and $p \to K^-$. The horizontal band is the signal, vertical and diagonal bands are the misidentification backgrounds described in the text.

is shown in Fig. 6.16, where on the right side the same fit with the y-axis in logarithmic scale is shown. The results of the fit are given in Tab. 6.8, where the last 4 lines shows the total number of signal (N_{bkg}) and background (N_{signal}) events, and the total number of signal ($N_{bkg}^{3\sigma}$) and background ($N_{signal}^{3\sigma}$) events in the 3 sigma region defined using the Gaussian sigma (σ_3) obtained from the fit. The same fit for the other trigger and polarity categories are shown in Appendix D. From this fit, the number of residual background events in the mass window $[2281.47, 2293.33]\,\text{MeV}/c^2$ is 2.89%. This window is selected using the standard deviation of the Gaussian σ_3 (which dominates the fit) and taking a window of $\pm\sigma_3$ around $\bar{x}$. The signal purity in the mass window is 97.12%. The fit to the $m_{pK^-\pi^+}$ invariant mass is used to extract signal events against background using the *sPlot* technique [210]. Fig. 6.17 shows the 2.89% residual background (in green) over the one-dimensional projection of the five phase space variables. The background is very small but it must be taken into account since it can contribute to the resonances lineshapes, as for instance for the $K^*(892)$ resonance in the $m_{K\pi}$ spectrum.

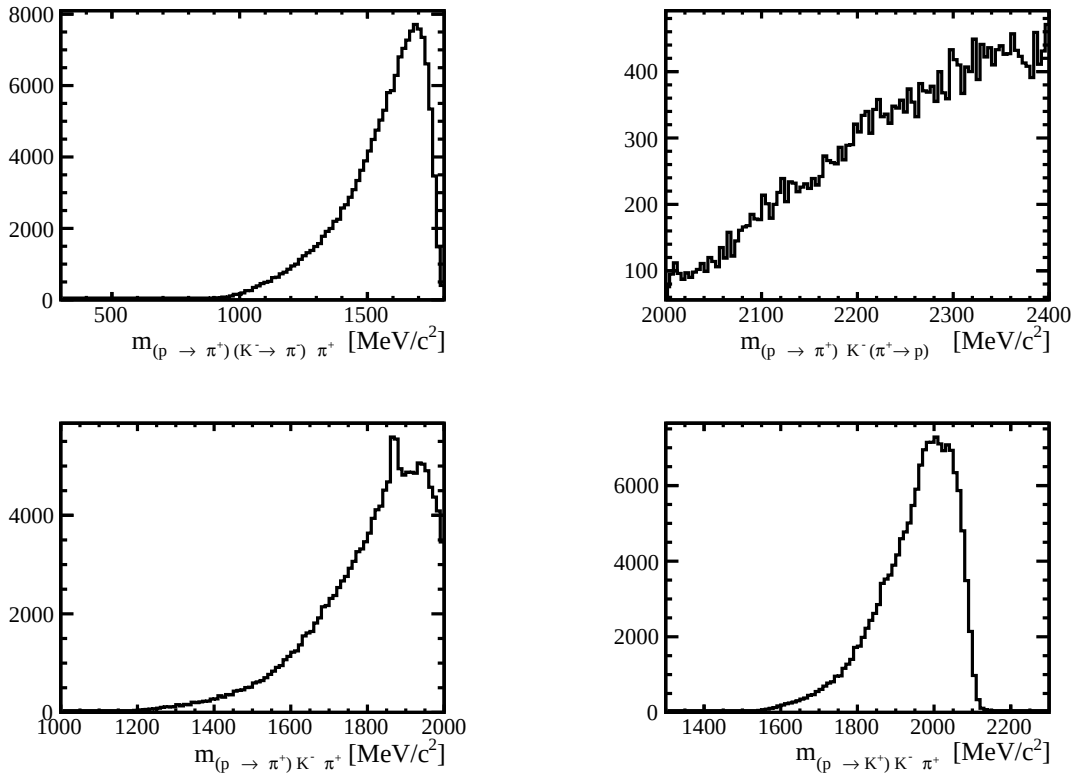

Figure 6.14: One dimensional projection of the $m_{pK^-\pi^+}$ invariant mass with different mass substitutions for reconstructed $\Lambda_c^+ \to pK^-\pi^+$ decays after offline selections. Top: double misidentification $p \to \pi^+$ and $K^- \to \pi^-$, double misidentification $p \to \pi^+$ and $\pi^+ \to p$. Bottom: simple misidentification $p \to \pi^+$ and $p \to K^-$. Two peaks appear around the mass of the D^+ (bottom left) and D_s^+ (bottom right), which correspond to the mother particles of the misidentified decays listed in Tab. 6.6.

6.2.7 Corrections to simulation

A Monte Carlo (MC) simulation is used to reproduce the $\Lambda_c^+ \to pK^-\pi^+$ decays and the detector response. In this analysis the simulation is mainly used to compute efficiencies in order to include it in the final amplitude fit. The simulation is performed within the LHCb software, more details can be found in Sec. 3.2.6, however due to the complexity of the LHCb detector and the variety of effects induced at each step of the detection chain, the simulation does not reproduce perfectly the data. For this reason the simulation sample has to be corrected for the L0 trigger response, the PID response and the Λ_c^+ kinematics, which includes the correction of the generated event multiplicity. The corrections are computed separately and added as weights to the simulation sample and will be included to the amplitude fit.

L0 trigger

The $L0$ trigger enters in the very beginning of the detection chain and it relies on the information of HCAL, ECAL and muon stations. The L0 Hadron TOS response is not well reproduced in the simulation and needs to be corrected using calibration samples obtained from D^0 and D^* decays

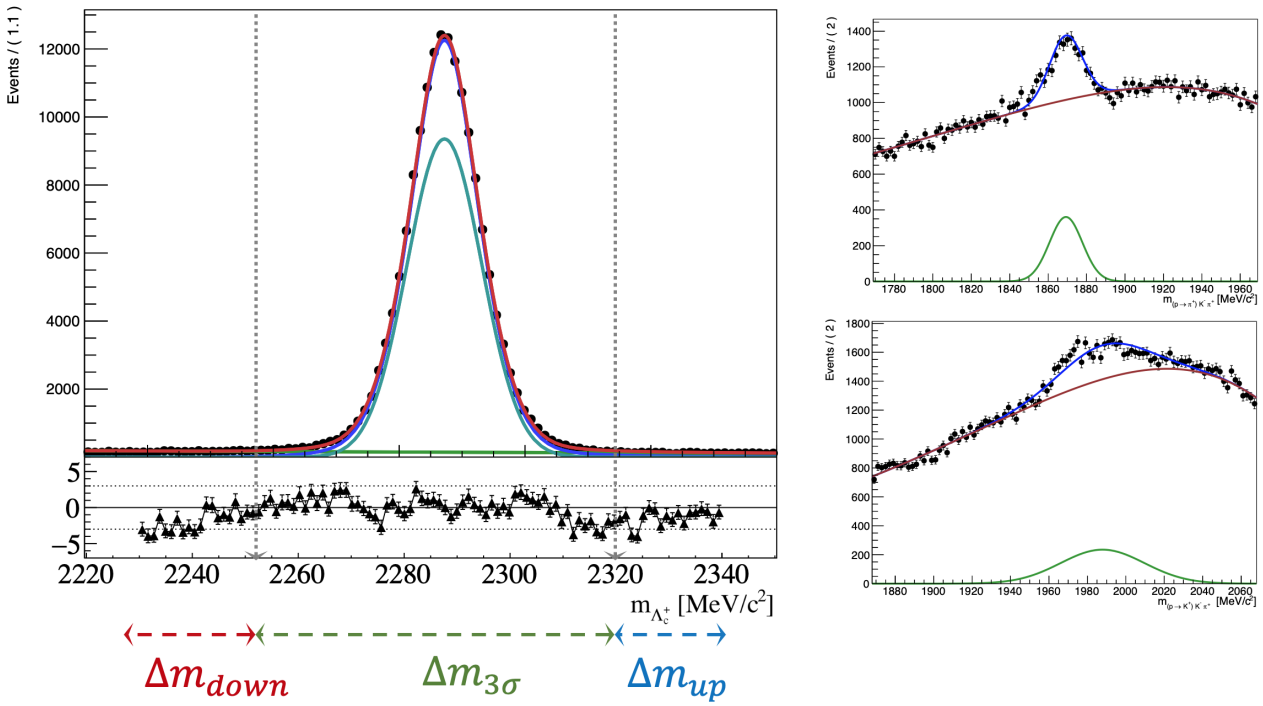

Figure 6.15: Left: invariant mass fit with three zones defined as: $\Delta m_{3\sigma}$ for the signal region, Δ_{down} and Δ_{up} outside the signal region. Right: fit to the invariant $m_{pK^-\pi^+}$ masses with swap hypothesis $p \to \pi^+$ and $p \to K^-$, for reconstructed $\Lambda_c^+ \to pK^-\pi^+$ decays before applying the offline selections.

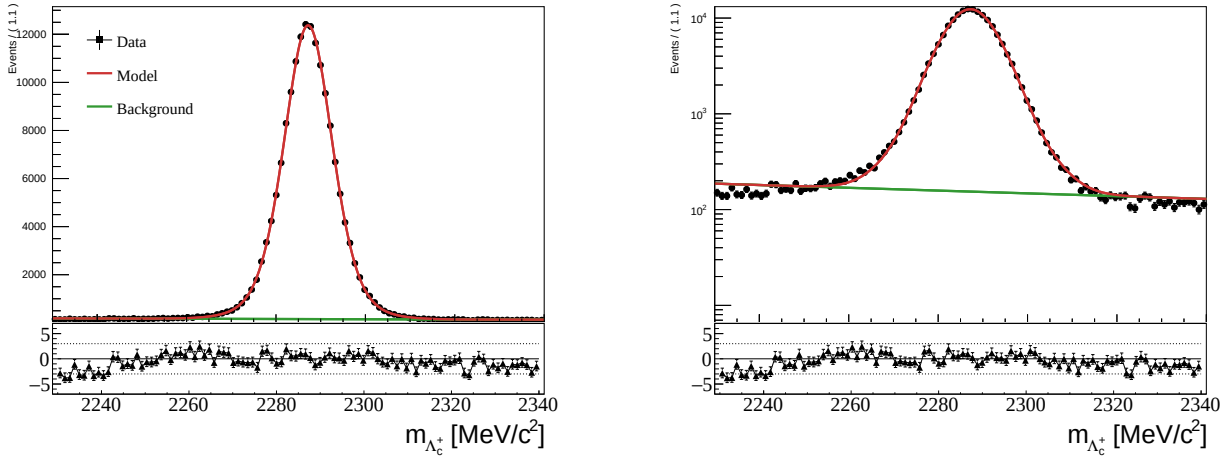

Figure 6.16: Left: fit to the $m_{pK^-\pi^+}$ invariant mass. Right: same fit, with the y-axis in logarithmic scale. Data are shown in black, the fit model (2CBs and a Gaussian function) is shown in red and the background (exponential) in green. The lower pads show the residues of the fit.

Fit result				
Trigger	TIS [%]		TOS[%]	
Polarity	Mag Up	Mag Down	Mag Up	Mag Down
Variable				
α_1	3.68 ± 0.79	2.58 ± 0.12	2.49 ± 0.030	3.69 ± 0.79
α_2	-4.78 ± 0.93	-4.784 ± 4.78	-4.94 ± 5.29	-4.78 ± 0.93
n_1	3.41 ± 5.69	2.06 ± 0.48	3.07 ± 0.47	3.41 ± 5.70
n_2	1.08 ± 6.47	10.00 ± 5.52	4.11 ± 6.16	1.81 ± 6.47
σ_1	3.50 ± 0.60	4.45 ± 0.13	3.89 ± 0.02	3.50 ± 0.60
σ_2	9.52 ± 0.40	10.36 ± 0.57	9.96 ± 0.04	9.52 ± 0.40
σ_3	5.51 ± 0.22	6.23 ± 0.31	5.73 ± 0.01	5.50 ± 0.22
f_{CB}	0.30 ± 0.20	0.84 ± 0.05	0.30 ± 0.20	0.30 ± 0.20
f_{Gauss}	0.28 ± 0.05	0.60 ± 0.08	0.28 ± 0.05	0.28 ± 0.05
$\bar{x}$	2287.2 ± 0.02	2287.4 ± 0.01	2287.2 ± 0.01	2287.2 ± 0.02
N_{bkg}	14967 ± 155	23161 ± 192	12716 ± 144	14967 ± 155
N_{signal}	152121 ± 0.00	219112 ± 0.00	136159 ± 0.00	152121 ± 0.00
$N_{bkg}^{3\sigma}$	3.23%	3.46%	2.85%	2.89%
$N_{signal}^{3\sigma}$	96.77%	96.53%	97.16%	97.12%

Table 6.8: Results of the fit to the $m_{pK^-\pi^+}$ invariant mass for the two trigger categories and polarities.

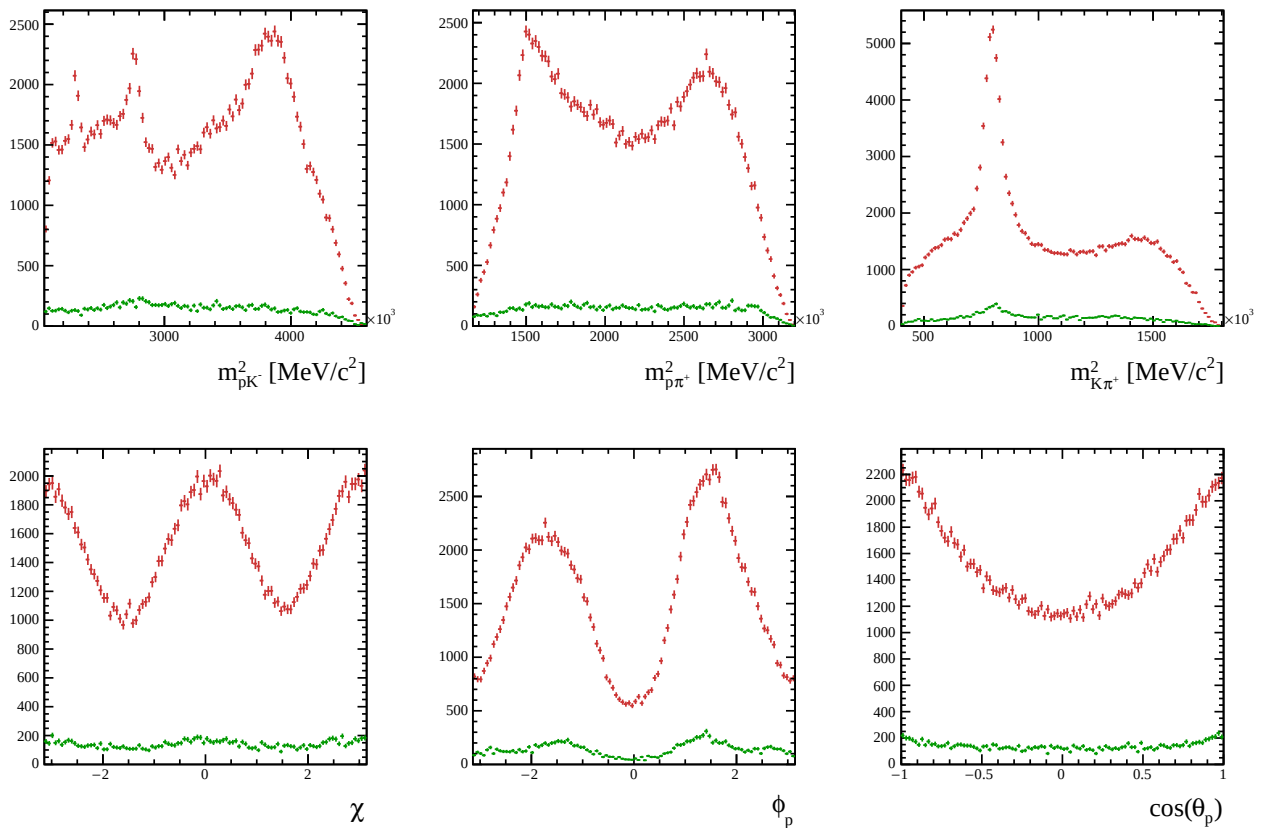

Figure 6.17: One-dimensional projections of the phase space variables. The red curves are the data after the offline selections, the green curve is the background estimated using the *sPlot* technique.

where well identified pion and kaon are obtained. For calibrating protons, $\Lambda \to p\pi^-$ and $\Lambda_c^+ \to pK^-\pi^+$ decays are used instead. Tables containing the L0 Hadron TOS decision efficiency as a function of the real transverse energy of the particles when arriving at the HCAL surface are provided. There exists one table per particle type, per region in the calorimeter (inner and outer), per data taking year and magnet polarity. More details on how the efficiency are computed from data can be found in Ref. [211]. The information per track contained in the tables needs to be combined and additional effects must be taken into account when doing that. For a three-body decay $a \to 1+2+3$, the efficiency of triggering on the event is a combination of the efficiencies of each one of the final tracks. Thus denoting ϵ_i the efficiency of track i, the combined L0 hadron efficiency ϵ_a is:

$$\epsilon_a = \epsilon_1 \times (1-(\epsilon_2+\epsilon_3)+\epsilon_2 \times (1-(\epsilon_1+\epsilon_3))+\epsilon_3 \times (1-(\epsilon_1+\epsilon_2))+ \\ \epsilon_1 \times \epsilon_2 \times (1-\epsilon_3)+\epsilon_1 \times \epsilon_3 \times (1-\epsilon_2)+\epsilon_2 \times \epsilon_3 \times (1-\epsilon_1)+\epsilon_1 \times \epsilon_2 \times \epsilon_3 \quad (6.5)$$

which includes the efficiency of triggering on only one particle (first three terms), on two particles and not the third one (next three terms) or triggering on the three at the same time (last term). The additional effects have been computed in separate tables and they include the overlap between signal track clusters, the average occupancy of the calorimeter separated in inner and outer regions, the relative calibration between HCAL cells which varies due to the aging of the detector, and the fraction of signal tracks with no energy deposit in the HCAL, since not all tracks reach the HCAL. All these additional tables are available per data taking year and magnet polarity, and instructions on how to correct the efficiency of Eq. 6.5 are given in [211]. The difference between the efficiency obtained from the simulation and the one obtained using the calibration tables is shown in Fig. 6.18 for a subsample of simulated events. In general, the simulation overestimates the efficiencies. Finally, an event-by-event weight containing the L0 Hadron TOS efficiency of the Λ_c^+ is added to the TOS category simulation samples. No reweighting procedure is necessary for the TIS trigger category used in this analysis since no L0Hadron TIS line are used.

PID

As for the L0 simulation, the PID response is not perfectly reproduced in the simulation and a calibration using data-drive methods is necessary. Within LHCb, there are few approaches available, described in Ref. [212] and [213], all based on dedicated calibration samples recorded in parallel to the data taking. In this analysis the PIDCorr package, described in Ref. [214] and provided within the LHCb collaboration is used. The classic PIDCalib approach uses the kinematics of the signal tracks to obtain event-by-event weights to correct for the PID response, whereas in the PIDCorr package the PID variables are transformed directly to match the data by mean of an unbinned calibration PDF. The calibration sample used in this analysis is obtained using the $\Lambda_b^0 \to \Lambda_c^+\pi^-$ decays for protons and $D^0 \to K^-\pi^+$ decays for kaons and pions. In Fig. 6.19, the simulated PID variables used in this analysis are compared with the background subtracted data, for the case with the PIDCorr correction (magenta) or without (cyan). Both curves have also the kinematic weights, explained in the next paragraph, applied. Overall, the agreement is improved, especially for $ProbNN_{pi}(p)$

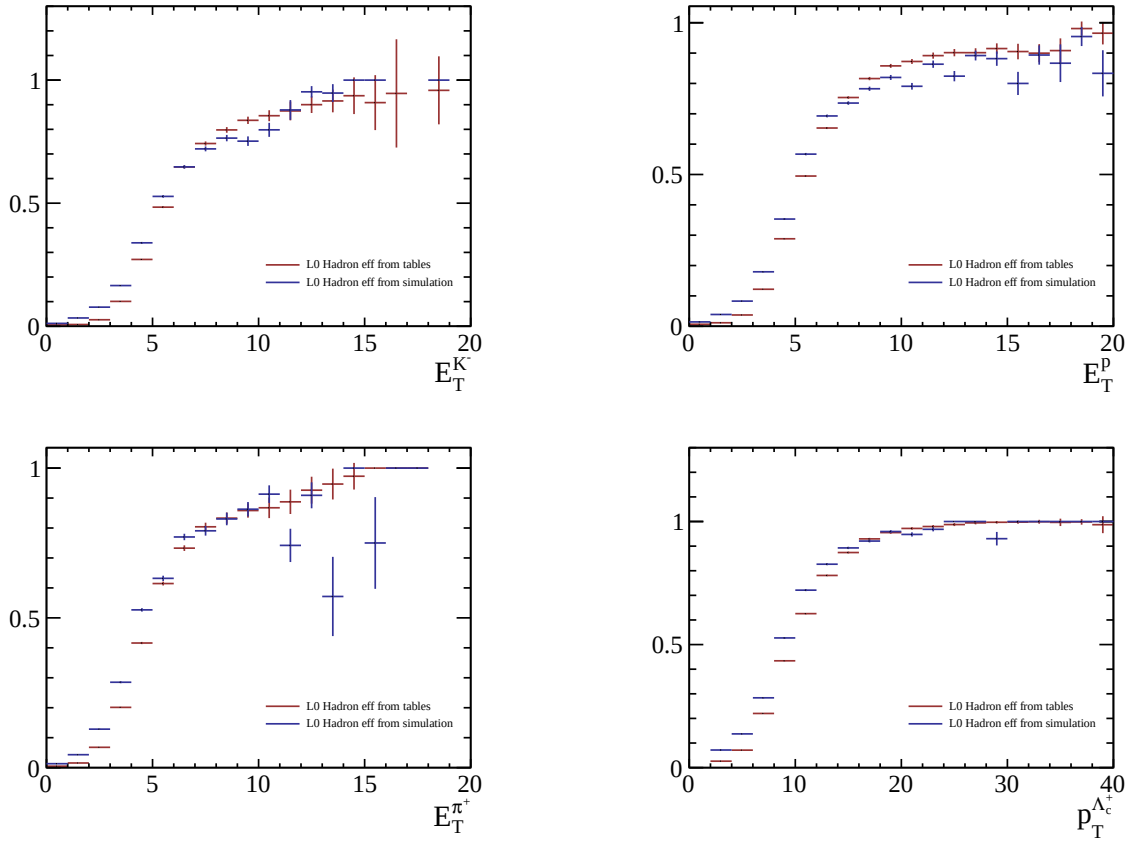

Figure 6.18: L0 Hadron efficiencies as a function of the transverse energy for the K^-, p and π^+ decay products, and as a function of the transverse momentum for the Λ_c^+, are shown. The efficiencies obtained with the LHCb simulation are shown in blue and with the calibration tables in red.

and $ProbNN_k(K)$, or equivalent, for $ProbNN_p(p)$ and $ProbNN_k(p)$, when applying the PIDCorr algorithm.

Kinematic reweighting

In order to have a better agreement over the kinematic variables (p, p_T, y, ...) between the simulated sample and the data, an additional correction is applied to the event multiplicity, the Λ_c^+ transverse momentum, rapidity and lifetime. This variables are not well reproduced in the simulation and by correcting them the simulation of the other variables will be also improved. The correction is calculated by comparing the simulation to the data and computing an event-by-event weight which will compensate for the difference between the two. This procedure is called kinematic and multiplicity reweighting and it is performed using the GBReweighter from the `hep_ml` library [215], which is a machine learning tool. The reweighter is trained with a subsample of the simulation against the sweighted data (to select only signal events). The input variables used are: the reconstructed Λ_c^+ transverse momentum $p_T^{\Lambda_c^+}$, the rapidity $y_{\Lambda_c^+}$, the lifetime $\tau(\Lambda_c^+)$ and the number of VELO tracks in the event ($nTracks$). The training is performed per trigger category and magnet polarity separately. Fig. 6.20 shows the distributions of the input variables from simulation, before (dashed green lines)

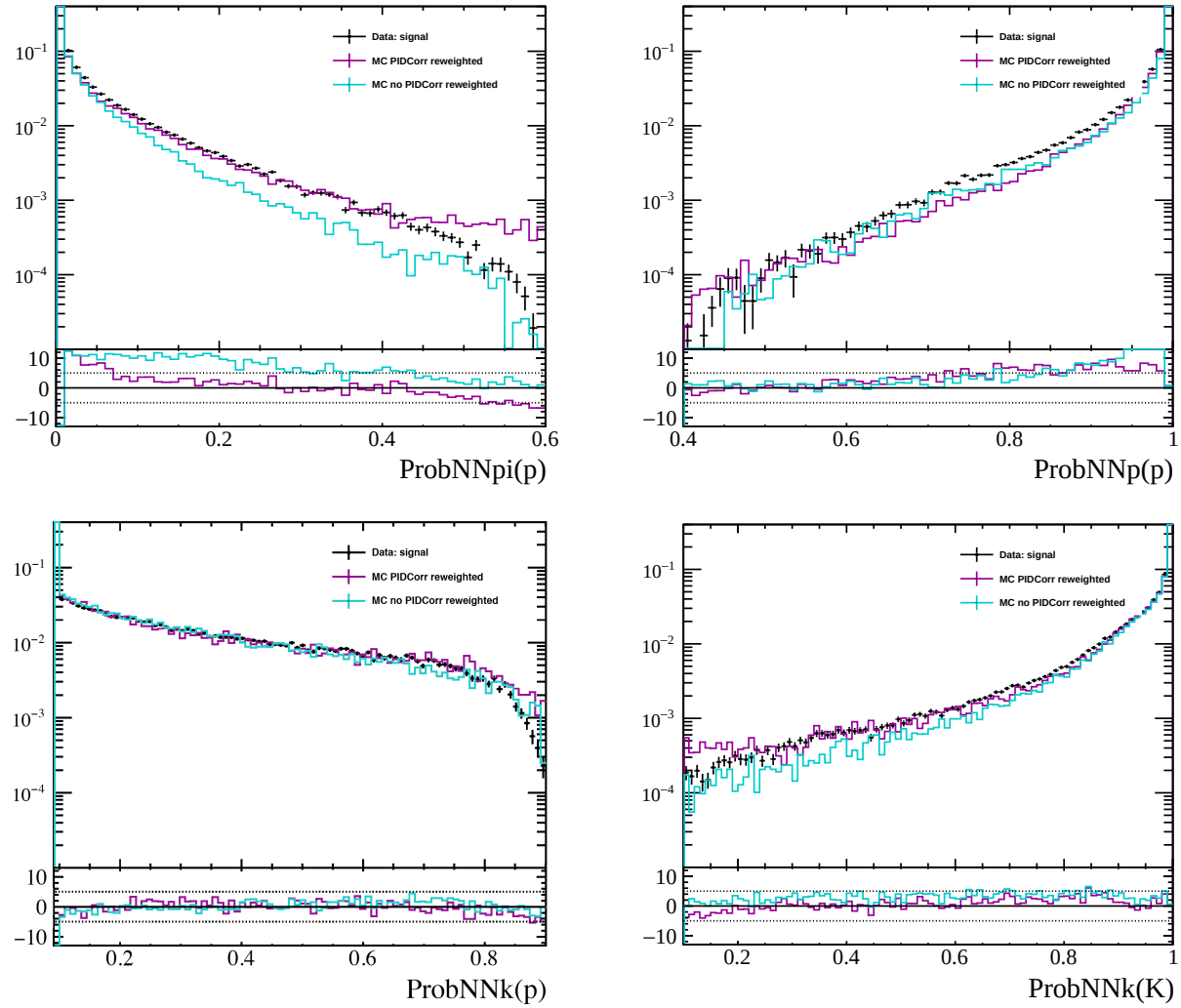

Figure 6.19: Comparison plots between data and simulation: the background subtracted data are shown in black for the signal, the simulation with PIDCorr is shown in magenta and without it in cyan.

and after (blue lines) the reweighting procedure, compared to the *sPlot* $\Lambda_c^+ \to pK^-\pi^+$ data. The lower pad shows the pulls between the simulation (with or without reweighting) and data. The Data/MC differences which where present before are now corrected for and the weighted simulation matches the data better. The effect of the reweighting procedure on the other relevant variables of the analysis is shown in Fig. 6.21 and Fig. 6.22. By looking at the pulls, one can see that the comparison for the probNN variables is less good than for the other variables, for this reason an additional verification is performed. To be sure that the simulation does not induce any bias over the phase space, profile histograms for each of the PID combination of variables used in the offline selection (see Tab. 6.4) featuring the phase space variables are build for simulation and data in order to compare them and verify that they behave similarly. An example for the $(ProbNN_p(p) - ProbNN_\pi(p))$ combination of variables is shown in Fig. 6.23. The two profiles look very similar and no bias seems to be introduced, hence the PID selections can be applied safely. Similar plots for the $(ProbNN_p(p) - ProbNN_K(p))$

and $ProbNN_K(K)$ variables are shown in Appendix C.

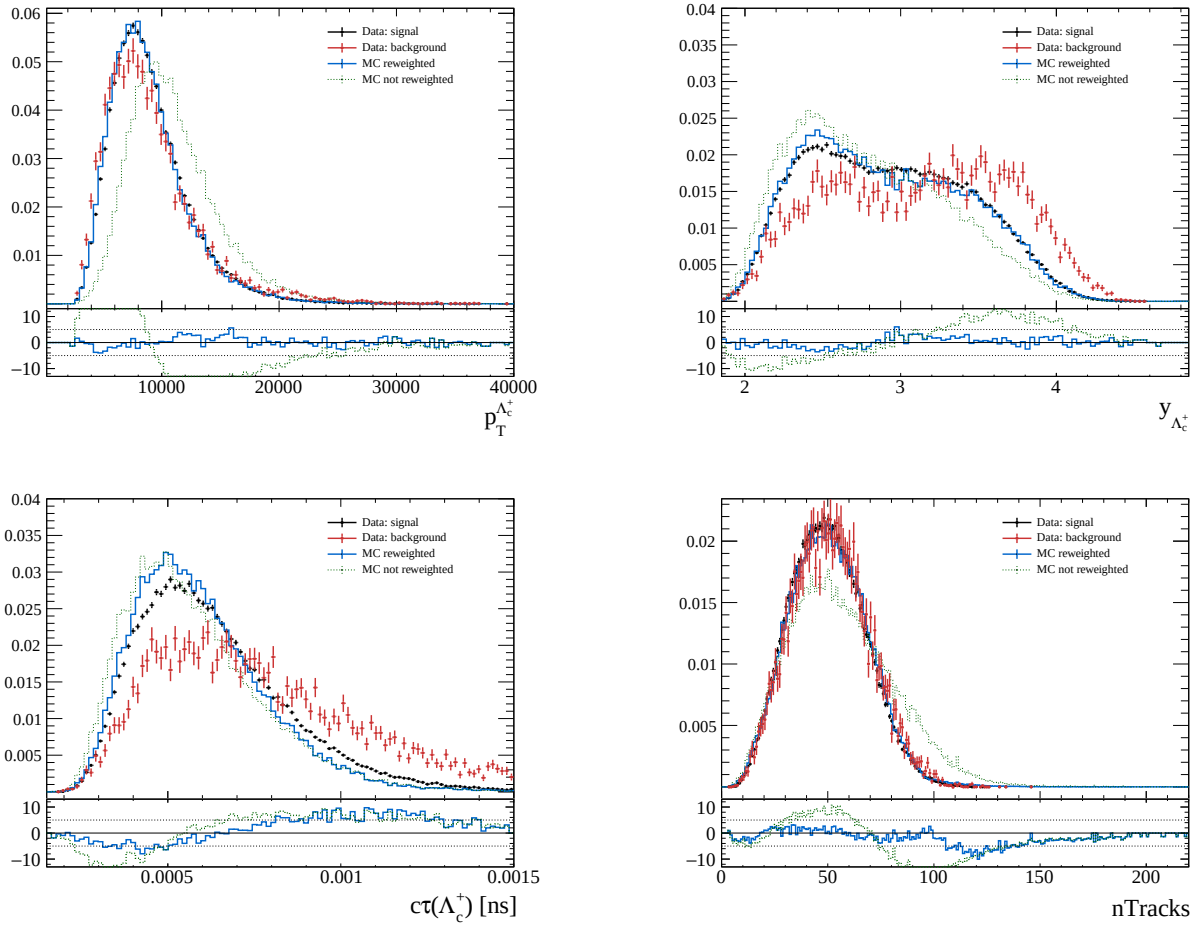

Figure 6.20: Comparison plots between data and MC for TOS Magnet Down $\Lambda_c^+ \to pK^-\pi^+$ samples. The sPlot data is shown in black for the signal and in red for the background, the simulation without corrections is shown in dashed green lines and the reweighted MC is shown in blue.

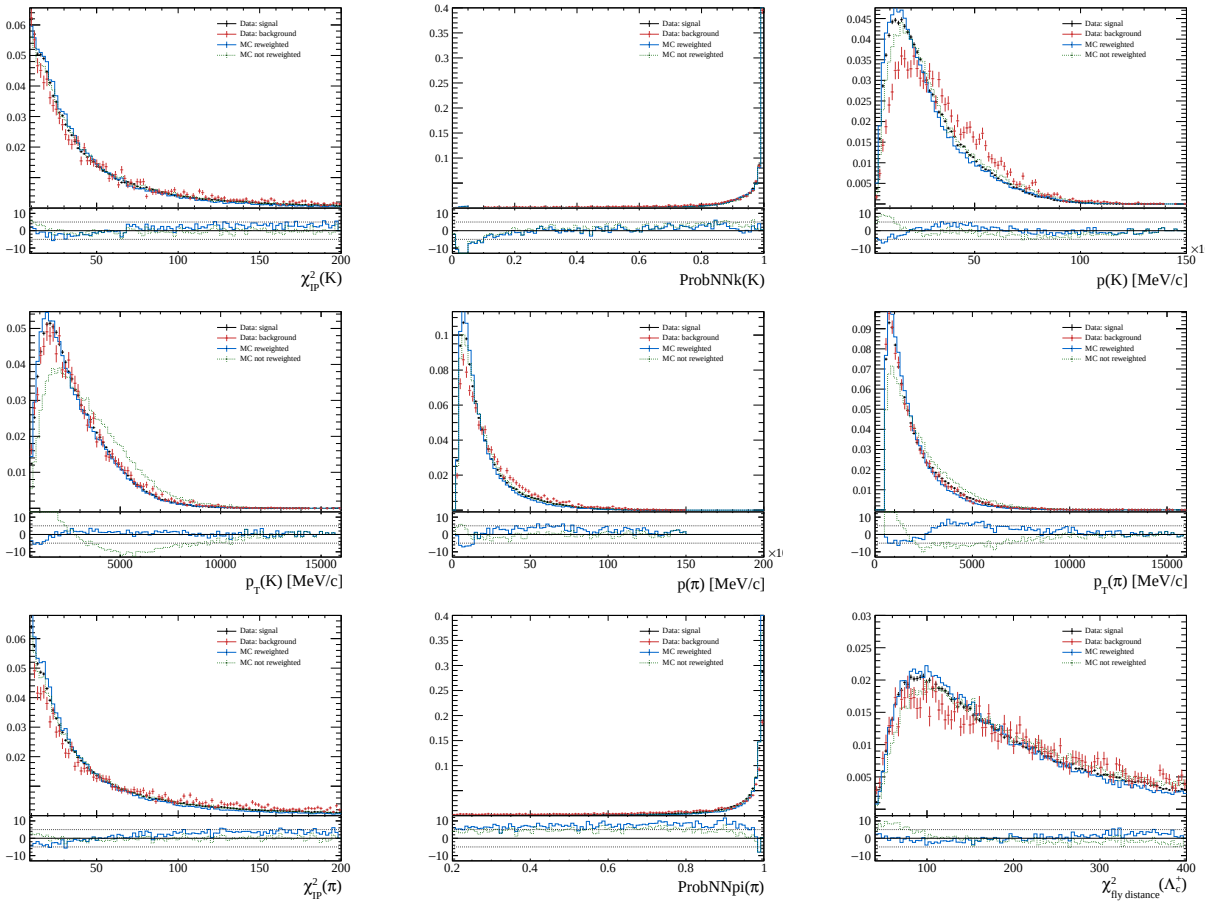

Figure 6.21: Comparison plots between data and MC for TOS Magnet Down $\Lambda_c^+ \to pK^-\pi^+$ samples. The sPlotted data is shown in black for the signal and in red for the background, the simulation without corrections is shown in dashed green lines and the reweighted MC is shown in blue.

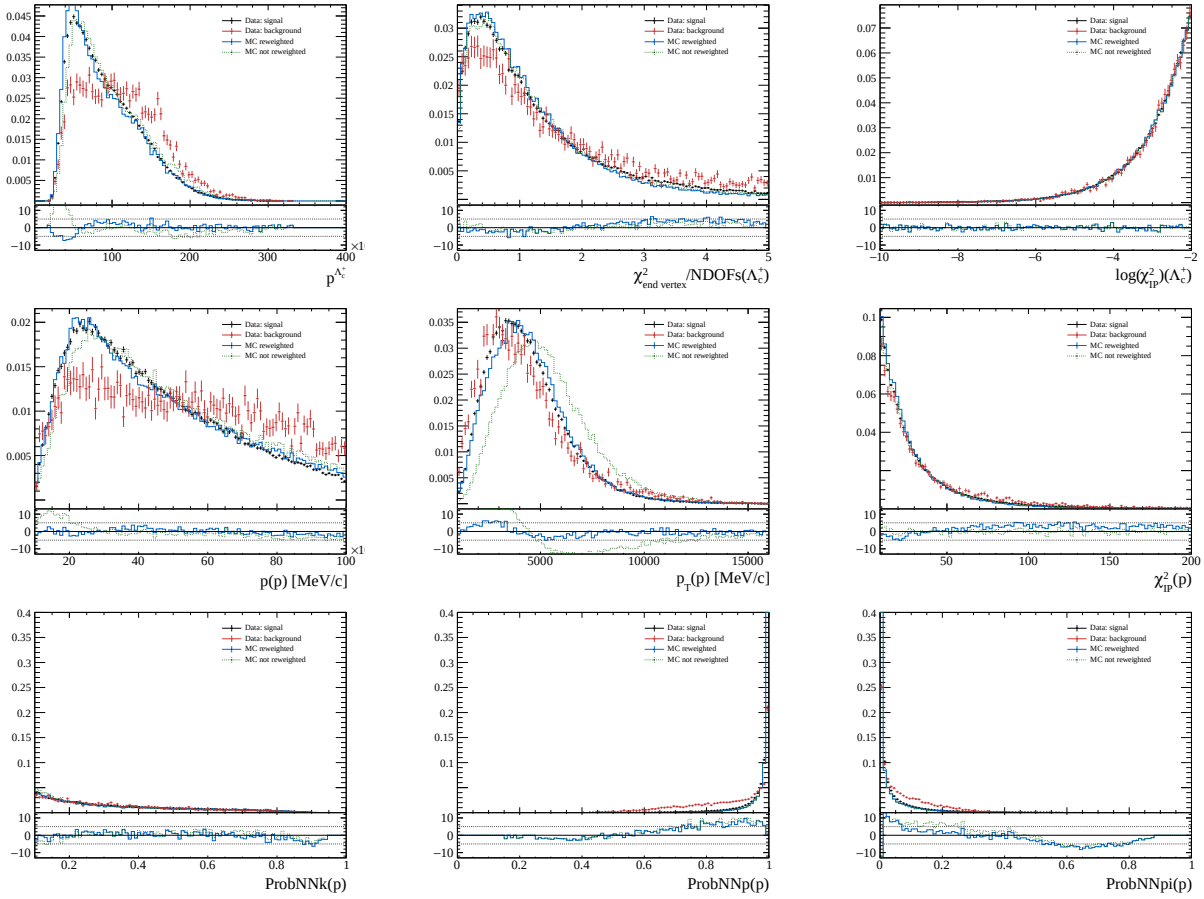

Figure 6.22: Comparison plots between data and MC for TOS Magnet Down $\Lambda_c^+ \to pK^-\pi^+$ samples. The sPlotted data is shown in black for the signal and in red for the background, the simulation without corrections is shown in dashed green lines and the reweighted MC is shown in blue.

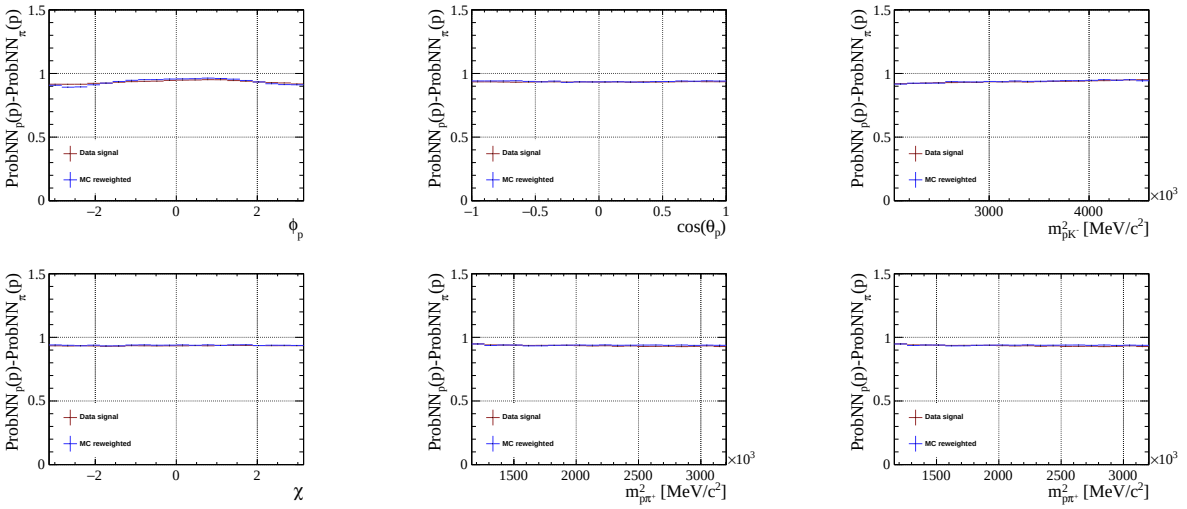

Figure 6.23: Profile histograms featuring the probNN distributions $(ProbNN_p(p) - ProbNN_\pi(p))$ versus the phase space variables $\left(m^2_{pK^-}, m^2_{p\pi^+}, \cos\theta_p, \phi_p, \chi\right)$, the mass $m^2_{K^-\pi^+}$ is also shown. The red dots are *sPlot* signal data, the blue dots the MC after the reweighting procedure. The results shown are for the TOS category and positive polarity.

6.2.8 Efficiencies

The total efficiency, ϵ_{TOT}, is the product of several efficiencies: the geometrical acceptance ϵ_{acc}, the kinematic offline selections ϵ_{sel}, including the stripping selections, the trigger $\epsilon_{trigger}$, including the L0 and HLT, the particle identification ϵ_{PID} and the reconstruction ϵ_{rec}. Thus,

$$\epsilon_{TOT} = \epsilon_{acc} \times \epsilon_{trigger} \times \epsilon_{sel} \times \epsilon_{PID} \times \epsilon_{rec}. \tag{6.6}$$

For the polarization measurement, there is no need to separate each contribution and the total efficiency is sufficient to describe the detector and selections effects. The total efficiency is obtained using the phase space MC simulation by dividing the number of reconstructed candidates matched to a true Λ_c^+ signal which passed all the selection chain (including the trigger and stripping steps) by the number of generated (signal) Λ_c^+. The kinematic reweights and L0 corrections discussed above are included. The efficiency over the Dalitz plot and the 3 angular variables are shown in Fig. 6.24, for the other magnet polarities and trigger categories see Appendix E. The efficiencies largely affect the shape of the angular distributions. In particular, the ϕ_p angle is asymmetric and depending on the trigger category studied the asymmetry changes, and this is mostly due to the L0 efficiency. This is one of the reason why the analysis is performed separately for the two L0 trigger categories, as explained in Sec. 6.2.1. The total efficiency is included in the PDF via the normalization sample, this is explained in Sec. 6.3.1, thus there is no need to parametrize it explicitly. However for the systematic studies, the efficiency needs to be included when producing the generated samples (toys). This is done using the efficiency maps, shown in Fig. 6.24 for the pair of variables $(m_{pK^-}, m_{p\pi^+})$ and for ϕ_p, $cos(\theta_p)$ and χ separately. Then, if the variables are not correlated, the total efficiency is simply the product of these four efficiencies. Consequently, one needs to check the correlations between each pair of variables to

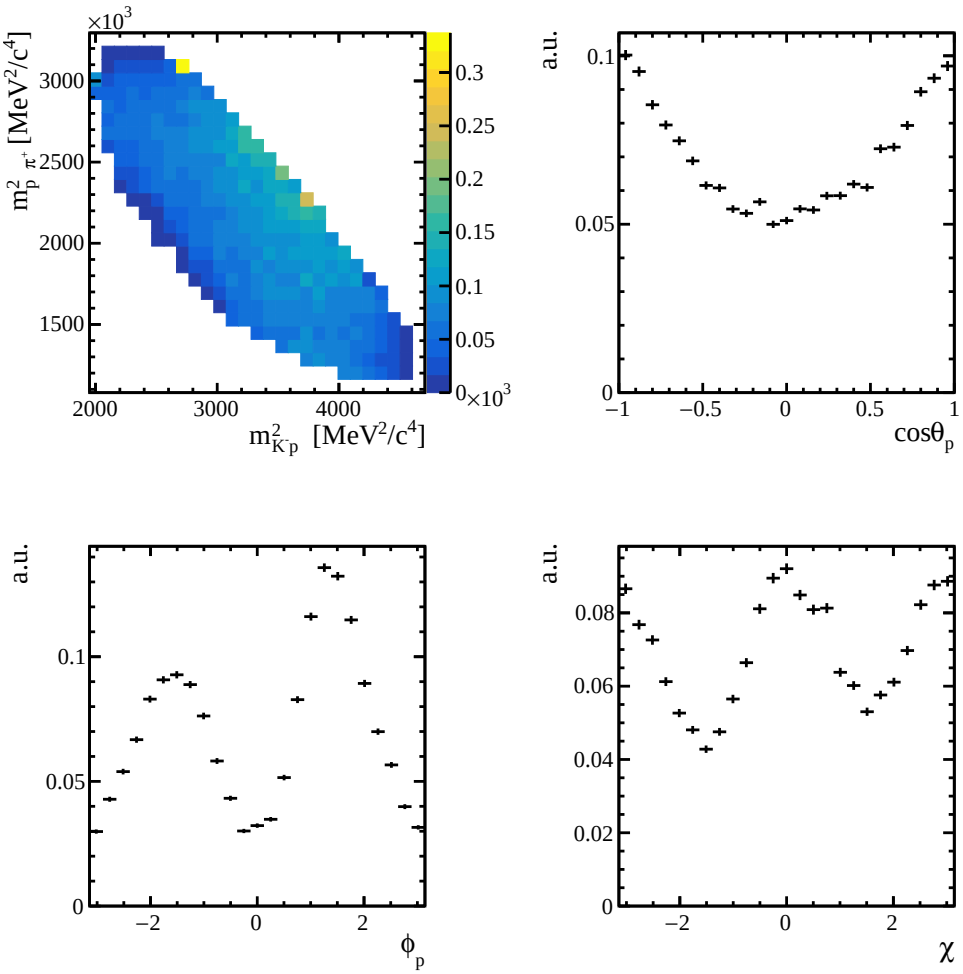

Figure 6.24: Efficiency distributions over the 2-dimensional plane $(m_{pK^-}, m_{p\pi^+})$ and the three angles ϕ_p, $cos(\theta_p)$ and χ for the trigger TOS category and $\Lambda_c^+ \to pK^-\pi^+$ decays. The units of the efficiency are arbitrary.

prove that this factorization holds. The correlation plots, 9 in total, are shown in Fig 6.25 where the correlation factor is overlaid on each sub-plot. The correlation coefficient, or Pearson's r correlation coefficients, for a given pair of variables X and Y are obtained as the ratio of the covariance between X and Y divided by the standard deviation of X and the one of Y. For a sample of variables (which corresponds here to the bin content (x_i, y_i) of the 2D histogram) the correlation factor becomes:

$$r_{xy} = \frac{\sum_{i=1}^{n}(x_i - \bar{x})(y_i - \bar{y})}{\sqrt{\sum_{i=1}^{n}(x_i - \bar{x})^2}\sqrt{\sum_{i=1}^{n}(y_i - \bar{y})^2}} \tag{6.7}$$

where n is the number of bins, (x_i, y_i) are the bin content of the i^{th} bin and $\bar{x} = 1/n\sum_i^n x_i$ is the mean value of x and similarly $\bar{y}$ is the mean value of y. The coefficient r_{xy} takes value between -1 (inverse correlation) and 1 (direct correlation), for values around 0 the correlation is null or very weak. In general, the correlations are found to be small, below 0.01 with the highest value around 0.11 for the correlation between χ and ϕ_p. When performing the systematic uncertainties studies, the small

correlation between χ and ϕ_p has been found to affect the measurement of the y component of the polarization hence the efficiency cannot be factorized.An alternative method to produce toys samples with the efficiency effects is used, see Sec. 6.3.7.

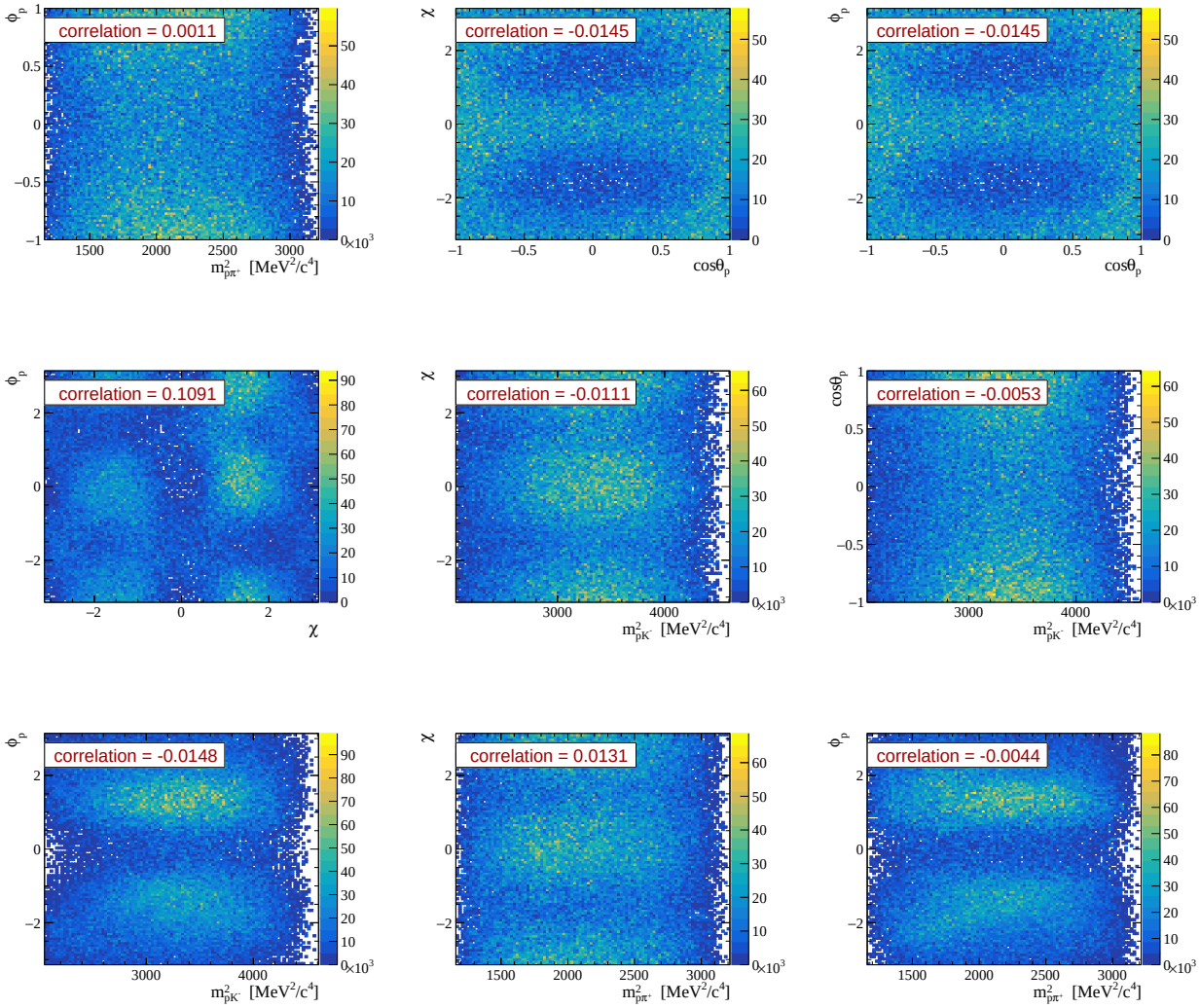

Figure 6.25: Correlation plots for the phase space variables obtained from the simulation sample after the selection chain. The correlation factor, described in the text, is overlaid in each sub-plot.

6.3 Amplitude fit

6.3.1 Likelihood and efficiency folding

The signal is described by the probability density function (PDF) composed by amplitude of Eq. 5.106 squared multiplied by the selection efficiency $\epsilon(m_{K^-\pi^+})$ and the phase space function $\Phi(m_{K^-\pi^+})$. The amplitude is a 5 dimensional (5D) function of the five variables $\Omega = \left(m^2_{pK^-}, m^2_{p\pi^+}, \cos\theta_p, \phi_p, \chi\right)$ and of the fit parameters $\vec{\omega} = \{\omega_1, \omega_2, ..., \omega_N\}$ which are the helicity couplings described in Sec. 5.4.4, the three components of the polarization vector and eventually some masses and widths of the resonances if they

are left free in the fit. The number of fit parameters N_{par} depends on the number of resonances included in the final model; for the Λ^*, Δ^{++} and the non resonant chains there are 2 parameters per resonance, for the K^* chain there are 4 parameters for spin 1 resonances, and 2 for spin 0. Each parameter is a complex number described by two real numbers (H, ϕ) as $He^{i\phi}$. The resonance lineshapes squared are numerically normalized to unity within the MINUIT fit. The amplitude parameters are determined by mean of an unbinned maximum likelihood fit to the 5D data which minimizes the negative logarithmic likelihood with respect to $\vec{\omega}$,

$$-2\ln\mathcal{L} = -2\sum_i \ln\mathcal{P}_{sig}(\Omega|\vec{\omega}) \tag{6.8}$$

where the signal PDF is

$$\mathcal{P}_{sig}(\Omega|\vec{\omega}) = \frac{|\mathcal{M}(\Omega|\vec{\omega})|^2\epsilon(\Omega)\Phi(m_{K^-\pi^+})}{I(\vec{\omega})} \tag{6.9}$$

$\Phi(m_{K^-\pi^+}) = pq$ is the phase space function and it is simply the product of the $K\pi$ (*i.e.* K^*) momentum p in the Λ_c^+ rest frame and the K momentum q in the K^* rest frame, and $I(\vec{\omega})$ is the normalization integral. The background is subtracted using the *sPlot* technique, explained in Sec. 6.2.2, which assign a weight sw_i according to the $m_{pK^-\pi^+}$ value of the candidate. Since the background is subtracted, the total PDF is the signal PDF, and using the logarithmic properties the likelihood can be written as:

$$-2\ln\mathcal{L} = -2\frac{\sum_i sw_i}{\sum_i sw_i^2}\sum_i sw_i \ln\mathcal{P}_{sig}(\Omega|\vec{\omega}) \tag{6.10}$$

$$= -2\frac{\sum_i sw_i}{\sum_i sw_i^2}\sum_i sw_i \left[\ln|\mathcal{M}(\Omega|\vec{\omega})|^2 + \ln[\epsilon(\Omega)\Phi(m_{K^-\pi^+})] - \ln I(\vec{\omega})\right] \tag{6.11}$$

$$\tag{6.12}$$

by writing $W_{tot} = \sum_i sw_i$ and $s_W = \frac{\sum_i sw_i}{\sum_i sw_i^2}$ and dropping the term which does not depend on the fitted parameters $\vec{\omega}$, the likelihood reduces to:

$$-2\ln\mathcal{L} = -2s_W\sum_i sw_i \ln|\mathcal{M}(\Omega|\vec{\omega})|^2 + 2s_W \ln I(\vec{\omega})W_{tot} \tag{6.13}$$

The integral $I(\vec{\omega})$ can be complicated to compute analytically since it would require the parameterization of the efficiency $\epsilon(\Omega)$,

$$I(\vec{\omega}) \equiv \int |\mathcal{M}(\Omega|\vec{\omega})|^2\epsilon(\Omega)\Phi(m_{K^-\pi^+})d\Omega \tag{6.14}$$

In order to avoid the parameterization of the efficiency over the phase space, a change of variable can be performed $d\Omega' = \epsilon(\Omega)\Phi(m_{K^-\pi^+})d\Omega$. Thus instead of integrating over the generated phase space the integration is performed over the simulated events that are generated uniformly in phase space and passed through the detector reconstruction and data selection procedure. In this way the simulation contains the efficiency effects which no longer need to be parametrized explicitly. Furthermore, the integration is performed numerically by summing the matrix element over the simulated events, and

the integral becomes:

$$I(\vec{\omega}) \propto \frac{1}{\sum_i w_i^{MC}} \sum_i^{N_{MC}} w_i^{MC} |\mathcal{M}(\Omega_i'|\vec{\omega})|^2 \tag{6.15}$$

where the w_i^{MC} are the kinematic weights computed in Sec. 6.2.7 to improve the data/MC agreement, the index i runs over the simulated events and N_{MC} is the number of simulated events.

The likelihood is implemented in C++ code in the RooFit framework [216] and it is a 5 dimensional function with up to 100 fit parameters. This makes the fit procedure very challenging and a simple fit using a hard-coded function analyzing the data sequentially could take up to a day. For this reason the amplitude fit is implemented using three tricks: first, as stated above, the normalization is optimized by running it over another sample, containing simulated events with the efficiency effects, as a different likelihood, this avoids to recompute the integral and the efficiency at each minimization step while fitting the data. The second trick consists in keeping in memory all the constant part of the complicated amplitude model (angles, lineshapes, d-wigners functions etc..) without computing them at each step. Finally the code analyses several groups of data (called "batches") in parallel on different CPUs at a time rather than sequentially computing the amplitude event after event. This is implemented using the customizable "batch evaluation" function of RooFit (available starting from version 6.20) and the OpenMP C++ library for the multi-threading. These optimizations allowed to speed up the code from 2 hours to 15 minutes. The minimization is performed using MINUIT [217], which employs the NLL minimization algorithm MIGRAD with the HESSE method to have a better estimate of the errors. The difference between the two is that MIGRAD computes at each step an approximation of the error matrix whereas HESSE calculates the full second-derivative matrix by finite differences and inverts it.

6.3.2 Fit fractions

The fit results are monitored by looking at the one dimensional projections of the fit results overlaid on data and numerically by looking at the fit fractions and the convergence status of MIGRAD. The fit fractions F_r give an idea of how much is a resonance contributing to the model, they are computed after the parameters have been obtained from the fit and they are defined as the ratio of the integral of the one resonance amplitude ($\mathcal{A}^r_{m,\lambda_p}$) to the integral of the full amplitude over the phase space $\vec{\Omega}$:

$$F_r = \frac{\int \sum_{m,\lambda_p} \left| \mathcal{X}_{\mathrm{BW}}(m_r) \mathcal{A}^r_{m,\lambda_p} \right|^2 d\vec{\Omega}}{\int \sum_{m,\lambda_p} \left| \sum_{r_i} \mathcal{X}_{\mathrm{BW}}(m_{r_i}) \mathcal{A}^{r_i}_{m,\lambda_p} \right|^2 d\vec{\Omega}} \tag{6.16}$$

where $\mathcal{X}_{\mathrm{BW}}(m_r)$ is the resonance lineshape and the sum on r_i runs over the resonances included in the model. The error on the fit fractions are estimated using a Gaussian multivariate approach, explained in the following. Around 100 toy samples are generated with different fit parameters obtained following a multi-dimensional Gaussian distribution, with means μ_i and covariance matrix elements $c_i j$, in order to take into account the correlations between the parameters. First, the covariance matrix C obtained

from the fit needs to be diagonalized as:

$$C = PDP^-1 \tag{6.17}$$

where the D is the diagonal matrix formed by the eigenvalues of C (e_i) and P is the transition matrix formed by the eigenvectors of C ($\vec{e_i}$). The square root of the eigenvalues gives the uncorrelated uncertainty, $s = \sqrt{e_i}$, of the parameter μ_i. Random numbers following a Gaussian distribution with a zero mean and standard deviation $s = \sqrt{e_i}$ are generated. Writing the generated numbers $r_i^{diagonal}$ in a vector $\vec{G}^{diagonal}$, they need to be rotated back to the non-diagonal space as:

$$\vec{G} = P\vec{G}^{diagonal} \tag{6.18}$$

Then a new set of parameters, μ_i' is obtained by adding to each parameter μ_i the corresponding shift obtained (r_i). In this way, the μ_i' parameters are generated randomly accounting for the correlations among them. The distribution of the μ_i' is Gaussian and its standard deviation μ_i' gives the error on F_r.

6.3.3 Asymmetry parameters

The asymmetry parameters for the resonance two body decays have been defined in Eq. 5.120, 5.122 and 5.125. They can be easily computed starting from the helicity couplings obtained from the fit to the data. The more general asymmetry parameter of the three-body decay $\Lambda_c^+ \to pK^-\pi^+$ cannot be expressed as a simple combination of the resonance helicity couplings. An effective α can be estimated by computing the sensitivity to the polarization S, as it is described in Ref. [218]; the relation between S and the effective α can be derived easily. Factorizing the total decay amplitude of Eq. 5.106, named here $\mathcal{P}(\Omega)$, as

$$\mathcal{P}(\Omega) = f(\Omega) + pg(\Omega) \tag{6.19}$$

where p is the polarization, Ω the usual five phase space variables and f and g are two functions to be specified depending on the decay studied. The total probability density function $\mathcal{P}$ is normalized to unity and the function f and g satisfy the normalization and positivity conditions:

$$\int \mathcal{P}(\Omega)d\Omega = 1, \qquad \int f(\Omega)d\Omega = 1, \qquad \int g(\Omega)d\Omega = 0 \tag{6.20}$$

with $f \geq 0$ and $|g| < f$. By introducing the variable $\omega = \frac{g(\Omega)}{f(\Omega)}$, the decay distribution becomes:

$$\hat{\mathcal{P}}(\Omega) = \hat{f}(\Omega)(1 + p\omega) \tag{6.21}$$

The second order momenta of $\hat{f}$ is $S^2(p = 0)$, which is the average information per event S^2 at zero polarization. Finally the sensitivity to the polarization is defined as:

$$S^2 = \frac{1}{N\sigma^2} = \left\langle \frac{g^2}{f^2}(\Omega) \right\rangle = \int \frac{g^2}{f} d\Omega \tag{6.22}$$

For the $\Lambda_c^+ \to pK^-\pi^+$ decay amplitude f and g can be found by factorizing P_z in Eq. 5.106

$$d\Gamma \propto (1+P_z)\left(|\mathcal{A}_{\frac{1}{2},\frac{1}{2}}|^2+|\mathcal{A}_{\frac{1}{2},-\frac{1}{2}}|^2\right)+(1-P_z)\left(|\mathcal{A}_{-\frac{1}{2},\frac{1}{2}}|^2+|\mathcal{A}_{-\frac{1}{2},-\frac{1}{2}}|^2\right) \tag{6.23}$$

$$\propto \underbrace{\left(|\mathcal{A}_{\frac{1}{2},\frac{1}{2}}|^2+|\mathcal{A}_{\frac{1}{2},-\frac{1}{2}}|^2+|\mathcal{A}_{-\frac{1}{2},\frac{1}{2}}|^2+|\mathcal{A}_{-\frac{1}{2},-\frac{1}{2}}|^2\right)}_{f(\Omega)} \tag{6.24}$$

$$+P_z\underbrace{\left(|\mathcal{A}_{\frac{1}{2},\frac{1}{2}}|^2+|\mathcal{A}_{\frac{1}{2},-\frac{1}{2}}|^2-|\mathcal{A}_{-\frac{1}{2},\frac{1}{2}}|^2-|\mathcal{A}_{-\frac{1}{2},-\frac{1}{2}}|^2\right)}_{g(\Omega)}. \tag{6.25}$$

Finally f and g are combinations of the decay amplitude for 0, -1 and 1 polarization:

$$f(\Omega) \propto \mathcal{P}(\Omega, P_z=0) \qquad \text{and} \qquad g(\Omega) \propto [\mathcal{P}(\Omega, P_z=1)-\mathcal{P}(\Omega, P_z=-1)] \tag{6.26}$$

The relation between the S average information and the decay asymmetry parameter α, is obtained inserting Eq. 5.113 (which has been already integrated w.r.t. ϕ_p,χ and the masses) in Eq. 6.22:

$$S^2 = \int \frac{g^2}{f} d\Omega = \int \frac{(\frac{1}{2}(2\alpha^2\cos^2\theta_p))^2}{\frac{1}{2}} d\Omega = \frac{4}{3}\alpha^2 \tag{6.27}$$

thus

$$S = \frac{2}{\sqrt{3}}|\alpha| \qquad \text{and} \qquad |\alpha| = \frac{\sqrt{3}}{2}S \tag{6.28}$$

As test, the asymmetry parameter obtained with this method is compared to the results obtained using the helicity couplings in the case of only one resonance decay at a time. The two values are found to agree as expected. As explained in Chapter 5 the asymmetry parameters α are composed of a parity violating and a parity conserving part, see for instance Eq. 5.123 or Eq. 5.126. If parity is conserved, then the asymmetry is zero. However if an alpha different from zero is measured, this is a sign of parity violation in the decay.

6.3.4 Model building

As explained in Sec. 5.4.4, all the resonances listed in Tab. 5.2 could be present in the data, however they do not have all the same impact on the total amplitude and some of them give such a small contribution that the fit is not sensitive to it. Furthermore, the contribution of a single resonance is influenced by the other resonances (in the same or in another channel) present in the model due to the interference effects. The amplitude is described by mean of the helicity amplitudes of Eq. 5.106 where the sum over the number of resonances in each channel depends on which isobars are included in the model. The "model building" consists in assessing which resonances are dominant in the data and which ones give a negligible contribution. In order to do so, the quality of the fit is monitored each time a new model (*i.e.* a new list of resonances) is tested by looking first at the visible discrepancies between the data and the model in the one dimensional projections of the phase space variables, and then looking at the χ^2/ndf and the fit fractions. The model histogram is obtained by weighting the phase space simulation, which contains efficiency effects, by the amplitude values obtained from the fit. Then the χ^2/ndf is computed for the one dimensional projections of ϕ_p, $\cos(\theta_p)$ and χ and the

two dimensional one of the pair $(m_{pK^-}, m_{p\pi^+})$ as:

$$\chi^2/\text{ndf} = \frac{1}{N - N_{par} - 1} \sum_i^N \frac{data[i] - model[i]}{err_{data}[i]^2 + err_{model}[i]^2} \tag{6.29}$$

where the index i runs over the histogram bins, $\{data[i], err_{data}[i]\}$ and $\{model[i], err_{model}[i]\}$ are the values of the bin i with its associated error for the data and for the fit model respectively, N is the number of bins (as default value N= 150), N_{par} the number of floating parameters in the fit. For the two dimensional case, the same formula applies with a double sum on the x and y bins. The distributions of the pull for each bin are displayed under each data/model comparison to give a fast qualitative visualization of the data/model discrepancies over the phase space. Furthermore, for a reasonable model the sum of fit fractions, given in Eq. 6.16, should be close to one, a value far from one indicates that there were large interference effects and in general models with small interferences are preferred.

For the model building procedure, the polarization vector is fixed to zero, since the polarization has no influence on the mass distributions but only on the angles. As a consequence the three angles, ϕ_p, $\cos(\theta_p)$ and χ, have a minor influence in the model building procedure. This is clear since even a first minimal model does describe correctly the angular variables within the errors even though the description of the invariant masses is not satisfactory. For this reason, the fit quality is mostly assessed looking at the masses rather than the angle's χ^2. The sample used is the TIS category with negative polarity with 150 000 events, and since similar results are expected for the TOS category, the building procedure is performed only on the TIS one. Furthermore, the decay $(\Lambda_c^+ \to pK^-\pi^+)$ and anti-decays $(\bar{\Lambda_c}^- \to \bar{p}K^+\pi^-)$ are mixed in order to have more statistics and to avoid biasing the model towards one of the two types of decays. In order to avoid local minima, four fits with randomized initial values are performed for each model and only the fit for which the computation of the covariance matrix converged and with the smallest negative likelihood is kept. For each model, the sum of fit fractions, the log-likelihood value and the χ^2/ndf given in Eq. 6.3.4 are calculated and compared. The resonance masses and widths are fixed to the known values from Ref. [11].

Regarding the choice of the models, the first resonances included are the one clearly visible by eye in the one dimensional distributions and in the 2 dimensional Dalitz plot shown in Fig. 6.26. In the pK spectrum two clear excesses appear as peaks in the one dimensional distributions and as bands on the Dalitz plot. They are compatible with the $\Lambda^*(1520)$ and $\Lambda^*(1670)$. Another excess appears on the high mass region above $1800\,\text{MeV}/c^2$, which is not clearly identified for now. The Σ resonances are expected to be suppressed since it is a transition involving an isospin difference of $\Delta I = 1$ (see discussion in Sec. 5.4.6), and they are not included in the model building. Furthermore they would be hard to separate from the favored $\Delta I = 0$ transitions, corresponding to the Λ^* resonances. However their influence on the final model needs to be studied, this is done when assessing the systematic uncertainties. For the $K\pi$ channel, the $K^*(892)$ resonance appears also clearly around 890 MeV/c^2 and as a diagonal band in the 2 dimensional Dalitz, here again an excess on the high $K\pi$ mass seems to indicate the presence of the $K^*(1430)$ resonance. Finally, for the $p\pi$ projection only the well established $\Delta^{++}(1232)$ appears on the left of the mass spectrum, the right side around $1600\,\text{MeV}/c^2$

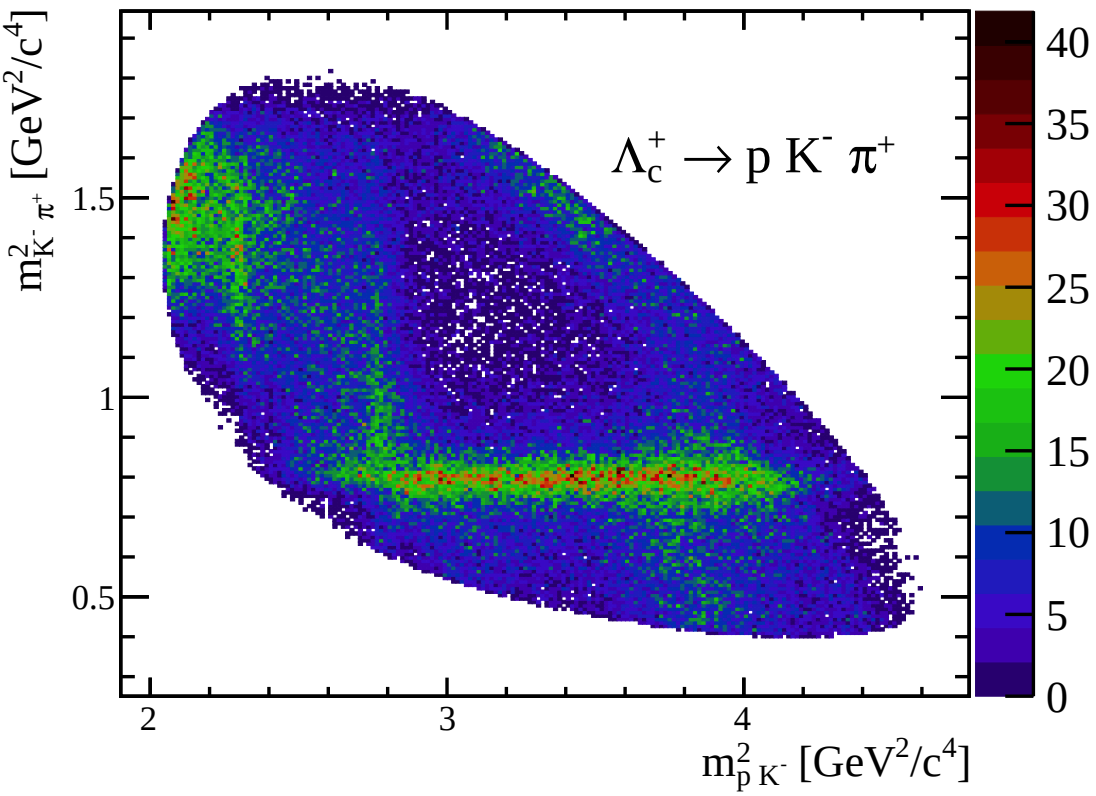

Figure 6.26: Dalitz plot of the background subtracted $\Lambda_c^+ \to pK^-\pi^+$ decays, the y axis shows the $m^2_{K\pi}$ invariant mass and the x axis the m^2_{pK} one.

may contains several resonances which cannot be distinguished by eye. Starting from this qualitative observation giving a "minimal model", labeled as "M0", other resonances can be added or removed. However, it is evident looking at the fit results for M0, shown in Fig. F.3 in Appendix F, that such a minimal model is not sufficient to described the data. Within the resonances listed in Tab. 5.2, all the ones that are well established, *i.e.* marked as "certain", are studied. An additive approach is first used to exclude models which are certainly not sufficient to describe the data. Then within the models giving reasonable results, few of them are very similar in which case the simplest one, with the smallest number of parameters, is kept.

Results of the model building The results of the model building are summarized concisely in Tab. 6.9 and Tab. 6.10, where each column, named as Mi (for instance: M0, M1, M2 etc..), is a different model. The resonance content is given by the ensemble of resonances with a green check mark whereas the red cross marks indicate that the resonance is not included in this model. The fit quality results are shown on the bottom part of the table.

M1 includes the well known $\Lambda(1405)$ resonance which has its pole mass outside the pK mass region and whose tail can contribute to the lower pK spectrum, it is parametrized using the Flatté lineshape

described in Sec. 5.3. In the second model a second resonance for the low pK mass spectrum, the $\Lambda(1600)$ is added. This fit model is already giving an acceptable $\chi^2/\text{ndf}(m^2_{pK}, m^2_{p\pi})$, however there is still room for improvement. Starting from M3, the 0^+ $K\pi$ contribution, including the two resonances $K^*(700)$, $K^*(1430)$, is added since it is expected to fill the high mass region of the $K\pi$ spectrum. The 0^+ is described using the LASS parametrization discussed in Sec. 5.3.5. Then, for models M4-M6, more Δ^{++} resonances are added recursively, the model M6 seems to have a very good $\chi^2/\text{ndf}(m^2_{pK}, m^2_{p\pi})$ and starting from this model, the majority of the following models looks very similar (within 3 standard deviations) when inspecting the data/model comparison by eye. Models M7-M11 are used to study the effects of additional Λ^* resonances in the presence of all the Δ^{++} contributions, the M7 and M10 appears to have a $\chi^2/\text{ndf}(m^2_{pK}, m^2_{p\pi})$ smaller than 5, and similar χ^2/ndf for the rest. However M10 has a sum of fit fractions closer to one. A test removing the $\Delta(1620)$ from M7 is performed in M12 and the fit quality is considerably worsened. From model M13 to M20, the Λ^* contribution around 1800 MeV/c^2 are studied; first the $\Lambda^*(2100)$ is included to try to fill the high pK mass, then the other 5 very close resonances around 1800 MeV/c^2 are added one by one. The best fits are the M17 and M18, however they both have significantly larger values with respect to the previous models for the one dimensional χ^2/ndf. Finally M21-M25 also study the Λ^* contribution around 1800 MeV/c^2, this time without the $\Lambda^*(2100)$ contribution replaced by a $\Lambda^*(2000)$ which is listed in the PDG as "poorly known" but which has been found to be significant in Ref. [219]. The best model is the M21, with a $\chi^2/\text{ndf}(m^2_{pK}, m^2_{p\pi})$ smaller than 5 and a sum of fit fractions close to 1. The $\Lambda^*(2100)$ resonance seems to fit well the high pK mass, this is why it has been included starting from the first models.

Conclusions on the model building The models which have a $\chi^2/\text{ndf}(m^2_{pK}, m^2_{p\pi})$ larger than 10 are automatically excluded, since better models are available. The models with a $\chi^2(m^2_{pK}, m^2_{p\pi})$ value around 10 are the M3, M4, M5 and the M15; these model are considered as satisfactory but not retained. Finally, the models with the best $\chi^2(m^2_{pK}, m^2_{p\pi})$ are, in decreasing order, the M7 and M21, and then M10, M6, M17, M18 and M2. Within the latter ones, M17 and M18 have large fit fractions, 1.13 and 1.4 respectively, resulting in large interference effects which are visible by eye in Fig. F.3 in Appendix F. The M21 has two more resonances, $\Lambda^*(1690)$ and $\Lambda^*(1890)$ with respect to M10, and by eye the two models give identical results. However, M21 has slightly worse single χ^2 with respect to M10, and requires more parameters (62 against 54), hence the M10 model is chosen over the M21, however the M21 is kept as second choice since it is the only model with one $\Lambda^*(1800)$ resonance giving good fit results. Within the last three models, M2 does not describe the $m_{K\pi}$ mass as well as the two others, there are discrepancies visible by eye in the very low and very high mass regions. Finally, M6 and M7 are very similar, the latter has one resonance more the $\Lambda^*(1690)$ and both models seems to indicate that the $K^*(1410)$ contribution is not necessary. As a conclusion, M10, M6 and M21 have been retained after the model building procedure. Since the three models are indistinguishable the simplest one, M6, is retained as baseline solution. The projections of the five phase space variables along with the third mass $m^2_{K\pi}$ are shown in Fig. 6.27. The black dots are the data points, the red line shows the full PDF model, the colored lines show the contributions of each resonance separately and

Res	M0	M1	M2	M3	M4	M5	M6	M7	M8	M9	M10	M11	M12
pK channel													
$\Lambda^*(1405)$	✗	✓	✓	✓	✓	✓	✓	✓	✓	✓	✓	✓	✓
$\Lambda^*(1520)$	✓	✓	✓	✓	✓	✓	✓	✓	✓	✓	✓	✓	✓
$\Lambda^*(1600)$	✗	✗	✓	✓	✓	✓	✓	✓	✗	✗	✓	✓	✓
$\Lambda^*(1670)$	✓	✓	✓	✓	✓	✓	✓	✓	✓	✓	✓	✓	✓
$\Lambda^*(1690)$	✗	✗	✗	✗	✗	✗	✗	✓	✓	✗	✗	✓	✓
$\Lambda^*(1800)$	✗	✗	✗	✗	✗	✗	✗	✗	✗	✗	✗	✗	✗
$\Lambda^*(1810)$	✗	✗	✗	✗	✗	✗	✗	✗	✗	✗	✗	✗	✗
$\Lambda^*(1820)$	✗	✗	✗	✗	✗	✗	✗	✗	✗	✗	✗	✗	✗
$\Lambda^*(1830)$	✗	✗	✗	✗	✗	✗	✗	✗	✗	✗	✗	✗	✗
$\Lambda^*(1890)$	✗	✗	✗	✗	✗	✗	✗	✗	✗	✗	✗	✗	✗
$\Lambda^*(2000)$	✗	✓	✓	✓	✓	✓	✓	✓	✓	✓	✓	✓	✓
$\Lambda^*(2100)$	✗	✗	✗	✗	✗	✗	✗	✗	✗	✗	✗	✗	✗
$\Lambda^*(2110)$	✗	✗	✗	✗	✗	✗	✗	✗	✗	✗	✗	✗	✗
$p\pi$ channel													
$\Delta^{++}(1232)$	✓	✓	✓	✓	✓	✓	✓	✓	✓	✓	✓	✓	✓
$\Delta^{++}(1600)$	✗	✗	✗	✗	✓	✓	✓	✓	✓	✓	✓	✓	✓
$\Delta^{++}(1620)$	✗	✗	✗	✗	✗	✗	✓	✓	✓	✓	✓	✓	✗
$\Delta^{++}(1700)$	✗	✗	✗	✗	✗	✓	✓	✓	✓	✓	✓	✓	✓
$K\pi$ channel													
$K^*(700)$	✗	✗	✗	✓	✓	✓	✓	✓	✓	✓	✓	✓	✓
$K^*(892)$	✓	✓	✓	✓	✓	✓	✓	✓	✓	✓	✓	✓	✓
$K^*(1410)$	✗	✗	✗	✗	✗	✗	✗	✗	✗	✗	✓	✓	✗
$K_0^*(1430)$	✗	✗	✗	✓	✓	✓	✓	✓	✓	✓	✓	✓	✓
Fit χ^2/ndf													
N_{par}	18	26	30	34	38	42	46	50	46	42	54	58	46
m^2_{pK}	217.17	40.66	9.18	10.80	12.18	12.30	11.85	13.39	15.23	12.44	12.92	16.24	14.5
$m^2_{K\pi}$	27.27	25.15	12.32	12.43	14.72	13.31	11.60	13.35	12.01	11.06	12.61	16.36	11.8
$m^2_{p\pi}$	55.82	22.64	10.60	12.24	12.50	11.82	11.12	12.02	12.10	10.47	14.44	15.12	13.9
$\cos(\theta_p)$	7.50	6.48	6.28	6.62	7.20	7.73	8.19	8.56	8.07	7.34	9.19	10.11	8.13
χ	6.59	5.44	5.50	5.57	6.35	6.68	7.05	7.63	7.04	6.62	8.30	9.18	7.36
ϕ_p	6.27	5.52	6.08	6.04	6.56	7.19	8.09	8.73	8.00	7.58	9.53	10.39	7.88
$m^2_{pK}, m^2_{p\pi}$	389.18	29.97	**7.32**	10.38	11.86	11.80	**5.04**	**4.72**	36.17	136.68	**4.92**	14.03	41.0
FF	1.030	0.932	1.100	1.030	1.119	1.102	1.129	1.125	1.106	1.113	1.065	1.136	1.094

Table 6.9: Summary of the model building procedure, each column identifies a different model (named M1, M2, M3 etc..), each line is a resonance from Ref. [11], the green tick marks indicate that the resonance is included in the model and the red crosses that it is excluded. The last 9 lines show the fit quality results for each model, including: the number of parameters, the single variables χ^2/ndf, the two-dimensional χ^2/ndf and the sum of fit fractions (FF). The χ^2/ndf values in green indicate the best models and in orange the reasonable ones.

Res	M13	M14	M15	M16	M17	M18	M19	M20	M21	M22	M23	M24	M25
pK channel													
$\Lambda^*(1405)$	✔	✔	✔	✔	✔	✔	✔	✔	✔	✔	✔	✔	✔
$\Lambda^*(1520)$	✔	✔	✔	✔	✔	✔	✔	✔	✔	✔	✔	✔	✔
$\Lambda^*(1600)$	✔	✔	✔	✔	✔	✔	✔	✔	✔	✔	✔	✔	✔
$\Lambda^*(1670)$	✔	✔	✔	✔	✔	✔	✔	✔	✔	✔	✔	✔	✔
$\Lambda^*(1690)$	✔	✗	✔	✔	✔	✔	✔	✔	✔	✔	✔	✔	✔
$\Lambda^*(1800)$	✗	✗	✗	✗	✗	✗	✔	✔	✗	✗	✗	✔	✔
$\Lambda^*(1810)$	✗	✗	✗	✗	✗	✗	✗	✔	✗	✗	✗	✗	✔
$\Lambda^*(1820)$	✗	✗	✗	✗	✔	✔	✔	✔	✗	✔	✔	✔	✔
$\Lambda^*(1830)$	✗	✗	✗	✗	✗	✔	✔	✔	✗	✗	✔	✔	✔
$\Lambda^*(1890)$	✗	✗	✗	✔	✔	✔	✔	✔	✔	✔	✔	✔	✔
$\Lambda^*(2000)$	✔	✗	✗	✗	✗	✗	✗	✗	✔	✔	✔	✔	✔
$\Lambda^*(2100)$	✔	✔	✔	✔	✔	✔	✔	✔	✗	✗	✗	✗	✗
$\Lambda^*(2110)$	✗	✗	✗	✗	✗	✗	✗	✗	✗	✗	✗	✗	✗
$p\pi$ channel													
$\Delta^{++}(1232)$	✔	✔	✔	✔	✔	✔	✔	✔	✔	✔	✔	✔	✔
$\Delta^{++}(1600)$	✔	✔	✔	✔	✔	✔	✔	✔	✔	✔	✔	✔	✔
$\Delta^{++}(1620)$	✔	✔	✔	✔	✔	✔	✔	✔	✔	✔	✔	✔	✔
$\Delta^{++}(1700)$	✔	✔	✔	✔	✔	✔	✔	✔	✔	✔	✔	✔	✔
$K\pi$ channel													
$K^*(700)$	✔	✔	✔	✔	✔	✔	✔	✔	✔	✔	✔	✔	✔
$K^*(892)$	✔	✔	✔	✔	✔	✔	✔	✔	✔	✔	✔	✔	✔
$K^*(1410)$	✔	✔	✔	✔	✔	✔	✔	✔	✔	✔	✔	✔	✔
$K_0^*(1430)$	✔	✔	✔	✔	✔	✔	✔	✔	✔	✔	✔	✔	✔
Fit χ^2/ndf													
N_{par}	62	54	58	62	66	70	74	78	62	66	70	74	78
m^2_{pK}	17.41	30.64	30.60	32.60	35	41.30	50.80	60.10	16.40	18.90	20.50	35.30	29.30
$m^2_{K\pi}$	14.66	12.44	15.70	13.90	19.10	22.80	31.60	44.10	18.10	18.50	22.80	32.30	38.30
$m^2_{p\pi}$	15.23	20.46	20.80	22.50	25.70	31.90	41.30	47.90	17.60	20.80	23.0	26.80	40.80
$\cos(\theta_p)$	11.37	8.96	9.99	10.60	12.20	14.0	16.90	19.90	11.40	12.80	14.30	17.90	19.60
χ	10.58	8.16	8.98	10.40	11.80	13.30	14.90	18.20	10.70	11.70	13.10	15.60	18.10
ϕ_p	12.43	9.21	10.40	12.20	13.80	15.60	17.30	20.80	12.20	13.30	15.0	15.60	20.80
$m^2_{pK}, m^2_{p\pi}$	13.23	16.06	10.50	30.50	**5.62**	**6.64**	405.0	385.0	**4.73**	855.0	5620	29.10	806.0
FF	1.225	1.098	1.141	1.116	1.132	1.142	1.088	1.147	1.090	1.145	1.231	1.505	1.359

Table 6.10: Summary of the model building procedure, each column identifies a different model (named M1, M2, M3 etc..), each line is a resonance from Ref. [11], the green tick marks indicate that the resonance is included in the model and the red crosses that it is excluded. The last 9 lines show the fit quality results for each model, including: the number of parameters, the single variables χ^2/ndf, the two-dimensional χ^2/ndf and the sum of fit fractions (FF). The χ^2/ndf values in green indicate the best models and in orange the reasonable ones.

the colour code is specified in the legend shown in the $m^2_{K\pi}$ mass projection, in general blue lines are K^* resonances, green lines Δ^{++} and brown-red lines Λ^*. The lower pads show the pulls between the data and the total model. The fit projections for models M10 and M21 can be found in the Appendix F.1.

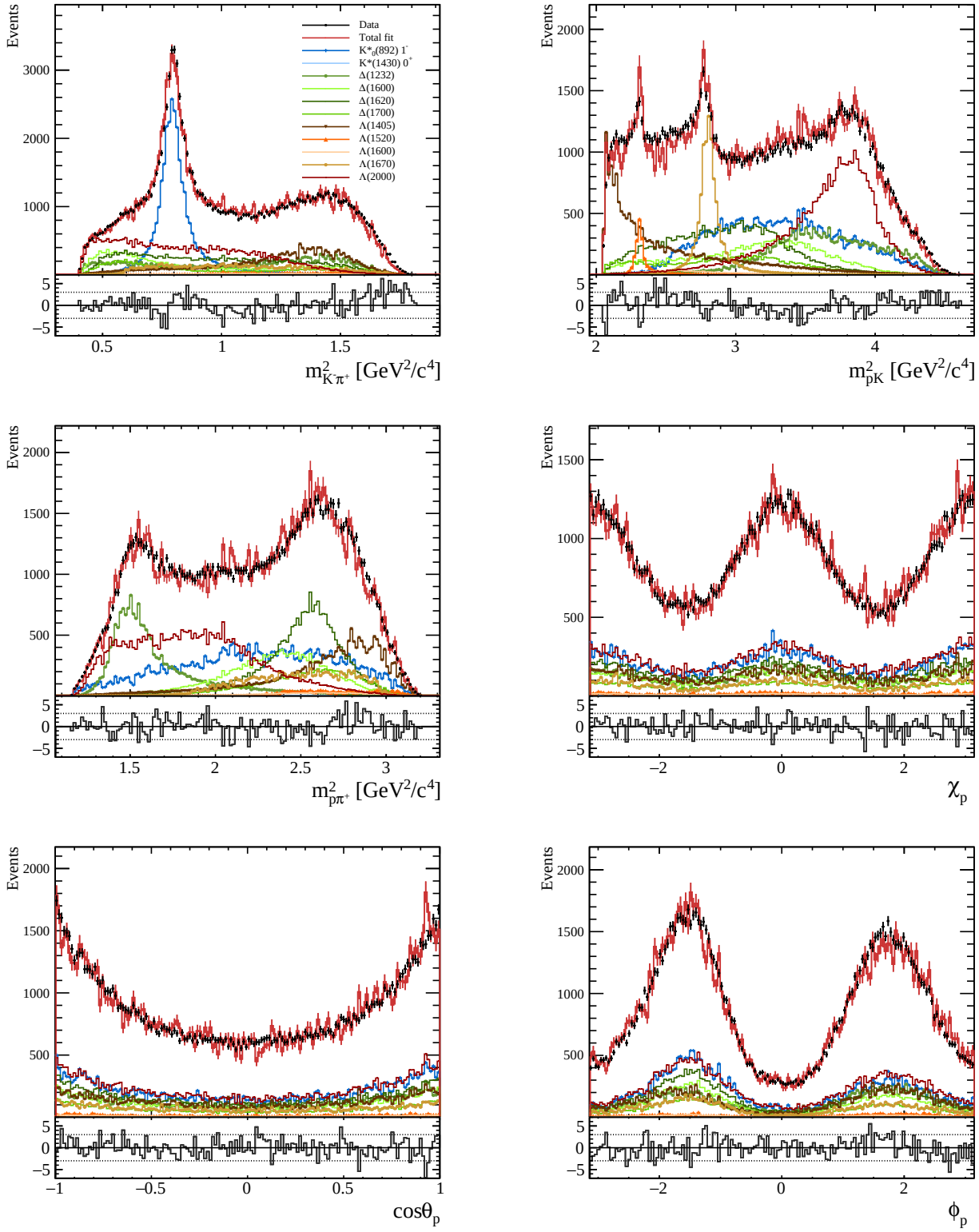

Figure 6.27: Example of fit with the model M6 on the TIS category, negative polarity, for Λ_c^+ and $\overline{\Lambda}_c^-$ decays mixed. The black dots are the data points, the red line shows the full PDF model, the colored lines shows the contributions of each resonance separately and the colour code is specified in the legend shown in the $m^2_{K\pi}$ mass projection, in general blue lines are K^* resonances, green lines Δ^{++} and brown-red lines Λ^*. The lower pads show the pulls between the data and the total model, the dashed horizontal lines show the limit of 3 standard deviations (3 σ).

6.3.5 Zero polarization test on the selected models

For the three models retained, the "zero polarization" test shown in Sec. 5.5 is performed using the helicity couplings obtained from the fit to the data. A generation of 10 M events without the efficiency effects for the three models (M10, M6 and M21) is performed to ensure that the angular distributions are flat if the polarization is set to 0. All three models behave correctly, an example of generation is shown in Fig. 6.28.

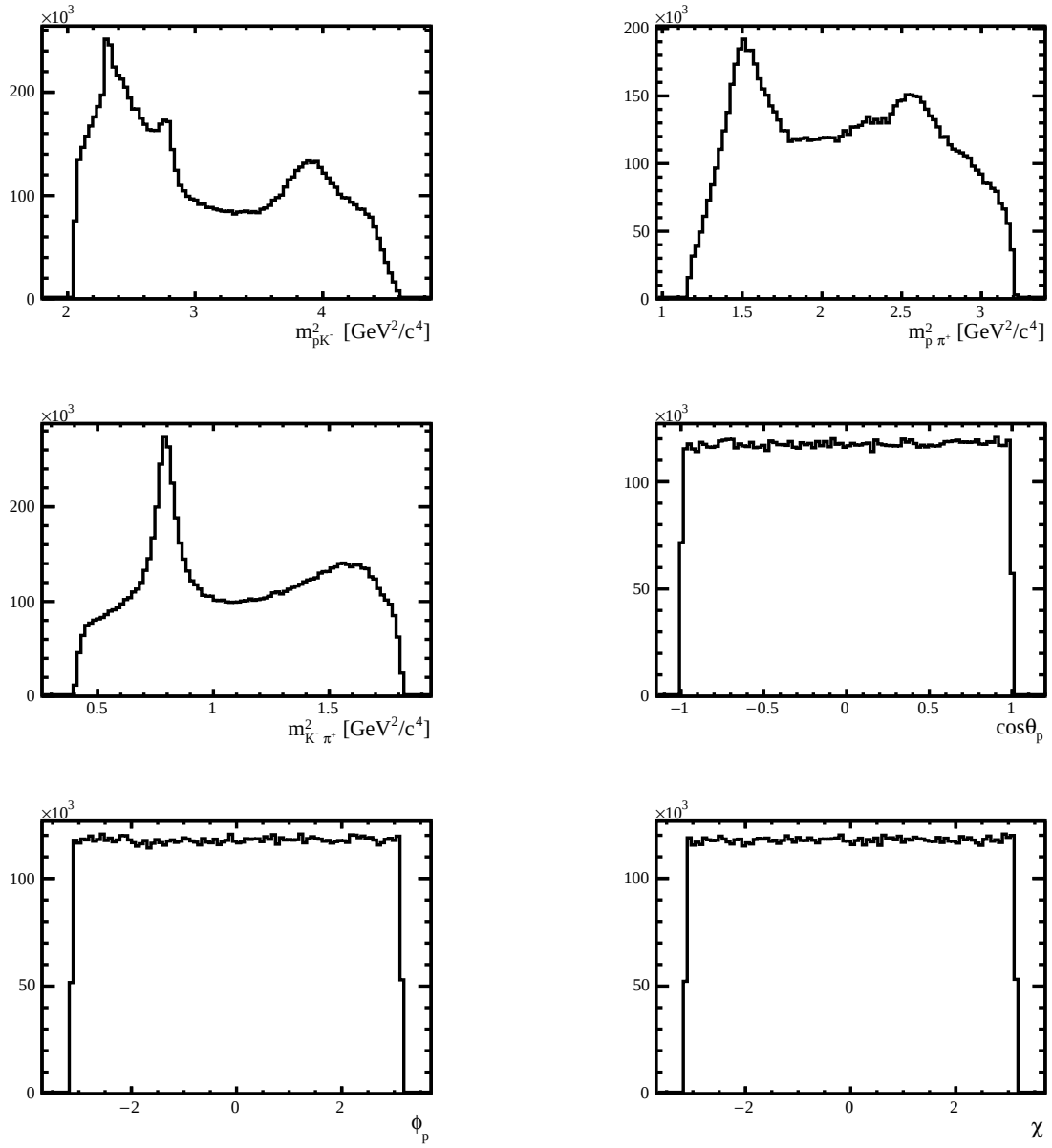

Figure 6.28: Toy generation of 10 M events using the model M10 with helicity couplings fixed to the fit results and zero polarization, without efficiency effects. The angular distributions are flat as expected.

	MagDown		MagUp	
MC	TIS	TOS	TIS	TOS
Λ_c^+	34 646	27 686	35 680	27 158
$\overline{\Lambda}_c^-$	34 398	28 523	34 488	28 643
Data	TIS	TOS	TIS	TOS
Λ_c^+	110 720	73 783	105 426	65 866
$\overline{\Lambda}_c^-$	108 394	78 340	104 852	70 295

Table 6.11: Number of events for the final fit for data and simulation, depending on the polarity, the trigger category and separating the Λ_c^+ from the $\overline{\Lambda}_c^-$ decays.

6.3.6 Fit Results

Within the model retained from the model building procedure, the simplest one is chosen as nominal model, M6, and the two others, M10 and M21, are used for the systematic uncertainty studies. The fit to the polarization is performed on the TIS and TOS trigger categories separately, for each magnet polarity (magnet up and magnet down) and separating the Λ_c^+ from the $\overline{\Lambda}_c^-$ decays. In total, 8 different and independent fits are performed. The number of events for each fit category are summarized in Tab. 6.11. The results of the fit to the TOS category for negative polarity and Λ_c^+ decays are shown in Tab. 6.12. The fit fractions, obtained using Eq. 6.16, are shown in Tab. 6.13, where the error is computed as explained in Sec 6.3.1 and the last line is the sum of fit fractions (called "SumofFF"). The helicity coupling are complex numbers of the form $H_k^{res}e^i\phi_k^{res}$, the superscript res indicate the resonance and the subscript k the number of couplings, which depends on the spin projection λ_p, the details on the helicity couplings are given in Sec. 5.4.4. The asymmetry parameters obtained following Eq. 5.120, 5.122 and 5.125 and the effective α computed as explained in Sec. 6.3.1 are reported in Tab. 6.14. Similar tables for the other fit categories can be found in Appendix G.

The fit projections of the five phase space variables along with the third mass $m^2_{K\pi}$ are shown in Fig. 6.29. The black dots are the data points, the red line shows the full PDF model, the colored lines shows the contributions of each resonance separately and the colour code is specified in the legend shown in the $m^2_{K\pi}$ mass projection, in general blue lines are K^* resonances, green lines Δ^{++} and brown-red lines Λ^*. The lower pads show the pulls between the data and the total model, the dashed horizontal lines show the limit of 3 standard deviations (3 σ). Overall the model matches the data reasonably well (within 3 σ) given the complicated fit. Discrepancies over 3 σ in the pulls can be seen at high $m^2_{K\pi}$ mass and at low m^2_{pK} mass, both seems to be due to the $\Lambda^*(1405)$ resonance however this is still under investigation at the time of writing this thesis.

6.3.7 Systematic uncertainties

The sources of systematic uncertainties affecting the measurement of the polarization and the helicity couplings are studied in this section. The general method used to estimate a systematic uncertainty on a measured value x_{mes} is to obtain the measurement of x in N different ways, where each way is simply a variation of the main method which explores other possible choices. A new toy sample is generated from the result of the measurement x_{mes}, then the measurement is performed again N

Parameter	Central value	Statistical uncertainty	Parameter	Central value	Statistical uncertainty
$H_1^{\Delta^{++}(1232)}$	0.756	0.02	$H_2^{\Delta^{++}(1232)}$	0.569	0.025
$H_1^{\Delta^{++}(1600)}$	0.659	0.02	$H_2^{\Delta^{++}(1600)}$	0.422	0.019
$H_1^{\Delta^{++}(1620)}$	0.625	0.01	$H_2^{\Delta^{++}(1620)}$	0.418	0.019
$H_1^{\Delta^{++}(1700)}$	0.547	0.016	$H_2^{\Delta^{++}(1700)}$	0.247	0.02
$H_1^{K^*(1430)}$	0.074	0.007	$H_2^{K^*(1430)}$	0.024	0.007
$H_2^{K^*(892)}$	0.595	0.028	$H_3^{K^*(892)}$	0.687	0.021
$H_4^{K^*(892)}$	0.534	0.03	$H_1^{\Lambda^*(1405)}$	0.623	0.014
$H_2^{\Lambda^*(1405)}$	0.591	0.021	$H_1^{\Lambda^*(1520)}$	0.341	0.034
$H_2^{\Lambda^*(1520)}$	0.356	0.034	$H_1^{\Lambda^*(1600)}$	0.164	0.016
$H_2^{\Lambda^*(1600)}$	0.027	0.014	$H_1^{\Lambda^*(1670)}$	0.333	0.011
$H_2^{\Lambda^*(1670)}$	0.341	0.013	$H_1^{\Lambda^*(2000)}$	0.614	0.012
$H_2^{\Lambda^*(2000)}$	0.648	0.017	$\phi_1^{\Delta^{++}(1232)}$	-0.529	0.061
$\phi_2^{\Delta^{++}(1232)}$	-3.525	0.087	$\phi_1^{\Delta^{++}(1600)}$	-4.419	0.066
$\phi_2^{\Delta^{++}(1600)}$	-1.082	0.084	$\phi_1^{\Delta^{++}(1620)}$	-3.995	0.057
$\phi_2^{\Delta^{++}(1620)}$	-0.683	0.081	$\phi_1^{\Delta^{++}(1700)}$	-1.383	0.05
$\phi_2^{\Delta^{++}(1700)}$	-1.354	0.127	$\phi_1^{K^*(1430)}$	-5.269	0.098
$\phi_2^{K^*(1430)}$	-5.217	0.316	$\phi_2^{K^*(892)}$	-0.113	0.062
$\phi_3^{K^*(892)}$	-6.5	0.008	$\phi_4^{K^*(892)}$	-3.353	0.1
$\phi_1^{\Lambda^*(1405)}$	-4.294	0.167	$\phi_2^{\Lambda^*(1405)}$	-4.325	0.168
$\phi_1^{\Lambda^*(1520)}$	-5.256	0.138	$\phi_2^{\Lambda^*(1520)}$	-1.154	0.133
$\phi_1^{\Lambda^*(1600)}$	-4.346	0.076	$\phi_2^{\Lambda^*(1600)}$	-5.887	0.546
$\phi_1^{\Lambda^*(1670)}$	-6.152	0.168	$\phi_2^{\Lambda^*(1670)}$	-6.373	0.148
$\phi_1^{\Lambda^*(2000)}$	0.544	0.17	$\phi_2^{\Lambda^*(2000)}$	-5.922	0.159
P_x	0.0	0.009	P_y	0.05	0.007
P_z	0.005	0.011			

Table 6.12: Result of the fit for model M6, MagDown polarity, TIS category and Λ_c^+ decays.

FF parameter	Central value	Statistical uncertainty
$\Delta^{++}(1232)$	0.12245	0.00011
$\Delta^{++}(1600)$	0.08202	0.00009
$\Delta^{++}(1620)$	0.15003	0.00454
$\Delta^{++}(1700)$	0.04804	0.00043
$K^*(1430)$	0.00322	0.00005
$K^*(892)$	0.19532	0.00012
$\Lambda^*(1405)$	0.19201	0.00056
$\Lambda^*(1520)$	0.03197	0.00011
$\Lambda^*(1600)$	0.00738	0.00009
$\Lambda^*(1670)$	0.06240	0.00059
$\Lambda^*(2000)$	0.22201	0.00036
$\sum F_{r_i}$	1.11685	0.00706

Table 6.13: Result of the fit for model M6, MagDown polarity, TIS category and Λ_c^+ decays.

Parameter	α	α statistical uncertainty
$\Delta^{++}(1232)$	0.2768	0.0474
$\Delta^{++}(1600)$	0.4184	0.0448
$\Delta^{++}(1620)$	0.3819	0.0412
$\Delta^{++}(1700)$	0.6613	0.0484
$K^*(1430)$	0.8096	0.1056
$K^*(892)$	0.3945	0.1282
$\Lambda^*(1405)$	0.0527	0.0419
$\Lambda^*(1520)$	-0.0430	0.1378
$\Lambda^*(1600)$	0.9472	0.0542
$\Lambda^*(1670)$	-0.0237	0.0504
$\Lambda^*(2000)$	-0.0538	0.0326
$\alpha_{effective}$	0.7147	0.0048

Table 6.14: Result of the fit for model M6, α parameters for MagDown polarity, TIS category and Λ_c^+ decays.

times on the toy data. The results of each new measurement x_i is slightly different from x_{mes} and the variation of the x_i with respect to x_{mes} give a measure of the systematic uncertainty. The distribution of the $\{x_1, x_2, ..., x_N\}$ new measurements is expected to be Gaussian with mean close to zero, the standard deviation σ_{sys} gives the systematic error on x. If only few "new" measurements are available, the uncertainty is chosen here as the maximum of the differences between the new fit results and the nominal ones. The source of systematic uncertainties and the method used to estimate it are listed below. The systematic uncertainties are studied for the polarization and the helicity couplings only since the fit fractions and the α parameters are derived from those. In the following, when a toy samples is generated, the number of events is the one of the real data or simulation, summarized in Table 6.11, depending if a toy emulating the data or of the simulation is generated.

Regarding the systematics due to the simulation samples, the sources studied are:

1. **Reweighting procedure:** the reweighting procedure described in Sec. 6.2.7 implies an implicit choice of the GBreweighter algorithm. To assess the effect of this choice, the weights are computed again in three different ways, using only 3 variables instead of four, with different combinations: (τ, P_T, y), $(nTracks, P_T, y)$ or $(nTracks, P_T, \tau)$. The fit with the nominal model is performed with these two alternative procedures. For these two new measurements, the difference with respect to the central value obtained with the nominal fit is computed and the maximum difference between the three is taken as systematic uncertainty.

2. **L0 trigger:** the L0 trigger has been corrected using tables obtained with a data-driven method. The weights used to correct the L0 TOS efficiencies are computed again by generating 100 new tables where the new values are obtained drawing random numbers following a normal distribution centered in the value of the original table with the value errors as standard deviation. The mean of the obtained distribution of new measurements is assigned as systematic uncertainty.

3. **PID Corr procedure:** the PID corrected variables are obtained using a calibration samples which has limited statistics. Alternative variables are generated using bootstrapped samples[1] with a different number of events. Furthermore, the PID variables are corrected for using a kernel PDF which can also be modified. A second set of variables is obtained using a modified kernel[2] width (50% wider). As for the first case, the maximum of the differences between the new measurements and the central value obtained with the nominal fit is taken as systematic uncertainty.

4. **MC size:** the simulation sample is used to include the efficiency effects in the PDF. However, this sample has a limited size. The systematic effect due to the finite size of the simulation sample is studied by generating toys with different efficiency maps and a large number of events (~ 500000). The new efficiency maps are obtained from the main simulation sample by drawing random numbers per each bin following a normal distribution centered in bin value with as standard deviation the statistical error of the bin. The $N = 100$ toys generated are fit back and

[1] Bootstrapping is a type of resampling technique where several smaller samples of the same size are repeatedly extracted from a single original sample.

[2] Kernel density estimation is a non parametric technique for density estimation in which a known density function (called the kernel) is averaged across the observed data points to create a smooth approximation of it.

the fit results distributions should be Gaussian. The mean of the parameters errors distribution is taken as systematic uncertainty.

Further sources of systematic uncertainties are the fit to the $m_{pK^-\pi^+}$ invariant mass from which the s-weights are extracted and the model choice, the latter gives the larger systematics. Finally the fit machinery could introduce a bias in the measurement, this effect is estimated building pull distributions as explained in the last bullet.

1. **Invariant mass fit:** the fit to the $m_{pK^-\pi^+}$ invariant mass is performed again with two new model which differs from the nominal one (which includes two CB functions, one Gaussian and an exponential function for the background). The first model uses only one CB and the second a polynomial function instead of exponential for the background.

2. **Model choice:** the nominal model (M6) has been chosen within the three models that passed the model: M6, M10 and M21. The effect of this choice is assessed by generating 100 toy data samples with the other alternative models (M10 and M21) and fitting it with the nominal model, setting as initial values the results obtained with the alternative models M10 and M21. The maximum variation of the result with respect to the nominal model is assigned as systematic uncertainty.

3. **Mass and widths of the resonances (RMW):** the masses and widths of the resonances are taken from Ref. [11], however the values reported have large uncertainties. For the resonances which have a major influence on the amplitude, *i.e.* the larger fit fractions, other fits are performed varying the mass and width values within their uncertainties. The maximum deviation from the fit results is assigned as systematic uncertainty.

4. **Bias of the fit machinery:** the final results obtained with the nominal model are used to generate N toy samples of the same size as the data sample, fixing the helicity couplings and polarization to the values obtained from the fit results, called $p_{nominal}$. The efficiency is included in the generation using the efficiency histogram obtained as explained in Sec. 6.2.8. A new phase space simulation sample, without the correlation effects, is produced using the same efficiency maps. This sample is then used in the likelihood to compute the integral of Eq. 6.14, which is needed for the full likelihood. The generated samples are then fit N times using the full fit machinery, with the likelihood defined as in Eq. 6.13. From the new fit results, p_{toy}, pull distributions are build for each helicity coupling parameter p as:

$$pull = \frac{p_{toy} - p_{nominal}}{\sigma_{toy}} \tag{6.30}$$

where $p_{nominal}$ is the result of the nominal fit to data for the parameter p and σ_{toy} the error on the fit to the toy data. Then the distributions of the pull obtained (for each parameter) should be a Gaussian with mean zero, if the fit is unbiased, and standard deviation close to one, if the error are computed correctly. If the standard deviation is larger (smaller) than 1 then the error are underestimated (overestimated). If this is the case, the statistical uncertainties are rescaled

by the pull standard deviation. If a bias is seen, the deviation from zero, multiplied by the statistical uncertainty on the fit result, is assigned as systematic uncertainty.

Finally, the detector resolution could affect the measurement of narrow resonances, for instance $\Lambda^*(1520)$ or $\Lambda^*(1670)$ which have widths 15^{+10}_{-8} and 19^{18}_{-2} MeV, see Tab. 5.2. The resolution on the Λ_c^+ mass is around 5 MeV, which is close to the lower limits of the $\Lambda^*(1520)$ or $\Lambda^*(1670)$ widths. The resolution on the m_{pK} mass in a 30 MeV and 40 MeV window around the $\Lambda^*(1520)$ and $\Lambda^*(1670)$ masses respectively is found to be 1.33 MeV and 1.93 MeV. Ultimately, the resolution is found to be smaller than the expected width hence the resolution effects are not considered.

A summary of the mean and standard deviation (called μ and σ) for the pulls of bullet 2, is given in Tab. 6.15. The total systematic uncertainty is the sum in quadrature of all the systematics. Table 6.16 and Table 6.17 shows the single systematic values as well as the final one for the helicity coupling and the polarization. The systematic uncertainty due to the model choice is not considered for the single helicity couplings since the resonant content changes when an alternative model is chosen and the value of the helicity couplings varies a lot since new degrees of freedom have been artificially added or removed. The larger source of systematic uncertainty on the polarization measurement is the model choice.

6.4 Results

The final results for the nominal fit to the samples of the TIS category, for negative polarity and Λ_c^+ decays are shown in Table 6.16 and Table 6.17. The preliminary measurement of the polarization is found to be compatible with zero, the measured values are:

$$\begin{aligned} P_x &= -0.0233 \pm 0.0046 \pm 0.0341 \\ P_y &= 0.0560 \pm 0.0044 \pm 0.0919 \\ P_z &= 0.0095 \pm 0.0063 \pm 0.0590 \end{aligned} \tag{6.31}$$

where the first uncertainty is statistical and the second systematic. The final precision is dominated by the systematic uncertainty which is in turn largely dominated by the model choice, see tab. 6.16. The systematic uncertainties for the other categories are still under study, hence no results are shown. This result is compatible with other baryons polarization measurements performed at the LHC. For instance, a zero polarization has been measured for Λ_b baryons at 7, 8 and 13 TeV by LHCb [80, 81], ATLAS [82] and CMS [83]; similarly for Λ baryons a zero polarization was measured by ATLAS [79]. As discussed in Sec. 2.3, there exists very few theoretical predictions to compare this result with, hence an input from theory would be very valuable. In the near future, the polarization measurement will be also performed in bins of transverse momentum in order to compare it to the results obtained in Ref. [204] and the theory prediction in [74].

The effective asymmetry parameter α is also measured and found to be $\alpha_{effective} = 0.715 \pm 0.005$, where the quoted uncertainty is statistical. The fit fractions are given in Table 6.13. Since the polarization is close to zero, the helicity couplings are degenerate. This can be understood looking at Eq. 5.106, where for $P_x = P_y = P_z = 0$, many terms cancel and some of the helicity couplings cannot be

Parameter	Pulls μ	Pulls σ	Parameter	Pulls μ	Pulls σ
$H_1^{\Delta^{++}(1232)}$	-0.5587	3.9680	$H_2^{\Delta^{++}(1232)}$	-2.9574	3.7598
$H_1^{\Delta^{++}(1600)}$	-8.0000	7.2137	$H_2^{\Delta^{++}(1600)}$	-3.5825	2.7508
$H_1^{\Delta^{++}(1620)}$	-6.4856	5.7826	$H_2^{\Delta^{++}(1620)}$	-3.8408	3.3337
$H_1^{\Delta^{++}(1700)}$	-8.0000	3.8707	$H_2^{\Delta^{++}(1700)}$	-3.1986	2.9016
$H_1^{K^*(1430)}$	-2.0537	1.7147	$H_2^{K^*(1430)}$	0.4622	1.5378
$H_2^{K^*(892)}$	-0.8185	2.5343	$H_3^{K^*(892)}$	-0.5820	1.8680
$H_4^{K^*(892)}$	-0.7063	3.1078	$H_1^{\Lambda^*(1405)}$	0.3918	2.6595
$H_2^{\Lambda^*(1405)}$	1.2118	4.8410	$H_1^{\Lambda^*(1520)}$	-1.2472	2.4137
$H_2^{\Lambda^*(1520)}$	1.9105	2.9364	$H_1^{\Lambda^*(1600)}$	2.1601	3.6046
$H_2^{\Lambda^*(1600)}$	1.2209	2.4301	$H_1^{\Lambda^*(1670)}$	2.2490	5.9748
$H_2^{\Lambda^*(1670)}$	1.3856	3.1968	$H_1^{\Lambda^*(2000)}$	-1.1563	4.1903
$H_2^{\Lambda^*(2000)}$	-0.2667	3.6883	$\phi_1^{\Delta^{++}(1232)}$	1.5636	2.3536
$\phi_2^{\Delta^{++}(1232)}$	2.8317	2.3506	$\phi_1^{\Delta^{++}(1600)}$	-0.0121	3.8001
$\phi_2^{\Delta^{++}(1600)}$	-0.8509	3.1850	$\phi_1^{\Delta^{++}(1620)}$	0.8705	3.7151
$\phi_2^{\Delta^{++}(1620)}$	0.6234	3.1173	$\phi_1^{\Delta^{++}(1700)}$	0.3515	3.0156
$\phi_2^{\Delta^{++}(1700)}$	1.3860	2.4544	$\phi_1^{K^*(1430)}$	1.0235	2.3184
$\phi_2^{K^*(1430)}$	0.7085	1.8923	$\phi_2^{K^*(892)}$	0.6868	2.7648
$\phi_3^{K^*(892)}$	2.2261	2.2294	$\phi_4^{K^*(892)}$	-0.1623	3.0591
$\phi_1^{\Lambda^*(1405)}$	7.0346	4.7345	$\phi_2^{\Lambda^*(1405)}$	4.4290	5.3364
$\phi_1^{\Lambda^*(1520)}$	1.7236	2.8946	$\phi_2^{\Lambda^*(1520)}$	3.9084	3.3489
$\phi_1^{\Lambda^*(1600)}$	-2.1545	2.5680	$\phi_2^{\Lambda^*(1600)}$	-1.2651	5.6300
$\phi_1^{\Lambda^*(1670)}$	8.0000	6.0450	$\phi_2^{\Lambda^*(1670)}$	8.0000	5.8281
$\phi_1^{\Lambda^*(2000)}$	3.3954	3.0595	$\phi_2^{\Lambda^*(2000)}$	1.8798	3.3733
P_x	-2.6501	1.9528	P_y	0.7588	1.6803
P_z	0.3719	1.7320			

Table 6.15: Results of the pulls for the uncertainties studies on helicity couplings and polarization for M6, MagDown polarity, TIS category and Λ_c^+ decays.

uniquely determined. Despite this, the effective asymmetry parameter is measurable since it includes all the amplitude components across the Dalitz plane. The large asymmetry measured implies that the method proposed to measure the polarization in the fixed-target sample can be used. If a small or zero value of $\alpha_{effective}$ was found instead, the sensitivity to the polarization would have been lost, preventing the use of this channel for the MDM measurement.

Resonance	mean fit	stat. unc.	Total sys.	Reweight	Mass fit	Pulls	Model	PID	RMW	MCsize
$H_1^{\Delta^{++}(1232)}$	0.7450	0.0050	0.4874	0.0040	0.0025	-0.0111	–	0.0064	0.4869	0.0179
$H_2^{\Delta^{++}(1232)}$	0.4959	0.0066	0.3153	0.0021	0.0042	-0.0734	–	0.0685	0.2981	0.0205
$H_1^{\Delta^{++}(1600)}$	0.5026	0.0027	0.1753	0.0031	0.0055	-0.1568	–	0.0228	0.0723	0.0190
$H_2^{\Delta^{++}(1600)}$	0.3549	0.0068	0.6662	0.0048	0.0031	-0.0672	–	0.0373	0.6614	0.0186
$H_1^{\Delta^{++}(1620)}$	0.5575	0.0018	0.0863	0.0017	0.0050	-0.0676	–	0.0109	0.0510	0.0117
$H_2^{\Delta^{++}(1620)}$	0.3470	0.0056	0.2235	0.0053	0.0051	-0.0715	–	0.0301	0.2090	0.0132
$H_1^{\Delta^{++}(1700)}$	0.4220	0.0040	0.2283	0.0026	0.0009	-0.1250	–	0.0114	0.1902	0.0147
$H_2^{\Delta^{++}(1700)}$	0.1818	0.0070	0.5714	0.0027	0.0043	-0.0652	–	0.0321	0.5664	0.0204
$H_1^{K^*(1430)}$	0.0599	0.0040	0.0171	0.0012	0.0008	-0.0140	–	0.0028	0.0065	0.0066
$H_2^{K^*(1430)}$	0.0275	0.0047	0.0890	0.0006	0.0008	0.0034	–	0.0046	0.0886	0.0064
$H_2^{K^*(892)}$	0.5727	0.0109	0.1767	0.0046	0.0109	-0.0227	–	0.0461	0.1673	0.0214
$H_3^{K^*(892)}$	0.6749	0.0115	0.0721	0.0070	0.0085	-0.0125	–	0.0115	0.0662	0.0200
$H_4^{K^*(892)}$	0.5132	0.0096	0.0976	0.0016	0.0014	-0.0210	–	0.0739	0.0498	0.0336
$H_1^{\Lambda^*(1405)}$	0.6286	0.0054	0.1212	0.0035	0.0037	0.0056	–	0.0129	0.1198	0.0113
$H_2^{\Lambda^*(1405)}$	0.6168	0.0043	0.2699	0.0067	0.0028	0.0254	–	0.0405	0.2648	0.0194
$H_1^{\Lambda^*(1520)}$	0.2977	0.0143	0.3512	0.0060	0.0026	-0.0430	–	0.0596	0.3426	0.0231
$H_2^{\Lambda^*(1520)}$	0.4208	0.0115	0.0773	0.0069	0.0051	0.0643	–	0.0319	0.0135	0.0240
$H_1^{\Lambda^*(1600)}$	0.1989	0.0045	0.0684	0.0006	0.0052	0.0351	–	0.0273	0.0501	0.0127
$H_2^{\Lambda^*(1600)}$	0.0444	0.0059	0.0243	0.0004	0.0026	0.0175	–	0.0101	0.0019	0.0131
$H_1^{\Lambda^*(1670)}$	0.3579	0.0018	0.0281	0.0015	0.0012	0.0246	–	0.0014	0.0094	0.0094
$H_2^{\Lambda^*(1670)}$	0.3589	0.0040	0.2358	0.0022	0.0010	0.0175	–	0.0291	0.2331	0.0109
$H_1^{\Lambda^*(2000)}$	0.5995	0.0030	0.0454	0.0029	0.0006	-0.0143	–	0.0112	0.0392	0.0134
$H_2^{\Lambda^*(2000)}$	0.6437	0.0046	0.2981	0.0038	0.0040	-0.0046	–	0.0459	0.2940	0.0173
P_x	-0.0233	0.0046	0.0341	0.0013	0.0008	-0.0238	0.0170	0.0059	0.0147	0.0075
P_y	0.0560	0.0044	0.0919	0.0004	0.0007	0.0056	0.0810	0.0136	0.0403	0.0069
P_z	0.0095	0.0063	0.0590	0.0020	0.0003	0.0041	0.0561	0.0156	0.0046	0.0072

Table 6.16: Systematic uncertainties on helicity couplings and polarization for M6, MagDown polarity, TIS category and Λ_c^+ decays.

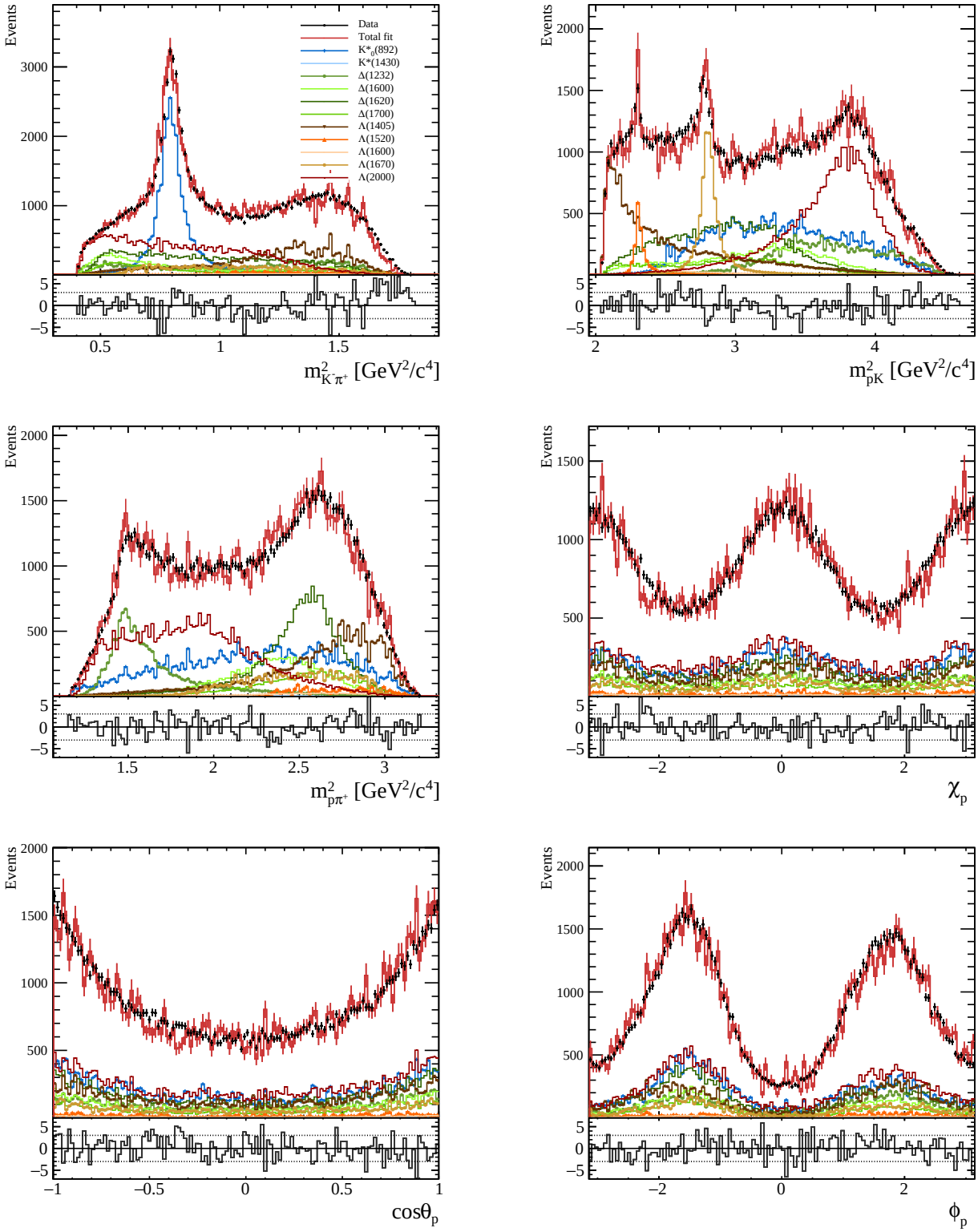

Figure 6.29: Example of fit with the model M6 on the TIS category, negative polarity, for Λ_c^+ decays only. The black dots are the data points, the red line shows the full PDF model, the colored lines shows the contributions of each resonance separately and the colour code is specified in the legend shown in the $m^2_{K\pi}$ mass projection, in general blue lines are K^* resonances, green lines Δ^{++} and brown-red lines Λ^*.

Resonance	mean fit	stat. unc.	Total sys.	Reweight	Mass fit	Pulls	Model	PID	RMW	MCsize
$\phi_1^{\Delta^{++}(1232)}$	-0.4345	0.0257	0.3992	0.0002	0.0113	0.0947	–	0.0357	0.3816	0.0584
$\phi_2^{\Delta^{++}(1232)}$	-3.2779	0.0371	0.6824	0.0044	0.0046	0.2466	–	0.0760	0.6283	0.0647
$\phi_1^{\Delta^{++}(1600)}$	-4.4194	0.0173	0.5541	0.0239	0.0034	-0.0008	–	0.0284	0.5498	0.0583
$\phi_2^{\Delta^{++}(1600)}$	-1.1534	0.0263	0.7006	0.0147	0.0030	-0.0714	–	0.0865	0.6878	0.0707
$\phi_1^{\Delta^{++}(1620)}$	-3.9450	0.0153	0.7614	0.0179	0.0038	0.0495	–	0.0331	0.7576	0.0449
$\phi_2^{\Delta^{++}(1620)}$	-0.6330	0.0259	1.1869	0.0002	0.0022	0.0503	–	0.0867	1.1814	0.0547
$\phi_1^{\Delta^{++}(1700)}$	-1.3656	0.0164	0.4796	0.0097	0.0016	0.0174	–	0.0301	0.4755	0.0507
$\phi_2^{\Delta^{++}(1700)}$	-1.1780	0.0516	0.7973	0.0092	0.0063	0.1756	–	0.1514	0.7578	0.0868
$\phi_1^{K^*(1430)}$	-5.1686	0.0424	1.1430	0.0113	0.0126	0.1005	–	0.1307	1.1270	0.0947
$\phi_2^{K^*(1430)}$	-4.9927	0.1670	0.6987	0.0598	0.0126	0.2240	–	0.1785	0.5939	0.2230
$\phi_2^{K^*(892)}$	-0.0708	0.0224	0.3808	0.0134	0.0036	0.0425	–	0.0751	0.3683	0.0423
$\phi_3^{K^*(892)}$	-6.4829	0.0034	0.0325	0.0000	0.0000	0.0171	–	0.0000	0.0000	0.0277
$\phi_4^{K^*(892)}$	-3.3695	0.0326	6.5842	0.0032	0.0042	-0.0162	–	0.1625	6.5818	0.0661
$\phi_1^{\Lambda^*(1405)}$	-3.1158	0.0354	1.3353	0.0246	0.0261	1.1779	–	0.1616	0.6024	0.0732
$\phi_2^{\Lambda^*(1405)}$	-3.5827	0.0314	1.0054	0.0290	0.0319	0.7422	–	0.1275	0.6545	-0.1157
$\phi_1^{\Lambda^*(1520)}$	-5.0181	0.0478	0.3145	0.0304	0.0102	0.2383	–	0.1772	0.0651	0.0736
$\phi_2^{\Lambda^*(1520)}$	-0.6333	0.0398	0.9580	0.0363	0.0073	0.5204	–	0.0942	0.7951	0.0670
$\phi_1^{\Lambda^*(1600)}$	-4.5098	0.0297	0.4374	0.0169	0.0265	-0.1642	–	0.0568	0.3958	0.0594
$\phi_2^{\Lambda^*(1600)}$	-6.5783	0.0971	1.7540	0.0251	0.1070	-0.6913	–	0.6130	0.6130	-1.3546
$\phi_1^{\Lambda^*(1670)}$	-4.8071	0.0278	1.3568	0.0241	0.0205	1.3450	–	0.1597	0.0123	0.0710
$\phi_2^{\Lambda^*(1670)}$	-5.1888	0.0254	1.2014	0.0237	0.0255	1.1840	–	0.1272	0.1272	0.0896
$\phi_1^{\Lambda^*(2000)}$	1.1213	0.0556	0.8083	0.0312	0.0276	0.5776	–	0.1655	0.5335	0.0773
$\phi_2^{\Lambda^*(2000)}$	-5.6232	0.0472	0.6675	0.0252	0.0339	0.2990	–	0.1186	0.5778	0.0804

Table 6.17: Systematic uncertainties on helicity couplings and polarization for M6, MagDown polarity, TIS category and Λ_c^+ decays.

7 Conclusions

In this thesis, the polarization of the charmed baryon Λ_c^+ has been measured for baryons produced promptly in proton-proton collisions, using the dataset collected by the LHCb detector in 2016, at a center of mass energy of 13 TeV. The main motivations for this measurements are threefold. On one hand, charmed baryon polarization is poorly known experimentally, the most relevant measurement has been performed 20 years ago [204], and no improvement has been made since then. On the other hand, there is no theory prediction available for charm baryons polarization at the LHC energy. Finally the Λ_c^+ polarization is a necessary input for the measurement of the Magnetic Dipole Moment (MDM) of the charm quark proposed in Ref. [1] [2] [3] [4] [5]. Along with the Λ_c^+ polarization measurement, this thesis presents the work done on the determination of the front-end electronics of the Plume detector, which will be installed for Run 3 in the LHCb experiment.

The five-dimensional amplitude analysis of the Cabibbo favoured three-body decay $\Lambda_c^+ \to pK^-\pi^+$ has been performed. The analysis can be broken down in three major steps: the development of the equations describing the amplitude of the decay, the treatment of the data to extract the promptly produced Λ_c^+ and finally the fit to the data to perform the polarization measurement. First the equations describing the amplitude of the $\Lambda_c^+ \to pK^-\pi^+$ decays have been derived within the helicity formalism. This was necessary since the formalism used in [204] was found to be incomplete, and many points needed to be clarified before proceeding with the analysis. In particular, the need of the Wigner rotations and the 2π factors described in Chapter 5 has been assessed. The formalism developed has been proven to be correct by testing it for specific configurations for which the output is known; it has also been proven to be equivalent to the one proposed in Ref. [202]. Regarding the signal extraction, during Run 2 the LHC has produced almost 1 MHz of $c\bar{c}$ pairs of which 600 Hz has been seen by the LHCb detector; this translates into a large amount of Λ_c^+ baryons and a very significant signal. Hence, the signal extraction was fairly straight-forward since the background contributions were small with respect to the signal. The most important selection for this analysis is the one on the Λ_c^+ impact parameter which allows to separate the prompt from the secondary decays. This is because the polarization depends on the production mechanism involved which differs between prompt and secondary production. A tight selection leaving less than 2% of contamination from secondaries has been applied. Finally the residual background, mostly from proton misidentification, is also below 2%. The main challenge of the selections procedure was the understanding of the L0

trigger effects on the angular variables, especially ϕ_p. In the end, the analysis has been performed for the two separated trigger categories in order to master those effects. The helicity amplitudes derived are then used to measure the Λ_c^+ and $\overline{\Lambda}_c^-$ polarization, the helicity couplings and the fit fractions of each intermediate resonant state, by means of a fit to the data. The asymmetry parameters of the single resonances as well as an effective asymmetry parameter for the whole decay have been extracted from the fit results. The resonance content of the model has been determined by adding only the resonances giving a significant contribution to the main amplitude and describing as good as possible the data. One nominal model and two additional models giving similar results have been retained. Once the nominal model determined, the final measurement has been performed for the two magnet polarities separately since the reconstruction is not exactly identical for the two polarities and the simulation does not reproduce those effects perfectly. The decays ($\Lambda_c^+ \to pK^-\pi^+$) and anti-decays ($\bar{\Lambda_c}^- \to \bar{p}K^+\pi^-$) have been also separated since the production of a Λ_c^+ baryon and a $\overline{\Lambda}_c^-$ antibaryon is different, hence the polarization may differs between the two. The measurement is performed for 8 different categories, depending on the trigger, polarity and type of decay. The polarization has been measured for the TIS, negative polarity sample of Λ_c^+ decays, as:

$$\begin{aligned} P_x &= -0.0233 \pm 0.0046 \pm 0.0341 \\ P_y &= 0.0560 \pm 0.0044 \pm 0.0919 \\ P_z &= 0.0095 \pm 0.0063 \pm 0.0590 \end{aligned} \tag{7.1}$$

where the first uncertainty is statistical and the second, systematic. The measurement is dominated by the systematic uncertainties which give an error up to 9% where the larger source of systematic uncertainties is the model choice. The most challenging parts of the analysis have been the understanding of the helicity amplitudes, the model construction and the development of the fit machinery. An incorrect amplitude can still give reasonable results when fitting the data. The equations have been carefully tested and studied to be sure that no unphysical definitions, which would not be seen in the fit, were used. The assessment of the resonance content of the model was also challenging since several equivalent models may give similar results, ultimately a choice is made by choosing the simplest model among the few similar models left. The fit machinery has been developed from scratch in C++ and it was also a challenging part of the analysis. The large amount of data and the complicated computations required an unavoidable optimization of the code using the most recent features of C++ libraries and RooFit. The code is parallelized, to run on several CPUs in parallel, and optimized in order to keep in memory any element of the amplitude which is not changing during the minimization of the likelihood. The usage of GPUs has been considered, however the larger number of CPUs available gave better performances than the small number of GPUs, hence this option has not been further investigated.

The amplitude analysis has been completed for the 8 categories, and the methods for the systematic uncertainties estimation have been developed. However the systematic uncertainties have been studied only for the TIS negative polarity sample of Λ_c^+ decays, they will be assessed for the other 7 categories during the analysis review. For the future prospects of this measurement, a higher statistic sample could be easily obtained by relaxing the selection on the impact parameter. The increased

contamination from secondary could be treated as a background component in the final likelihood. Furthermore, the entire analysis could be performed for the $\Xi_c^+ \to pK^-\pi^+$ baryons decays, which share the same final state and same helicity amplitudes. Finally, the model obtained in this analysis, will be used to measured the polarization in a completely different system, the pNe collisions collected by LHCb in 2017 at a center of mass energy of 68 GeV. The estimated statistical uncertainty for the 2017 pNe sample ranges from 10% to 14% depending on the final number of signal events extracted, which can vary from 200 to 400 signal events. Thus, the measurement of the Λ_c^+ polarization in this sample will be dominated by the statistical uncertainty. During Run 3, thanks to SMOG2, a data sample with a larger signal is expected. For a sample containing 300 000 Λ_c^+ baryons, a statistical uncertainty of 0.4% is expected, in this case the polarization measurement will be dominated by the systematic uncertainty due to the model choice, which is around 5%. In other words, the precision on the polarization measurement for future SMOG2 samples will be systematically limited to 5%.

Along with the data analysis and the development of the helicity amplitudes formalism, a more hardware related work has been done in this thesis, concerning the determination of the front-end electronics of the Plume detector. The Plume detector is a luminosity detector conceived for the LHCb experiment. The journey from the conception to the construction of the Plume detector was definitely exciting. The tests performed aimed at proving that the front-end electronic of the electromagnetic calorimeter of LHCb could be adapted for the PLUME needs. The ECAL FEBs have been designed to integrate a signal within 25 ns, and removing eventual leaks outside this window. The expected signal for PLUME however is much shorter, around 3 ns, and the electronics was not optimized for such a short pulse. In this work, it has been proven that it is possible to use the ECAL FEBs for PLUME. Furthermore, a new timing measurement is proposed aiming at monitoring the shift of the LHCb clock with respect to the main LHC clock. The first results are promising, an expected time resolution of less than the 0.5 ns obtained with the OT during Run 1 seems achievable. Few possible improvements for the timing measurement have been identified, including the conception of a better splitter to divide the signal in 8 copies and an optimization of the step size of the timing scan. This measurement will be beneficial for the performances of the LHCb detector during Run 3 since it will allow to monitor the time synchronization in quasi real time with a good precision.

8 Synthèse

Le modèle standard de la physique des particules (MS) est une théorie élégante qui décrit la structure fondamentale de la matière qui nous entoure. Il se concentre sur la description des particules élémentaires, par exemple les quarks q, et la façon dont ils se combinent en éléments plus complexes, par exemple les baryons (qqq) ou les mésons ($\bar{q}q$). Parmi les baryons, les protons et les neutrons forment la matière ordinaire telle que nous la connaissons. Les interactions entre ces particules sont également décrites dans le MS : pour chaque type de force (électromagnétique, faible et forte), il existe un "porteur de force", qui véhicule l'interaction entre les particules. Bien que le grand nombre de prédictions réussies ait fait du MS une théorie bien établie, il existe quelques observations expérimentales qui ne sont pas prises en compte. Parmi celles-ci, l'asymétrie significative entre la matière et l'antimatière que nous observons dans notre Univers, n'est pas expliquée par le MS. La violation des symétries de charge et de parité, appelée violation de CP, pourrait aider à comprendre pourquoi la matière et l'antimatière ne sont pas présentes en même quantité, mais elle n'est toujours pas suffisante pour expliquer une différence aussi importante.

Le besoin de modèles physiques allant au-delà du MS pousse les recherches expérimentales à tester les limites de ses prédictions et à rechercher de la nouvelle physique (NP) au-delà de celui-ci. Dans le référentiel de ces recherches, la mesure du moment dipolaire magnétique (MDM) des baryons charmés et finalement du quark charmé, permet de tester la validité des prédictions du MS et surtout de la théorie de la chromodynamique quantique (QCD). Le moment magnétique d'une particule μ est une propriété induite par le spin. Pour les particules de spin $S = 1/2$, le moment magnétique μ s'écrit, en unités naturelles $\hbar = c = 1$,

$$\vec{\mu} = \frac{g}{2}\frac{q}{2m}\vec{S} \quad \text{et} \quad \mu = \frac{g}{2}\frac{q}{2m} \tag{8.1}$$

où q est la charge électrique du fermion, m est sa masse et g est le facteur gyromagnétique. Au niveau classique, $g = 2$, cependant les corrections quantiques dues aux effets de boucle peuvent modifier cette valeur. Le moment magnétique anormal est défini comme $a_p \equiv \frac{g-2}{2}$, où l'indice p indique la particule, et est couramment utilisé pour quantifier les contributions d'ordre supérieur, qui sont calculées très précisément par la QED. Toute déviation de a_p par rapport à la prédiction MS indiquerait la présence d'effets de nouvelle physique. Les moments magnétiques de l'électron et du muon ont été mesurés très précisément : $g_e/2 = 1,00115965218073(28)$ [89] et $a_\mu = 116592061(41) \times 10^{-11}$ [90]. Les prédictions

théoriques sont également calculées avec une très bonne précision, ce qui se traduit par une tension de 4.2 σ entre la théorie et l'expérience pour le moment magnétique du muon. Il s'agit de l'une des preuves les plus significatives de nouvelle physique à ce jour. Le MDM du tau est techniquement plus difficile à mesurer en raison de sa très courte durée de vie ; à ce jour, le MDM anormal du tau est connu avec une précision de seulement 10^{-2}, ce qui n'est pas compétitif avec la précision de 10^{-8} du MS. De même, pour le MDM des baryons et des quark charmés, quelques prédictions existent mais il n'y a pas de mesure expérimentale disponible pour les confirmer ou les rejeter, d'où la nécessité d'une nouvelle mesure.

Du point de vue théorique, le MDM des baryons peut être prédit, dans le référentiel du modèle des quarks, à partir du moment magnétique des constituants. Le moment magnétique d'un baryon $|B\rangle$ s'écrit donc :

$$\mu_B = \langle B|(\vec{\mu}_1 + \vec{\mu}_2 + \vec{\mu}_3) \cdot \vec{S}|B\rangle = \sum_i \langle B|\frac{g_i}{2}\frac{q_i}{2m_i}|B\rangle \tag{8.2}$$

Dans cette thèse, le baryon charmé Λ_c^+ est étudié, son moment magnétique s'écrit simplement: $\mu_{\Lambda_c^+} = \mu_c$. La mesure du MDM du Λ_c^+ permettrait donc d'accéder au MDM du quark charm. Il existe un grand nombre de prédictions théoriques pour le MDM du Λ_c^+ basées sur des modèles différents, donnant des valeurs comprises entre $[0.15 - 0.52]\mu_N$ et jusqu'à présent il n'existe pas de mesure expérimentale permettant de déterminer lequel parmi ces modèles est correct.

Une expérience de mesure du MDM des baryons charmés est proposée dans les références suivantes : [1][2][3][4][5]. Toutes ces propositions sont basées sur le même principe physique bien connu (utilisé en outre pour mesurer le moment magnétique du muon), à savoir la précession des particules chargées dans un champ magnétique. L'idée de ces expériences est de mesurer l'angle de précession du vecteur spin des baryons, ce qui donne accès au MDM du baryon même. Cependant, la durée de vie des baryons charmés est très courte (environ quelques centaines de fm) donc pour que la précession se produise avant la désintégration du baryon un champ magnétique très puissant (de l'ordre 10^3 T) est nécessaire. Jusqu'à présent, les aimants conventionnels ne peuvent pas produire un tel champ magnétique[1]. Une solution possible est de canaliser les baryons dans un cristal, où le champ magnétique entre les plans de la structure cristallographique est suffisamment élevé pour que la précession se produise avant la désintégration du baryon ; cette méthode a été utilisée avec succès dans le passé pour mesurer le MDM du baryon Σ^+ [6]. La manière dont les baryons charmés pourraient être produits au Large Hadron Collider (LHC) et ensuite redirigés vers le cristal de précession fait l'objet d'un vaste programme de recherche. L'un des montages proposés comprend une séquence de deux cristaux où un cristal déflecteur est utilisé pour extraire les protons du halo du faisceau du LHC afin de les diriger sur un second cristal, un cristal-cible, qui est utilisé pour produire les baryons charmés. Le cristal dédié à la précession du vecteur polarisation est placé juste après ces deux autres cristaux; un dessin est montré un figure 8.1. Afin de mesurer le moment magnétique, la polarisation initiale du baryon (avant qu'il ne pénètre dans le cristal) est une donnée nécessaire. En principe, la polarisation initiale pourrait être obtenue à partir d'autres expériences fonctionnant dans des conditions similaires à celles de l'installation à double cristal, par exemple une expérience produisant des baryons à partir de l'interaction d'un faisceau de protons avec une cible. L'expérience LHCb [7] est adaptée à cette

[1]Le champ magnétique plus puissant jamais produit sur terre s'élève à 45.5 T [220].

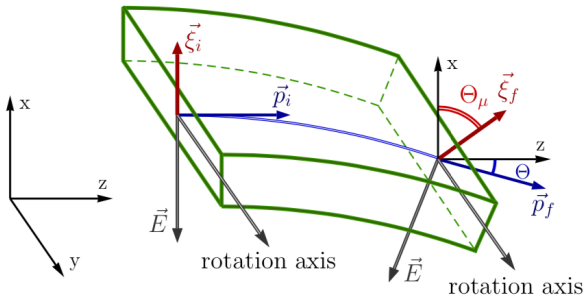

Figure 8.1: Esquisse de la précession du vecteur polarisation (en rouge) dans le cristal, l'angle de précession Θ_μ est également représenté. D'après Ref.[2].

mesure car elle peut fonctionner en mode cible fixe grâce au système SMOG, qui permet d'injecter de petites quantités de gaz à proximité du point d'interaction. L'échantillon pNe à cible fixe collecté avec le détecteur LHCb à une énergie dans le centre de masse de $\sqrt{s} = 68$ GeV en 2017 reproduit des conditions similaires à celles requises pour la mesure de la polarisation d'entrée discutée ci-dessus. Cependant, en raison du manque de statistiques dans cet échantillon (environ 250 Λ_c^+ sont observés dans les données) et de la complexité de l'analyse d'amplitude qui est nécessaire pour mesurer la polarisation, une mesure préliminaire de la polarisation est effectuée en utilisant les échantillons à haute statistique contenant des collisions pp. Cela permet de fixer certains des paramètres du modèle (les couplages d'hélicité ainsi que la liste de résonances inclues) qui ne dépendent pas du mécanisme impliqué dans la production de baryons et qui sont donc indépendants de l'expérience. C'est le sujet de ce travail. Le modèle construit sur les données pp sera ensuite utilisé pour mesurer la polarisation dans l'échantillon à cible fixe.

8.1 La polarisation des baryons

De manière générale, la polarisation de production d'un baryon avec un spin 1/2 donne une indication de quelle projection est la plus fréquente entre les deux valeurs possibles: $+1/2$ et $+1/2$. L'information sur la polarisation est extraite en examinant la distribution angulaire des produits de désintégration, qui dépend à la fois de la polarisation originale du baryon et de l'asymétrie de désintégration. Dans le cas d'une désintégration à deux corps du type $\Lambda_c^+ \to X + Y$, la distribution angulaire s'écrit, dans le référentiel du Λ_c^+, comme

$$\frac{1}{N}\frac{dN}{d\cos\theta} = \frac{1}{2}(1 + \alpha P \cos\theta) \tag{8.3}$$

où P est la projection de la polarisation Λ_c^+, θ est l'angle entre l'axe de polarisation et la direction finale du baryon X, et α est le paramètre d'asymétrie de désintégration. D'une part, le paramètre d'asymétrie α est indépendant des conditions de production et représente l'asymétrie entre les amplitudes de la désintégration qui violent la parité et celles qui la conservent. Cela signifie que si la désintégration conserve la parité, α sera nul et la distribution angulaire sera plate, ce qui empêcherait la mesure de la polarisation. En effet, l'asymétrie est non nulle pour les désintégrations induites par des interactions violant la parité et la sensibilité à la polarisation dépend de la valeur de α; plus α est grand plus la

sensibilité est élevée. D'autre part, la polarisation dépend strictement du mécanisme de production et par conséquent de l'expérience, c'est-à-dire qu'elle dépend du type de faisceau, du mode de collision (cible fixe ou non), du canal de désintégration, de l'énergie du centre de masse du système.

Au LHC, Λ_c^+ peut être produit via des interactions fortes juste après la collision ou via des interactions faibles dans une désintégration secondaire (par exemple $\Lambda_b \to \Lambda_c^+ l\nu_l$). Pour acquérir une polarisation, les Λ_c^+ doivent être produits à partir d'une particule ayant un spin et polarisée. Pour l'interaction faible, cette particule est le boson faible $W^\pm$. Dans le cas de l'interaction forte, les Λ_c^+ peuvent être produits par différents mécanismes (par exemple, la fusion des gluons, l'interaction qg, etc.). Cependant, au moment où le quark c est créé et hadronisé en un Λ_c^+, de nombreuses interactions intermédiaires se produisent et la polarisation est diluée. Comme le nombre de particules produites et d'interactions augmente avec les énergies, la perte de polarisation augmente également. Après sa production, la particule se désintègre via une interaction forte ou faible. Dans le premier cas, comme la parité est conservée, l'amplitude de désintégration doit être symétrique sous inversion d'espace et la polarisation ne peut pas être mesurée puisqu'il n'y a pas d'asymétrie dans la désintégration, c'est-à-dire que $\alpha = 0$. En revanche, pour les Λ_c^+ faiblement produits, une violation de parité peut se produire et $\alpha \neq 0$, donc la polarisation est mesurable. La désintégration de $\Lambda_c^+ \to pK^-\pi^+$ est une désintégration faible, ce qui signifie que la polarisation est accessible.

Il existe des mesures de polarisation pour différents baryons, en particulier pour les baryons contenant un quark étrange, les hypérons. Pour le baryon Λ_c^+, la première mesure a été effectuée en 1992 au CERN-SPS, dans l'expérience NA32 qui a fait entrer en collision 230 GeV/c π^- sur une cible en Cu, ils ont recueilli 121 désintégrations $\Lambda_c^+ \to pK^-\pi^+$ et ont trouvé le produit αP à $-0.65^{+0.22}_{-0.18}$ pour un $p_T > 1.1\,\text{GeV}/c$ [73]. Puis, en 1999, l'expérience E791 a étudié la même désintégration pour des collisions pion-noyau de $500\,\text{GeV}/c$, avec 946 ± 38 de désintégrations reconstruites. Les résultats ont montré une polarisation de plus en plus négative en fonction de p_T^2, la polarisation la plus élevée étant de -0.67 ± 0.15 dans le bin $1.24 < p_T^2 < 5.20$ GeV$^2/c^2$. La dépendance de la polarisation en fonction de p_T est bien décrite par le modèle proposé dans [74], où les fonctions de fragmentation dépendantes du spin sont calculées dans un modèle quark-diquark. Cependant, le formalisme utilisé dans l'expérience E791 était incomplet; une partie du travail de cette thèse a été dédié à l'étude et au développement du formalisme d'hélicité utilisé pour décrire la désintégration $\Lambda_c^+ \to pK^-\pi^+$. Dans un deuxième temps, les équations obtenues sont utilisées pour décrire les données collectées par l'expérience LHCb contenant des collisions pp collectées avec le détecteur LHCb en 2016, à une énergie dans le centre de masse de 13 TeV. Cette mesure, et en particulier la mesure du paramètre d'asymétrie α est une donnée fondamentale pour la mesure des MDM des baryons charmés en utilisant les cristaux, non seulement pour l'expérience en elle mêmes mais aussi pour la phase de développement des prototypes de l'expérience. En effet, la précision sur le facteur gyromagnétique g dépend de la précision avec laquelle α est connu. Après cette thèse, il sera possible de déterminer plus précisément le nombre de jours de prise de données nécessaires afin d'atteindre une précision de 0.1 sur g.

En conclusion, cette thèse s'articule sur trois axes principaux : d'un côté les développements du formalisme d'hélicité et l'analyse en amplitude des données LHCb, de l'autre un travail hardware portant sur la détermination de l'électronique frontale du détecteur PLUME a été aussi effectué. Ces trois axes sont résumés ci-dessous.

8.2 Formalisme d'hélicité

Dans le référentiel du modèle isobar, la désintégration à 3 corps $\Lambda_c^+ \to pK^-\pi^+$ peut être décomposée en désintégrations successives à deux corps. Les états de résonances intermédiaires sont appelés "isobars" et sont décrits par des fonctions dynamiques, généralement appelées *lineshapes*, qui doivent être paramétrées en choisissant un modèle spécifique. Pour une désintégration à trois corps $A \to a+b+c$, il existe trois combinaisons possibles donnant trois isobars différentes : $A \to (R_1 \to a+b)+c$, $A \to a+(R_2 \to b+c)$ et $A \to (R_3 \to c+a)+b$. L'amplitude de désintégration est factorisée en une partie dynamique $\Delta_{r_i}(m_{r_i})$ et une partie angulaire $\psi_{r_i}(\vec{\Omega})$:

$$\mathscr{A}(\vec{\Omega}) = \sum_i \psi_{r_i}(\vec{\Omega})\Delta_{r_i}(m_{r_i}) \tag{8.4}$$

où $\vec{\Omega}$ sont les variables de l'espace des phases, r_i est la résonance i et m_{r_i} sa masse. Le choix de la paramétrisation de la *linsehape* $\Delta_{r_i}(m_{r_i})$ est guidé par des données expérimentales ou des modèles existants et introduit un biais dans les amplitudes puisqu'il nécessite une modélisation spécifique. Les amplitudes angulaires ψ_{r_i} sont au contraire dérivées des premiers principes de la mécanique quantique sans aucune hypothèse a priori sur le processus physique étudié. Elles peuvent être décrites par différentes approches et elles ne dépendent que du spin et du moment angulaire des particules. Dans ce travail, le formalisme de l'hélicité est choisi. Ce formalisme a été développé dans les années 60 dans la référence [203], mais il présente toutefois des subtilités pour les désintégrations incluant des particules avec un spin différent de zéro dans l'état finale, dans cette thèse ce formalisme est étudié et développé en détail pour la désintégration $\Lambda_c^+ \to pK^-\pi^+$ (avec spin-parité $J^P : \frac{1}{2}^+ \to \frac{1}{2}^+ + 0^+ + 0^+$). En partant de la décomposition de l'équation 8.4, l'amplitude finale de la désintégration à trois corps est obtenue en additionnant de manière cohérente les différents isobars, qui peuvent avoir un spin différent, et de manière incohérente les hélicités des états initial et final.

Cinématique de la désintégration La cinématique de la désintégration à trois corps de Λ_c^+ est décrite par les quatre impulsions des 3 particules filles, ce qui donne $3 \times 4 = 12$ degrés de liberté (dofs). En fixant les 3 masses et en utilisant la conservation de l'énergie et du moment, il ne reste que 5 degrés de liberté. Dans le référentiel au repos du Λ_c, les produits de désintégration sont dans le même plan et les angles entre eux sont déterminés par deux paires de masses invariantes. L'orientation du plan est donnée par 3 angles d'Euler, l'angle polaire et l'angle azimutal du proton (θ_p, ϕ_p), et l'angle χ, qui est l'angle entre les plans formés par l'axe z et la direction du proton et le plan formé par le produit de désintégration de résonance, comme le montre la figure 8.2. Les cinq variables de l'espace des phases sont donc $\Omega = \left(m^2_{pK^-}, m^2_{p\pi^+}, \cos\theta_p, \phi_p, \chi\right)$. Pour une polarisation nulle, il n'y a pas de dépendance aux trois angles d'Euler et la désintégration est entièrement déterminée par deux variables, généralement les deux masses invariantes. Pour une polarisation non nulle, la désintégration aura une dépendance angulaire non triviale. Cela signifie que les effets de la polarisation peuvent être vus dans la distribution angulaire de la désintégration et non sur les distributions des masses invariantes. Le choix de l'axe est arbitraire mais il peut être guidé par des considérations de physique; dans le cas d'une production de baryons via des interactions fortes, la polarisation est attendue perpendiculaire au plan de production,

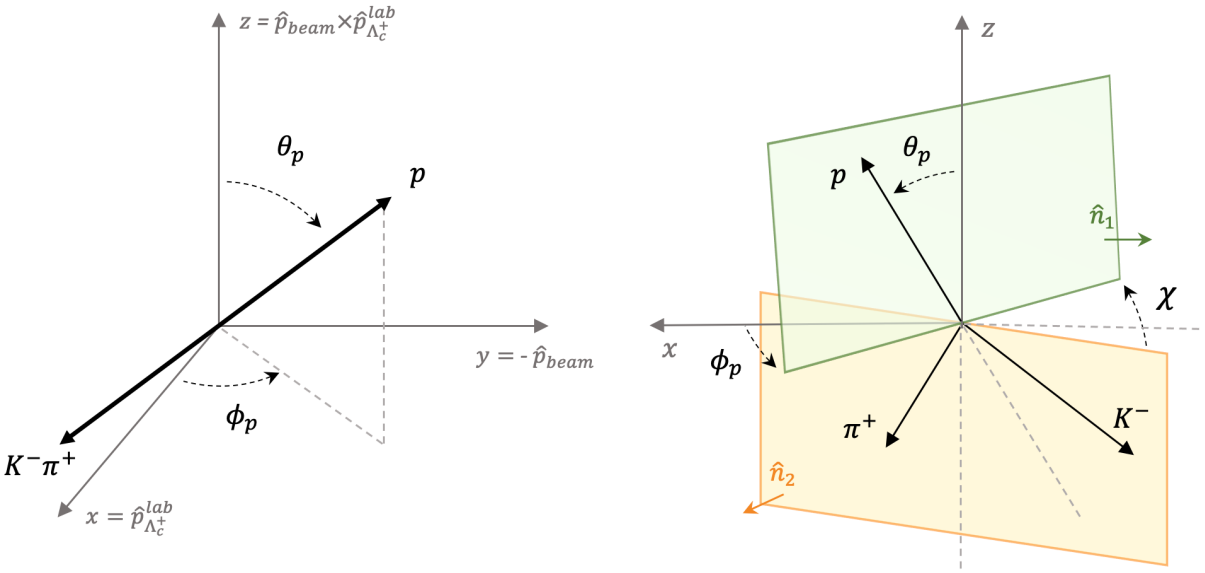

Figure 8.2: Définitions des angles d'Euler dans le référentiel de polarisation. À gauche : angles θ_p et ϕ_p. À droite : angle χ. Le plan $(\vec{p},z)$ est représenté en vert et le plan (K^-,π^+) en orange. Les vecteurs unitaires, $\hat{n}_1$ et $\hat{n}_2$, perpendiculaires à ces plans sont également représentés.

dans lequel les vecteurs impulsion du proton incident et du baryon se trouvent.

L'opérateur d'hélicité Considérons une particule de moment angulaire total $\vec{J} = \vec{L} + \vec{S}$ où $\vec{S}$ est le vecteur spin et $\vec{L}$ le moment angulaire orbital. L'opérateur d'hélicité Λ est défini comme la projection du moment angulaire total le long du moment de la particule :

$$\hat{\Lambda} = \frac{\vec{J} \cdot \vec{p}}{\|\vec{p}\|} = (\hat{L} + \hat{S}) \cdot \hat{\mathbf{p}} = \hat{S} \cdot \hat{\mathbf{p}}. \tag{8.5}$$

Λ commute avec $\vec{J}$ et $\vec{S}^2$, nous pouvons donc construire une base d'états propres simultanés de $\vec{J}^2$, J_z, $\vec{S}^2$ et Λ. Une propriété très utile de l'opérateur d'hélicité est son invariance sous les rotations, puisque $\hat{\mathbf{p}}$ et $\vec{S}$ sont tournés en même temps, le produit des deux est invariant. Ainsi si l'impulsion de la particule est alignée avec l'axe de projection (souvent noté z), alors la projection du moment angulaire total de la particule le long de l'axe z coïncide par construction avec l'hélicité. Ensuite, en utilisant une séquence de rotations et de transformations de Lorentz il est possible de définir l'état de spin d'une particule pour n'importe quelle valeur de l'impulsion, ce qui n'était pas trivial car le spin d'une particule relativiste pas au repos n'est pas une quantité bien définie.

Amplitude de la désintégration La désintégration $a \to 1+2+3$ peut être décomposée en deux désintégrations séquentielles à deux corps, par exemple $a \to (R \to 1+2)+3$, où l'état final et les particules intermédiaires ont des hélicités $\lambda_1, \lambda_2, \lambda_3, \lambda_R$ et des spins s_1, s_2, s_3, s_R. L'amplitude de ce

processus peut être écrite comme suit

$$\mathscr{A}_{M,\lambda_1,\lambda_2,\lambda_3}(a \to 1+2+3) = \sum_{\lambda_1} D^{*J}_{M,\lambda_R-\lambda_3}(\phi_1,\theta_1,-\phi_1) D^{*s_R}_{\lambda_R,\lambda_1-\lambda_2}(\phi_3,\theta_3,-\phi_3) H^{a\to R3}_{\lambda_R,\lambda_3} H^{R\to 12}_{\lambda_1,\lambda_2} \quad (8.6)$$

où $H^{a\to R3}_{\lambda_1,\lambda_2}$ sont les couplages d'hélicité pour la désintégration de la particule mère vers la résonance R et $H^{R\to 12}_{\lambda_3,\lambda_4}$ celui pour la désintégration de la résonance R vers ses produits de désintégration. Les angles sont calculés à chaque fois dans le référentiel au repos de la particule, ainsi θ_1 et ϕ_1 sont calculés dans le référentiel de référence a atteint à partir du référentiel de laboratoire et θ_3 et ϕ_3 sont calculés dans le référentiel de référence R atteint à partir du référentiel de référence a. Il s'agit d'un point crucial ; les états de spin des produits de désintégration a et R sont définis dans des référentiels d'hélicité obtenus à partir de points de départ différents, les hélicités sont donc projetées sur des axes différents.

Le référentiel d'hélicité du proton est atteint à partir du référentiel d'hélicité des résonances via une rotation et un boost le long du moment du proton. Lorsque l'on effectue le boost pour aller dans le référentiel au repos de la résonance et ensuite dans le référentiel au repos du proton, le proton a un rôle différent selon la chaîne que nous examinons. Le référentiel au repos du proton atteint à partir de la chaine du K^* et celle du Λ^* et Δ^{++} est montré en figure 8.3. En revanche, l'amplitude de désintégration finale est obtenue en additionnant de manière cohérente les amplitudes des différentes résonances, défini en utilisant le même axe de quantification (qui est défini par rapport au Λ_c^+) pour les trois chaînes. Si nous mesurons la projection du spin du proton en utilisant comme axe de quantification pour toutes les désintégrations dans le référentiel du proton au repos, la direction du proton dans le référentiel Λ_c, on doit faire tourner l'axe de projection (ou de manière équivalente l'état d'hélicité du proton) de la chaîne qui n'est pas alignée avec cet axe de quantification. Ces rotations sont appelées rotations de Wigner et elles contiennent une partie azimutale (ϕ'_K) et une partie polaire (β_{res}), elles s'écrivent comme $R(0,\beta_{\text{res}},\phi'_K)$ et elles apparaissent lorsqu'on combine les amplitudes des trois chaînes.

Maintenant que tous les éléments nécessaires ont été introduits, les amplitudes d'hélicité pour les désintégrations $\Lambda_c^+ \to pK^-\pi^+$ sont dérivées d'abord pour chaque chaîne séparément et finalement pour l'amplitude totale, y compris la matrice de densité de spin.

L'amplitude finale est obtenue en additionnant les hélicités finales (puisqu'elles ne peuvent être mesurées) et en incluant la polarisation. Dans ce cas, la seule hélicité finale non nulle est celle du proton. Pour pouvoir faire cette somme, il faut inclure la rotation de Wigner pour avoir une définition cohérente de l'axe de quantification, d'où l'utilisation des fonctions D habituelles pour représenter les rotations, l'amplitude pour chaque configuration d'hélicité $\mathcal{A}^{\Lambda_c^+\to pK^-\pi^+}_{m,\lambda_p,\lambda_{K^-},\lambda_{\pi^+}} = \mathcal{A}_{m,\lambda_p}$:

$$\mathcal{A}_{m,\lambda_p}(\Omega) = \mathcal{A}^{K^*}_{m,\lambda_p}(\Omega_{K^*}) + \sum_{\lambda'_p} \mathcal{A}^{\Lambda^*}_{m,\lambda'_p}(\Omega_{\Lambda^*})\, D(\alpha_1,\beta_{\Lambda^*},\phi'_{K^-}) + \sum_{\lambda'_p} \mathcal{A}^{\Delta^{++}}_{m,\lambda'_p}(\Omega_{\Delta^{++}})\, D(\alpha_2,\beta_{\Delta^*},\phi'_{K^-}) \quad (8.7)$$

où

$$\alpha_1 = \begin{cases} 2\pi & \text{if } |\phi_p - \phi_\pi| > \pi \\ 0 & \text{else} \end{cases} \qquad \alpha_2 = \begin{cases} 2\pi & \text{if } |\phi_p - \phi_K| > \pi \\ 0 & \text{else} \end{cases} \quad (8.8)$$

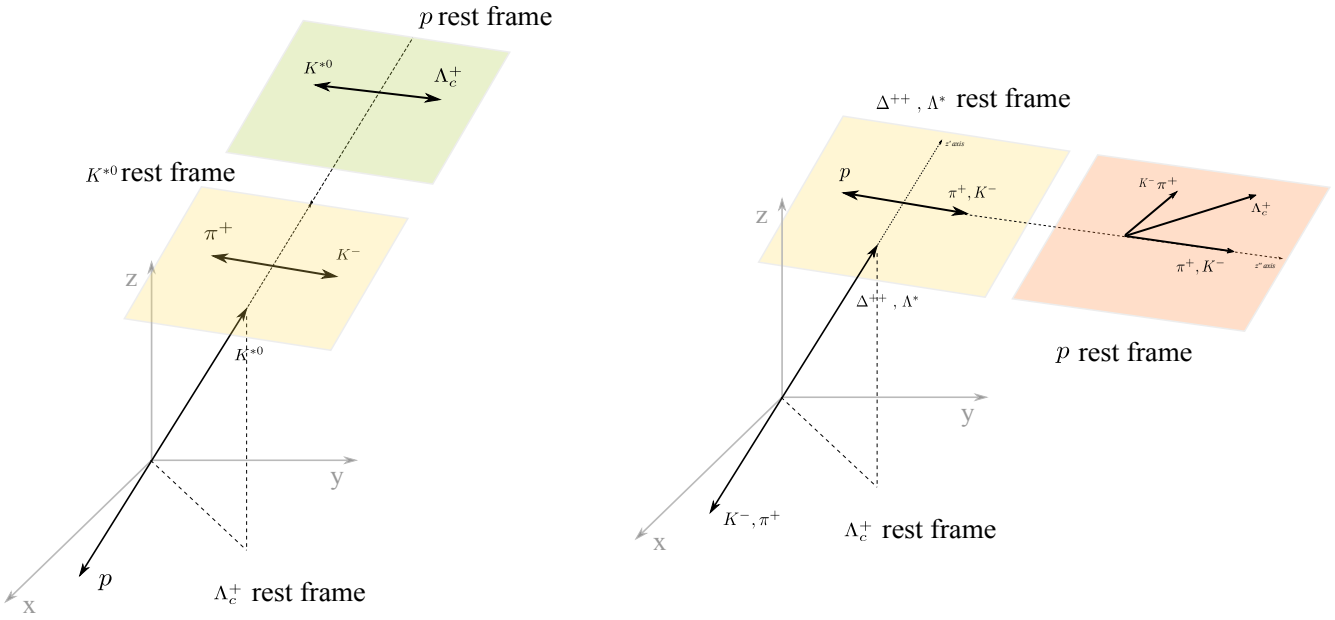

Figure 8.3: Définition des référentiels et des angles pour les trois chaînes de désintégration, K^* à gauche, Δ^{++} et Λ^* à droite.

Les conditions alpha (α_1, α_2) proviennent du fait que les particules de spin $\frac{1}{2}$ ne sont pas invariantes sous une rotation de 2π mais sous une rotation de 4π.

La polarisation est incluse au moyen de la matrice spin densité ρ; dans le cas de $\Lambda_c^+ \to pK^-\pi^+$, $j = \frac{1}{2}$ donc ρ est une matrice 2×2 paramétrée par 3 nombres réels. La façon la plus générale d'écrire ρ est d'utiliser les matrices de Pauli σ_i et la matrice identité $\mathcal{I}$.

$$\rho = \frac{1}{2}\left(\mathcal{I} + \vec{P}\cdot\vec{\sigma}\right) = \begin{pmatrix} \rho_{\frac{1}{2},\frac{1}{2}} & \rho_{\frac{1}{2},-\frac{1}{2}} \\ \rho_{-\frac{1}{2},\frac{1}{2}} & \rho_{-\frac{1}{2},-\frac{1}{2}} \end{pmatrix} = \frac{1}{2}\begin{pmatrix} 1+P_z & P_x - iP_y \\ P_x + iP_y & 1-P_z \end{pmatrix} \tag{8.9}$$

$\vec{P} = \{P_x, P_y, P_z\}$ est le vecteur polarisation représentant le degré et la direction de l'orientation du spin de l'état. Un état pur correspond à un état totalement polarisé avec $P = \pm 1$. En introduisant la matrice de densité de spin, le taux de désintégration devient :

$$d\Gamma(\Omega) \propto \sum_{\{\lambda_i\}} \sum_{m,m'} \rho_{m,m'} \mathscr{A}_{m,\lambda_1,\lambda_2,\lambda_3} \mathscr{A}^*_{m',\lambda_1,\lambda_2,\lambda_3} \tag{8.10}$$

où Ω décrit l'espace des phases. Par rapport aux équations données dans la Réf.[204], ces amplitudes incluent les rotations de Wigner et les facteurs additionnels α, définis dans l'Eq. 8.8, qui compensent l'homomorphisme deux à un $SU(2) \to SO(3)$.

Tests du formalisme Trois tests ont été développés pour s'assurer que le formalisme développé soit correct. Ces tests se basent sur les propriétés physiques de la désintégration dans certaines conditions particulières, notamment :

- La linéarité de la distribution angulaire dans le cas d'une désintégration incluant un seul état

intermédiaire (*i.e.* une seule résonance)

- Si la conservation de la parité est imposée pour la désintégration $\Lambda_c^+ \to Rh$ alors les distributions angulaires doivent être uniformes
- Si la polarisation du Λ_c^+ est nulle, alors les distributions angulaires doivent aussi être uniformes

Un exemple de ces tests est montré en figure 8.4, dans lequel les distributions angulaires pour les trois chaines intermédiaires avec une polarisation nulle sont montrées avec le formalisme complet (gauche) et en enlevant la condition 2π (droite). Les distributions ne sont plus plates dans le deuxième cas, ceci indique que la condition 2π est nécessaire pour que le formalisme soit correct. En conclusion,

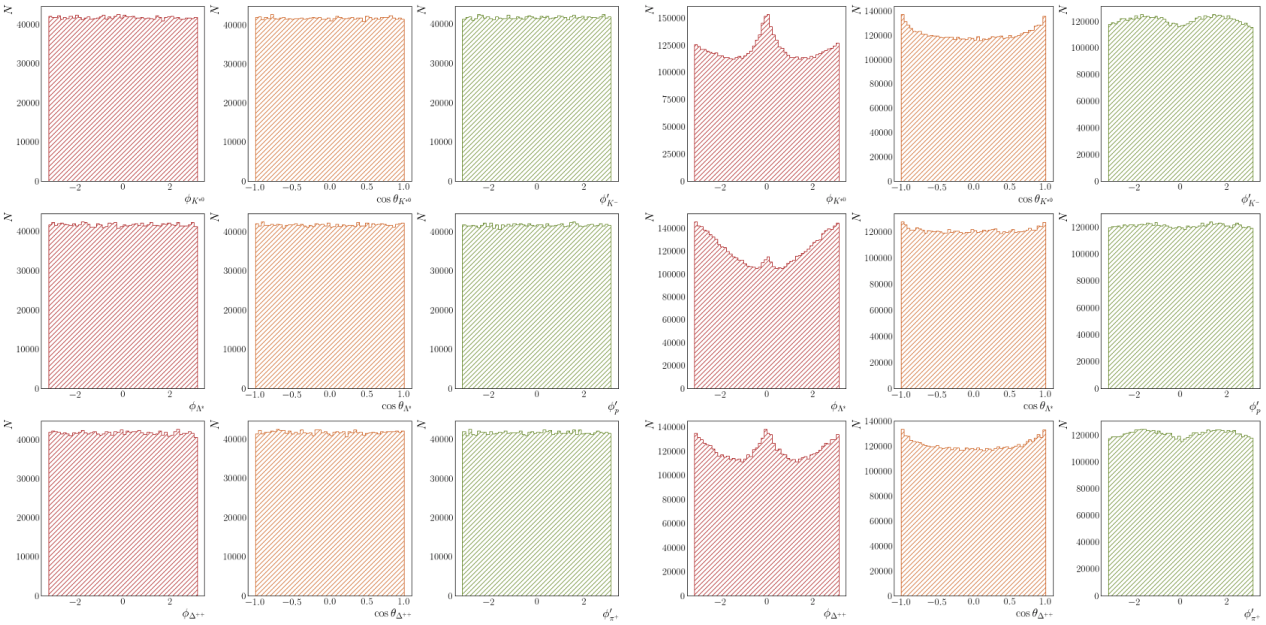

Figure 8.4: Simulation de l'espace de phase de 1M événements avec $\vec{P} = \{0.0, 0\}$ et BW=1, incluant seulement trois résonances : $K^*(890)$, $\Lambda^*(1520)$ et $\Delta^{++}(1232)$ avec les couplages d'hélicité aléatoires indiqués dans le texte. De la colonne de gauche à celle de droite, les distributions angulaires pour les trois angles d'Euler sont montrées. De la ligne du haut vers la ligne du bas, les chaînes K^*, Λ^* et Δ^{++} sont représentées. À gauche : la partie azimutale de la rotation de Wigner a été supprimée. À droite: la condition "2π " a été supprimée.

les résultats de ces tests démontrent que le formalisme développé dans cette thèse est correct, en outre les tests développés peuvent être utilisés pour s'assurer que n'importe quel autre formalisme soit correcte car les principes utilisés sont toujours vrais.

8.3 Analyse en amplitude de la désintégration $\Lambda_c^+ \to pK^-\pi^+$

Dans cette thèse, l'analyse d'amplitude de la désintégration à trois corps $\Lambda_c^+ \to pK^-\pi^+$ est présentée. Le but de cette analyse est d'établir un modèle décrivant cette désintégration et d'extraire le vecteur polarisation du baryon Λ_c^+. Le choix de ce canal est guidé par deux raisons : premièrement la nécessité pour une désintégration faible afin d'être sensible à la polarisation, puisque l'amplitude est

proportionnelle au paramètre d'asymétrie α qui est non nul seulement dans le cas d'interactions violant la parité ; deuxièmement, le fait que ce canal a un grand rapport d'embranchement ce qui permet d'avoir un échantillon de données plus grand. De plus, cette désintégration permet l'existence d'états intermédiaires qui peuvent interférer entre eux, ce qui augmente la sensibilité à la polarisation. Malgré la complexité de l'analyse à trois corps, le gain en sensibilité est important. En effet, une désintégration à deux corps (comme $\Lambda_c^+ \to K_s^0 p$) pourrait aussi être utilisée pour mesurer la polarisation et serait plus simple à analyser. En revanche, le rapport d'embranchement étant plus petits, elles ne seront pas visibles dans les données cible fixe et en plus dans le cas où le paramètre d'asymétrie α serait nul alors la polarisation ne pourrait pas être mesurée, ce qui n'est pas vrai pour les désintégrations à 3 corps qui présentent une structure plus riche permettant de mesurer la polarisation pour n'importe quelle valeur du paramètre d'asymétrie α.

La mesure est effectuée sur les données contenant des collisions pp collectées avec le détecteur LHCb en 2016, à une énergie dans le centre de masse de 13 TeV. L'analyse est effectuée pour les baryons Λ_c^+ "prompts" et "secondaires". Une série de coupures est appliquée sur les candidats p, K^- et π^+ ainsi que la particule mère Λ_c^+, afin de choisir uniquement les particules provenant de la désintégration étudiée : $\Lambda_c^+ \to pK^-\pi^+$, que l'on appelle évènements de signal. Ces coupures s'appliquent sur les quantités suivantes: le moment transverse, l'impulsion, la qualité des traces et la qualité de l'identification des particules (appelé PID). Concernant le Λ_c^+, la coupure la plus importante est celle qui permet de séparer les Λ_c^+ produit directement après la collision de ceux qui viennent de la désintégration d'un autre baryon (Λ_c^+ secondaires). Cette coupure est optimisée afin d'avoir une contamination résiduelle provenant de Λ_c^+ secondaires inferieure à 2%. Après avoir appliqué toutes les coupures, le bruit de fond résiduel est inférieur à 3 %. Environ 800 000 désintégrations prompts ont été sélectionnées avec des contributions de fond négligeables et une contamination résiduelle des désintégrations secondaires négligeable. L'ajustement de la masse invariante, montré en figure 8.5, est effectué sur l'échantillon après sélections ; il est utilisé pour séparer les évènements de signal du bruit de fond restant dans la suite de l'analyse en utilisant la technique du *sPlot*.

Une simulation Monte Carlo (MC) des évènements de signal est utilisée pour évaluer les efficacités de reconstruction et de sélection des candidats. Cette simulation est corrigée à l'aide d'un algorithme de *machine learning* qui permet d'améliorer la comparaison entre les données et la simulation. Ces corrections sont appliquées sous forme de poids évènement par évènement et elles portent sur la cinématique de la désintégration, la simulation du PID ainsi que celle du trigger hardware (L0 trigger).

Mesure de polarisation La polarisation est mesurée au moyen d'un ajustement à cinq dimensions utilisant la méthode du maximum de vraisemblance, qui minimise le logarithme de la densité de probabilité (PDF) par rapport aux paramètres qui doivent être mesurés (les couplages d'hélicité). La PDF contient l'amplitude décrite à l'aide des équations développées dans cette thèse, l'efficacité et l'intégrale de normalisation.

Pour chaque état intermédiaire (ou chaque chaine), ils peuvent y avoir plusieurs états résonants, en revanche tous ces états ne contribuent pas forcément de façon significative à l'amplitude finale ; certains ne sont pas visibles dans les données étudiées. Ainsi, un modèle d'amplitude doit être construit en utilisant une procédure itérative dans laquelle les résonances intermédiaires sont ajoutées une par

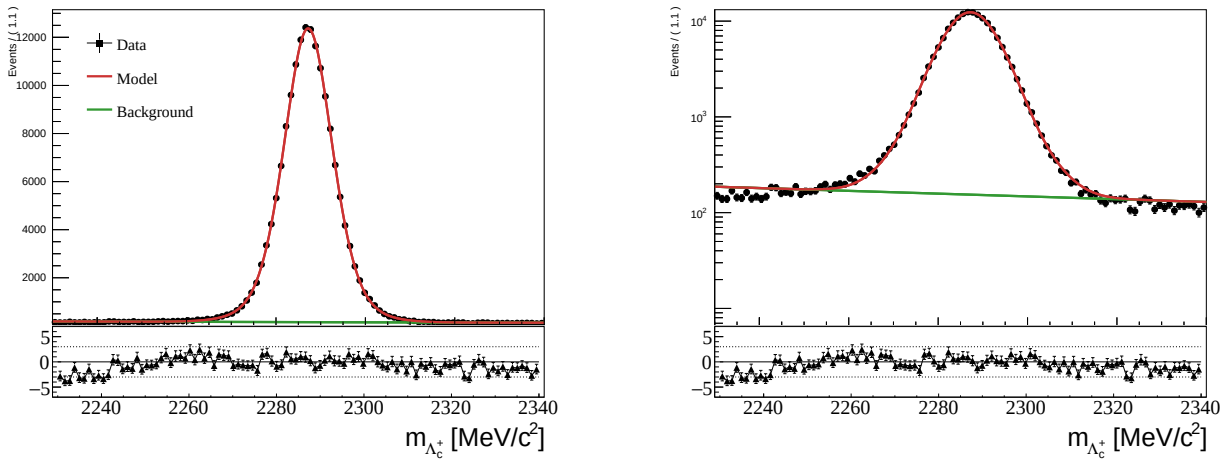

Figure 8.5: Gauche : ajustement de la masse invariante $m_{pK^-\pi^+}$. A droite : même ajustement, avec l'axe y en échelle logarithmique. Les données sont représentées en noir, le modèle d'ajustement (2 Crystal Ball et une fonction Gaussienne) est représenté en rouge et le bruit de fond (exponentiel) en vert. Les subfigures inférieures montrent les résidus de l'ajustement.

une jusqu'à ce que le modèle n'arrive plus à les discerner. Les premières résonances ajoutées sont celles que l'on peut voir en regardant directement le plan de Dalitz, qui est donnée dans la figure 8.6; les résonances apparaissent comment des lignes foncées, les plus visibles sont: $\Lambda^*(1520)$, $\Lambda^*(1670)$, $K^*(890)$ and $\Delta^{++}(1232)$. Pour chaque nouveau modèle (*i.e.* chaque nouvelle liste de résonances) 4

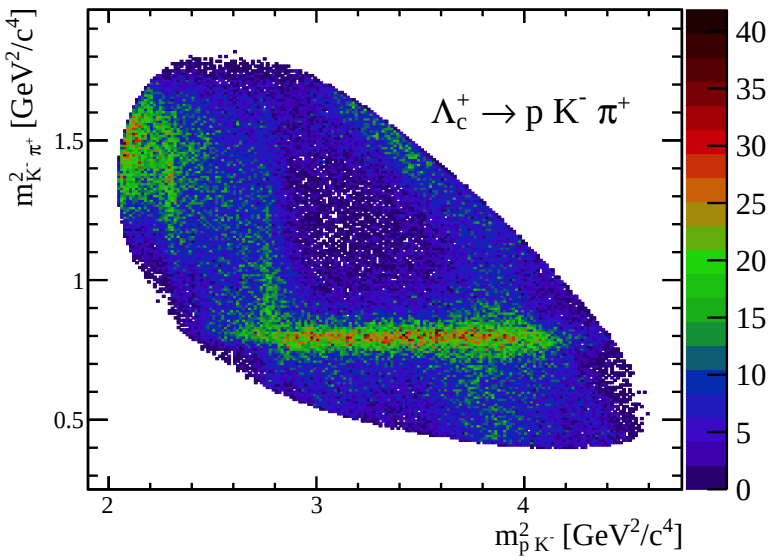

Figure 8.6: Diagramme de Dalitz des désintégrations $\Lambda_c^+ \to pK^-\pi^+$ soustraites du bruit de fond, l'axe y montre la masse invariante $m^2_{K\pi}$ et l'axe x celle m^2_{pK}.

ajustements sont effectués pour éviter de se retrouver dans un minimum local lors de la minimisation de la PDF. Le χ^2/ndf est utilisé pour évaluer la qualité du modèle, les 3 meilleurs modèles sont gardés. Le

	MagDown		MagUp	
MC	TIS	TOS	TIS	TOS
Λ_c^+	34 646	27 686	35 680	27 158
$\overline{\Lambda}_c^-$	34 398	28 523	34 488	28 643
Data	TIS	TOS	TIS	TOS
Λ_c^+	110 720	73 783	105 426	65 866
$\overline{\Lambda}_c^-$	108 394	78 340	104 852	70 295

Table 8.1: Nombre d'événements pour l'ajustement final des données et de la simulation, en fonction de la polarité, de la catégorie de déclenchement et de la séparation des désintégrations Λ_c^+ et $\overline{\Lambda}_c^-$.

modèle nominal contient les résonances : $\Lambda^*(1405)$, $\Lambda^*(1520)$, $\Lambda^*(1600)$, $\Lambda^*(1670)$, $\Lambda^*(2000)$, $K^*(700)$, $K^*(890)$, $K^*(1430)$ et $\Delta^{++}(1232)$, $\Delta^{++}(1600)$, $\Delta^{++}(1620)$, $\Delta^{++}(1700)$. Ce modèle est utilisé pour mesurer le vecteur polarisation et les couplages d'hélicité, ainsi que les paramètres d'asymétrie et les fractions d'ajustement. L'ajustement obtenu avec le modèle nominal est montré dans la figure 8.7, chaque ligne de couleur représente une résonance. Les deux autres modèles, sont utilisés pour les études systématiques ; le premier inclue une résonance $K^-\pi^+$ en plus, le $K^*(1410)$, le deuxième deux autres résonances pK^- (en plus du $K^*(1410)$), le $\Lambda^*(1690)$ et $\Lambda^*(1890)$.

La mesure est effectuée séparément pour les désintégrations Λ_c^+ et $\overline{\Lambda}_c^-$, car des mécanismes de production différents sont impliqués pour les baryons et les antibaryons et leur polarisation peut différer. En outre, les échantillons de données sont séparés selon la polarité de l'aimant LHCb (MagUp ou MagDown) et selon la catégorie de trigger hardware étudiée (TIS ou TOS). Le tableau 8.1 montre le nombre d'événements final par catégories pour les données et la simulation (MC).

Erreurs systématiques Les erreurs systématiques sont évaluées à l'aide de pseudo-expériences pour chacune des 8 catégories séparément. Elles peuvent être séparées en trois catégories : les erreurs liées à la simulation, aux données ou à la façon de faire l'ajustement. Dans le premier cas, les ajustements sont faits à nouveau en changeant le poids de correction de la simulation (incluant les poids corrigeant PID et le trigger). La taille de l'échantillon de simulation rajoute aussi une systématique qui est évaluée en générant une pseudo-expérience avec un grand nombre d'évènements et ajustant la 100 fois avec 100 tableaux d'efficacité différents génèrés à partir du tableau principal. Pour les systématiques liées au données, l'ajustement de la masse invariante est effectué en utilisant une PDF différente. Le choix du modèle, entre les trois modèles sélectionnés après la procédure itérative décrite ci-dessus, introduit une systématique. Cette dernière est évaluée en générant des pseudo-expériences avec les deux autres modèles alternatifs qui sont ensuite ajustés avec le modèle nominal. Enfin les masses et les largeurs des résonances sont connues avec des larges incertitudes, les ajustements sont effectués à nouveau avec des nouvelles valeurs. La dernière systématique est due au biais qui pourrait être introduit par l'ajustement. Un grand nombre de pseudo-échantillons sont générés à partir de cet ajustement. Enfin, chacun de ces pseudo-échantillons est ajusté à nouveau et les résultats sont comparés aux valeurs initiales utilisées pour générer les pseudo-échantillons. Le biais ainsi mis en évidence est assigné comme une erreur systématique.

Résultats La mesure de polarisation est obtenue pour l'échantillon contenant des Λ_c^+, avec une polarité de l'aimant LHCb négative (MagDown) et pour la catégorie de trigger TIS. Les valeurs obtenues sont:

$$\begin{aligned} P_x &= -0.0233 \pm 0.0046 \pm 0.0341 \\ P_y &= 0.0560 \pm 0.0044 \pm 0.0919 \\ P_z &= 0.0095 \pm 0.0063 \pm 0.0590 \end{aligned} \tag{8.11}$$

où la première incertitude est statistique et la seconde systématique. L'erreur systématique est plus grande que l'erreur statistique et elle est dominée l'incertitude due au choix modèle. La figure 8.8 montre la comparaison des résultats (pour la composante P_z) entre les différentes catégories en incluant seulement les erreurs statistiques et la seule erreur systématique qui n'est pas corrélée (celle liée à la taille de l'échantillon de simulation). Les résultats sont compatibles dans un maximum de deux écarts types.

Ce résultat est compatible avec d'autres mesures de polarisation de baryons réalisées au LHC. Par exemple, une polarisation nulle a été mesurée pour les baryons Λ_b à 7, 8 et 13 TeV par LHCb [80, 81], ATLAS [82] et CMS [83] ; de même pour les baryons Λ une polarisation nulle a été mesurée par ATLAS [79]. Il existe très peu de prédictions théoriques avec lesquelles comparer ce résultat, donc un apport de la théorie serait très précieux. Dans un futur proche, la mesure de la polarisation sera également effectuée dans des bins de moment transverse afin de la comparer aux résultats obtenus dans la Réf. [204] et à la prédiction théorique dans [74].

Le paramètre d'asymétrie effective α est également mesuré: $\alpha_{effective} = 0.715 \pm 0.005$, l'incertitude citée étant statistique. Les fractions d'ajustement sont aussi mesurées. Comme la polarisation est proche de zéro, les couplages d'hélicité sont dégénérés et ils ne peuvent pas être déterminés de manière unique. Malgré cela, le paramètre d'asymétrie effective est mesurable puisqu'il inclut toutes les composantes d'amplitude à travers le plan Dalitz. La grande asymétrie mesurée implique que la méthode proposée pour mesurer la polarisation dans l'échantillon à cible fixe peut être utilisée. Si une valeur faible ou nulle de $\alpha_{effective}$ avait été trouvée à la place, la sensibilité à la polarisation aurait été perdue, empêchant l'utilisation de ce canal pour la mesure MDM.

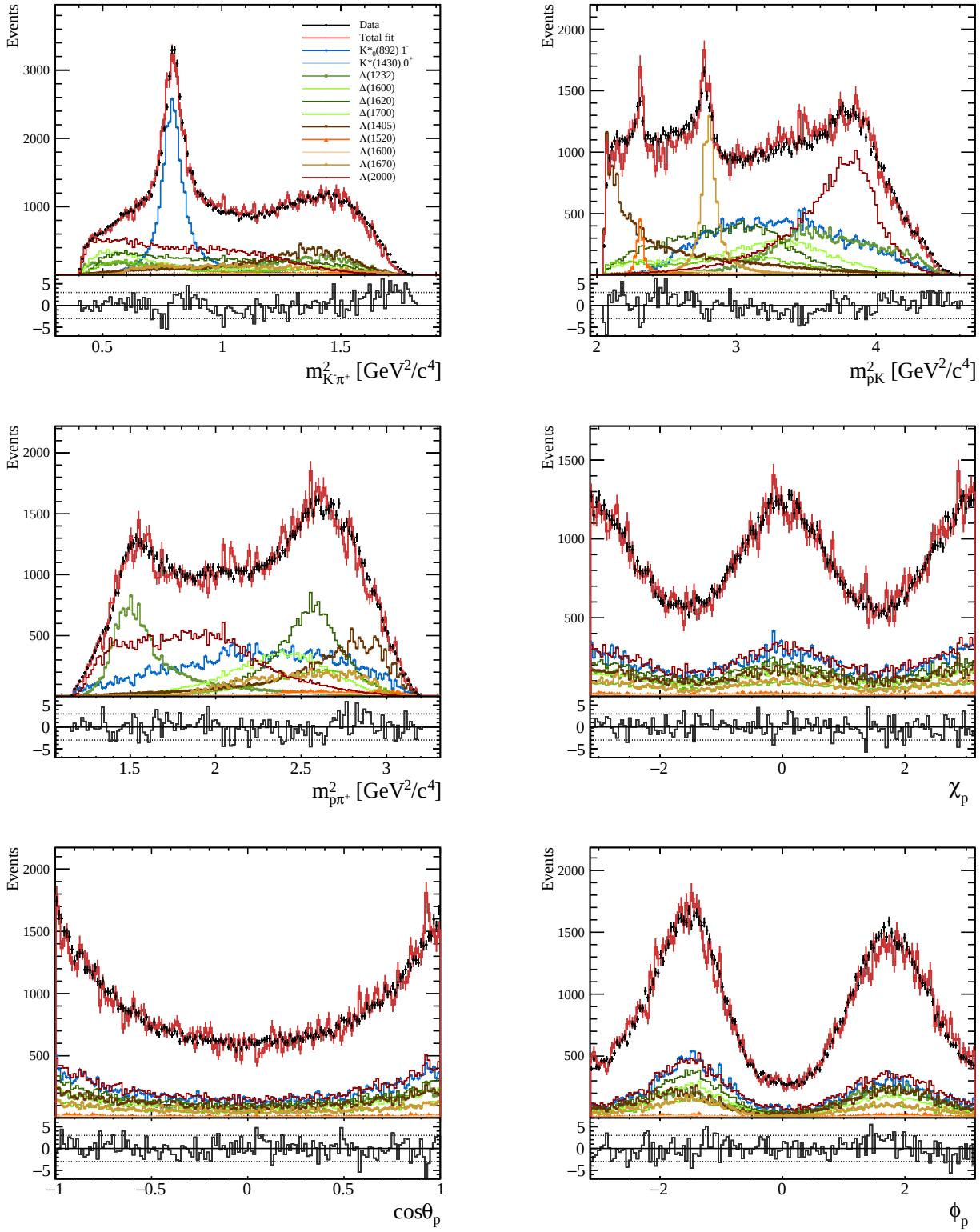

Figure 8.7: Exemple d'ajustement avec le modèle nominal sur la catégorie TIS, polarité négative, pour les désintégrations Λ_c^+ et $\overline{\Lambda}_c^-$ mélangées. Les points noirs sont les points de données, la ligne rouge montre le modèle PDF total, les lignes colorées montrent les contributions de chaque résonance séparément et le code couleur est spécifié dans la légende de la projection de masse $m^2_{K\pi}$, en général les lignes bleues sont les résonances K^*, les lignes vertes Δ^{++} et les lignes marron-rouge Λ^*. Les subfigures inférieurs montrent les différences entre les données et le modèle total, les lignes horizontales en pointillés montrent la limite de 3 écarts types (3 σ).

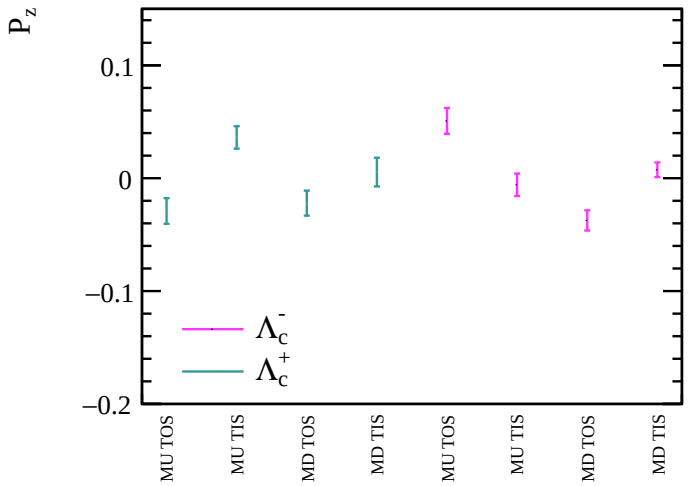

Figure 8.8: Comparaisons de la mesure de P_z pour les 8 catégories d'ajustement. Le point en cyan montre la mesure pour les Λ_c^+ et en rose pour $\overline{\Lambda}_c^-$. Les erreurs n'incluent pas les systématiques corrélées.

8.4 L'électronique frontale du détecteur PLUME

L'expérience LHCb a été mise à niveau pour pouvoir prendre des données au cours des trois prochaines années dans les conditions prévues pour le Run 3 (2022-2025). Le nouveau détecteur fonctionnera à un niveau de luminosité cinq fois supérieur à celui des cycles précédents, Run 1 et Run 2. Toutefois, les performances du détecteur LHCb, même dans sa version améliorée, se dégradent en cas d'occupation élevée, car il a été conçu pour fonctionner à un niveau de luminosité inférieur à ATALS et CMS. Pour cette raison, la luminosité est volontairement réduite au point d'interaction de LHCb et cette procédure, appelée *luminosity levelling*, s'appuie sur la mesure de la luminosité en temps réel. En outre, au cours du Run 3, le détecteur LHCb passera à un système de déclenchement entièrement software, ce qui nécessite une connaissance très précise des conditions de fonctionnement de l'expérience. Ce ne sont là que quelques-unes des raisons qui ont motivé la construction d'un nouveau détecteur de luminosité, le détecteur PLUME, qui sera installé près du point d'interaction de LHCb. Le détecteur PLUME est conçu pour déterminer s'il y a eu ou non une interaction lors des collisions des paquets de protons du faisceau et il est basé sur la mesure de la lumière Cherenkov produite par les particules chargées qui traversent le détecteur.

Dans cette thèse, l'électronique frontale (FEE) du détecteur PLUME est présenté a été défini ; elle sera basée sur l'électronique frontale du calorimètre électromagnétique de LHCb qui s'est avérée être adapté à la forme du signal obtenu lors des tests de faisceau. L'adaptabilité de l'électronique du calorimètre LHCb n'était pas trivial car cette électronique a été conçue pour un signal plus long ; typiquement 25 ns contre le 3 ns du signal attendu pour PLUME. Le premier test effectué consiste en l'utilisation d'un montage, reproduisant les conditions de fonctionnement de PLUME, composé par : un laser, un des photomultiplicateurs (PMTs) de PLUME, les cartes d'acquisition du calorimètre et une carte de contrôle (3CU). Les données ont été prises avec un système d'acquisition (DAQ) similaire à celui de LHCb. Les résultats de ces tests prouvent que le FEB du ECAL peuvent être utilisées pour PLUME.

Ensuite, la possibilité d'utiliser le détecteur PLUME pour mesurer le décalage de l'horloge de LHCb par rapport à l'horloge principale du LHC est également explorée. Afin de lire de manière synchrone l'ensemble du détecteur LHCb lorsqu'une collision se produit, une horloge globale réglée par le LHC est utilisée pour suivre les bunches qui se croisent. L'électronique de chacun des sous-détecteurs est synchronisée par rapport à l'horloge du LHC pour échantillonner correctement le signal dans un délai de 25 ns. L'horloge du LHC arrive à l'expérience LHCb par des fibres optiques souterraines. En raison des variations de température, l'horloge peut subir un décalage de quelques ns avant d'arriver à LHCb, ce qui entraîne une désynchronisation de la lecture du détecteur par rapport aux collisions du LHC. Pendant le Run 1 et le Run 2, un décalage d'horloge a été observé et il a été corrigé en utilisant la mesure de timing du Outer Tracker (OT) avec une résolution de 0.5 ns. Ce décalage doit être surveillé afin d'obtenir des performances optimales pendant le Run 3, notamment en ce qui concerne l'étalonnage et l'alignement du détecteur. Le OT sera retiré pendant le Run 3. Pour cette raison, une mesure du retard d'horloge utilisant le détecteur PLUME est proposée dans cette thèse. Cette mesure exploite les caractéristiques de la puce ICECAL, détaillées ci-dessous.

L'intégration du signal est réalisée dans la puce ICECAL qui contient deux lignes d'intégration

fonctionnant en parallèle à 20 MHz chacune, alternant 25 ns d'intégration et 25 ns de mode repos. Une vue schématique du processus d'intégration se déroulant dans l'ICECAL est présentée à la figure 8.9. De haut en bas, l'horloge du LHC, l'impulsion PMT, l'intégration et les systèmes *track and hold* (T/H) sont représentés en fonction du temps, avec les deux lignes d'intégration dessinées en vert et en rouge. Ce dessin n'est pas à l'échelle, il a pour but de guider le lecteur dans l'explication. L'impulsion d'entrée (provenant des PMTs) est intégrée par le premier intégrateur pendant 25 ns. En même temps, la charge de sortie est transférée vers les condensateurs de maintien du système T/H. Pendant ce temps, l'autre intégrateur reste en état de réinitialisation. Pendant les 25 ns suivantes, le premier intégrateur passe en mode de réinitialisation et le second réalise l'intégration de la queue du signal qui ne rentrait pas dans la première fenêtre d'intégration. Ici encore, le signal est transféré au (deuxième) système T/H. Ensuite, le multiplexeur combine les deux signaux pour les envoyer aux pilotes ADC après avoir sélectionné le canal d'intégration correct. La phase de l'horloge T/H peut

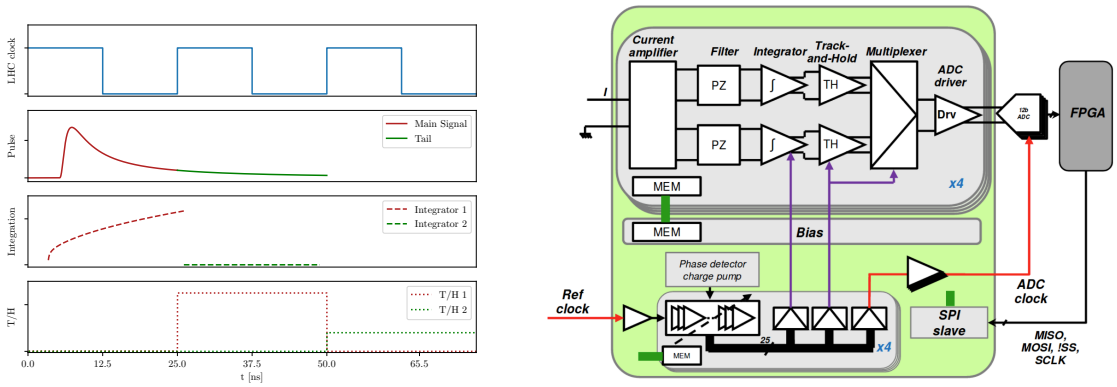

Figure 8.9: A gauche : schéma du processus d'intégration dans la puce ICECAL (unités arbitraires sur l'axe des y) pour un signal de type ECAL. Droite : Croquis du processus d'intégration dans la puce ICECAL (unités arbitraires sur l'axe des y) pour un signal de type ECAL.

être ajustée, ce qui implique que la charge de sortie de l'intégrateur est déplacée vers le T/H et de maintien plus tôt (ou plus tard selon le retard). Cela revient à modifier le début (t_0^{int}) du processus d'intégration du signal et donc à appliquer un retard par rapport à l'horloge du LHC. En déplaçant t_0^{int}, le premier intégrateur n'intègre plus la totalité du signal et le deuxième intégrateur intègre une plus grande partie du signal plutôt que seulement la queue. Ainsi, en augmentant progressivement les délais de 0 à 25 ns, il est possible d'effectuer un balayage, en surveillant le déplacement progressif du signal d'un intégrateur à l'autre.

Si l'horloge du LHCb est parfaitement synchronisée avec celle du LHC, pour un retard de $d_{split} = 12,5$ ns, le signal devrait être divisé en deux entre les deux intégrateurs. En traçant la différence de signaux entre les deux intégrateurs en fonction du retard appliqué, il est possible de mesurer où se situe le point de partage en deux. Cela devrait donner une courbe, avec une forme typique en S, où le point d'inflexion correspond à d_{split}. La courbe idéale en forme de S que l'on devrait obtenir est représentée sur la figure 8.10 (gauche); celle obtenue dans cette étude est montrée dans la même figure, à droite.

La résolution visée est au moins inférieure à 250 ps et peut être améliorée jusqu'à 70 ps. Bien que très préliminaires, ces résultats ouvrent la voie à une mesure de temps supplémentaire prometteuse et

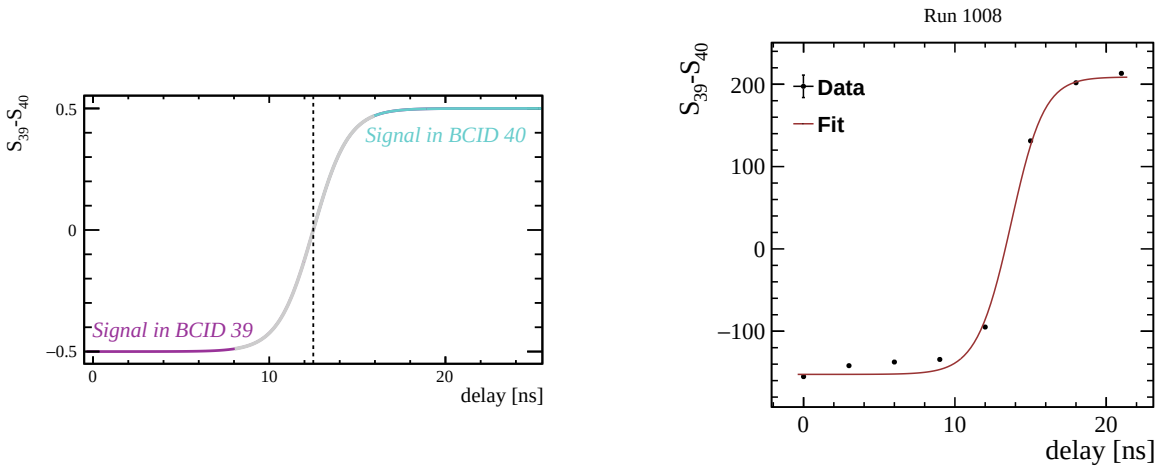

Figure 8.10: Gauche: S-shape idéale pour des retards de 0 à 25 ns. La ligne verticale pointillée indique le point $d_{split} = 12,5$ ns. La région magenta correspond à un signal intégré par les intégrateurs marqués BCID 39 et la région cyan à l'intégrateur BCID 40. La partie grise de la courbe représente la région où l'intégration du signal passe progressivement d'un intégrateur à l'autre. Droite: S-shape obtenu dans cette thèse avec les montage décrit dans le texte.

inattendue que le détecteur PLUME pourrait effectuer. A l'issue de ce travail, les FEBs de l'ECAL ont été choisies pour l'électronique frontale du futur détecteur PLUME et une mesure préliminaire du temps a été effectuée, donnant des résultats prometteurs.

8.5 Conclusions

Dans cette thèse, la polarisation du baryon charmé Λ_c^+ a été mesurée pour des baryons prompt dans des collisions proton-proton, en utilisant l'échantillon de données collecté par le détecteur LHCb en 2016, à une énergie dans le centre de masse de 13 TeV. Les principales motivations de cette mesure sont: d'une part la polarisation des baryons charmés est mal connue expérimentalement, la mesure la plus pertinente a été réalisée il y a 20 ans [204], et aucune amélioration n'a été apportée depuis. D'autre part, aucune prédiction théorique n'est disponible pour la polarisation des baryons charmés à l'énergie du LHC. Enfin, la polarisation Λ_c^+ est une donnée nécessaire pour la mesure du moment dipolaire magnétique (MDM) du quark charmé proposée dans la Réf. [1] [2] [3] [4] [5]. En plus de la mesure de polarisation Λ_c^+, cette thèse présente le travail effectué sur la détermination de l'électronique frontale du détecteur Plume, qui sera installé pour le Run 3 de l'expérience LHCb.

L'analyse en amplitude de la désintégration $\Lambda_c^+ \to pK^-\pi^+$ peut être décomposée en trois étapes majeures : le développement des équations décrivant l'amplitude de la désintégration, le traitement des données pour extraire le Λ_c^+ prompt et enfin l'ajustement aux données pour effectuer la mesure de la polarisation. Tout d'abord, les équations qui décrivent l'amplitude de la désintégration de $\Lambda_c^+ \to pK^-\pi^+$ ont été dérivées dans le cadre du formalisme de l'hélicité. Cela était nécessaire car le formalisme utilisé dans [204] s'est avéré incomplet, et de nombreux points devaient être clarifiés avant de poursuivre l'analyse. En particulier, la nécessité des rotations de Wigner et des facteurs de 2π a

été démontrée. De plus, il a été prouvé que le formalisme développé est correct en le testant pour des configurations spécifiques. L'extraction du signal a été relativement simple puisque les contributions du bruit de fond étaient faibles par rapport au signal. La sélection la plus importante pour cette analyse est celle du paramètre d'impact Λ_c^+ qui permet de séparer les désintégrations prompt des secondaires. En effet, la polarisation dépend du mécanisme de production impliqué, qui diffère entre la production prompte et secondaire. Une sélection rigoureuse laissant moins de 2% de contamination par les secondaires a été appliquée. Enfin, le bruit de fond résiduel, provenant principalement d'une mauvaise identification des protons, est également inférieur à 2%. Le principal défi de la procédure de sélection a été la compréhension des effets du déclenchement du L0 sur les variables angulaires, en particulier le ϕ_p. Finalement, l'analyse a été effectuée pour les deux catégories de déclencheurs séparés afin de maîtriser ces effets. Les amplitudes d'hélicité dérivées sont ensuite utilisées pour mesurer la polarisation Λ_c^+ et $\overline{\Lambda}_c^-$, les couplages d'hélicité et les fractions d'ajustement de chaque état résonant intermédiaire, au moyen d'un ajustement aux données. Les paramètres d'asymétrie des résonances individuelles ainsi que le paramètre d'asymétrie effectif pour l'ensemble de la désintégration ont été extraits des résultats de l'ajustement. Le contenu de résonance du modèle a été déterminé en ajoutant seulement les résonances donnant une contribution significative à l'amplitude principale et décrivant aussi bien que possible les données. Un modèle nominal et deux modèles supplémentaires donnant des résultats similaires ont été retenus. Une fois le modèle nominal déterminé, la mesure finale a été effectuée pour les deux polarités de l'aimant séparément car la reconstruction n'est pas exactement identique entre les deux et la simulation ne reproduit pas parfaitement ces effets. Les désintégrations ($\Lambda_c^+ \to pK^-\pi^+$) et sont anti-désintégration ($\bar{\Lambda_c}^- \to \bar{p}K^+\pi^-$) ont également été séparées car la production d'un baryon Λ_c^+ et d'un antibaryon $\overline{\Lambda}_c^-$ est différente, donc la polarisation peut différer entre les deux. Ainsi, la mesure est effectuée pour 8 catégories différentes, en fonction du trigger, de la polarité et du type de désintégration. La polarisation a été mesurée pour l'échantillon TIS, de polarité négative, de désintégrations Λ_c^+ :

$$\begin{aligned} P_x &= -0.0233 \pm 0.0046 \pm 0.0341 \\ P_y &= 0.0560 \pm 0.0044 \pm 0.0919 \\ P_z &= 0.0095 \pm 0.0063 \pm 0.0590 \end{aligned} \tag{8.12}$$

où la première incertitude est statistique et la seconde systématique. La mesure est dominée par les incertitudes systématiques qui donnent une erreur allant jusqu'à 9% où la plus grande source d'incertitudes systématiques est celle liée au le choix du modèle. La partie la plus difficile de l'analyse a été la compréhension des amplitudes d'hélicité, la construction du modèle et le développement du mécanisme d'ajustement. Une amplitude incorrecte peut encore donner des résultats raisonnables lors de l'ajustement des données. Les équations ont été soigneusement testées et étudiées pour s'assurer qu'aucune définition non physique, qui n'apparaîtrait pas dans l'ajustement, n'était utilisée. L'évaluation du contenu de résonance du modèle a également été un défi, car plusieurs modèles équivalents peuvent donner des résultats similaires. Le mécanisme d'ajustement a été développé à partir de zéro en C++ et il a également constitué une partie difficile de l'analyse. La grande quantité de données et les calculs complexes ont nécessité une optimisation inévitable du code en utilisant

les fonctionnalités les plus récentes des bibliothèques C++ et RooFit. Le code est parallélisé, pour fonctionner sur plusieurs CPU en même temps, et optimisé afin de garder en mémoire tout élément de l'amplitude qui ne change pas pendant la minimisation de la PDF. L'utilisation de GPUs a été envisagée, mais le grand nombre de CPUs disponibles a donné de meilleures performances que le petit nombre de GPUs, donc cette option n'a pas été étudiée plus.

Pour les perspectives de cette mesure, un échantillon statistique plus élevé pourrait être facilement obtenu en relâchant la sélection du paramètre d'impact. L'augmentation de la contamination secondaire pourrait être traitée comme une composante de fond dans la PDF finale. En outre, l'analyse complète pourrait être effectuée pour les désintégrations des baryons $\Xi_c^+ \to pK^-\pi^+$, qui partagent le même état final et donc les mêmes équations. Enfin, le modèle obtenu dans cette analyse, sera utilisé pour mesurer la polarisation dans des collisions pNe collectées par LHCb en 2017 à une énergie dans le centre de masse de 68 GeV. L'incertitude statistique estimée pour l'échantillon pNe de 2017 est comprise entre 10% et 14% selon le nombre final d'événements de signal extraits, qui peut varier de 200 à 400 événements. Ainsi, la mesure de la polarisation Λ_c^+ dans cet échantillon sera dominée par l'incertitude statistique. Au cours du Run 3, grâce à SMOG2, un échantillon de données avec un signal plus important est attendu. Pour un échantillon contenant 300 000 baryons de Λ_c^+, une incertitude statistique de $0,4\%$ est attendue, dans ce cas la mesure de la polarisation sera dominée par l'incertitude systématique due au choix du modèle, qui est d'environ 5%. En d'autres termes, la précision de la mesure de la polarisation pour les futurs échantillons SMOG2 sera systématiquement limitée à 5%.

Parallèlement à l'analyse des données et au développement du formalisme des amplitudes d'hélicité, un travail hardware a été effectué dans cette thèse, concernant la détermination de l'électronique frontale du détecteur Plume. Le détecteur Plume est un détecteur de luminosité conçu pour l'expérience LHCb. Le parcours de la conception à la construction du détecteur Plume a été passionnant. Les tests effectués visaient à prouver que l'électronique frontale du calorimètre électromagnétique de LHCb pouvait être adaptée aux besoins de PLUME. Les FEB de l'ECAL ont été conçus pour intégrer un signal dans un délai de 25 ns, et éliminer les éventuelles fuites en dehors de cette fenêtre. Le signal attendu pour PLUME est cependant beaucoup plus court, environ 3 ns, et l'électronique n'a pas été optimisée pour un signal aussi court. Dans ce travail, il a été prouvé qu'il est possible d'utiliser les FEB de l'ECAL pour le PLUME. De plus, une nouvelle mesure de temps est proposée afin de surveiller le décalage de l'horloge de LHCb par rapport à l'horloge principale du LHC. Les premiers résultats sont prometteurs, une résolution temporelle inférieure à 0.5 ns obtenue avec l'OT pendant le Run 1 semble réalisable. Quelques améliorations possibles pour la mesure du temps ont été identifiées, y compris la conception d'un meilleur séparateur pour diviser le signal en 8 copies et une optimisation de la taille du pas du scan de temps. Cette mesure sera bénéfique pour les performances du détecteur LHCb pendant le Run 3 car elle permettra de contrôler la synchronisation temporelle en temps quasi réel avec une bonne précision.

A Plume FEB tests

More plot for the signal shapes obtained in the *Split mode*. The runs shown are the last three of Table 4.3: 1049, 1051 and 1053. The numerical results of the fits are shown in Tab. A.1, Table A.2 and Table A.3.

Channel	ΔS[ADCs]	Error [ADCs]	Delay [ns]
8	86.4	0.2	0
9	79.4	0.2	3
10	73.9	0.4	6
11	74.6	0.2	9
12	79.2	0.1	12
13	-6.9	0.1	15
14	-75.0	0.3	18
15	-106.5	0.1	21

Table A.1: Fit result after pedestal substraction for Run 1049.

Channel	ΔS[ADCs]	Error [ADCs]	Delay [ns]
8	75.4	0.9	0
9	68.3	0.8	3
10	36.8	0.1	6
11	-30.4	0.1	9
12	-74.7	0.5	12
13	-113.0	0.2	15
14	-109.8 0	0.	18
15	-109.0	0.3 21	

Table A.2: Fit result after pedestal substraction for Run 1051.

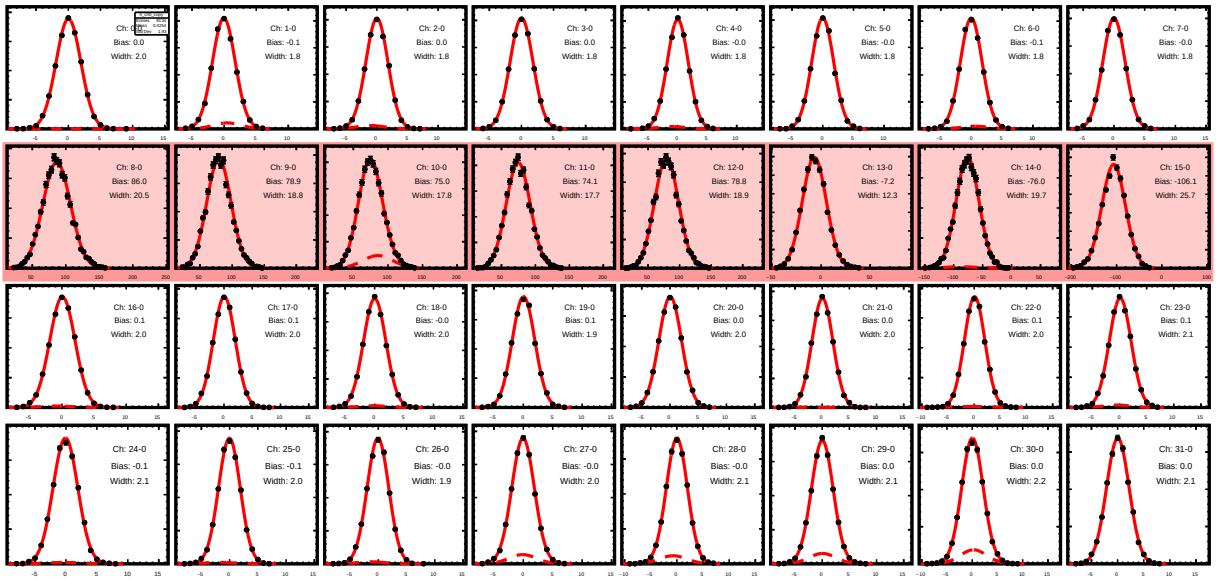

Figure A.1: ΔS distributions for Feb 4, 32 channels (Run 1049) as a function of the ADC counts after pedestal substraction. The red bold lines are double gaussian fits to the distributions and the bais and width values are shown on the subplots. The red shaded channels have a non zero mean and correspond to the channels where a signal is seen.

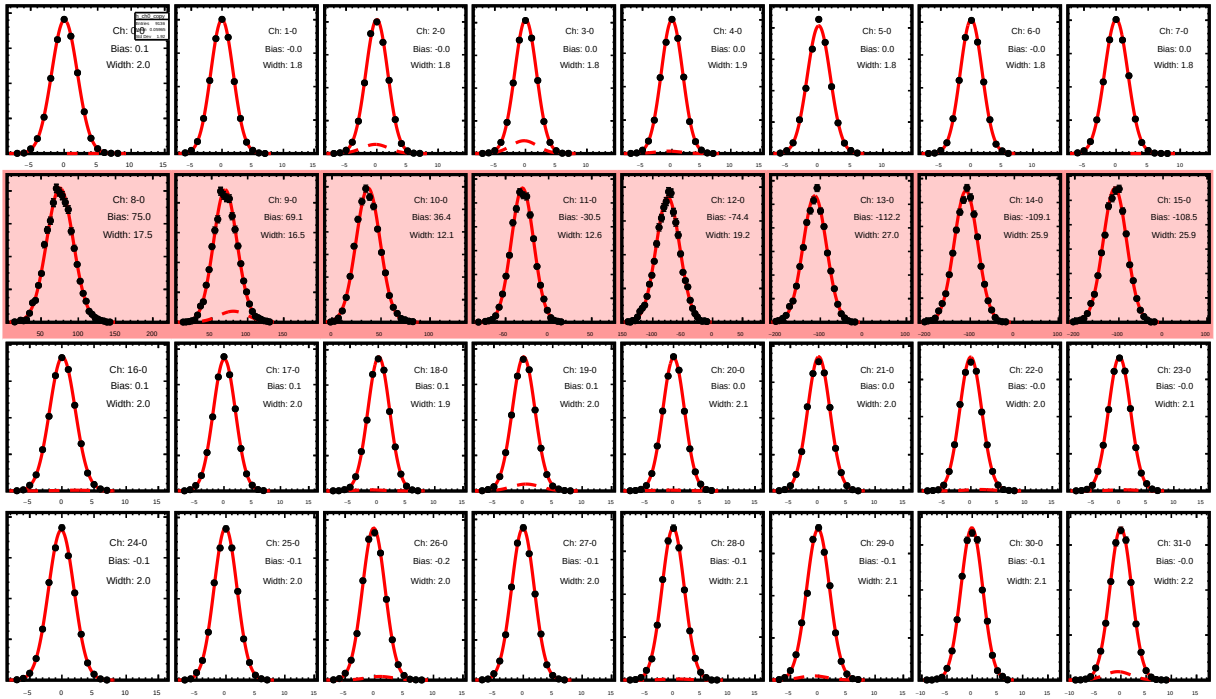

Figure A.2: ΔS distributions for Feb 4, 32 channels (Run 1051) as a function of the ADC counts after pedestal substraction. The red bold lines are double gaussian fits to the distributions and the bais and width values are shown on the subplots. The red shaded channels have a non zero mean and correspond to the channels where a signal is seen.

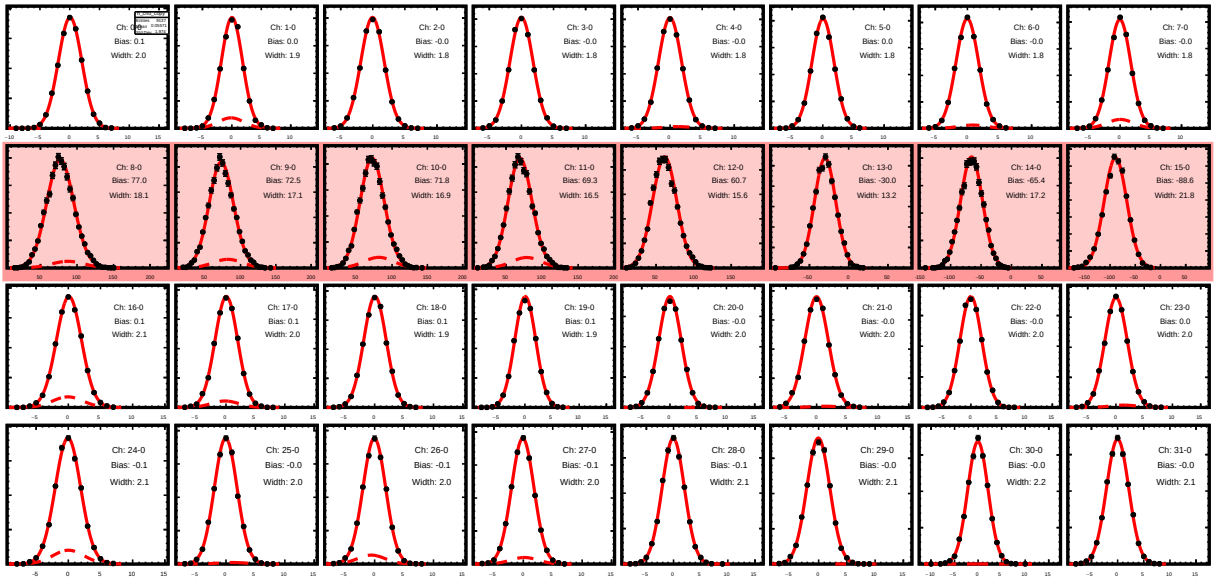

Figure A.3: ΔS distributions for Feb 4, 32 channels (Run 1053) as a function of the ADC counts after pedestal substraction. The red bold lines are double gaussian fits to the distributions and the bais and width values are shown on the subplots. The red shaded channels have a non zero mean and correspond to the channels where a signal is seen.

Channel	ΔS[ADCs]	Error [ADCs]	Delay [ns]
8	76.6	0.4	0
9	72.0	0.4	3
10	71.5	0.4	6
11	68.7	0.4	9
12	61.3	0.2	12
13	-30.0	0.1	15
14	-65.62	0.2	18
15	-89.2	0.2	21

Table A.3: Fit result after pedestal substraction for Run 1053.

B Mis-ID backgrounds

Full mid-identification plots for TIS and TOS categories.

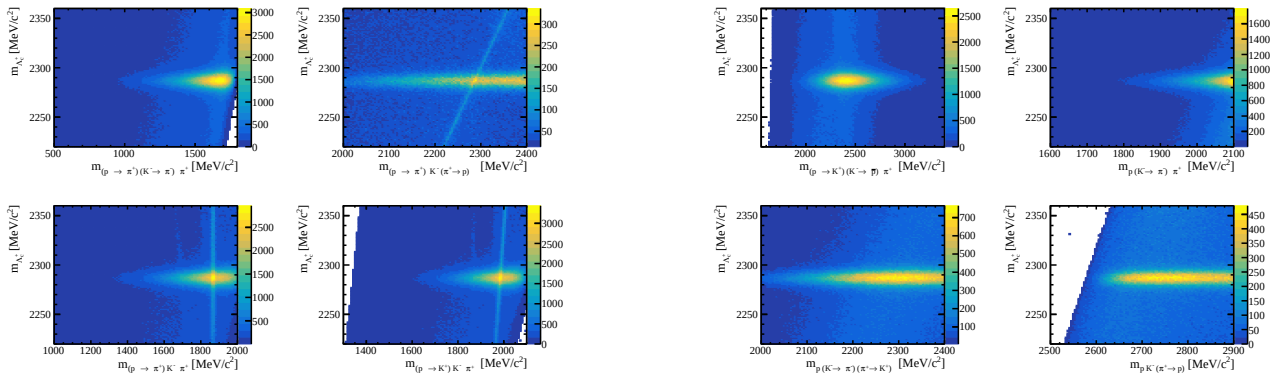

Figure B.1: TIS category, before selections, invariant mass with different mass hypothesis.

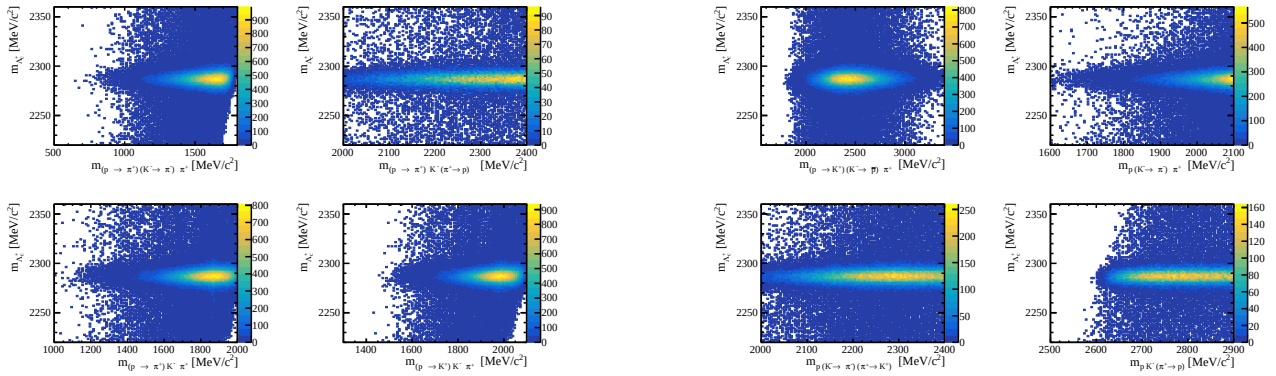

Figure B.2: TIS category, after final selections, invariant mass with different mass hypothesis.

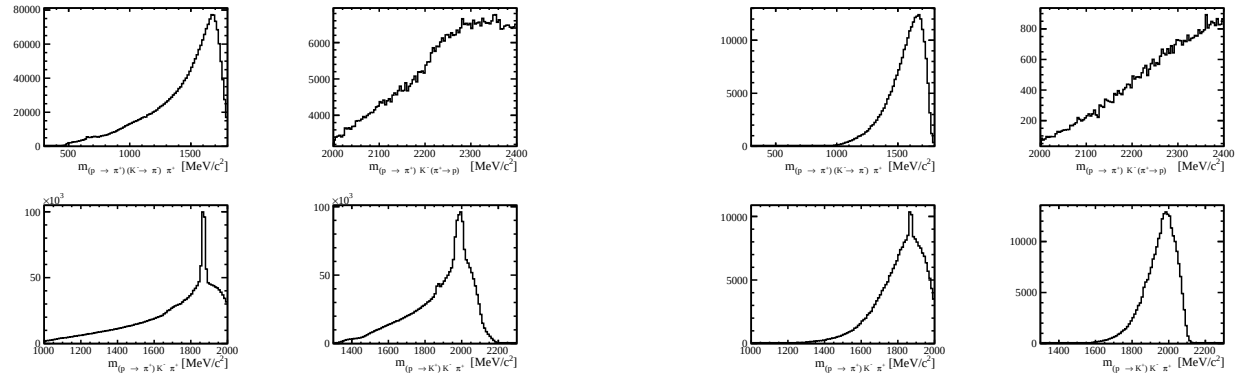

Figure B.3: TIS category, one dimensional projections. Left: before selections. Rigth: after selections. Only the relevant masses giving significant backgrounds from misidentification are shown.

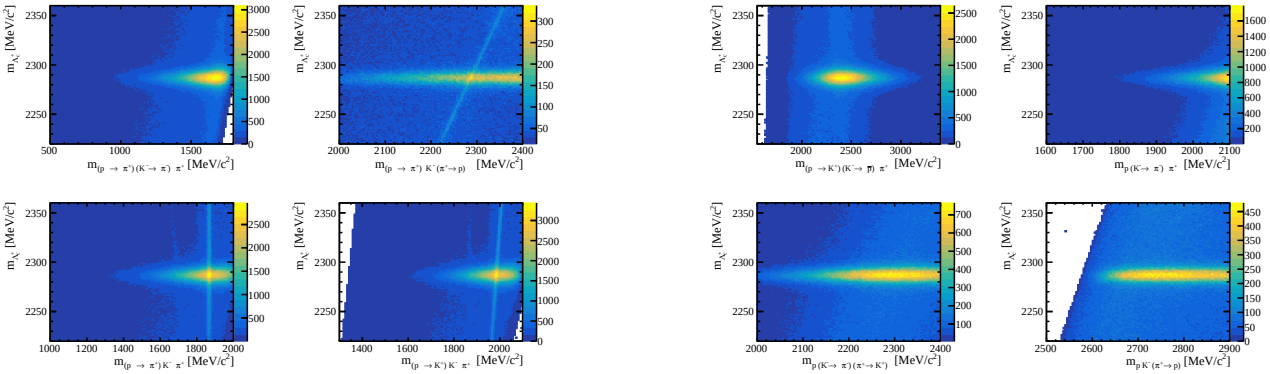

Figure B.4: TOS category, before selections, invariant mass with different mass hypothesis.

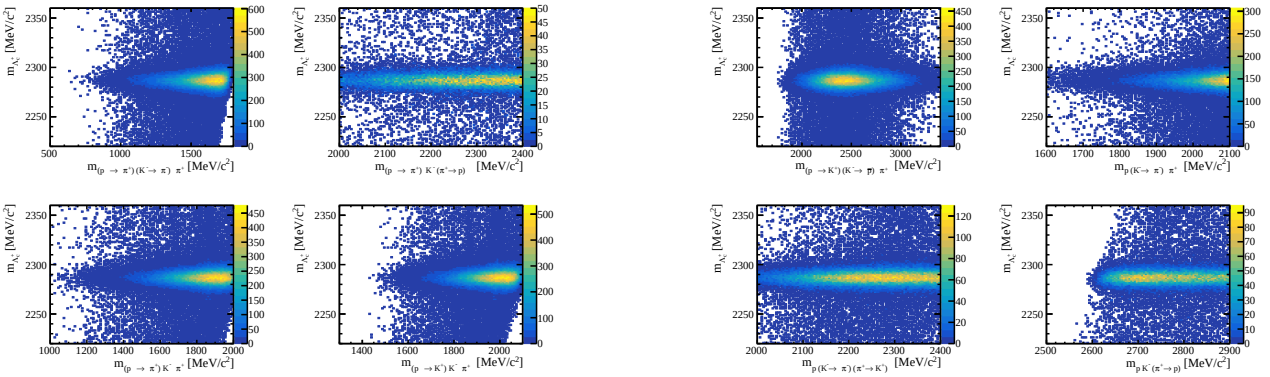

Figure B.5: TOS category, after final selections, invariant mass with different mass hypothesis.

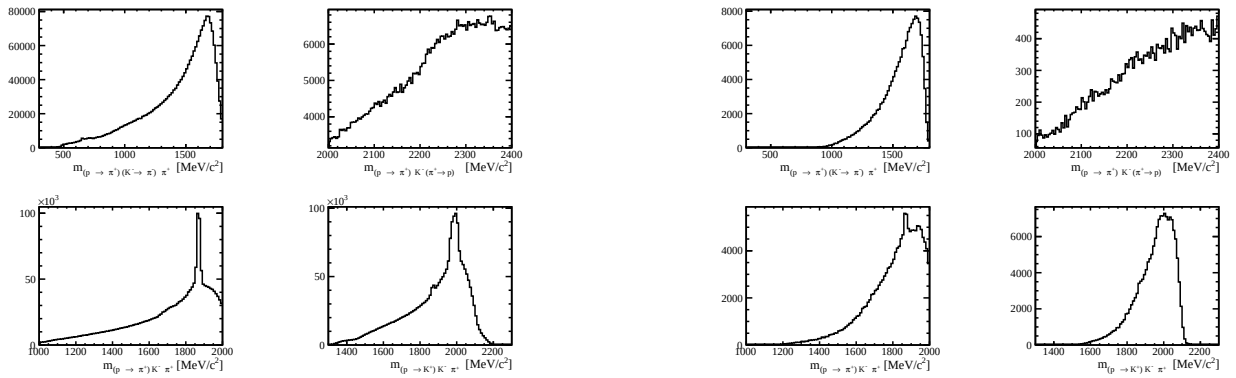

Figure B.6: TOS category, one dimensional projections. Left: before selections. Rigth: after selections. Only the relevant masses giving significant backgrounds from misidentification are shown.

C Additional Data/MC comparisons

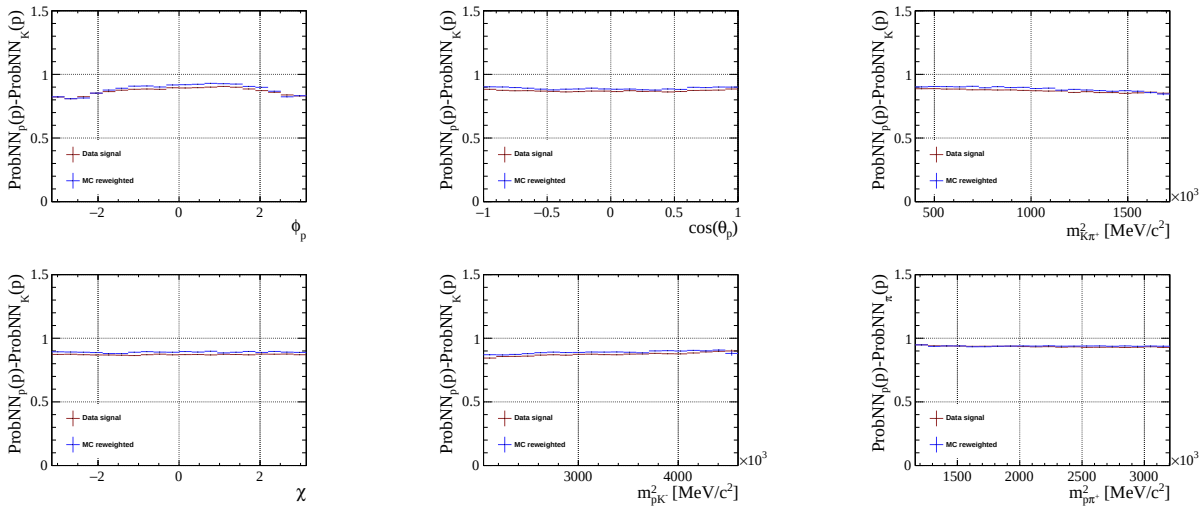

Figure C.1: Profile histograms featuring the probNN distributions $(ProbNN_p(p) - ProbNN_K(p))$ versus the phase space variables $\left(m^2_{pK^-}, m^2_{p\pi^+}, \cos\theta_p, \phi_p, \chi\right)$, the mass $m^2_{K^-\pi^+}$ is also shown. The red dots are *sPlot* signal data, the blue dots the MC after the reweighting procedure. The results shown are for the TOS category and negative polarity.

D Invariant mass fits

In this appendix, the invariant mass fit for the categories TIS MagDown, TIS MagUp and TOS MagUp are shown.

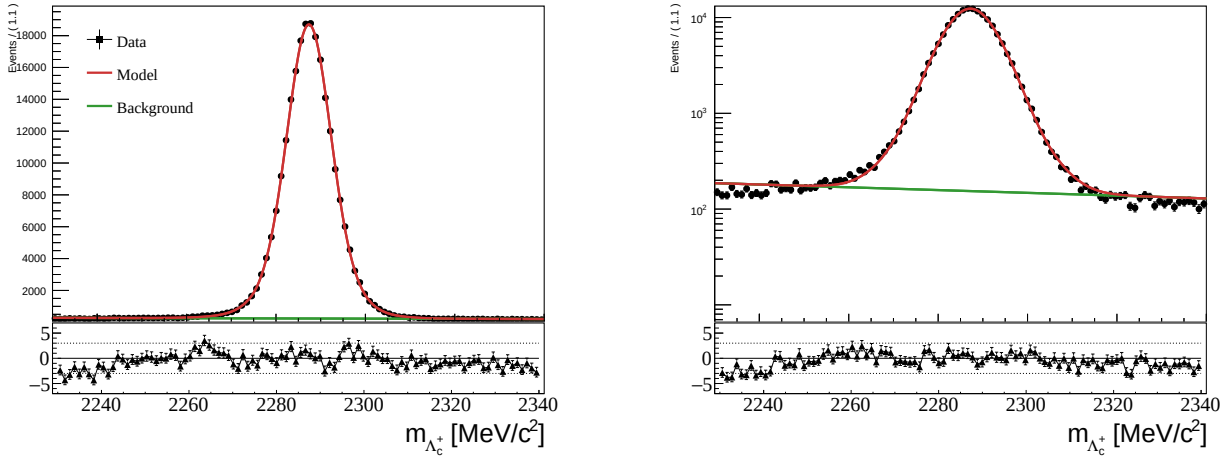

Figure D.1: Left: fit to the $m_{pK^-\pi^+}$ invariant mass. Right: same fit, with the y-axis in logarithmic scale. Data are shown in black, the fit model (2CBs and a Gaussian function) is shown in red and the background (exponential) in green. The lower pads show the residues of the fit. Trigger category TOS and negative polarity

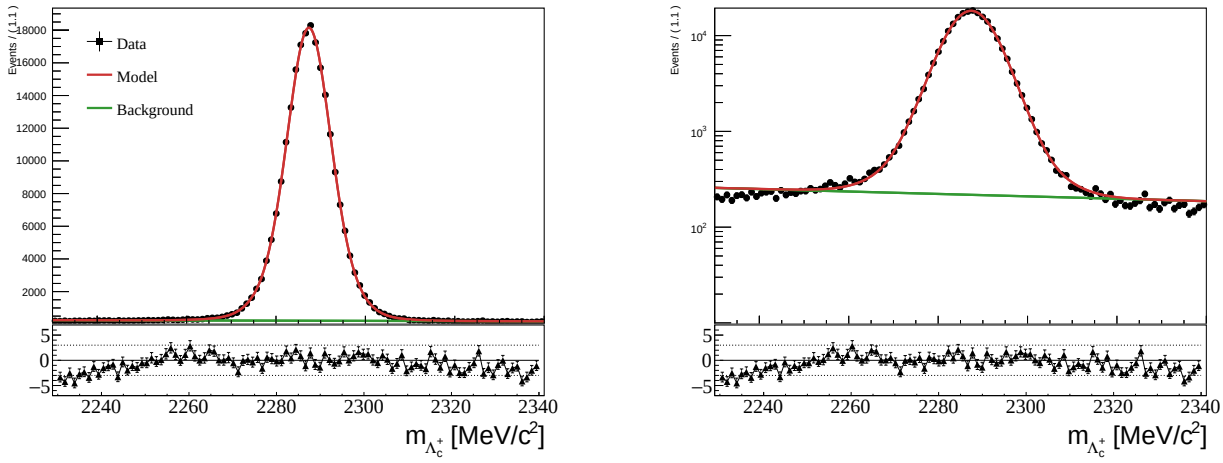

Figure D.2: Left: fit to the $m_{pK^-\pi^+}$ invariant mass. Right: same fit, with the y-axis in logarithmic scale. Data are shown in black, the fit model (2CBs and a Gaussian function) is shown in red and the background (exponential) in green. The lower pads show the residues of the fit. Trigger category TIS and positive polarity

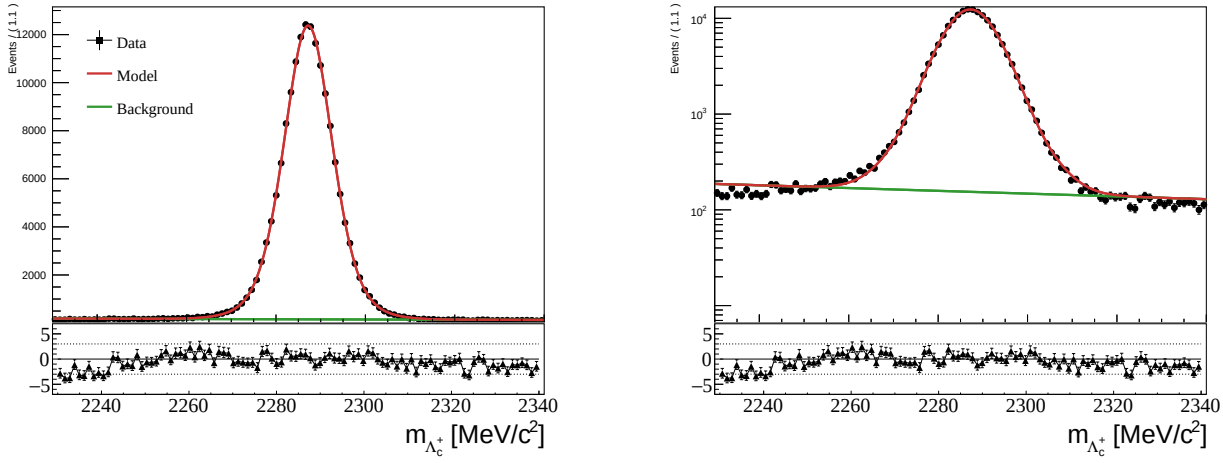

Figure D.3: Left: fit to the $m_{pK^-\pi^+}$ invariant mass. Right: same fit, with the y-axis in logarithmic scale. Data are shown in black, the fit model (2CBs and a Gaussian function) is shown in red and the background (exponential) in green. The lower pads show the residues of the fit. Trigger category TOS and negative polarity

E Additional efficiency plots

Efficiency distributions for the other magnet polarity and trigger category: magnet up TOS, magnet down TIS, magnet up TIS.

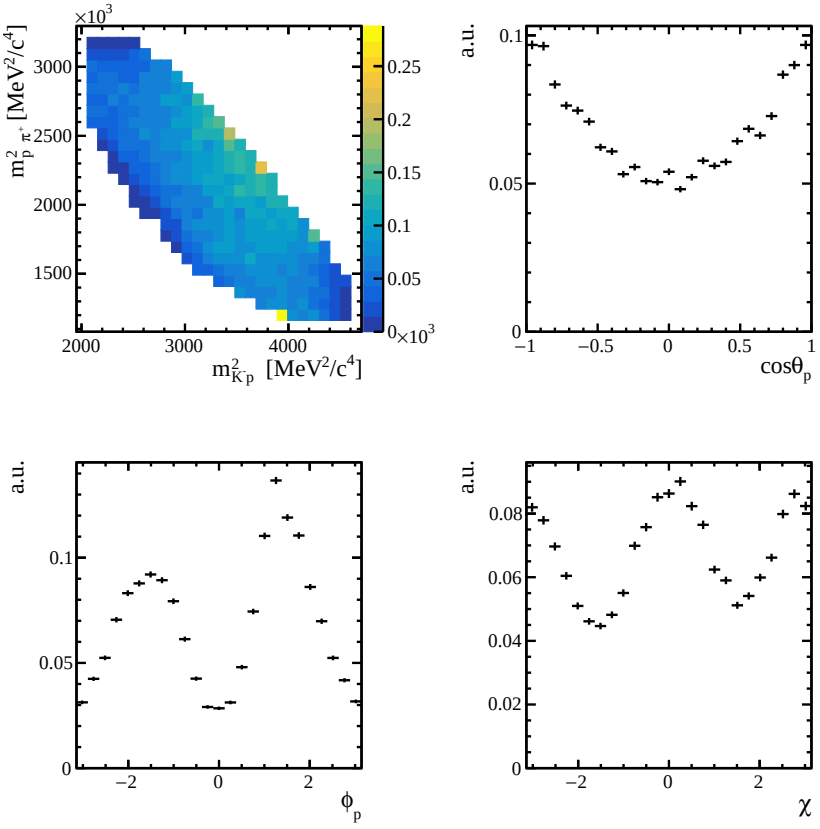

Figure E.1: Efficiency distributions over the 2 dimensional plane (m_{pK^-},$m_{p\pi^+}$) and the three angles ϕ_p, $cos(\theta_p)$ and χ for the trigger TOS category, magnet up. The units of the efficiency are arbitrary.

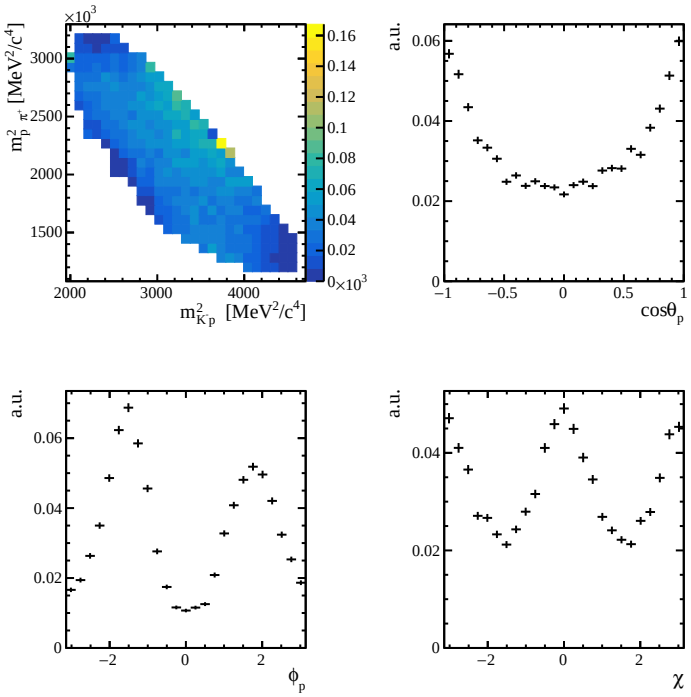

Figure E.2: Efficiency distributions over the 2 dimensional plane $(m_{pK^-}, m_{p\pi^+})$ and the three angles ϕ_p, $cos(\theta_p)$ and χ for the trigger TIS category, magnet down. The units of the efficiency are arbitrary.

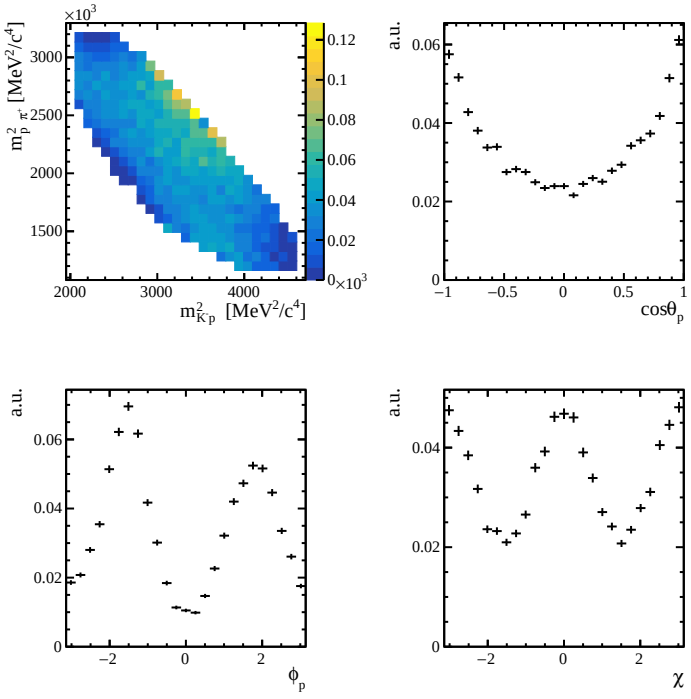

Figure E.3: Efficiency distributions over the 2 dimensional plane $(m_{pK^-}, m_{p\pi^+})$ and the three angles ϕ_p, $cos(\theta_p)$ and χ for the trigger TIS category, magnet up. The units of the efficiency are arbitrary.

F Model building

F.1 Fit results for the two supplementary models M10 and M21

The fit for the other two models selected from the model building procedure are shown here. In all Figures, the black dots are the data points, the red line shows the full PDF model, the colored lines shows the contributions of each resonance separately and the colour code is specified in the legend shown in the $m^2_{K\pi}$ mass projection, in general blue lines are K^* resonances, green lines Δ^{++} and brown-red lines Λ^*. The lower pads show the pulls between the data and the total model, the dashed horizontal lines show the limit of 3 standard deviations (3 σ).

F.2 Discarded models

Examples of fit results for which have been discussed in the text and discarded are shown here. Especially, one example of how the minimal model (M0) is not sufficient to describe the data and two other models (M17,M18) which may seem good but which have large interferencce effects, only the M17 is shown.

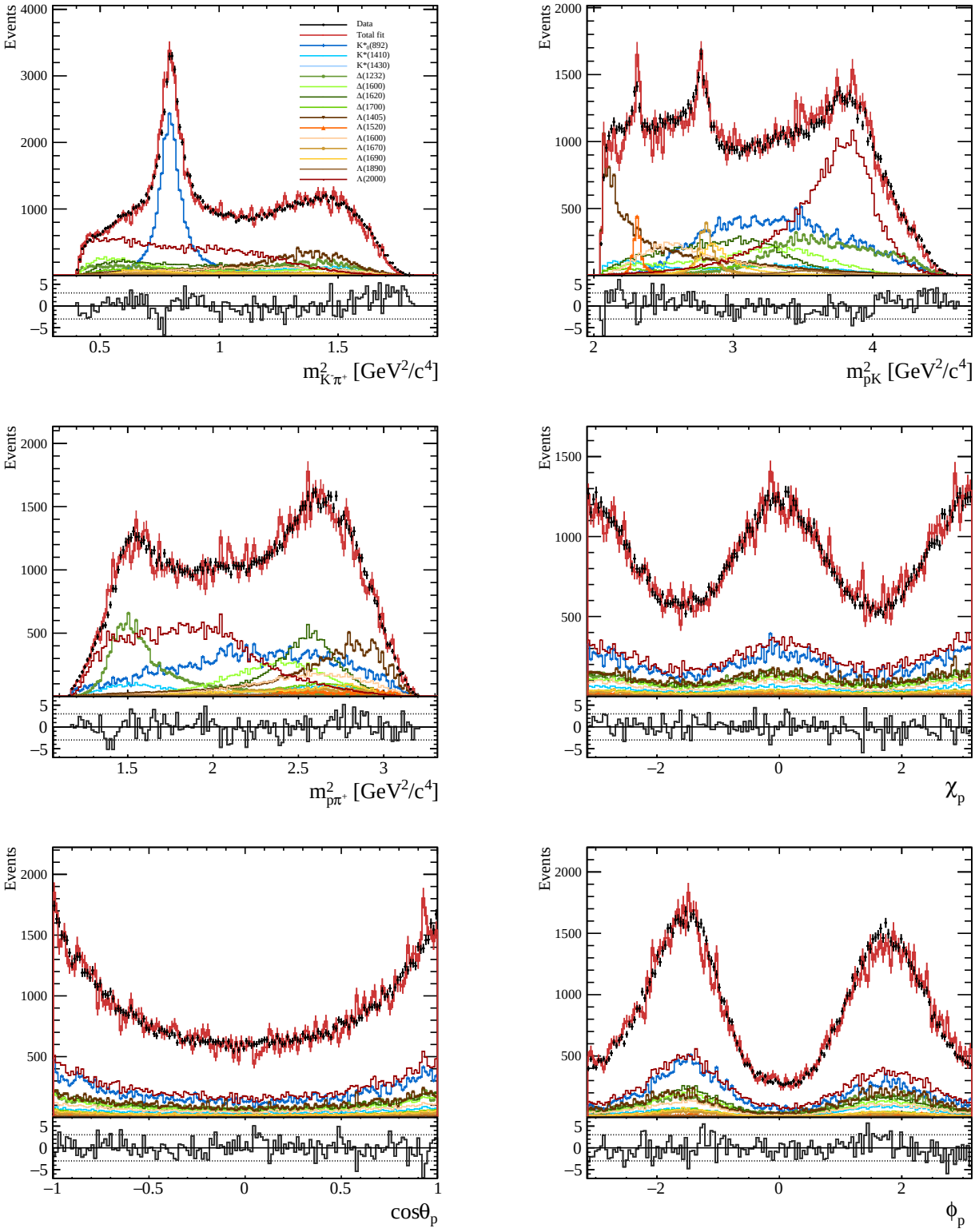

Figure F.1: Example of fit with the model M21 on the TIS category, negative polarity, for Λ_c^+ and $\overline{\Lambda}_c^-$ decays mixed.

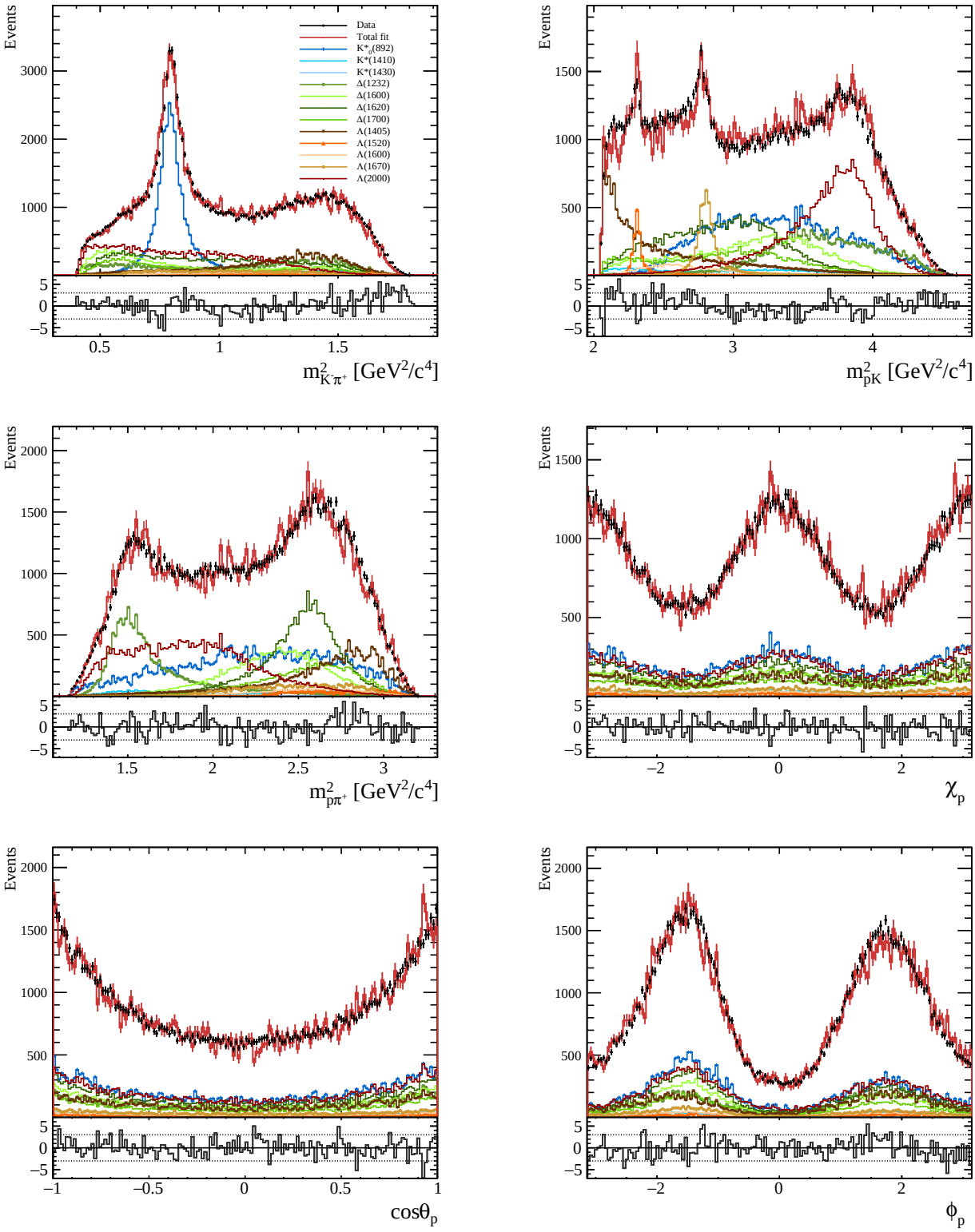

Figure F.2: Example of fit with the model M10 on the TIS category, negative polarity, for Λ_c^+ and $\overline{\Lambda}_c^-$ decays mixed.

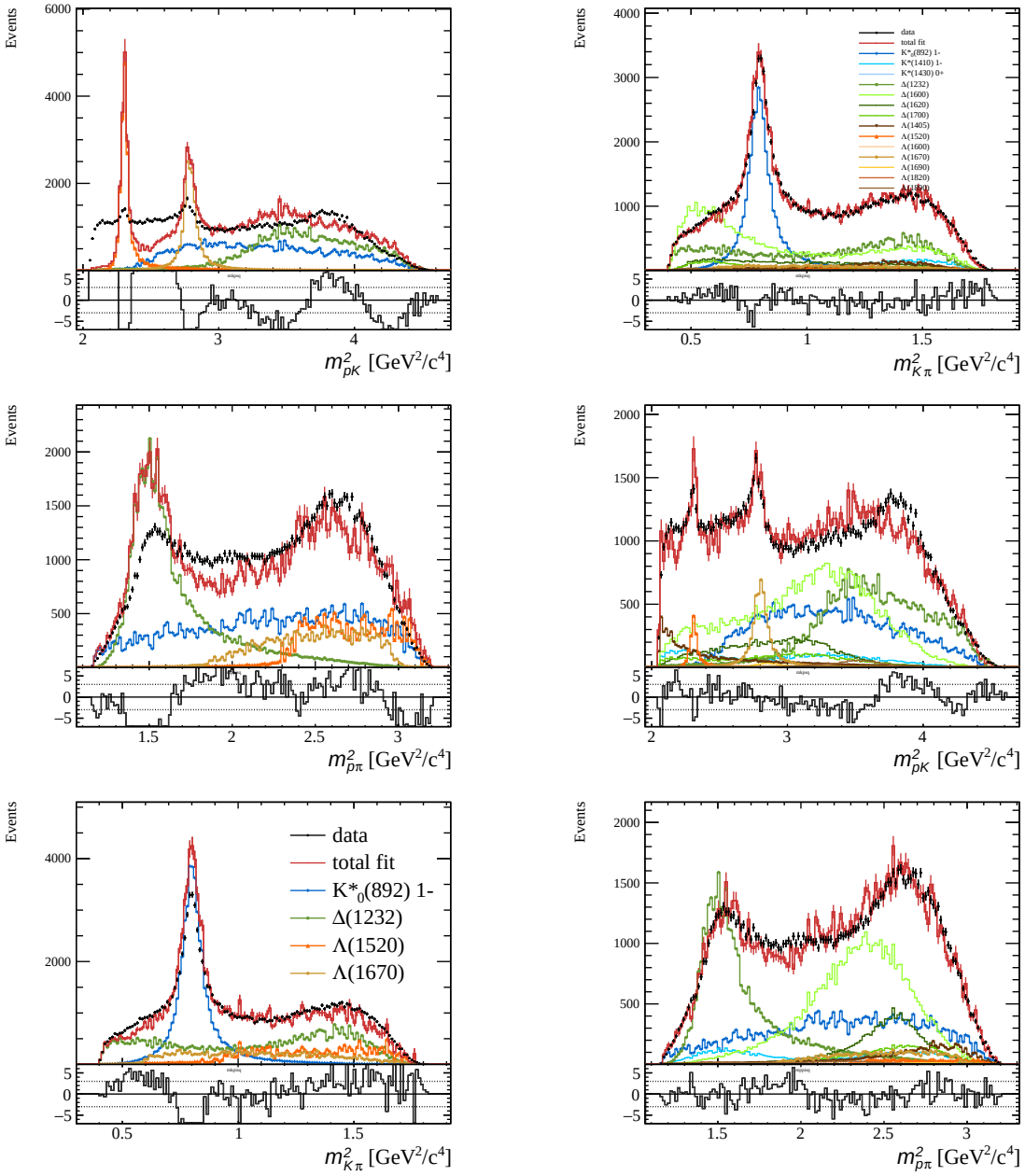

Figure F.3: One dimensional projections of the masses m^2_{pK},$m^2_{p\pi}$ and $m^2_{K\pi}$. The first column shows the projections for the minimal model M0, the right column for M17. The latter shows large interference effects from the $\Delta(1232)$ and $\Delta(1600)$ resonances.

G Fit results

The fit results for the other catergories of model 6 (M6) and for the alternative models (M10 and M21) are shown here. The uncertainties cited are only statistical.

G.1 Results for model 6

FF parameter	Central value	Statistical uncertainty
$\Delta^{++}(1232)$	0.16004	0.00106
$\Delta^{++}(1600)$	0.12063	0.00024
$\Delta^{++}(1620)$	0.16727	0.00081
$\Delta^{++}(1700)$	0.05793	0.00048
$K^{*}(1430)$	0.00008	0.00004
$K^{*}(890)$	0.18556	0.00016
$\Lambda^{*}(1405)$	0.13295	0.00031
$\Lambda^{*}(1520)$	0.03817	0.00151
$\Lambda^{*}(1600)$	0.00933	0.00006
$\Lambda^{*}(1670)$	0.05921	0.00068
$\Lambda^{*}(2000)$	0.20962	0.00042
$\sum F_{r_i}$	1.14080	0.00576

Table G.1: Result of the fit for model M6, MagDown polarity, TIS category and $\overline{\Lambda}_c^-$ decays.

Parameter	α	α statistical uncertainty
$\Delta^{++}(1232)$	0.4810	0.0403
$\Delta^{++}(1600)$	0.5669	0.0416
$\Delta^{++}(1620)$	0.5305	0.0301
$\Delta^{++}(1700)$	0.6936	0.0473
$K^{*}(1430)$	-1.0000	0.0000
$K^{*}(890)$	0.3994	0.1241
$\Lambda^{*}(1405)$	0.2283	0.0391
$\Lambda^{*}(1520)$	0.4991	0.0699
$\Lambda^{*}(1600)$	-0.7733	0.0920
$\Lambda^{*}(1670)$	-0.0749	0.0485
$\Lambda^{*}(2000)$	-0.0321	0.0318
$\alpha_{effective}$	0.7071	0.0042

Table G.2: Result of the fit for model M6, α parameters for MagDown polarity, TIS category and $\overline{\Lambda}_c^-$ decays.

Parameter	Central value	Statistical uncertainty	Parameter	Central value	Statistical uncertainty
$H_1^{\Delta^{++}(1232)}$	0.946	0.026	$H_2^{\Delta^{++}(1232)}$	0.56	0.025
$H_1^{\Delta^{++}(1600)}$	0.854	0.022	$H_2^{\Delta^{++}(1600)}$	0.449	0.025
$H_1^{\Delta^{++}(1620)}$	0.706	0.012	$H_2^{\Delta^{++}(1620)}$	0.391	0.015
$H_1^{\Delta^{++}(1700)}$	0.616	0.015	$H_2^{\Delta^{++}(1700)}$	0.262	0.023
$H_1^{K^*(1430)}$	0.0	0.008	$H_2^{K^*(1430)}$	0.012	0.007
$H_2^{K^*(890)}$	0.517	0.021	$H_3^{K^*(890)}$	0.669	0.023
$H_4^{K^*(890)}$	0.595	0.034	$H_1^{\Lambda^*(1405)}$	0.569	0.012
$H_2^{\Lambda^*(1405)}$	0.451	0.016	$H_1^{\Lambda^*(1520)}$	0.474	0.015
$H_2^{\Lambda^*(1520)}$	0.274	0.024	$H_1^{\Lambda^*(1600)}$	0.064	0.014
$H_2^{\Lambda^*(1600)}$	0.179	0.012	$H_1^{\Lambda^*(1670)}$	0.321	0.011
$H_2^{\Lambda^*(1670)}$	0.346	0.012	$H_1^{\Lambda^*(2000)}$	0.613	0.014
$H_2^{\Lambda^*(2000)}$	0.633	0.014	$\phi_1^{\Delta^{++}(1232)}$	-0.618	0.06
$\phi_2^{\Delta^{++}(1232)}$	-3.364	0.114	$\phi_1^{\Delta^{++}(1600)}$	-3.869	0.061
$\phi_2^{\Delta^{++}(1600)}$	-1.123	0.098	$\phi_1^{\Delta^{++}(1620)}$	-3.677	0.059
$\phi_2^{\Delta^{++}(1620)}$	-0.532	0.095	$\phi_1^{\Delta^{++}(1700)}$	-0.977	0.053
$\phi_2^{\Delta^{++}(1700)}$	-1.493	0.135	$\phi_1^{K^*(1430)}$	-6.48	9.59
$\phi_2^{K^*(1430)}$	-4.367	0.578	$\phi_2^{K^*(890)}$	0.202	0.065
$\phi_3^{K^*(890)}$	-6.5	0.012	$\phi_4^{K^*(890)}$	-2.803	0.073
$\phi_1^{\Lambda^*(1405)}$	-4.953	0.048	$\phi_2^{\Lambda^*(1405)}$	-4.915	0.063
$\phi_1^{\Lambda^*(1520)}$	-5.929	0.055	$\phi_2^{\Lambda^*(1520)}$	-2.118	0.091
$\phi_1^{\Lambda^*(1600)}$	-3.954	0.2	$\phi_2^{\Lambda^*(1600)}$	-5.566	0.08
$\phi_1^{\Lambda^*(1670)}$	-6.5	0.01	$\phi_2^{\Lambda^*(1670)}$	-6.4	0.055
$\phi_1^{\Lambda^*(2000)}$	-0.059	0.05	$\phi_2^{\Lambda^*(2000)}$	-6.464	0.056
P_x	-0.004	0.009	P_y	-0.019	0.007
P_z	0.012	0.007			

Table G.3: Result of the fit for model M6, MagDown polarity, TIS category and $\overline{\Lambda}_c^-$ decays.

Parameter	Central value	Statistical uncertainty	Parameter	Central value	Statistical uncertainty
$H_1^{\Delta^{++}(1232)}$	0.832	0.018	$H_2^{\Delta^{++}(1232)}$	0.54	0.022
$H_1^{\Delta^{++}(1600)}$	0.663	0.022	$H_2^{\Delta^{++}(1600)}$	0.501	0.019
$H_1^{\Delta^{++}(1620)}$	0.587	0.012	$H_2^{\Delta^{++}(1620)}$	0.374	0.013
$H_1^{\Delta^{++}(1700)}$	0.55	0.016	$H_2^{\Delta^{++}(1700)}$	0.317	0.031
$H_1^{K^*(1430)}$	0.009	0.006	$H_2^{K^*(1430)}$	0.012	0.007
$H_2^{K^*(890)}$	0.37	0.025	$H_3^{K^*(890)}$	0.706	0.018
$H_4^{K^*(890)}$	0.556	0.035	$H_1^{\Lambda^*(1405)}$	0.553	0.014
$H_2^{\Lambda^*(1405)}$	0.522	0.017	$H_1^{\Lambda^*(1520)}$	0.259	0.024
$H_2^{\Lambda^*(1520)}$	0.3	0.024	$H_1^{\Lambda^*(1600)}$	0.172	0.015
$H_2^{\Lambda^*(1600)}$	0.101	0.013	$H_1^{\Lambda^*(1670)}$	0.309	0.012
$H_2^{\Lambda^*(1670)}$	0.382	0.011	$H_1^{\Lambda^*(2000)}$	0.616	0.017
$H_2^{\Lambda^*(2000)}$	0.597	0.014	$\phi_1^{\Delta^{++}(1232)}$	-0.672	0.068
$\phi_2^{\Delta^{++}(1232)}$	-3.8	0.117	$\phi_1^{\Delta^{++}(1600)}$	-4.214	0.065
$\phi_2^{\Delta^{++}(1600)}$	-0.821	0.078	$\phi_1^{\Delta^{++}(1620)}$	-3.927	0.059
$\phi_2^{\Delta^{++}(1620)}$	-0.614	0.091	$\phi_1^{\Delta^{++}(1700)}$	-1.241	0.052
$\phi_2^{\Delta^{++}(1700)}$	-1.927	0.09	$\phi_1^{K^*(1430)}$	-6.5	0.218
$\phi_2^{K^*(1430)}$	-5.11	0.62	$\phi_2^{K^*(890)}$	-0.352	0.131
$\phi_3^{K^*(890)}$	-6.5	0.064	$\phi_4^{K^*(890)}$	-2.936	0.089
$\phi_1^{\Lambda^*(1405)}$	-3.909	0.129	$\phi_2^{\Lambda^*(1405)}$	-3.98	0.12
$\phi_1^{\Lambda^*(1520)}$	-5.477	0.102	$\phi_2^{\Lambda^*(1520)}$	-1.041	0.078
$\phi_1^{\Lambda^*(1600)}$	-3.84	0.068	$\phi_2^{\Lambda^*(1600)}$	-5.813	0.131
$\phi_1^{\Lambda^*(1670)}$	-5.676	0.138	$\phi_2^{\Lambda^*(1670)}$	-5.858	0.09
$\phi_1^{\Lambda^*(2000)}$	0.996	0.121	$\phi_2^{\Lambda^*(2000)}$	-5.495	0.12
P_x	0.02	0.008	P_y	0.032	0.007
P_z	0.004	0.007			

Table G.4: Result of the fit for model M6, MagUp polarity, TIS category and Λ_c^+ decays.

FF parameter	Central value	Statistical uncertainty
$\Delta^{++}(1232)$	0.14793	0.00091
$\Delta^{++}(1600)$	0.10154	0.00018
$\Delta^{++}(1620)$	0.14129	0.00111
$\Delta^{++}(1700)$	0.05903	0.00029
$K^*(1430)$	0.00012	0.00011
$K^*(890)$	0.19792	0.00015
$\Lambda^*(1405)$	0.16574	0.00035
$\Lambda^*(1520)$	0.02273	0.00004
$\Lambda^*(1600)$	0.01165	0.00012
$\Lambda^*(1670)$	0.07294	0.00055
$\Lambda^*(2000)$	0.22550	0.00017
$\sum F_{r_i}$	1.14640	0.00399

Table G.5: Result of the fit for model M6, MagUp polarity, TIS category and Λ_c^+ decays.

Parameter	α	α statistical uncertainty
$\Delta^{++}(1232)$	0.4072	0.0385
$\Delta^{++}(1600)$	0.2731	0.0466
$\Delta^{++}(1620)$	0.4225	0.0331
$\Delta^{++}(1700)$	0.5013	0.0764
$K^*(1430)$	-0.2800	0.8164
$K^*(890)$	0.5412	0.1167
$\Lambda^*(1405)$	0.0576	0.0411
$\Lambda^*(1520)$	-0.1459	0.1198
$\Lambda^*(1600)$	0.4872	0.1186
$\Lambda^*(1670)$	-0.2090	0.0462
$\Lambda^*(2000)$	0.0313	0.0362
$\alpha_{effective}$ 0.7343	0.0018	

Table G.6: Result of the fit for model M6, α parameters for MagUp polarity, TIS category and Λ_c^+ decays.

Parameter	Central value	Statistical uncertainty	Parameter	Central value	Statistical uncertainty
$H_1^{\Delta^{++}(1232)}$	0.838	0.021	$H_2^{\Delta^{++}(1232)}$	0.653	0.024
$H_1^{\Delta^{++}(1600)}$	0.726	0.024	$H_2^{\Delta^{++}(1600)}$	0.439	0.018
$H_1^{\Delta^{++}(1620)}$	0.547	0.012	$H_2^{\Delta^{++}(1620)}$	0.379	0.012
$H_1^{\Delta^{++}(1700)}$	0.567	0.013	$H_2^{\Delta^{++}(1700)}$	0.253	0.023
$H_1^{K^*(1430)}$	0.002	0.007	$H_2^{K^*(1430)}$	0.054	0.007
$H_2^{K^*(890)}$	0.446	0.02	$H_3^{K^*(890)}$	0.568	0.019
$H_4^{K^*(890)}$	0.565	0.036	$H_1^{\Lambda^*(1405)}$	0.561	0.012
$H_2^{\Lambda^*(1405)}$	0.424	0.018	$H_1^{\Lambda^*(1520)}$	0.381	0.016
$H_2^{\Lambda^*(1520)}$	0.124	0.024	$H_1^{\Lambda^*(1600)}$	0.164	0.014
$H_2^{\Lambda^*(1600)}$	0.114	0.014	$H_1^{\Lambda^*(1670)}$	0.347	0.009
$H_2^{\Lambda^*(1670)}$	0.348	0.013	$H_1^{\Lambda^*(2000)}$	0.555	0.014
$H_2^{\Lambda^*(2000)}$	0.587	0.014	$\phi_1^{\Delta^{++}(1232)}$	-0.982	0.064
$\phi_2^{\Delta^{++}(1232)}$	-4.027	0.084	$\phi_1^{\Delta^{++}(1600)}$	-4.314	0.056
$\phi_2^{\Delta^{++}(1600)}$	-1.136	0.086	$\phi_1^{\Delta^{++}(1620)}$	-4.131	0.054
$\phi_2^{\Delta^{++}(1620)}$	-0.815	0.075	$\phi_1^{\Delta^{++}(1700)}$	-1.297	0.049
$\phi_2^{\Delta^{++}(1700)}$	-1.932	0.113	$\phi_1^{K^*(1430)}$	-6.5	0.791
$\phi_2^{K^*(1430)}$	-6.073	0.132	$\phi_2^{K^*(890)}$	0.155	0.066
$\phi_3^{K^*(890)}$	-6.5	0.036	$\phi_4^{K^*(890)}$	-2.78	0.08
$\phi_1^{\Lambda^*(1405)}$	-4.601	0.044	$\phi_2^{\Lambda^*(1405)}$	-4.511	0.055
$\phi_1^{\Lambda^*(1520)}$	-6.159	0.077	$\phi_2^{\Lambda^*(1520)}$	-1.122	0.189
$\phi_1^{\Lambda^*(1600)}$	-4.103	0.069	$\phi_2^{\Lambda^*(1600)}$	-6.239	0.107
$\phi_1^{\Lambda^*(1670)}$	-6.5	0.026	$\phi_2^{\Lambda^*(1670)}$	-6.237	0.048
$\phi_1^{\Lambda^*(2000)}$	0.188	0.05	$\phi_2^{\Lambda^*(2000)}$	-6.139	0.052
P_x	0.015	0.008	P_y	0.01	0.007
P_z	0.017	0.008			

Table G.7: Result of the fit for model M6, MagUp polarity, TIS category and $\overline{\Lambda}_c^-$ decays.

FF parameter	Central value	Statistical uncertainty
$\Delta^{++}(1232)$	0.17351	0.00253
$\Delta^{++}(1600)$	0.10851	0.00028
$\Delta^{++}(1620)$	0.13212	0.00125
$\Delta^{++}(1700)$	0.05787	0.00099
$K^{*}(1430)$	0.00172	0.00012
$K^{*}(890)$	0.19182	0.00012
$\Lambda^{*}(1405)$	0.14467	0.00042
$\Lambda^{*}(1520)$	0.02379	0.00012
$\Lambda^{*}(1600)$	0.01198	0.00014
$\Lambda^{*}(1670)$	0.07451	0.00071
$\Lambda^{*}(2000)$	0.20430	0.00011
$\sum F_{r_i}$	1.12478	0.00680

Table G.8: Result of the fit for model M6, MagUp polarity, TIS category and $\overline{\Lambda}_c^-$ decays.

Parameter	α	α statistical uncertainty
$\Delta^{++}(1232)$	0.2444	0.0418
$\Delta^{++}(1600)$	0.4645	0.0413
$\Delta^{++}(1620)$	0.3513	0.0338
$\Delta^{++}(1700)$	0.6679	0.0519
$K^{*}(1430)$	-0.9973	0.0192
$K^{*}(890)$	0.4370	0.1052
$\Lambda^{*}(1405)$	0.2729	0.0440
$\Lambda^{*}(1520)$	0.8084	0.0686
$\Lambda^{*}(1600)$	0.3484	0.1314
$\Lambda^{*}(1670)$	-0.0029	0.0455
$\Lambda^{*}(2000)$	-0.0560	0.0346
$\alpha_{effective}$	0.7202	0.0018

Table G.9: Result of the fit for model M6, α parameters for MagUp polarity, TIS category and $\overline{\Lambda}_c^-$ decays.

Parameter	Central value	Statistical uncertainty	Parameter	Central value	Statistical uncertainty
$H_1^{\Delta^{++}(1232)}$	0.805	0.002	$H_2^{\Delta^{++}(1232)}$	0.65	0.001
$H_1^{\Delta^{++}(1600)}$	0.688	0.002	$H_2^{\Delta^{++}(1600)}$	0.488	0.002
$H_1^{\Delta^{++}(1620)}$	0.623	0.001	$H_2^{\Delta^{++}(1620)}$	0.442	0.001
$H_1^{\Delta^{++}(1700)}$	0.565	0.002	$H_2^{\Delta^{++}(1700)}$	0.287	0.002
$H_1^{K^*(1430)}$	0.053	0.001	$H_2^{K^*(1430)}$	0.039	0.001
$H_2^{K^*(890)}$	0.472	0.002	$H_3^{K^*(890)}$	0.645	0.002
$H_4^{K^*(890)}$	0.639	0.002	$H_1^{\Lambda^*(1405)}$	0.705	0.001
$H_2^{\Lambda^*(1405)}$	0.654	0.002	$H_1^{\Lambda^*(1520)}$	0.369	0.002
$H_2^{\Lambda^*(1520)}$	0.346	0.003	$H_1^{\Lambda^*(1600)}$	0.164	0.001
$H_2^{\Lambda^*(1600)}$	0.0	0.28	$H_1^{\Lambda^*(1670)}$	0.314	0.001
$H_2^{\Lambda^*(1670)}$	0.386	0.001	$H_1^{\Lambda^*(2000)}$	0.659	0.001
$H_2^{\Lambda^*(2000)}$	0.688	0.001	$\phi_1^{\Delta^{++}(1232)}$	-0.099	0.003
$\phi_2^{\Delta^{++}(1232)}$	-3.005	0.004	$\phi_1^{\Delta^{++}(1600)}$	-3.806	0.003
$\phi_2^{\Delta^{++}(1600)}$	-0.498	0.004	$\phi_1^{\Delta^{++}(1620)}$	-3.432	0.002
$\phi_2^{\Delta^{++}(1620)}$	-0.138	0.003	$\phi_1^{\Delta^{++}(1700)}$	-0.891	0.003
$\phi_2^{\Delta^{++}(1700)}$	-0.966	0.006	$\phi_1^{K^*(1430)}$	-6.5	0.0
$\phi_2^{K^*(1430)}$	-2.592	0.025	$\phi_2^{K^*(890)}$	-0.051	0.007
$\phi_3^{K^*(890)}$	-6.5	0.001	$\phi_4^{K^*(890)}$	-3.225	0.005
$\phi_1^{\Lambda^*(1405)}$	-4.683	0.003	$\phi_2^{\Lambda^*(1405)}$	-4.476	0.002
$\phi_1^{\Lambda^*(1520)}$	-5.711	0.009	$\phi_2^{\Lambda^*(1520)}$	-1.898	0.01
$\phi_1^{\Lambda^*(1600)}$	-4.382	0.008	$\phi_2^{\Lambda^*(1600)}$	-6.476	7.17
$\phi_1^{\Lambda^*(1670)}$	-6.412	0.005	$\phi_2^{\Lambda^*(1670)}$	-6.471	0.004
$\phi_1^{\Lambda^*(2000)}$	0.247	0.002	$\phi_2^{\Lambda^*(2000)}$	-6.031	0.002
P_x	0.009	0.001	P_y	0.009	0.001
P_z	-0.017	0.001			

Table G.10: Result of the fit for model M6, MagDown polarity, TOS category and Λ_c^+ decays.

FF parameter	Central value	Statistical uncertainty
$\Delta^{++}(1232)$	0.13665	0.00050
$\Delta^{++}(1600)$	0.08888	0.00002
$\Delta^{++}(1620)$	0.14433	0.00004
$\Delta^{++}(1700)$	0.04999	0.00003
$K^*(1430)$	0.00214	0.00001
$K^*(890)$	0.17695	0.00007
$\Lambda^*(1405)$	0.22446	0.00007
$\Lambda^*(1520)$	0.03141	0.00008
$\Lambda^*(1600)$	0.00671	0.00002
$\Lambda^*(1670)$	0.06341	0.00010
$\Lambda^*(2000)$	0.23578	0.00010
$\sum F_{r_i}$	1.16070	0.00103

Table G.11: Result of the fit for model M6, MagDown polarity, TOS category and Λ_c^+ decays.

Parameter	α	α statistical uncertainty
$\Delta^{++}(1232)$	0.2107	0.0028
$\Delta^{++}(1600)$	0.3306	0.0045
$\Delta^{++}(1620)$	0.3304	0.0025
$\Delta^{++}(1700)$	0.5898	0.0051
$K^*(1430)$	0.2975	0.0290
$K^*(890)$	0.3834	0.1048
$\Lambda^*(1405)$	0.0749	0.0034
$\Lambda^*(1520)$	0.0643	0.0102
$\Lambda^*(1600)$	1.0000	0.0000
$\Lambda^*(1670)$	-0.2036	0.0039
$\Lambda^*(2000)$	-0.0430	0.0021
$\alpha_{effective}$	0.7196	0.0002

Table G.12: Result of the fit for model M6, α parameters for MagDown polarity, TOS category and Λ_c^+ decays.

Parameter	Central value	Statistical uncertainty	Parameter	Central value	Statistical uncertainty
$H_1^{\Delta^{++}(1232)}$	0.769	0.023	$H_2^{\Delta^{++}(1232)}$	0.682	0.044
$H_1^{\Delta^{++}(1600)}$	0.635	0.024	$H_2^{\Delta^{++}(1600)}$	0.549	0.051
$H_1^{\Delta^{++}(1620)}$	0.589	0.016	$H_2^{\Delta^{++}(1620)}$	0.478	0.043
$H_1^{\Delta^{++}(1700)}$	0.573	0.02	$H_2^{\Delta^{++}(1700)}$	0.259	0.033
$H_1^{K^*(1430)}$	0.044	0.008	$H_2^{K^*(1430)}$	0.0	0.002
$H_2^{K^*(890)}$	0.525	0.042	$H_3^{K^*(890)}$	0.618	0.024
$H_4^{K^*(890)}$	0.736	0.061	$H_1^{\Lambda^*(1405)}$	0.602	0.027
$H_2^{\Lambda^*(1405)}$	0.681	0.033	$H_1^{\Lambda^*(1520)}$	0.42	0.042
$H_2^{\Lambda^*(1520)}$	0.315	0.037	$H_1^{\Lambda^*(1600)}$	0.193	0.016
$H_2^{\Lambda^*(1600)}$	0.024	0.017	$H_1^{\Lambda^*(1670)}$	0.335	0.015
$H_2^{\Lambda^*(1670)}$	0.399	0.02	$H_1^{\Lambda^*(2000)}$	0.585	0.021
$H_2^{\Lambda^*(2000)}$	0.661	0.029	$\phi_1^{\Delta^{++}(1232)}$	0.105	0.188
$\phi_2^{\Delta^{++}(1232)}$	-2.807	0.208	$\phi_1^{\Delta^{++}(1600)}$	-3.696	0.168
$\phi_2^{\Delta^{++}(1600)}$	-0.083	0.182	$\phi_1^{\Delta^{++}(1620)}$	-3.325	0.168
$\phi_2^{\Delta^{++}(1620)}$	0.215	0.191	$\phi_1^{\Delta^{++}(1700)}$	-0.784	0.137
$\phi_2^{\Delta^{++}(1700)}$	-0.485	0.315	$\phi_1^{K^*(1430)}$	-6.297	0.218
$\phi_2^{K^*(1430)}$	-6.5	9.239	$\phi_2^{K^*(890)}$	0.725	0.199
$\phi_3^{K^*(890)}$	-5.894	0.157	$\phi_4^{K^*(890)}$	-3.454	0.099
$\phi_1^{\Lambda^*(1405)}$	-3.973	0.126	$\phi_2^{\Lambda^*(1405)}$	-3.942	0.119
$\phi_1^{\Lambda^*(1520)}$	-5.244	0.112	$\phi_2^{\Lambda^*(1520)}$	-1.46	0.14
$\phi_1^{\Lambda^*(1600)}$	-3.73	0.123	$\phi_2^{\Lambda^*(1600)}$	-6.5	1.745
$\phi_1^{\Lambda^*(1670)}$	-5.917	0.131	$\phi_2^{\Lambda^*(1670)}$	-5.923	0.103
$\phi_1^{\Lambda^*(2000)}$	0.795	0.125	$\phi_2^{\Lambda^*(2000)}$	-5.517	0.116
P_x	-0.03	0.011	P_y	-0.002	0.011
P_z	-0.036	0.011			

Table G.13: Result of the fit for model M6, MagDown polarity, TOS category and $\overline{\Lambda}_c^-$ decays.

FF parameter	Central value	Statistical uncertainty
$\Delta^{++}(1232)$	0.13544	0.00023
$\Delta^{++}(1600)$	0.08843	0.00015
$\Delta^{++}(1620)$	0.14308	0.00128
$\Delta^{++}(1700)$	0.04950	0.00097
$K^*(1430)$	0.00098	0.00005
$K^*(890)$	0.19089	0.00224
$\Lambda^*(1405)$	0.20169	0.00029
$\Lambda^*(1520)$	0.03405	0.00008
$\Lambda^*(1600)$	0.00951	0.00005
$\Lambda^*(1670)$	0.06983	0.00056
$\Lambda^*(2000)$	0.20368	0.00043
$\sum F_{r_i}$	1.12710	0.00632

Table G.14: Result of the fit for model M6, MagDown polarity, TOS category and $\overline{\Lambda}_c^-$ decays.

Parameter	α	α statistical uncertainty
$\Delta^{++}(1232)$	0.1195	0.0701
$\Delta^{++}(1600)$	0.1445	0.0982
$\Delta^{++}(1620)$	0.2058	0.0900
$\Delta^{++}(1700)$	0.6607	0.0744
$K^*(1430)$	1.0000	0.0000
$K^*(890)$	0.2567	0.1554
$\Lambda^*(1405)$	-0.1227	0.0650
$\Lambda^*(1520)$	0.2800	0.1422
$\Lambda^*(1600)$	0.9695	0.0428
$\Lambda^*(1670)$	-0.1731	0.0652
$\Lambda^*(2000)$	-0.1215	0.0559
$\alpha_{effective}$	0.6971	0.0010

Table G.15: Result of the fit for model M6, α parameters for MagDown polarity, TOS category and $\overline{\Lambda}_c^-$ decays.

Parameter	Central value	Statistical uncertainty	Parameter	Central value	Statistical uncertainty
$H_1^{\Delta^{++}(1232)}$	0.815	0.021	$H_2^{\Delta^{++}(1232)}$	0.498	0.03
$H_1^{\Delta^{++}(1600)}$	0.586	0.027	$H_2^{\Delta^{++}(1600)}$	0.416	0.029
$H_1^{\Delta^{++}(1620)}$	0.599	0.014	$H_2^{\Delta^{++}(1620)}$	0.378	0.017
$H_1^{\Delta^{++}(1700)}$	0.496	0.019	$H_2^{\Delta^{++}(1700)}$	0.33	0.028
$H_1^{K^*(1430)}$	0.034	0.008	$H_2^{K^*(1430)}$	0.023	0.008
$H_2^{K^*(890)}$	0.39	0.038	$H_3^{K^*(890)}$	0.652	0.022
$H_4^{K^*(890)}$	0.581	0.044	$H_1^{\Lambda^*(1405)}$	0.558	0.022
$H_2^{\Lambda^*(1405)}$	0.579	0.022	$H_1^{\Lambda^*(1520)}$	0.508	0.028
$H_2^{\Lambda^*(1520)}$	0.231	0.054	$H_1^{\Lambda^*(1600)}$	0.166	0.021
$H_2^{\Lambda^*(1600)}$	0.088	0.018	$H_1^{\Lambda^*(1670)}$	0.383	0.019
$H_2^{\Lambda^*(1670)}$	0.302	0.021	$H_1^{\Lambda^*(2000)}$	0.625	0.018
$H_2^{\Lambda^*(2000)}$	0.57	0.017	$\phi_1^{\Delta^{++}(1232)}$	-0.273	0.099
$\phi_2^{\Delta^{++}(1232)}$	-3.514	0.193	$\phi_1^{\Delta^{++}(1600)}$	-4.454	0.106
$\phi_2^{\Delta^{++}(1600)}$	-1.01	0.129	$\phi_1^{\Delta^{++}(1620)}$	-3.972	0.091
$\phi_2^{\Delta^{++}(1620)}$	-0.816	0.158	$\phi_1^{\Delta^{++}(1700)}$	-1.295	0.092
$\phi_2^{\Delta^{++}(1700)}$	-1.614	0.131	$\phi_1^{K^*(1430)}$	-6.147	0.259
$\phi_2^{K^*(1430)}$	-3.701	0.389	$\phi_2^{K^*(890)}$	-0.611	0.143
$\phi_3^{K^*(890)}$	-6.5	0.068	$\phi_4^{K^*(890)}$	-3.069	0.134
$\phi_1^{\Lambda^*(1405)}$	-3.471	0.166	$\phi_2^{\Lambda^*(1405)}$	-3.59	0.134
$\phi_1^{\Lambda^*(1520)}$	-5.406	0.107	$\phi_2^{\Lambda^*(1520)}$	-1.174	0.215
$\phi_1^{\Lambda^*(1600)}$	-3.898	0.097	$\phi_2^{\Lambda^*(1600)}$	-6.049	0.219
$\phi_1^{\Lambda^*(1670)}$	-5.43	0.122	$\phi_2^{\Lambda^*(1670)}$	-5.823	0.145
$\phi_1^{\Lambda^*(2000)}$	1.325	0.146	$\phi_2^{\Lambda^*(2000)}$	-5.075	0.152
P_x	-0.019	0.011	P_y	0.03	0.011
P_z	-0.028	0.009			

Table G.16: Result of the fit for model M6, MagUp polarity, TOS category and Λ_c^+ decays.

FF parameter	Central value	Statistical uncertainty
$\Delta^{++}(1232)$	0.13028	0.00014
$\Delta^{++}(1600)$	0.07227	0.00013
$\Delta^{++}(1620)$	0.13881	0.00104
$\Delta^{++}(1700)$	0.04951	0.00029
$K^*(1430)$	0.00094	0.00001
$K^*(890)$	0.18533	0.00049
$\Lambda^*(1405)$	0.17600	0.00051
$\Lambda^*(1520)$	0.04285	0.00011
$\Lambda^*(1600)$	0.00984	0.00019
$\Lambda^*(1670)$	0.06835	0.00084
$\Lambda^*(2000)$	0.20847	0.00035
$\sum F_{r_i}$	1.08263	0.00409

Table G.17: Result of the fit for model M6, MagUp polarity, TOS category and Λ_c^+ decays.

Parameter	α	α statistical uncertainty
$\Delta^{++}(1232)$	0.4563	0.0519
$\Delta^{++}(1600)$	0.3298	0.0745
$\Delta^{++}(1620)$	0.4304	0.0413
$\Delta^{++}(1700)$	0.3863	0.0792
$K^*(1430)$	0.3721	0.3618
$K^*(890)$	0.4885	0.1294
$\Lambda^*(1405)$	-0.0369	0.0547
$\Lambda^*(1520)$	0.6573	0.1364
$\Lambda^*(1600)$	0.5612	0.1647
$\Lambda^*(1670)$	0.2332	0.0808
$\Lambda^*(2000)$	0.0919	0.0411
$\alpha_{effective}$	0.7198	0.0034

Table G.18: Result of the fit for model M6, α parameters for MagUp polarity, TOS category and Λ_c^+ decays.

Parameter	Central value	Statistical uncertainty	Parameter	Central value	Statistical uncertainty
$H_1^{\Delta^{++}(1232)}$	0.763	0.021	$H_2^{\Delta^{++}(1232)}$	0.559	0.026
$H_1^{\Delta^{++}(1600)}$	0.648	0.025	$H_2^{\Delta^{++}(1600)}$	0.47	0.031
$H_1^{\Delta^{++}(1620)}$	0.535	0.014	$H_2^{\Delta^{++}(1620)}$	0.4	0.019
$H_1^{\Delta^{++}(1700)}$	0.55	0.019	$H_2^{\Delta^{++}(1700)}$	0.291	0.028
$H_1^{K^*(1430)}$	0.032	0.008	$H_2^{K^*(1430)}$	0.044	0.008
$H_2^{K^*(890)}$	0.407	0.023	$H_3^{K^*(890)}$	0.604	0.019
$H_4^{K^*(890)}$	0.478	0.032	$H_1^{\Lambda^*(1405)}$	0.557	0.018
$H_2^{\Lambda^*(1405)}$	0.574	0.023	$H_1^{\Lambda^*(1520)}$	0.412	0.028
$H_2^{\Lambda^*(1520)}$	0.211	0.044	$H_1^{\Lambda^*(1600)}$	0.201	0.021
$H_2^{\Lambda^*(1600)}$	0.111	0.022	$H_1^{\Lambda^*(1670)}$	0.367	0.016
$H_2^{\Lambda^*(1670)}$	0.354	0.017	$H_1^{\Lambda^*(2000)}$	0.608	0.015
$H_2^{\Lambda^*(2000)}$	0.566	0.017	$\phi_1^{\Delta^{++}(1232)}$	-0.612	0.134
$\phi_2^{\Delta^{++}(1232)}$	-3.629	0.19	$\phi_1^{\Delta^{++}(1600)}$	-4.229	0.143
$\phi_2^{\Delta^{++}(1600)}$	-0.802	0.207	$\phi_1^{\Delta^{++}(1620)}$	-3.958	0.137
$\phi_2^{\Delta^{++}(1620)}$	-0.631	0.204	$\phi_1^{\Delta^{++}(1700)}$	-1.261	0.118
$\phi_2^{\Delta^{++}(1700)}$	-1.532	0.256	$\phi_1^{K^*(1430)}$	-6.5	0.166
$\phi_2^{K^*(1430)}$	-4.551	0.236	$\phi_2^{K^*(890)}$	-0.052	0.221
$\phi_3^{K^*(890)}$	-6.441	0.144	$\phi_4^{K^*(890)}$	-3.185	0.164
$\phi_1^{\Lambda^*(1405)}$	-4.028	0.119	$\phi_2^{\Lambda^*(1405)}$	-4.122	0.11
$\phi_1^{\Lambda^*(1520)}$	-5.461	0.113	$\phi_2^{\Lambda^*(1520)}$	-1.393	0.165
$\phi_1^{\Lambda^*(1600)}$	-3.885	0.085	$\phi_2^{\Lambda^*(1600)}$	-6.199	0.162
$\phi_1^{\Lambda^*(1670)}$	-5.848	0.112	$\phi_2^{\Lambda^*(1670)}$	-6.158	0.108
$\phi_1^{\Lambda^*(2000)}$	0.724	0.106	$\phi_2^{\Lambda^*(2000)}$	-5.688	0.112
P_x	0.042	0.01	P_y	-0.027	0.01
P_z	0.052	0.01			

Table G.19: Result of the fit for model M6, MagUp polarity, TOS category and $\overline{\Lambda}_c^-$ decays.

FF parameter	Central value	Statistical uncertainty
$\Delta^{++}(1232)$	0.13738	0.00018
$\Delta^{++}(1600)$	0.09635	0.00025
$\Delta^{++}(1620)$	0.13298	0.00085
$\Delta^{++}(1700)$	0.05795	0.00054
$K^*(1430)$	0.00174	0.00056
$K^*(890)$	0.18300	0.00013
$\Lambda^*(1405)$	0.18693	0.00035
$\Lambda^*(1520)$	0.03166	0.00008
$\Lambda^*(1600)$	0.01589	0.00035
$\Lambda^*(1670)$	0.08030	0.00079
$\Lambda^*(2000)$	0.21578	0.00044
$\sum F_{r_i}$	1.13996	0.00451

Table G.20: Result of the fit for model M6, MagUp polarity, TOS category and $\overline{\Lambda}_c^-$ decays.

Parameter	α	α statistical uncertainty
$\Delta^{++}(1232)$	0.3014	0.0491
$\Delta^{++}(1600)$	0.3106	0.0690
$\Delta^{++}(1620)$	0.2829	0.0499
$\Delta^{++}(1700)$	0.5626	0.0699
$K^*(1430)$	-0.3081	0.2798
$K^*(890)$	0.5519	0.0994
$\Lambda^*(1405)$	-0.0301	0.0514
$\Lambda^*(1520)$	0.5844	0.1444
$\Lambda^*(1600)$	0.5326	0.1605
$\Lambda^*(1670)$	0.0360	0.0648
$\Lambda^*(2000)$	0.0715	0.0387
$\alpha_{effective}$	0.7277	0.0035

Table G.21: Result of the fit for model M6, α parameters for MagUp polarity, TOS category and $\overline{\Lambda}_c^-$ decays.

G.2 Results for model 10

Parameter	Central value	Statistical uncertainty	Parameter	Central value	Statistical uncertainty
$H_1^{\Delta^{++}(1232)}$	0.748	0.043	$H_2^{\Delta^{++}(1232)}$	1.211	0.109
$H_1^{\Delta^{++}(1600)}$	0.594	0.04	$H_2^{\Delta^{++}(1600)}$	1.067	0.105
$H_1^{\Delta^{++}(1620)}$	0.335	0.031	$H_2^{\Delta^{++}(1620)}$	0.978	0.093
$H_1^{\Delta^{++}(1700)}$	0.671	0.033	$H_2^{\Delta^{++}(1700)}$	0.815	0.099
$H_1^{K^*(1410)}$	0.259	0.053	$H_2^{K^*(1410)}$	0.449	0.061
$H_3^{K^*(1410)}$	0.297	0.055	$H_4^{K^*(1410)}$	0.102	0.047
$H_1^{K^*(1430)}$	0.061	0.012	$H_2^{K^*(1430)}$	0.08	0.014
$H_2^{K^*(890)}$	0.827	0.075	$H_3^{K^*(890)}$	1.063	0.093
$H_4^{K^*(890)}$	1.504	0.163	$H_1^{\Lambda^*(1405)}$	0.662	0.042
$H_2^{\Lambda^*(1405)}$	1.002	0.104	$H_1^{\Lambda^*(1520)}$	0.629	0.056
$H_2^{\Lambda^*(1520)}$	0.613	0.068	$H_1^{\Lambda^*(1600)}$	0.303	0.03
$H_2^{\Lambda^*(1600)}$	0.515	0.05	$H_1^{\Lambda^*(1670)}$	0.208	0.04
$H_2^{\Lambda^*(1670)}$	0.437	0.029	$H_1^{\Lambda^*(2000)}$	0.844	0.075
$H_2^{\Lambda^*(2000)}$	0.849	0.07	$\phi_1^{\Delta^{++}(1232)}$	0.497	0.111
$\phi_2^{\Delta^{++}(1232)}$	4.027	0.074	$\phi_1^{\Delta^{++}(1600)}$	2.958	0.12
$\phi_2^{\Delta^{++}(1600)}$	6.5	0.007	$\phi_1^{\Delta^{++}(1620)}$	-3.053	0.153
$\phi_2^{\Delta^{++}(1620)}$	0.755	0.031	$\phi_1^{\Delta^{++}(1700)}$	5.216	0.055
$\phi_2^{\Delta^{++}(1700)}$	0.162	0.038	$\phi_1^{K^*(1410)}$	0.123	0.22
$\phi_2^{K^*(1410)}$	-1.638	0.132	$\phi_3^{K^*(1410)}$	1.119	0.182
$\phi_4^{K^*(1410)}$	-1.13	0.676	$\phi_1^{K^*(1430)}$	3.068	0.166
$\phi_2^{K^*(1430)}$	1.266	0.151	$\phi_2^{K^*(890)}$	1.336	0.14
$\phi_3^{K^*(890)}$	1.219	0.095	$\phi_4^{K^*(890)}$	2.229	0.059
$\phi_1^{\Lambda^*(1405)}$	-0.538	0.1	$\phi_2^{\Lambda^*(1405)}$	-1.367	0.074
$\phi_1^{\Lambda^*(1520)}$	-0.244	0.105	$\phi_2^{\Lambda^*(1520)}$	0.607	0.1
$\phi_1^{\Lambda^*(1600)}$	1.884	0.101	$\phi_2^{\Lambda^*(1600)}$	-1.425	0.067
$\phi_1^{\Lambda^*(1670)}$	-0.527	0.178	$\phi_2^{\Lambda^*(1670)}$	0.528	0.077
$\phi_1^{\Lambda^*(2000)}$	-1.12	0.089	$\phi_2^{\Lambda^*(2000)}$	-1.006	0.085
P_x	-0.042	0.009	P_y	-0.019	0.01
P_z	0.073	0.008			

Table G.22: Result of the fit for model M10, polarity, TIS category and Λ_c^+ decays.

FF parameter	Central value	Statistical uncertainty
$\Delta^{++}(1232)$	0.11437	0.00045
$\Delta^{++}(1600)$	0.08243	0.00389
$\Delta^{++}(1620)$	0.11701	0.00407
$\Delta^{++}(1700)$	0.06131	0.00051
$K^*(1410)$	0.01341	0.00004
$K^*(1430)$	0.00221	0.00002
$K^*(890)$	0.19374	0.00045
$\Lambda^*(1405)$	0.15502	0.00034
$\Lambda^*(1520)$	0.04183	0.00043
$\Lambda^*(1600)$	0.03942	0.00747
$\Lambda^*(1670)$	0.02650	0.00376
$\Lambda^*(2000)$	0.16477	0.00136
$\sum F_{r_i}$	1.01201	0.02278

Table G.23: Result of the fit for model M10, MagDown polarity, TIS category and Λ_c^+ decays.

Parameter	α	α statistical uncertainty
$\Delta^{++}(1232)$	-0.4477	0.0854
$\Delta^{++}(1600)$	-0.5268	0.0861
$\Delta^{++}(1620)$	-0.7900	0.0499
$\Delta^{++}(1700)$	-0.1920	0.1262
$K^*(1410)$	-0.5007	0.1841
$K^*(1430)$	-0.2647	0.2448
$K^*(890)$	-0.1608	0.3191
$\Lambda^*(1405)$	-0.3923	0.1029
$\Lambda^*(1520)$	0.0258	0.1421
$\Lambda^*(1600)$	-0.4857	0.1060
$\Lambda^*(1670)$	-0.6306	0.1225
$\Lambda^*(2000)$	-0.0059	0.1212
$\alpha_{effective}$	0.6981	0.0059

Table G.24: Result of the fit for model M10, α parameters for MagDown polarity, TIS category and Λ_c^+ decays.

Parameter	Central value	Statistical uncertainty	Parameter	Central value	Statistical uncertainty
$H_1^{\Delta^{++}(1232)}$	0.697	0.034	$H_2^{\Delta^{++}(1232)}$	0.733	0.035
$H_1^{\Delta^{++}(1600)}$	0.905	0.022	$H_2^{\Delta^{++}(1600)}$	0.319	0.021
$H_1^{\Delta^{++}(1620)}$	0.609	0.015	$H_2^{\Delta^{++}(1620)}$	0.423	0.023
$H_1^{\Delta^{++}(1700)}$	0.585	0.017	$H_2^{\Delta^{++}(1700)}$	0.249	0.021
$H_1^{K^*(1410)}$	0.216	0.018	$H_2^{K^*(1410)}$	0.314	0.025
$H_3^{K^*(1410)}$	0.0	0.005	$H_4^{K^*(1410)}$	0.0	0.003
$H_1^{K^*(1430)}$	0.04	0.007	$H_2^{K^*(1430)}$	0.023	0.007
$H_2^{K^*(890)}$	0.624	0.025	$H_3^{K^*(890)}$	0.516	0.025
$H_4^{K^*(890)}$	0.465	0.028	$H_1^{\Lambda^*(1405)}$	0.55	0.016
$H_2^{\Lambda^*(1405)}$	0.402	0.018	$H_1^{\Lambda^*(1520)}$	0.507	0.013
$H_2^{\Lambda^*(1520)}$	0.194	0.018	$H_1^{\Lambda^*(1600)}$	0.039	0.016
$H_2^{\Lambda^*(1600)}$	0.135	0.015	$H_1^{\Lambda^*(1670)}$	0.285	0.013
$H_2^{\Lambda^*(1670)}$	0.298	0.011	$H_1^{\Lambda^*(2000)}$	0.583	0.014
$H_2^{\Lambda^*(2000)}$	0.612	0.015	$\phi_1^{\Delta^{++}(1232)}$	-0.575	0.092
$\phi_2^{\Delta^{++}(1232)}$	3.353	0.083	$\phi_1^{\Delta^{++}(1600)}$	2.631	0.069
$\phi_2^{\Delta^{++}(1600)}$	5.863	0.199	$\phi_1^{\Delta^{++}(1620)}$	-3.418	0.079
$\phi_2^{\Delta^{++}(1620)}$	0.138	0.117	$\phi_1^{\Delta^{++}(1700)}$	5.419	0.075
$\phi_2^{\Delta^{++}(1700)}$	-0.794	0.183	$\phi_1^{K^*(1410)}$	-0.839	0.117
$\phi_2^{K^*(1410)}$	-1.931	0.099	$\phi_3^{K^*(1410)}$	2.081	10.425
$\phi_4^{K^*(1410)}$	-1.24	9.125	$\phi_1^{K^*(1430)}$	-2.836	0.172
$\phi_2^{K^*(1430)}$	0.635	0.289	$\phi_2^{K^*(890)}$	0.215	0.098
$\phi_3^{K^*(890)}$	-0.098	0.108	$\phi_4^{K^*(890)}$	3.09	0.12
$\phi_1^{\Lambda^*(1405)}$	0.451	0.082	$\phi_2^{\Lambda^*(1405)}$	0.603	0.084
$\phi_1^{\Lambda^*(1520)}$	-0.042	0.069	$\phi_2^{\Lambda^*(1520)}$	3.17	0.173
$\phi_1^{\Lambda^*(1600)}$	2.328	0.355	$\phi_2^{\Lambda^*(1600)}$	0.734	0.095
$\phi_1^{\Lambda^*(1670)}$	-1.055	0.094	$\phi_2^{\Lambda^*(1670)}$	-0.778	0.09
$\phi_1^{\Lambda^*(2000)}$	-0.888	0.089	$\phi_2^{\Lambda^*(2000)}$	-0.806	0.077
P_x	0.049	0.009	P_y	-0.023	0.008
P_z	0.002	0.008			

Table G.25: Result of the fit for model M10, polarity, TIS category and $\overline{\Lambda}_c^-$ decays.

FF parameter	Central value	Statistical uncertainty
$\Delta^{++}(1232)$	0.15310	0.00054
$\Delta^{++}(1600)$	0.13492	0.00034
$\Delta^{++}(1620)$	0.15945	0.00013
$\Delta^{++}(1700)$	0.05901	0.00050
$K^*(1410)$	0.01401	0.00164
$K^*(1430)$	0.00121	0.00001
$K^*(890)$	0.18964	0.00084
$\Lambda^*(1405)$	0.13229	0.00084
$\Lambda^*(1520)$	0.04237	0.00057
$\Lambda^*(1600)$	0.00578	0.00020
$\Lambda^*(1670)$	0.05097	0.00131
$\Lambda^*(2000)$	0.21780	0.00102
$\sum F_{r_i}$	1.16055	0.00794

Table G.26: Result of the fit for model M10, MagDown polarity, TIS category and $\overline{\Lambda}_c^-$ decays.

Parameter	α	α statistical uncertainty
$\Delta^{++}(1232)$	-0.0503	0.0681
$\Delta^{++}(1600)$	0.7790	0.0276
$\Delta^{++}(1620)$	0.3491	0.0524
$\Delta^{++}(1700)$	0.6932	0.0463
$K^*(1410)$	-0.3576	0.1005
$K^*(1430)$	0.5031	0.2622
$K^*(890)$	0.3529	0.1086
$\Lambda^*(1405)$	0.3036	0.0485
$\Lambda^*(1520)$	0.7446	0.0429
$\Lambda^*(1600)$	-0.8459	0.1209
$\Lambda^*(1670)$	-0.0446	0.0586
$\Lambda^*(2000)$	-0.0485	0.0342
$\alpha_{effective}$	0.6885	0.0026

Table G.27: Result of the fit for model M10, α parameters for MagDown polarity, TIS category and $\overline{\Lambda}_c^-$ decays.

Parameter	Central value	Statistical uncertainty	Parameter	Central value	Statistical uncertainty
$H_1^{\Delta^{++}(1232)}$	0.768	0.026	$H_2^{\Delta^{++}(1232)}$	0.686	0.043
$H_1^{\Delta^{++}(1600)}$	0.504	0.024	$H_2^{\Delta^{++}(1600)}$	0.716	0.032
$H_1^{\Delta^{++}(1620)}$	0.466	0.016	$H_2^{\Delta^{++}(1620)}$	0.536	0.031
$H_1^{\Delta^{++}(1700)}$	0.669	0.023	$H_2^{\Delta^{++}(1700)}$	0.357	0.036
$H_1^{K^*(1410)}$	0.403	0.043	$H_2^{K^*(1410)}$	0.187	0.034
$H_3^{K^*(1410)}$	0.161	0.026	$H_4^{K^*(1410)}$	0.395	0.041
$H_1^{K^*(1430)}$	0.029	0.007	$H_2^{K^*(1430)}$	0.046	0.008
$H_2^{K^*(890)}$	0.609	0.042	$H_3^{K^*(890)}$	0.666	0.029
$H_4^{K^*(890)}$	0.67	0.057	$H_1^{\Lambda^*(1405)}$	0.579	0.026
$H_2^{\Lambda^*(1405)}$	0.616	0.028	$H_1^{\Lambda^*(1520)}$	0.404	0.02
$H_2^{\Lambda^*(1520)}$	0.114	0.024	$H_1^{\Lambda^*(1600)}$	0.255	0.016
$H_2^{\Lambda^*(1600)}$	0.124	0.019	$H_1^{\Lambda^*(1670)}$	0.306	0.02
$H_2^{\Lambda^*(1670)}$	0.416	0.017	$H_1^{\Lambda^*(2000)}$	0.63	0.02
$H_2^{\Lambda^*(2000)}$	0.723	0.032	$\phi_1^{\Delta^{++}(1232)}$	0.056	0.059
$\phi_2^{\Delta^{++}(1232)}$	3.654	0.077	$\phi_1^{\Delta^{++}(1600)}$	3.046	0.062
$\phi_2^{\Delta^{++}(1600)}$	6.5	0.033	$\phi_1^{\Delta^{++}(1620)}$	-3.023	0.046
$\phi_2^{\Delta^{++}(1620)}$	0.595	0.034	$\phi_1^{\Delta^{++}(1700)}$	5.463	0.042
$\phi_2^{\Delta^{++}(1700)}$	-0.205	0.077	$\phi_1^{K^*(1410)}$	0.21	0.1
$\phi_2^{K^*(1410)}$	-0.526	0.113	$\phi_3^{K^*(1410)}$	5.478	0.184
$\phi_4^{K^*(1410)}$	-2.352	0.106	$\phi_1^{K^*(1430)}$	-1.186	0.243
$\phi_2^{K^*(1430)}$	1.465	0.168	$\phi_2^{K^*(890)}$	0.912	0.082
$\phi_3^{K^*(890)}$	0.476	0.07	$\phi_4^{K^*(890)}$	2.48	0.071
$\phi_1^{\Lambda^*(1405)}$	1.82	0.109	$\phi_2^{\Lambda^*(1405)}$	1.916	0.126
$\phi_1^{\Lambda^*(1520)}$	0.971	0.076	$\phi_2^{\Lambda^*(1520)}$	-1.86	0.305
$\phi_1^{\Lambda^*(1600)}$	2.242	0.069	$\phi_2^{\Lambda^*(1600)}$	-1.826	0.142
$\phi_1^{\Lambda^*(1670)}$	-0.079	0.133	$\phi_2^{\Lambda^*(1670)}$	0.12	0.091
$\phi_1^{\Lambda^*(2000)}$	0.539	0.126	$\phi_2^{\Lambda^*(2000)}$	0.408	0.109
P_x	0.041	0.008	P_y	-0.026	0.009
P_z	0.022	0.008			

Table G.28: Result of the fit for model M10, polarity, TIS category and Λ_c^+ decays.

FF parameter	Central value	Statistical uncertainty
$\Delta^{++}(1232)$	0.13497	0.00044
$\Delta^{++}(1600)$	0.09558	0.00023
$\Delta^{++}(1620)$	0.12444	0.00022
$\Delta^{++}(1700)$	0.07138	0.00065
$K^*(1410)$	0.03120	0.00029
$K^*(1430)$	0.00148	0.00001
$K^*(890)$	0.19499	0.00085
$\Lambda^*(1405)$	0.17310	0.00031
$\Lambda^*(1520)$	0.02160	0.00038
$\Lambda^*(1600)$	0.02010	0.00017
$\Lambda^*(1670)$	0.06807	0.00359
$\Lambda^*(2000)$	0.23852	0.00082
$\sum F_{r_i}$	1.17543	0.00798

Table G.29: Result of the fit for model M10, MagUp polarity, TIS category and Λ_c^+ decays.

Parameter	α	α statistical uncertainty
$\Delta^{++}(1232)$	0.1124	0.0703
$\Delta^{++}(1600)$	-0.3374	0.0579
$\Delta^{++}(1620)$	-0.1390	0.0660
$\Delta^{++}(1700)$	0.5567	0.0735
$K^*(1410)$	0.6457	0.1229
$K^*(1430)$	-0.4312	0.2422
$K^*(890)$	0.2756	0.1605
$\Lambda^*(1405)$	-0.0619	0.0637
$\Lambda^*(1520)$	0.8525	0.0591
$\Lambda^*(1600)$	0.6175	0.1024
$\Lambda^*(1670)$	-0.2978	0.0702
$\Lambda^*(2000)$	-0.1368	0.0534
$\alpha_{effective}$	0.6999	0.0033

Table G.30: Result of the fit for model M10, α parameters for MagUp polarity, TIS category and Λ_c^+ decays.

Parameter	Central value	Statistical uncertainty	Parameter	Central value	Statistical uncertainty
$H_1^{\Delta^{++}(1232)}$	0.822	0.021	$H_2^{\Delta^{++}(1232)}$	0.628	0.033
$H_1^{\Delta^{++}(1600)}$	0.768	0.024	$H_2^{\Delta^{++}(1600)}$	0.402	0.022
$H_1^{\Delta^{++}(1620)}$	0.522	0.011	$H_2^{\Delta^{++}(1620)}$	0.372	0.018
$H_1^{\Delta^{++}(1700)}$	0.588	0.015	$H_2^{\Delta^{++}(1700)}$	0.212	0.026
$H_1^{K^*(1410)}$	0.176	0.028	$H_2^{K^*(1410)}$	0.136	0.027
$H_3^{K^*(1410)}$	0.109	0.022	$H_4^{K^*(1410)}$	0.246	0.035
$H_1^{K^*(1430)}$	0.021	0.008	$H_2^{K^*(1430)}$	0.074	0.007
$H_2^{K^*(890)}$	0.53	0.019	$H_3^{K^*(890)}$	0.451	0.022
$H_4^{K^*(890)}$	0.519	0.036	$H_1^{\Lambda^*(1405)}$	0.6	0.011
$H_2^{\Lambda^*(1405)}$	0.37	0.017	$H_1^{\Lambda^*(1520)}$	0.405	0.024
$H_2^{\Lambda^*(1520)}$	0.011	0.15	$H_1^{\Lambda^*(1600)}$	0.177	0.014
$H_2^{\Lambda^*(1600)}$	0.109	0.012	$H_1^{\Lambda^*(1670)}$	0.357	0.01
$H_2^{\Lambda^*(1670)}$	0.307	0.01	$H_1^{\Lambda^*(2000)}$	0.574	0.012
$H_2^{\Lambda^*(2000)}$	0.568	0.012	$\phi_1^{\Delta^{++}(1232)}$	-1.101	0.047
$\phi_2^{\Delta^{++}(1232)}$	2.176	0.056	$\phi_1^{\Delta^{++}(1600)}$	1.941	0.058
$\phi_2^{\Delta^{++}(1600)}$	5.079	0.07	$\phi_1^{\Delta^{++}(1620)}$	-4.176	0.051
$\phi_2^{\Delta^{++}(1620)}$	-0.787	0.047	$\phi_1^{\Delta^{++}(1700)}$	4.945	0.086
$\phi_2^{\Delta^{++}(1700)}$	-2.138	0.102	$\phi_1^{K^*(1410)}$	-0.326	0.315
$\phi_2^{K^*(1410)}$	-0.578	0.173	$\phi_3^{K^*(1410)}$	3.4	0.353
$\phi_4^{K^*(1410)}$	-2.212	0.182	$\phi_1^{K^*(1430)}$	-2.041	0.337
$\phi_2^{K^*(1430)}$	0.046	0.09	$\phi_2^{K^*(890)}$	0.252	0.062
$\phi_3^{K^*(890)}$	-0.173	0.068	$\phi_4^{K^*(890)}$	3.862	0.065
$\phi_1^{\Lambda^*(1405)}$	1.097	0.084	$\phi_2^{\Lambda^*(1405)}$	1.198	0.101
$\phi_1^{\Lambda^*(1520)}$	-0.194	0.101	$\phi_2^{\Lambda^*(1520)}$	-0.093	9.467
$\phi_1^{\Lambda^*(1600)}$	1.803	0.091	$\phi_2^{\Lambda^*(1600)}$	-0.772	0.125
$\phi_1^{\Lambda^*(1670)}$	-0.771	0.081	$\phi_2^{\Lambda^*(1670)}$	-0.373	0.069
$\phi_1^{\Lambda^*(2000)}$	-0.368	0.082	$\phi_2^{\Lambda^*(2000)}$	-0.333	0.057
P_x	0.024	0.008	P_y	0.005	0.007
P_z	0.018	0.008			

Table G.31: Result of the fit for model M10, polarity, TIS category and $\overline{\Lambda}_c^-$ decays.

FF parameter	Central value	Statistical uncertainty
$\Delta^{++}(1232)$	0.17177	0.00028
$\Delta^{++}(1600)$	0.11789	0.00069
$\Delta^{++}(1620)$	0.12771	0.00014
$\Delta^{++}(1700)$	0.06109	0.00053
$K^{*}(1410)$	0.01262	0.00288
$K^{*}(1430)$	0.00366	0.00003
$K^{*}(890)$	0.19056	0.00014
$\Lambda^{*}(1405)$	0.15190	0.00033
$\Lambda^{*}(1520)$	0.02536	0.00062
$\Lambda^{*}(1600)$	0.01358	0.00037
$\Lambda^{*}(1670)$	0.07118	0.00365
$\Lambda^{*}(2000)$	0.21298	0.00100
$\sum F_{r_i}$	1.16031	0.01068

Table G.32: Result of the fit for model M10, MagUp polarity, TIS category and $\overline{\Lambda}_c^-$ decays.

Parameter	α	α statistical uncertainty
$\Delta^{++}(1232)$	0.2629	0.0544
$\Delta^{++}(1600)$	0.5699	0.0426
$\Delta^{++}(1620)$	0.3264	0.0472
$\Delta^{++}(1700)$	0.7699	0.0510
$K^{*}(1410)$	0.2523	0.2382
$K^{*}(1430)$	-0.8509	0.1083
$K^{*}(890)$	0.3724	0.1001
$\Lambda^{*}(1405)$	0.4490	0.0395
$\Lambda^{*}(1520)$	0.9985	0.0402
$\Lambda^{*}(1600)$	0.4501	0.1081
$\Lambda^{*}(1670)$	0.1498	0.0420
$\Lambda^{*}(2000)$	0.0105	0.0297
$\alpha_{effective}$	0.7139	0.0075

Table G.33: Result of the fit for model M10, α parameters for MagUp polarity, TIS category and $\overline{\Lambda}_c^-$ decays.

Parameter	Central value	Statistical uncertainty	Parameter	Central value	Statistical uncertainty
$H_1^{\Delta^{++}(1232)}$	0.782	0.033	$H_2^{\Delta^{++}(1232)}$	0.756	0.041
$H_1^{\Delta^{++}(1600)}$	0.711	0.042	$H_2^{\Delta^{++}(1600)}$	0.617	0.046
$H_1^{\Delta^{++}(1620)}$	0.571	0.022	$H_2^{\Delta^{++}(1620)}$	0.513	0.036
$H_1^{\Delta^{++}(1700)}$	0.597	0.035	$H_2^{\Delta^{++}(1700)}$	0.421	0.042
$H_1^{K^*(1410)}$	0.378	0.04	$H_2^{K^*(1410)}$	0.166	0.031
$H_3^{K^*(1410)}$	0.145	0.034	$H_4^{K^*(1410)}$	0.156	0.041
$H_1^{K^*(1430)}$	0.077	0.01	$H_2^{K^*(1430)}$	0.025	0.009
$H_2^{K^*(890)}$	0.595	0.044	$H_3^{K^*(890)}$	0.602	0.037
$H_4^{K^*(890)}$	0.75	0.063	$H_1^{\Lambda^*(1405)}$	0.844	0.04
$H_2^{\Lambda^*(1405)}$	0.589	0.048	$H_1^{\Lambda^*(1520)}$	0.46	0.031
$H_2^{\Lambda^*(1520)}$	0.311	0.036	$H_1^{\Lambda^*(1600)}$	0.212	0.023
$H_2^{\Lambda^*(1600)}$	0.195	0.027	$H_1^{\Lambda^*(1670)}$	0.329	0.021
$H_2^{\Lambda^*(1670)}$	0.38	0.024	$H_1^{\Lambda^*(2000)}$	0.737	0.034
$H_2^{\Lambda^*(2000)}$	0.706	0.046	$\phi_1^{\Delta^{++}(1232)}$	0.298	0.09
$\phi_2^{\Delta^{++}(1232)}$	3.753	0.102	$\phi_1^{\Delta^{++}(1600)}$	3.165	0.084
$\phi_2^{\Delta^{++}(1600)}$	6.5	0.025	$\phi_1^{\Delta^{++}(1620)}$	-2.742	0.064
$\phi_2^{\Delta^{++}(1620)}$	0.695	0.043	$\phi_1^{\Delta^{++}(1700)}$	5.806	0.08
$\phi_2^{\Delta^{++}(1700)}$	-0.197	0.084	$\phi_1^{K^*(1410)}$	-0.336	0.237
$\phi_2^{K^*(1410)}$	-0.841	0.18	$\phi_3^{K^*(1410)}$	4.642	0.224
$\phi_4^{K^*(1410)}$	2.819	0.462	$\phi_1^{K^*(1430)}$	-1.056	0.141
$\phi_2^{K^*(1430)}$	-1.922	0.367	$\phi_2^{K^*(890)}$	0.193	0.149
$\phi_3^{K^*(890)}$	-0.041	0.137	$\phi_4^{K^*(890)}$	2.716	0.11
$\phi_1^{\Lambda^*(1405)}$	1.148	0.097	$\phi_2^{\Lambda^*(1405)}$	1.341	0.124
$\phi_1^{\Lambda^*(1520)}$	0.206	0.103	$\phi_2^{\Lambda^*(1520)}$	4.047	0.215
$\phi_1^{\Lambda^*(1600)}$	1.349	0.117	$\phi_2^{\Lambda^*(1600)}$	-2.183	0.127
$\phi_1^{\Lambda^*(1670)}$	5.547	0.116	$\phi_2^{\Lambda^*(1670)}$	-0.52	0.092
$\phi_1^{\Lambda^*(2000)}$	-0.223	0.106	$\phi_2^{\Lambda^*(2000)}$	-0.212	0.107
P_x	-0.038	0.01	P_y	0.036	0.01
P_z	-0.02	0.009			

Table G.34: Result of the fit for model M10, polarity, TOS category and Λ_c^+ decays.

FF parameter	Central value	Statistical uncertainty
$\Delta^{++}(1232)$	0.13573	0.00025
$\Delta^{++}(1600)$	0.09961	0.00060
$\Delta^{++}(1620)$	0.13121	0.00759
$\Delta^{++}(1700)$	0.05975	0.00045
$K^*(1410)$	0.01600	0.00061
$K^*(1430)$	0.00291	0.00005
$K^*(890)$	0.17719	0.00084
$\Lambda^*(1405)$	0.23142	0.00095
$\Lambda^*(1520)$	0.03401	0.00055
$\Lambda^*(1600)$	0.01863	0.00239
$\Lambda^*(1670)$	0.05809	0.00335
$\Lambda^*(2000)$	0.24377	0.00157
$\sum F_{r_i}$	1.20831	0.01921

Table G.35: Result of the fit for model M10, MagDown polarity, TOS category and Λ_c^+ decays.

Parameter	α	α statistical uncertainty
$\Delta^{++}(1232)$	0.0338	0.0686
$\Delta^{++}(1600)$	0.1409	0.0932
$\Delta^{++}(1620)$	0.1067	0.0791
$\Delta^{++}(1700)$	0.3357	0.1027
$K^*(1410)$	0.6766	0.1164
$K^*(1430)$	0.8093	0.1321
$K^*(890)$	0.1957	0.1663
$\Lambda^*(1405)$	0.3450	0.0831
$\Lambda^*(1520)$	0.3726	0.1153
$\Lambda^*(1600)$	0.0834	0.1747
$\Lambda^*(1670)$	-0.1431	0.0880
$\Lambda^*(2000)$	0.0429	0.0797
$\alpha_{effective}$	0.7195	0.0045

Table G.36: Result of the fit for model M10, α parameters for MagDown polarity, TOS category and Λ_c^+ decays.

Parameter	Central value	Statistical uncertainty	Parameter	Central value	Statistical uncertainty
$H_1^{\Delta^{++}(1232)}$	0.787	0.025	$H_2^{\Delta^{++}(1232)}$	0.609	0.04
$H_1^{\Delta^{++}(1600)}$	0.81	0.032	$H_2^{\Delta^{++}(1600)}$	0.297	0.043
$H_1^{\Delta^{++}(1620)}$	0.75	0.024	$H_2^{\Delta^{++}(1620)}$	0.028	0.044
$H_1^{\Delta^{++}(1700)}$	0.475	0.022	$H_2^{\Delta^{++}(1700)}$	0.314	0.036
$H_1^{K^*(1410)}$	0.283	0.057	$H_2^{K^*(1410)}$	0.108	0.047
$H_3^{K^*(1410)}$	0.308	0.061	$H_4^{K^*(1410)}$	0.291	0.041
$H_1^{K^*(1430)}$	0.036	0.009	$H_2^{K^*(1430)}$	0.041	0.008
$H_2^{K^*(890)}$	0.544	0.025	$H_3^{K^*(890)}$	0.577	0.029
$H_4^{K^*(890)}$	0.571	0.044	$H_1^{\Lambda^*(1405)}$	0.665	0.033
$H_2^{\Lambda^*(1405)}$	0.424	0.062	$H_1^{\Lambda^*(1520)}$	0.497	0.023
$H_2^{\Lambda^*(1520)}$	0.188	0.039	$H_1^{\Lambda^*(1600)}$	0.106	0.021
$H_2^{\Lambda^*(1600)}$	0.206	0.021	$H_1^{\Lambda^*(1670)}$	0.238	0.022
$H_2^{\Lambda^*(1670)}$	0.18	0.02	$H_1^{\Lambda^*(2000)}$	0.517	0.016
$H_2^{\Lambda^*(2000)}$	0.543	0.023	$\phi_1^{\Delta^{++}(1232)}$	0.186	0.091
$\phi_2^{\Delta^{++}(1232)}$	3.062	0.095	$\phi_1^{\Delta^{++}(1600)}$	2.851	0.089
$\phi_2^{\Delta^{++}(1600)}$	6.5	0.484	$\phi_1^{\Delta^{++}(1620)}$	-2.919	0.103
$\phi_2^{\Delta^{++}(1620)}$	0.795	1.0	$\phi_1^{\Delta^{++}(1700)}$	5.747	0.096
$\phi_2^{\Delta^{++}(1700)}$	-1.213	0.125	$\phi_1^{K^*(1410)}$	4.38	0.126
$\phi_2^{K^*(1410)}$	1.16	0.472	$\phi_3^{K^*(1410)}$	4.698	0.239
$\phi_4^{K^*(1410)}$	0.732	0.168	$\phi_1^{K^*(1430)}$	5.824	0.262
$\phi_2^{K^*(1430)}$	3.13	0.213	$\phi_2^{K^*(890)}$	-0.165	0.093
$\phi_3^{K^*(890)}$	-0.225	0.104	$\phi_4^{K^*(890)}$	3.294	0.151
$\phi_1^{\Lambda^*(1405)}$	1.191	0.151	$\phi_2^{\Lambda^*(1405)}$	2.593	0.222
$\phi_1^{\Lambda^*(1520)}$	-0.488	0.097	$\phi_2^{\Lambda^*(1520)}$	-1.199	0.18
$\phi_1^{\Lambda^*(1600)}$	3.848	0.246	$\phi_2^{\Lambda^*(1600)}$	0.825	0.15
$\phi_1^{\Lambda^*(1670)}$	-3.093	0.129	$\phi_2^{\Lambda^*(1670)}$	0.826	0.162
$\phi_1^{\Lambda^*(2000)}$	1.301	0.227	$\phi_2^{\Lambda^*(2000)}$	1.278	0.244
P_x	-0.068	0.01	P_y	0.021	0.01
P_z	0.004	0.01			

Table G.37: Result of the fit for model M10, polarity, TOS category and $\overline{\Lambda}_c^-$ decays.

FF parameter	Central value	Statistical uncertainty
$\Delta^{++}(1232)$	0.14490	0.00022
$\Delta^{++}(1600)$	0.10658	0.00015
$\Delta^{++}(1620)$	0.16009	0.00027
$\Delta^{++}(1700)$	0.04633	0.00051
$K^{*}(1410)$	0.02567	0.00016
$K^{*}(1430)$	0.00171	0.00001
$K^{*}(890)$	0.19385	0.00039
$\Lambda^{*}(1405)$	0.17335	0.00038
$\Lambda^{*}(1520)$	0.03969	0.00141
$\Lambda^{*}(1600)$	0.01542	0.00027
$\Lambda^{*}(1670)$	0.02623	0.00116
$\Lambda^{*}(2000)$	0.16796	0.00181
$\sum F_{r_i}$	1.10179	0.00675

Table G.38: Result of the fit for model M10, MagDown polarity, TOS category and $\overline{\Lambda}_c^-$ decays.

Parameter	α	α statistical uncertainty
$\Delta^{++}(1232)$	0.2509	0.0684
$\Delta^{++}(1600)$	0.7630	0.0627
$\Delta^{++}(1620)$	0.9972	0.0087
$\Delta^{++}(1700)$	0.3918	0.1047
$K^{*}(1410)$	0.7458	0.2128
$K^{*}(1430)$	-0.1293	0.3118
$K^{*}(890)$	0.3637	0.1254
$\Lambda^{*}(1405)$	0.4219	0.1269
$\Lambda^{*}(1520)$	0.7496	0.0931
$\Lambda^{*}(1600)$	-0.5813	0.1475
$\Lambda^{*}(1670)$	0.2723	0.1338
$\Lambda^{*}(2000)$	-0.0490	0.0523
$\alpha_{effective}$	0.7376	0.0049

Table G.39: Result of the fit for model M10, α parameters for MagDown polarity, TOS category and $\overline{\Lambda}_c^-$ decays.

Parameter	Central value	Statistical uncertainty	Parameter	Central value	Statistical uncertainty
$H_1^{\Delta^{++}(1232)}$	0.962	0.044	$H_2^{\Delta^{++}(1232)}$	1.025	0.177
$H_1^{\Delta^{++}(1600)}$	0.736	0.05	$H_2^{\Delta^{++}(1600)}$	0.92	0.142
$H_1^{\Delta^{++}(1620)}$	0.588	0.038	$H_2^{\Delta^{++}(1620)}$	0.737	0.131
$H_1^{\Delta^{++}(1700)}$	0.289	0.068	$H_2^{\Delta^{++}(1700)}$	0.89	0.126
$H_1^{K^*(1410)}$	0.423	0.048	$H_2^{K^*(1410)}$	0.576	0.102
$H_3^{K^*(1410)}$	0.324	0.047	$H_4^{K^*(1410)}$	0.0	0.044
$H_1^{K^*(1430)}$	0.061	0.014	$H_2^{K^*(1430)}$	0.074	0.013
$H_2^{K^*(890)}$	0.652	0.086	$H_3^{K^*(890)}$	0.726	0.079
$H_4^{K^*(890)}$	1.11	0.196	$H_1^{\Lambda^*(1405)}$	0.424	0.064
$H_2^{\Lambda^*(1405)}$	0.809	0.134	$H_1^{\Lambda^*(1520)}$	0.321	0.062
$H_2^{\Lambda^*(1520)}$	0.748	0.075	$H_1^{\Lambda^*(1600)}$	0.153	0.03
$H_2^{\Lambda^*(1600)}$	0.223	0.034	$H_1^{\Lambda^*(1670)}$	0.392	0.033
$H_2^{\Lambda^*(1670)}$	0.161	0.06	$H_1^{\Lambda^*(2000)}$	0.707	0.058
$H_2^{\Lambda^*(2000)}$	0.675	0.091	$\phi_1^{\Delta^{++}(1232)}$	-0.67	0.193
$\phi_2^{\Delta^{++}(1232)}$	1.875	0.186	$\phi_1^{\Delta^{++}(1600)}$	2.404	0.207
$\phi_2^{\Delta^{++}(1600)}$	4.862	0.187	$\phi_1^{\Delta^{++}(1620)}$	-3.338	0.153
$\phi_2^{\Delta^{++}(1620)}$	-1.292	0.173	$\phi_1^{\Delta^{++}(1700)}$	5.329	0.279
$\phi_2^{\Delta^{++}(1700)}$	-2.056	0.126	$\phi_1^{K^*(1410)}$	-1.58	0.155
$\phi_2^{K^*(1410)}$	0.94	0.134	$\phi_3^{K^*(1410)}$	3.891	0.252
$\phi_4^{K^*(1410)}$	1.082	10.145	$\phi_1^{K^*(1430)}$	6.285	0.228
$\phi_2^{K^*(1430)}$	1.877	0.238	$\phi_2^{K^*(890)}$	-1.798	0.262
$\phi_3^{K^*(890)}$	-1.741	0.213	$\phi_4^{K^*(890)}$	3.965	0.06
$\phi_1^{\Lambda^*(1405)}$	0.418	0.137	$\phi_2^{\Lambda^*(1405)}$	1.592	0.123
$\phi_1^{\Lambda^*(1520)}$	-0.46	0.215	$\phi_2^{\Lambda^*(1520)}$	2.479	0.113
$\phi_1^{\Lambda^*(1600)}$	2.839	0.207	$\phi_2^{\Lambda^*(1600)}$	-0.149	0.122
$\phi_1^{\Lambda^*(1670)}$	-4.556	0.189	$\phi_2^{\Lambda^*(1670)}$	-2.22	0.317
$\phi_1^{\Lambda^*(2000)}$	0.917	0.157	$\phi_2^{\Lambda^*(2000)}$	1.173	0.182
P_x	0.019	0.011	P_y	-0.04	0.011
P_z	-0.023	0.011			

Table G.40: Result of the fit for model M10, polarity, TOS category and Λ_c^+ decays.

FF parameter	Central value	Statistical uncertainty
$\Delta^{++}(1232)$	0.15770	0.00096
$\Delta^{++}(1600)$	0.10831	0.00025
$\Delta^{++}(1620)$	0.13755	0.00636
$\Delta^{++}(1700)$	0.06809	0.00058
$K^*(1410)$	0.03175	0.00026
$K^*(1430)$	0.00289	0.00003
$K^*(890)$	0.17198	0.00109
$\Lambda^*(1405)$	0.12655	0.00104
$\Lambda^*(1520)$	0.05082	0.00019
$\Lambda^*(1600)$	0.01144	0.00023
$\Lambda^*(1670)$	0.02874	0.00415
$\Lambda^*(2000)$	0.15512	0.00240
$\sum F_{r_i}$	1.05095	0.01754

Table G.41: Result of the fit for model M10, MagUp polarity, TOS category and Λ_c^+ decays.

Parameter	α	α statistical uncertainty
$\Delta^{++}(1232)$	-0.0633	0.1779
$\Delta^{++}(1600)$	-0.2195	0.1605
$\Delta^{++}(1620)$	-0.2221	0.1798
$\Delta^{++}(1700)$	-0.8092	0.0948
$K^*(1410)$	-0.2993	0.1915
$K^*(1430)$	-0.1908	0.2785
$K^*(890)$	-0.0409	0.2931
$\Lambda^*(1405)$	-0.5690	0.1515
$\Lambda^*(1520)$	-0.6890	0.1143
$\Lambda^*(1600)$	-0.3599	0.2162
$\Lambda^*(1670)$	0.7113	0.1887
$\Lambda^*(2000)$	0.0463	0.1575
$\alpha_{effective}$	0.7130	0.0088

Table G.42: Result of the fit for model M10, α parameters for MagUp polarity, TOS category and Λ_c^+ decays.

Parameter	Central value	Statistical uncertainty	Parameter	Central value	Statistical uncertainty
$H_1^{\Delta^{++}(1232)}$	0.87	0.043	$H_2^{\Delta^{++}(1232)}$	1.126	0.072
$H_1^{\Delta^{++}(1600)}$	0.958	0.044	$H_2^{\Delta^{++}(1600)}$	0.951	0.081
$H_1^{\Delta^{++}(1620)}$	0.558	0.021	$H_2^{\Delta^{++}(1620)}$	0.638	0.036
$H_1^{\Delta^{++}(1700)}$	0.288	0.027	$H_2^{\Delta^{++}(1700)}$	0.859	0.048
$H_1^{K^*(1410)}$	0.353	0.051	$H_2^{K^*(1410)}$	0.322	0.065
$H_3^{K^*(1410)}$	0.373	0.048	$H_4^{K^*(1410)}$	0.159	0.051
$H_1^{K^*(1430)}$	0.051	0.011	$H_2^{K^*(1430)}$	0.073	0.011
$H_2^{K^*(890)}$	0.541	0.041	$H_3^{K^*(890)}$	0.694	0.041
$H_4^{K^*(890)}$	0.96	0.073	$H_1^{\Lambda^*(1405)}$	0.432	0.03
$H_2^{\Lambda^*(1405)}$	0.681	0.044	$H_1^{\Lambda^*(1520)}$	0.528	0.033
$H_2^{\Lambda^*(1520)}$	0.416	0.03	$H_1^{\Lambda^*(1600)}$	0.154	0.023
$H_2^{\Lambda^*(1600)}$	0.142	0.022	$H_1^{\Lambda^*(1670)}$	0.298	0.019
$H_2^{\Lambda^*(1670)}$	0.346	0.029	$H_1^{\Lambda^*(2000)}$	0.592	0.023
$H_2^{\Lambda^*(2000)}$	0.634	0.033	$\phi_1^{\Delta^{++}(1232)}$	-1.283	0.136
$\phi_2^{\Delta^{++}(1232)}$	1.683	0.099	$\phi_1^{\Delta^{++}(1600)}$	2.227	0.102
$\phi_2^{\Delta^{++}(1600)}$	5.058	0.099	$\phi_1^{\Delta^{++}(1620)}$	-3.741	0.106
$\phi_2^{\Delta^{++}(1620)}$	-0.937	0.101	$\phi_1^{\Delta^{++}(1700)}$	4.673	0.208
$\phi_2^{\Delta^{++}(1700)}$	-1.739	0.088	$\phi_1^{K^*(1410)}$	-1.237	0.116
$\phi_2^{K^*(1410)}$	1.158	0.152	$\phi_3^{K^*(1410)}$	4.444	0.156
$\phi_4^{K^*(1410)}$	2.848	0.29	$\phi_1^{K^*(1430)}$	1.499	0.225
$\phi_2^{K^*(1430)}$	1.532	0.173	$\phi_2^{K^*(890)}$	-1.56	0.158
$\phi_3^{K^*(890)}$	-1.954	0.14	$\phi_4^{K^*(890)}$	3.697	0.072
$\phi_1^{\Lambda^*(1405)}$	0.707	0.109	$\phi_2^{\Lambda^*(1405)}$	1.473	0.102
$\phi_1^{\Lambda^*(1520)}$	-0.322	0.097	$\phi_2^{\Lambda^*(1520)}$	2.656	0.13
$\phi_1^{\Lambda^*(1600)}$	3.071	0.139	$\phi_2^{\Lambda^*(1600)}$	0.121	0.152
$\phi_1^{\Lambda^*(1670)}$	2.683	0.124	$\phi_2^{\Lambda^*(1670)}$	3.554	0.109
$\phi_1^{\Lambda^*(2000)}$	1.397	0.12	$\phi_2^{\Lambda^*(2000)}$	1.593	0.126
P_x	0.095	0.011	P_y	-0.015	0.01
P_z	0.043	0.01			

Table G.43: Result of the fit for model M10, polarity, TOS category and $\overline{\Lambda}_c^-$ decays.

FF parameter	Central value	Statistical uncertainty
$\Delta^{++}(1232)$	0.18745	0.00029
$\Delta^{++}(1600)$	0.16517	0.00038
$\Delta^{++}(1620)$	0.12903	0.00578
$\Delta^{++}(1700)$	0.07411	0.00054
$K^*(1410)$	0.02347	0.00015
$K^*(1430)$	0.00284	0.00003
$K^*(890)$	0.16917	0.00050
$\Lambda^*(1405)$	0.11471	0.00099
$\Lambda^*(1520)$	0.04026	0.00066
$\Lambda^*(1600)$	0.00792	0.00009
$\Lambda^*(1670)$	0.03880	0.00510
$\Lambda^*(2000)$	0.14203	0.00152
$\sum F_{r_i}$	1.09496	0.01603

Table G.44: Result of the fit for model M10, MagUp polarity, TOS category and $\overline{\Lambda}_c^-$ decays.

Parameter	α	α statistical uncertainty
$\Delta^{++}(1232)$	-0.2524	0.0757
$\Delta^{++}(1600)$	0.0073	0.0968
$\Delta^{++}(1620)$	-0.1332	0.0666
$\Delta^{++}(1700)$	-0.7979	0.0397
$K^*(1410)$	0.0917	0.2462
$K^*(1430)$	-0.3440	0.2320
$K^*(890)$	0.0992	0.1907
$\Lambda^*(1405)$	-0.4261	0.0776
$\Lambda^*(1520)$	0.2340	0.0902
$\Lambda^*(1600)$	0.0809	0.2138
$\Lambda^*(1670)$	-0.1482	0.1030
$\Lambda^*(2000)$	-0.0684	0.0646
$\alpha_{effective}$	0.7119	0.0040

Table G.45: Result of the fit for model M10, α parameters for MagUp polarity, TOS category and $\overline{\Lambda}_c^-$ decays.

G.3 Results for model 21

FF parameter	Central value	Statistical uncertainty
$\Delta^{++}(1232)$	0.10458	0.00010
$\Delta^{++}(1600)$	0.06091	0.00012
$\Delta^{++}(1620)$	0.09569	0.00013
$\Delta^{++}(1700)$	0.03993	0.00037
$K^*(1410)$	0.00771	0.00181
$K^*(1430)$	0.00192	0.00002
$K^*(890)$	0.19860	0.00362
$\Lambda^*(1405)$	0.17559	0.00087
$\Lambda^*(1520)$	0.04361	0.00037
$\Lambda^*(1600)$	0.06097	0.00045
$\Lambda^*(1670)$	0.03535	0.00258
$\Lambda^*(1690)$	0.01892	0.00029
$\Lambda^*(1890)$	0.00627	0.00003
$\Lambda^*(2000)$	0.23244	0.00026
$\sum F_{r_i}$	1.08250	0.01100

Table G.46: Result of the fit for model M21, MagDown polarity, TIS category and Λ_c^+ decays.

Parameter	α	α statistical uncertainty
$\Delta^{++}(1232)$	0.1525	0.0661
$\Delta^{++}(1600)$	0.1101	0.0812
$\Delta^{++}(1620)$	0.2101	0.0664
$\Delta^{++}(1700)$	-0.1956	0.0784
$K^*(1410)$	0.3764	0.4484
$K^*(1430)$	-0.1327	0.2251
$K^*(890)$	0.0077	0.2118
$\Lambda^*(1405)$	-0.0278	0.0564
$\Lambda^*(1520)$	-0.1938	0.1153
$\Lambda^*(1600)$	-0.2728	0.0813
$\Lambda^*(1670)$	-0.6144	0.0528
$\Lambda^*(1690)$	1.0000	0.0000
$\Lambda^*(1890)$	-0.7598	0.0920
$\Lambda^*(2000)$	-0.1797	0.0489
$\alpha_{effective}$	0.7441	0.0047

Table G.47: Result of the fit for model M21, α parameters for MagDown polarity, TIS category and Λ_c^+ decays.

Parameter	Central value	Statistical uncertainty	Parameter	Central value	Statistical uncertainty
$H_1^{\Delta^{++}(1232)}$	0.821	0.035	$H_2^{\Delta^{++}(1232)}$	0.704	0.037
$H_1^{\Delta^{++}(1600)}$	0.621	0.03	$H_2^{\Delta^{++}(1600)}$	0.556	0.037
$H_1^{\Delta^{++}(1620)}$	0.578	0.024	$H_2^{\Delta^{++}(1620)}$	0.467	0.026
$H_1^{\Delta^{++}(1700)}$	0.429	0.02	$H_2^{\Delta^{++}(1700)}$	0.523	0.035
$H_1^{K^*(1410)}$	0.104	0.041	$H_2^{K^*(1410)}$	0.07	0.024
$H_3^{K^*(1410)}$	0.0	0.002	$H_4^{K^*(1410)}$	0.343	0.034
$H_1^{K^*(1430)}$	0.049	0.008	$H_2^{K^*(1430)}$	0.056	0.009
$H_2^{K^*(890)}$	0.77	0.037	$H_3^{K^*(890)}$	0.809	0.035
$H_4^{K^*(890)}$	1.018	0.058	$H_1^{\Lambda^*(1405)}$	0.708	0.021
$H_2^{\Lambda^*(1405)}$	0.728	0.035	$H_1^{\Lambda^*(1520)}$	0.452	0.041
$H_2^{\Lambda^*(1520)}$	0.55	0.043	$H_1^{\Lambda^*(1600)}$	0.356	0.026
$H_2^{\Lambda^*(1600)}$	0.471	0.023	$H_1^{\Lambda^*(1670)}$	0.195	0.014
$H_2^{\Lambda^*(1670)}$	0.399	0.018	$H_1^{\Lambda^*(1690)}$	0.462	0.019
$H_2^{\Lambda^*(1690)}$	0.0	0.006	$H_1^{\Lambda^*(1890)}$	0.092	0.019
$H_2^{\Lambda^*(1890)}$	0.249	0.017	$H_1^{\Lambda^*(2000)}$	0.723	0.024
$H_2^{\Lambda^*(2000)}$	0.867	0.033	$\phi_1^{\Delta^{++}(1232)}$	3.357	0.097
$\phi_2^{\Delta^{++}(1232)}$	0.545	0.111	$\phi_1^{\Delta^{++}(1600)}$	-0.505	0.079
$\phi_2^{\Delta^{++}(1600)}$	-3.731	0.084	$\phi_1^{\Delta^{++}(1620)}$	0.093	0.06
$\phi_2^{\Delta^{++}(1620)}$	3.333	0.071	$\phi_1^{\Delta^{++}(1700)}$	-3.97	0.093
$\phi_2^{\Delta^{++}(1700)}$	2.535	0.064	$\phi_1^{K^*(1410)}$	1.025	0.307
$\phi_2^{K^*(1410)}$	1.155	0.424	$\phi_3^{K^*(1410)}$	5.459	10.573
$\phi_4^{K^*(1410)}$	1.812	0.085	$\phi_1^{K^*(1430)}$	-1.653	0.19
$\phi_2^{K^*(1430)}$	-1.936	0.161	$\phi_2^{K^*(890)}$	-2.494	0.094
$\phi_3^{K^*(890)}$	-2.566	0.082	$\phi_4^{K^*(890)}$	3.12	0.053
$\phi_1^{\Lambda^*(1405)}$	5.336	0.061	$\phi_2^{\Lambda^*(1405)}$	5.463	0.072
$\phi_1^{\Lambda^*(1520)}$	4.475	0.095	$\phi_2^{\Lambda^*(1520)}$	2.172	0.074
$\phi_1^{\Lambda^*(1600)}$	2.643	0.062	$\phi_2^{\Lambda^*(1600)}$	-0.465	0.056
$\phi_1^{\Lambda^*(1670)}$	3.25	0.121	$\phi_2^{\Lambda^*(1670)}$	3.494	0.081
$\phi_1^{\Lambda^*(1690)}$	6.5	0.012	$\phi_2^{\Lambda^*(1690)}$	6.166	10.261
$\phi_1^{\Lambda^*(1890)}$	4.562	0.173	$\phi_2^{\Lambda^*(1890)}$	-1.245	0.084
$\phi_1^{\Lambda^*(2000)}$	3.871	0.068	$\phi_2^{\Lambda^*(2000)}$	3.705	0.076
P_x	-0.007	0.008	P_y	0.085	0.008
P_z	0.014	0.007			

Table G.48: Result of the fit for model M21, polarity, TIS category and Λ_c^+ decays.

Parameter	Central value	Statistical uncertainty	Parameter	Central value	Statistical uncertainty
$H_1^{\Delta^{++}(1232)}$	0.658	0.059	$H_2^{\Delta^{++}(1232)}$	1.296	0.055
$H_1^{\Delta^{++}(1600)}$	0.765	0.041	$H_2^{\Delta^{++}(1600)}$	1.012	0.061
$H_1^{\Delta^{++}(1620)}$	0.548	0.024	$H_2^{\Delta^{++}(1620)}$	0.902	0.042
$H_1^{\Delta^{++}(1700)}$	0.522	0.027	$H_2^{\Delta^{++}(1700)}$	0.682	0.046
$H_1^{K^*(1410)}$	0.168	0.03	$H_2^{K^*(1410)}$	0.477	0.067
$H_3^{K^*(1410)}$	0.365	0.042	$H_4^{K^*(1410)}$	0.329	0.046
$H_1^{K^*(1430)}$	0.065	0.01	$H_2^{K^*(1430)}$	0.015	0.01
$H_2^{K^*(890)}$	0.999	0.047	$H_3^{K^*(890)}$	0.737	0.051
$H_4^{K^*(890)}$	1.304	0.075	$H_1^{\Lambda^*(1405)}$	0.748	0.036
$H_2^{\Lambda^*(1405)}$	0.647	0.036	$H_1^{\Lambda^*(1520)}$	0.562	0.034
$H_2^{\Lambda^*(1520)}$	0.548	0.04	$H_1^{\Lambda^*(1600)}$	0.317	0.032
$H_2^{\Lambda^*(1600)}$	0.311	0.039	$H_1^{\Lambda^*(1670)}$	0.437	0.02
$H_2^{\Lambda^*(1670)}$	0.276	0.021	$H_1^{\Lambda^*(1690)}$	0.0	0.024
$H_2^{\Lambda^*(1690)}$	0.416	0.038	$H_1^{\Lambda^*(1890)}$	0.059	0.024
$H_2^{\Lambda^*(1890)}$	0.128	0.023	$H_1^{\Lambda^*(2000)}$	0.997	0.044
$H_2^{\Lambda^*(2000)}$	0.749	0.038	$\phi_1^{\Delta^{++}(1232)}$	1.947	0.108
$\phi_2^{\Delta^{++}(1232)}$	-1.962	0.057	$\phi_1^{\Delta^{++}(1600)}$	-2.838	0.068
$\phi_2^{\Delta^{++}(1600)}$	-4.985	0.06	$\phi_1^{\Delta^{++}(1620)}$	-2.03	0.094
$\phi_2^{\Delta^{++}(1620)}$	1.483	0.059	$\phi_1^{\Delta^{++}(1700)}$	-5.883	0.084
$\phi_2^{\Delta^{++}(1700)}$	0.831	0.065	$\phi_1^{K^*(1410)}$	-0.791	0.211
$\phi_2^{K^*(1410)}$	4.52	0.093	$\phi_3^{K^*(1410)}$	6.343	0.091
$\phi_4^{K^*(1410)}$	1.353	0.108	$\phi_1^{K^*(1430)}$	3.398	0.152
$\phi_2^{K^*(1430)}$	-1.705	0.699	$\phi_2^{K^*(890)}$	-4.907	0.066
$\phi_3^{K^*(890)}$	-4.631	0.098	$\phi_4^{K^*(890)}$	2.626	0.044
$\phi_1^{\Lambda^*(1405)}$	6.5	0.011	$\phi_2^{\Lambda^*(1405)}$	6.457	0.063
$\phi_1^{\Lambda^*(1520)}$	6.47	0.068	$\phi_2^{\Lambda^*(1520)}$	2.303	0.07
$\phi_1^{\Lambda^*(1600)}$	3.56	0.079	$\phi_2^{\Lambda^*(1600)}$	0.984	0.075
$\phi_1^{\Lambda^*(1670)}$	5.025	0.054	$\phi_2^{\Lambda^*(1670)}$	4.84	0.089
$\phi_1^{\Lambda^*(1690)}$	6.498	12.528	$\phi_2^{\Lambda^*(1690)}$	-1.882	0.072
$\phi_1^{\Lambda^*(1890)}$	-0.4	0.269	$\phi_2^{\Lambda^*(1890)}$	-3.147	0.163
$\phi_1^{\Lambda^*(2000)}$	4.977	0.038	$\phi_2^{\Lambda^*(2000)}$	5.151	0.06
P_x	0.021	0.009	P_y	-0.001	0.007
P_z	-0.019	0.007			

Table G.49: Result of the fit for model M21, polarity, TIS category and $\overline{\Lambda}_c^-$ decays.

FF parameter	Central value	Statistical uncertainty
$\Delta^{++}(1232)$	0.14544	0.00491
$\Delta^{++}(1600)$	0.10843	0.00982
$\Delta^{++}(1620)$	0.14882	0.00596
$\Delta^{++}(1700)$	0.04952	0.00051
$K^*(1410)$	0.02214	0.00055
$K^*(1430)$	0.00118	0.00002
$K^*(890)$	0.19767	0.00471
$\Lambda^*(1405)$	0.12820	0.00019
$\Lambda^*(1520)$	0.04080	0.00043
$\Lambda^*(1600)$	0.02654	0.00742
$\Lambda^*(1670)$	0.03699	0.00009
$\Lambda^*(1690)$	0.01181	0.00007
$\Lambda^*(1890)$	0.00136	0.00001
$\Lambda^*(2000)$	0.21819	0.00103
$\sum F_{r_i}$	1.13707	0.03572

Table G.50: Result of the fit for model M21, MagDown polarity, TIS category and $\overline{\Lambda}_c^-$ decays.

Parameter	α	α statistical uncertainty
$\Delta^{++}(1232)$	-0.5901	0.0647
$\Delta^{++}(1600)$	-0.2727	0.0747
$\Delta^{++}(1620)$	-0.4608	0.0503
$\Delta^{++}(1700)$	-0.2612	0.0792
$K^*(1410)$	-0.7793	0.0892
$K^*(1430)$	0.8989	0.1314
$K^*(890)$	-0.2724	0.2579
$\Lambda^*(1405)$	0.1440	0.0720
$\Lambda^*(1520)$	0.0252	0.0947
$\Lambda^*(1600)$	0.0191	0.1609
$\Lambda^*(1670)$	0.4297	0.0724
$\Lambda^*(1690)$	-1.0000	0.0000
$\Lambda^*(1890)$	-0.6495	0.2571
$\Lambda^*(2000)$	0.2785	0.0620
$\alpha_{effective}$	0.7242	0.0041

Table G.51: Result of the fit for model M21, α parameters for MagDown polarity, TIS category and $\overline{\Lambda}_c^-$ decays.

Parameter	Central value	Statistical uncertainty	Parameter	Central value	Statistical uncertainty
$H_1^{\Delta^{++}(1232)}$	0.965	0.115	$H_2^{\Delta^{++}(1232)}$	1.521	0.156
$H_1^{\Delta^{++}(1600)}$	0.776	0.056	$H_2^{\Delta^{++}(1600)}$	1.514	0.163
$H_1^{\Delta^{++}(1620)}$	0.824	0.091	$H_2^{\Delta^{++}(1620)}$	1.152	0.127
$H_1^{\Delta^{++}(1700)}$	0.514	0.041	$H_2^{\Delta^{++}(1700)}$	1.1	0.143
$H_1^{K^*(1410)}$	0.892	0.144	$H_2^{K^*(1410)}$	0.306	0.067
$H_3^{K^*(1410)}$	0.219	0.056	$H_4^{K^*(1410)}$	0.651	0.139
$H_1^{K^*(1430)}$	0.033	0.014	$H_2^{K^*(1430)}$	0.047	0.015
$H_2^{K^*(890)}$	1.295	0.145	$H_3^{K^*(890)}$	0.986	0.138
$H_4^{K^*(890)}$	1.911	0.257	$H_1^{\Lambda^*(1405)}$	0.917	0.103
$H_2^{\Lambda^*(1405)}$	1.167	0.146	$H_1^{\Lambda^*(1520)}$	0.404	0.05
$H_2^{\Lambda^*(1520)}$	0.7	0.088	$H_1^{\Lambda^*(1600)}$	0.151	0.035
$H_2^{\Lambda^*(1600)}$	0.314	0.083	$H_1^{\Lambda^*(1670)}$	0.737	0.083
$H_2^{\Lambda^*(1670)}$	0.484	0.061	$H_1^{\Lambda^*(1690)}$	0.129	0.039
$H_2^{\Lambda^*(1690)}$	0.106	0.038	$H_1^{\Lambda^*(1890)}$	0.107	0.033
$H_2^{\Lambda^*(1890)}$	0.159	0.033	$H_1^{\Lambda^*(2000)}$	1.266	0.14
$H_2^{\Lambda^*(2000)}$	1.216	0.158	$\phi_1^{\Delta^{++}(1232)}$	1.305	0.089
$\phi_2^{\Delta^{++}(1232)}$	-2.166	0.066	$\phi_1^{\Delta^{++}(1600)}$	-2.383	0.101
$\phi_2^{\Delta^{++}(1600)}$	-5.495	0.056	$\phi_1^{\Delta^{++}(1620)}$	-1.872	0.064
$\phi_2^{\Delta^{++}(1620)}$	1.01	0.046	$\phi_1^{\Delta^{++}(1700)}$	-6.5	0.016
$\phi_2^{\Delta^{++}(1700)}$	0.524	0.052	$\phi_1^{K^*(1410)}$	-0.226	0.083
$\phi_2^{K^*(1410)}$	-0.623	0.179	$\phi_3^{K^*(1410)}$	6.5	0.042
$\phi_4^{K^*(1410)}$	2.877	0.134	$\phi_1^{K^*(1430)}$	-0.78	0.389
$\phi_2^{K^*(1430)}$	-4.424	0.276	$\phi_2^{K^*(890)}$	-4.781	0.081
$\phi_3^{K^*(890)}$	-4.566	0.107	$\phi_4^{K^*(890)}$	2.38	0.059
$\phi_1^{\Lambda^*(1405)}$	6.5	0.006	$\phi_2^{\Lambda^*(1405)}$	6.5	0.012
$\phi_1^{\Lambda^*(1520)}$	6.429	0.116	$\phi_2^{\Lambda^*(1520)}$	2.318	0.064
$\phi_1^{\Lambda^*(1600)}$	2.336	0.282	$\phi_2^{\Lambda^*(1600)}$	-2.395	0.14
$\phi_1^{\Lambda^*(1670)}$	4.909	0.053	$\phi_2^{\Lambda^*(1670)}$	4.677	0.069
$\phi_1^{\Lambda^*(1690)}$	3.332	0.198	$\phi_2^{\Lambda^*(1690)}$	-3.118	0.381
$\phi_1^{\Lambda^*(1890)}$	5.527	0.238	$\phi_2^{\Lambda^*(1890)}$	-3.617	0.21
$\phi_1^{\Lambda^*(2000)}$	5.109	0.031	$\phi_2^{\Lambda^*(2000)}$	5.229	0.035
P_x	0.003	0.009	P_y	-0.02	0.007
P_z	-0.005	0.008			

Table G.52: Result of the fit for model M21, polarity, TIS category and Λ_c^+ decays.

FF parameter	Central value	Statistical uncertainty
$\Delta^{++}(1232)$	0.12617	0.00265
$\Delta^{++}(1600)$	0.11012	0.01044
$\Delta^{++}(1620)$	0.15132	0.00438
$\Delta^{++}(1700)$	0.05591	0.00062
$K^*(1410)$	0.03415	0.00401
$K^*(1430)$	0.00050	0.00001
$K^*(890)$	0.19209	0.00072
$\Lambda^*(1405)$	0.16293	0.00113
$\Lambda^*(1520)$	0.02442	0.00022
$\Lambda^*(1600)$	0.00924	0.00074
$\Lambda^*(1670)$	0.06070	0.00505
$\Lambda^*(1690)$	0.00108	0.00007
$\Lambda^*(1890)$	0.00141	0.00032
$\Lambda^*(2000)$	0.24419	0.00020
$\sum F_{r_i}$	1.17424	0.03056

Table G.53: Result of the fit for model M21, MagUp polarity, TIS category and Λ_c^+ decays.

Parameter	α	α statistical uncertainty
$\Delta^{++}(1232)$	-0.4260	0.1287
$\Delta^{++}(1600)$	-0.5839	0.0854
$\Delta^{++}(1620)$	-0.3231	0.1398
$\Delta^{++}(1700)$	-0.6416	0.0897
$K^*(1410)$	0.7894	0.1025
$K^*(1430)$	-0.3396	0.4697
$K^*(890)$	-0.4598	0.4218
$\Lambda^*(1405)$	-0.2365	0.1587
$\Lambda^*(1520)$	-0.5003	0.1323
$\Lambda^*(1600)$	-0.6244	0.2145
$\Lambda^*(1670)$	0.3974	0.1423
$\Lambda^*(1690)$	0.1939	0.4513
$\Lambda^*(1890)$	-0.3766	0.3190
$\Lambda^*(2000)$	0.0403	0.1703
$\alpha_{effective}$	0.7117	0.0032

Table G.54: Result of the fit for model M21, α parameters for MagUp polarity, TIS category and Λ_c^+ decays.

Parameter	Central value	Statistical uncertainty	Parameter	Central value	Statistical uncertainty
$H_1^{\Delta^{++}(1232)}$	1.558	0.066	$H_2^{\Delta^{++}(1232)}$	1.152	0.059
$H_1^{\Delta^{++}(1600)}$	0.915	0.054	$H_2^{\Delta^{++}(1600)}$	1.158	0.072
$H_1^{\Delta^{++}(1620)}$	0.878	0.036	$H_2^{\Delta^{++}(1620)}$	0.897	0.039
$H_1^{\Delta^{++}(1700)}$	0.485	0.029	$H_2^{\Delta^{++}(1700)}$	0.928	0.052
$H_1^{K^*(1410)}$	0.119	0.05	$H_2^{K^*(1410)}$	0.086	0.041
$H_3^{K^*(1410)}$	0.0	0.009	$H_4^{K^*(1410)}$	0.374	0.046
$H_1^{K^*(1430)}$	0.0	0.005	$H_2^{K^*(1430)}$	0.112	0.012
$H_2^{K^*(890)}$	0.654	0.049	$H_3^{K^*(890)}$	1.126	0.046
$H_4^{K^*(890)}$	1.907	0.077	$H_1^{\Lambda^*(1405)}$	0.748	0.03
$H_2^{\Lambda^*(1405)}$	0.949	0.045	$H_1^{\Lambda^*(1520)}$	0.575	0.044
$H_2^{\Lambda^*(1520)}$	0.633	0.046	$H_1^{\Lambda^*(1600)}$	0.314	0.041
$H_2^{\Lambda^*(1600)}$	0.462	0.039	$H_1^{\Lambda^*(1670)}$	0.311	0.029
$H_2^{\Lambda^*(1670)}$	0.672	0.032	$H_1^{\Lambda^*(1690)}$	0.39	0.041
$H_2^{\Lambda^*(1690)}$	0.136	0.031	$H_1^{\Lambda^*(1890)}$	0.088	0.035
$H_2^{\Lambda^*(1890)}$	0.163	0.038	$H_1^{\Lambda^*(2000)}$	0.912	0.037
$H_2^{\Lambda^*(2000)}$	1.18	0.043	$\phi_1^{\Delta^{++}(1232)}$	3.345	0.099
$\phi_2^{\Delta^{++}(1232)}$	0.368	0.144	$\phi_1^{\Delta^{++}(1600)}$	0.187	0.091
$\phi_2^{\Delta^{++}(1600)}$	-3.658	0.073	$\phi_1^{\Delta^{++}(1620)}$	0.243	0.091
$\phi_2^{\Delta^{++}(1620)}$	3.145	0.085	$\phi_1^{\Delta^{++}(1700)}$	-3.231	0.123
$\phi_2^{\Delta^{++}(1700)}$	2.599	0.079	$\phi_1^{K^*(1410)}$	3.087	0.426
$\phi_2^{K^*(1410)}$	-0.076	0.425	$\phi_3^{K^*(1410)}$	6.082	10.184
$\phi_4^{K^*(1410)}$	2.589	0.133	$\phi_1^{K^*(1430)}$	-3.952	10.706
$\phi_2^{K^*(1430)}$	-1.637	0.131	$\phi_2^{K^*(890)}$	-2.036	0.132
$\phi_3^{K^*(890)}$	-2.269	0.075	$\phi_4^{K^*(890)}$	3.405	0.059
$\phi_1^{\Lambda^*(1405)}$	6.142	0.051	$\phi_2^{\Lambda^*(1405)}$	6.5	0.023
$\phi_1^{\Lambda^*(1520)}$	4.805	0.081	$\phi_2^{\Lambda^*(1520)}$	2.691	0.077
$\phi_1^{\Lambda^*(1600)}$	2.877	0.154	$\phi_2^{\Lambda^*(1600)}$	-0.311	0.113
$\phi_1^{\Lambda^*(1670)}$	4.676	0.106	$\phi_2^{\Lambda^*(1670)}$	4.661	0.045
$\phi_1^{\Lambda^*(1690)}$	6.5	0.059	$\phi_2^{\Lambda^*(1690)}$	4.749	0.184
$\phi_1^{\Lambda^*(1890)}$	2.885	0.36	$\phi_2^{\Lambda^*(1890)}$	-0.354	0.127
$\phi_1^{\Lambda^*(2000)}$	4.875	0.065	$\phi_2^{\Lambda^*(2000)}$	4.739	0.046
P_x	-0.022	0.008	P_y	0.046	0.008
P_z	0.008	0.009			

Table G.55: Result of the fit for model M21, polarity, TIS category and $\overline{\Lambda}_c^-$ decays.

FF parameter	Central value	Statistical uncertainty
$\Delta^{++}(1232)$	0.16662	0.00060
$\Delta^{++}(1600)$	0.09465	0.00013
$\Delta^{++}(1620)$	0.13570	0.00016
$\Delta^{++}(1700)$	0.04749	0.00024
$K^*(1410)$	0.00463	0.00028
$K^*(1430)$	0.00216	0.00001
$K^*(890)$	0.19038	0.00281
$\Lambda^*(1405)$	0.12328	0.00070
$\Lambda^*(1520)$	0.03119	0.00061
$\Lambda^*(1600)$	0.02710	0.00014
$\Lambda^*(1670)$	0.04881	0.00436
$\Lambda^*(1690)$	0.00750	0.00018
$\Lambda^*(1890)$	0.00152	0.00001
$\Lambda^*(2000)$	0.20113	0.00024
$\sum F_{r_i}$	1.08216	0.01047

Table G.56: Result of the fit for model M21, MagUp polarity, TIS category and $\overline{\Lambda}_c^-$ decays.

Parameter	α	α statistical uncertainty
$\Delta^{++}(1232)$	0.2931	0.0608
$\Delta^{++}(1600)$	-0.2313	0.0811
$\Delta^{++}(1620)$	-0.0214	0.0597
$\Delta^{++}(1700)$	-0.5709	0.0552
$K^*(1410)$	0.3138	0.5729
$K^*(1430)$	-1.0000	0.0000
$K^*(890)$	-0.2837	0.3032
$\Lambda^*(1405)$	-0.2336	0.0587
$\Lambda^*(1520)$	-0.0958	0.1046
$\Lambda^*(1600)$	-0.3681	0.1344
$\Lambda^*(1670)$	-0.6472	0.0608
$\Lambda^*(1690)$	0.7832	0.0971
$\Lambda^*(1890)$	-0.5486	0.3223
$\Lambda^*(2000)$	-0.2521	0.0511
$\alpha_{effective}$	0.6972	0.0038

Table G.57: Result of the fit for model M21, α parameters for MagUp polarity, TIS category and $\overline{\Lambda}_c^-$ decays.

Parameter	Central value	Statistical uncertainty	Parameter	Central value	Statistical uncertainty
$H_1^{\Delta^{++}(1232)}$	1.028	0.041	$H_2^{\Delta^{++}(1232)}$	0.832	0.043
$H_1^{\Delta^{++}(1600)}$	0.742	0.047	$H_2^{\Delta^{++}(1600)}$	0.916	0.055
$H_1^{\Delta^{++}(1620)}$	0.572	0.03	$H_2^{\Delta^{++}(1620)}$	0.479	0.033
$H_1^{\Delta^{++}(1700)}$	0.603	0.029	$H_2^{\Delta^{++}(1700)}$	0.421	0.072
$H_1^{K^*(1410)}$	0.168	0.049	$H_2^{K^*(1410)}$	0.138	0.038
$H_3^{K^*(1410)}$	0.405	0.043	$H_4^{K^*(1410)}$	0.357	0.046
$H_1^{K^*(1430)}$	0.047	0.011	$H_2^{K^*(1430)}$	0.037	0.011
$H_2^{K^*(890)}$	0.46	0.039	$H_3^{K^*(890)}$	0.821	0.059
$H_4^{K^*(890)}$	0.939	0.083	$H_1^{\Lambda^*(1405)}$	0.795	0.094
$H_2^{\Lambda^*(1405)}$	0.798	0.059	$H_1^{\Lambda^*(1520)}$	0.235	0.099
$H_2^{\Lambda^*(1520)}$	0.656	0.038	$H_1^{\Lambda^*(1600)}$	0.28	0.05
$H_2^{\Lambda^*(1600)}$	0.349	0.046	$H_1^{\Lambda^*(1670)}$	0.212	0.027
$H_2^{\Lambda^*(1670)}$	0.363	0.023	$H_1^{\Lambda^*(1690)}$	0.391	0.042
$H_2^{\Lambda^*(1690)}$	0.161	0.05	$H_1^{\Lambda^*(1890)}$	0.147	0.021
$H_2^{\Lambda^*(1890)}$	0.195	0.025	$H_1^{\Lambda^*(2000)}$	0.825	0.037
$H_2^{\Lambda^*(2000)}$	0.74	0.04	$\phi_1^{\Delta^{++}(1232)}$	3.192	0.179
$\phi_2^{\Delta^{++}(1232)}$	-0.023	0.242	$\phi_1^{\Delta^{++}(1600)}$	0.528	0.2
$\phi_2^{\Delta^{++}(1600)}$	-2.595	0.151	$\phi_1^{\Delta^{++}(1620)}$	1.008	0.156
$\phi_2^{\Delta^{++}(1620)}$	4.196	0.198	$\phi_1^{\Delta^{++}(1700)}$	-3.439	0.135
$\phi_2^{\Delta^{++}(1700)}$	3.359	0.207	$\phi_1^{K^*(1410)}$	-1.202	0.291
$\phi_2^{K^*(1410)}$	2.14	0.464	$\phi_3^{K^*(1410)}$	-4.03	0.137
$\phi_4^{K^*(1410)}$	1.996	0.096	$\phi_1^{K^*(1430)}$	2.885	0.228
$\phi_2^{K^*(1430)}$	-4.562	0.283	$\phi_2^{K^*(890)}$	-3.476	0.386
$\phi_3^{K^*(890)}$	-3.234	0.203	$\phi_4^{K^*(890)}$	3.012	0.061
$\phi_1^{\Lambda^*(1405)}$	5.063	0.134	$\phi_2^{\Lambda^*(1405)}$	5.549	0.134
$\phi_1^{\Lambda^*(1520)}$	4.165	0.282	$\phi_2^{\Lambda^*(1520)}$	2.322	0.087
$\phi_1^{\Lambda^*(1600)}$	2.566	0.153	$\phi_2^{\Lambda^*(1600)}$	-0.389	0.108
$\phi_1^{\Lambda^*(1670)}$	3.053	0.294	$\phi_2^{\Lambda^*(1670)}$	3.3	0.122
$\phi_1^{\Lambda^*(1690)}$	6.5	0.018	$\phi_2^{\Lambda^*(1690)}$	4.303	0.244
$\phi_1^{\Lambda^*(1890)}$	5.036	0.235	$\phi_2^{\Lambda^*(1890)}$	-1.506	0.139
$\phi_1^{\Lambda^*(2000)}$	3.659	0.123	$\phi_2^{\Lambda^*(2000)}$	3.664	0.161
P_x	0.033	0.01	P_y	0.026	0.01
P_z	0.013	0.009			

Table G.58: Result of the fit for model M21, polarity, TOS category and Λ_c^+ decays.

FF parameter	Central value	Statistical uncertainty
$\Delta^{++}(1232)$	0.16995	0.00047
$\Delta^{++}(1600)$	0.13225	0.00043
$\Delta^{++}(1620)$	0.10502	0.00014
$\Delta^{++}(1700)$	0.05126	0.00077
$K^*(1410)$	0.02125	0.00019
$K^*(1430)$	0.00136	0.00002
$K^*(890)$	0.18202	0.00126
$\Lambda^*(1405)$	0.23454	0.00148
$\Lambda^*(1520)$	0.04535	0.00043
$\Lambda^*(1600)$	0.03807	0.01285
$\Lambda^*(1670)$	0.03443	0.00193
$\Lambda^*(1690)$	0.01720	0.00026
$\Lambda^*(1890)$	0.00576	0.00004
$\Lambda^*(2000)$	0.24327	0.00030
$\sum F_{r_i}$	1.28172	0.02059

Table G.59: Result of the fit for model M21, MagDown polarity, TOS category and Λ_c^+ decays.

Parameter	α	α statistical uncertainty
$\Delta^{++}(1232)$	0.2084	0.0624
$\Delta^{++}(1600)$	-0.2076	0.0835
$\Delta^{++}(1620)$	0.1756	0.0839
$\Delta^{++}(1700)$	0.3446	0.1566
$K^*(1410)$	0.1942	0.3860
$K^*(1430)$	0.2348	0.3575
$K^*(890)$	0.2098	0.2038
$\Lambda^*(1405)$	-0.0038	0.1394
$\Lambda^*(1520)$	-0.7725	0.1715
$\Lambda^*(1600)$	-0.2168	0.2115
$\Lambda^*(1670)$	-0.4913	0.1079
$\Lambda^*(1690)$	0.7101	0.1629
$\Lambda^*(1890)$	-0.2753	0.1774
$\Lambda^*(2000)$	0.1083	0.0694
$\alpha_{effective}$	0.7389	0.0067

Table G.60: Result of the fit for model M21, α parameters for MagDown polarity, TOS category and Λ_c^+ decays.

Parameter	Central value	Statistical uncertainty	Parameter	Central value	Statistical uncertainty
$H_1^{\Delta^{++}(1232)}$	1.071	0.057	$H_2^{\Delta^{++}(1232)}$	0.654	0.055
$H_1^{\Delta^{++}(1600)}$	0.45	0.035	$H_2^{\Delta^{++}(1600)}$	0.834	0.06
$H_1^{\Delta^{++}(1620)}$	0.599	0.038	$H_2^{\Delta^{++}(1620)}$	0.666	0.044
$H_1^{\Delta^{++}(1700)}$	0.315	0.034	$H_2^{\Delta^{++}(1700)}$	0.564	0.046
$H_1^{K^*(1410)}$	0.0	0.018	$H_2^{K^*(1410)}$	0.0	0.007
$H_3^{K^*(1410)}$	0.229	0.057	$H_4^{K^*(1410)}$	0.219	0.041
$H_1^{K^*(1430)}$	0.068	0.012	$H_2^{K^*(1430)}$	0.032	0.011
$H_2^{K^*(890)}$	0.531	0.048	$H_3^{K^*(890)}$	0.932	0.05
$H_4^{K^*(890)}$	1.242	0.092	$H_1^{\Lambda^*(1405)}$	0.577	0.039
$H_2^{\Lambda^*(1405)}$	0.894	0.056	$H_1^{\Lambda^*(1520)}$	0.282	0.052
$H_2^{\Lambda^*(1520)}$	0.754	0.048	$H_1^{\Lambda^*(1600)}$	0.382	0.033
$H_2^{\Lambda^*(1600)}$	0.422	0.034	$H_1^{\Lambda^*(1670)}$	0.203	0.027
$H_2^{\Lambda^*(1670)}$	0.47	0.028	$H_1^{\Lambda^*(1690)}$	0.318	0.033
$H_2^{\Lambda^*(1690)}$	0.148	0.038	$H_1^{\Lambda^*(1890)}$	0.02	0.025
$H_2^{\Lambda^*(1890)}$	0.235	0.025	$H_1^{\Lambda^*(2000)}$	0.707	0.036
$H_2^{\Lambda^*(2000)}$	0.876	0.051	$\phi_1^{\Delta^{++}(1232)}$	3.039	0.128
$\phi_2^{\Delta^{++}(1232)}$	0.075	0.216	$\phi_1^{\Delta^{++}(1600)}$	-0.751	0.199
$\phi_2^{\Delta^{++}(1600)}$	-4.101	0.11	$\phi_1^{\Delta^{++}(1620)}$	-0.269	0.142
$\phi_2^{\Delta^{++}(1620)}$	2.837	0.125	$\phi_1^{\Delta^{++}(1700)}$	-4.2	0.224
$\phi_2^{\Delta^{++}(1700)}$	2.163	0.118	$\phi_1^{K^*(1410)}$	0.199	9.816
$\phi_2^{K^*(1410)}$	2.268	10.518	$\phi_3^{K^*(1410)}$	6.5	0.029
$\phi_4^{K^*(1410)}$	1.79	0.18	$\phi_1^{K^*(1430)}$	3.488	0.169
$\phi_2^{K^*(1430)}$	-1.785	0.361	$\phi_2^{K^*(890)}$	-2.794	0.254
$\phi_3^{K^*(890)}$	-2.992	0.157	$\phi_4^{K^*(890)}$	3.075	0.066
$\phi_1^{\Lambda^*(1405)}$	5.756	0.138	$\phi_2^{\Lambda^*(1405)}$	5.824	0.106
$\phi_1^{\Lambda^*(1520)}$	5.134	0.309	$\phi_2^{\Lambda^*(1520)}$	1.904	0.102
$\phi_1^{\Lambda^*(1600)}$	2.993	0.119	$\phi_2^{\Lambda^*(1600)}$	-0.159	0.103
$\phi_1^{\Lambda^*(1670)}$	3.961	0.231	$\phi_2^{\Lambda^*(1670)}$	3.76	0.122
$\phi_1^{\Lambda^*(1690)}$	6.5	0.708	$\phi_2^{\Lambda^*(1690)}$	4.649	0.206
$\phi_1^{\Lambda^*(1890)}$	5.317	1.407	$\phi_2^{\Lambda^*(1890)}$	-1.302	0.11
$\phi_1^{\Lambda^*(2000)}$	4.224	0.131	$\phi_2^{\Lambda^*(2000)}$	4.09	0.115
P_x	-0.012	0.009	P_y	0.002	0.009
P_z	-0.023	0.01			

Table G.61: Result of the fit for model M21, polarity, TOS category and $\overline{\Lambda}_c^-$ decays.

FF parameter	Central value	Statistical uncertainty
$\Delta^{++}(1232)$	0.12289	0.00034
$\Delta^{++}(1600)$	0.06855	0.00013
$\Delta^{++}(1620)$	0.12132	0.00010
$\Delta^{++}(1700)$	0.03179	0.00028
$K^*(1410)$	0.00507	0.00094
$K^*(1430)$	0.00173	0.00008
$K^*(890)$	0.19518	0.00075
$\Lambda^*(1405)$	0.16813	0.00094
$\Lambda^*(1520)$	0.04866	0.00328
$\Lambda^*(1600)$	0.04955	0.00016
$\Lambda^*(1670)$	0.04111	0.00420
$\Lambda^*(1690)$	0.00953	0.00114
$\Lambda^*(1890)$	0.00433	0.00003
$\Lambda^*(2000)$	0.20152	0.00014
$\sum F_{r_i}$	1.06937	0.01250

Table G.62: Result of the fit for model M21, MagDown polarity, TOS category and $\overline{\Lambda}_c^-$ decays.

Parameter	α	α statistical uncertainty
$\Delta^{++}(1232)$	0.4568	0.0788
$\Delta^{++}(1600)$	-0.5490	0.0740
$\Delta^{++}(1620)$	-0.1056	0.0906
$\Delta^{++}(1700)$	-0.5245	0.0981
$K^*(1410)$	-999.0000	19.2939
$K^*(1430)$	0.6374	0.2294
$K^*(890)$	0.0119	0.2434
$\Lambda^*(1405)$	-0.4119	0.0765
$\Lambda^*(1520)$	-0.7546	0.0840
$\Lambda^*(1600)$	-0.0993	0.1170
$\Lambda^*(1670)$	-0.6856	0.0772
$\Lambda^*(1690)$	0.6439	0.1621
$\Lambda^*(1890)$	-0.9856	0.0358
$\Lambda^*(2000)$	-0.2111	0.0739
$\alpha_{effective}$	0.7392	0.0062

Table G.63: Result of the fit for model M21, α parameters for MagDown polarity, TOS category and $\overline{\Lambda}_c^-$ decays.

Parameter	Central value	Statistical uncertainty	Parameter	Central value	Statistical uncertainty
$H_1^{\Delta^{++}(1232)}$	0.685	0.044	$H_2^{\Delta^{++}(1232)}$	1.174	0.115
$H_1^{\Delta^{++}(1600)}$	0.499	0.047	$H_2^{\Delta^{++}(1600)}$	0.656	0.072
$H_1^{\Delta^{++}(1620)}$	0.531	0.055	$H_2^{\Delta^{++}(1620)}$	0.547	0.067
$H_1^{\Delta^{++}(1700)}$	0.288	0.031	$H_2^{\Delta^{++}(1700)}$	0.459	0.072
$H_1^{K^*(1410)}$	0.0	0.006	$H_2^{K^*(1410)}$	0.291	0.061
$H_3^{K^*(1410)}$	0.111	0.05	$H_4^{K^*(1410)}$	0.213	0.042
$H_1^{K^*(1430)}$	0.052	0.012	$H_2^{K^*(1430)}$	0.061	0.014
$H_2^{K^*(890)}$	0.487	0.053	$H_3^{K^*(890)}$	0.833	0.089
$H_4^{K^*(890)}$	1.009	0.176	$H_1^{\Lambda^*(1405)}$	0.703	0.044
$H_2^{\Lambda^*(1405)}$	0.627	0.09	$H_1^{\Lambda^*(1520)}$	0.645	0.072
$H_2^{\Lambda^*(1520)}$	0.485	0.068	$H_1^{\Lambda^*(1600)}$	0.378	0.038
$H_2^{\Lambda^*(1600)}$	0.591	0.053	$H_1^{\Lambda^*(1670)}$	0.206	0.032
$H_2^{\Lambda^*(1670)}$	0.461	0.053	$H_1^{\Lambda^*(1690)}$	0.408	0.036
$H_2^{\Lambda^*(1690)}$	0.21	0.039	$H_1^{\Lambda^*(1890)}$	0.237	0.029
$H_2^{\Lambda^*(1890)}$	0.13	0.036	$H_1^{\Lambda^*(2000)}$	0.69	0.048
$H_2^{\Lambda^*(2000)}$	0.939	0.09	$\phi_1^{\Delta^{++}(1232)}$	5.782	0.253
$\phi_2^{\Delta^{++}(1232)}$	2.352	0.151	$\phi_1^{\Delta^{++}(1600)}$	0.113	0.212
$\phi_2^{\Delta^{++}(1600)}$	-3.327	0.148	$\phi_1^{\Delta^{++}(1620)}$	0.852	0.174
$\phi_2^{\Delta^{++}(1620)}$	4.062	0.153	$\phi_1^{\Delta^{++}(1700)}$	-2.517	0.254
$\phi_2^{\Delta^{++}(1700)}$	3.655	0.141	$\phi_1^{K^*(1410)}$	-0.094	9.671
$\phi_2^{K^*(1410)}$	-0.202	0.187	$\phi_3^{K^*(1410)}$	5.685	0.414
$\phi_4^{K^*(1410)}$	3.996	0.465	$\phi_1^{K^*(1430)}$	4.771	0.22
$\phi_2^{K^*(1430)}$	1.083	0.24	$\phi_2^{K^*(890)}$	-1.895	0.206
$\phi_3^{K^*(890)}$	-2.233	0.14	$\phi_4^{K^*(890)}$	3.69	0.112
$\phi_1^{\Lambda^*(1405)}$	5.216	0.104	$\phi_2^{\Lambda^*(1405)}$	5.457	0.128
$\phi_1^{\Lambda^*(1520)}$	4.572	0.147	$\phi_2^{\Lambda^*(1520)}$	0.957	0.218
$\phi_1^{\Lambda^*(1600)}$	2.28	0.154	$\phi_2^{\Lambda^*(1600)}$	-0.793	0.091
$\phi_1^{\Lambda^*(1670)}$	2.693	0.204	$\phi_2^{\Lambda^*(1670)}$	3.647	0.148
$\phi_1^{\Lambda^*(1690)}$	6.426	0.124	$\phi_2^{\Lambda^*(1690)}$	2.654	0.207
$\phi_1^{\Lambda^*(1890)}$	4.23	0.117	$\phi_2^{\Lambda^*(1890)}$	-1.255	0.206
$\phi_1^{\Lambda^*(2000)}$	3.571	0.131	$\phi_2^{\Lambda^*(2000)}$	3.682	0.107
P_x	0.078	0.011	P_y	-0.041	0.01
P_z	0.022	0.01			

Table G.64: Result of the fit for model M21, polarity, TOS category and Λ_c^+ decays.

FF parameter	Central value	Statistical uncertainty
$\Delta^{++}(1232)$	0.15032	0.00016
$\Delta^{++}(1600)$	0.05407	0.00017
$\Delta^{++}(1620)$	0.09170	0.01052
$\Delta^{++}(1700)$	0.02331	0.00037
$K^*(1410)$	0.00750	0.00000
$K^*(1430)$	0.00203	0.00003
$K^*(890)$	0.16259	0.00041
$\Lambda^*(1405)$	0.13760	0.00075
$\Lambda^*(1520)$	0.05094	0.00186
$\Lambda^*(1600)$	0.07836	0.00168
$\Lambda^*(1670)$	0.04171	0.00370
$\Lambda^*(1690)$	0.01702	0.00031
$\Lambda^*(1890)$	0.00593	0.00005
$\Lambda^*(2000)$	0.22531	0.00011
$\sum F_{r_i}$	1.04840	0.02011

Table G.65: Result of the fit for model M21, MagUp polarity, TOS category and Λ_c^+ decays.

Parameter	α	α statistical uncertainty
$\Delta^{++}(1232)$	-0.4920	0.0888
$\Delta^{++}(1600)$	-0.2669	0.1343
$\Delta^{++}(1620)$	-0.0297	0.1603
$\Delta^{++}(1700)$	-0.4350	0.1542
$K^*(1410)$	-1.0000	0.0000
$K^*(1430)$	-0.1583	0.3173
$K^*(890)$	0.1487	0.2687
$\Lambda^*(1405)$	0.1139	0.1546
$\Lambda^*(1520)$	0.2776	0.1654
$\Lambda^*(1600)$	-0.4194	0.1110
$\Lambda^*(1670)$	-0.6671	0.1072
$\Lambda^*(1690)$	0.5811	0.1362
$\Lambda^*(1890)$	0.5374	0.2153
$\Lambda^*(2000)$	-0.2987	0.1079
$\alpha_{effective}$	0.7543	0.0147

Table G.66: Result of the fit for model M21, α parameters for MagUp polarity, TOS category and Λ_c^+ decays.

Parameter	Central value	Statistical uncertainty	Parameter	Central value	Statistical uncertainty
$H_1^{\Delta^{++}(1232)}$	1.27	0.006	$H_2^{\Delta^{++}(1232)}$	0.93	0.007
$H_1^{\Delta^{++}(1600)}$	0.624	0.006	$H_2^{\Delta^{++}(1600)}$	1.076	0.007
$H_1^{\Delta^{++}(1620)}$	0.724	0.004	$H_2^{\Delta^{++}(1620)}$	0.901	0.004
$H_1^{\Delta^{++}(1700)}$	0.517	0.007	$H_2^{\Delta^{++}(1700)}$	0.781	0.008
$H_1^{K^*(1410)}$	0.133	0.013	$H_2^{K^*(1410)}$	0.158	0.01
$H_3^{K^*(1410)}$	0.147	0.01	$H_4^{K^*(1410)}$	0.508	0.01
$H_1^{K^*(1430)}$	0.072	0.004	$H_2^{K^*(1430)}$	0.0	0.278
$H_2^{K^*(890)}$	0.965	0.008	$H_3^{K^*(890)}$	0.8	0.009
$H_4^{K^*(890)}$	1.748	0.005	$H_1^{\Lambda^*(1405)}$	0.909	0.006
$H_2^{\Lambda^*(1405)}$	1.012	0.004	$H_1^{\Lambda^*(1520)}$	0.321	0.014
$H_2^{\Lambda^*(1520)}$	0.906	0.007	$H_1^{\Lambda^*(1600)}$	0.422	0.006
$H_2^{\Lambda^*(1600)}$	0.402	0.005	$H_1^{\Lambda^*(1670)}$	0.588	0.004
$H_2^{\Lambda^*(1670)}$	0.412	0.005	$H_1^{\Lambda^*(1690)}$	0.2	0.007
$H_2^{\Lambda^*(1690)}$	0.448	0.007	$H_1^{\Lambda^*(1890)}$	0.181	0.006
$H_2^{\Lambda^*(1890)}$	0.095	0.006	$H_1^{\Lambda^*(2000)}$	1.149	0.004
$H_2^{\Lambda^*(2000)}$	0.964	0.004	$\phi_1^{\Delta^{++}(1232)}$	2.188	0.008
$\phi_2^{\Delta^{++}(1232)}$	-1.324	0.012	$\phi_1^{\Delta^{++}(1600)}$	-2.067	0.012
$\phi_2^{\Delta^{++}(1600)}$	-5.221	0.008	$\phi_1^{\Delta^{++}(1620)}$	-1.53	0.008
$\phi_2^{\Delta^{++}(1620)}$	1.577	0.007	$\phi_1^{\Delta^{++}(1700)}$	-5.381	0.013
$\phi_2^{\Delta^{++}(1700)}$	1.089	0.008	$\phi_1^{K^*(1410)}$	-0.12	0.065
$\phi_2^{K^*(1410)}$	-0.876	0.064	$\phi_3^{K^*(1410)}$	4.987	0.06
$\phi_4^{K^*(1410)}$	1.498	0.023	$\phi_1^{K^*(1430)}$	4.212	0.057
$\phi_2^{K^*(1430)}$	-6.481	10.151	$\phi_2^{K^*(890)}$	-4.357	0.012
$\phi_3^{K^*(890)}$	-3.923	0.015	$\phi_4^{K^*(890)}$	2.863	0.009
$\phi_1^{\Lambda^*(1405)}$	6.498	0.005	$\phi_2^{\Lambda^*(1405)}$	6.5	0.001
$\phi_1^{\Lambda^*(1520)}$	5.827	0.042	$\phi_2^{\Lambda^*(1520)}$	2.289	0.016
$\phi_1^{\Lambda^*(1600)}$	3.196	0.014	$\phi_2^{\Lambda^*(1600)}$	-0.019	0.014
$\phi_1^{\Lambda^*(1670)}$	4.741	0.011	$\phi_2^{\Lambda^*(1670)}$	4.591	0.015
$\phi_1^{\Lambda^*(1690)}$	6.315	0.031	$\phi_2^{\Lambda^*(1690)}$	-1.767	0.017
$\phi_1^{\Lambda^*(1890)}$	6.332	0.03	$\phi_2^{\Lambda^*(1890)}$	-1.409	0.069
$\phi_1^{\Lambda^*(2000)}$	4.891	0.006	$\phi_2^{\Lambda^*(2000)}$	4.991	0.007
P_x	-0.078	0.003	P_y	-0.002	0.003
P_z	-0.02	0.003			

Table G.67: Result of the fit for model M21, polarity, TOS category and $\overline{\Lambda}_c^-$ decays.

FF parameter	Central value	Statistical uncertainty
$\Delta^{++}(1232)$	0.12162	0.00087
$\Delta^{++}(1600)$	0.07433	0.00003
$\Delta^{++}(1620)$	0.12715	0.00004
$\Delta^{++}(1700)$	0.04200	0.00007
$K^*(1410)$	0.01020	0.00024
$K^*(1430)$	0.00098	0.00001
$K^*(890)$	0.18706	0.00171
$\Lambda^*(1405)$	0.17294	0.00007
$\Lambda^*(1520)$	0.04360	0.00056
$\Lambda^*(1600)$	0.03256	0.00044
$\Lambda^*(1670)$	0.05075	0.00110
$\Lambda^*(1690)$	0.01175	0.00010
$\Lambda^*(1890)$	0.00205	0.00000
$\Lambda^*(2000)$	0.22477	0.00020
$\sum F_{r_i}$	1.10177	0.00544

Table G.68: Result of the fit for model M21, MagUp polarity, TOS category and $\overline{\Lambda}_c^-$ decays.

Parameter	α	α statistical uncertainty
$\Delta^{++}(1232)$	0.3019	0.0081
$\Delta^{++}(1600)$	-0.4967	0.0087
$\Delta^{++}(1620)$	-0.2153	0.0068
$\Delta^{++}(1700)$	-0.3906	0.0144
$K^*(1410)$	-0.1706	0.1131
$K^*(1430)$	1.0000	0.0000
$K^*(890)$	-0.4171	0.2711
$\Lambda^*(1405)$	-0.1069	0.0076
$\Lambda^*(1520)$	-0.7769	0.0176
$\Lambda^*(1600)$	0.0485	0.0188
$\Lambda^*(1670)$	0.3414	0.0123
$\Lambda^*(1690)$	-0.6676	0.0212
$\Lambda^*(1890)$	0.5680	0.0483
$\Lambda^*(2000)$	0.1738	0.0053
$\alpha_{effective}$	0.7143	0.0006

Table G.69: Result of the fit for model M21, α parameters for MagUp polarity, TOS category and $\overline{\Lambda}_c^-$ decays.

Bibliography

[1] L Burmistrov, G Calderini, Yu Ivanov, L Massacrier, P Robbe, W Scandale, and A Stocchi. Measurement of short living baryon magnetic moment using bent crystals at SPS and LHC. Technical report, CERN, Geneva, Jun 2016. URL https://cds.cern.ch/record/2194564.

[2] A. S. Fomin, A. Yu. Korchin, A. Stocchi, O. A. Bezshyyko, L. Burmistrov, S. P. Fomin, I. V. Kirillin, L. Massacrier, A. Natochii, P. Robbe, and et al. Feasibility of measuring the magnetic dipole moments of the charm baryons at the LHC using bent crystals. *Journal of High Energy Physics*, 2017(8), Aug 2017. ISSN 1029-8479. doi: 10.1007/jhep08(2017)120. URL http://dx.doi.org/10.1007/JHEP08(2017)120.

[3] A. S. Fomin, S. Barsuk, A. Yu. Korchin, V. A. Kovalchuk, E. Kou, M. Liul, A. Natochii, E. Niel, P. Robbe, and A. Stocchi. The prospect of charm quark magnetic moment determination. *Eur. Phys. J. C*, 80(5):358, 2020. doi: 10.1140/epjc/s10052-020-7891-0. URL https://doi.org/10.1140/epjc/s10052-020-7891-0.

[4] F. J. et al. Botella. On the search for the electric dipole moment of strange and charm baryons at LHC. *The European Physical Journal C*, 77(3), Mar 2017. ISSN 1434-6052. doi: 10.1140/epjc/s10052-017-4679-y. URL http://dx.doi.org/10.1140/epjc/s10052-017-4679-y.

[5] E. et al. Bagli. Electromagnetic dipole moments of charged baryons with bent crystals at the LHC. *The European Physical Journal C*, 77(12), Dec 2017. ISSN 1434-6052. doi: 10.1140/epjc/s10052-017-5400-x. URL http://dx.doi.org/10.1140/epjc/s10052-017-5400-x.

[6] D. et al. Chen. First observation of magnetic moment precession of channeled particles in bent crystals. *Phys. Rev. Lett.*, 69:3286–3289, 1992. doi: 10.1103/PhysRevLett.69.3286. URL https://journals.aps.org/prl/abstract/10.1103/PhysRevLett.69.3286.

[7] A. A. Alves et al. The LHCb detector at the LHC. *JINST*, 3:S08005, 2008. doi: 10.1088/1748-0221/3/08/S08005. URL https://iopscience.iop.org/article/10.1088/1748-0221/3/08/S08005/meta.

[8] Jeffrey D. Richman. An Experimenter's Guide to the Helicity Formalism. 6 1984.

[9] G. Aad et al. Observation of a new particle in the search for the standard model higgs boson with the atlas detector at the lhc. *Physics Letters B*, 716(1):1–29, Sep 2012. ISSN 0370-2693. doi: 10.1016/j.physletb.2012.08.020. URL http://dx.doi.org/10.1016/j.physletb.2012.08.020.

[10] et al. S. Chatrchyan. Observation of a new boson at a mass of 125 GeV with the CMS experiment at the LHC. *Physics Letters B*, 716(1):30–61, Sep 2012. ISSN 0370-2693. doi: 10.1016/j.physletb.2012.08.021. URL http://dx.doi.org/10.1016/j.physletb.2012.08.021.

[11] P. A. Zyla et al. Review of particle physics. *Prog. Theor. Exp. Phys.*, 2020(8):083C01, 2020. doi: 10.1093/ptep/ptaa104.

[12] S.-K. et al. Choi. Observation of a narrow charmonium-like state in exclusive $B^{\pm} \to K^{\pm}\pi^{+}\pi^{-}J/\psi$ i decays. *Phys. Rev. Lett.*, 91:262001, Dec 2003. doi: 10.1103/PhysRevLett.91.262001. URL https://link.aps.org/doi/10.1103/PhysRevLett.91.262001.

[13] B. et al. Aubert. Study of the $B^{-} \to J/\psi\ iK^{-}\pi^{+}\pi^{-}$ decay and measurement of the $B^{-} \to x(3872)K^{-}$ branching fraction. *Phys. Rev. D*, 71:071103, Apr 2005. doi: 10.1103/PhysRevD.71.071103. URL https://link.aps.org/doi/10.1103/PhysRevD.71.071103.

[14] R. Aaij et al. Observation of $J/\psi p$ resonances consistent with pentaquark states in $\Lambda_b^0 \to J/\psi p K^{-}$ decays. *Phys. Rev. Lett.*, 115:072001, 2015. doi: 10.1103/PhysRevLett.115.072001. URL https://journals.aps.org/prl/abstract/10.1103/PhysRevLett.115.072001.

[15] R. Aaij et al. Search for beautiful tetraquarks in the $\Upsilon\mu^{+}\mu^{-}$ invariant-mass spectrum. 2018. submitted to JHEP.

[16] Raymond Davis, Don S. Harmer, and Kenneth C. Hoffman. Search for neutrinos from the sun. *Phys. Rev. Lett.*, 20:1205–1209, May 1968. doi: 10.1103/PhysRevLett.20.1205. URL https://link.aps.org/doi/10.1103/PhysRevLett.20.1205.

[17] Y. et al. Fukuda. Evidence for oscillation of atmospheric neutrinos. *Phys. Rev. Lett.*, 81:1562–1567, Aug 1998. doi: 10.1103/PhysRevLett.81.1562. URL https://link.aps.org/doi/10.1103/PhysRevLett.81.1562.

[18] Y. et al. Abe. Indication of reactor $\overline{\nu}_e$ disappearance in the Double Chooz experiment. *Phys. Rev. Lett.*, 108:131801, Mar 2012. doi: 10.1103/PhysRevLett.108.131801. URL https://link.aps.org/doi/10.1103/PhysRevLett.108.131801.

[19] Michael E. Peskin and Daniel V. Schroeder. *An Introduction to quantum field theory*. Addison-Wesley, Reading, USA, 1995. ISBN 978-0-201-50397-5.

[20] David J Griffiths. *Introduction to elementary particles; 2nd rev. version*. Physics textbook. Wiley, New York, NY, 2008. URL https://cds.cern.ch/record/111880.

[21] A. D. Martin and T. D. Spearman. *Elementary particle theory*. North-Holland Publishing Company, 1970.

[22] C. S. Wu, E. Ambler, R. W. Hayward, D. D. Hoppes, and R. P. Hudson. Experimental test of parity conservation in beta decay. *Phys. Rev.*, 105:1413–1415, Feb 1957. doi: 10.1103/PhysRev.105.1413. URL https://link.aps.org/doi/10.1103/PhysRev.105.1413.

[23] Vardanet al. Khachatryan. Measurement and QCD analysis of double-differential inclusive jet cross sections in pp collisions at $\sqrt{s} = 8$ TeV and cross section ratios to 2.76 and 7 TeV. *Journal of High Energy Physics*, 2017, 03 2017. doi: 10.1007/JHEP03(2017)156. URL https://link.springer.com/article/10.1007/JHEP03(2017)156.

[24] M. Banner et al. Observation of single isolated electrons of high transverse momentum in events with missing transverse energy at the cern *pp* collider. *Physics Letters B*, 122(5):476–485, 1983. ISSN 0370-2693. doi: https://doi.org/10.1016/0370-2693(83)91605-2. URL https://www.sciencedirect.com/science/article/pii/0370269383916052.

[25] G. Arniso et al. Experimental observation of lepton pairs of invariant mass around 95 GeV/c^2 at the CERN SPS collider. *Physics Letters B*, 126(5):398–410, 1983. ISSN 0370-2693. doi: https://doi.org/10.1016/0370-2693(83)90188-0. URL https://www.sciencedirect.com/science/article/pii/0370269383901880.

[26] F. Englert and R. Brout. Broken symmetry and the mass of gauge vector mesons. *Phys. Rev. Lett.*, 13:321–323, Aug 1964. doi: 10.1103/PhysRevLett.13.321. URL https://link.aps.org/doi/10.1103/PhysRevLett.13.321.

[27] Peter W. Higgs. Broken symmetries and the masses of gauge bosons. *Phys. Rev. Lett.*, 13:508–509, Oct 1964. doi: 10.1103/PhysRevLett.13.508. URL https://link.aps.org/doi/10.1103/PhysRevLett.13.508.

[28] T. D. Lee and C. N. Yang. Parity nonconservation and a two-component theory of the neutrino. *Phys. Rev.*, 105:1671–1675, Mar 1957. doi: 10.1103/PhysRev.105.1671. URL https://link.aps.org/doi/10.1103/PhysRev.105.1671.

[29] C. S. Wu, E. Ambler, R. W. Hayward, D. D. Hoppes, and R. P. Hudson. Experimental test of parity conservation in beta decay. *Phys. Rev.*, 105:1413–1415, Feb 1957. doi: 10.1103/PhysRev.105.1413. URL https://link.aps.org/doi/10.1103/PhysRev.105.1413.

[30] J. H. Christenson, J. W. Cronin, V. L. Fitch, and R. Turlay. Evidence for the 2π decay of the k_2^0 meson. *Phys. Rev. Lett.*, 13:138–140, Jul 1964. doi: 10.1103/PhysRevLett.13.138. URL https://link.aps.org/doi/10.1103/PhysRevLett.13.138.

[31] Nicola Cabibbo. Unitary symmetry and leptonic decays. *Phys. Rev. Lett.*, 10:531–533, Jun 1963. doi: 10.1103/PhysRevLett.10.531. URL https://link.aps.org/doi/10.1103/PhysRevLett.10.531.

[32] S. L. Glashow, J. Iliopoulos, and L. Maiani. Weak interactions with lepton-hadron symmetry. *Phys. Rev. D*, 2:1285–1292, Oct 1970. doi: 10.1103/PhysRevD.2.1285. URL https://link.aps.org/doi/10.1103/PhysRevD.2.1285.

[33] J. E. et al. Augustin. Discovery of a narrow resonance in e^+e^- annihilation. *Phys. Rev. Lett.*, 33:1406–1408, Dec 1974. doi: 10.1103/PhysRevLett.33.1406. URL https://link.aps.org/doi/10.1103/PhysRevLett.33.1406.

[34] J. J. et al. Aubert. Experimental observation of a heavy particle J. *Phys. Rev. Lett.*, 33:1404–1406, Dec 1974. doi: 10.1103/PhysRevLett.33.1404. URL https://link.aps.org/doi/10.1103/PhysRevLett.33.1404.

[35] Makoto Kobayashi and Toshihide Maskawa. CP-Violation in the renormalizable theory of weak interaction. *Progress of Theoretical Physics*, 49(2):652–657, 02 1973. ISSN 0033-068X. doi: 10.1143/PTP.49.652. URL https://doi.org/10.1143/PTP.49.652.

[36] S. W. et al. Herb. Observation of a dimuon resonance at 9.5 GeV in 400-GeV proton-nucleus collisions. 39:252–255, Aug 1977. doi: 10.1103/PhysRevLett.39.252. URL https://link.aps.org/doi/10.1103/PhysRevLett.39.252.

[37] F. et al. Abe. Evidence for top quark production in p$\bar{p}$ collisions at $\sqrt{s}$ =1.8 TeV. *Phys. Rev. Lett.*, 73:225–231, Jul 1994. doi: 10.1103/PhysRevLett.73.225. URL https://link.aps.org/doi/10.1103/PhysRevLett.73.225.

[38] Lincoln Wolfenstein. Parametrization of the Kobayashi-Maskawa matrix. *Phys. Rev. Lett.*, 51:1945–1947, Nov 1983. doi: 10.1103/PhysRevLett.51.1945. URL https://link.aps.org/doi/10.1103/PhysRevLett.51.1945.

[39] CKMfitter Group (J. Charles et al.). Study of the $B^- \to J/\psi\ iK^-\pi^+\pi^-$ decay and measurement of the $B^- \to X(3872)K^-$ branching fraction. *Eur. Phys. J.*, C41:1–131, Apr 2005. URL http://ckmfitter.in2p3.fr.

[40] M. Bona et al. Constraints on new physics from the quark mixing unitarity triangle. *Phys. Rev. Lett.*, 97:151803, 2006. doi: 10.1103/PhysRevLett.97.151803.

[41] Y. et al. Ashie. Evidence for an oscillatory signature in atmospheric neutrino oscillations. *Phys. Rev. Lett.*, 93:101801, Sep 2004. doi: 10.1103/PhysRevLett.93.101801. URL https://link.aps.org/doi/10.1103/PhysRevLett.93.101801.

[42] Q. R. Ahmad et al. Measurement of the rate of $\nu_e + d \to p + p + e^-$ interactions produced by ^{8}B solar neutrinos at the Sudbury Neutrino Observatory. *Phys. Rev. Lett.*, 87:071301, 2001. doi: 10.1103/PhysRevLett.87.071301.

[43] J. M. et al. Pendlebury. Revised experimental upper limit on the electric dipole moment of the neutron. *Phys. Rev. D*, 92:092003, Nov 2015. doi: 10.1103/PhysRevD.92.092003. URL https://link.aps.org/doi/10.1103/PhysRevD.92.092003.

[44] R. Aaij et al. Measurement of the $B_s \to \mu^+\mu^-$ properties and search for the $b^0 \to \mu^+\mu^-$ and the $B_s \to \mu^+\mu^-\gamma$ decays. in preparation.

[45] Roel et al. Aaij. Test of lepton universality in beauty-quark decays. 3 2021.

[46] B. et al. Abi. Measurement of the positive muon anomalous magnetic moment to 0.46 ppm. *Phys. Rev. Lett.*, 126:141801, Apr 2021. doi: 10.1103/PhysRevLett.126.141801. URL https://link.aps.org/doi/10.1103/PhysRevLett.126.141801.

[47] M. Gell-Mann. A schematic model of baryons and mesons. *Physics Letters*, 8(3):214–215, 1964. ISSN 0031-9163. doi: https://doi.org/10.1016/S0031-9163(64)92001-3. URL https://www.sciencedirect.com/science/article/pii/S0031916364920013.

[48] G. Zweig. An SU(3) model for strong interaction symmetry and its breaking. 1 1964.

[49] Fogli Gianluigi Costa, Giovanni. *Symmetries and Group Theory in Particle Physics*. Springer-Verlag, Berlin Heidelberg, 2012. ISBN 978-3-642-15481-2.

[50] Ken J. Barnes. *Group Theory for the Standard Model of Particle Physics and Beyond.* CRC Press, 2010. ISBN 978-1-420-07874-9.

[51] Wikipedia. Baryon octect. https://commons.wikimedia.org/wiki/File:Baryon-octet.svg, .

[52] Wikipedia. Baryon decuplet. https://commons.wikimedia.org/wiki/File:Baryon-decuplet-small.svg, .

[53] J. G. Korner and H. W. Siebert. Charm baryons: theory and experiment. *Ann. Rev. Nucl. Part. Sci.*, 41:511–545, 1991. doi: 10.1146/annurev.ns.41.120191.002455. URL https://doi.org/10.1146/annurev.ns.41.120191.002455.

[54] Marco S Sozzi. *Discrete symmetries and CP violation: from experiment to theory.* Oxford graduate texts. Oxford Univ. Press, New York, NY, 2008. doi: 10.1093/acprof:oso/9780199296668.001.0001. URL https://cds.cern.ch/record/1087897.

[55] G. Bunce et al. Λ^0 hyperon polarization in inclusive production by 300-GeV protons on beryllium. *Phys. Rev. Lett.*, 36:1113–1116, 1976. doi: 10.1103/PhysRevLett.36.1113. URL https://link.aps.org/doi/10.1103/PhysRevLett.36.1113.

[56] Kenneth J. Heller et al. Polarization of Λ and anti-Λ produced by 400-GeV protons. *Phys. Rev. Lett.*, 41:607, 1978. doi: 10.1103/PhysRevLett.41.607. URL https://link.aps.org/doi/10.1103/PhysRevLett.41.607. [Erratum: Phys.Rev.Lett. 45, 1043 (1980)].

[57] B. S. et al. Yuldashev. Neutral-strange-particle production in p^{20}Ne and pN interactions at 300 GeV. *Phys. Rev. D*, 43:2792–2802, May 1991. doi: 10.1103/PhysRevD.43.2792. URL https://link.aps.org/doi/10.1103/PhysRevD.43.2792.

[58] B. et al. Lundberg. Polarization in inclusive Λ and $\overline{\Lambda}$ production at large p_T. *Phys. Rev. D*, 40:3557–3567, Dec 1989. doi: 10.1103/PhysRevD.40.3557. URL https://link.aps.org/doi/10.1103/PhysRevD.40.3557.

[59] E.J. Ramberg et al. Polarization of Λ and Λ produced by 800-GeV protons. *Physics Letters B*, 338(2):403–408, 1994. ISSN 0370-2693. doi: https://doi.org/10.1016/0370-2693(94)91397-8. URL https://www.sciencedirect.com/science/article/pii/0370269394913978.

[60] B. et al. Lundberg. Polarization in inclusive Λ and $\overline{\Lambda}$ production at large p_T. *Phys. Rev. D*, 40: 3557–3567, Dec 1989. doi: 10.1103/PhysRevD.40.3557. URL https://link.aps.org/doi/10.1103/PhysRevD.40.3557.

[61] K. B. et al. Luk. Polarization of ω^- hyperons produced in 800 GeV proton-beryllium collisions. *Phys. Rev. Lett.*, 70:900–903, Feb 1993. doi: 10.1103/PhysRevLett.70.900. URL https://link.aps.org/doi/10.1103/PhysRevLett.70.900.

[62] A. et al. Morelos. Polarization of σ^+ andσ^- hyperons produced by 800-GeV/c protons. *Phys. Rev. Lett.*, 71:2172–2175, Oct 1993. doi: 10.1103/PhysRevLett.71.2172. URL https://link.aps.org/doi/10.1103/PhysRevLett.71.2172.

[63] I. Abt and et al. Polarization of Λ and Λ^- in 920 GeV fixed-target proton-nucleus collisions. *Physics Letters B*, 638(5):415–421, 2006. ISSN 0370-2693. doi: https://doi.org/10.1016/j.physletb.2006.05.040. URL https://www.sciencedirect.com/science/article/pii/S0370269306006216.

[64] V. Fanti et al. A measurement of the transverse polarization of Λ-hyperons produced in inelastic pN-reactions at 450 GeV proton energy. *The European Physical Journal C - Particles and Fields*, 6(2):265–269, 1999. doi: 10.1007/s100529801045. URL https://doi.org/10.1007/s100529801045.

[65] R. et al. Rameika. Measurements of production polarization and decay asymmetry for Ξ^- hyperons. *Phys. Rev. D*, 33:3172–3179, Jun 1986. doi: 10.1103/PhysRevD.33.3172. URL https://link.aps.org/doi/10.1103/PhysRevD.33.3172.

[66] L. H. et al. Trost. New measurement of the production polarization and magnetic moment of the Ξ^- hyperon. *Phys. Rev. D*, 40:1703–1707, Sep 1989. doi: 10.1103/PhysRevD.40.1703. URL https://link.aps.org/doi/10.1103/PhysRevD.40.1703.

[67] P. M. Ho, M. J. Longo, A. Nguyen, K. B. Luk, C. James, R. Rameika, J. Duryea, G. Guglielmo, K. Heller, K. Johns, H. T. Diehl, S. Teige, G. B. Thomson, and Y. Zou. Production polarization and magnetic moment of Ξ^+ antihyperons produced by 800-GeV/c protons. *Phys. Rev. Lett.*, 65: 1713–1716, Oct 1990. doi: 10.1103/PhysRevLett.65.1713. URL https://link.aps.org/doi/10.1103/PhysRevLett.65.1713.

[68] J. Duryea, G. Guglielmo, K. Heller, K. Johns, M. Shupe, K. Thorne, C. James, K. B. Luk, R. Rameika, P. M. Ho, M. J. Longo, H. T. Diehl, S. Teige, and G. B. Thomson. Polarization of Ξ^- hyperons produced by 800- GeV protons. *Phys. Rev. Lett.*, 67:1193–1196, Sep 1991. doi: 10.1103/PhysRevLett.67.1193. URL https://link.aps.org/doi/10.1103/PhysRevLett.67.1193.

[69] K. et al. Heller. Polarization of Ξ^0 and Λ hyperons produced by 400-GeV/c protons. *Phys. Rev. Lett.*, 51:2025–2028, Nov 1983. doi: 10.1103/PhysRevLett.51.2025. URL https://link.aps.org/doi/10.1103/PhysRevLett.51.2025.

[70] J. Lach. Hyperon polarization: An experimental overview. 1992.

[71] P. M. et al. Ho. Production polarization and magnetic moment of Ξ^{-+} antihyperons produced by 800-GeV/c protons. *Phys. Rev. Lett.*, 65:1713–1716, Oct 1990. doi: 10.1103/PhysRevLett.65.1713. URL https://link.aps.org/doi/10.1103/PhysRevLett.65.1713.

[72] K. B. Luk et al. Production polarization and magnetic moment of Anti-Ξ^+ and Ω^- hyperons: Preliminary results from FNAL E-756. In *9th International Symposium on High-energy Spin Physics*, 9 1990.

[73] M. Jezabek, K. Rybicki, and R. Rylko. Experimental study of spin effects in hadroproduction and decay of Λ_c^+. *Phys. Lett. B*, 286:175–179, 1992. doi: 10.1016/0370-2693(92)90177-6. URL https://inspirehep.net/literature/339924.

[74] Gary R. Goldstein. Spin dependent fragmentation functions for heavy flavor baryons and single heavy hyperon polarization0. *Czech. J. Phys.*, 51:A135–A143, 2001. doi: 10.1007/s10582-001-0016-6.

[75] S. Carrillo, C. Castromonte, and C. Oropeza. Polarization Study Of Λ_c^+ Baryon Using Data From The Fermilab E831 Experiment. *AIP Conference Proceedings*, 1026(1):303–305, 2008. doi: 10.1063/1.2965068. URL https://aip.scitation.org/doi/abs/10.1063/1.2965068.

[76] Y. Guan et al. Observation of Transverse $\Lambda/\bar{\Lambda}$ Hyperon Polarization in e^+e^- Annihilation at Belle. *Phys. Rev. Lett.*, 122(4):042001, 2019. doi: 10.1103/PhysRevLett.122.042001.

[77] Polarization and entanglement in baryon–antibaryon pair production in electron–positron annihilation. *Nature Physics*, 15(7):631–634, May 2019. ISSN 1745-2481. doi: 10.1038/s41567-019-0494-8. URL http://dx.doi.org/10.1038/s41567-019-0494-8.

[78] S. Erhan, W. Lockman, M. Medinnis, T. Meyer, J. Rander, P. Schlein, R. Webb, A. Boehm, H. Foeth, A. Staude, R. Ellis, B. Naroska, P. Strolin, and J. Zsembery. $\lambda 0$ polarization in proton-proton interactions at $\sqrt{s} = 53$ and 62 GeV. *Physics Letters B*, 82(2):301–304, 1979. ISSN 0370-2693. doi: https://doi.org/10.1016/0370-2693(79)90761-5. URL https://www.sciencedirect.com/science/article/pii/0370269379907615.

[79] G. Aad, B. Abbott, J. Abdallah, S. Abdel Khalek, O. Abdinov, R. Aben, B. Abi, M. Abolins, O. S. AbouZeid, H. Abramowicz, and et al. Measurement of the transverse polarization of Λ and $\overline{\Lambda}$ hyperons produced in proton-proton collisions at $\sqrt{s}$ =7 TeV using the ATLAS detector. *Physical Review D*, 91(3), Feb 2015. ISSN 1550-2368. doi: 10.1103/physrevd.91.032004. URL http://dx.doi.org/10.1103/PhysRevD.91.032004.

[80] R. Aaij, C. Abellan Beteta, T. Ackernley, B. Adeva, M. Adinolfi, H. Afsharnia, C. A. Aidala, S. Aiola, Z. Ajaltouni, and et al. Measurement of the $\Lambda_b^0 \to J/\psi\,\Lambda$ angular distribution and the Λ_b^0 polarisation in pp collisions. *Journal of High Energy Physics*, 2020(6), Jun 2020. ISSN 1029-8479. doi: 10.1007/jhep06(2020)110. URL http://dx.doi.org/10.1007/JHEP06(2020)110.

[81] R. Aaij et al. Measurements of the $\Lambda_b^0 \to J/\psi\Lambda$ decay amplitudes and the Λb0 polarisation in pp collisions at s=7 TeV. *Physics Letters B*, 724(1):27–35, 2013. ISSN 0370-2693. doi: https://doi.org/10.1016/j.physletb.2013.05.041. URL https://www.sciencedirect.com/science/article/pii/S0370269313004231.

[82] G. et al. Aad. Measurement of the parity-violating asymmetry parameter α_b and the helicity amplitudes for the decay $\Lambda_b^0 \to J/\psi\Lambda^0$ with the ATLAS detector. *Phys. Rev. D*, 89:092009, May 2014. doi: 10.1103/PhysRevD.89.092009. URL https://link.aps.org/doi/10.1103/PhysRevD.89.092009.

[83] A. M. et al. Sirunyan. Measurement of the Λ_b polarization and angular parameters in $\Lambda_b \to J\psi\Lambda$ decays from *pp* collisions at $\sqrt{s} = 7$ and 8 TeV. *Phys. Rev. D*, 97:072010, Apr 2018. doi: 10.1103/PhysRevD.97.072010. URL https://link.aps.org/doi/10.1103/PhysRevD.97.072010.

[84] Jaroslav Adam et al. Polarization of Λ ($\bar{\Lambda}$) hyperons along the beam direction in Au + Au collisions at $\sqrt{s_{NN}} = 200$ GeV. *Phys. Rev. Lett.*, 123(13):132301, 2019. doi: 10.1103/PhysRevLett.123.132301. URL https://link.aps.org/doi/10.1103/PhysRevLett.123.132301.

[85] Shreyasi Acharya et al. Global polarization of $\Lambda\bar{\Lambda}$ hyperons in Pb-Pb collisions at $\sqrt{s_{NN}} = 2.76$ and 5.02 TeV. *Phys. Rev. C*, 101(4):044611, 2020. doi: 10.1103/PhysRevC.101.044611. URL https://link.aps.org/doi/10.1103/PhysRevC.101.044611.

[86] Iurii Karpenko and Francesco Becattini. Λ polarization in heavy ion collisions: from RHIC BES to LHC energies. *Nucl. Phys. A*, 982:519–522, 2019. doi: 10.1016/j.nuclphysa.2018.10.067. URL https://www.sciencedirect.com/science/article/pii/S0375947418303488.

[87] Bálint Boldizsár, Márton I. Nagy, and Máté Csanád. Polarized baryon production in heavy ion collisions: An analytic hydrodynamical study. *Universe*, 5(5):101, 2019. doi: 10.3390/universe5050101. URL https://www.mdpi.com/2218-1997/5/5/101.

[88] M. Anselmino, D. Boer, U. D'Alesio, and F. Murgia. Λ polarization in unpolarized hadron reactions. *Czechoslovak Journal of Physics*, 51(1):A107–A113, 2001. doi: 10.1007/s10582-001-0012-x. URL https://doi.org/10.1007/s10582-001-0012-x.

[89] D. Hanneke, S. Fogwell, and G. Gabrielse. New measurement of the electron magnetic moment and the fine structure constant. *Physical Review Letters*, 100(12), Mar 2008. ISSN 1079-7114. doi: 10.1103/physrevlett.100.120801. URL http://dx.doi.org/10.1103/PhysRevLett.100.120801.

[90] B. et al. Abi. Measurement of the positive muon anomalous magnetic moment to 0.46 ppm. *Phys. Rev. Lett.*, 126:141801, Apr 2021. doi: 10.1103/PhysRevLett.126.141801. URL https://link.aps.org/doi/10.1103/PhysRevLett.126.141801.

[91] A. G. Grozin. Introduction to the heavy quark effective theory. part 1. 12 1992.

[92] Howard Georgi. An effective field theory for heavy quarks at low energies. *Physics Letters B*, 240 (3):447–450, 1990. ISSN 0370-2693. doi: https://doi.org/10.1016/0370-2693(90)91128-X. URL https://www.sciencedirect.com/science/article/pii/037026939091128X.

[93] Estia Eichten and Brian Hill. An effective field theory for the calculation of matrix elements involving heavy quarks. *Physics Letters B*, 234(4):511–516, 1990. ISSN 0370-2693. doi: https://doi.org/10.1016/0370-2693(90)92049-O. URL https://www.sciencedirect.com/science/article/pii/037026939092049O.

[94] Shi-lin Zhu, W-Y. P. Hwang, and Ze-sen Yang. Σ_c and Λ_c magnetic moments from QCD spectral sum rules. *Phys. Rev. D*, 56:7273–7275, Dec 1997. doi: 10.1103/PhysRevD.56.7273. URL https://link.aps.org/doi/10.1103/PhysRevD.56.7273.

[95] Guang-Juan Wang, Lu Meng, Hao-Song Li, Zhan-Wei Liu, and Shi-Lin Zhu. Magnetic moments of the spin-$\frac{1}{2}$ singly charmed baryons in chiral perturbation theory. *Phys. Rev. D*, 98:054026, Sep 2018. doi: 10.1103/PhysRevD.98.054026. URL https://link.aps.org/doi/10.1103/PhysRevD.98.054026.

[96] B. Silvestre-Brac. Spectrum and static properties of heavy baryons. *Few Body Syst.*, 20:1–25, 1996. doi: 10.1007/s006010050028. URL https://inspirehep.net/literature/431028.

[97] N. Barik and M. Das. Magnetic moments of confined quarks and baryons in an independent-quark model based on dirac equation with power-law potential. *Phys. Rev. D*, 28:2823–2829, Dec 1983. doi: 10.1103/PhysRevD.28.2823. URL https://link.aps.org/doi/10.1103/PhysRevD.28.2823.

[98] Ajay Kumar Rai Bhavin Patel and P C Vinodkumar. Masses and magnetic moments of heavy flavour baryons in the hyper central model. *J. Phys. G: Nucl. Part. Phys*, 35(065001), 2008. doi: https://doi-org.proxy.scd.u-psud.fr/10.1088/0954-3899/35/6/065001. URL https://iopscience-iop-org.proxy.scd.u-psud.fr/article/10.1088/0954-3899/35/6/065001.

[99] C.S. An. The $qqqq\bar{q}$ components and the magnetic moments of the charmed and the bottomed baryons. *Nuclear Physics A*, 797(3):131–144, 2007. ISSN 0375-9474. doi: https://doi.org/10.1016/j.nuclphysa.2007.10.002. URL https://www.sciencedirect.com/science/article/pii/S037594740700735X.

[100] Martin J. Savage. Magnetic moment of the Λ_c, Ξ_{c1}^+ and Ξ_{c1}^0. *Phys. Lett. B*, 326:303–306, 1994. doi: 10.1016/0370-2693(94)91326-9. URL https://www.sciencedirect.com/science/article/pii/0370269394913269.

[101] D.O Riska. Physics of charmed baryons and their magnetic moments. *Nuclear Instruments and Methods in Physics Research Section B: Beam Interactions with Materials and Atoms*, 119(1): 259–265, 1996. ISSN 0168-583X. doi: https://doi.org/10.1016/0168-583X(95)01382-2. URL https://www.sciencedirect.com/science/article/pii/0168583X95013822.

[102] Neetika Sharma, Harleen Dahiya, P. K. Chatley, and Manmohan Gupta. Spin $\frac{1}{2}^+$, spin $\frac{3}{2}^+$, and transition magnetic moments of low lying and charmed baryons. *Phys. Rev. D*, 81:073001, Apr 2010. doi: 10.1103/PhysRevD.81.073001. URL https://link.aps.org/doi/10.1103/PhysRevD.81.073001.

[103] T. M. Aliev, A. Ozpineci, and M. Savci. The Magnetic moments of Λ_b^0 and Λ_c^+ baryons in light cone QCD sum rules. *Phys. Rev. D*, 65:056008, 2002. doi: 10.1103/PhysRevD.65.056008. URL https://journals.aps.org/prd/abstract/10.1103/PhysRevD.65.056008.

[104] Andrius Bernotas and Vytautas Simonis. Magnetic moments of heavy baryons in the bag model re-examined, 9 2012. URL https://inspirehep.net/literature/1185432.

[105] Amand Faessler, Th. Gutsche, M. A. Ivanov, J. G. Körner, V. E. Lyubovitskij, D. Nicmorus, and K. Pumsa-ard. Magnetic moments of heavy baryons in the relativistic three-quark model. *Phys. Rev. D*, 73:094013, May 2006. doi: 10.1103/PhysRevD.73.094013. URL https://link.aps.org/doi/10.1103/PhysRevD.73.094013.

[106] Peter Cho. Chiral perturbation theory for hadrons containing a heavy quark. The sequel. *Physics Letters B*, 285(1):145–152, 1992. ISSN 0370-2693. doi: https://doi.org/10.1016/0370-2693(92)91314-Y. URL https://www.sciencedirect.com/science/article/pii/037026939291314Y.

[107] A.A. Greenenko and N.F. Shul'ga. Turning a beam of high-energy charged particles by means of scattering by atomic rows of a curved crystal. *JETP*, 54:524, 1991. URL https://inspirehep.net/literature/326398.

[108] A.A. Greenenko and N.F. Shul'ga. Deflection of high energy particles during multiple scattering by atomic strings of a bent crystal. *Nuclear Instruments and Methods in Physics Research Section B: Beam Interactions with Materials and Atoms*, 90(1):179–182, 1994. ISSN 0168-583X. doi: https://doi.org/10.1016/0168-583X(94)95537-9. URL https://www.sciencedirect.com/science/article/pii/0168583X94955379.

[109] A.A. Greenenko and N.F. Shul'ga. Spin rotation and deflection of high energy charged particles in a bent crystal due to multiple scattering by atomic strings. *Nuclear Instruments and Methods in Physics Research Section B: Beam Interactions with Materials and Atoms*, 67(1):212–216, 1992. ISSN 0168-583X. doi: https://doi.org/10.1016/0168-583X(92)95804-Z. URL https://www.sciencedirect.com/science/article/pii/0168583X9295804Z.

[110] Ick Joh Kim. Magnetic moment measurement of baryons with heavy-flavored quarks by planar channeling through a bent crystal. *Nuclear Physics B*, 229(1):251–268, 1983. ISSN 0550-3213. doi: https://doi.org/10.1016/0550-3213(83)90363-2. URL https://www.sciencedirect.com/science/article/pii/0550321383903632.

[111] D. Mirarchi, A. S. Fomin, S. Redaelli, and W. Scandale. Layouts for fixed-target experiments and dipole moment measurements of short-lived baryons using bent crystals at the LHC. *The European Physical Journal C*, 80(10), Oct 2020. ISSN 1434-6052. doi: 10.1140/epjc/s10052-020-08466-x. URL http://dx.doi.org/10.1140/epjc/s10052-020-08466-x.

[112] Frederic Fleuret, Benjamin Audurier, Felipe Andres Garcia Rosales, and Emilie Amandine Maurice. Global event cuts for 2017 pNe SMOG data. Technical report, CERN, Geneva, Jun 2020. URL https://cds.cern.ch/record/2720461.

[113] L. Evans and P. Bryant. LHC machine. *Journal of Instrumentation*, 3(08):S08001–S08001, aug 2008. doi: 10.1088/1748-0221/3/08/s08001. URL https://doi.org/10.1088/1748-0221/3/08/s08001.

[114] Esma Mobs. The cern accelerator complex - 2019. Jul 2019. URL https://cds.cern.ch/record/2684277. General Photo.

[115] G. Aad et al. The ATLAS experiment at the CERN large hadron collider. *Journal of Instrumentation*, 3(08):S08003–S08003, aug 2008. doi: 10.1088/1748-0221/3/08/s08003. URL https://doi.org/10.1088/1748-0221/3/08/s08003.

[116] S. Chatrchyan et al. The CMS Collaboration. The CMS experiment at the CERN LHC. *Journal of Instrumentation*, 3(08):S08004–S08004, aug 2008. doi: 10.1088/1748-0221/3/08/s08004. URL https://doi.org/10.1088/1748-0221/3/08/s08004.

[117] K. Aamodt et al. The ALICE experiment at the CERN LHC. *JINST*, 3:S08002, 2008. doi: 10.1088/1748-0221/3/08/S08002. URL https://iopscience.iop.org/article/10.1088/1748-0221/3/08/S08002.

[118] Sascha Caron. SUSY searches at ATLAS. In *46th Rencontres de Moriond on Electroweak Interactions and Unified Theories*, pages 111–118, 6 2011.

[119] Georges Aad et al. Search for light long-lived neutral particles produced in pp collisions at $\sqrt{s} =$ 13 TeV and decaying into collimated leptons or light hadrons with the ATLAS detector. *Eur. Phys. J. C*, 80(5):450, 2020. doi: 10.1140/epjc/s10052-020-7997-4. URL https://doi.org/10.1140/epjc/s10052-020-7997-4.

[120] P J Oddone. Introduction to physics studies at an asymmetric e^+e^- b-factory. URL https://www.osti.gov/biblio/10103588.

[121] Christian Elsässer. $\bar{b}b$ production angle plots. URL https://lhcb.web.cern.ch/lhcb/speakersbureau/html/bb_ProductionAngles.html.

[122] R. Aaij et al. Prompt charm production in pp collisions at $\sqrt{s} = 7$ TeV. *Nucl. Phys. B*, 871: 1–20, 2013. doi: 10.1016/j.nuclphysb.2013.02.010.

[123] R. Aaij et al. Measurements of prompt charm production cross-sections in pp collisions at $\sqrt{s} = 13$ TeV. *JHEP*, 03:159, 2016. doi: 10.1007/JHEP03(2016)159,10.1007/JHEP09(2016)013,10.1007/JHEP05(2017)074. URL https://link.springer.com/article/10.1007/JHEP03(2016)159. [Erratum: JHEP09,013(2016); Erratum: JHEP05,074(2017)].

[124] R. et al. Aaji. Measurement of B hadron production fractions in 7 TeV pp collisions. *Physical Review D*, 85(3), Feb 2012. ISSN 1550-2368. doi: 10.1103/physrevd.85.032008. URL http://dx.doi.org/10.1103/PhysRevD.85.032008.

[125] Rafal Maciula and Antoni Szczurek. Production of Λ_c^+ baryons at the LHC within the kT-factorization approach and independent parton fragmentation picture. *Physical Review D*, 98 (1), Jul 2018. ISSN 2470-0029. doi: 10.1103/physrevd.98.014016. URL http://dx.doi.org/10.1103/PhysRevD.98.014016.

[126] A. Zupanc et al. Measurement of the Branching Fraction $\mathcal{B}(\Lambda_c^+ \to pK^-\pi^+)$. *Phys. Rev. Lett.*, 113(4):042002, 2014. doi: 10.1103/PhysRevLett.113.042002. URL https://journals.aps.org/prl/abstract/10.1103/PhysRevLett.113.042002.

[127] M. Ablikim et al. Measurements of absolute hadronic branching fractions of Λ_c^+ baryon. *Phys. Rev. Lett.*, 116(5):052001, 2016. doi: 10.1103/PhysRevLett.116.052001. URL https://link.aps.org/doi/10.1103/PhysRevLett.116.052001.

[128] LHCb Collaboration. *LHCb VELO (VErtex LOcator): Technical Design Report.* Technical design report. LHCb. CERN, Geneva, 2001. URL https://cds.cern.ch/record/504321.

[129] LHCb detector performance. *International Journal of Modern Physics A*, 30(07):1530022, Mar 2015. ISSN 1793-656X. doi: 10.1142/s0217751x15300227. URL http://dx.doi.org/10.1142/S0217751X15300227.

[130] Steven R. Blusk. Measurements of the Λ_c^+, Ξ_c^+ and Ξ_c^0 baryon lifetimes using semileptonic beauty decays. Feb 2019. URL https://cds.cern.ch/record/2657989.

[131] LHCb inner tracker: Technical Design Report, 2002.

[132] LHCb Collaboration. *LHCb inner tracker: Technical Design Report.* Technical design report. LHCb. CERN, Geneva, 2002. URL https://cds.cern.ch/record/582793. revised version number 1 submitted on 2002-11-13 14:14:34.

[133] LHCb outer tracker: Technical Design Report, 2001.

[134] W.D. Hulsbergen. The global covariance matrix of tracks fitted with a kalman filter and an application in detector alignment. *Nuclear Instruments and Methods in Physics Research Section A: Accelerators, Spectrometers, Detectors and Associated Equipment*, 600(2):471–477, Mar 2009. ISSN 0168-9002. doi: 10.1016/j.nima.2008.11.094. URL http://dx.doi.org/10.1016/j.nima.2008.11.094.

[135] The LHCb collaboration. Measurement of the track reconstruction efficiency at LHCb. *Journal of Instrumentation*, 10(02):P02007–P02007, feb 2015. doi: 10.1088/1748-0221/10/02/p02007. URL https://doi.org/10.1088/1748-0221/10/02/p02007.

[136] Aaij et al. Design and performance of the LHCb trigger and full real-time reconstruction in Run 2 of the LHC. *Journal of Instrumentation*, 14(04):P04013–P04013, Apr 2019. ISSN 1748-0221. doi: 10.1088/1748-0221/14/04/p04013. URL http://dx.doi.org/10.1088/1748-0221/14/04/P04013.

[137] LHCb calorimeters: Technical Design Report, 2000.

[138] Martino Borsato. Study of the $B^0 \to K^{*0}e^+e^-$ decay with the LHCb detector and development of a novel concept of PID detector: the Focusing DIRC, 2015. URL https://cds.cern.ch/record/2104825. Presented 08 Sep 2015.

[139] Amato et al. *LHCb RICH: Technical Design Report*. Technical design report. LHCb. CERN, Geneva, 2000. URL https://cds.cern.ch/record/494263.

[140] Denis Derkach et al. Machine-learning-based global particle-identification algorithms at the LHCb experiment. *Journal of Physics: Conference Series*, 1085:042038, sep 2018. doi: 10.1088/1742-6596/1085/4/042038. URL https://doi.org/10.1088/1742-6596/1085/4/042038.

[141] M. Adinolfi et al. Performance of the LHCb RICH detector at the LHC. *Eur. Phys. J. C*, 73:2431, 2013. doi: 10.1140/epjc/s10052-013-2431-9. URL https://link.springer.com/article/10.1140/epjc/s10052-013-2431-9.

[142] A. Papanestis and C. D'Ambrosio. Performance of the LHCb RICH detectors during the LHC Run II. *Nucl. Instrum. Meth. A*, 876:221–224, 2017. doi: 10.1016/j.nima.2017.03.009. URL https://cds.cern.ch/record/2255885/files/10.1016_j.nima.2017.03.009.pdf.

[143] LHCb Collaboration. *LHCb muon system: Technical Design Report*. Technical design report. LHCb. CERN, Geneva, 2001. URL https://cds.cern.ch/record/504326.

[144] A. A. Alves et al. Performance of the LHCb muon system. *Journal of Instrumentation*, 8(02): P02022–P02022, feb 2013. doi: 10.1088/1748-0221/8/02/p02022. URL https://doi.org/10.1088/1748-0221/8/02/p02022.

[145] F Archilli et al. Performance of the muon identification at LHCb. *Journal of Instrumentation*, 8 (10):P10020–P10020, oct 2013. doi: 10.1088/1748-0221/8/10/p10020. URL https://doi.org/10.1088/1748-0221/8/10/p10020.

[146] Aaij et al. Optimization of the muon reconstruction algorithms for LHCb Run 2. Technical Report LHCb-PUB-2017-007. CERN-LHCb-PUB-2017-007, CERN, Geneva, Feb 2017. URL https://cds.cern.ch/record/2253050.

[147] The LHCb collaboration. Precision luminosity measurements at LHCb. *Journal of Instrumentation*, 9(12):P12005–P12005, Dec 2014. ISSN 1748-0221. doi: 10.1088/1748-0221/9/12/p12005. URL http://dx.doi.org/10.1088/1748-0221/9/12/P12005.

[148] LHCb Collaboration. LHCb SMOG Upgrade. Technical Report CERN-LHCC-2019-005. LHCB-TDR-020, CERN, Geneva, May 2019. URL https://cds.cern.ch/record/2673690.

[149] Roel Aaij et al. Measurement of Antiproton Production in pHe Collisions at $\sqrt{s_{NN}} = 110$ GeV. *Phys. Rev. Lett.*, 121(22):222001, 2018. doi: 10.1103/PhysRevLett.121.222001. URL https://link.aps.org/doi/10.1103/PhysRevLett.121.222001.

[150] Roel Aaij et al. First Measurement of charm production in its Fixed-Target configuration at the LHC. *Phys. Rev. Lett.*, 122(13):132002, 2019. doi: 10.1103/PhysRevLett.123.239901,10.1103/PhysRevLett.122.132002. URL http://dx.doi.org/10.1103/PhysRevLett.122.132002.

[151] Trigger schemes, . URL http://lhcb.web.cern.ch/lhcb/speakersbureau/html/TriggerScheme.html.

[152] M Clemencic, G Corti, S Easo, C R Jones, S Miglioranzi, M Pappagallo, and P Robbe and. The LHCb Simulation Application, Gauss: Design, Evolution and Experience. *Journal of Physics: Conference Series*, 331(3):032023, dec 2011. doi: 10.1088/1742-6596/331/3/032023. URL https://doi.org/10.1088/1742-6596/331/3/032023.

[153] . URL https://lhcb.github.io/starterkit-lessons/first-analysis-steps/run-2-data-flow.html.

[154] The moore project, . URL http://lhcb-releasearea.web.cern.ch/LHCb-release-area/DOC/moore(2012).

[155] The WLCG Project, . URL https://wlcg-public.web.cern.ch.

[156] M Clemencic et al. The LHCb simulation application, gauss: Design, evolution and experience. *Journal of Physics: Conference Series*, 331(3):032023, dec 2011. doi: 10.1088/1742-6596/331/3/032023. URL https://doi.org/10.1088/1742-6596/331/3/032023.

[157] Torbjörn Sjöstrand, Stephen Mrenna, and Peter Skands. A brief introduction to PYTHIA 8.1. *Computer Physics Communications*, 178(11):852–867, 2008. ISSN 0010-4655. doi: https://doi.org/10.1016/j.cpc.2008.01.036. URL https://www.sciencedirect.com/science/article/pii/S0010465508000441.

[158] I Belyaev, T Brambach, N H Brook, N Gauvin, G Corti, K Harrison, P F Harrison, J He, C R Jones, M Lieng, G Manca, S Miglioranzi, P Robbe, V Vagnoni, M Whitehead, and J Wishahi and. Handling of the generation of primary events in Gauss, the LHCb simulation framework. *Journal of Physics: Conference Series*, 331(3):032047, dec 2011. doi: 10.1088/1742-6596/331/3/032047. URL https://doi.org/10.1088/1742-6596/331/3/032047.

[159] T. Pierog, Iu. Karpenko, J. M. Katzy, E. Yatsenko, and K. Werner. EPOS LHC: Test of collective hadronization with data measured at the CERN Large Hadron Collider. *Physical Review C*, 92(3), Sep 2015. ISSN 1089-490X. doi: 10.1103/physrevc.92.034906. URL http://dx.doi.org/10.1103/PhysRevC.92.034906.

[160] Xin-Nian Wang and Miklos Gyulassy. Hijing: A Monte Carlo model for multiple jet production in pp, pA, and AA collisions. *Phys. Rev. D*, 44:3501–3516, Dec 1991. doi: 10.1103/PhysRevD.44.3501. URL https://link.aps.org/doi/10.1103/PhysRevD.44.3501.

[161] Spencer R. Klein, Joakim Nystrand, Janet Seger, Yuri Gorbunov, and Joey Butterworth. STARlight: A Monte Carlo simulation program for ultra-peripheral collisions of relativistic ions. *Computer Physics Communications*, 212:258–268, Mar 2017. ISSN 0010-4655. doi: 10.1016/j.cpc.2016.10.016. URL http://dx.doi.org/10.1016/j.cpc.2016.10.016.

[162] David J. Lange. The EvtGen particle decay simulation package. *Nuclear Instruments and Methods in Physics Research Section A: Accelerators, Spectrometers, Detectors and Associated Equipment*, 462(1):152–155, 2001. ISSN 0168-9002. doi: https://doi.org/10.1016/S0168-9002(01)00089-4. URL https://www.sciencedirect.com/science/article/pii/S0168900201000894. BEAUTY2000, Proceedings of the 7th Int. Conf. on B-Physics at Hadron Machines.

[163] P. Golonka and Z. Was. PHOTOS Monte Carlo: a precision tool for QED correctionsin Z and W decays. *The European Physical Journal C - Particles and Fields*, 45(1):97–107, 2006. doi: 10.1140/epjc/s2005-02396-4. URL https://doi.org/10.1140/epjc/s2005-02396-4.

[164] S. Agostinelli et al. Geant4 a simulation toolkit. *Nuclear Instruments and Methods in Physics Research Section A: Accelerators, Spectrometers, Detectors and Associated Equipment*, 506(3): 250–303, 2003. ISSN 0168-9002. doi: https://doi.org/10.1016/S0168-9002(03)01368-8. URL https://www.sciencedirect.com/science/article/pii/S0168900203013688.

[165] J.Allison et al. Geant4 developments and applications. *IEEE Transactions on Nuclear Science*, 53(1):270–278, 2006. doi: 10.1109/TNS.2006.869826.

[166] LHCb Tracker Upgrade Technical Design Report, 2014.

[167] LHCb VELO Upgrade Technical Design Report, 2013.

[168] T. Poikela, R. Ballabriga, J. Buytaert, X. Llopart, W. Wong, M. Campbell, K. Wyllie, M. van Beuzekom, J. Schipper, S. Miryala, and V. Gromov. The VeloPix ASIC. *Journal of Instrumentation*, 12(01):C01070–C01070, jan 2017. doi: 10.1088/1748-0221/12/01/c01070. URL https://doi.org/10.1088/1748-0221/12/01/c01070.

[169] Sz. Bugiel, R. Dasgupta, M. Firlej, T. Fiutowski, M. Idzik, M. Kuczynska, J. Moron, K. Swientek, and T. Szumlak. SALT, a dedicated readout chip for high precision tracking silicon strip detectors at the LHCb upgrade. *Journal of Instrumentation*, 11(02):C02028–C02028, feb 2016. doi: 10.1088/1748-0221/11/02/c02028. URL https://doi.org/10.1088/1748-0221/11/02/c02028.

[170] Sajan Easo. Overview of LHCb-RICH upgrade. *Nucl. Instrum. Meth. A*, 876:160–163, 2017. doi: 10.1016/j.nima.2017.02.061.

[171] L. Cassina. Photodetectors and front-end electronics for the LHCb RICH upgrade. *Nucl. Instrum. Meth. A*, 876:217–220, 2017. doi: 10.1016/j.nima.2017.03.008.

[172] P Carniti, M De Matteis, A Giachero, C Gotti, M Maino, and G Pessina. CLARO-CMOS, a very low power ASIC for fast photon counting with pixellated photodetectors. *Journal of Instrumentation*, 7(11):P11026–P11026, nov 2012. doi: 10.1088/1748-0221/7/11/p11026. URL https://doi.org/10.1088/1748-0221/7/11/p11026.

[173] Albert et al. Bursche. Physics opportunities with the fixed-target program of the LHCb experiment using an unpolarized gas target. Technical report, CERN, Geneva, Dec 2018. URL https://cds.cern.ch/record/2649878.

[174] LHCb Trigger and Online Upgrade Technical Design Report. Technical Report CERN-LHCC-2014-016. LHCB-TDR-016, May 2014. URL https://cds.cern.ch/record/1701361.

[175] LHCb Trigger and Online Technical Design Report, 2014.

[176] R. Aaij, J. Albrecht, M. Belous, P. Billoir, T. Boettcher, A. Brea Rodríguez, D. vom Bruch, D. H. Cámpora Pérez, A. Casais Vidal, D. C. Craik, and et al. Allen: A High-Level Trigger on GPUs for LHCb. *Computing and Software for Big Science*, 4(1), Apr 2020. ISSN 2510-2044. doi: 10.1007/s41781-020-00039-7. URL http://dx.doi.org/10.1007/s41781-020-00039-7.

[177] G. et al Antchev. Luminosity-independent measurement of the proton-proton total cross section at $\sqrt{s} = 8$ TeV. *Phys. Rev. Lett.*, 111:012001, Jul 2013. doi: 10.1103/PhysRevLett.111.012001. URL https://link.aps.org/doi/10.1103/PhysRevLett.111.012001.

[178] S van der Meer. Calibration of the effective beam height in the ISR. Technical Report CERN-ISR-PO-68-31. ISR-PO-68-31, CERN, Geneva, 1968. URL https://cds.cern.ch/record/296752.

[179] M.Ferro-Luzzi. Proposal for an absolute luminosity determination in colliding beam experiments using vertex detection of beam–gas interactions. *Nuclear Instruments and Methods in Physics Research Section A: Accelerators, Spectrometers, Detectors and Associated Equipment*, 553(3): 388–399, 2005. ISSN 0168-9002. doi: https://doi.org/10.1016/j.nima.2005.07.010. URL https://www.sciencedirect.com/science/article/pii/S0168900205014130.

[180] G. Papotti, X. Buffat, W. Herr, Rossano Giachino, and Tatiana Pieloni. Observations of beam-beam effects at the lhc. 09 2014.

[181] Michael Schmelling. Luminosity calibration for the leading bunch nobias-triggered data from the 2015 early measurement runs. Technical Report LHCb-INT-2017-015. CERN-LHCb-INT-2017-015, CERN, Geneva, Jun 2017. URL https://cds.cern.ch/record/2271152.

[182] N Yu Zaitsev. Study of the LHCb pile-up trigger and $B_s \to J/\psi\,\phi$ decay, 2000. URL https://cds.cern.ch/record/473383. Presented on 27 Oct 2000.

[183] O. Okhrimenko, S. Barsuk, F. Alessio, and V. Pugatch. LHCb RMS status and operation at 13 TeV. In *3rd French-Ukrainian workshop on the instrumentation developments for HEP*, pages 61–65, 2015.

[184] F Alessio, R Dzhelyadin, and R Jacobsson. A Cherenkov-based Beam Loss Scintillator system for beam, background and online luminosity monitoring at the LHCb experiment at CERN. Technical Report LHCb-PUB-2013-006. CERN-LHCb-PUB-2013-006, CERN, Geneva, Jun 2013. URL http://cds.cern.ch/record/1547517.

[185] Ch. Ilgner, M. Domke M. Lieng, M. Nedos, J. Sauerbrey, S. Schleich, B. Spaan, K. Warda, and J. Wishahi. The Beam Conditions Monitor of the LHCb Experiment, 2010.

[186] Barsuk S. et al. Probe for LUminosity MEasurement in LHCb. Technical Report LHCb-PUB-2020-008. CERN-LHCb-PUB-2020-008, CERN, Geneva, Oct 2020. URL http://cds.cern.ch/record/2743098.

[187] G.L. Alberghi et al. Choice and characterization of photomultipliers for the new ATLAS LUCID detector. *Journal of Instrumentation*, 11(05):P05014–P05014, may 2016. doi: 10.1088/1748-0221/11/05/p05014. URL https://doi.org/10.1088/1748-0221/11/05/p05014.

[188] G. Avoni et al. The new LUCID-2 detector for luminosity measurement and monitoring in ATLAS. *Journal of Instrumentation*, 13(07):P07017–P07017, jul 2018. doi: 10.1088/1748-0221/13/07/p07017. URL https://doi.org/10.1088/1748-0221/13/07/p07017.

[189] Matthias Karacson. *Evaluation of the radiation environment of the LHCb experiment.* PhD thesis, 2016. URL https://cds.cern.ch/record/2243499.

[190] CERN (Meyrin) LHCb Collaboration. LHCb PLUME: Probe for LUminosity MEasurement. Technical Report CERN-LHCC-2021-002. LHCB-TDR-022, CERN, Geneva, Jan 2021. URL https://cds.cern.ch/record/2750034.

[191] Valentina Cicero. *Neutron radiation resistance of photomultipliers for the LUCID detector in the ATLAS experiment at LHC.* PhD thesis, 2015. URL https://amslaurea.unibo.it/9410/1/cicero_valentina_tesi.pdf.

[192] Iouri et al. Guz. Upgrade of the monitoring system of LHCb ECAL. Technical Report LHCb-PUB-2016-018. CERN-LHCb-PUB-2016-018, CERN, Geneva, 7 2016. URL https://cds.cern.ch/record/2196516.

[193] Yasmine Sara Amhis, Christophe Beigbeder-Beau, Olivier Duarte, Vitalii Lisovskyi, Frederic Machefert, Monique Anne-Marie Taurigna Quere, and Joao Coelho. The Front-End board of the upgraded LHCb Calorimeter. Technical Report LHCb-INT-2019-004. CERN-LHCb-INT-2019-004, CERN, Geneva, Jan 2019. URL https://cds.cern.ch/record/2655086.

[194] J.P. Cachemiche, P.Y. Duval, F. Hachon, R. Le Gac, and F. Réthoré. The PCIe-based readout system for the LHCb experiment. *Journal of Instrumentation*, 11(02):P02013–P02013, feb 2016. doi: 10.1088/1748-0221/11/02/p02013. URL https://doi.org/10.1088/1748-0221/11/02/p02013.

[195] Yasmine Sara Amhis, Christophe Beigbeder-Beau, Olivier Duarte, Yiming Li, Vitalii Lisovskyi, Frederic Machefert, and Monique Anne-Marie Taurigna Quere. 3CU Calorimeter Control Card Unit. Technical report, CERN, Geneva, Jan 2019. URL https://cds.cern.ch/record/2654820.

[196] E Picatoste, D Gascón, C Abellán, J Lefrançois, F Machefert, O Duarte, E Grauges, L Garrido, and X Vilasis. Low noise front end ICECAL ASIC for the upgrade of the LHCb calorimeter. *Journal of Instrumentation*, 7(01):C01080–C01080, jan 2012. doi: 10.1088/1748-0221/7/01/c01080. URL https://doi.org/10.1088/1748-0221/7/01/c01080.

[197] R. Arink et al. Performance of the LHCb Outer Tracker. *JINST*, 9:P01002, 2014. doi: 10.1088/1748-0221/9/01/P01002.

[198] Walther Gerlach and Otto Stern. Das magnetische moment des silberatoms. *Zeitschrift für Physik*, 9(1):353–355, 1922. doi: 10.1007/BF01326984. URL https://doi.org/10.1007/BF01326984.

[199] L. Thomas. The motion of the spinning electron. *Nature*, (117):514, 1926. URL https://doi.org/10.1038/117514a0.

[200] Jun John Sakurai. *Modern quantum mechanics; rev. ed.* Addison-Wesley, Reading, MA, 1994. URL https://cds.cern.ch/record/1167961.

[201] Claude Cohen-Tannoudji, Bernard Diu, and Franck Laloë. *Quantum mechanics; 1st ed.* Wiley, New York, NY, 1977. URL https://cds.cern.ch/record/101367. Trans. of : Mécanique quantique. Paris : Hermann, 1973.

[202] M. Mikhasenko et al. Dalitz-plot decomposition for three-body decays. *Phys. Rev. D*, 101(3):034033, 2020. doi: 10.1103/PhysRevD.101.034033.

[203] M. Jacob and G. C. Wick. On the General Theory of Collisions for Particles with Spin. *Annals Phys.*, 7:404–428, 1959. doi: 10.1016/0003-4916(59)90051-X.

[204] E.M. Aitala, S. Amato, J.C. Anjos, J.A. Appel, D. Ashery, S. Banerjee, I. Bediaga, G. Blaylock, S.B. Bracker, P.R. Burchat, and et al. Multidimensional resonance analysis of $\Lambda_c^+ \to pK^-\pi^+$. *Physics Letters B*, 471(4):449–459, Jan 2000. ISSN 0370-2693. doi: 10.1016/s0370-2693(99)01397-0. URL http://dx.doi.org/10.1016/S0370-2693(99)01397-0.

[205] D. Aston aet al. A study of $K^-\pi^+$ scattering in the reaction $K - p \to K^-\pi^+ n$ at 11 GeV/c. *Nuclear Physics B*, 296(3):493–526, 1988. ISSN 0550-3213. doi: https://doi.org/10.1016/0550-3213(88)90028-4. URL https://www.sciencedirect.com/science/article/pii/0550321388900284.

[206] S.M. Flatté. Coupled-channel analysis of the $\pi\eta$ and $K\bar{K}$ systems near $K\bar{K}$ threshold. *Physics Letters B*, 63(2):224–227, 1976. ISSN 0370-2693. doi: https://doi.org/10.1016/0370-2693(76)90654-7. URL https://www.sciencedirect.com/science/article/pii/0370269376906547.

[207] Avital Dery, Mitrajyoti Ghosh, Yuval Grossman, and Stefan Schacht. SU(3)F analysis for beauty baryon decays. *Journal of High Energy Physics*, 2020(3):165, 2020. doi: 10.1007/JHEP03(2020)165. URL https://doi.org/10.1007/JHEP03(2020)165.

[208] From private communication with Emi Kou.

[209] Wouter D. Hulsbergen. Decay chain fitting with a Kalman filter. *Nuclear Instruments and Methods in Physics Research Section A: Accelerators, Spectrometers, Detectors and Associated Equipment*, 552(3):566–575, 2005. ISSN 0168-9002. doi: https://doi.org/10.1016/j.nima.2005.06.078. URL https://www.sciencedirect.com/science/article/pii/S0168900205013963.

[210] M. Pivk and F.R. Le Diberder. splots: A statistical tool to unfold data distributions. *Nuclear Instruments and Methods in Physics Research Section A: Accelerators, Spectrometers, Detectors and Associated Equipment*, 555(1):356–369, 2005. ISSN 0168-9002. doi: https://doi.org/10.1016/j.nima.2005.08.106. URL https://www.sciencedirect.com/science/article/pii/S0168900205018024.

[211] L0hadron efficiency correction. https://twiki.cern.ch/twiki/bin/view/LHCbPhysics/CalorimeterObjectsToolsGroupDOC#L0_Hadron_trigger_efficiencies.

[212] O. et al. Lupton. Calibration samples for particle identification at LHCb in Run 2. Technical report, CERN, Geneva, Mar 2016. URL https://cds.cern.ch/record/2134057.

[213] Roel et al. Aaij. Selection and processing of calibration samples to measure the particle identification performance of the LHCb experiment in Run 2. *EPJ Techniques and Instrumentation*, 6(1), Feb 2019. ISSN 2195-7045. doi: 10.1140/epjti/s40485-019-0050-z. URL http://dx.doi.org/10.1140/epjti/s40485-019-0050-z.

[214] Anton Poluektov. Correction of simulated particle identification response in LHCb using kernel density estimation. Technical report, CERN, Geneva, Apr 2017. URL https://cds.cern.ch/record/2260281.

[215] Alex Rogozhnikov. Reweighting with boosted decision trees. *Journal of Physics: Conference Series*, 762:012036, Oct 2016. ISSN 1742-6596. doi: 10.1088/1742-6596/762/1/012036. URL http://dx.doi.org/10.1088/1742-6596/762/1/012036.

[216] Wouter Verkerke and David P. Kirkby. The RooFit toolkit for data modeling. *eConf*, C0303241: MOLT007, 2003.

[217] F. James and M. Roos. Minuit - a system for function minimization and analysis of the parameter errors and correlations. *Computer Physics Communications*, 10(6):343–367, 1975. ISSN 0010-4655. doi: https://doi.org/10.1016/0010-4655(75)90039-9. URL https://www.sciencedirect.com/science/article/pii/0010465575900399.

[218] M. Davier, L. Duflot, F. Le Diberder, and A. Rougé. The optimal method for the measurement of tau polarization. *Physics Letters B*, 306(3):411–417, 1993. ISSN 0370-2693. doi: https:

//doi.org/10.1016/0370-2693(93)90101-M. URL https://www.sciencedirect.com/science/article/pii/037026939390101M.

[219] Daniele Marangotto. *Amplitude analysis and polarisation measurement of the Λ_c^+ baryon in $pK^-\pi^+$ final state for electromagnetic dipole moment experiment.* PhD thesis, Milan U., 2020.

[220] Seungyong Hahn, Kwanglok Kim, Kwangmin Kim, Xinbo Hu, Thomas Painter, Iain Dixon, Seokho Kim, Kabindra R. Bhattarai, So Noguchi, Jan Jaroszynski, and David C. Larbalestier. 45.5-tesla direct-current magnetic field generated with a high-temperature superconducting magnet. *Nature*, 570(7762):496–499, 2019. doi: 10.1038/s41586-019-1293-1. URL https://doi.org/10.1038/s41586-019-1293-1.

université PARIS-SACLAY

ÉCOLE DOCTORALE
Particules, hadrons, énergie et noyau : instrumentation, imagerie, cosmos et simulation (PHENIICS)

Titre: Mesures précises des propriétés des baryons charmés avec le détecteur LHCb au LHC.

Mots clés: Polarization, baryons charmés, interactions electrofaible, moment dipolaire magnétique, analyse en amplitude, luminosité, physique des particules.

Résumé: La polarisation des baryons charmés n'est pas prédite par la théorie et constitue une donnée nécessaire pour la mesure du moment dipolaire magnétique (MDM) des baryons charmés qui est prévue au LHC. Elle a été mesurée pour les baryons étranges (Λ) et beaux (Λ_b^0) dans différents systèmes de collision, mais aucune mesure n'existe à ce jour pour les baryons charmés. Dans cette thèse, la polarisation du baryon Λ_c^+ est mesurée au moyen d'une analyse d'amplitude à cinq dimensions de la désintégration faible à trois corps $\Lambda_c^+ \to pK^-\pi^+$ pour des Λ_c^+ produits dans des collisions pp à une énergie de 13 TeV dans le centre de masse.

La désintégration $\Lambda_c^+ \to pK^-\pi^+$ passe par des états résonants intermédiaires qui interfèrent entre eux et qui doivent être inclus dans l'amplitude. Tout d'abord, les équations décrivant l'amplitude de cette désintégration à trois corps ont été dérivées dans le cadre du formalisme d'hélicité. La polarisation est prise en compte au moyen de la matrice de densité de spin et les états résonants intermédiaires sont décrits à l'aide du modèle isobare. Ce travail a permis de mieux comprendre les amplitudes d'hélicité et peut être facilement étendu à d'autres désintégrations baryoniques à trois corps comportant des particules avec spin dans l'état final.

Ensuite, les amplitudes d'hélicité obtenues sont utilisées pour décrire les données collectées par le détecteur LHCb au CERN en 2016 (Run 2), correspondant à une luminosité intégrée de 1.7 fb^{-1}. Comme la polarisation dépend du mécanisme de production impliqué, il est important de séparer les Λ_c^+ produits directement après les collisions pp via des interactions fortes (production dite "prompt"), des Λ_c^+ produits via une désintégration faible d'autres baryons (production secondaire) ; dans cette analyse, les Λ_c^+" prompt" sont étudiés. La désintégration $\Lambda_c^+ \to pK^-\pi^+$, avec un rapport d'embranchement de $6.28 \pm 0.32\%$, est le mode de désintégration de Λ_c^+ le plus abondant et l'échantillon de données final, après l'optimisation de la chaîne de sélection, contient environ ∼500 000 événements de signal ; la pureté du signal est de $\sim 97\%$ et la contamination due aux Λ_c^+ venant de B est inférieure à 2%. Les paramètres d'asymétrie, qui sont des combinaisons des couplages d'hélicité contenus dans l'amplitude, sont également mesurés ainsi que les contributions individuelles des résonances à l'amplitude totale. Les résultats de l'analyse en amplitude de la désintégration $\Lambda_c^+ \to pK^-\pi^+$ seront utilisés pour mesurer la polarisation des Λ_c^+ produits dans des collisions proton-gaz (pNe), en utilisant un échantillon de données collectées par le détecteur LHCb en 2017, à une énergie de 68 GeV dans le centre de masse.

La prochaine phase d'acquisition de données, prévue en 2022, verra une augmentation du taux de collision d'un facteur 5 à LHCb. Un nouveau détecteur, appelé PLUME, a été conçu pour effectuer une mesure de luminosité dans les nouvelles conditions de fonctionnement. Dans cette thèse, l'électronique frontale du calorimètre de LHCb a été testée pour prouver qu'elle est adaptée aux besoins du détecteur PLUME et elle est maintenant l'électronique de base pour PLUME. Enfin, une mesure du décalage de l'horloge de LHCb à l'aide du détecteur PLUME est proposée. L'horloge de LHCb peut être désynchronisée de l'horloge principale du LHC ; un décalage allant jusqu'à 1 ns a été mesuré pendant les Run 1 et 2, en utilisant le Outer Tracker (OT), avec une résolution temporelle de 0,5 ns. Au cours du Run 3, l'OT sera supprimé et LHCb collectera des données à 40 MHz avec un nouveau schéma de déclenchement entièrement « software ». Des conditions de fonctionnement stables sont essentielles pour qu'un tel schéma fonctionne, et le décalage de l'horloge pourrait avoir un impact important sur les performances du détecteur LHCb. PLUME pourrait être utilisé pour surveiller le décalage de l'horloge du LHCb. Dans cette thèse, la faisabilité de la mesure du décalage en temps est étudiée.

Title: Precise measurements of charmed baryon properties with the LHCb detector at the LHC.

Keywords: Polarization, charmed baryons, weak interactions, magnetic dipole moment, amplitude analysis, luminosity, particle physics

Abstract: Charmed baryon polarization is not predicted by theory and it is a necessary input for the measurement of the charmed baryons magnetic dipole moment (MDM) which is foreseen at the LHC. Baryon's polarization has been measured for strange (Λ) and beauty (Λ_b^0) baryons in different colliding systems, however, no measurement exists for charmed baryons as of today. In this thesis, the Λ_c^+ polarization is measured by means of a five-dimensional amplitude analysis of the three-body weak decay $\Lambda_c^+ \to pK^-\pi^+$ of Λ_c^+ produced in pp collisions at a center of mass energy of 13 TeV.

The $\Lambda_c^+ \to pK^-\pi^+$ decay passes through intermediate resonant states which interfere with each other, and which need to be included in the amplitude. First, the equations describing the amplitude of this three-body decay have been derived within the helicity formalism. The polarization is accounted for by means of the spin density matrix and the intermediate resonant states are described using the isobar model factorization. This work allowed to better understand the helicity amplitudes and can be easily extended to other three-body baryonic decays featuring particles with spin in the final state.

Then, the helicity amplitudes obtained are used to describe the data collected by the LHCb detector at CERN during the 2016 data taking period (Run 2), corresponding to an integrated luminosity of 1.7 fb^{-1}. Since the polarization depends on the production mechanism involved, it is important to separate the Λ_c^+ produced directly after the pp collisions via strong interactions (prompt production), from the Λ_c^+ produced via a weak decay of other baryons (secondary production). In this analysis, the promptly produced Λ_c^+ are studied.

The $\Lambda_c^+ \to pK^-\pi^+$ decay, with a branching ratio of $6.28 \pm 0.32\%$, is the most abundant Λ_c^+ decay mode and the final data sample, after the optimization of the selection chain, contains around $\sim$500 000 signal events, it has a signal purity of $\sim 97\%$ and the contamination due to secondary Λ_c^+ is less than 2%. The asymmetry parameters of the intermediate decays, which are combinations of the helicity couplings contained in the amplitude, are also measured along with the fit fractions, which describe the contribution of each resonance to the total amplitude. The results of the $\Lambda_c^+ \to pK^-\pi^+$ amplitude analysis will be used to measure the polarization of Λ_c^+ baryons produced in proton gas (pNe) collisions, using a data sample collected by the LHCb detector during 2017 at a center of mass energy of 68 GeV.

The next data acquisition phase, foreseen in 2022, will see an increase of the collision rate by a factor of 5 at LHCb. A new detector, called PLUME, has been designed to perform a luminosity measurement in the new running conditions. In this thesis, the front-end electronics of the LHCb calorimeter has been tested to prove that it is adapted for the PLUME detector needs and it is now the baseline electronics for PLUME. Finally, a measurement of the LHCb clock shift using the PLUME detector is proposed. The LHCb clock can be desynchronized from the LHC main clock; a shift up to 1 ns has been measured during Run 1 and Run 2, using the Outer Tracker (OT), with a time resolution of 0.5 ns. During Run 3 the OT will be removed and LHCb will collect data at 40 MHz with a new triggering scheme based on an entire software trigger. Stable running conditions are essential for such a scheme to work, and the clock shift could have a large impact on the LHCb detector performances. PLUME could be used to monitor the LHCb clock shift and in this thesis a preliminary timing measurement is performed probing the feasibility of such a measurement and opening the route to further studies.

Université Paris-Saclay
Espace Technologique / Immeuble Discovery
Route de l'Orme aux Merisiers RD 128 / 91190 Saint-Aubin, France